

Handbook of Soil Mechanics

Volume 3

**Soil Mechanics of Earthworks, Foundations
and Highway Engineering**

by

Árpád Kézdi

and

László Rétháti



Elsevier

Amsterdam · Oxford · New York · Tokyo 1988

Joint edition published by Elsevier Science Publishers, Amsterdam,
and Akadémiai Kiadó, Budapest

Handbook of Soil Mechanics

Vol. 1. Soil Physics

Vol. 2. Soil Testing

Vol. 3. Soil Mechanics of Earthworks, Foundations and Highway Engineering

Vol. 4. Application of Soil Mechanics in Practice: Examples and Case Histories

This is the revised and enlarged version of the German Handbuch der Bodenmechanik. Band 2: Bodenmechanik im Erd-, Grund- und Straßenbau, published by Akadémiai Kiadó, Budapest in co-edition with VEB Verlag für Bauwesen, Berlin (GDR)

Translated by H. Héjj

The distribution of this book is being handled by the following publishers for the USA and Canada

Elsevier Science Publishing Co. Inc.
52 Vanderbilt Avenue
New York, New York 10017, USA

for the East European countries, Democratic People's Republic of Korea, People's Republic of Mongolia, Republic of Cuba and Socialist Republic of Vietnam

Kultura Hungarian Foreign Trading Company
P. O. Box 149, H-1389 Budapest 62, Hungary

for all remaining areas

Elsevier Science Publishers
25 Sara Burgerhartstraat
P. O. Box 211, 1000 AE Amsterdam, The Netherlands

Library of Congress Cataloging-in-Publication Data

Kézdi, Árpád
[Bodenmechanik im Erd-, Grund-, und Strassenbau. English]
Soil mechanics of earthworks, foundations, and highway engineering
by Árpád Kézdi and László Rétháti; [translated by H. Héjj].
p. cm. — (Handbook of soil mechanics; v. 3)
Translation of the rev. & enl. version of: Bodenmechanik im Erd-,
Grund-, und Strassenbau, originally published as Bd. 2 of Handbuch
der Bodenmechanik.
Bibliography: p.
Includes index.
ISBN 0-444-98929-3 (U.S.)
1. Soil mechanics — Handbooks, manuals, etc. I. Rétháti, László.
II. Title. III. Series: Kézdi, Árpád. Handbuch der Bodenmechanik.
English: v. 3.
TA710.K4913 1979 vol. 3
624.1'513 s—dc 19
[624.1'5136]

88-2363
CIP

With 561 Illustrations and 46 Tables

© Akadémiai Kiadó, Budapest 1988

All rights reserved.

No part of this publication may be reproduced, stored in a retrieval system or transmitted in any form or by any means, electronic, mechanical, photocopying, recording, or otherwise without the prior written permission of the copyright owner.

Preface

The first and second volumes of the Handbook of Soil Mechanics, published in 1974 and 1979, were a great success in the field of soil mechanics. This third volume deals mainly with practical problems. This is a revised and enlarged version of the second volume of the Handbuch der Bodenmechanik, published in German jointly by the Akadémiai Kiadó and VEB Verlag für Bauwesen (GDR).

Unfortunately, the senior author, Árpád Kézdi was unable to complete the initially planned four volumes of this series due to his sickness and untimely death. As a colleague and friend I have been most honoured to help in updating this third volume which has been based on the literature of the past twenty years and on my own research having added several new sections. As to the reference list we ask the readers' understanding for its being incomplete due to the untimely death of Professor Kézdi.

My aim in this book has been concordant with Árpád Kézdi's to summarize the results of soil mechanics describing at the same time the trends of development of this field.

The assistance and encouragement of the Akadémiai Kiadó and Elsevier Science Publishers are gratefully acknowledged.

LÁSZLÓ RÉTHÁTI

Chapter 1.

Soil mechanics of earthwork

1.1 Introduction

Construction of earthworks involving billions of cubic meters are carried out every year in connection with civil engineering. They serve many purposes: they may be used as the foundation or as a part of a structure, or they may be made with the sole purpose of providing the necessary space for construction, as in the case of foundation pits. The stability and durability of the earthwork are prerequisites for the stability and durability of the superstructure and for economy of construction. Shortsighted planning or poor workmanship in carrying out earthworks may have detrimental consequences: swelling or shrinkage of the earth material, excessive deformation or subsidence of the fill, slips of slopes, ground failure, etc. Once the damage has occurred, reconstruction or remedial measures usually cost a multiple of what would have been required for adequate preliminary soil exploration, design and construction.

During construction as well as after completion, earthworks are constantly effected by weather and exposed to atmospheric agents. Continually changing temperature, precipitation, physical and chemical weathering, stagnant or flowing surface water and groundwater, frost and ice are the most important factors that endanger stability. Among these the action of water deserves particular attention: earth stability problems are, as a rule, closely linked with those of drainage. Because of the ever-changing character of the influencing factors, stability problems should never be regarded as static. The variation in soil conditions and environment and the dynamic character of the factors must always be taken into consideration.

Only this kind of approach will enable the civil engineer to understand the manifold interactions between natural environment and man-made earthworks and to tackle stability problems successfully. It should also be pointed out that even a most meticulous preliminary soil survey is not likely to reveal all the hazards and influencing factors and it is therefore impracticable to attempt to solve stability and drainage problems in advance in every detail. There will always be

contingencies to be dealt with during the course of construction on the basis of careful observation of site conditions. Even a thorough soil survey might not detect some seemingly minor, but in fact important changes in soil conditions which, if brought to light during construction, may necessitate a complete revision of the original — and often only tentative — plans in order to match the changed conditions.

Site observations should be extended not only to soil conditions but also to the geology, hydrology, meteorology and vegetation of the area in question, and the combined effect of all these factors must be taken into consideration in stability analyses.

This chapter deals with stability problems of various earthworks. The treatment is essentially theoretical and is based on mechanics. Nevertheless, we shall never omit to point out, where appropriate, the importance of the influencing factors mentioned in this paragraph.

1.2 Stability of slopes

1.2.1 General remarks

When an artificial earthwork, cutting or embankment (Fig. 1) is to be constructed, the inclination of its lateral boundary surfaces, called the slopes, cannot be selected arbitrarily, since this depends on the internal resistance of the earth material. The inclination of a slope is usually expressed as the tangent of its angle to the horizontal. $\tan \beta$ values are conveniently written in the form of a fraction whose numerator is always 1, thus: 1 in 1 ($\rho = \cot \beta = 4/4$), 1 in 1.5 ($\rho = 6/4$), 1 in 2 ($\rho = 8/4$) etc. Typical uses of slopes are those of embankments and cuts for roads, railways, canals, waterways, excavations, foundation pits, spoil tips, and the like.

If a slope is made steeper than would be permitted by the available shear strength of the soil, or if the intrinsic shear resistance of the soil in an originally stable slope has been reduced, for example through softening of the material, a slip or slide results; part of the sloping soil mass begins to move downward and outward as shown

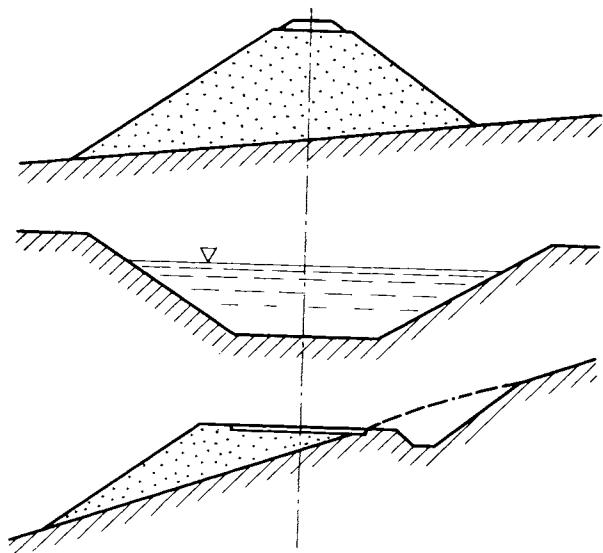


Fig. 1. Earthworks confined within slopes

in Fig. 2. Similar movements — commonly known as landslides — occur in natural slopes and on hillsides.

The causes of instability of slopes are many, and the resulting movements are very different in character. An exhaustive discussion of this topic is beyond the scope of this book. We shall therefore be concerned primarily with the basic problem of finding criteria for the stability of a given slope in a given soil, in order to ascertain what is the safety factor against failure. It should be emphasized, however, that stability problems must never be treated mechanically without regard to environmental effects. The geology of the area, the stratification of the soil and various external effects such as surcharge, incidental loads, infiltration, groundwater seepage, the action of vegetation, should all be considered in their dialectic interaction with due regard to their variations with time. In this chapter we shall discuss the mechanical principles and methods necessary for stability analysis.

Concern frequently arises in the preliminary design stage about the stability of natural or artificial slopes on hillsides or in mountainous areas. The efficiency of such engineering considerations can be largely enhanced by using the maps of recorded landslides or sliding areas.

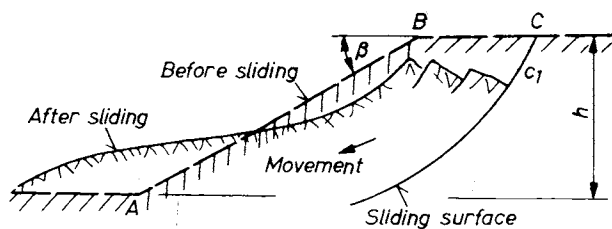


Fig. 2. Slope failure

These maps are being elaborated in an ever-widening range in most countries. During recent years there has been a growing interest in hazard and risk mapping, which is certainly due to an increase of human activity in the realm of critical areas. As geology surely plays an important role in landslide development, the problem of mapping has also been included on the agenda of the International Association of Engineering Geology (Symposium at Newcastle, 1979; Congress in Paris, 1980).

1.2.2 Cohesionless granular soils

In dry, clean sands the internal resistance is entirely due to interparticle friction. An embankment made of such soil remains stable, irrespective of its height, as long as the angle of its slope β is smaller than the angle of internal friction Φ measured in the loose state of the soil. For this case the safety factor ν against slip can be defined as:

$$\nu = \frac{\tan \Phi}{\tan \beta}.$$

When $\beta = \Phi$, the slope is in a limiting state of equilibrium. In an infinite slope two sets of failure planes are developed, one being parallel to the slope and the other vertical (See Vol. 1, Chapter 9).

The assumption of the Mohr failure theory that the intermediate principal stress σ_2 is irrelevant to the state of failure is not fully satisfied in dry sands in that the limiting value of the slope angle seems to depend also on the state of stress, i.e., on whether we have to do with a two-dimensional or a three-dimensional problem. When dry sand is heaped up to form a conical fill, $\sigma_1 > (\sigma_2 = \sigma_3)$, the safe angle of slope is smaller than it would be for an infinite slope (plane strain, $\sigma_1 > \sigma_2 > \sigma_3$). Finally, the slope will be steepest when a conical hollow is made in a semi-infinite horizontal sand mass, in which case $(\sigma_1 = \sigma_2) > \sigma_3$ (Fig. 3). Here an arching effect also comes into play and it is more pronounced the smaller the top radius of the hollow. This explains, in part, why vertical boreholes remain stable without casing to a considerable depth in moist sands having only a slight cohesion.

The stability of slopes in sand may be greatly endangered by forces resulting from vibration and seepage. Dynamic effects caused, for example, by an earthquake or by pile driving may result, even in dry sands, in a radical reduction of the angle of internal friction and as a consequence in the flattening of the slope. In saturated or quasi-saturated sands, quick-sand conditions may arise (see Vol. 1, Section 6.2).

In the literature we find reports of catastrophic landslides triggered by violent earthquakes. For example, the 1923 earthquake in Japan caused a huge mass of saturated and completely liquefied

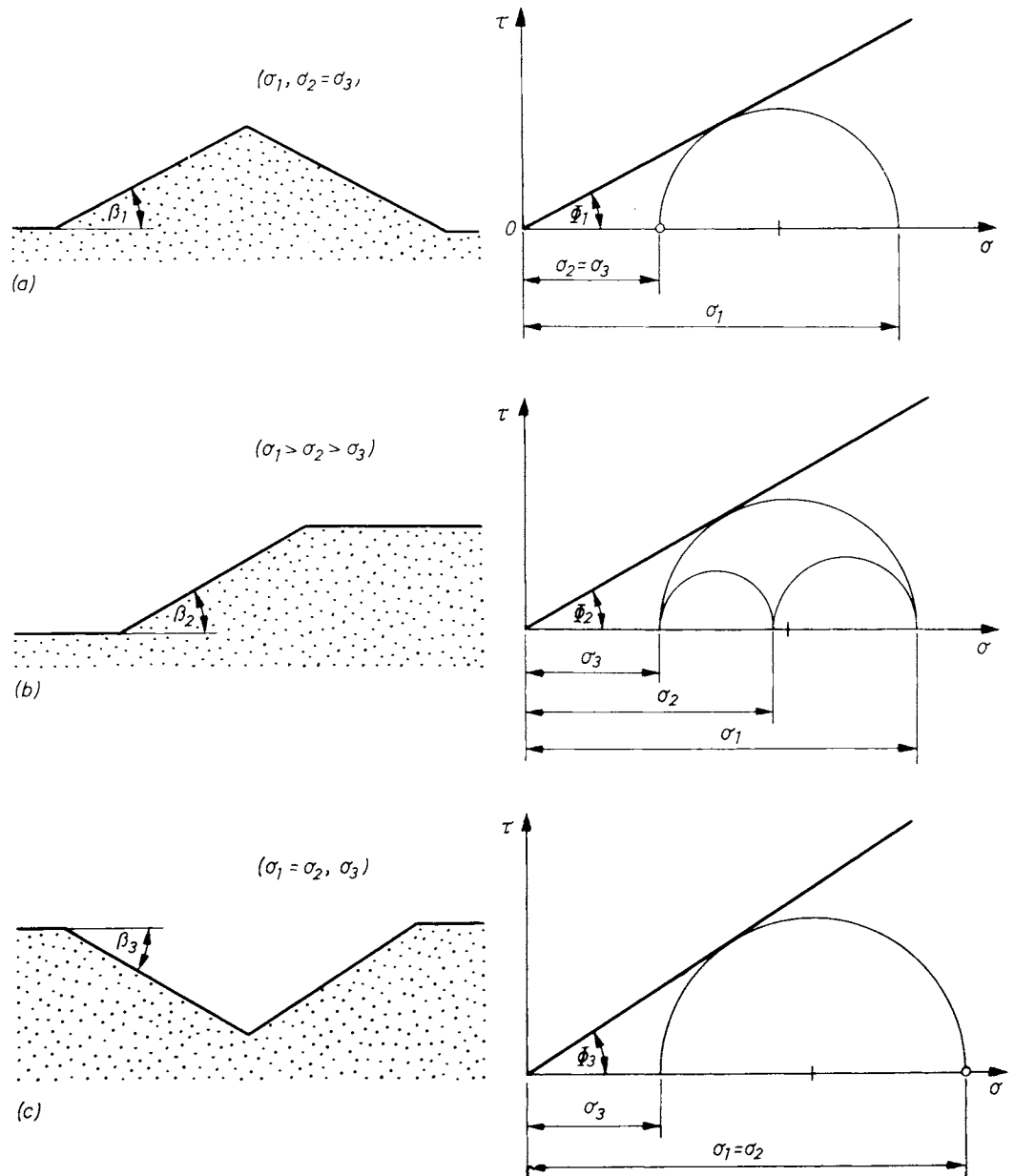


Fig. 3. Inclination of free slopes as a function of stress conditions

soil to rush downslope at the enormous speed of one kilometre per minute (CASAGRANDE and SHANON, 1948). A similar phenomenon known as "mur" occurs frequently in the Alps; in this case, however, the seepage force of flowing groundwater also comes into play (see Vol. 1, Section 5.2).

It is interesting to note that quick condition may occur even in dry cohesionless soils. We can easily produce this phenomenon if we open a cement bag and empty its content onto a smooth plane surface so quickly that there is not enough time for the air entrapped in the voids between the particles to escape. As a result a considerable portion of the stresses has to be borne temporarily by the por air and the shear strength of the

cement powder will be reduced to a very small value. Such peculiar conditions, on a large scale, might account for the devastating loess flow which occurred in the Kansu province of China in 1922, and which took a toll of well over 100 000 lives. Following an earthquake, vast banks of loess over 100 m in height completely lost their stability, collapsed and spread at an incredible speed over several square kilometres of the valley floor. As a contemporary report described the case, "...villages became buried and rivers dammed up within seconds". A probable explanation, gathered from the study of photographs of the catastrophe-stricken area, was that the shear strength of the material had been reduced to a fraction of its

original value within a very short time. As violent shocks had destroyed the structure of the loess (see Vol. 1, Section 3.4.2) a large portion of the pore air became entrapped in the debris with practically no time to escape. Thus a large portion of the stresses due to the weight of the affected mass was transferred to the pore air and caused a radical decrease in shear strength and an instantaneous liquefaction of the soil.

Seepage of water induces neutral stresses in the slope. Since the total stresses in a given slope are constant, an increase in the neutral stress will result in an equal decrease in the effective stress. As a consequence, the stability of the slope will also be reduced. An especially dangerous situation arises when water is suddenly removed from the face of a submerged slope (rapid draw-down).

The effect of stagnant and percolating water on the stability of slopes will be discussed in Section 1.3.

1.2.3 Slopes in homogeneous cohesive soils

1.2.3.1 General remarks

For cohesive soils the shear strength is given by the general Coulomb equation:

$$\tau = \sigma \tan \Phi + c .$$

In such soils, cuts with vertical walls will stand without bracing up to a certain limiting height. For greater heights the slope must be flattened. The stable height of the slope can thus be expressed as a function of the slope angle: $h = f(\beta)$. The failure of a slope may occur in such a manner that a body of soil breaks away from the adjacent soil mass and slips down on a single and well-defined rupture surface. In other cases no such definite slip surface exists. The first type of failure is characteristic of a stiff homogeneous

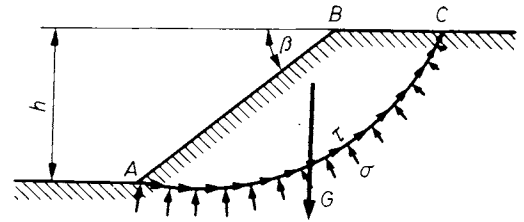


Fig. 4. Forces acting on the sliding mass

soil whose compressive stress-strain diagram shows a sharp definite failure (see Vol. 1, Fig. 239). Only this case will be discussed in this chapter.

Failure usually starts with the formation of tension cracks some distance from the crest of the slope and this is followed by the sliding down of a large mass of soil on a rotational slip surface, as was shown in Fig. 2. The slip surface resembles an elliptical arc, with the sharpest curvature near the upper end and with a relatively flat central section.

The forces that act on the sliding soil mass are shown in Fig. 4. Sliding is caused by the weight of the moving soil mass itself, while internal friction and cohesion mobilized along the slip surface tend to restrain motion.

In a homogeneous soil, failure may either take the form of a slope failure along a slip surface that passes through or sometimes above the toe A of the slope (Fig. 5a) or it may occur along a slip surface that passes below the toe and intersects the free surface at a point some distance from it (base failure, Fig. 5b). The shape and position of the critical slip surface are governed by two factors, the inclination of the slope and the shear strength of the soil. (This is valid for homogeneous soil only.)

In the design of slopes we usually have to answer one of the following two questions: first, given the height and gradient of a slope and the shear strength of its material, what safety factor

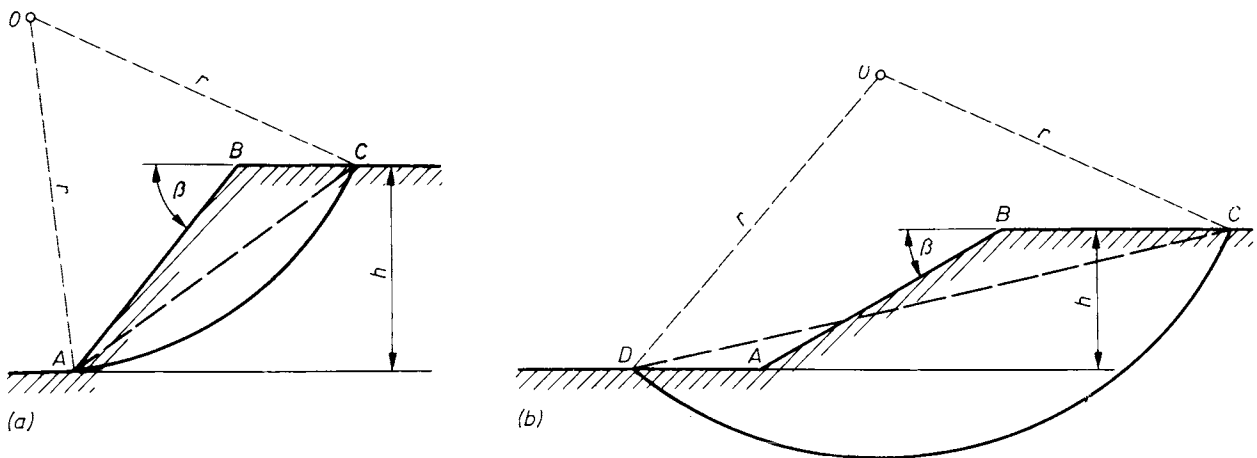


Fig. 5. a — Toe failure; b — base failure in homogeneous subsoil

against failure exists, and second, given the height of the slope and the physical properties of the soil, what should the slope angle be to secure a required safety factor. A number of methods, both analytical and graphical, are available for the solution of these problems. The most widely used is the procedure in which we work with arbitrarily selected slip surfaces, determine the conditions under which failure along such surfaces just occurs and find, by trial, the critical position of the slip surface along which the danger of failure is greatest. The exact mathematical equation of the slip surface is known only for certain particular cases such as the semi-infinite half space with horizontal or sloping surface (see Vol. 1, Chapter 9). In practical stability analysis, the actual slip surface is replaced by some relatively simple surface which is more amenable to mathematical or graphical treatment. Such surfaces are, as is known from the theory of earth pressure, the plane and the cylindrical surface with a circular or a logarithmic spiral arc.

In this chapter we first discuss an early method based on a plane surface of sliding, then we deal with more advanced methods which assume circular slip surfaces.

1.2.3.2 Stability analysis using a plane slip surface

The first attempt to treat the problem of slope stability mathematically was made by CULMANN (1866). He assumed a plane slip surface. As was shown in the introduction to this chapter, such an oversimplified assumption by no means reflects reality, since slope failures, particularly in homogeneous cohesive soil masses, invariably occur along curved rotational surfaces. Culmann's plane slip surface theory is therefore mainly of historical significance.

Given a slope of height h , making an angle β with the horizontal (Fig. 6) let us find the plane of rupture \overline{AB} along which the resistance to sliding is a minimum. The force that causes the slope to fail is the weight of the wedge ABC . The

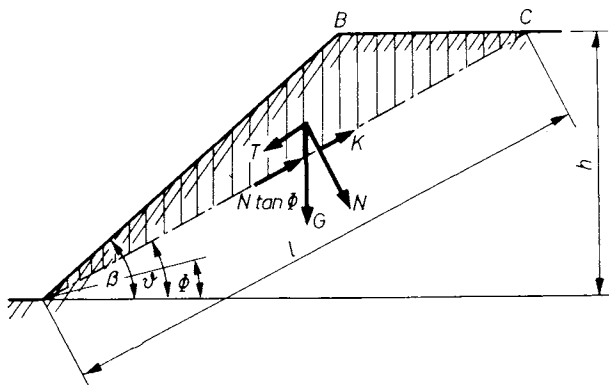


Fig. 6. Stability analysis on a plane

restraining forces are, according to Coulomb's failure theory, those due to internal friction and cohesion. In the limiting state of equilibrium:

$$T - C - N \tan \Phi = 0.$$

In order to find the most dangerous position of the slip surface \overline{AC} , we have to determine the angle at which the force of cohesion required to maintain equilibrium is a maximum. The cohesive force can be written as the length of the slip surface multiplied by the cohesion, per unit area, of the soil: $C = cl$. The weight W of the sliding wedge ABC , as well as its perpendicular components N and T , can be expressed, by geometry, as functions of the inclination angle of the rupture plane. The weight can be written as:

$$W = \frac{h^2 \gamma}{2} (\cot \beta - \cot \alpha)$$

and hence, by using equilibrium conditions, we obtain the cohesion required to just maintain equilibrium:

$$c = \frac{h \gamma}{2} \frac{\sin(\beta - \alpha) \sin(\alpha - \Phi)}{\sin \beta \cos \Phi} \tag{1}$$

To find the maximum of c we differentiate the above expression with respect to α and then solve the equation $dc/d\alpha = 0$, whence

$$\alpha = \frac{\beta + \Phi}{2}$$

In words, the most dangerous failure plane bisects the angle between the slope and the "natural slope" i.e. the line with an inclination of Φ .

By substituting this value of the angle α in the expression for c and solving it for h , we obtain the following relationship which furnishes for any given slope angle β , the maximum height h at which the slope is just in a limiting state of equilibrium:

$$h = \frac{4c}{\gamma} \frac{\sin \beta \cos \Phi}{1 - \cos(\beta - \Phi)} \tag{2}$$

Here c is the cohesion and γ is the unit weight of the soil.

From Eq. (2) it can be shown that for slopes in a limiting state of equilibrium, the locus of point B , as the slope angle β changes, is a parabola, known as Culmann's cohesion parabola. Its focus coincides with the toe A of the slope and its axis makes an angle Φ with the horizontal. The distance from the focus to the directrix is equal to:

$$q = \frac{4c}{\gamma} \cos \Phi.$$

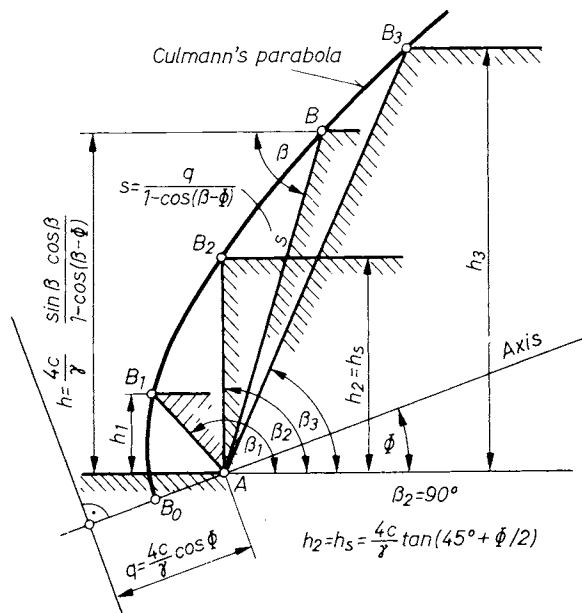


Fig. 7. Culmann's cohesion parabola

Using polar co-ordinates, the equation of the parabola becomes:

$$s = \frac{q}{1 - \cos(\beta - \Phi)}$$

(For notation see Fig. 7.)

With the aid of the Culmann parabola, the limiting height can readily be determined for any given slope angle β . An important value is the limiting height at which a vertical bank in cohesive soil stands without lateral support. Incorporating $\beta = 90^\circ$ in Eq. (2) gives

$$h_0 = \frac{4c}{\gamma} \tan\left(45^\circ + \frac{\Phi}{2}\right) \quad (3)$$

If the height of the slope is smaller than h_0 , even a slightly overhanging slope may remain stable.

JÁKY (1925) has shown on the basis of the cohesion parabola that the theoretical profile of a slope in the limiting state of equilibrium is curved. Let h denote the limiting height of a slope inclined at an angle β to the horizontal (Fig. 8). If we consider an upper part of height h_1 separately from the rest of the slope, this part would stand in a slope steeper than the overall slope corresponding to the total height h . Let us now divide the height h into, say, four equal parts. Using the Culmann parabola we can construct the limiting slope angles corresponding to heights $h/4, h/2, 3h/4$, respectively. Clearly, the lower the slope in question, the steeper it can be. By drawing the respective slope for each height in such a manner that the total weight of the sliding wedge does not change, we obtain a profile made up of broken lines (Fig. 8). If we use sufficiently small divisions and continue the construction in the manner previously described, eventually a smooth curve results. This is called the theoretical slope. From first principles, JÁKY also derived the mathematical equation of the theoretical slope and he developed a method for its construction.

In practice, it would be rather awkward to form a slope exactly to such a profile. Nevertheless, bell-shaped and bowl-shaped slopes, which approximate the theoretical profile fairly well, are often used for high embankments and deep cuttings, respectively, in order to minimize the land area occupied.

The idea of the theoretical slope, although it was originally developed on the assumption of a plane surface of failure, can readily be applied to other, more realistic, curved slip surfaces. Providing a graph relating the limiting height to the slope angle is available, a theoretical profile can always be constructed by the procedure illustrated in Fig. 8. This can then be used to design safe and economic curved slopes.

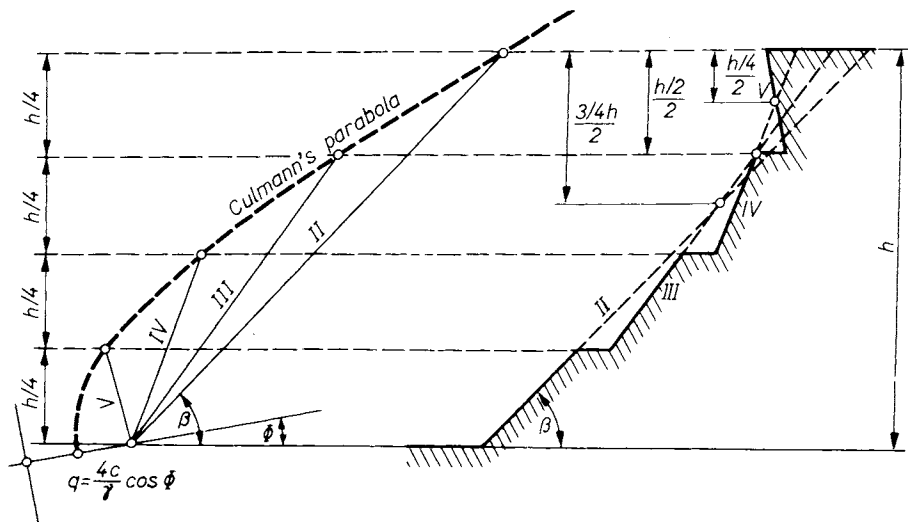


Fig. 8. The theoretical slope constructed using Culmann's parabola

1.2.3.3 Stability analysis based on the assumption that $\Phi = 0$

The assumption that the slip surface is plane offers a simple solution to the problem of slope stability, but it is certainly not a satisfactory one since experience has shown that actual slip surfaces deviate considerably from the plane. Yet, considering the many uncertainties in the values of the soil properties on which the calculation is based, this discrepancy would seem to be of minor significance as long as the results obtained are on the safe side. However, this is not so: for given soil properties and geometry, the analysis based on a curved slip surface always leads to smaller safety heights than are obtainable by the slip plane assumption. Safety is thus the main factor which justifies the introduction of curved slip surfaces into the following discussion.

If the soil of a slope is such that it has a constant undrained shear strength, i.e. $\Phi = 0$ and $\tau = c$, the stability of the slope can be investigated by using a circular slip surface. For this particular case the circular cylinder is the exact solution, as has been shown by the senior author. The $\Phi = 0$ condition applies to the undrained shear of homogeneous, saturated clays, when their shear strength is given as a function of the total normal stress. The circular slip surface was assumed, on the basis of previous observations, in some early investigations and was first used for the $\Phi = 0$ analysis by FELLENIUS (1927, 1936). The method became known as the Swedish method.

According to this method, as a first step we have to find the position and radius of that circle which replaces the actual slip surface. This circle, known as the critical circle, must satisfy the condition that the ratio of the moment of restraining forces acting along the slip surface to the moment of driving forces be a minimum. The ratio obtained is then taken as the safety factor. If it has a value equal to 1, the slope is on the verge of imminent failure. For stable slopes the safety factor must be $\nu > 1$.

Figure 9 shows a slope AB inclined at angle β to the horizontal. Let \widehat{AC} be the arc of a trial slip surface. Its position in relation to the slope is determined by two angles: the central angle 2θ , and the angle α which the chord \widehat{AC} makes with the horizontal.

Let W = weight of mass tending to slide,
 a = lever arm of force W with respect to centre of slip surface,
 r = radius of slip circle,
 l_a = length of slip surface,
 l_c = length of chord of slip surface,
 c = cohesion on slip surface.

Since there is no friction, the only force tending to restrain sliding is the cohesive force C . Writing

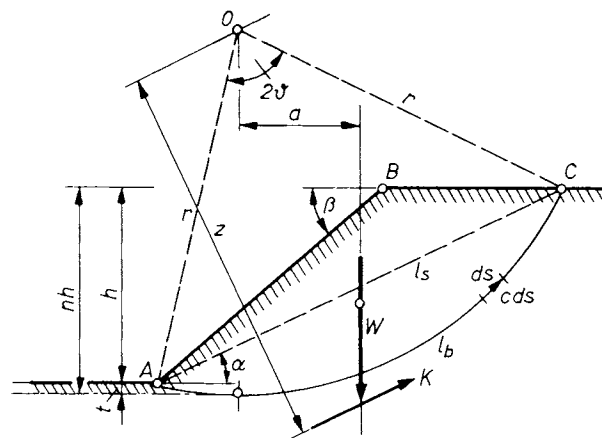


Fig. 9. Circular sliding surface beneath the slope

the moment equation of equilibrium,

$$Wa - Cz = 0. \quad (4)$$

C is the resultant of the elementary cohesive forces acting along the arc \widehat{AC} . Its magnitude is proportional to the length of the chord \widehat{AC} : $C = cl$ and the distance of its action line from the centre of rotation O is $z = rl_a/l_c$ (see Vol. 1, Section 10.5.2).

From Eq. (4) the cohesion per unit area required to prevent rotational sliding along the surface \widehat{AC} is obtained as

$$c = \frac{Wa}{rl_a}. \quad (5)$$

The quantities W , a and l_a can be expressed by geometry (Fig. 9). Substituting the resulting expressions into Eq. (5) gives

$$c = h\gamma \frac{1}{f(\alpha, \beta, \theta)}, \quad (6)$$

where γ = unit weight of soil,

h = stable height of slope,

$f(\alpha, \beta, \theta)$ = a dimensionless number.

The most dangerous or critical circular slip surface is the one along which the cohesive resistance needed for stability is maximum. For a given slope the angle β is constant and the position of the critical circle is thus governed by the equations:

$$\left. \begin{aligned} \frac{\partial c}{\partial \alpha} &= 0, \\ \frac{\partial c}{\partial \theta} &= 0, \end{aligned} \right\} \quad (7)$$

If we solve Eqs (7) and substitute the resulting values of α and θ into Eq. (6), we obtain:

$$c = h\gamma \frac{1}{f(\alpha, \beta, \theta)} = h\gamma N_c. \quad (8)$$

In this formula N_c is a dimensionless number called the stability number.

Supposing that N_c is known for any given angle β , the cohesion required to maintain stability can be expressed from Eq. (8). The available cohesion of the material of the slope can be determined experimentally and, hence, the safety factor can be obtained:

$$v = c_{\text{available}}/c_{\text{required}}$$

On the other hand, if the determination of the maximum stable height for a slope with given angle β and cohesion c is required, Eq. (8) should be solved for h :

$$h = \frac{c}{\gamma N_c} \tag{9}$$

The location of the critical circle was investigated by FELLENIUS (1927). His results are shown in Fig. 10, where values of the angles α and θ are plotted against the slope angle β . With these angles known, the critical slip surface can be constructed and, making use of the moment equation of equilibrium, the cohesion needed for stability can be calculated. By repeating the calculation for varying angles of β , we obtain a graph giving the stability number N_c as a function of β (Fig. 11).

Let, for example, $\beta = 90^\circ$. From the graph we find $N_c = 0.266$, whence $h = c/\gamma N_c = 3.76 c/\gamma$. Similarly for $\beta = 0$, $N_c = 0.1196$ and $h = 8.36 c/\gamma$. When $\beta = 60^\circ$, the angles θ and α have the same values and the critical circle has a horizontal tangent at the toe of the slope. If the slope angle β is greater than 60° , the slip circle has a rising tangent at the toe, whereas in the case of $\beta < 60^\circ$, the slip surface has a falling tangent at the toe, i.e. it penetrates below the base of the slope. This portion of the graph in Fig. 11 is therefore valid only if the material of the slope and that of its base are identical.

The statements in the preceding paragraph hold only for the condition that the soil is homogeneous

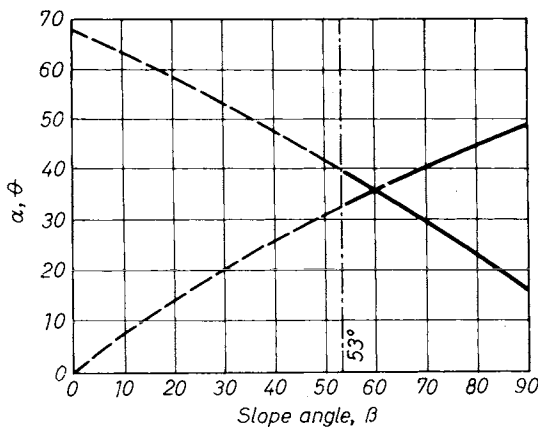


Fig. 10. Angles defining the location of the critical circle (FELLENIUS, 1927)

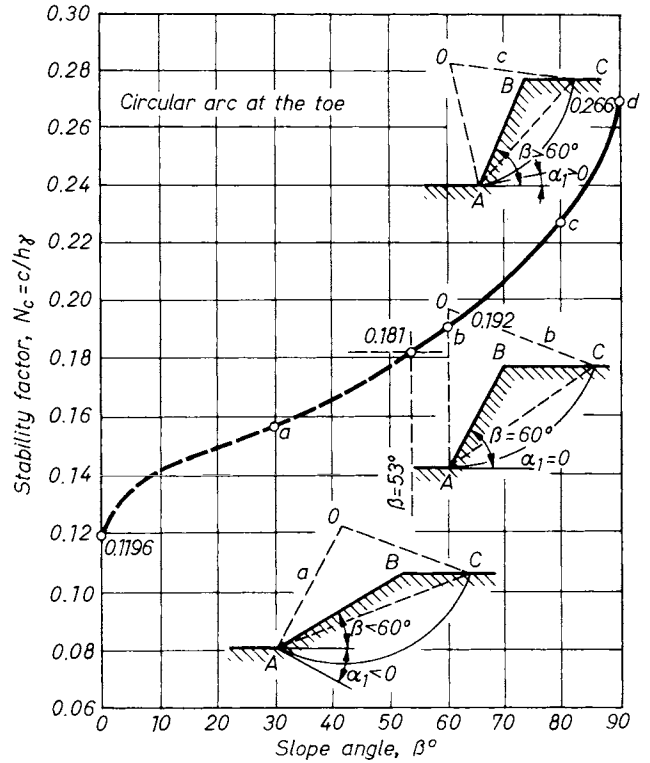


Fig. 11. Stability coefficient N_c for slope failure calculations

and the slip surface passes through the toe A . The location of the critical surface has been shown previously to be governed by Eq. (7). The question arises, however, whether the most dangerous slip surface is always a toe circle?

Observation of slides that occurred in flat slopes has shown that the critical slip surface does not as a rule pass through the toe but penetrates below it and cuts the free surface at some distance from it. The same situation arises when a slope is made on a very soft base.

In order to determine the equilibrium condition for such base failures, let us consider a slope in a homogeneous soft soil as shown in Fig. 12. As can be seen from the following reasoning, the centre of the critical circle must be located on the vertical that intersects the slope at the mid-point. In Fig. 12 the circular slip surface \widehat{CD} is such that the above condition is fulfilled. The cohesion required to maintain stability is obtained from Eq. (5) as

$$c = \frac{W a}{r l_a}$$

where l_a is the length of arc \widehat{CD} . Since $\Phi = 0$, the only internal resistance available is cohesion. If we fix the position of the centre O and of the arc \widehat{DC} and then move the face of the slope \widehat{AB} by a distance of Δl to the left, the weight of the sliding mass will be increased by ΔW and the

moment about the centre of rotation O will be decreased by $\Delta W \Delta l / 2$. If the plane of the slope is shifted by Δl to the right, the weight is decreased by ΔW , and the moment about O is again decreased by $\Delta W \Delta l / 2$. In either case the disturbing moment is reduced while the restraining moment remains unchanged. It follows that the disturbing moment is indeed a maximum when the centre of rotation is located on the vertical passing through the mid-point of the slope \overline{AB} .

To fix the position of the slip surface with respect to the slope, two additional data are needed. One is the depth factor, defined as

$$n = \frac{h + t}{h} = 1 + \frac{t}{h}, \quad (10)$$

which signifies the depth to which rupture can penetrate below the elevation of the toe (Fig. 13). The difference between the elevations of the highest and lowest points of the slip surface is nh . The other datum required is the radius of the circle r . Taking the moment equation of equilibrium, the cohesion required for stability can be computed from Eq. (5). Expressing W , a , r and l from the geometry of the slope and substituting into Eq. (5) leads to the following general formula:

$$c = h\gamma \frac{1}{f(\beta, r, n)}. \quad (11)$$

The most dangerous circular slip surface can again be found from the extremum conditions:

$$\frac{\partial c}{\partial n} = 0 \text{ and } \frac{\partial c}{\partial r} = 0. \quad (12)$$

By solving Eq. (12), it can be shown that, regardless of the value of angle β ,

$$\text{when } n \rightarrow \infty, \quad h = \frac{c}{\gamma} \frac{1}{0.181} = 5.54c/\gamma.$$

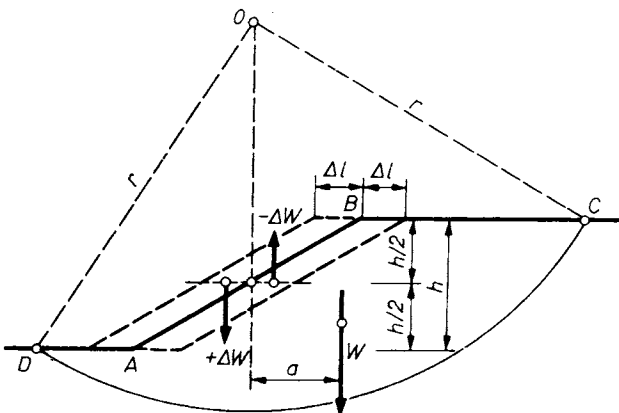


Fig. 12. For a base failure, the centre of the critical sliding circle is along the vertical line dividing the slope in two halves

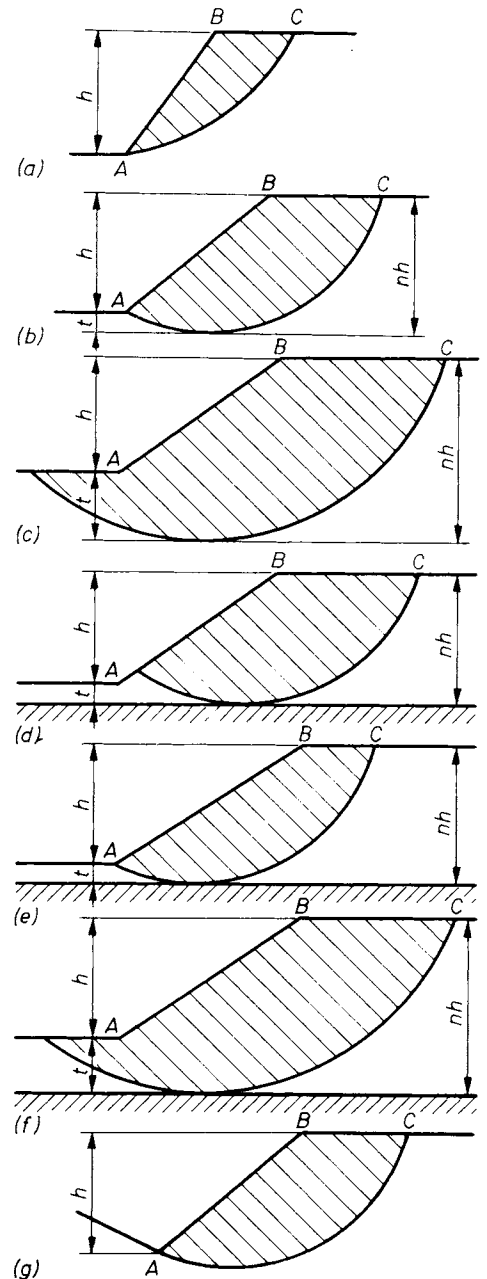


Fig. 13. Characteristic locations of the critical sliding surface

If we plot this value of the stability number on the vertical axis in Fig. 11, and draw a horizontal projection line at $N_c = 0.181$, it will intersect the curve representing the critical toe circle at $\beta = 53^\circ$. This means that if $\beta < 53^\circ$ and the ground surface at the toe is horizontal with no surcharge acting on it, then in a homogeneous soil a critical circle that passes below the toe is likely to develop. If, however, the surface at the toe is rising, as shown in Fig. 13g, a toe circle will be the critical one.

An underlying firm stratum may prevent the slip surface from extending to greater depths below the toe, and the critical slip surface, whether it is a toe circle or passes below the toe, can only

touch the surface of the hard stratum. There are three possible cases: (i) If the slope is not too flat and a firm stratum is located at a depth relatively near the toe, the critical circle will touch the surface of the firm stratum and intersect the slope above the toe A (case d, Fig. 13). (ii) If a firm stratum is encountered at increasingly greater depths, a toe circle is likely to be the critical one (case e), whereas (iii) for flat slopes with a firm stratum at very great depths, the critical slip surface always passes below the toe (case f). In all such cases the ratio n is known and the location of the critical slip surface is governed only by the second equation given in Eq. (12). Hence, the radius of the critical circle can be determined and the cohesion needed for stability and the safety factor can be computed.

Numerical values of the stability factor N_c were determined by TAYLOR (1937, 1948) on the basis of the analysis described above, for both toe circles and circles passing below the toe and also taking into account the depth factor. The results of his investigations are summarized in the chart shown in Fig. 14. According to this figure — and summing up the main conclusions of the previous discussion — the following important statements can be made concerning the stability of slopes in soft clays whose angle of internal friction is very near to zero.

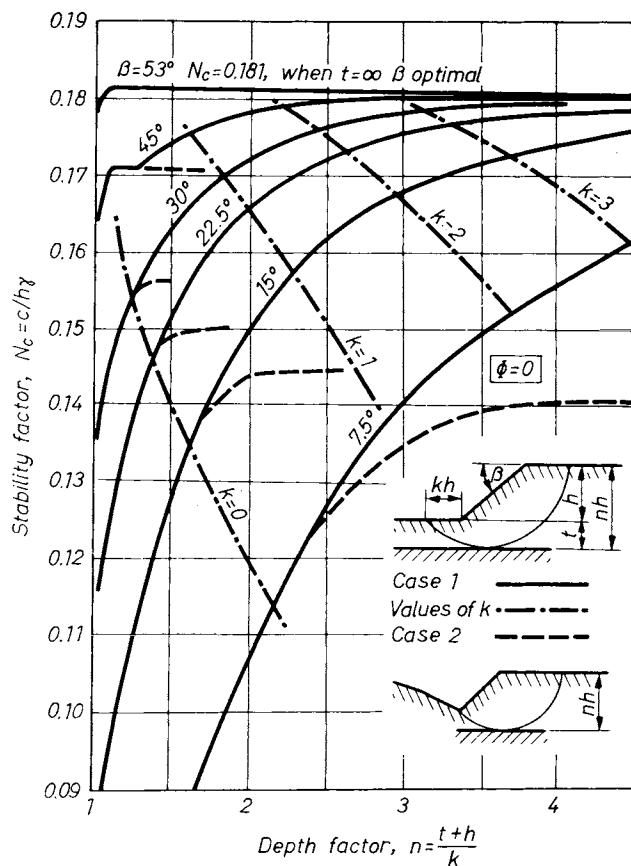


Fig. 14. Values of the stability coefficient N_c as a function of the depth coefficient in the case of $\Phi = 0$

1. For slope angles greater than 60° , the critical circle is a toe circle and is located entirely above the level of the toe. Relevant stability factor values are contained in the portion II-III-IV of the curve in Fig. 14.

2. If β is between 53° and 60° , the slip surface is still a toe circle but one which penetrates below the elevation of the toe. Should, however, a firm base be located at a small depth below the toe, i.e. the depth factor n is only slightly greater than 1, the critical circle may be a slope circle that is tangential to the firm base and intersects the slope above the toe.

3. If β is smaller than 53° , the value of the stability factor depends greatly on the value of the depth factor n . Figure 14 gives the relationship between depth factor and stability factor for different values of slope angle β .

As can be seen from the figure, if n is greater than 4, the stability factor is practically independent of the value of the slope angle β , and apart from very flat slopes ($\beta < 15^\circ$) it can be taken as a constant, $N_c = 0.181$.

For all other values of β and n , the stability factor can be obtained from the curves in Fig. 14. If the type of failure is similar to that shown in Fig. 13g, a base failure is not likely to occur. For such cases the dashed curves of Fig. 14 should be used; here, too, N_c depends on the depth factor n .

Figure 14 also shows values of the factor k , by means of which we can compute, in the case of a base failure, the distance from the toe at which the critical circle intersects the lower, free surface. This distance is kh . The dash-dot curves in Fig. 14 correspond to constant values of k .

Summing up the $\Phi = 0$ method, it is based on the assumption that the shear strength is constant, and that no volume change occurs during failure. Such conditions exist only in saturated soils with a permeability low enough to prevent any perceptible change in water content, i.e., any volume change during shear. In such cases the shear strength is indeed independent of the total normal stress.

1.2.3.4 Stability analysis when $\Phi \neq 0$ and $c \neq 0$

We now examine the case where there is a linear dependence of the shear strength upon the normal stress, i.e. the failure condition is of the form

$$\tau = \bar{\sigma} \tan \Phi + c,$$

where $\bar{\sigma}$ is the effective normal stress acting on the surface of sliding. Since the manner in which the normal stress is distributed along the slip surface is not known, the problem is statically indeterminate and can be solved only with certain simplifying assumptions.

In practical stability analysis, two methods are in general use. In one, we consider a sliding mass

separated by a circular slip surface from the rest of the soil mass and examine the conditions under which this rigid, free body is in a limiting state of equilibrium. In the other, we subdivide the sliding mass into a number of vertical slices, and perform the stability analysis by taking into consideration all the forces acting on these slices (method of slices). The second method is the more accurate since it permits equilibrium conditions and failure conditions to be satisfied rigorously. This method will be discussed first.

Only the two-dimensional case will be considered (plane state of strain). The first step is to make an assumption for the shape of the slip surface. The circular cylinder is the most commonly used assumption. This, together with other suggested geometrical curves, is shown in Fig. 15. Type (a) is the usual circular slip surface. Type (b) is composed of two circular arcs of different radii which form a smooth curve so as to fit the actual surface of sliding better. Type (c) is a logarithmic spiral for a weightless material with internal friction. Type (d) shows an example of how a rotational slip surface may be distorted by the presence of a dipping ledge or of a firm layer located near the disturbed zone. Finally, type (e) represents the extreme case of the circular slip surface, i.e. a plane parallel to the ground surface. This is used in the stability analysis of an infinite slope with no cohesion.

If there are no excess pore pressures in a soil mass bounded by a slope, or when the stability analysis is performed on the basis of shear strength referred to total stress for partially saturated soils this does not necessarily imply that the angle Φ is equal to zero, simplified methods of analysis can be employed. One of these, known as the friction circle method, was developed by TAYLOR (1938). He assumed that the resultant qds of the elementary normal force σds and tangential force τds acting on an element of the slip surface is inclined at the angle Φ to the normal to the slip surface so that it is tangential to a circle of radius $r \sin \Phi$ whose centre coincides with that of the slip circle. Consequently, the resultant Q of elementary forces qds on all such elements must also be tangential to that circle. (This assumption was already discussed in connection with earth pressure problems in Vol. 1, Chapter 10.)

The procedure of the friction circle method is illustrated by Fig. 16.

Let l_a be the length of the arc \widehat{AC} and l_c be the length of the chord \overline{AC} . Assuming a uniform cohesion along the slip surface, the moment arm of the resultant cohesion C is given by

$$z = r \frac{l_a}{l_c}.$$

Its line of action is parallel to the chord \overline{AC} . The vertical line of action of the weight W of the sliding mass ABC can be found by a graphical

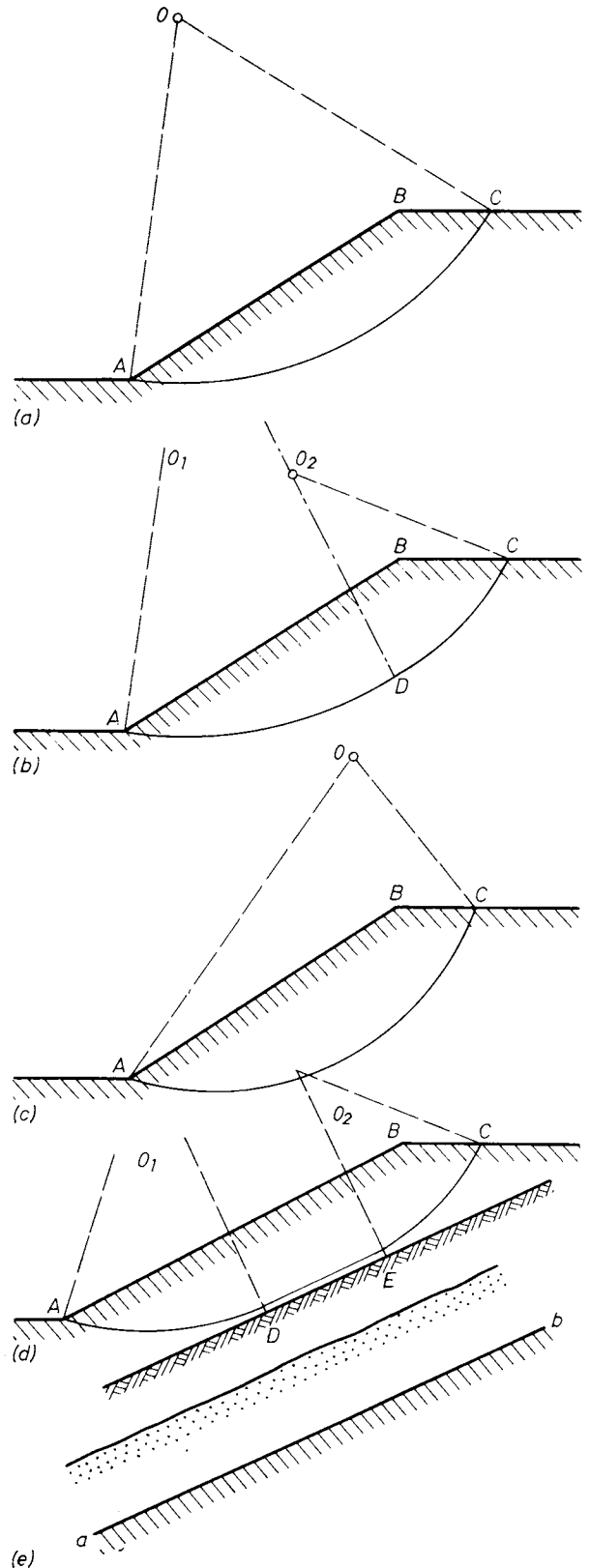


Fig. 15. Patterns of sliding surfaces to be used in the case of the method of slices:

a — circle; b — compound curve; c — logarithmic spiral; d — composite elongated sliding surface; e — plane

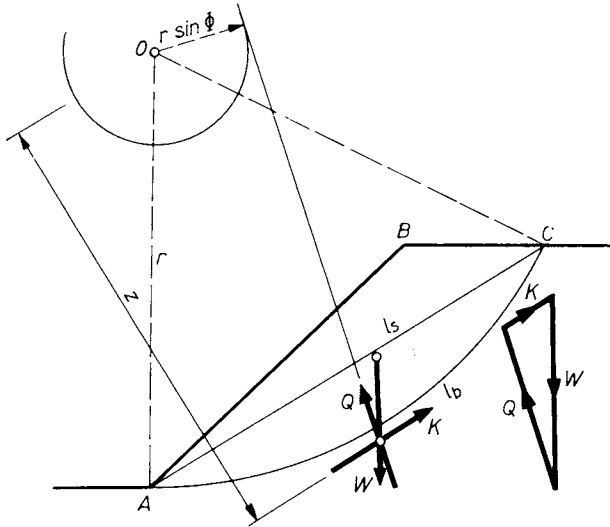


Fig. 16. Stability analysis for soils of friction and cohesion, according to Taylor's method (1938)

construction. If ABC is a regular figure, we may divide it into a triangle and a circular segment, and find their common centre of gravity. If the sliding mass is bounded by an irregular surface, we divide the mass into vertical slices and determine the line of action of W by means of a string polygon. The point of intersection of the forces C and W can thus be found. For equilibrium, the unknown resultant Q of the normal and frictional forces acting on the slip surface must also pass through that point. On the other hand, Q must be tangential to the circle of radius $r \sin \Phi$ and hence its line of action can be drawn. Since the mass ABC in Fig. 16 tends to slide downwards from the right to the left, while the restraining forces act in the opposite sense, the line of action of Q should be tangential to the friction circle on the right. Equilibrium also requires that the vector polygon of the forces W , C and Q must close. Since the magnitude and direction of W are known, and the lines of action of the forces C and Q are furnished by the construction just described, the force triangle can readily be completed. The resultant cohesion C needed for equilibrium can be scaled off from the figure and the cohesion per unit area c computed from the expression $c = C/l_c$.

By repeating the construction with a sufficient number of trial slip surfaces, the most dangerous circle, i.e., the one giving the maximum cohesion necessary for equilibrium, can be found. Hence the safety factor can be computed as the ratio of the cohesion available along the slip surface to the maximum cohesion obtained from the construction:

$$v = \frac{c_{\text{available}}}{c_{\text{required}}}$$

The assumption on which the construction is based can only be considered as an approximation

since it can easily be seen that the resultant force Q on the slip surface is not exactly tangential to the circle of radius $r \sin \Phi$, missing tangency by a small amount as shown in Fig. 17. This discrepancy is due to the fact that the elementary forces acting on the slip surface do not intersect on the perimeter of the circle of radius $r \sin \Phi$ but, depending on the mode of distribution of the restraining forces along the slip surface, some small distance away from it. For example, two such elementary forces Q_1 and Q_6 intersect at point D in Fig. 17. By making simple assumptions for the distribution of stresses along the slip surface, the error can be determined mathematically.

The distance of the line of action of the tangential component T of force Q from the centre of rotation can be given by the general expression

$$z_2 = rf(\theta),$$

where θ is half of the central angle subtended by the arc \widehat{AC} . The function $f(\theta)$ has been evaluated by FRÖHLICH (1950) for three different modes of stress distribution shown in Fig. 18. The respective formulae, together with numerical values of the quantity $(Z/r - 1)$ plotted against the angle θ , are shown in Fig. 19. Pattern b in Fig. 18 bears, in most cases, the closest resemblance to the actual stress distribution. Pattern a, which is tacitly assumed in the friction circle method, is only an approximation. Pattern c shows the probable distribution of stresses in cases where there is some restraint at point A preventing the free development of the slip surface \widehat{AC} .

The stability analysis based on the friction circle method can also be treated mathematically.

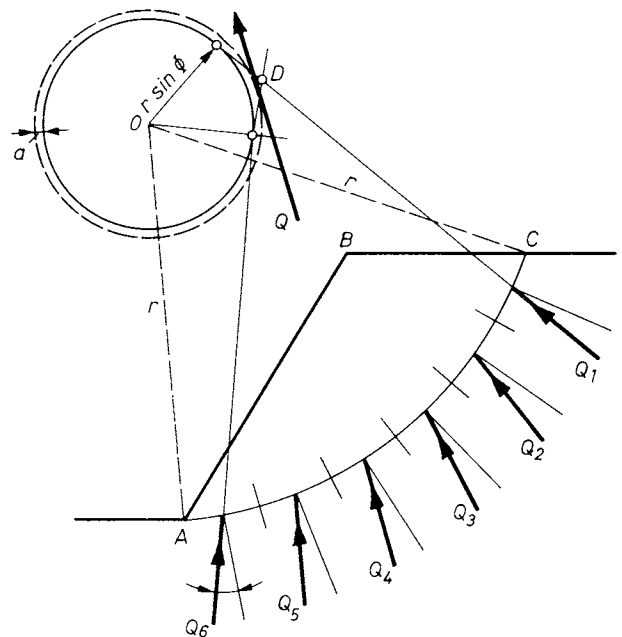
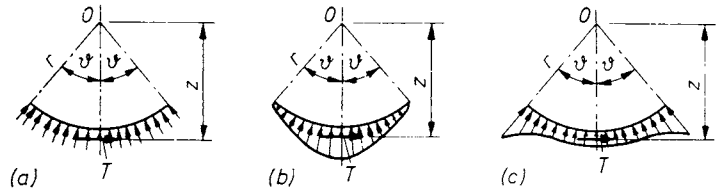


Fig. 17. Direction of reactive forces on a sliding surface

Fig. 18. Three alternatives for the establishment of the acting point of reactive forces in the case of different normal stress distributions



It can be shown that the expression furnishing the cohesion necessary for equilibrium is similar to Eq. (8), except that in this case the function F contains an additional variable: the angle of internal friction Φ . The location of the critical circle is again determined by the extremum criteria

$$\frac{\partial c}{\partial \alpha} = 0 \quad \text{and} \quad \frac{\partial c}{\partial \theta} = 0.$$

By solving the equations, the cohesion necessary for equilibrium can be expressed as

$$c = \frac{h\gamma}{F(\alpha, \beta, \theta, \Phi)} = h\gamma N_c, \quad (13)$$

whence the height of stable slope becomes

$$h = \frac{c}{\gamma N_c}. \quad (14)$$

Numerical values of the stability number N_c against the slope angle β for various values of Φ are given in Fig. 20. The graph is divided by a dash-dot line into two zones. In zone I the critical circle is always a toe circle, with its lowest point at the toe. In zone II, which corresponds to moderate and flat slopes, there are three variant cases to be considered. Case I is likely to occur in homogeneous soils. The most dangerous circle passes through the toe but it may penetrate slightly below the elevation of the toe, i.e. the depth factor may be greater than unity. Case 2 is valid for Φ values of less than 5° . The critical circle passes below the toe and cuts the free surface at some distance from it. In case 3 there is a ledge or firm stratum that limits the depth to which, the slip surface can penetrate. For small Φ angles, a deep-seated failure cannot occur and the slip surface finishes on the slope above the toe A . The three cases are represented by different types of line in the chart, each being shown only where the occurrence of the respective case is possible or critical.

As can be seen from the chart, a base failure is to be expected only when the friction angle is less than 5° . Conversely, from the occurrence of a base failure in a homogeneous soil, it can be inferred that at the time of failure the friction angle Φ was probably very close to zero. In the range of small Φ values the depth factor has a marked influence

on the stability of the slope, but it becomes negligible as Φ increases.

Taylor's friction circle method was further developed by JÁKY (1944) in so far as he suggested that instead of laborious trials the critical circle can be found in one step on the basis that at the lower end of the slip surface the soil is in a state of uniaxial compression and at the upper end in uniaxial tension, and thus the slopes of tangents to the circle are determined at those points (Fig. 21). It follows from the geometry of the circle that the chord \overline{AC} of the critical circle makes an angle of $(\beta + \Phi)/2$ with the horizontal. These conditions determine the location of the critical slip surface unequivocally.

Although the assumptions made by Jáky on the state of stress of the slope hold true, the actual slip surface is not circular but is a curved surface having the sharpest curvature near the upper end C and becoming gradually flatter towards point A . Therefore, the slope angles of the initial and final tangents to the substituting circular surface cannot be assumed to be known and, in fact, the greatest deviations from the actual slip surface occur at points A and C . In spite of this, if we calculate the stability number N_c from the fol-

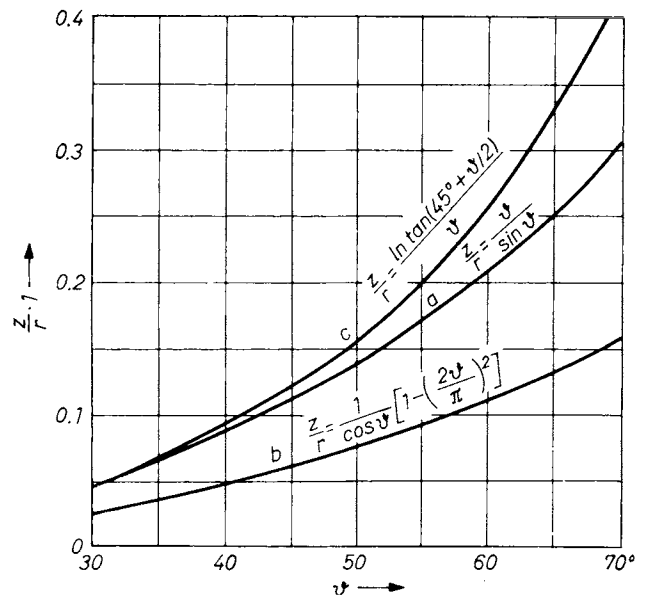


Fig. 19. Finding the location where the force Q acts (FRÖHLICH, 1950)

lowing formula furnished by Jáky's analytical method (JÁKY, 1944),

$$\frac{1}{N} = 4 \cos \Phi \frac{\sin \frac{\beta + \Phi}{2}}{\sin \frac{\beta - \Phi}{2}} \cdot \frac{\cos \beta}{(\cos \Phi - \cos \beta) \cot \beta + \tan \left(45^\circ + \frac{\beta}{2} \right) \left(\frac{\pi}{2} - \beta - \cos \beta \right)} \quad (15)$$

and plot the N_c values obtained on Taylor's stability chart (Fig. 20), the difference between the two sets of values will be negligible. The good agreement is all the more conspicuous since the differences between the locations and radii of the critical circles are indeed very significant. For practical purposes, the Taylor curves can be

replaced, especially in the range of higher Φ values, by Eq. (15) or by the equation of a well fitting hyperbola,

$$\frac{1}{N_c} = 4 \left(\frac{4\Phi}{\beta - \Phi} + 1.6 - 0.04\Phi \right) \quad (16)$$

(β and Φ in degrees), both of which furnish reliable values of N_c .

BISHOP (1955) developed an analytical solution for the method of slices which takes into account the difference of the earth pressures acting on the two vertical sides of a slice. This method also makes it possible to allow for pore pressure acting in the slope.

Consider a rotational slide occurring along a toe circle, as shown in Fig. 22. The pore-water pressure u at any point can be expressed in terms of the ratio

$$r_u = \frac{u}{h\gamma},$$

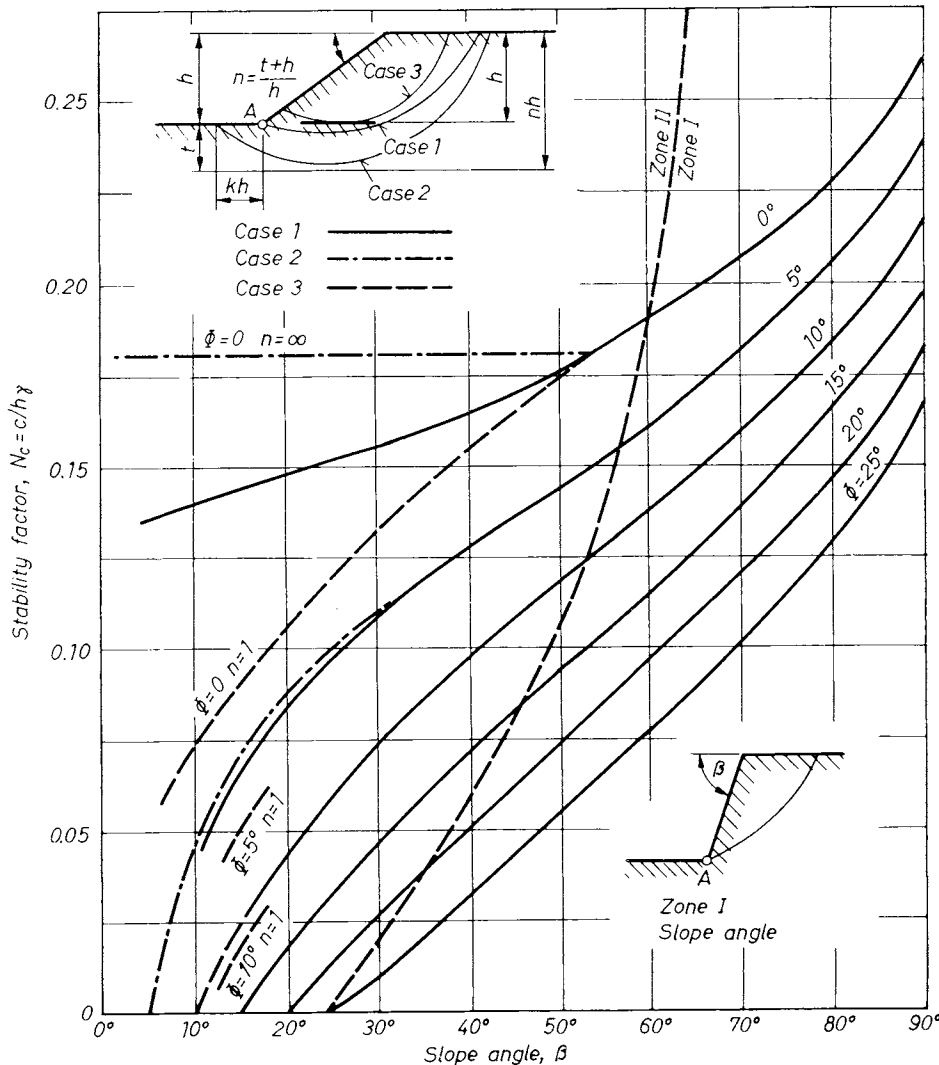


Fig. 20. Stability numbers as a function of the slope angle

Hence

$$N - ul = N' = \frac{W + E_n - E_{n+1} - ul \cos \alpha - \frac{c'}{v} l \sin \alpha}{\cos \alpha + \sin \alpha \frac{\tan \Phi'}{v}} \quad (22)$$

Substituting into Eq. (20) gives

$$v = \frac{r}{\Sigma W x}$$

$$\cdot \sum \left[c'l + \tan \Phi' \frac{W + E_n - E_{n+1} - ul \cos \alpha - \frac{c'}{v} l \sin \alpha}{\cos \alpha + \sin \alpha \frac{\tan \Phi'}{v}} \right] \quad (23)$$

From Fig. 23 it can be readily seen that

$$x = r \sin \alpha,$$

$$b = l \cos \alpha$$

and

$$\frac{ub}{W} = \frac{u}{h\gamma} = r_u.$$

Substituting these expressions into Eq. (23), we obtain

$$v = \frac{1}{\Sigma W \sin \alpha} \sum \left[c'b + [W(1 - r_u) + (E_n - E_{n+1})] \tan \Phi' + \frac{\sec \alpha}{1 + \frac{\tan \alpha \tan \Phi'}{v}} \right] \quad (24)$$

The values of $\Delta E_n = E_n - E_{n+1}$ are determined by successive approximation on the basis that

$$\left. \begin{aligned} \Sigma(E_n - E_{n+1}) &= \Sigma \Delta E_n = 0, \\ \Sigma(E_t - E_{t+1}) &= \Sigma \Delta E_t = 0, \end{aligned} \right\} \quad (25)$$

and that the condition of moment equilibrium must also be satisfied.

The procedure is as follows. Resolving the force acting on a slice tangentially and using the condition of equilibrium, we obtain

$$(W + \Delta E_n) \sin \alpha + \Delta E_t \cos \alpha = T$$

or $\Delta E_t = T \sec \alpha - (W + \Delta E_n) \tan \alpha. \quad (26)$

Now, if Eq. (24) is written in the form

$$v = \frac{1}{\Sigma W \sin \alpha} \Sigma [m]$$

then

$$T = \frac{m}{v},$$

and hence

$$\Sigma \Delta E_t = \Sigma \left[\frac{m}{v} \sec \alpha - (W + \Delta E_n) \tan \alpha \right]. \quad (27)$$

The E_n values must therefore also satisfy the condition that

$$\Sigma \left[\frac{m}{v} \sec \alpha - (W + \Delta E_n) \tan \alpha \right] = 0.$$

In practice, as a first approximation, a value of v is computed from Eq. (24) on the assumption that $\Delta E_n = 0$. Several trial values of v are then assumed and entered into the right-hand side of Eq. (24). Finally, assumed and computed v values are compared. The correct solution when

$$v_{\text{assumed}} = v_{\text{computed}}$$

can be obtained by graphical interpolation. The solution obtained will thus satisfy Eq. (24), but not Eq. (27). Suitably assumed ΔE_n values are then introduced into Eq. (27) and adjusted by iteration, until the correct value which satisfies Eq. (27) is found. BISHOP (1954) noted that there are a number of different distributions of ΔE_n which all satisfy Eq. (27), but the corresponding variations in the value of v are less than 1%.

The Bishop method is primarily adaptable to the stability analysis of earth dams, normally built with gentle slopes, in which high pore-water pressure is likely to build up and the critical slip surface penetrates deep below the toe and has a great central angle.

The simplified method of Janbu (JANBU *et al.*, 1956) takes account of the shear forces between the slices by using a corrective factor f_0 which depends on Φ and c , and the shape of the sliding surface. The normal force P can be calculated from the equilibrium of vertical forces, i.e., from Eqs (28) and (29), as follows:

$$W - (X_R - X_L - P \cos \alpha - S_m \sin \alpha) = 0, \quad (28)$$

$$P = \left[W - \frac{c'l \sin \alpha}{F} + \frac{ul \tan \Phi' \sin \alpha}{F} \right] m_\alpha, \quad (29)$$

where u means the pore-water pressure, F the safety factor and

$$m_\alpha = \cos \alpha + (\sin \alpha \tan \Phi') : F. \quad (30)$$

(The other symbols are illustrated in Fig. 24.)

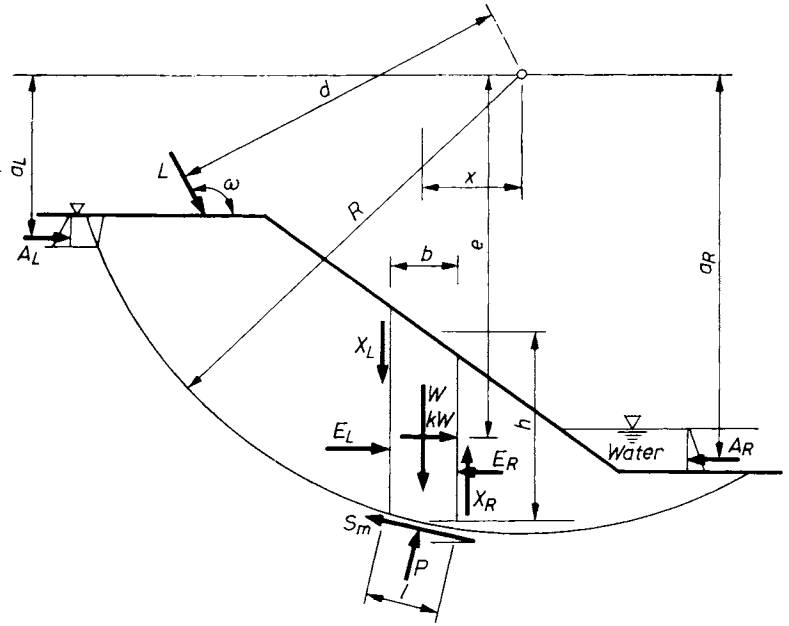
The formula

$$\Sigma (E_L - E_P) + \Sigma P \sin \alpha - \Sigma S_m \cos \alpha + \Sigma kW \pm A - L \cos \omega = 0 \quad (31)$$

representing the equilibrium of the horizontal forces can be used to calculate the safety factor in the following form

$$F_0 = \frac{\Sigma [c'l \cos \alpha + (P - ul) \tan \Phi' \cos \alpha]}{\Sigma P \sin \alpha + \Sigma kW \pm A - L \cos \omega}. \quad (32)$$

Fig. 24. Acting forces for the method of slices



(In this equation A means the resultant water forces, and ω the angle of the line load from the horizontal.)

The final (corrected) form of the safety factor is then:

$$F = f_0 F_0. \quad (33)$$

Janbu elaborated a "rigorous method" as well, in which it is supposed that the point where the interslice forces act can be defined with the help of the "line of thrust". New terms involved are then defined as follows (see Fig. 25):

– t_L, t_R = vertical distance from the base of the slice to the line of thrust (on the left and right sides of the slice, respectively);

– α_t = angle between the line of thrust on the right side of a slice and the horizontal.

The normal force P can be found from the equilibrium of all vertical forces:

$$P = \left[W - (X_R - X_L) - \frac{c'l \sin \alpha}{F} + \frac{ul \tan \Phi' \sin \alpha}{F} \right] : m_\alpha \quad (34)$$

and the safety factor from the equilibrium of all horizontal forces:

$$F = \frac{\Sigma [c'b + \tan \Phi'(W - ub + X_n - X_{n-1})]}{(E_a - E_b + \Sigma W \tan \alpha) \frac{1 + \frac{\tan \Phi' \tan \alpha}{F}}{1 + \tan^2 \alpha}} \quad (35)$$

JANBU'S rigorous analysis differs from the simplified analysis in that the shear forces are retained in the derivation of the normal force.

To solve Eq. (35) the shear forces between the slices should first be established. An iteration is applied after that, in which the first step is to assume the shear forces to be equal to zero. The next step is to calculate interslice forces from the summary of moments that act on the centre of each slice base:

$$X_L \frac{b}{2} + X_R \frac{b}{2} - E_L \left(t_L + \frac{b \tan \alpha}{2} \right) + E_R \left(t_L + \frac{b}{2} \tan \alpha - b \tan \alpha_t \right) - k \frac{Wh}{2} = 0. \quad (36)$$

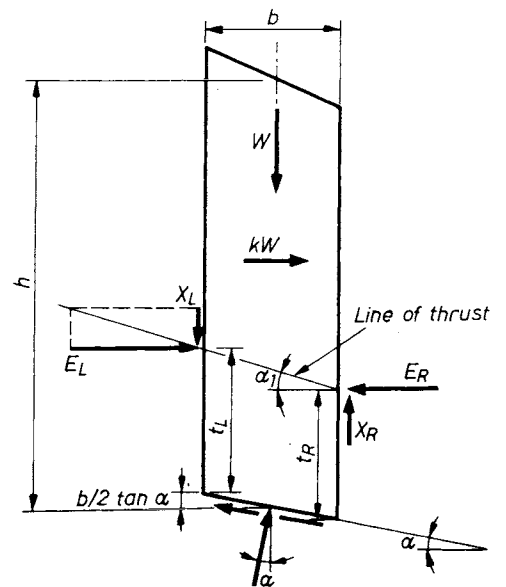


Fig. 25. Forces acting on each slice in the case of Janbu's "rigorous" method

After rearranging Eq. (36), several terms become as negligible as the width dx . These terms are:

$$(X_R - X_L) \frac{b}{2}; (E_R - E_L) \frac{b \tan \alpha}{2}; (E_R - E_L) b \tan \alpha_t.$$

After eliminating these terms, and dividing by the width of the slice, the shear force X_R becomes:

$$X_R = E_R \tan \alpha_t - (E_R - E_L) \frac{t_R}{b} + \frac{kW}{b} \cdot \frac{h}{2}. \quad (37)$$

The horizontal interslice forces required to solve Eq. (37) are obtained by combining the summation of vertical and horizontal forces on each slice:

$$(E_R - E_L) = [W - (X_R - X_L)] \tan \alpha - \frac{S_m}{\cos \alpha} + kW. \quad (38)$$

The horizontal interslice forces are obtained by integration from left to right across the slope. The magnitude of the interslice shear forces in Eq. (38) lag by one iteration. Each iteration gives a new set of shear forces.

MORGENSTERN and PRICE (1965) assume an arbitrarily taken function to describe the direction of the interslice forces:

$$\lambda f(x) = \frac{X}{E}. \quad (39)$$

In this expression λ represents a constant to be evaluated for solving the safety factor, and $f(x)$ is the functional variable with respect to x . The final solution is based on the summation of all tangential and normal forces. The force equilibrium equations were combined and then the Newton-Raphson numerical technique was used to solve moment and force equations for the safety factor and λ .

FREDLUND and KRAHN (1977) presented an alternative method for the same problem. The combined procedure consists essentially in the following. The normal force is derived from Eq. (34). Two safety factor equations are computed, one in respect to the equilibrium of moments, and the other in respect to the equilibrium of forces. (The former is allocated to a common point; even if the sliding surface is a composite one, a fictitious common centre can be used.) The equation is the same as that obtained for the simplified Bishop method. The safety factor with respect to force equilibrium (F_f) is defined with the Eq. (32). The interslice shear forces are computed in a manner similar to that presented before as Janbu's rigorous method. On the first iteration, the vertical shear forces are set to zero. On subsequent iterations, the horizontal interslice forces are first computed (Eq. [38]) and then it

comes to the vertical shear forces using an assumed λ value and side force function:

$$X_R = E_R \lambda f(x). \quad (40)$$

The side forces are recomputed after each iteration. The moment and force equilibrium safety factors are solved for a range of λ values and a specified side force function. These safety factors are plotted in a manner similar to Fig. 26. The safety factors vs. λ are fit by a second-order polynomial regression and the point of intersection satisfies both force and moment equilibrium.

Spencer's method (1967) applies the premises illustrated in Fig. 27. Accordingly, the equilibrium of the following five forces should be analysed:

- (a) The weight (W);
- (b) The total reaction (P) normal to the base of the slice. This force has two components: (i) the force P' due to inter-granular effective stresses, and (ii) the force ($ub \sec \alpha$) due to the pore pressure (u). Thus:

$$P = P' + ub \sec \alpha. \quad (41)$$

- (c) The mobilized shear force ($S_m = S/F$), where

$$S = c'b \sec \alpha + P' \tan \Phi', \quad (42)$$

i.e.:

$$S_m = \frac{c'b}{F} \sec \alpha + P' \frac{\tan \Phi'}{F}. \quad (43)$$

- (d) The interslice forces (Z_n and Z_{n+1}). For equilibrium, the resultant (Q) of these two forces has to pass through the point of intersection of the other three forces.

By dividing the five forces shown in Fig. 27 into the components normal and parallel to the base of the slice the following expression is obtained for the resultant (Q) of the two interslice forces:

$$Q = \frac{\frac{c'b}{F} \sec \alpha + \frac{\tan \Phi'}{F} (W \cos \alpha - ub \sec \alpha) - W \sin \alpha}{\cos (\alpha - \theta) \left[1 + \frac{\tan \Phi'}{F} \tan (\alpha - \theta) \right]} \quad (44)$$

As $W = \gamma bh$ and $u = r_u \gamma h$ (where r_u is a pore-pressure coefficient proposed by Bishop and Morgenstern). Equation (44) can now be transformed and rewritten in a dimensionless form as follows:

$$Q = \frac{\frac{c'}{F\gamma H} + \frac{h \tan \Phi'}{2HF} (1 - 2r_u + \cos 2\alpha) - \frac{h}{2H} \sin 2\alpha}{\cos \alpha \cos (\alpha - \theta) \left[1 + \frac{\tan \Phi'}{F} \tan (\alpha - \theta) \right]}, \quad (45)$$

where H represents the height of the slope.

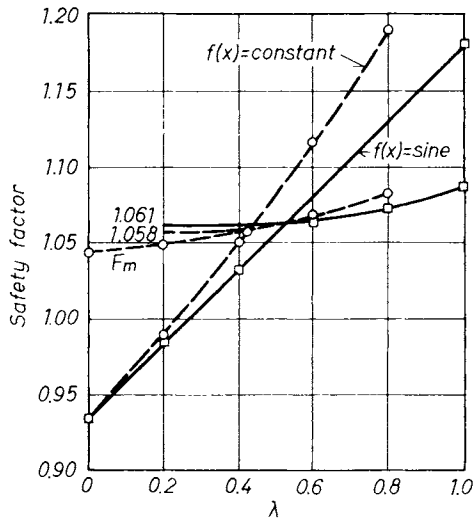


Fig. 26. Variation of F with respect to moment and force equilibrium versus λ for the MORGENSTERN and PRICE (1965) method; soil properties: $c'/\gamma h = 0.02$, $\Phi' = 40^\circ$, $r_u = 0.5$, geometry: $\beta = 26.5^\circ$, height = 30 m

If all external forces on the slope are in equilibrium, the sum of interslice forces has to be zero, i.e., the sum of both the horizontal and vertical components of interslice forces has to be zero:

$$\Sigma(Q \cos \theta) = 0, \tag{46}$$

and

$$\Sigma(Q \sin \theta) = 0. \tag{47}$$

Furthermore, if the sum of the moments of external forces about the centre of rotation is zero, the sum of the moments of interslice forces must also be zero:

$$\Sigma[QR \cos(\alpha - \theta)] = 0. \tag{48}$$

There are thus three equations to be solved in a given problem: two in respect of forces (Eqs (46) and (47)) and one in respect of moments (Eq. (48)). Proper values should be found in respect of F and θ to satisfy all three equations, and it has to be noted that although, for a given slice, the value of θ will be the same, the forces between the slices will not necessarily be parallel throughout.

As MORGENSTERN and PRICE (1965) have proved that the dispersion of F -values belonging to different types of θ -distributions is small, SPENCER saw the merit of the allowable supposition that the interslice forces are parallel to each other (i.e., $\theta = \text{const.}$). In this manner, Eqs (46) and (47) would be identical:

$$\Sigma Q = 0 \tag{49}$$

and only two equations remain to be solved (Eqs (48) and (49)). Following these considerations, the procedure consists of the following steps.

(a) Several values of θ are assumed, and for each, a value of F should be found to satisfy both

Eqs (48) and (49). Using the force-equilibrium equation (49), the value of F obtained will be designated as F_f , the other as F_m . The value of the safety factor from the moment equation, while θ was taken as zero, will be marked as F_{m0} .

(b) A curve should then be plotted to find the relationship between F_f and θ , and a second curve on the same graph to show the relation between F_m and Q . The intersection of the two curves will represent the value of the safety factor (F_i) which satisfies both equations and the corresponding incline (θ_i) of interslice forces (see Fig. 26).

(c) These values of F_i and θ_i are then substituted in Eq. (45) to obtain the values of resultant interslice forces. Hence, proceeding from the first slice to the last, the values of every interslice force can be established.

(d) Then, working again from the first slice to the last, the acting points of the interslice forces can be found by calculating the moments to the middle points on the base of each slice. The position of the points of action should then be marked on the sections of the slopes.

Examination of practical examples prompted SPENCER (1967) to derive the following conclusions:

(a) the value of θ_i was less than the slope of the embankment (β);

(b) the variation of θ values influenced the F_f values to a much greater extent than those of F_m . In fact, when θ was less than θ_i , the variation in F_m was very small indeed. Consequently, there was not much difference between the values of F_{m0} and F_i ;

(c) the line passing through the points of action of the interslice forces fit very closely to the lower

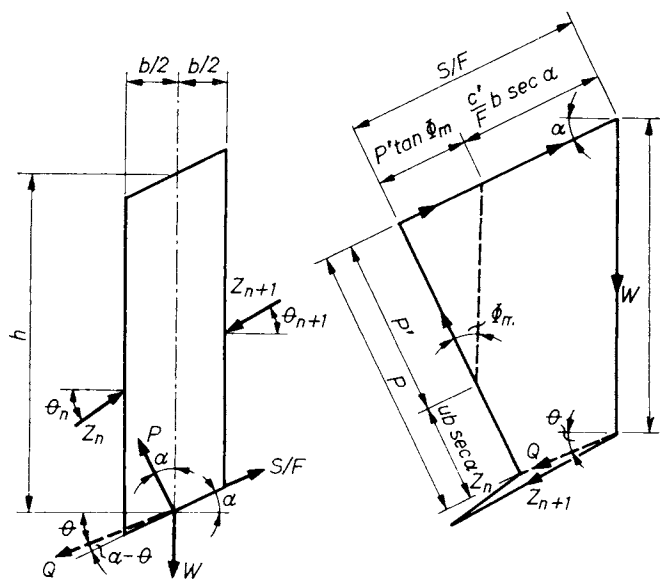


Fig. 27. Forces on a slice for Spencer's method (1967)

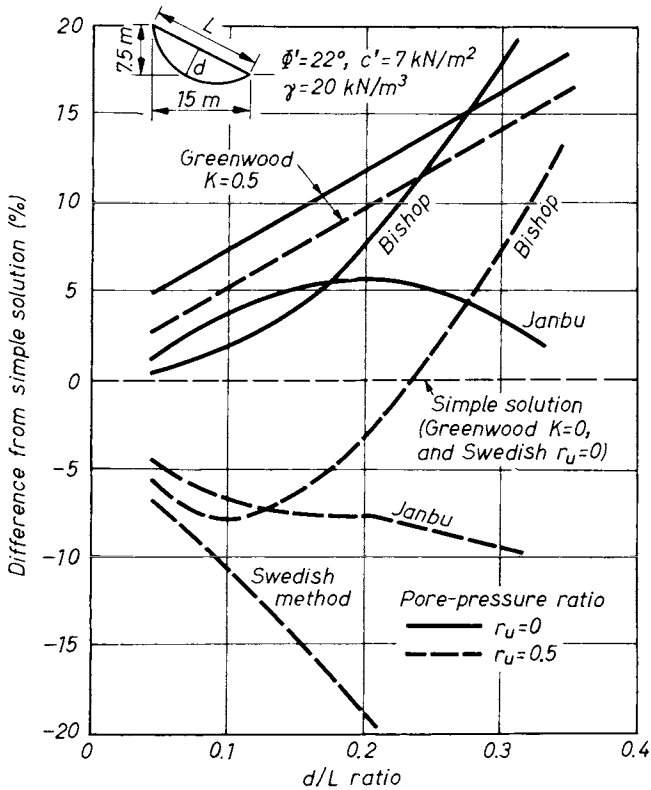


Fig. 28. Comparison between Greenwood's solution (1983) and other solutions for a typical slope with circles of varying depths

“third-point” on the interface of the slices. This implies an approximately triangular stress distribution on these boundaries, which is a quite acceptable result.

Using a numerical example, SPENCER also investigated, how the number of slices (*n*) influenced the value of the safety factor (*F*) and found:

<i>n</i>	8	16	32	64	128
<i>F</i>	1.233	1.245	1.249	1.251	1.251

The results of this comparison have shown that though the accuracy of Bishop's simplified method decreases slightly as the slope of the embankment, *r_u* and Φ' increase or the parameter $c'/\gamma H$ decreases, the error was less than 1% in most of the cases considered. The worst combination of these factors resulted in an error in the safety factor of 4%.

GREENWOOD (1983) elaborated an approximate solution. Based on it, the safety factor can be estimated from the following equation:

$$F = \frac{1}{\sum W \sin \alpha} \sum [c' b \sec \alpha + W(1 - r_u)(1 + K \tan^2 \alpha) \cdot \cos \alpha \tan \Phi'] \tag{50}$$

in which — additionally to the previous ones — the symbol *K* means the ratio of horizontal to

vertical effective stresses. Supposing the situation $K = 0$, the case of FELLENIUS will be reinstated. Figure 28 compares this procedure with other methods.

PAPADOPOULOS and ANAGNOSTOPOULOS (1981) argue that, according to observations, the sliding surface is not always a circle, the more so not in over-consolidated and anisotropic soils. They suggested applying an alternative approach in such cases, for example, to describe the sliding surface by the following function:

$$x = -\frac{\lambda}{H} z^2 + \lambda H. \tag{51}$$

The authors conducted a comparative analysis to demonstrate in which case the circle and when the parable supplied lower safety factor values. Three fundamental situations were examined:

- the soil mass was isotropic or
- anisotropic ($K = c_{\max}/c_{\min}$);
- the cohesion varied according to depth.

Cases have been found in all three situations when the parable supplied the lower values for safety. In the first situation, for example, the circle was more perilous for a slope with low incline and/or when the shear resistance was small, in the opposite cases the parable was more perilous.

1.2.3.5 Criticism of theories and general considerations

The authors who attempted criticism on theoretical works mostly examined the following four problems:

- fulfilment of equilibrium conditions;
- distribution of normal stresses;
- the safety factor along the sliding surface;
- the influence of the “stress-path”.

It can be stated unanimously on the basis of facts described in Section 1.2.3.4 that the method of Fellenius, the simplified method of Bishop, and all theories which apply the “stiff mass” assump-

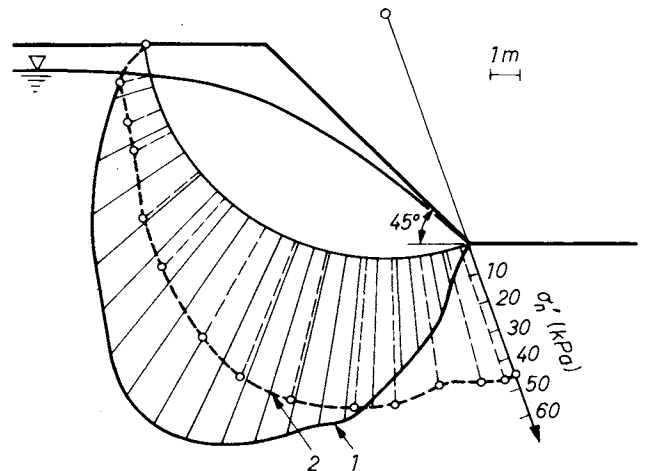
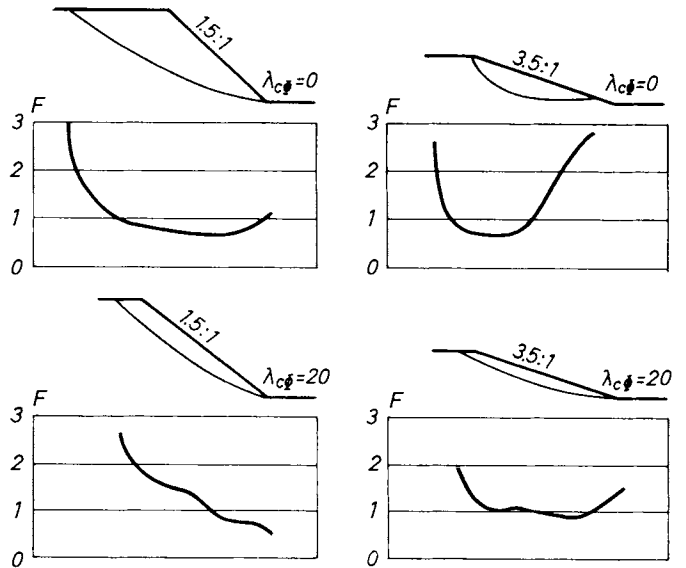


Fig. 29. Effective normal stresses (σ'_n) in an excavated slope: 1 — in Bishop's stability analysis (1955) and 2 — from an elastic solution

Fig. 30. Effective normal stresses (σ'_n) under an embankment in Bishop's stability analysis (1955) and from a non-linear elasto-plastic solution



tion, would not satisfy the requirements for equilibrium.

With respect to normal stress distribution, the deficiencies in the supposition will be clearly visible in Fig. 29, where the stress distribution in a cutting calculated by Bishop's method is compared with the actual one which has been measured by La Rochelle using the photo-elasticity method (TAVENAS *et al.*, 1980). There are very important differences between the two stress distributions. They reveal a strong overestimation of σ'_n and thus of the available clay strength along the upper part of the failure surface, and an even more pronounced underestimation of σ'_n and τ at the toe of the slope. A similar outcome can be observed generally at the foundations of embankments. Figure 30 shows a typical comparison between the normal stresses obtained from a finite-element method (FEM) analysis — using a hyperbolic stress-strain relationship — and those computed according to the modified Bishop method.

Similar results have been obtained by WRIGHT *et al.* (1973), when it was stated that the differences

between the normal stress distributions as assumed in stability analyses and that obtained from elasticity theories decrease when the incline of the slope decreases.

The safety factor as determined by means of stability theories is assumed to be the same for every slice, and thus to be constant for each point on the shear surface. The values calculated from the linear elastic stress distribution (WRIGHT *et al.*, 1973), however, are not constant, as can be seen in Fig. 31. For the cases studied, it was found that along about one-third to one-half of the shear surface the F values calculated by using linear elastic stresses were below the average on the slope. From these results it is possible to determine the minimum value of an overall safety factor required so that F would not be less than unity at any point on the shear surface, i.e., the value of F required to prevent overstress according to linear elastic theory. These values are shown in Table 1. (The definition of $\lambda_{c\phi}$ will be explained later.) Consequently, for a wide range of conditions, a safety factor equal to 1.5 would be sufficiently large to prevent any local elastic overstress.

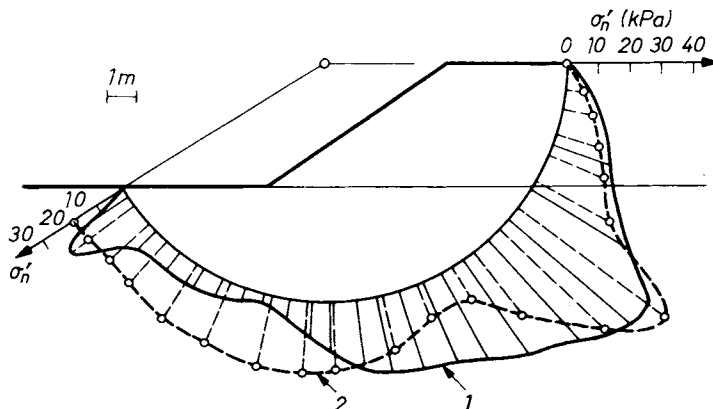


Fig. 31. Variation of the safety factor along the shear surface as calculated by the finite element method (simplified Bishop method (1955), $F = 1.0$)

Table 1. Values of F required to prevent local elastic overstress along critical shear surface

$\lambda_{c\Phi}$	Shape ratio		
	1.5 : 1	2.5 : 1	3.5 : 1
0	1.46	1.44	1.49
2	1.32	1.23	1.23
5	1.34	1.18	1.14
20	2.27	1.21	1.10
50	4.36	1.37	1.12

Inadequate inference of the stress path is illustrated in Fig. 32 by the example originally used by TAVENAS *et al.* (1980). At present, there are no means yet available by which these facts could be evaluated.

Theories can also be classified according to the number of equations necessary to achieve a proper solution (WRIGHT *et al.*, 1973). All methods employ assumptions to reduce the number of unknowns to be equal to the number of equilibrium equations. However, not all of the methods satisfy the same conditions of equilibrium. Janbu's generalized procedure of slices, and Morgenstern and Price's procedure do satisfy all conditions. These provide two equations for force equilibrium and one equation for moment equilibrium at each slice, and thus $3n$ equations are derived (n is the number of slices). Bishop's simplified method, and the ordinary method of slices do not satisfy all conditions of equilibrium. Bishop's method satisfies the requirement for vertical equilibrium at each slice and that for the overall moment equilibrium, but does not satisfy horizontal equilibrium or moment equilibrium requirements at each slice; as a result, the number of equations is $n + 1$.

The ordinary method satisfies only overall moment equilibrium requirements, but does not satisfy the moment or force equilibrium conditions at the individual slices; as a result, there is just one equation at hand.

Several researchers attempted to compare the individual procedures. This would require the invention of a complex common parameter to make the comparison unambiguous, as the geometry of the slope and the characteristics of the soil provide a great variety of possible combinations. Accepted parameters for such purpose include for example the central angle of the sliding surface (HUDER, 1977), or the d/L ratio described in Fig. 28. One of the best propositions has been introduced by JANBU (1957) where the dimensionless parameter

$$\lambda_{c\Phi} = \frac{\gamma H \tan \Phi}{c} \tag{52}$$

was suggested.

Janbu's investigations have proved that the results of a stability analysis might be expressed uniquely in terms of $\lambda_{c\Phi}$ and two other dimensionless coefficients, $F\gamma H/c$ and $\tan \beta$. Thus for any combination of $\lambda_{c\Phi}$ and β , the value of $F\gamma H/c$ calculated by any method is unique, i.e., any combination of γ , H , c , and Φ which gives the same value of $\lambda_{c\Phi}$ will result in the same value of $F\gamma H/c$. In addition, the distribution of normal stresses on the shear surface as determined by any method is precisely similar on any two slopes which have the same incline and $\lambda_{c\Phi}$ values.

FREDLUND and KRAHN (1977) have suggested that in perusing the differences among the theories the equations for the safety factor and the normal

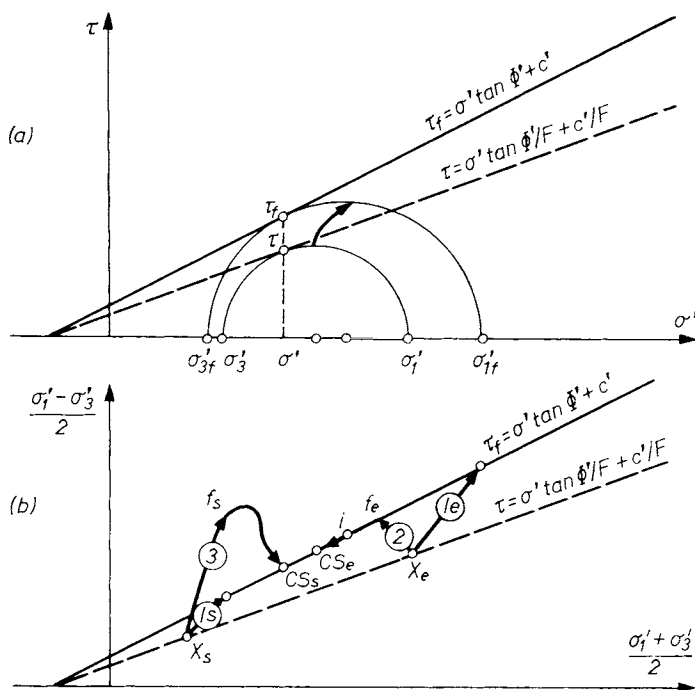


Fig. 32. Effective stress path up to failure, as implied in all methods of stability analysis (a); comparison between actual and assumed stress path up to failure in a slope or in the base of an embankment (b):

1 — effective stress path as implied in $\tau = (c' + \sigma' \tan \Phi')$; 2 — typical stress path in the soft clay base of an embankment; 3 — typical stress path for excavation in overconsolidated clay

forces should be compared separately. They stated, among other things, that Bishop's equation for the calculation of F is identical to that of the Swedish method, and difference exists only in the calculation of P . Spencer proclaimed two equations for the safety factor: one for the moments, and the other for the forces acting parallel to those at the interfaces of slices. The former is identical with the equation in Bishop's and in the Swedish methods. The present authors have summarized the results of their investigation as follows:

(a) All methods of slices that satisfy the overall moment equilibrium requirement can be written in the same form:

$$F_m = \frac{\Sigma c'lR + \Sigma (P - ul) R \tan \Phi'}{\Sigma Wx - \Sigma Pf + \Sigma kW_e \pm Aa + Ld} \quad (53)$$

(see the key in Fig. 24 for symbols).

(b) All methods satisfying overall force equilibrium have the following form for the safety factor equation:

$$F_f = \frac{\Sigma c'l \cos \alpha + \Sigma (P - ul) \tan \Phi' \cos \alpha}{\Sigma P \sin \alpha + \Sigma kW \pm A - L \cos \omega} \quad (54)$$

From the theoretical standpoint, the derived safety factor equations differ in (i) the equations of statics satisfied explicitly for the overall slope and (ii) in the assumption of making the problem determinate. The assumption used causes altering the determination of interslice forces in the normal force equation. The latter — with the exception of the ordinary method — has the same form:

$$P = \left[W - (X_R - X_L) - \frac{c'l \sin \alpha}{F} + \frac{ul \tan \Phi' \sin \alpha}{F} \right] : m_\alpha \quad (55)$$

It is possible to analyse the analytical aspects of slope stability in terms of one safety factor equation which satisfies overall moment equilibrium

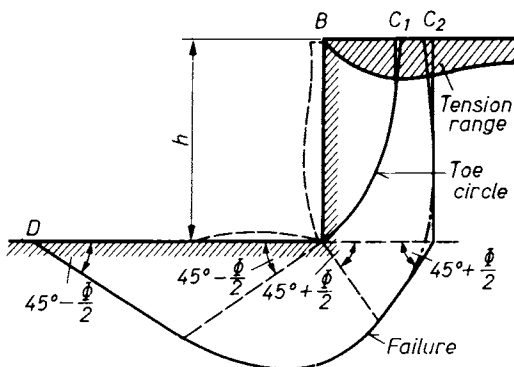


Fig. 33. Stability analysis of a vertical earth wall — determination of the sliding surface

and another satisfying overall force equilibrium requirements. In this way each method becomes a special case of the "best-fit regression" solution to the Morgenstern-Price method.

1.2.3.6 Stability of vertical banks

The stability of vertical earth banks requires special consideration, partly because it represents a limiting case of slope stability, and partly on account of its importance for the stability of trench walls and excavations.

Figure 33 shows a cross-section through a vertical bank in a cohesive soil. During the process of excavation, deformations occur in the soil mass, and the originally vertical face of the bank assumes a slightly curved shape as indicated by a dashed line in the figure. Within the shaded zone near the ground surface, the soil is in a state of tension which eventually leads to the formation of tension cracks. Excessive shrinkage due to desiccation of the soil may aggravate the situation and cause the cracks to penetrate even deeper. Temperature changes and infiltrating precipitation may also add to the formation and widening of such cracks. As a consequence, the shear strength is greatly reduced or even ceases to exist in the uppermost part of the bank. The effective length of the surface of rupture upon which resistance depends will be decreased until finally the bank fails along a curved surface normally passing through the toe.

A base failure is also possible. This sort of failure is likely to occur when the underlying soil is much softer than the material of the bank itself, and yields under the weight of a bank of height h .

In the simplest method of stability analysis, we assume that the soil along the vertical face is in the active Rankine state. In this case the surface of rupture is plane, rising at an angle of $45^\circ + \Phi/2$ from the horizontal. In a cohesive soil, the earth pressure acting on a wall of height h is given by the expression

$$E_{aR} = \frac{h^2 \gamma}{2} \tan^2 \left(45^\circ - \frac{\Phi}{2} \right) - 2ch \tan \left(45^\circ - \frac{\Phi}{2} \right).$$

E_{aR} becomes zero, when

$$h = h_0 = \frac{4c}{\gamma} \tan \left(45^\circ + \frac{\Phi}{2} \right). \quad (56)$$

Equation (56) would give the theoretical value of the critical height of an unsupported vertical bank. However, the assumptions underlying the derivation of Eq. (56) are not correct. The Rankine theory is strictly applicable to the semi-infinite half-space in a state of plastic equilibrium. In the Rankine state, the upper part of a vertical section is indeed acted upon by tensile and the lower part by compressive normal stresses as suggested,

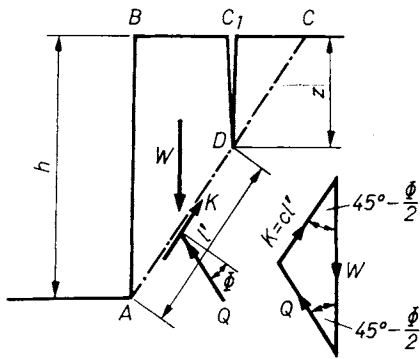


Fig. 34. Stability analysis of a vertical earth wall — static design

but along the vertical face of a bank, the normal stresses must be zero everywhere. In addition, the sliding wedge above a potential surface of sliding is not in a state of plastic equilibrium. Only a single slip surface exists, which, however, is not plane but, as shown by experience, slightly curved. Assuming a circular surface of sliding, Fellenius showed that the critical height is given by

$$h = 3.85 \frac{c}{\gamma} \tag{57}$$

The difference between the values obtained by Eqs (56) and (57) is less than 5%, and thus, considering the many uncertainties involved, for practical stability analyses the assumption of a plane surface of rupture will be quite satisfactory.

On the other hand, we must take into consideration the effect of the tensile cracks which may be formed in the upper part of the bank (Fig. 34). If one such crack penetrates so deep that it reaches the potential surface of sliding, then the body of soil C_1CD no longer participates in the failure.

The condition of equilibrium may be expressed from the force polygon as

$$\begin{aligned} W &= \frac{1}{2} \gamma (h^2 - z^2) \tan \left(45^\circ - \frac{\Phi}{2} \right) = \\ &= 2C \cos \left(45^\circ - \frac{\Phi}{2} \right) = 2c(h - z), \end{aligned}$$

since

$$C = \frac{c(h - z)}{\cos \left(45^\circ - \frac{\Phi}{2} \right)}$$

Considering Eq. (56), the critical height h'_0 can be written as

$$h = h'_0 = \frac{4c}{\gamma} \tan \left(45^\circ + \frac{\Phi}{2} \right) - z = h_0 - z.$$

The depth of tension cracks does not normally exceed one half of the height of the vertical bank. Thus, assuming $z = h'_0/2$, we obtain

$$h'_0 = \frac{2h_0}{3} = \frac{2.67c}{\gamma} \tan \left(45^\circ + \frac{\Phi}{2} \right). \tag{58}$$

It can be proved that in a homogeneous soil a slip surface passing through the foot of the vertical bank is always more dangerous than one passing below it, therefore, depending on whether or not tension cracks are likely to develop, the critical height of a vertical bank can be computed by either Eq. (58), or Eq. (56).

1.2.4 Slopes in nonhomogeneous and stratified soils

As was previously stated, the slip surface always follows the line of least resistance. Therefore, in practical cases the most dangerous slip surface determined by theory often cannot develop. Should, for example, the shear strength increase with depth, then the actual surface of rupture will deviate from the theoretical one as is shown in Fig. 35a. The presence of a layer with a low shear strength may also cause a distortion of the slip surface (Fig. 35b). Such cases can seldom be handled by exact methods of stability analysis and we should rather rely on experience in judging the stability of a slope. It is important that the engineer should correctly recognize the factors that may influence stability.

When dealing with stratified soils, we must always bear in mind that the shear strength of highly cohesive soils may deteriorate substantially

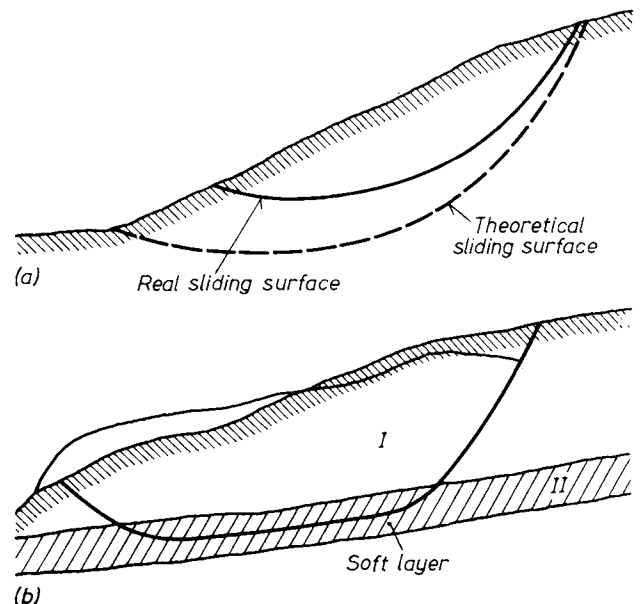


Fig. 35. Transformation of the theoretical sliding surface: a — soil strength increases with depth; b — interwoven soft layer at greater depth

because of lasting exposure to shear stresses. It follows that failure conditions will usually not be reached at one and the same time in every layer out across by a potential slip surface. Let us consider, for example, the situation shown in Fig. 35b. A stiff clay (I) which tends to fail with a relatively small shear deformation is underlain by a layer of soft clay (II) which exhibits a large deformation before it fails. Under such conditions, a relatively small displacement may be sufficient to bring layer I to the verge of failure, while in layer II only a small portion of the shear resistance is mobilized. On the other hand, deformations large enough to mobilize the shear strength in layer II completely, will long before have caused failure in layer I. As a result, the resistance to sliding in layer I becomes greatly reduced or ceases entirely. Should the shear resistance in either layer alone be insufficient to prevent failure, then we must assume, for the purpose of a stability analysis, a maximum resistance in layer II combined with a strength greatly reduced due to remoulding of the soil in layer I.

In the following, some examples are given of those cases of instability for which a quantitative analysis is possible, provided that reliable information on stratification and soil properties is available.

Figure 36 shows the cross-section of a typical slide. A large mass of earth moves outwards along the approximately plane interface of two different soil strata. There is a likelihood of such a type of failure if a permeable layer — usually sand, coarse silt, fissured clay, etc. — is underlain by an impermeable clay stratum which has a sidelong surface. The clay sucks in infiltrating rain water and swells. As a result, its shear strength may be reduced to such a level that the total frictional resistance along the plane of sliding plus the tensile strength in the upper layer are no longer sufficient to balance the tangential component of the weight of the sliding mass. Then instant sliding takes place. Locally, where small deformations have already taken place, the shear strength may drop to its ultimate value which for certain soils may be substantially smaller than the peak strength value. The upper permeable layer usually consists of sand, coarse silt or fissured clay.

The stability of such natural slopes cannot, as a rule, be investigated on the basis of some exact mathematical slip surface, since in this case the surface of rupture is determined by the geological conditions. A rough estimate of the degree of stability is possible using the following method. Figure 37 shows the cross-section of an unstable hillside. An arbitrary vertical section 1-2 is acted upon by an active earth pressure. The resultant earth pressure E_a is a tensile force when the height h is smaller than the limiting height of a vertical slope h_c and it is a thrust when h is greater than h_c . Because of tensile stresses acting in the zone near the surface, cracks will develop to a depth of

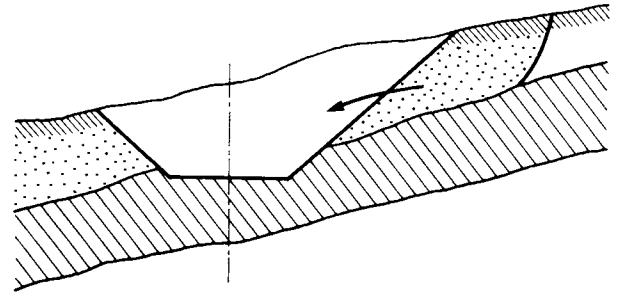


Fig. 36. Sliding in the narrow sense of the word: motion atop the stiff layer

$$h'_0 = \frac{2.67c}{\gamma} \tan(45^\circ + \Phi/2).$$

The most dangerous situation arises when, during a rainstorm, such a crack becomes filled with water, which exerts an additional pressure U on the sides of the crack. The forces which tend to cause sliding are the earth pressure E_a , the incidental water pressure U and the weight W of the block of soil $AB12$. Their resultant R is obtained by a force polygon. R can be resolved into components normal and tangential to the surface of sliding. The normal component N makes an angle α with the direction of the resultant. As for the restraining forces, there is a frictional resistance $N \tan \varphi$ on the section $A2$ of the surface of sliding. (φ denotes the angle of surface friction on the boundary of the two layers.) Equilibrium exists only if the angle α obtained from the force polygon is smaller than φ . The preceding construction is repeated several times for various positions of the vertical section 1-2. By plotting the variation of $\tan \alpha$ and comparing it with $\tan \varphi$, as is shown in Fig. 37, we can judge the degree of the stability of the hillside.

When the upper boundary of the firm stratum does not intersect the free surface of the slope,

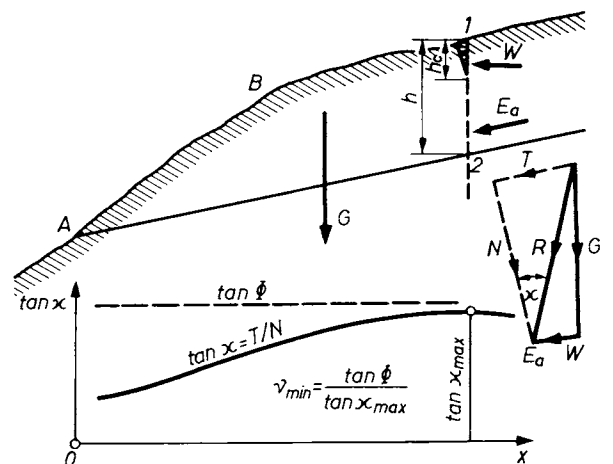


Fig. 37. Stability analysis when the sliding surface intersects the slope

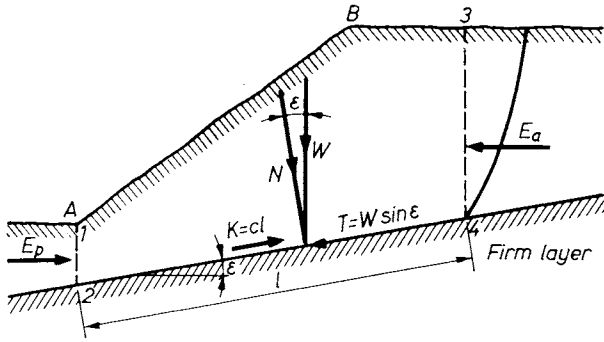


Fig. 38. Stability analysis when the sliding surface lies at some depth below the toe

but passes below its foot, the slide takes the form shown in Fig. 38. The least resistance to sliding exists at the toe of the slope, where failure occurs along a curved slip surface joining the boundary of the firm stratum tangentially at point 2. The passive earth pressure mobilized at the toe may have an appreciable value and should be entered into the stability computation. By determining the passive earth pressure E_p on the vertical section 1-2 and the active earth pressure E_a on an arbitrary section 3-4, we can compute the safety factor with respect to sliding by the formula

$$v = \frac{cl + N \tan \varphi + E_p \cos \epsilon}{T + E_a \cos \epsilon}$$

If the layers are approximately horizontal and their shear strength parameters do not differ considerably, a rotational slip is likely to occur and it is possible to perform a stability analysis on the basis of the values of Φ and c determined for the individual layers. Figure 39 shows the cross-

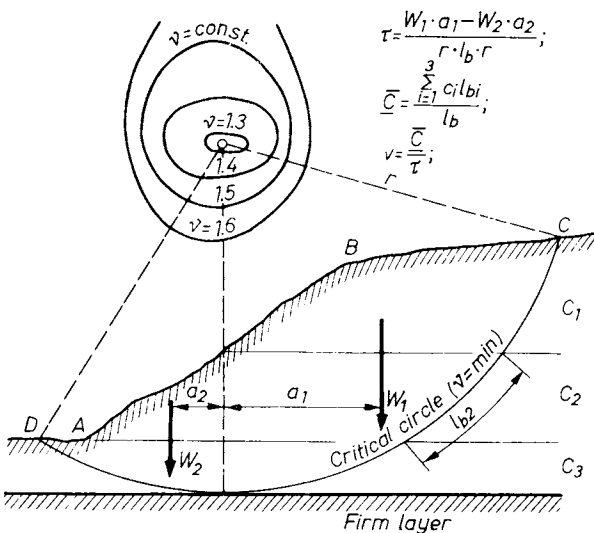


Fig. 39. Investigation of slope stability in the case of approximately horizontal stratification

section of such a stratified soil. The slip surface cuts across several layers. Obviously, the most dangerous slip surface is such that the section of its arc located within the softest layer is as long as possible. The manner in which a slope fails depends on the relative cohesions of the individual layers. Should, for example, a soft layer be located in the upper or mid-part of the slope, the occurrence of a firm stratum at some greater depth is not likely to influence stability. On the other hand, if there is a soft layer, for example, layer 3 in Fig. 39, located just below the toe, a base failure will most probably occur. The critical slip surface will just touch the surface of the firm base. Such considerations will help us greatly in finding the location of the most dangerous slip surface.

The stability analysis may be performed on the assumption that $\Phi = 0$. By tracing a trial circle, we compute the average shear resistance τ that would be required along the slip surface to prevent sliding. From Fig. 39, we have

$$\tau_{\text{required}} = \frac{W_1 a_1 - W_2 a_2}{r l_a}$$

where a_1 and a_2 are the lever arms with respect to the centre O of the forces W_1 and W_2 , respectively, and l_a is the total length of the arc \widehat{CD} . The weighted average of the available cohesions of the individual strata is computed by the formula

$$c_{\text{average}} = \frac{\sum_{i=1}^n c_i \Delta l_{ai}}{l_a}$$

where c_i is the cohesion of the i th layer and Δl_{ai} is the length of the arc of the section of slip surface in the i th layer. The safety factor with respect to sliding can be written as

$$v = \frac{c_{\text{average}}}{\tau_{\text{required}}}$$

The investigation is repeated for different trial slip surfaces in order to find the least value of v . By performing a sufficient number of investigations and assigning to the centre of each one of the trial circles the corresponding value of v , we can trace a set of contours representing equal v values as shown in Fig. 39. The lowest point furnishes the centre of the critical circle and at the same time the desired value of v_{min} .

For the case $\Phi \neq 0$, the investigation can be carried out by any of the methods discussed in Section 1.2.3.4. For the method of slices, vertical division lines can conveniently be drawn at every point where the slip surface intersects the boundaries of the layers so that there is only a single value of c for each slice.

1.3 Factors influencing the stability of slopes

1.3.1 Introduction

Earthworks are constantly exposed to various physical and chemical effects. Ever-changing environmental conditions influence the stability of slopes through a variety of processes causing deformations, erosion or other damage. The work of the various agencies and the extent of the damage may be extremely diverse. Some minor decays may ruin the appearance of a slope without endangering its stability or proper use. However, if the start of damage is neglected or its cause remains unrevealed, the situation may rapidly deteriorate and initially small trouble spots may extend over increasingly large masses of soil, so that finally the earthwork completely fails to serve its purpose.

The harmful effects on the stability of slopes can be categorized with regard to many different characteristics. Table 2 shows an example of such a categorization. Three main groups can be distinguished. The effects of weather — precipitation, variation in temperature, movement of air — listed in group *I* are the most important. Other natural forces form group *II*, and effects due to activities of man are listed in group *III*.

Among atmospheric effects, the work of water is the most significant. Surface water causes erosion. Initially narrow and shallow gullies cut by run-off water become widened and deepened in the course of time, while the debris of erosion is deposited at some lower elevations. All these effects may considerably damage surface drainage works. Water percolating in the soil exerts seepage forces and in loss it may cause collapse of the soil structure. Cohesive soils undergo seasonal swelling and shrinkage. Hydrostatic pressure induces neutral stresses in the soil with a consequent reduction

in the shear strength. The slopes of dykes and canals are continually exposed to erosion by wash and wave effects.

A rise of temperature causes water to evaporate from the near surface zone of the soil. This leads to the formation of shrinkage cracks. Water may fill the cracks and penetrate to great depths. Frost causes the formation of ice lenses in fine-grained soils. During subsequent thaw periods large masses of frozen soil become softened resulting in a destruction of structure and an almost total loss of strength. Wind is likely to cause serious damage to slopes of fine sand.

Chemical effects rarely cause slope failure. Decomposition of the solid part of the soil, reduction in shear strength because of cation exchange, etc., may be mentioned in this sub-group. The presence of carbon dioxide in the atmosphere can be very injurious to calcareous stone.

Sometimes tectonic effects come into play. Slow movements in the earth's crust cause a steepening of slopes, usually associated with soil-creep. Earthquakes may have violent effects. Shear waves that propagate near the ground surface give rise to horizontal forces which change the magnitude and direction of the resultant body force acting on the slope essentially and cause additional shear stresses in the soil.

Biological effects of plants and animal life can occasionally be very significant. Holes burrowed by moles and other pests pipe water through or beneath embankments and dykes and may have catastrophic consequences.

It is commonly recognized that vegetation provides an effective means of slope protection, but sometimes it can be harmful. Plant roots growing in construction joints exert a wedging effect, and they can also clog outlet of drains. Growth of weeds on roadsides and in railway ballasts can be very harmful.

Table 2. Harmful effects on earthworks

I. Physical influence of the atmosphere	II. Further impact of nature	III. Artificial impacts
1. Activity of water (a) Erosion caused by run-off water (b) Rainwater infiltrating in the underground (c) Activity of the groundwater: Permanent groundwater table Gravitational flow Capillary rise 2. Influence of temperature (plus water) (a) Drying, shrinkage (b) Penetration of frost (c) Warm springs 3. Air movement (a) Wind erosion (b) Abrasion	1. Actions of water (a) Scour caused by water, lakes and lakelets, river, wave action (b) Impact of springs 2. Influence of gravitation; slow deformations 3. Chemical effects (a) Exchange of bases (b) Other chemical processes (leakage, dissolution, etc.) 4. Tectonic movements (a) Slow creep of the crust (b) Earthquake 5. Biological effects (a) Animal (b) Vegetation (c) Bacteria	1. Influence of water (a) Development of water pressure, water head, pore-water pressure, seepage from ducts 2. Loads (a) Own-weight (b) External load 3. Dynamic effect (a) Traffic (b) Miscellaneous activities (pile driving, etc.) 4. Further activities (a) Overcompaction (b) Stabilization

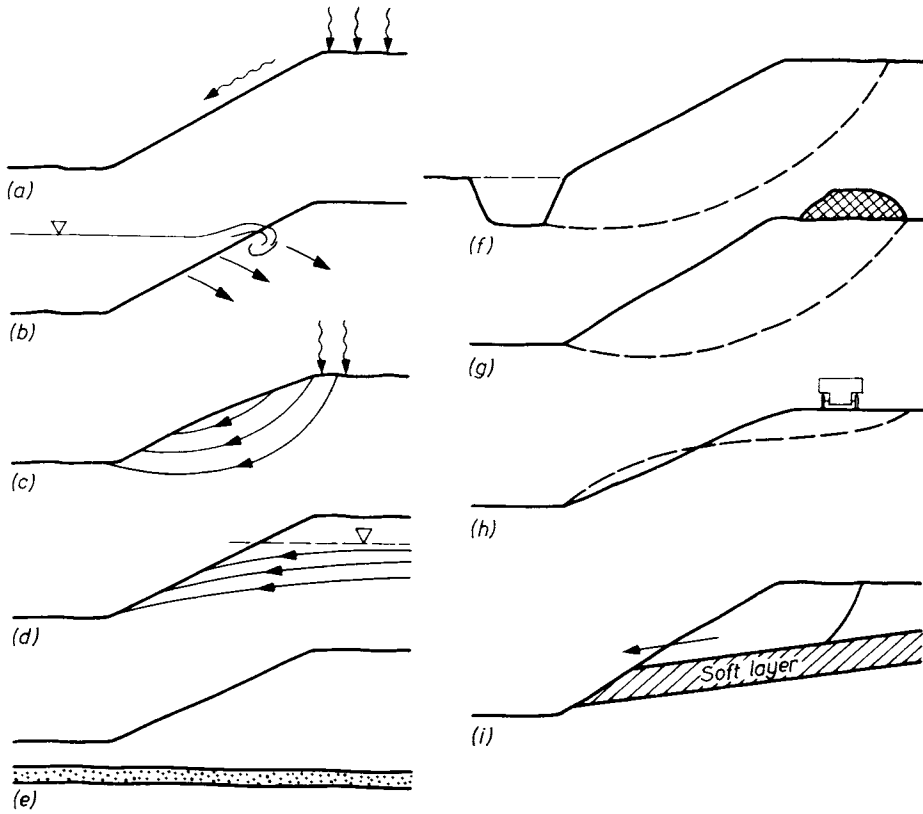


Fig. 40. Some harmful instances which may influence the stability of slope:
 a — erosion caused by runoff water; b — wave action; c — increased seepage pressure due to infiltrating rain water; d — lowering the groundwater table; e — increased water pressure in thin embedded sand layers; f — excavation at the toe; g — surcharge load; h — trembling due to traffic; i — slide on the surface of a stiff inclined layer

Exceptionally, bacteria may cause damage to slopes.

In group III — man's interference — overstressing of the slope should be mentioned first. In this respect, the term 'overstressing' is used for

all such changes in load which tend to increase the shear stresses in the danger zone of a slope. For example, a minor excavation or cutting down at the toe also increases the shear stresses on a potential slip surface. Initially, soil-creep takes

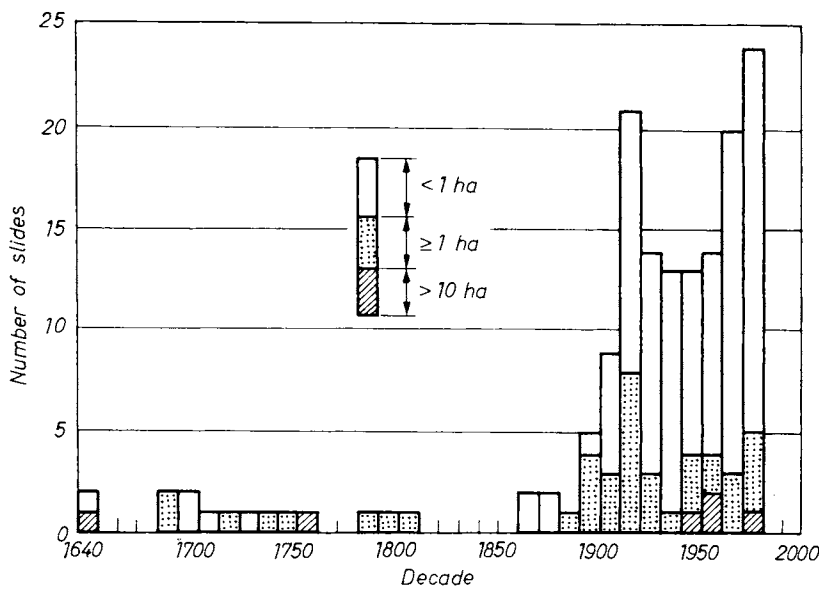


Fig. 41. Landslide frequency with time in Sweden (VIBERG, 1981)

place, resulting in a further reduction of the shear resistance. Inadequately compacted fills subside under their own weight and may become badly deformed. Additional loading at the top of the slope due to spoil tipping, buildings, plants, etc. may be the cause of imminent sliding. It is worth noting that not only loading, but also unloading of a slope may have detrimental consequences.

Dynamic effects caused by traffic, operating machines, pile driving, etc., can be dangerous, especially in cohesionless soils.

Some of the factors endangering the stability of slopes are illustrated in Fig. 40.

Interesting statistical inventories have been compiled in Sweden relating the frequencies of extended landslides in the last three and a half centuries (VIBERG, 1981). As can be seen from Fig. 41, the number of landslides covering areas between one and ten hectares became markedly significant after 1890 and 1940. The reasons for these increases are probably mainly due to the construction of the railway system at the end of the 19th century and the rapid urban development after World War II. Before 1850, the frequency of landslides was probably only affected by natural causes. There were long periods without large landslides and this implies that such landslides are triggered by transient rapid causes such as extremely wet years and earthquakes rather than slow continuous processes such as land upheaval or annual erosion.

1.3.2 The effect of water and precipitation on the stability of slopes

In Vol. 1, Chapter 5, we discussed the body forces that are induced by the flow of water in a mass of soil and the different ways of combining all body forces to obtain their resultant. For such computations it is required that a flow net be constructed on the basis of which the resultant water pressure acting on a potential slip surface can be determined and the stability of a slope investigated by means of the methods discussed in Section 1.2.

Figure 42 shows a slope which is entirely submerged. The soil is saturated and the water is at rest. A body of soil bounded by a potential slip surface AC is acted upon by its own weight and by water pressure on the face of the slope and along the slip surface, respectively. The total weight of the body ABC may be written as

$$V\gamma_{\text{sat}} = V(\gamma'_{\text{sat}} + \gamma_w)$$

Along the boundary surfaces, neutral pressures act. Since there is no flow of water, these can be determined as hydrostatic pressures. The resultants of the boundary water pressures are the forces U_1 and U_2 . These two, added vectorially to the total weight W , give the resultant body force R which, as can be seen from the force polygon in Fig. 42, is equal to the submerged weight

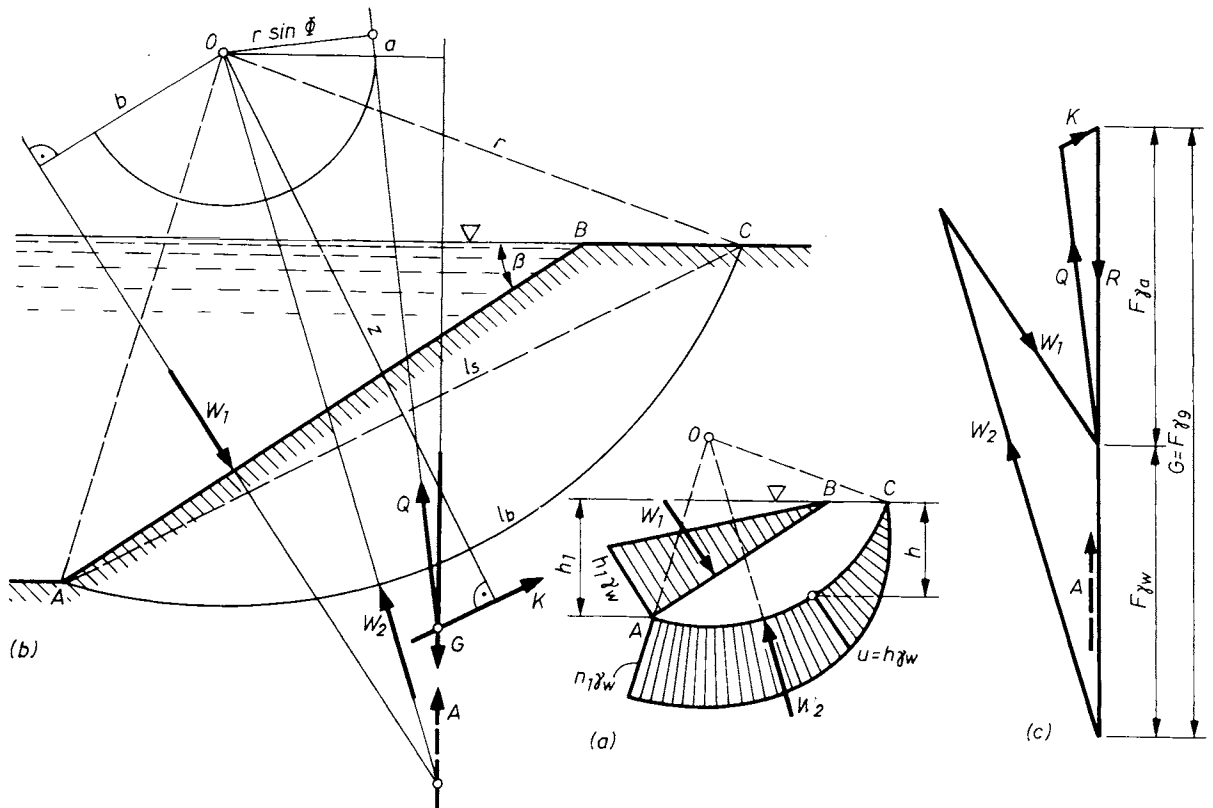


Fig. 42. Stability analysis of a slope below free water level:
 a — distribution of the water pressure on the sliding wedge; b — forces acting on the sliding wedge; c — diagram of forces

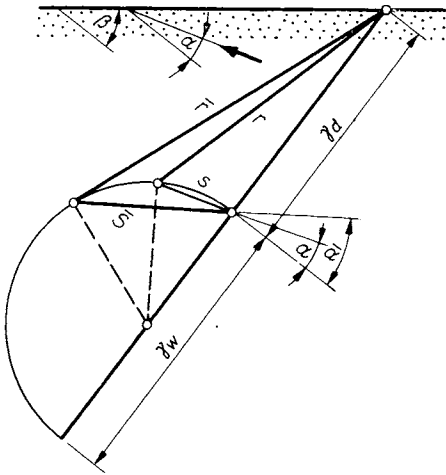


Fig. 45. Determination of the critical flow direction

and

$$\beta = \tan^{-1} \left(\frac{\gamma_{sat}}{\gamma'_{sat}} \tan \varepsilon \right). \quad (60)$$

A slope in a cohesionless soil remains stable only if $\beta < \Phi$. The limiting angle of the slope ε can be obtained by setting $\beta = \Phi$. Assuming that $\gamma'_{sat} \approx \gamma_{sat}/2$ we obtain $\tan \varepsilon_{max} \approx 1/2 \tan \Phi$, as was derived by BERNATZIK (1947).

If the seepage is not parallel to the surface of the slope, the critical flow direction can be determined as follows.

Figure 44 shows the cross-section of an infinite cohesionless slope. Consider an element of unit volume located immediately beneath the surface. The forces acting on the element are the submerged unit weight γ'_{sat} and the seepage force p . The slope is in a limiting state of equilibrium when the quotient of the forces parallel and normal to the surface of the slope is equal to the friction coefficient $\tan \Phi$. In Fig. 45 the triangle of force is shown in a cross-section of the slope. The submerged unit weight is represented by the vector OO' . Prolonging this vertical line, we also plot γ_w on it and using this as diameter, we construct a circle. The resultant body force pertaining to an arbitrary seepage direction can be determined by drawing a line from the lower end of vector

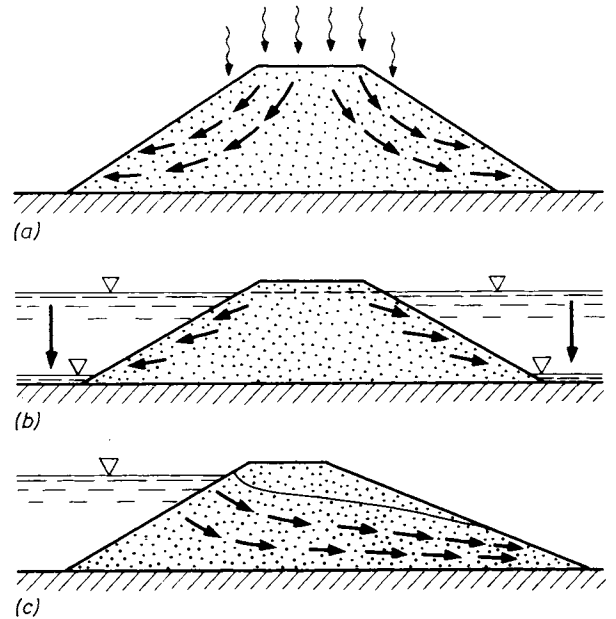


Fig. 47. Seepage pressure in the body of a dam owing to: a — long lasting rain; b — sudden depression of the water level; c — permanent seepage

γ'_{sat} parallel to the direction of flow. Its point of intersection with the circle furnishes the vector of the seepage force p . The resultant body force per unit volume is represented by the vector r . The magnitude and direction of the most dangerous resultant can be determined by drawing a vector from O tangential to the circle. The critical direction of seepage can be obtained from the expression

$$\cos 2\alpha_{cr} = \frac{\gamma_w}{2\gamma'_{sat} + \gamma_w}.$$

Figure 46 shows, for $\Phi = 30^\circ$, the limiting angle β of an infinite slope as a function of direction of seepage.

Let us now consider the seepage which arises when an embankment is exposed to a heavy rainstorm, or when the free water level adjoining the slope is suddenly lowered (rapid drawdown). The embankment (Fig. 47) is made of sand having no or a negligibly small cohesion. The base of the fill is assumed to be practically impermeable.

In dry weather the water is held in the voids of the soil by capillary forces. The neutral stresses have negative values, and since the shear strength of the soil is governed by the general relationship $\tau = (\sigma - u) \tan \Phi$, a negative value of u causes an increase in shear strength. As a result, the embankment is more stable than it would be if the soil were completely dry.

During a heavy rainstorm, water enters the fill through the crest and the slopes and drains out through the lower part of the slopes (Fig. 47a). Under unfavourable conditions, this may lead to a permanent flow in the fill.

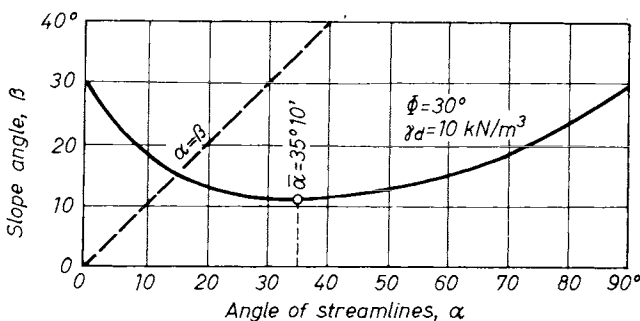


Fig. 46. Critical slope angle as a function of flow direction

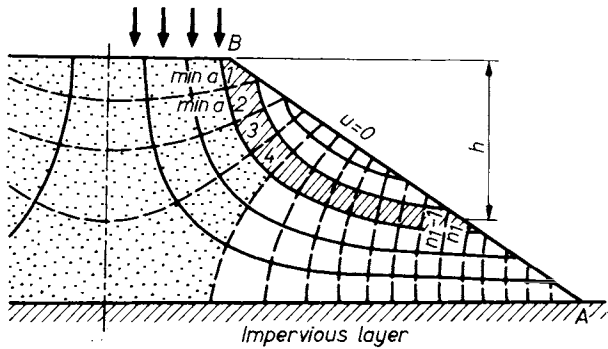


Fig. 48. Flow net diagram in a dam over an impermeable subsoil in the case of stormy rains or abrupt loss of water head

The boundary conditions required for the construction of the flow net are as follows: the impervious base and the axis of symmetry of the section are flow lines; the crest of the embankment is an equipotential line; the neutral stress at any point along the face of the slope is zero. Figure 48 shows the complete flow net. In order to maintain a permanent flow, a certain intensity of rain is necessary. The quantity of water which enters the embankment between two adjacent flow lines must be the same in each one of the channels. Therefore, the rate of precipitation per unit of area of the surface of entry is greatest where the distance between two consecutive flow lines is smallest. This condition exists at the edges of the crest. Let the width of the channel formed here be a_{min} . The total head lost as water seeps through the channel is h , and since the number of drops passed is n_1 , the potential drop as water moves from one equipotential line to the next is $\Delta h = h/n_1$. Near the edge of the crest (point B) the hydraulic gradient is $i = \Delta h/a_{min}$. The intensity of rain (i.e., the quantity of water per unit of area and unit of time) necessary to maintain a steady flow of water through the embankment is

$$v = ki = k \frac{\Delta h}{a_{min}} = \frac{k}{a_{min}} \frac{h}{n_1}$$

During heavy rainstorms this condition is normally satisfied for every embankment made of fine or silty sand.

A similar seepage occurs in an embankment which had been flooded on both sides for a sufficiently long period of time to become fully saturated and where the water level is suddenly lowered (Fig. 47b). The water draining out of the embankment exerts a seepage pressure acting outwards on the material of the fill; since the neutral stresses have positive values, the shear strength of the soil is greatly reduced, as is the stability of the embankment. Experience shows that in embankments made of very fine sand most troubles occur during heavy rainstorms or immediately after a sudden drawdown. A different flow net is developed in an earth dam through which

seepage of water occurs toward the downstream slope (Fig. 47c). This case is all the more involved since the location of the top flow line is indeterminate. (For a detailed discussion of this problem see Section 1.5). Whichever is the case, the flow of water induces seepage forces inside the embankment which must be taken into account in the stability analysis.

The stability analysis is illustrated by Fig. 49. We assume a circular slip surface which starts at a point near the centre of the crest and is tangential to the impervious base of the embankment. The most dangerous slip surface can be found by trial and error. Drawing a trial circle, we determine the weight W_1 of the sliding mass using the saturated unit weight γ_{sat} of the soil. The weight acts at the centre of gravity of the sliding body. In a cohesionless soil the only resistance to sliding is that due to internal friction. In the instant of failure, the resultant of the elementary frictional forces is tangential to the friction circle drawn with radius $r \sin \Phi$ from the centre of the slip surface. The neutral stresses induced by seepage are normal to the slip surface, and pass through the centre O . The neutral stress at an arbitrary point such as P is given by the expression $u = h' \gamma_w$, where h' is the difference in elevation between the point P and the point where the equipotential line passing through P

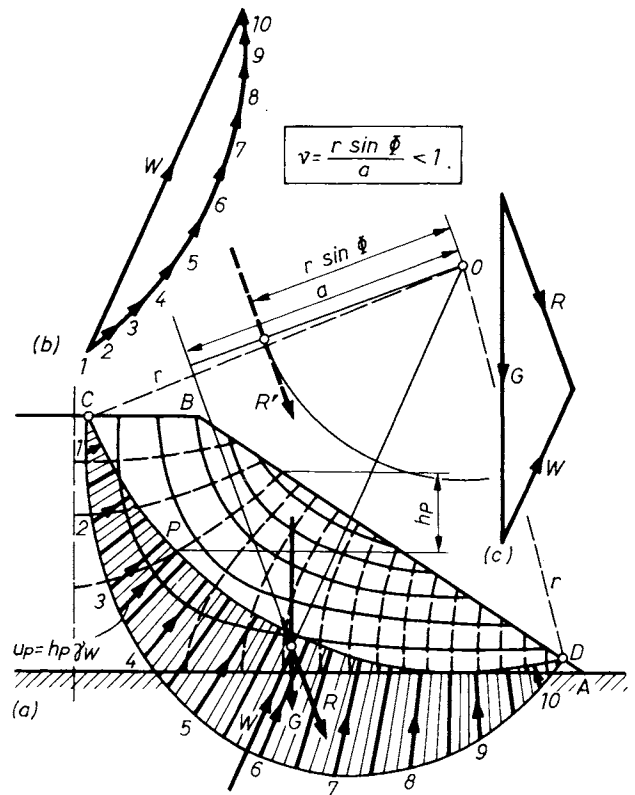


Fig. 49. Investigation of slope stability in sandy soil after the sudden lowering of the water level: a — cross-section of the dam, flow net diagram and pressure distribution; b — determination of resulting water pressures; c — diagram of forces

intersects the surface of the slope. Hence the distribution of neutral stresses along the slip surface is known. The elementary forces acting on small sections of the slip surface can be computed and their resultant U_1 determined by means of a polygon of force.

In the case of equilibrium the three forces, W_1 , U_1 and Q , must be concurrent and their vector polygon must close. Unless the force Q obtained from the construction intersects or just touches the friction circle, the seepage induced by a rain-storm or by a rapid drawdown causes failure of the slope. The safety factor with respect to sliding is

$$v = \frac{r \sin \Phi}{d}$$

If the material of an embankment has an appreciable cohesion, it can be taken into account in the same way as in the usual methods for stability analysis of slopes (Fig. 50). We draw the action line of the force of cohesion parallel to the chord of the slip surface, at a distance $z = rl_a/l_c$ from the centre O , and determine the cohesion c_1 , required to maintain stability. To this end we construct the resultant Q_1 of the forces W_1 and U_1 and make its line of action intersect the force C_1 . From the point thus obtained we draw the action line of Q so that it is tangential to the circle of friction. The polygon of forces furnishes the magnitude of the required cohesion C_1 . By comparing this force with the available cohesion of the soil, the degree of stability can be estimated. In order to obtain a numerical value for the safety factor, we determine, by drawing a line parallel to O_1M in the force polygon, the cohesion that would be required if there were no frictional resistance. Its magnitude is equal to $C_1 + S$. Hence the safety factor is

$$v = \frac{S + C_{\text{available}}}{S + C_1}$$

The method just described can be applied to the investigation of any stability problem associated with seepage; for once the flow net is constructed, the neutral stresses induced by seepage can readily be determined and entered in the stability analysis.

The method explained in the foregoing is rather tedious, since the whole procedure should be repeated a number of times in order to find the lowest value of the safety factor. Besides, the flow net may, in reality, be greatly influenced by local variations in the permeability of the soil, and an approximate method will often do just as well. One such method which is applicable to flat slopes ($\rho > 10/4$), is illustrated in Fig. 51. In the case the equipotential lines shown, are approximately vertical and the error we make by assuming that they are truly vertical is negligible. The resultant U of the neutral stresses can thus be

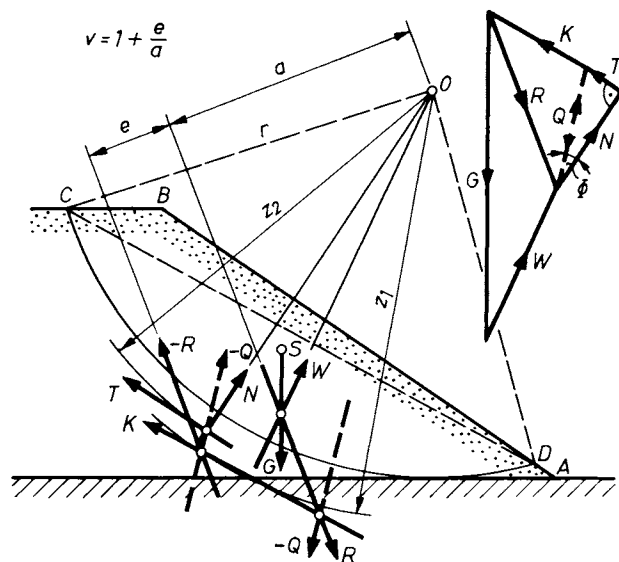


Fig. 50. Slope stability analysis ($c \neq 0$) after sudden lowering of the water level (application of Fröhlich's method (1950))

assumed to pass through both the center of gravity of the potential sliding body and the centre O of the slip surface. Let the angle it makes with the vertical be α . The vertical component of the resultant water pressure U is approximately equal to the cross-sectional area A of the sliding body multiplied by the unit weight of water γ_w . Therefore the resultant U need not be determined from the force polygon, but can simply be written

$$U = \frac{A\gamma_w}{\cos \alpha}$$

With U known, the further procedure is the same as that used in the examples previously discussed.

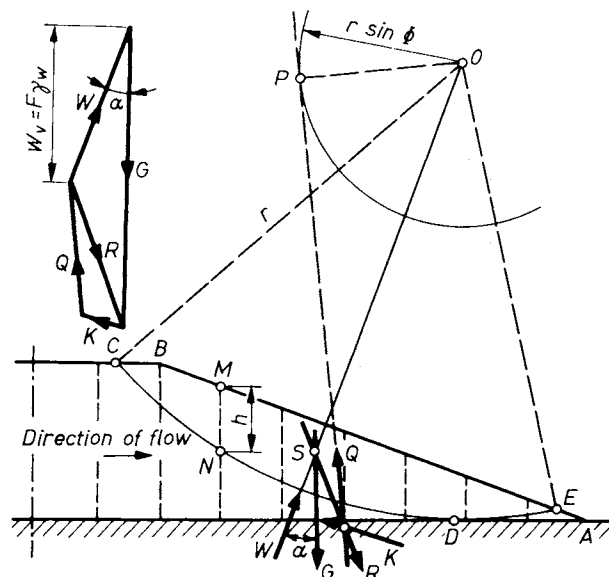


Fig. 51. Simplified stability analysis: assumption of horizontal flow lines

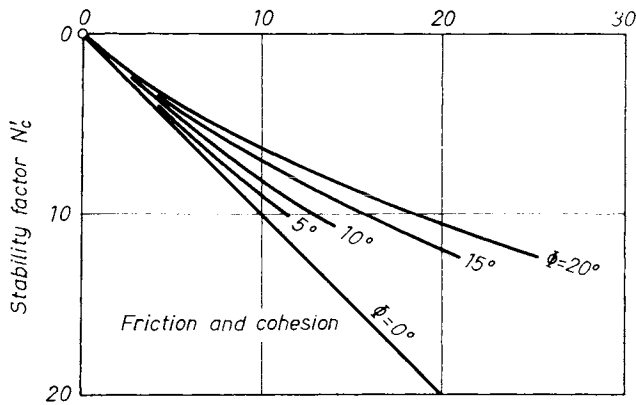


Fig. 52. Values of the stability coefficient N'_c in the case of an abrupt decrease in water level

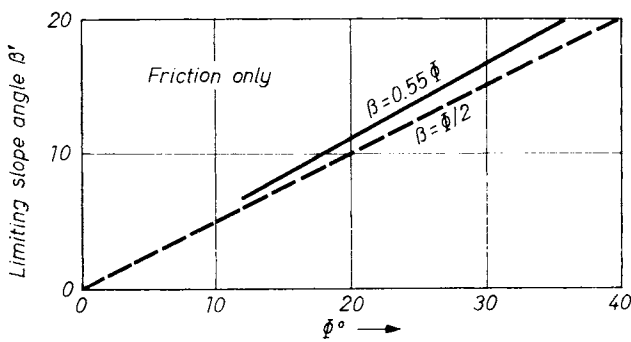


Fig. 53. Inclination limit of a sand slope in the case of an abrupt decrease in water level

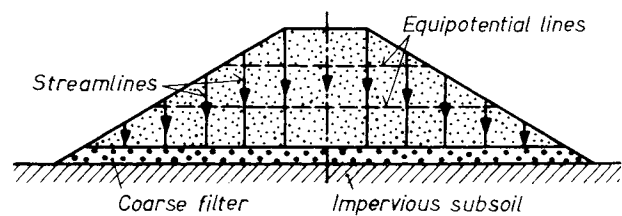


Fig. 54. Vertical stream lines resulting from a horizontal permeable layer constructed at the base of the dam

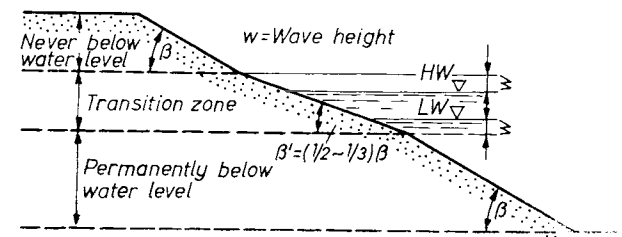


Fig. 55. Construction of a dam slope with respect to fluctuation of the water level

For details see Fig. 51. The minimum of the safety factor can again be obtained by iteration.

Another short cut in the stability analysis is provided by the use of design charts based on

stability numbers taking into account the effect of seepage. An analytical approach would have been far too complicated and therefore stability numbers, corrected for seepage, have been determined by a great number of graphic constructions. The results are shown in Fig. 52. Reciprocals of Taylor's stability numbers are plotted on the horizontal axis and $1/N'_c$ values on the vertical axis, where N'_c is the stability number corrected for the seepage case shown in Fig. 48. Numerical values for various angles of internal friction Φ can be read off from the set of curves.

Let, for example, $\Phi = 20^\circ$ and $N_c = 15$. From Fig. 52, the stability factor corrected for seepage is $N'_c = 8.6$. For a slope 15 m high with a unit weight of soil $\gamma_{sat} = 20 \text{ kN/m}^3$, the cohesion required for stability when no seepage is occurring is

$$c = h\gamma_{sat}/N_c = 15 \times 20/15 = 20 \text{ kN/m}^2.$$

After a sudden drawdown the slope only remains stable if the available cohesion is not less than

$$c = h\gamma_{sat}/N'_c = 15 \times 20/8.6 = 35 \text{ kN/m}^2.$$

For cohesionless soils an approximate relationship for the safe angle of slopes subjected to seepage effect is given in Fig. 53. According to this, the slope of an embankment in which a flow net similar to that shown in Fig. 48 is developed, does not remain stable unless its angle to the horizontal is less than 0.55Φ .

The preceding discussion has clearly shown how seriously the stability of a slope could be affected by seepage of water. Fortunately, there are a number of ways of preventing failure. For example, if a coarse-grained filter is placed immediately beneath the base of the embankment, all the flow lines become approximately vertical and the equipotential lines horizontal (Fig. 54). It follows that the neutral stresses inside the fill become zero and thus will not affect the stability of the embankment during rainstorms.

Another precautionary measure consists of flattening the slope. Figure 55 shows a typical profile recommended for slopes of canals and reservoirs in cohesionless soils when a wide variation in water levels is expected. The surface of such slopes can be divided into three parts. The highest water level plus the wave height a gives the upper limit and the lowest water level minus the wave height a gives the lower limit of that central zone which is likely to be affected by seepage. Above this buffer zone the slope never becomes submerged and below it the slope is constantly under water. The top and bottom sections of the slope can be made with a safe angle β normally permitted for static conditions, but the central part must be flattened with a reduced slope angle of $\beta/2$ to $2/3\beta$.

Among the many effects of water on the stability of slopes, yet another, the pressure of water

filling tension cracks near the surface, is worth mentioning. Embankments made of, and cuttings excavated in cohesive soils are subject to desiccation during dry spells, especially if their slopes are not yet protected by vegetation. As a consequence, deep, wide cracks may develop in the tension zone near the surface. If they become filled with water during torrential rain, the stability of an otherwise safe slope may be seriously endangered. The primary cause of reduced stability is normally not the decrease in cohesion of the soil due to soaking by water, since this is a relatively long process, but the instantaneous effect that the outward pressure of the water filling a crack exerts on its side. In such case the stability analysis can be performed according to Fig. 56. The depths to which the cracks penetrate can be assumed to be approximately equal to

$$z_0 = \frac{2.67c}{\gamma} \tan \left(45^\circ + \frac{\Phi}{2} \right) = 1.33q_u/\gamma$$

The effect of water pressure in the cracks may occasionally be very significant. Taking, for example, a cutting 10 m deep with slopes $\rho = 6/4$, the safety factor with respect to sliding may drop from $v = 2$ to $v = 1.4$.

The significance of precipitation can duly be proved by histograms which show, in a monthly arrangement the frequencies of the precipitation and slides (VIBERG, 1981). In Fig. 57 the number of slides — that occurred in Sweden — is plotted against the month in which a slide was observed. There are two peaks in the histogram for the whole of Sweden, one in the spring and one in the autumn. The geographical separation of the slides illustrates that the slide frequency is greatest during the autumn months in southern Sweden and during the spring months in northern Sweden. A similar pattern exists in Norway (note that a continental climate prevails in both countries). Most slides occur during the wet seasons when pore pressures and the activity of erosion are at their peak. Obviously, the fact that evaporation is at a low rate and evapotranspiration is completely absent in autumn and winter may contribute to this outcome.

In sensitive clay deposits in Quebec, Canada, LEBUIS and RISSMAN (1979) have established a histogram which gives a very predominant peak during the months of April and May when snowmelt combined with rain can produce the worst possible conditions of infiltration. The groundwater recharge due to snowmelt is also a predominant factor in Quebec; in fact, nearly all the major landslides in Eastern Canada have occurred during springtime.

MANFREDINI *et al.* (1981) have observed in the Sinni-Valley in Italy that the rate of transient landslides depends not only on the intensity of the precipitation which occurs during the observation period, but also on that of the directly

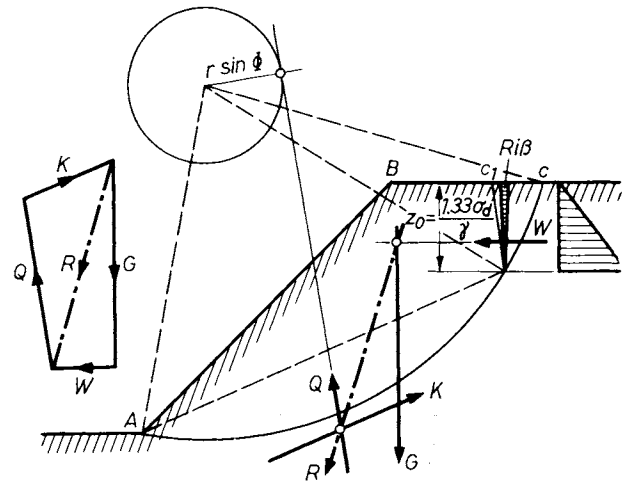


Fig. 56. Stability analysis with respect to the water pressure in tension cracks

previous period. The maximum sliding velocity ensues normally in one month after the maximum rainfall. In the first years of the study, the speed of the slide approached 0.5 m per year, with marked absence in summer. The speed has gained impetus since 1976 probably due to the beginning of a long-lasting wet epoch. Inclinometers that have been embedded in the sliding mass have also proved that sliding was always initiated in winter. (It has to be noted that the climate in that region

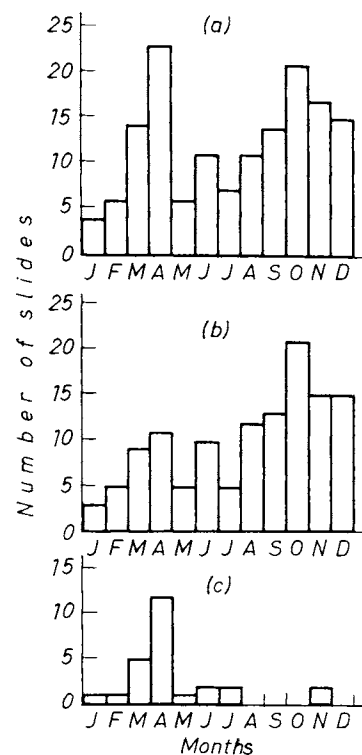


Fig. 57. Monthly distribution of landslide frequencies (VIBERG, 1981):

a — in the whole of Sweden; b — the southern and c — northern Sweden

is Mediterranean — contrary to Sweden and Norway — and most of the precipitation occurs in autumn and winter).

1.3.3 Effect of excess pore-water pressure

The stability of a natural hillside or an artificial earthwork can be seriously endangered if the subsoil contains water-bearing seams or lenses of sand in which high pore-water pressures may develop. It is characteristic of this type of failure that a relatively gentle slope or hillside, which has previously been stable, moves out suddenly or slumps while the ground in front of the toe bulges. An explanation of this phenomenon was given by Terzaghi. He showed that if the pore pressure in the seam of sand is great enough to reduce the shear strength to zero, the critical height of the overlying slope is equal to the critical height of a vertical slope, regardless of the actual slope angle. This statement can be verified as follows.

Figure 58 shows a cutting of depth h which has been excavated in a clay. The base of the slope, as well as every horizontal plane located further below, is acted upon by shear stresses, because the soil mass adjoining the slope tends to settle vertically and, at the same time, to expand laterally under its own weight. Beneath the base, there is a water-bearing seam of sand, 1-2, in which the pore water is under pressure. The shear strength of the sand is determined by the equation $\tau_s = (\sigma - u) \tan \Phi$. A critical condition arises when $u = \sigma$ and hence $\tau_s = 0$. The equilibrium of the soil body, $a12b$, depends on the ratio of the active and passive earth pressures acting on the vertical sections $a1$ and $b2$, respectively. In the limiting state of equilibrium

$$E_a = E_p.$$

Assuming zero friction, we get

$$E_a = \frac{1}{2} \gamma(h + h_1)^2 - 2c(h + h_1)$$

and

$$E_p = \frac{1}{2} \gamma h_1^2 + 2ch_1.$$

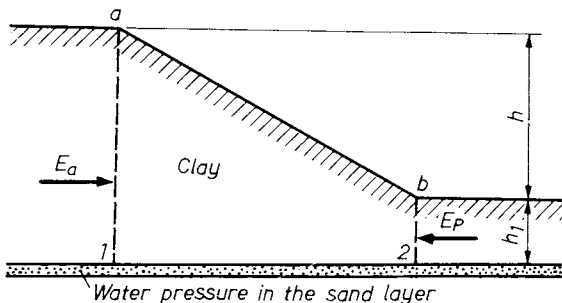


Fig. 58. Investigation of equilibrium conditions of a slope block: there is water pressure in the sand layer, effective stress is zero

Equating E_a and E_p gives

$$h_{cr} = h_0 = \frac{4c}{\gamma},$$

which is the theoretical expression for the critical height of a vertical slope in the case that $\Phi = 0$.

Geological conditions favourable for the build-up, from time to time, of exceptionally high pore-water pressures in thin layers of sand are responsible for recurring landslides on the highway and railway line along the NE shore of Lake Balaton in Hungary, which is flanked by high banks in which all prerequisites for failure by spreading occur. The soils of the bank are generally wet and soft with an average water content of 35 to 45%. Their shear strength is very low, even if the effect of pore-water pressure is not taken into consideration. Relatively thick strata of silt and impervious clay are interspersed with water-bearing seams of sand and coarse silt, some of which apparently communicate with a layer of gravel which covers large areas of the upper terrain. During wet seasons, rain water infiltrates the soil and percolates through the seams towards the lake, thereby causing the piezometric levels in the seams to rise considerably. Usual remedial works utilizing buttress drains, shafts and headings, etc., have not proven successful, at least on an economic scale, in arresting the movement of the sliding masses. The affected section of the highway and railway track therefore had to be abandoned altogether. A new dual rockfill embankment was built in the lake bed at a safe distance of 100 to 150 m from the shoreline.

If the seam of sand is not horizontal, and the pore-water pressures acting in it are known, the stability of the slope can be investigated according to Fig. 59. A section through the slope is shown in Fig. 59a. The dashed line indicates the piezometric level for the pore water in the seam 1-2. We have to determine the forces acting on the block of soil $a12b$. The vertical sections $a1$ and $b2$ are acted upon by active and passive earth pressures, respectively. The weight of the block induces normal and shear stresses on the plane 1-2. These are given by the expressions $\sigma = h\gamma \cos^2 \epsilon$ and $\tau = h\gamma \sin \epsilon \cos \epsilon$. σ is the total normal stress, whence the effective normal stress can be obtained by subtracting the neutral stress: $\bar{\sigma} = \sigma - u = \sigma - h' \gamma_w$. The shear strength expressed in terms of effective stresses, is

$$\tau_s = \bar{\sigma} \tan \Phi = (\sigma - h' \gamma_w) \tan \Phi.$$

The distribution along the plane 1-2 of the shear and normal stresses and of the frictional resistance are shown by the graphs (b), (c) and (d) in the lower part of Fig. 59. The safety factor against sliding can be computed as the sum of the forces which resist sliding divided by the sum of the forces which tend to produce it

$$v = \frac{E_p \cos \epsilon + \int_1^2 \tau_s dx}{E_a \cos \epsilon + \int_1^2 \tau dx}.$$

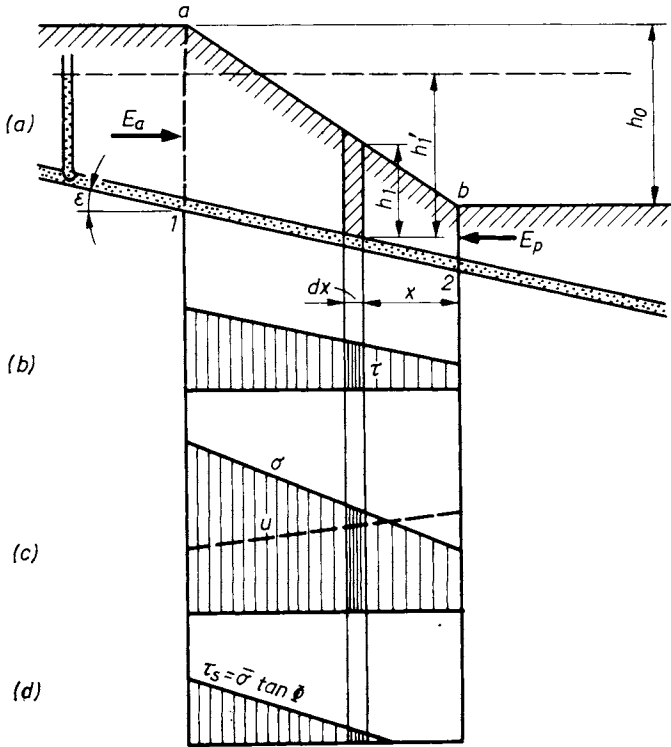


Fig. 59. Investigation of equilibrium conditions in a slope block with known piezometric heads and an inclined sand layer in it:

a — cross-section and piezometric head; b — shear stresses; c — normal stresses; d — shear resistance

High pore-water pressures in seams of sand can be very dangerous to natural slopes even if the seams outcrop at the surface. Such geological conditions are common in flood-plain deposits which were formed during alternating flood-water and low-water periods, and also in delta deposits. The subsequent formation of erosion valleys or river beds in such layered deposits may create extremely treacherous conditions involving a perpetual danger to the stability of banks and hillsides. Flood-plain deposits are, as a rule, not horizontal since the original terrain itself had been very uneven and undulating. It is possible that some of the thin water-bearing layers outcrop on the surface at some higher elevations. At such spots precipitation may soak away through a vein of sand. The piezometric level in the seam drops constantly towards the lower end where water issues freely and its pressure diminishes to zero, but locally very high pore-water pressures may develop on intermediate sections of the seam. Particularly high pore-water pressures are likely to occur if the permeability of the sand gradually decreases at lower elevations, or if the seam is choked up, for example, by frost action.

Figure 60 shows the stability analysis of a natural slope in a soil containing a water-bearing seam. In the first step we compute the normal and shear stresses along the plane 1-2. Next we determine the neutral stresses in the seam (Fig. 60b). It is only the effective normal stresses that

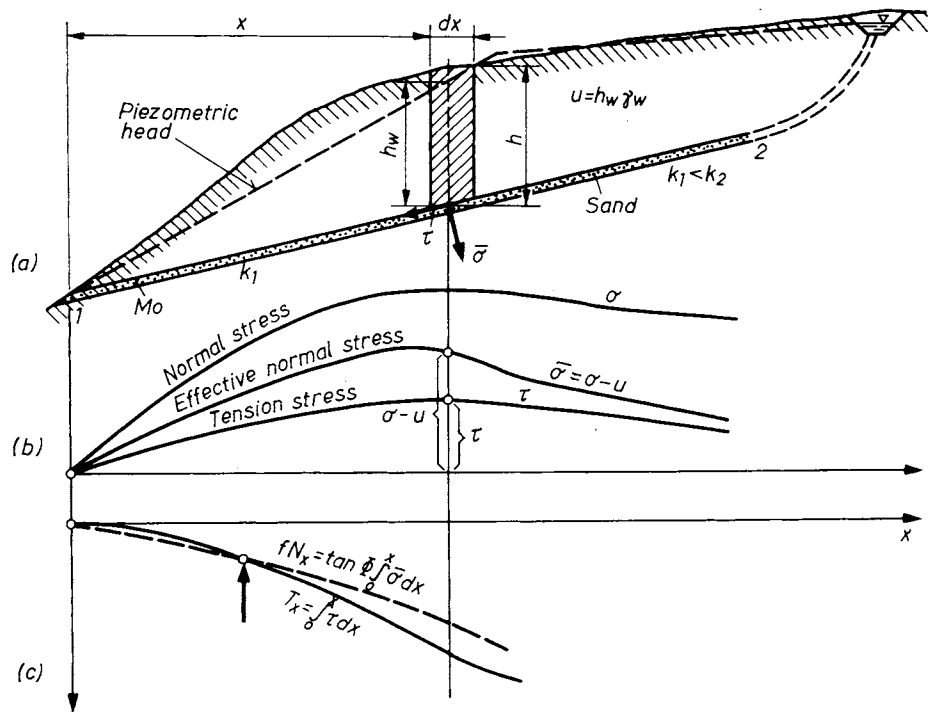


Fig. 60. Establishing the location of the critical vertical section

produce frictional resistance. The total of the shear resistance up to a section at some arbitrary distance from the outlet is given by the integral

$$fN_x = \tan \Phi \int_0^x (\sigma - u) dx.$$

The two curves in Fig. 60c show the variation with x of the integrals of the shear resistance fN_x and of the shear stresses $T_x = \int_0^x \tau dx$, respectively.

Failure starts over that section where T_x exceeds the value of fN_x .

Among the manifold effects of water on the stability of slopes we have not yet mentioned its lubricating action. As we pointed out in Vol. 1 (Chapter 7) water, in its interaction with solid mineral particles, is an antilubricant. The common observation that the strength of a cohesive soil is rapidly reduced with increasing water content is due to the fact that the void ratio increases with increasing water content and the structure of the soil becomes looser. A saturated clay cannot take up more water unless it swells. It is therefore not the lubricating effect of water, but the swelling of the soil or the action of neutral stresses and seepage forces that cause a reduction in shear strength and ultimately leads to slope failure.

1.3.4 Stabilizing effect of a revetment

Heavy facings made of stones or concrete blocks provide an extra protection for slopes in various ways. Firstly they prevent erosion caused by surface flow and by wind or wave action. They also have an insulating effect, whereby volume changes are greatly reduced. In addition, they

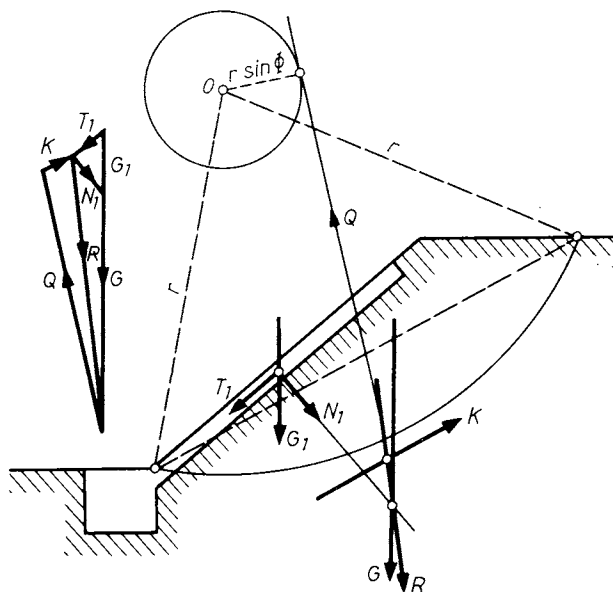


Fig. 61. Effect of lining — stability analysis

increase the stability of the slope in cases where the critical slip surface is a toe circle. This last effect can be evaluated quantitatively as follows (Fig. 61).

The weight of the facing W_1 represents a uniformly distributed pressure on the surface of the slope. W_1 can be resolved into the components N_1 and T_1 . The component T_1 is counteracted either by the frictional resistance on the interface of the slope and the protective lining or by the passive earth pressure at the toe. If the component N_1 is added vectorially to the weight W of the sliding body, the resultant R will decline from the horizontal towards the inside of the earth mass. As a result, the shear resistance necessary to maintain equilibrium is reduced. The cohesive force C required for stability is determined by the polygon of force shown in Fig. 61.

Example. A 1 in 1.25 slope, 8 m high, was provided with a protective concrete layer, 30 cm thick. The cohesion of the soil was $c = 20 \text{ kN/m}^2$, the angle of internal friction $\Phi = 15^\circ$ and the unit weight of the soil $\gamma = 19 \text{ kN/m}^3$. The safety factor for the unprotected slope was $v = 1.5$. With concrete facing it was increased to $v = 1.7$.

1.3.5 Slopes in some peculiar soils

Certain soils show a peculiar behaviour from the point of view of slope stability. Stiff fissured clays with a mosaic structure are an example. The properties of this type of soil were discussed in detail in Vol. 1, Chapter 3. The stability of cut slopes on such soils may be greatly endangered by the slow deterioration of the shear strength of the soil caused by relief from overburden pressure or by weathering.

Example. A 6 m deep cutting was excavated in Hungary in a brown fat clay with a mosaic structure ($w_L = 110\%$, $w_p = 25\%$, $w = 20\%$, $q_u = 300$ to 600 kN/m^2). Temporarily the cut was made with nearly vertical slopes which showed no signs of deterioration for several months. Shortly after the final slopes of 1 to 1 had been made, giving an increased height of 8 m (Fig. 62), a sliding took place. The usual methods of stability analysis, based on a preliminary soil investigation, showed the safety factor to have varied between 3 and 4. The cause of instability was, therefore, to be found in a reduction of the in situ shear strength of the clay. Many factors may have contributed to this effect. Because of the mosaic structure of this soil, the strength measured on a small and intact laboratory sample is invariably greater than the average strength of a large mass of soil, since in reality the surface of rupture tends to follow the lines of least resistance. Furthermore, the negative pore pressures which may develop in a laboratory sample also result in an increase in the compressive strength of the sample. In addition the clay in question was highly expansive, with a linear shrinkage of 18 to 20% and this property led to the formation of shrinkage cracks near the face of the slope. Blasting operations carried out nearby added to the widening of fissures and cracks. The combined action of all these factors inevitably led to failure. In order to estimate the actual value of cohesion that had existed at the time of failure, the equilibrium of the slope was re-examined by a method proposed by FRONTARD (1922). This method is especially suitable for the stability analysis of slopes in stiff fissured clays tending to lose a greater portion of their strength immediately after sliding has begun (FRONTARD, 1954). The analysis based on the observed shape and

location of the slip surface and on the soil properties given in Fig. 62 showed the cohesion at the time of failure to have been as low as 8 to 10 kN/m².

In Hungary, slopes in mosaic clays have been successfully stabilized by means of buttress drains combined, where necessary, with removal of the disturbed masses of soil and replacement by better material (KÉZDI and MARKÓ, 1969).

Loess with a macroporous structure (see Vol. 1, Chapter 3) is extraordinarily susceptible to the effect of water. Very great heights of vertical loess banks can stand provided that the groundwater table is at great depths and the vertical surfaces are not exposed to erosion. Unless protected by vegetation, slopes of cuttings excavated in loess readily deteriorate by erosion. Run-off water erodes deep channels and near-vertical caverns in the loess and causes sloughing and slumps of the slopes. For the reasons mentioned it is recommended that cuts with nearly vertical slopes in loess should be made as shown in Fig. 63. Even such a precaution would not prevent the falling down of large blocks of soil from time to time, and for reasons of safety it is advisable to leave a sufficiently wide berm at the toe of the bank. Deep cuttings should be made with terraced slopes.

Quick clay slides frequently start without any warning and develop very rapidly embracing an area of several hundred thousand of square metres within a few minutes or less. AAS (1981) for example, reported that in Norway about one million cubic metres of earth mass is moving in each fourth year. A nearly horizontal sliding surface and a very gently inclined average slope are characteristic features of this type of motion. The extent of the slide area in the direction of sliding is of the order of 7 to 15 times the corresponding difference in terrain level. The typical quick clay slide is generally described in the literature as a combination of a minor initial slide and a progressive failure process developing very rapidly and spreading in all directions. According to examples in AAS (1981) another common failure mechanism implies a clay mass sliding out as a huge flake. It seems that the failure in quick clay slides might be initiated by:

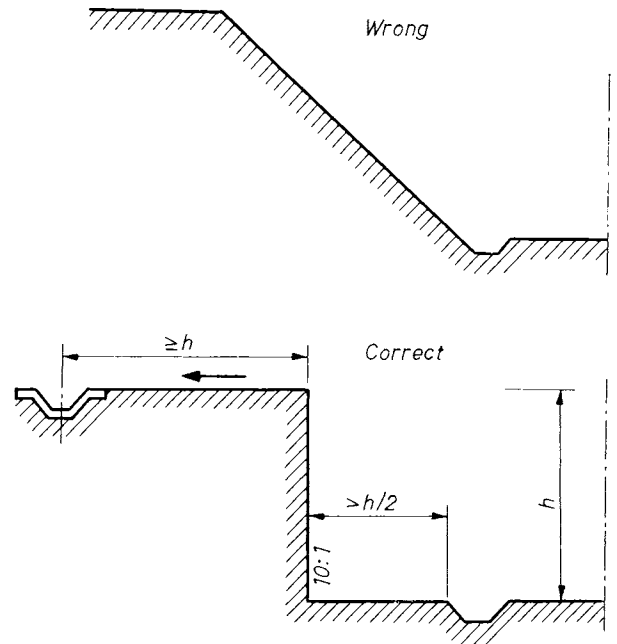


Fig. 63. Proper shape of a cut in loess

— the increase of shear stresses due to intensive erosion caused by the rivers;
 — the increase of the density in the upper layer due to infiltration;
 — agricultural earthwork activities;
 — overloading of the slopes with dumping materials.

Aas conceived that the difference between normal and quick clays consists in the fact that the neutral stress Δu_w increases abruptly in the latter when the indicator

$$\sin \Phi'_{\text{mob}} = \frac{\sigma_1 - \sigma_3}{\sigma'_1 - \sigma'_3}$$

reaches a critical value.

In the case of slides in quick clays in Sweden, Norway and Canada the minimal angle of the terrain was 7 degrees to the horizontal, and VIBERG (1981) concluded from this fact that a stability analysis should always be conducted when the slope has an incline over 6 degrees. According to the author's observations, the char-

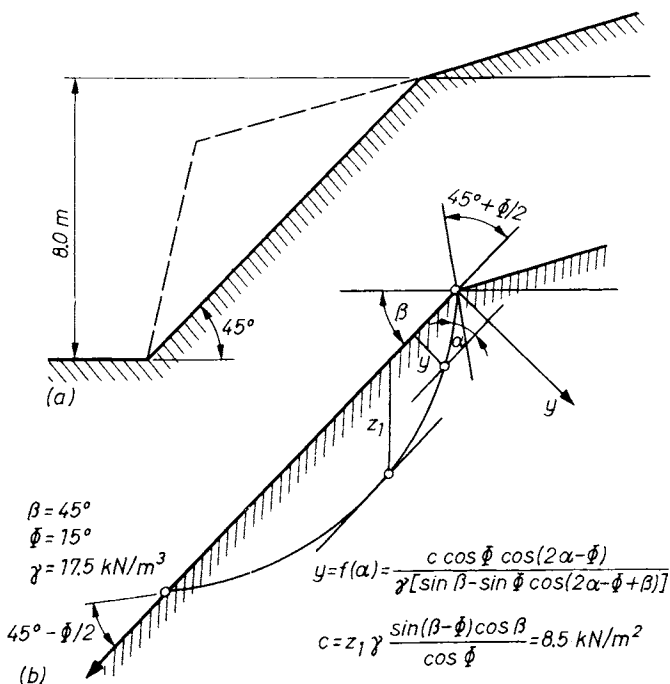


Fig. 62. Sliding of a slope in fissured clay:
 a — flattening the incline; b — assumed sliding surface after FRONTARD (1954)

acteristic shape of quick clay slides is of the "bottleneck" pattern.

It often occurs that a slide of an earth mass ensues over a thin but weak clayey surface. Such has been the mechanism of the "Kimola-sliding" in Finland, described by LEONARDS (1982). Here the slide was triggered because the shear resistance of the sensitive clay was at a low grade. It is probable that tension cracks developed earlier in the ground surface which then became filled with rain water from a sudden storm and thereby the layer became soaked.

1.3.6 Effect of a linear load on the stability of slopes

Should a linear load (p^0) act parallel at some distance (A) from the crest of a slope, two basic situations should be distinguished.

(a) The bearing capacity of the soil is predominant in the case when the shear surface does not intersect the slope and, therefore, the problem will be limited to investigating the neighbourhood of the load (bearing capacity theories would apply to such modes of failure).

(b) Slope failure should be analysed where the critical shear surface extends beyond the crest and hence also a part of the slope is involved in the problem.

The latter case has been studied and solved by BALIGH *et al.* (1977). The authors applied the generalized method of Taylor (see Section 1.2.3.4). The critical curves belonging to various

normalized edge distances (A/H) have been selected first, then the relative p_{cr}^0 values have been calculated. Results are given on Fig. 64. Here also, the particular values of $(\gamma H/c)_{cr}$ are given which correspond to Taylor's solution for failure when the slope is exposed to its own weight alone. The results for steep slopes ($\beta \geq 45^\circ$) show that

1. for small values of $\gamma H/c$ compared to $(\gamma H/c)_{cr}$ the p_{cr}^0/cH value increases linearly with A/H . This linearity basically means that for given values of β , γ , c and A , the critical load is independent of H if the slope has a high safety factor for its own-weight only;
2. for large values of $\gamma H/c$, the surcharge load is small; at the limit, when $\gamma H/c = (\gamma H/c)_{cr}$, p_{cr}^0/cH equals zero;
3. the influence of β can be seen by comparing the results obtained for different values of β ; for given values of $\gamma H/c$ and A/H , p_{cr}^0/cH decreases as β increases, i.e., the steeper the slope, the more important is the influence of gravity, and hence, the smaller the surcharge load. (This decrease in p_{cr}^0/cH with β is also more pronounced for large values of $\gamma H/c$.)

For a flat slope, p_{cr}^0/cH is significantly affected by the location of the bedrock. For given values of $\gamma H/c$ and β , the slope becomes more stable as the depth to bedrock decreases; this results in larger values of p_{cr}^0/cH .

The authors have also investigated the three-dimensional case (when the finite length of the linear load is L_p). In this case, the critical load is:

$$P_{cr} = f_L P_{cr}^0 \quad (61)$$

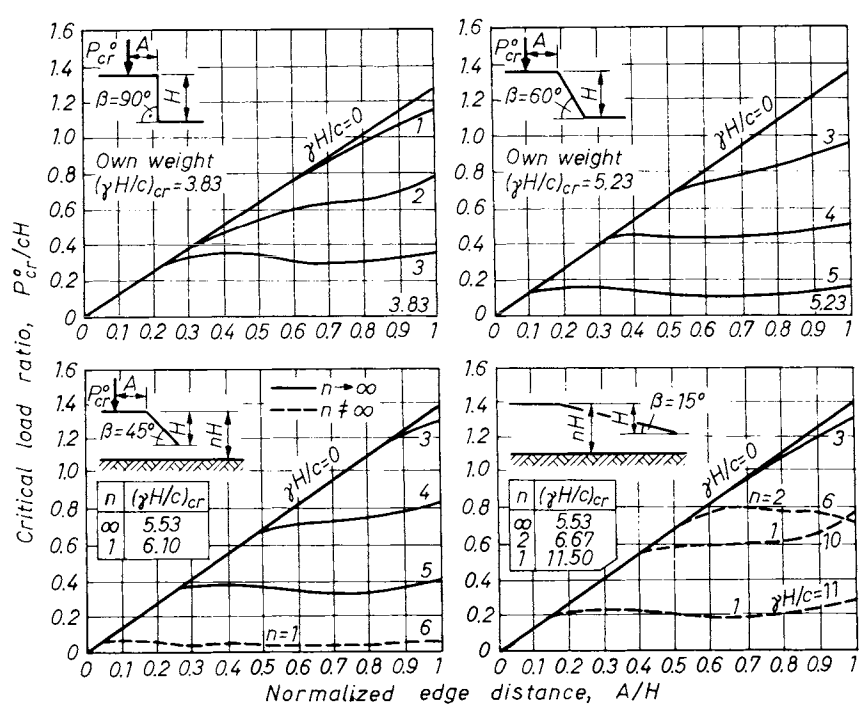


Fig. 64. Stability charts for line loads of infinite extent (BALIGH *et al.*, 1977)

The results of these calculations can be expressed as follows:

- f_L decreases when L_p/H increases;
- the end effect can be very significant (f_L may increase up to 20), the more so, when $\gamma H/c$ approaches the critical value;
- for a given β , f_L increases with $\gamma H/c$ and A/H ;
- f_L shows hardly any dependence on β with low values of $\gamma H/c$.

1.4 Time effect and stability of slopes

If we considered merely the momentary state of a slope, we would often fail to explain satisfactorily why and how a landslide occurred, for both the external and the internal forces that determine the stability are time-dependent. Instability of a slope always results from the most unfavourable combination of disturbing forces and resistances. Unpredictable events, such as accidental rainstorms or sudden thaw, may all affect stability. Such events might of course have occurred frequently in the past without ever provoking a landslide, and if a natural slope suddenly begins to move, it clearly must be due to some extraordinary disturbance or to a slow gradual deterioration of the shear strength of the soil. (The latter is the case in mosaic clays.)

Figure 65 shows, after SKEMPTON (1948), typical examples of gradual reduction in the shear strength of clays with time. Skempton made a comprehensive study of slides occurring in the London clay, a stiff clay with pronounced mosaic structure. He found that banks in this soil with vertical faces 5 to 6 m high stood only for a few weeks, after which they invariably failed without any apparent disturbance from weather or other factors. Slopes of 2 horizontal to 1 vertical are likely to remain stable for 10 to 20 years and those of 3 to 1 for as long as 50 years. The inclination of permanently stable natural slopes seldom exceeds a value of 10 degrees to the horizontal. On the basis of this observation, Skempton found the shear strength versus time relationships for various clays shown in Fig. 65. Such empirical curves permit a reliable assessment of the long-term stability of slopes which would prove extremely difficult merely on the basis of laboratory testing of the clays. Also much valuable information can be gathered from field observations and from the study of case histories.

Further examples of variation in the safety factor with time are given after TERZAGHI in Fig. 66. The curve *a* represents the case when a natural slope gradually becomes steeper due to tectonic action, or the shear strength of the soil of a slope is gradually reduced, for example, by physical or chemical weathering. Minor irregularities on the curve indicate temporary decreases

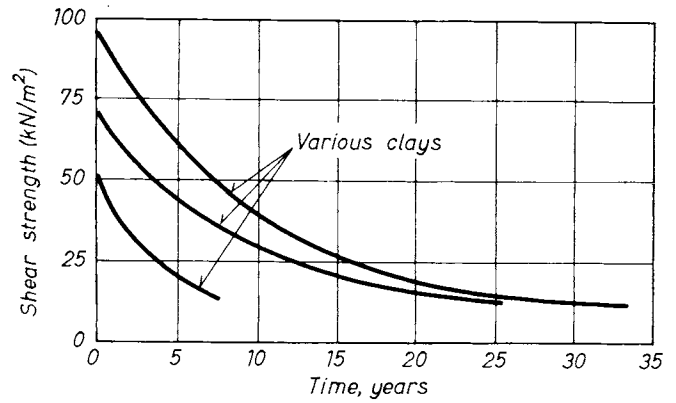


Fig. 65. Diminishing shear strength in London clay as a function of time (as observed by SKEMPTON, 1948)

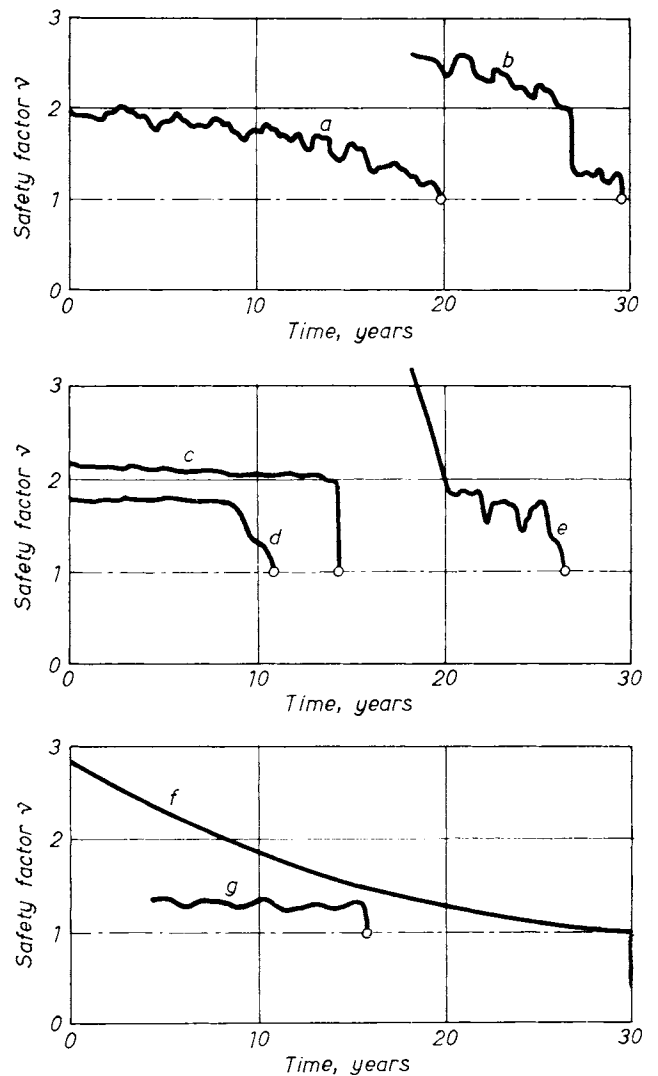


Fig. 66. Variation of the stability coefficient as a function of time, owing to:

- a — chemical decomposition, creep, increasing inclination due to tectonic movements; b — the same, with the addition of an excavation at the toe; c — liquefaction due to dynamic effect; d — infiltration and increased water pressure due to construction of a canal above the shoulder of the slope; e — newly excavated cutting, swell, decreased stability coefficient, slide after a heavy rain; f — creep, swell, loss of shear strength due to dissolved capillary tension in the course of flooding over the slope; g — abrupt sinking of the water level

in the safety factor due to incidental rains, thaw, etc. Although curve *a* has a noticeable falling trend and the safety factor would sooner or later drop to a critical value, it is in all probability one of these incidental effects that triggers sliding.

The tendency of the resisting forces to decrease with time becomes greatly accelerated when a slope is undercut at the toe (curve *b*). Such a drastic interference with stability is reflected by a sharp drop on the curve.

In case *c*, instability is due to quicksand conditions; vibrations, earthquake or explosions may produce such an effect. Curve *d* shows the effect of the construction of a channel near the top of a slope. The water seeping away from the channel induces seepage forces in the slope and causes swelling of the soil leading to a gradual reduction of its shear strength. Curve *e* represents the case of an embankment slope that failed during an unprecedentedly violent rainstorm.

If capillary pressures cease to exist in a soil because of saturation of the voids, the relief from hydrostatic pressure causes the soil skeleton to swell. Fine-grained soils take up a considerable amount of water during swelling and as a result their shear strength is greatly reduced. Under unfavourable conditions this effect may ultimately lead to failure (curve *f*). Curve *g* corresponds to a slope in which periodical rises and falls of the water table take place. Failure occurs when the water level sinks at an exceptionally fast rate.

1.5 Problems of embankments and earth dams

1.5.1 Stresses in embankments

In Section 1.2 the stability of slopes was treated on the basis of failure theory. A slip surface was assumed to develop in the slope and the conditions for limiting equilibrium of the sliding body were sought. Stability was investigated in terms of forces, and the stresses acting within the sliding body were of little concern and were not determined. However, there may be cases in which it

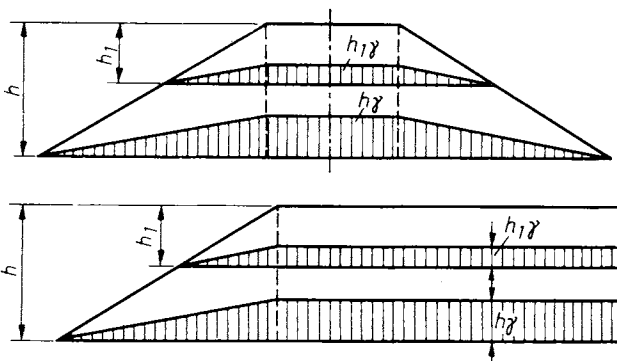


Fig. 67. Simple assumption of stress distribution inside the dam

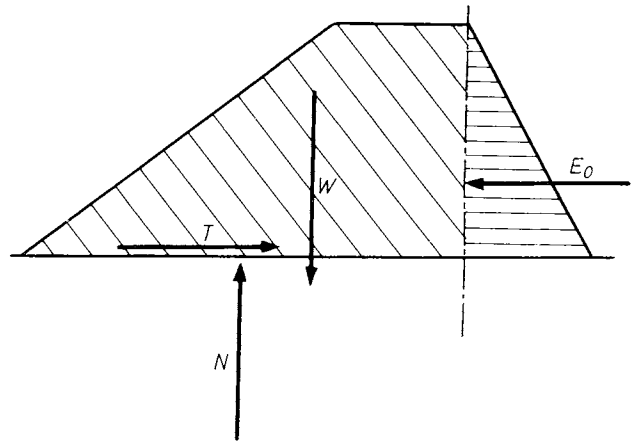


Fig. 68. Equilibrium of forces in one half of the embankment

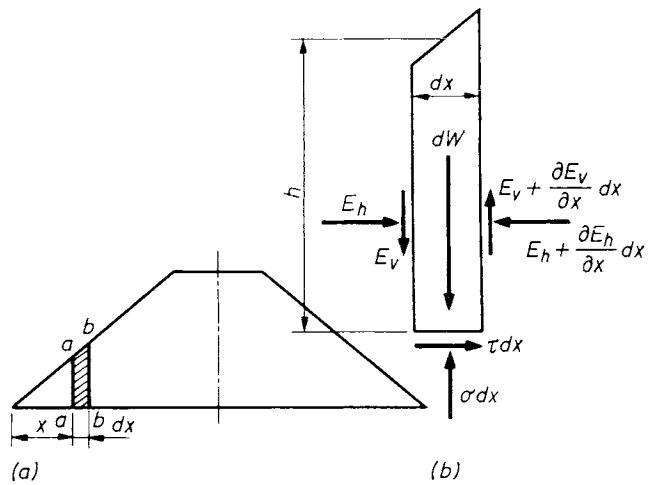


Fig. 69. Determination of stresses at the base of an embankment:

a — cross-section; b — forces acting on an element

is required that one has an idea about the distribution of stresses within the embankment before it is brought to a limiting state of equilibrium. In the following, we shall deal with this problem and investigate the state of stress of a dam. These considerations can, however, be readily extended to semi-infinite slopes.

The simplest assumption used for the computation of stresses inside an embankment is illustrated by Fig. 67. It can be useful in determining the settlement of an embankment or the compression of the fill itself under its own weight. But this assumption is inadequate in the case of high dams or when a greater accuracy is required, in that it fails to satisfy the conditions of equilibrium and does not furnish stresses other than vertical. In reality, there are also horizontal stresses acting along the base and on every horizontal section of the embankment, as can easily be seen from the sketch in Fig. 68. Supposing that one half of the embankment is removed and the support it pro-

vides for the remaining half is replaced by a corresponding earth pressure; then equilibrium is only maintained if a horizontal force equal to the earth pressure acts along the base of the fill.

The distribution of the forces N and T can be determined by the method of RENDULIĆ (1936).

Consider the equilibrium of an elementary slice of the fill, shown in Fig. 69. The lateral earth pressures acting on the section $a-a$ and $b-b$ are resolved into horizontal and vertical components. The weight of the slice is

$$dW = h\gamma dx.$$

Equilibrium requires that

$$\tau = \frac{\partial E_h}{\partial x} \tag{62}$$

and

$$\sigma = h\gamma + \frac{\partial E_v}{\partial x}. \tag{63}$$

In order to determine the distribution of the shear stresses over the base of the embankment, the components E_h and E_v of the earth pressure on every vertical section must also be known. Rendulić used Engesser's graphical procedure (cf. Vol. 1, Chapter 9), for this purpose and assumed that the conditions for an active limiting state are fulfilled within the embankment.

The construction is illustrated by Fig. 70. We determine first the earth pressure acting from the right-hand side on a vertical section such as $a-b$. We select a number of trial planes of rupture and draw the direction of the reaction acting on it for each plane. The weights of the sliding wedges are plotted in a force diagram. The envelope to the lines of the slip surface reaction gives the Engesser curve e_1 . In a similar manner, we determine the earth pressures acting from the left-hand side and obtain the curve e_2 . Equilibrium requires that the earth pressures E and E' are equal and opposite. Therefore, we must select such a direction for these earth pressures that the condition of equality is fulfilled. By projecting the curve e_1 radially about point P , we obtain the auxiliary curve e'_1 . The point A' where the curve e'_1 intersects the curve e_2 gives one end of the vector E' sought. By repeating the whole construction for a number of arbitrarily selected vertical sections, we can determine the variation of the components E_h and E_v along the base of the fill. The resulting diagrams are similar to those shown in Fig. 71. The unknown values of $\partial E_h/\partial x$ in Eqs (62) and (63) can be obtained from these curves graphically.

Figure 72 shows the results of two numerical examples. The stresses are plotted in terms of the ratios $\sigma/h\gamma$ and $\tau/h\gamma$. In the first example (Fig. 72a), the values of the normal stress differ only slightly from $h\gamma$. The maximum value of the shear stress is $0.144h\gamma$.

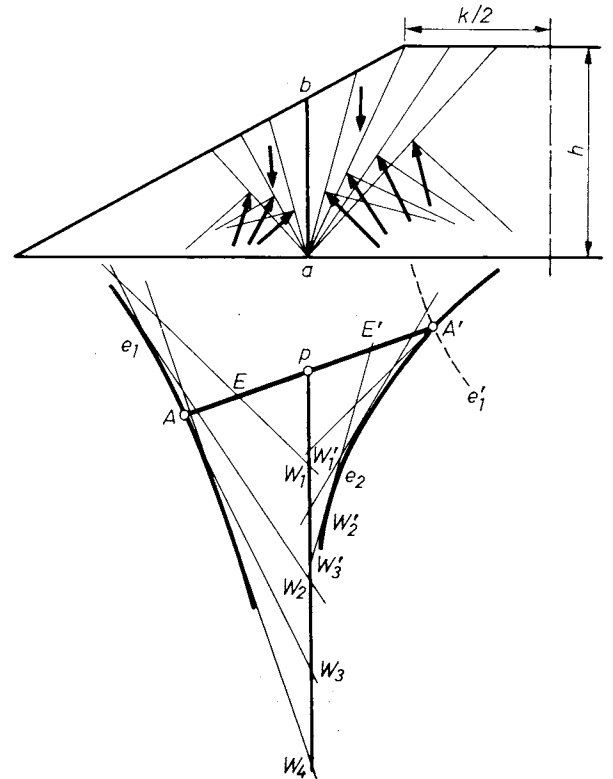


Fig. 70. Determination of earth pressure in a vertical section ($a-b$) across the slope (Engesser's method)

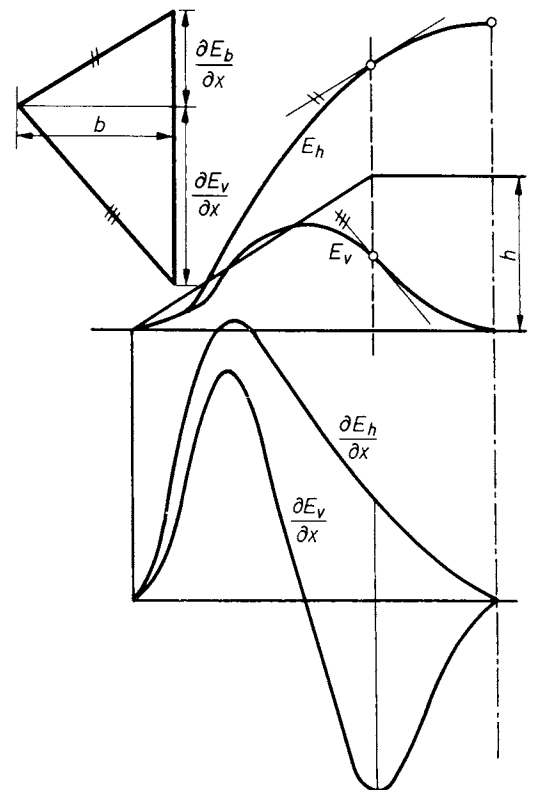


Fig. 71. Variation of earth pressure in the horizontal direction

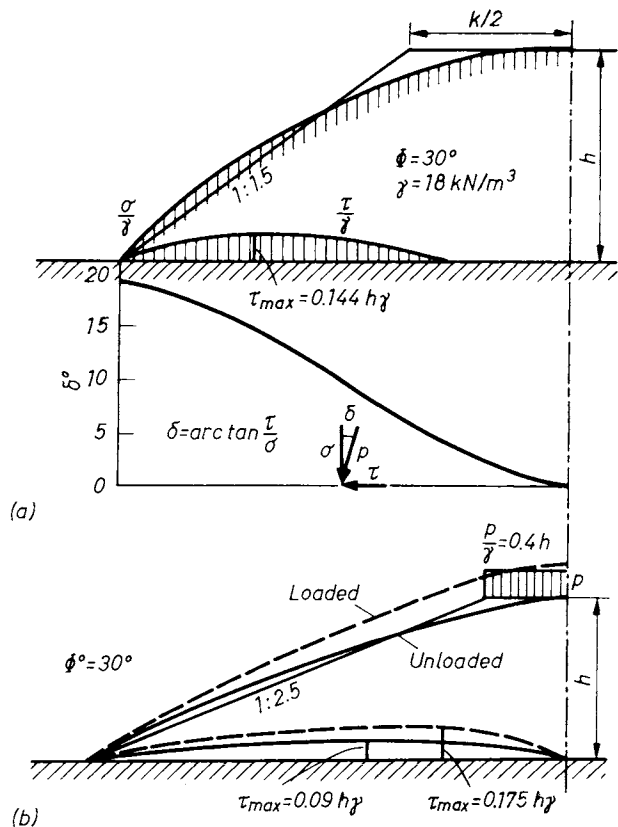


Fig. 72. Numerical example for the determination of stresses at the base of a dam

The resultant stress on the base of the embankment makes an angle δ with the vertical. This angle of obliquity is a maximum at the toe of the fill, whereas in the centre it diminishes to zero. Figure 72a also shows the variations in the angle δ over the base. The horizontal stresses τ may cause failure of the embankment under unfavourable conditions.

The preceding method is open to objection on the grounds that it assumes the earth pressures to be active forces. The mode of distribution and, particularly, the magnitude of the deformations that occur within the fill are normally not sufficient to produce an active limiting state throughout, unless the embankment is actually brought to the verge of failure. Otherwise the earth pressure is essentially higher than the value obtained on the assumption of an active state. In certain cases the coefficient of earth pressure may be as high as 0.6. If we can form a reasonable estimate of the degree to which the shear resistance is mobilized in the fill, we can compute a reduced angle of shear resistance and use it for determining the stresses along the base. Supposing that the embankment is in a state of rest and the earth pressure coefficient at rest, K_0 , is known, the reduced friction angle Φ_{red} can be obtained from the equation

$$K_0 = \tan^2 \left(45^\circ - \frac{\Phi_{red}}{2} \right).$$

SCHWARZ (1963) extended the Rendulic method to the general case when the embankment is built on a sloping base. (Fig. 73). For this case, the normal and tangential stresses on the base are given by the following expressions:

$$\sigma = \cos \alpha \left(h\gamma + \frac{\partial E_v}{\partial x} \right) - \sin \alpha \frac{\partial E_h}{\partial x}$$

$$\tau = \sin \alpha \left(h\gamma + \frac{\partial E_v}{\partial x} \right) + \cos \alpha \frac{\partial E_h}{\partial x}.$$

E_v and E_h are determined by the Engesser method. By comparing the available shear strength on the base computed by the formula $\tau = \sigma \tan \Phi_2 + c_2$, with the shear stresses acting on the base, we can judge whether or not a danger of failure exists.

For an embankment in which the deformation can be assumed to be mainly elastic, the stresses can be computed by means of the theory of elasticity. CHRISTENSEN (1950) presented a method for this. It is based on the assumption that the stresses at a point such as O inside the fill (Fig. 74) are due to the weight of a soil wedge having its lower boundaries inclined at an angle ψ to the vertical. The stresses can be computed by formulae derived by STROHSCHNEIDER (1932). The value of the limiting angle ψ depends on the shape of the cross-section and on the freedom of lateral deformations. In practice, we usually take $\psi = 90^\circ - \beta$. The stress components at point O are determined by the following expressions:

$$\left. \begin{aligned} \sigma_x &= \gamma c \Delta \theta \Sigma r \sin \theta \tan \theta (1 - \cot^2 \psi \tan^2 \theta) \\ \sigma_y &= \gamma c \Delta \theta \Sigma r \cos \theta (1 - \cot^2 \psi \tan^2 \theta) \\ \tau_{xy} &= \gamma c \Delta \theta \Sigma r \sin \theta (1 - \cot^2 \psi \tan^2 \theta), \end{aligned} \right\} (64)$$

where

$$c = \frac{\sin^2 \psi}{2\psi - \sin^2 \psi}.$$

The graphs in Fig. 75 give influence values c_y , c_x and c_{xy} , respectively, for the stresses σ_y , σ_x and τ_{xy} , for an embankment with slopes of $\cot \beta = 1.5$. Values of $100c$ are plotted as func-

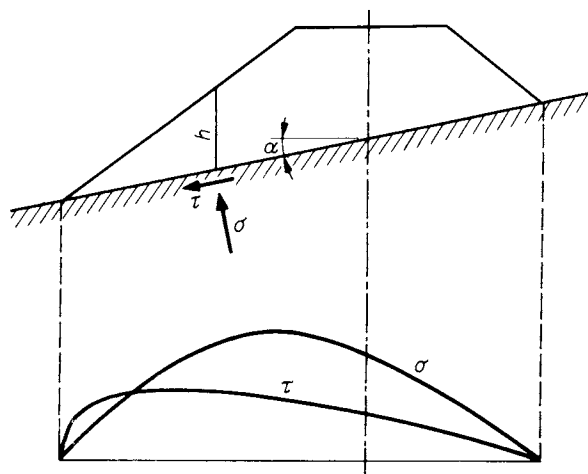


Fig. 73. Stress distribution at the base of an embankment on inclined ground

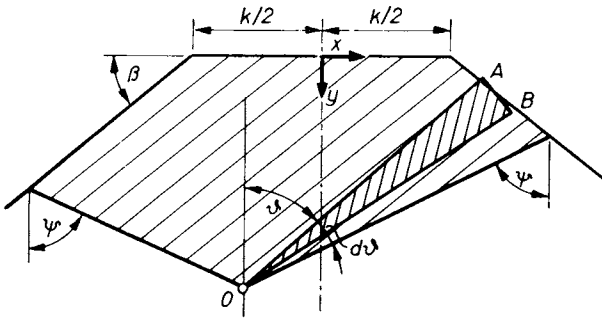


Fig. 74. Element showing the stress conditions inside a dam

tions of the dimensionless numbers x/k and y/k where k denotes the crest width of the embankment. A value of $\psi = 90^\circ - \beta = 56.3^\circ$ is assumed for the limiting angle throughout.

Numerical example. Given $k = 6.00$ m and $\gamma = 20$ kN/m³, evaluate the stress components at a depth $y = 7.00$ m and at a distance $x = 9.00$ m from the centre line of the fill. With $y/k = 1.25$ and $x/k = 1.50$, we obtain from the graphs the influence values $c_y = 0.66$, $c_x = 0.25$ and $c_{xy} = 0.146$. Hence, the desired stress components are

$$\begin{aligned} \sigma_y &= 0.66 \cdot 6.00 \cdot 20 = 79 \text{ kN/m}^2, \\ \sigma_x &= 0.25 \cdot 6.00 \cdot 20 = 30 \text{ kN/m}^2, \\ \tau_{xy} &= 0.146 \cdot 6.00 \cdot 20 = 17.5 \text{ kN/m}^2. \end{aligned}$$

1.5.2 Base failure beneath embankments

The stability of an embankment may be endangered by base failure in cases where the subsoil is very soft or where it contains undesirable layers. The quality of the fill itself can be controlled by selecting suitable fill materials and using appropriate construction methods. But even a properly built embankment is subject to damage if it rests on a troublesome subsoil. The formation of a slip surface is to be expected in places where the shear strength is originally very low or where it decreases with time. A reduction in shear strength is mostly due to a build-up of excess pore-water pressures with a subsequent decrease in effective stresses.

In the following we shall examine the different ways in which base failures may occur. The stresses beneath the base of an embankment can be computed by means of the theory of elasticity provided that the magnitude of the stresses does not exceed a certain limit. This problem, together with the computation of settlements, will be studied in Chapter 2. This section deals only with the problems of stability.

Three characteristic types of base failure can be distinguished. In the first case, the fill rests upon a thick, very soft, saturated layer of clay. Because of the very low permeability of the clay it can be assumed that undrained conditions prevail in the subsoil not only during construction but also for some time thereafter. It is therefore permissible to carry out the stability analysis in terms of total stresses, on the assumption that $\Phi = 0$. The soft layer yields laterally under the weight of the fill until failure occurs along a deep-seated and approximately circular slip surface (Fig. 76). The conditions for such a base failure were investigated by JÁKY (1948). He showed, on the basis of the theoretical analysis of the $\Phi = 0$ case, that the shear pattern is similar to that shown in Fig. 77. The slip surfaces consist of two plane sections connected by a circular section. Failure takes place when the vertical pressure on the base of the fill reaches a critical value given by the expression

$$\sigma = 2c \left(1 + \frac{\pi}{2} \right).$$

According to this formula, the maximum allowable height of an embankment built on a soft

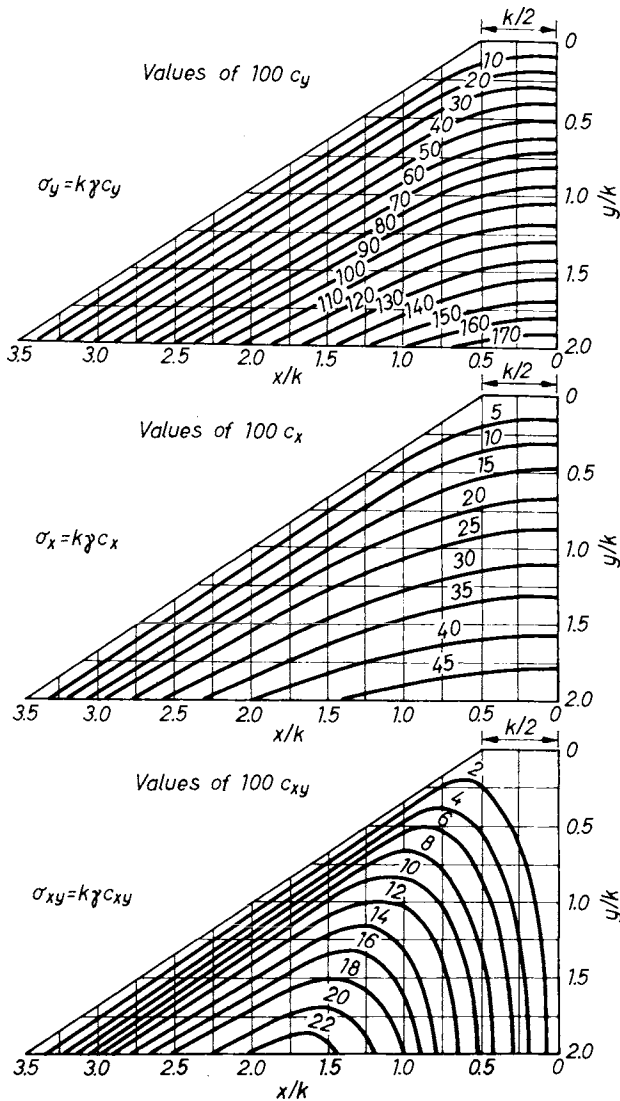


Fig. 75. Influence diagrams for the determination of stress conditions inside a dam

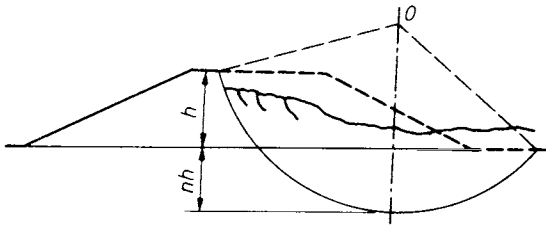


Fig. 76. Base failure due to the soft subsoil below the dam

subsoil is equal to

$$h_{\max} = \frac{\sigma}{r\gamma} = \frac{2c}{r\gamma} \left(1 + \frac{\pi}{2} \right). \quad (65)$$

In Eq. (65), the cohesion c can be assumed to have a value equal to half of the unconfined compression strength q_u .

If there is a danger of this type of base failure, the embankment can be stabilized by means of a counterweight. The necessary weight of the stabilizing mass can be determined by the following formula (Fig. 78):

$$W = \nu \frac{W_1 a_1 - W_2 a_2 - c l_a r}{a}$$

In a cutting, base failure can be averted by the removal of a sufficiently large mass of soil from the top of the slope (Fig. 78b). If both the material of the slope and the subsoil to a considerable depth consist of a soft clay, longitudinal subsurface drains should be constructed at the toe of the slope assisted if necessary by stone-filled buttress drains, as a precautionary or remedial measure.

The second type of base failure occurs if a relatively thin layer of soft clay is located at some depth below the base of the embankment. In this case the surface of rupture assumes a composite shape similar to that shown in Fig. 79. Inside the embankment a curved slip surface is formed (ab), which is joined by a planar section (bc) located on the surface of, or inside, the soft layer. The central soil block bb_1cc_1 acts in a similar manner to a retaining wall which rotates about the upper edge or is displaced horizontally. This block is acted upon by an active earth pressure on the

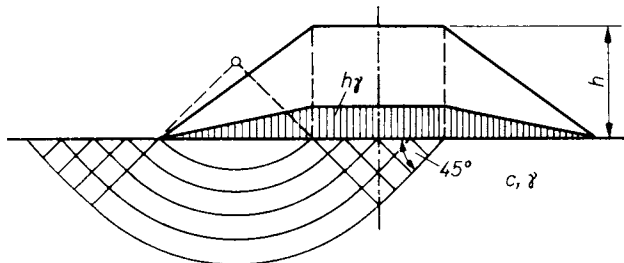


Fig. 77. Development of sliding surfaces below an embankment for the case $\Phi = 0$

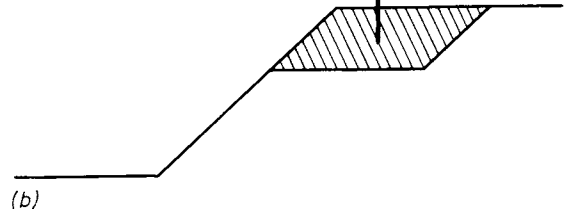
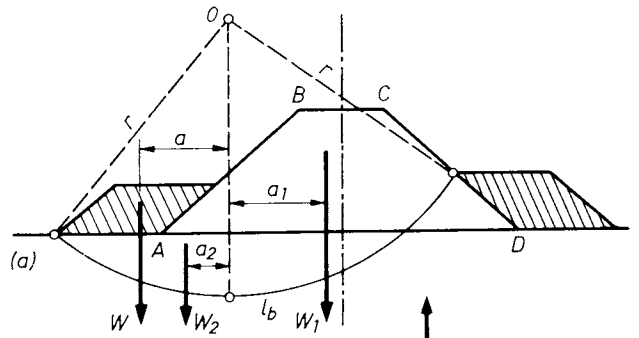


Fig. 78. Increasing the stability of an embankment by: a — berms; b — displacement of loads

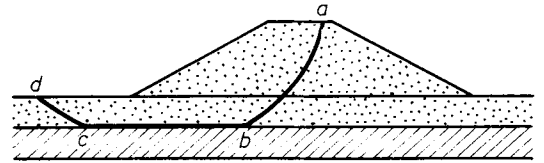


Fig. 79. Base failure below an embankment; rupture along the top of the stiff layer

vertical face bb_1 and, at the same time, it exerts a lateral thrust on the soil located in the vicinity of the toe, thereby mobilizing a passive earth pressure. Accordingly, the slip surface has a curved final section $c-d$.

The method of stability analysis is illustrated by Fig. 80. We consider the equilibrium of the soil block bcc_1b_1 . The vertical section $b-b_1$ is acted upon by an active earth pressure E_a , which is counteracted by the shear resistance T_1 along the plane bc and the passive earth pressure E_p on the vertical section cc_1 . There is no danger of failure if

$$E_a < E_p + cl + T_1.$$

The magnitude of T_1 is determined by the expression $T_1 = N_1 \mu_f = W_1 \mu_f$, where μ_f is the coefficient of friction on the surface of contact between the two layers. It is assumed that the line of action of the passive earth pressure E_p is horizontal, and that the surface of rupture for E_p is a plane. Hence

$$E_p = \frac{h^2 \gamma}{2} \tan^2 \left(45^\circ + \frac{\Phi}{2} \right) + 2ch \tan \left(45^\circ + \frac{\Phi}{2} \right).$$

In order to determine the maximum value of the active earth pressure, the investigation must be repeated for different positions of the section bb_1 . It is on the safe side to assume that the action

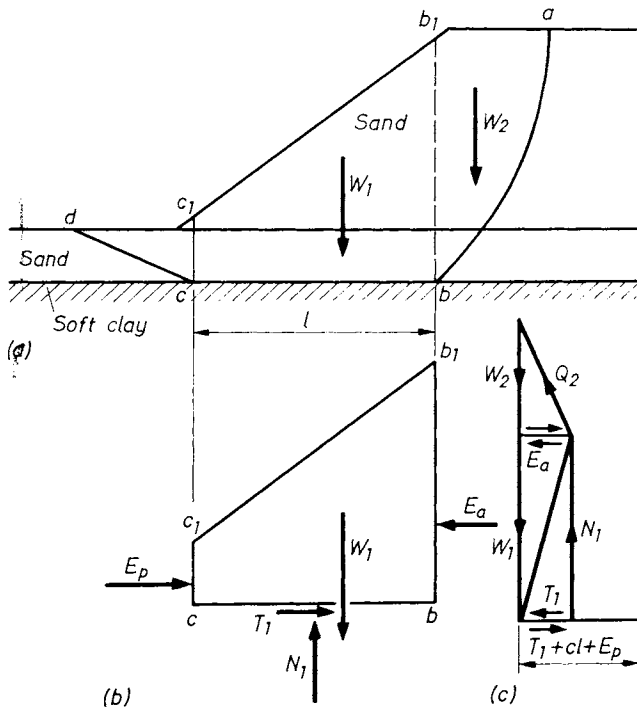


Fig. 80. Static investigation of the base failure according to the block method :
 a — cross-section; b — forces acting; c — force diagram

line of E_a is also horizontal. The most dangerous position of the vertical section bb_1 is found by trial and error.

The investigation can be greatly simplified if we assume plane surfaces of rupture for both the active and the passive earth pressure. E_a and E_p can then be calculated with the aid of charts or tabulated values of the earth pressure coefficients K_a and K_p . Examples of the stability analysis are shown in Fig. 81. For the purpose of such investigations, we should use the shear strength parameters Φ_m and c_m which represent the mobilized

portion of the ultimate shear strength, i.e., the actual value of Φ and c divided by an arbitrarily selected value of the safety factor. The analysis can be carried out by the method of slices. That value of the safety factor at which equilibrium conditions are satisfied can be found by successive approximation.

The third type of base failure is due to excess pore-water pressures in the soil beneath the fill. Fig. 82 shows a dam whose subsoil contains a thin layer of homogeneous clay. The load due to the weight of the fill induces excess pore-water pressures in the soft layer which dissipate slowly during the course of consolidation. At an initial stage these neutral pressures must be taken into consideration in the stability analysis. The maximum neutral pressures exist along the mid-height

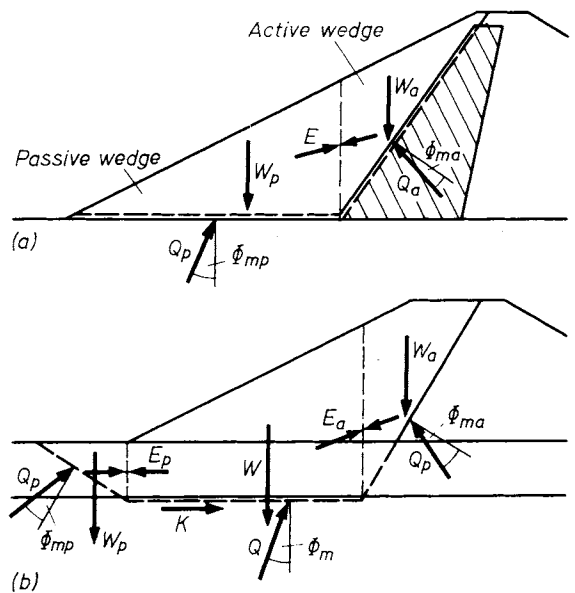


Fig. 81. Examples of plane failure surfaces:
 a — earth dam with impermeable core; b — soft layer at some depth below the dam

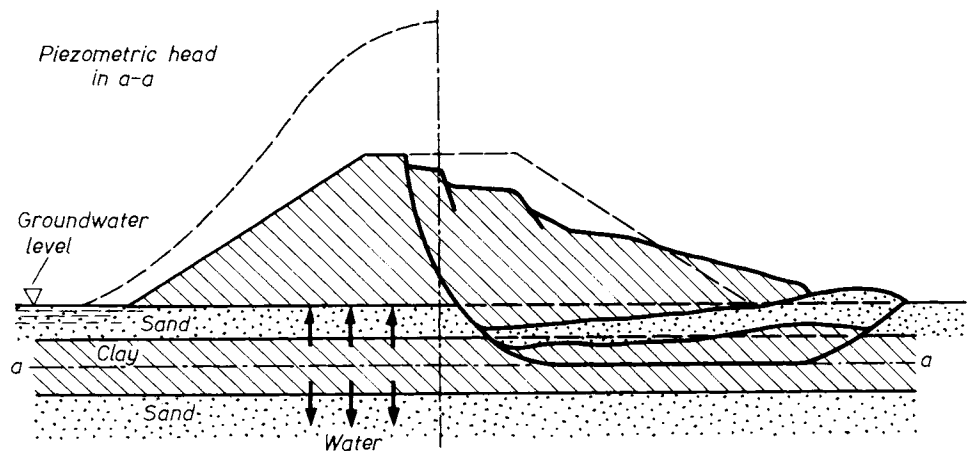


Fig. 82. Base failure due to increased neutral stresses in the clay layer in some depth below the dam

of the soft layer and hence the surface of sliding also follows this line (*a-a*). The piezometric level along *a-a* is indicated by a dashed line in Fig. 82.

The likelihood of a base failure of this type should be investigated with regard to the process of consolidation. An example of a detailed analysis is given in Fig. 83. First, we compute the total normal stresses along the mid-height of the clay layer. These are due to the weight of the upper half of the clay layer itself plus the weight of the fill. The normal stresses caused by the weight of the clay layer located above *a-a* are effective stresses, while the excess normal stresses induced by the fill are partly effective and partly neutral, their ratio being dependent on the degree of consolidation. In the example it is estimated that the effective stresses amount to 40% of the total

excess normal stresses (Fig. 83b). With the effective stresses known, we can compute the shear strength available along the surface of sliding *a₁-c₁*. Figure 83d shows the distribution of the shear stresses τ . The distribution is approximately parabolic. The maximum ordinate τ_{max} can be determined on the basis that the shear stresses along *a₁-c₁* must be in equilibrium with the earth pressure at rest E_0 acting on the vertical section *a-a₁* in the centre line of the dam. Let us consider an arbitrary vertical section such as *b-b₁*. The safety factor for the block of soil *aa₁ bb₁* with respect to sliding can be determined by the following expression

$$v = \frac{\int_{c_1}^{b_1} (\bar{\sigma} \tan \Phi + c) dx + E_p}{\int_{c_1}^{b_1} \tau dx} \quad (66)$$

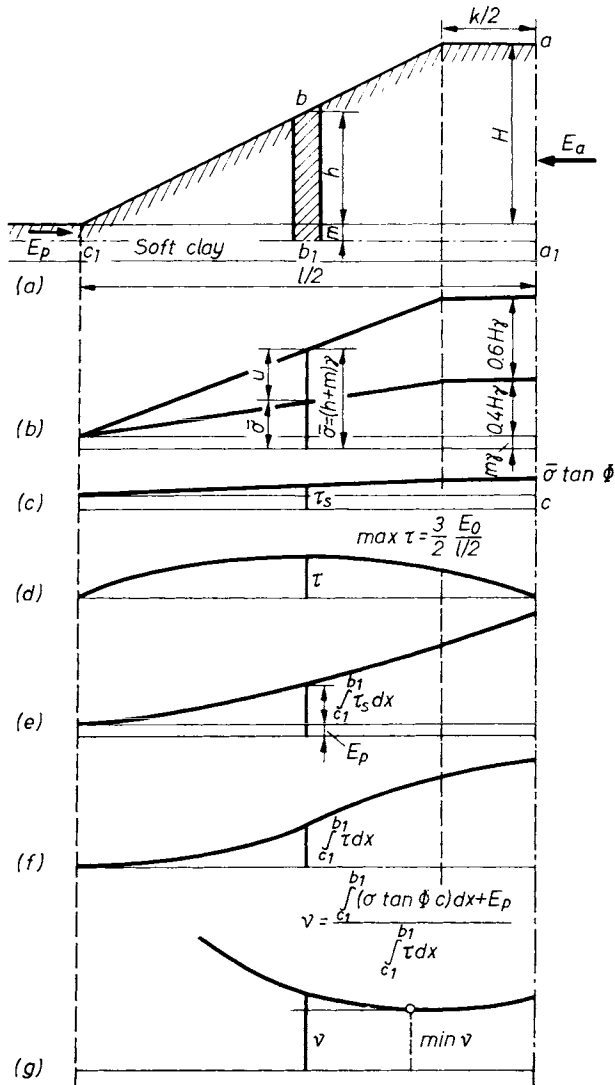


Fig. 83. Investigation of a base failure taking account of effective and neutral stresses; determination of the critical vertical section:

a — cross-section; b — normal stresses; c — shear strength; d — shear stress distribution; e — distribution of resistance forces; f — shear force; g — coefficient of stability

The integrals to be entered in Eq. (66) are shown diagrammatically in Figs 83e and f. By changing the position of the vertical section *b-b₁*, we can compute a safety factor for each vertical and plot the variation of *v* as shown in Fig. 83g. The lowest point of the curve furnishes the minimum safety factor. The described method is very useful in the stability analysis of earth dams. For dams, the hydrostatic pressure acting on the upstream slope must also be taken into account as a force tending to cause sliding.

The occurrence of lenses or seams of sand, without adequate drainage, in a clay stratum also constitutes a serious risk of base failure (Fig. 84). The cause is again the build-up of high excess pore-water pressures, so this type of failure can be considered as a variant of the case discussed in connection with Fig. 82. The pore-water squeezed out of the clay stratum consolidating under the weight of the fill drains into the pervious seam of sand and there causes the hydrostatic pressures to increase considerably. The dashed line in Fig. 84 indicates the approximate piezometric levels in the sand seam. The shear strength of the sand becomes drastically reduced especially in places where the difference between the excess pore-water pressure and the weight of the overlying soil and fill is greatest. The worst situation arises near the toe of the embankment, where the only resistance to sliding is the passive earth pressure in the layer located above the surface of rupture. If the horizontal driving force exceeds the available resistance near the toe, failure takes places almost instantaneously. The central part of the crest subsides, leaving a depression as shown in Fig. 84.

In the case that an embankment is to be constructed on a clay subsoil, a thorough survey of the stratification of the soil is very important. If the geological conditions are such that a base failure of the types described is to be expected, the risk of failure can be avoided by one of the

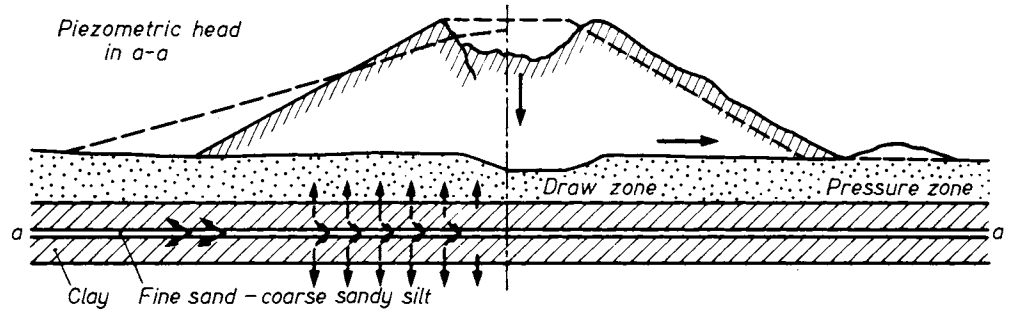


Fig. 84. Base failure due to increase in neutral stresses in a thin sand layer

following precautionary measures. The fill should be made with very flat slopes, or the construction should proceed so slowly that sufficient time is left for excess pore pressures to dissipate already during construction. The process of consolidation can be greatly accelerated by means of vertical sand drains, which serve additionally as a means of reducing settlements.

1.5.3 Construction of a flow net in an earth dam

First we consider a homogeneous dam on an impervious base and determine the flow net (Fig. 85). In Section 1.4 we dealt only with flow cases in which a mass of soil was assumed to be saturated throughout, and which was joined on both sides to free water surfaces. In an earth dam the conditions are different in that the zone in which seepage occurs is bounded by a top flow line the location of which is, however, not exactly defined. We only know that along this line the hydrostatic pressure must be zero.

We know various methods for locating the top flow line. Solutions for two simple cases of dam cross-section will be shown first, although typical earth dams usually have composite sections. The study of these simple cases will furnish a good picture of the conditions characteristic of any top flow line. Furthermore, a top flow line determined for a simple case can often be used as a first approximation in constructing the flow net for a more complicated case.

Figure 86 shows one of the principal conditions that the top flow line must obey. Along this line atmospheric pressure exists, therefore the piezometric head above the elevation head must be zero at every point. It follows that the differences in elevation between the points at which successive equipotential lines intersect the top flow line must be equal as shown in Fig. 86.

Water seeping along the top flow line enters the dam at the elevation of the upstream water surface. At its starting point, the top flow line must be normal to the face of the upstream slope since the latter is an equipotential line (Fig. 87a). Should, however, the angle γ be less than 90° , the rule just mentioned does not hold, and the

top flow line is different. This is the case, for example, when a wedge-shaped part of the cross-section adjacent to the toe is made of a coarse-grained material (Fig. 87b). The permeability of this material can be so high that it offers almost no resistance to flow. It follows that the rear boundary $a-b$ of this wedge is an equipotential line. But contrary to the case shown in Fig. 87a, the top flow line cannot be normal to the surface $a-b$ since the water cannot rise above the upstream water level without violating the rule illustrated in Fig. 86. Consequently, the top flow line has a horizontal tangent at the point b . This also means that the initial gradient, and hence the initial velocity, are both zero. The 'zero condition' explains why the flow lines do not intersect the initial equipotential line $a-b$ perpendicularly. If

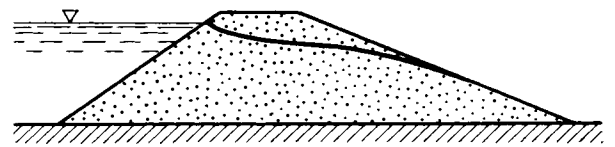


Fig. 85. Homogeneous earth dam resting on an impervious underground

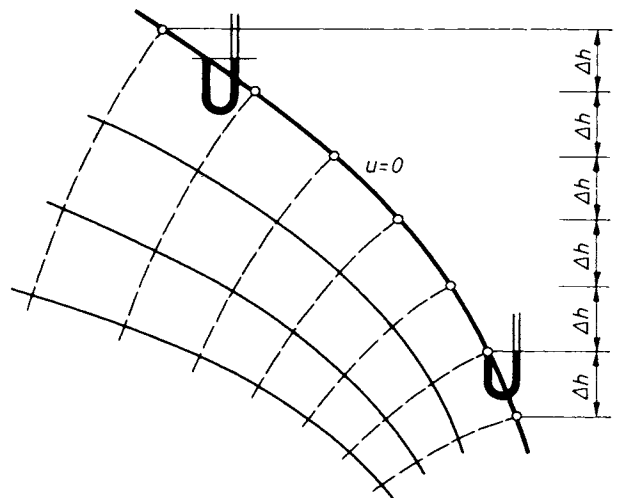


Fig. 86. Conditions for the uppermost seepage line

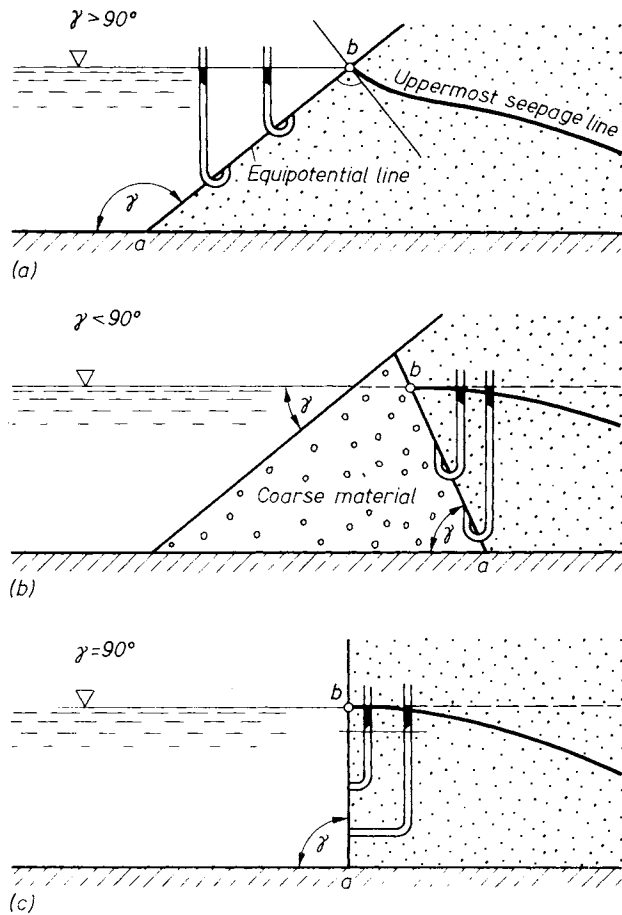


Fig. 87. Initial conditions for the uppermost seepage line: a — homogeneous earth dam; b — coarse internal material on the upwater side; c — vertical boundary

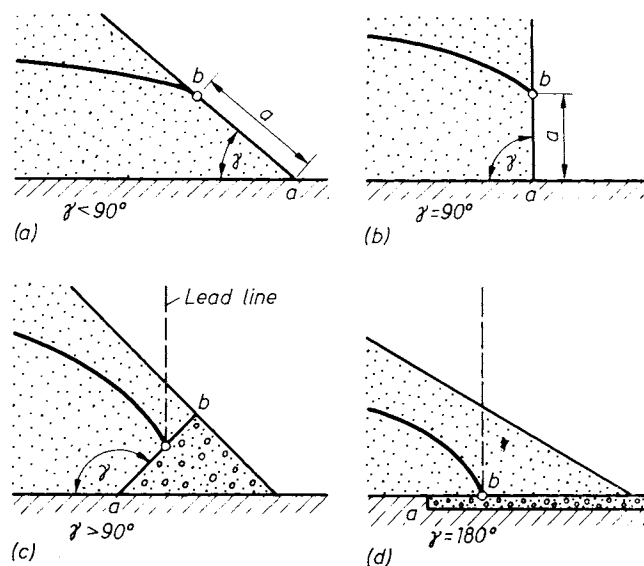


Fig. 88. Situation of the uppermost seepage line at the exit point for different angles of γ

the upstream boundary is vertical (Fig. 87c), the conditions illustrated by Figs 87a and b lead to the same result.

Between the exit point of the top flow line and the toe of the downstream slope, the particles of water tend to follow the direction of gravity. As a result, the downstream section of the top flow line will have the forms shown in Fig. 88 for different values of the angle γ . Figure 88d shows the case when a horizontal filter is located at the downstream toe of the dam. By means of this arrangement the water can be prevented from emerging on the face of the slope and from causing erosion there. The filter material is many times more permeable than the material of the dam, so that the pressure in the filter is atmospheric. The upper boundary of the filter is an equipotential line and the flow lines intersect it at right angles. In addition to the cases already mentioned, Fig. 89 shows further possibilities for the formation of flow lines when water flows across a boundary between soils with different permeabilities. In certain cases, a discontinuity on the boundary is also possible (Fig. 89d), if the layer of lower permeability cannot yield a sufficient amount of water into the more permeable layer. The magnitude of the drop depends on the angle ω and on the ratio of the two permeabilities, k_1/k_2 . The relationships illustrated by Fig. 89 must be taken into consideration in the study of flow nets in dams having composite cross-sections.

One of the simplest solutions of the Laplace equation of potential flow (Vol. 1, Chapter 6) consists of confocal parabolas (Fig. 90). For the hypothetical case, in which all the boundaries of a cross-section are either flow lines or equipotential lines conforming in shape to the curves in Fig. 90, this set of confocal parabolas furnishes the flow net. Such a flow net is shown in Fig. 91. Here the lines BC and DF are flow lines, and BD and FC are equipotential lines. In reality, a dam has a cross-section similar to that shown in Fig. 91b, for which the flow net will deviate from that given in Fig. 91a. Nevertheless, the shape of the zone in which seepage occurs will be similar for the two cases. Analysis has shown the top flow line to deflect from a true parabola only in the vicinity of point B . CASAGRANDE (1939) proposed starting the construction of the parabola from a point E located on the upstream water surface, where the distance \overline{EB} is equal to three-tenths of the horizontal projection \overline{AD} of the submerged slope: $\overline{EB} = 0.3\overline{AD}$. The parabola can thus be constructed. The correction near point B can readily be sketched in freehand.

The equation of the parabola — the top flow line — is derived as follows (Fig. 92). By definition, the distance of any point on the parabola from the focus is equal to its distance from the directrix. Hence, from Fig. 92, we obtain

$$\sqrt{x^2 + z^2} = x + p,$$

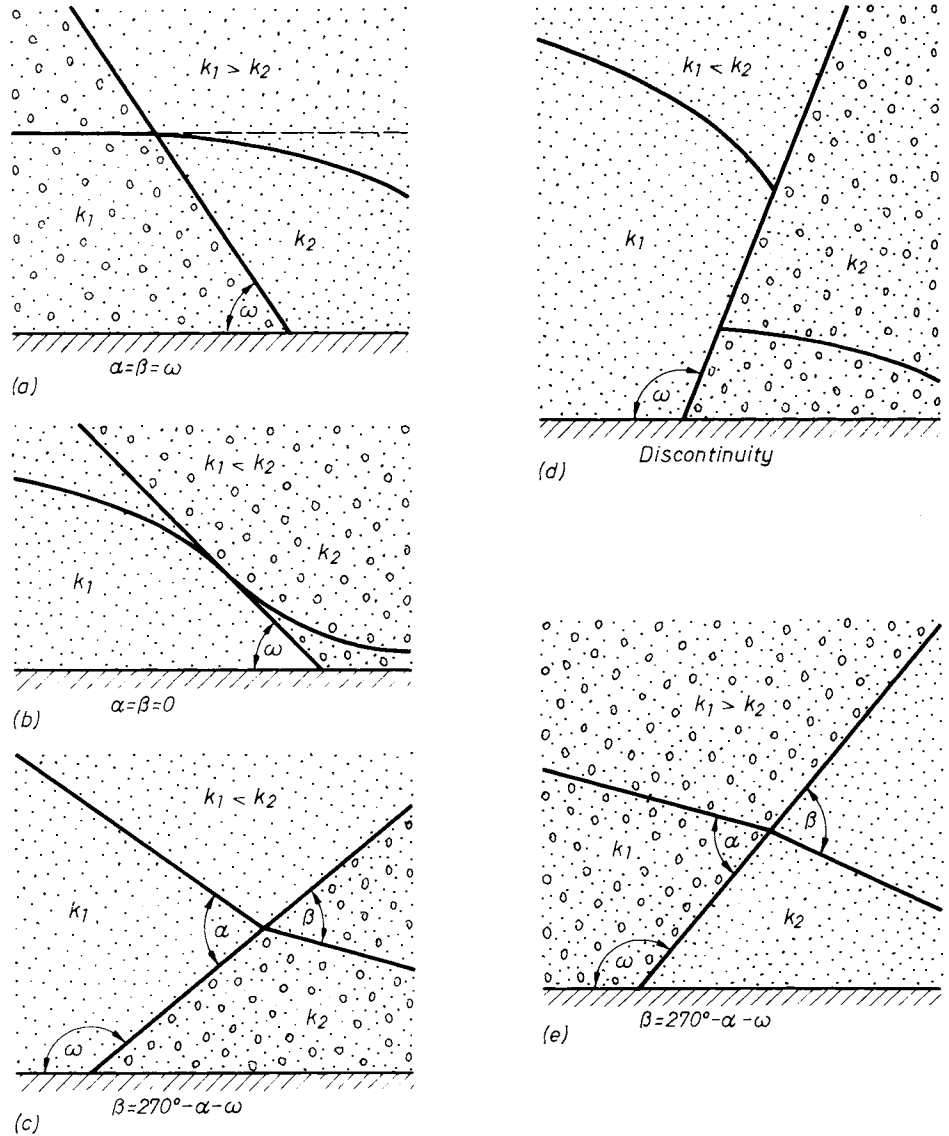


Fig. 89. Development of the seepage line on the interface of materials of different permeabilities

whence

$$x = \frac{z^2 - p^2}{2p} \tag{67}$$

At point A , $z = h$ and $x = d$. Therefore,

$$p = \sqrt{d^2 + h^2} - d \tag{68}$$

The distance p is obtained from the construction shown in Fig. 92. With point E as centre we draw a circle of radius \overline{EF} , which intersects the prolongation of the upstream water level at point J . The distance \overline{KJ} is equal to p . Having thus fixed the locations of the vertex C ($\overline{FC} = p/2$) and of point G ($\overline{FG} = p$), we can easily complete the construction.

The quantity of seepage can be computed by applying Eq. (116) in Vol. 1 to the portion $CCFH$

of the flow net. The total head at point G equals to the elevation head p , and the head loss between the equipotential lines GH and FC is also p . By symmetry, the numbers of the squares n_1 and n_2 are the same, and hence

$$q = kp \tag{69}$$

The construction for another case is shown in Fig. 93. Since there is no underfilter, the top flow line emerges on the downstream slope.

With the focus located at the toe of the slope, A , the parabola can be constructed by the method shown in Fig. 92. It intersects the downstream slope at point C . The distance \overline{AC} is determined by the formula

$$\overline{AC} = \sqrt{x_c^2 + z_c^2} = x_c + p$$

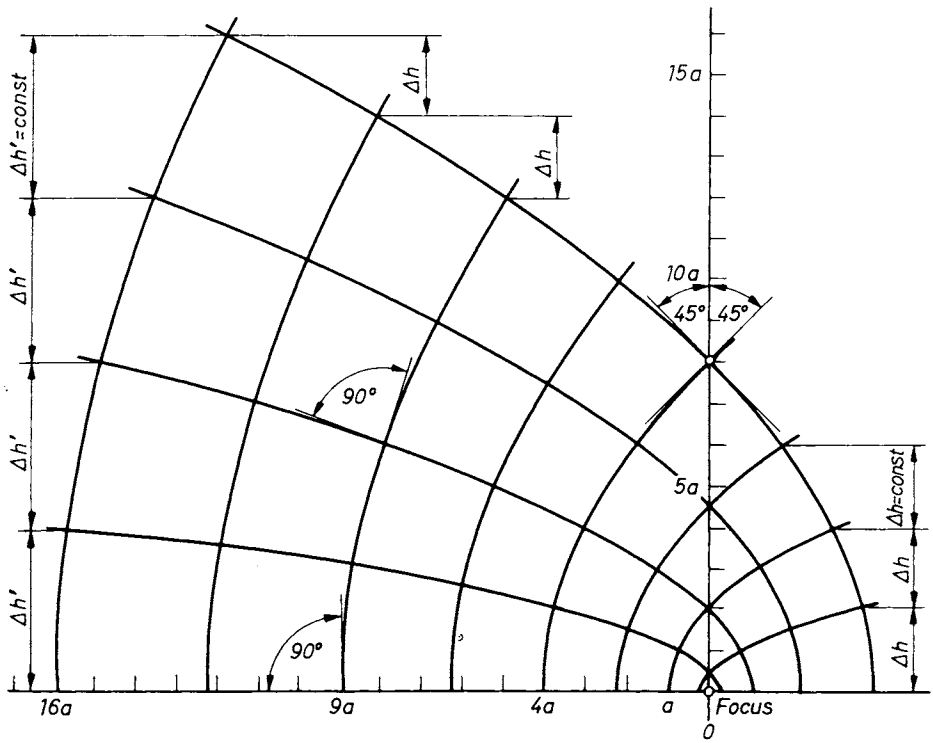


Fig. 90. Set of parabolas with common focus

With
we obtain

$$x_c = \overline{AC} \cos \beta$$

$$\overline{AC} = \frac{P}{1 - \cos \beta} \quad (70)$$

The actual breakout point of the top flow line is C' . Its distance from the toe can be expressed as

$$\overline{AC'} = \epsilon \overline{AC}.$$

As was shown by Casagrande, the ratio ϵ is a

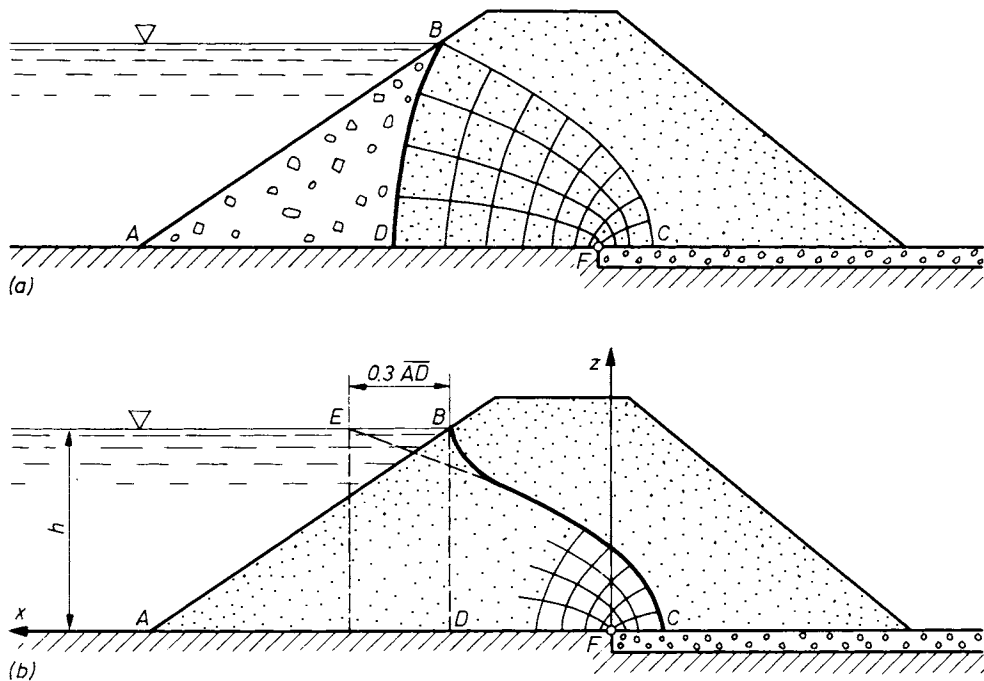


Fig. 91. a — cross-section of a dam in which the flow net is composed from parabolas with common focus; b — application of the above condition for a common dam

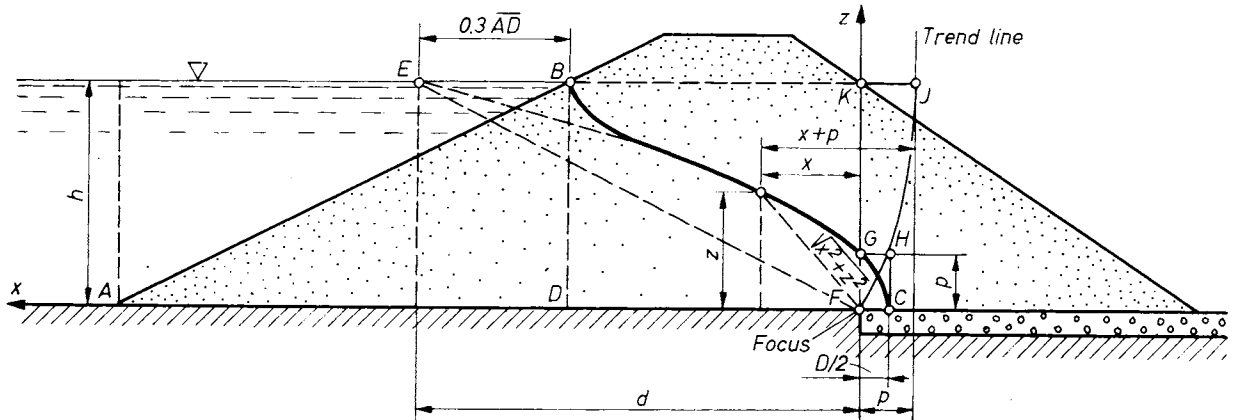


Fig. 92. Determination of the uppermost seepage line when a horizontal filter layer has been provided

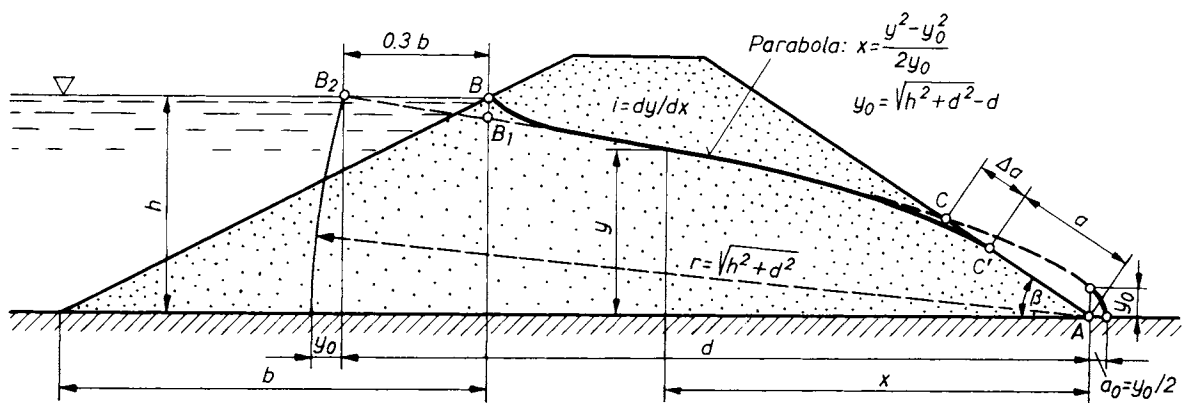


Fig. 93. Determination of the uppermost seepage line (impermeable subsoil) after CASAGRANDE (1937)

function of the slope angle β . The relationship is given in Fig. 94.

On the basis of the Dupuit formula, CASAGRANDE (1937) developed the following approximate solution for the determination of the distance $\overline{AC'}$:

$$\overline{AC'} = a = \frac{d}{\cos \beta} - \sqrt{\frac{d^2}{\cos^2 \beta} - \frac{h^2}{\sin^2 \beta}} \quad (71)$$

A more accurate solution was given by GILBOY (1940). This method is represented by the chart shown in Fig. 95.

The quantity of seepage can again be estimated by Eq. (69). For the case where $\beta < 30^\circ$, the approximate formula

$$q = k \sqrt{h^2 + d^2} - \sqrt{d^2 - h^2 \cot^2 \beta \sin^2 \beta} \quad (72)$$

can be used.

For the purpose of the stability analysis of a cross-section, it is necessary to construct the complete flow net. Once the top flow line has been obtained on the basis of the preceding considerations, the boundary conditions can be stated and the flow lines and equipotential lines can be readily sketched in. An example of the use of

flow net in stability analysis is given in Fig. 96. Values of the safety factor are indicated for both the upstream and downstream slopes under different seepage conditions. For comparison, the top figure shows the case when there is no seepage through the dam. It can be seen that as a result

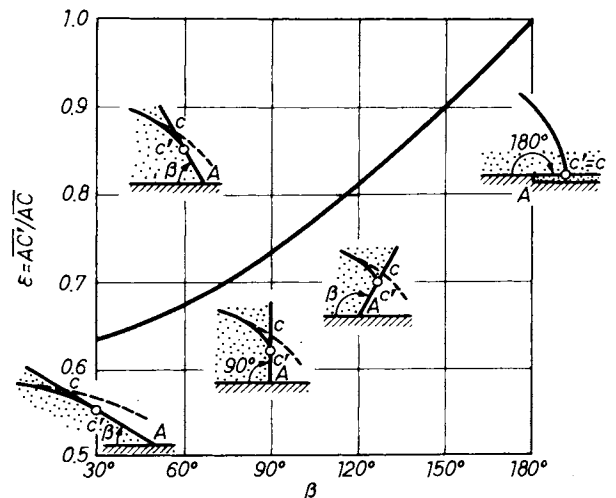


Fig. 94. Diagram for the determination of the exit point of the uppermost seepage line

of seepage the safety factor is increased for the upstream slope and decreased for the downstream slope.

In the preceding discussion it was assumed that the boundary conditions are constant and do not change with time. In reality, however, there are cases where we have to deal with time-dependent conditions, for example, when the water level on the upstream face of an earth dam rises or sinks. Similar conditions may arise in levees. A rising or sinking water level causes the zone of saturation to change within the dam. As a result, either dry soil becomes wetted and saturated, or air is forced into the previously saturated soil and the degree of saturation drops below unity. Within the zone of saturation the conditions of continuity are fulfilled; hence a flow net can be constructed. Such flow nets differ from those obtained in the steady seepage case in that flow lines may intersect the line of saturation (phreatic line). If the line of saturation is lowered, water is draining out of the soil above, so flow lines must start at the line of saturation (Fig. 97). In the case of a rising water level, flow lines end at the advancing saturation front.

1.6 Calculation and assumption of safety

1.6.1 Safety as a function in the coordinate system of $\tan \Phi'$ and c

In stability analyses, assuming a rigid sliding body an alternative safety factor can be defined by the following consideration. Let us assume, for

the sake of simplicity, a regular slope in a homogeneous soil with plane boundary surfaces and with no surcharge and no other body force (seepage force, pore pressure, etc.) but the weight of the soil.

If the available shear strength of the soil be given by the equation

$$\tau = \sigma \tan \Phi + c$$

and the greatest value of the actual shear stress along the slip surface is τ_1 , then the ratio

$$v = \frac{\tau}{\tau_1}$$

could be regarded as the safety factor. But since both τ and τ_1 depend on the normal stress σ , the above ratio cannot be evaluated. Instead, we may proceed as follows. We assume various fictitious values of the friction angle Φ' and for each one we determine the value of the cohesion c' that must act on the critical slip surface to secure stability. Using any pair of corresponding Φ' and c' values, it is possible to compute two safety factors, one with respect to friction

$$v_\Phi = \frac{\tan \Phi}{\tan \Phi'} \tag{73}$$

and another with respect to cohesion

$$v_c = \frac{c}{c'} \tag{74}$$

The two values are interrelated, i.e. for a given critical circle one can be computed from the other.

Let us examine the interdependence of the safety factors v_Φ and v_c in a numerical example. Given a 1.5 to 1 slope ($\beta = 33^\circ 40'$), 15 m high, in a homogeneous soil having a friction angle of $\Phi = 15^\circ$, a cohesion of $c = 30 \text{ kN/m}^2$ and a unit weight of $\gamma = 20 \text{ kN/m}^3$. Assuming a set of Φ' values ranging from 0 to β , we determine on the basis of a circular slip surface the corresponding set of c' values that are necessary to maintain equilibrium. The location of the critical circles will of course be different for different Φ' values. The results of the computation are tabulated below.

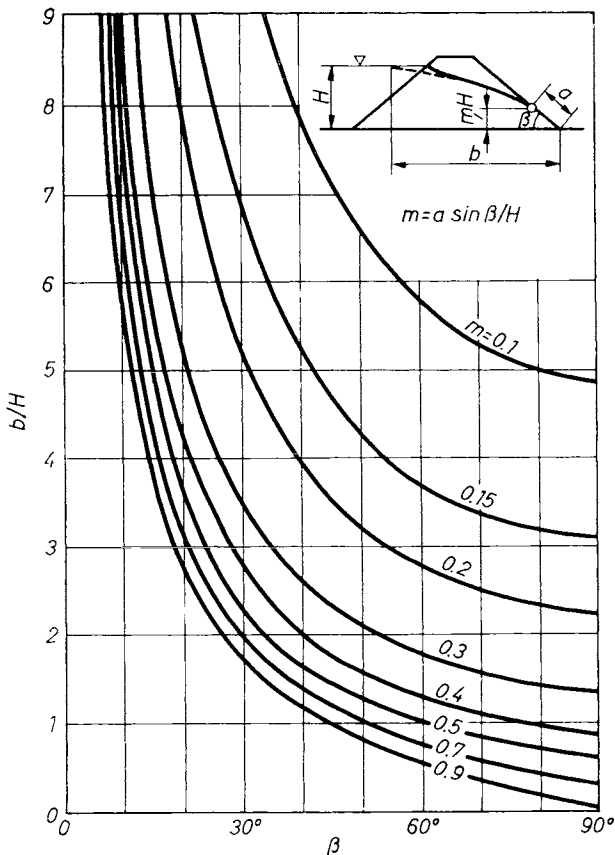


Fig. 95. Gilboy's method (1940) of finding the length of the seepage surface

Φ' [degrees]	$\tan \Phi'$	c' [kN/m ²]
0	0.000	48.0
5	0.087	35.1
10	0.176	25.2
15	0.268	16.8
20	0.364	10.2
25	0.466	5.2
30	0.577	2.1
33° 40'	0.667	0

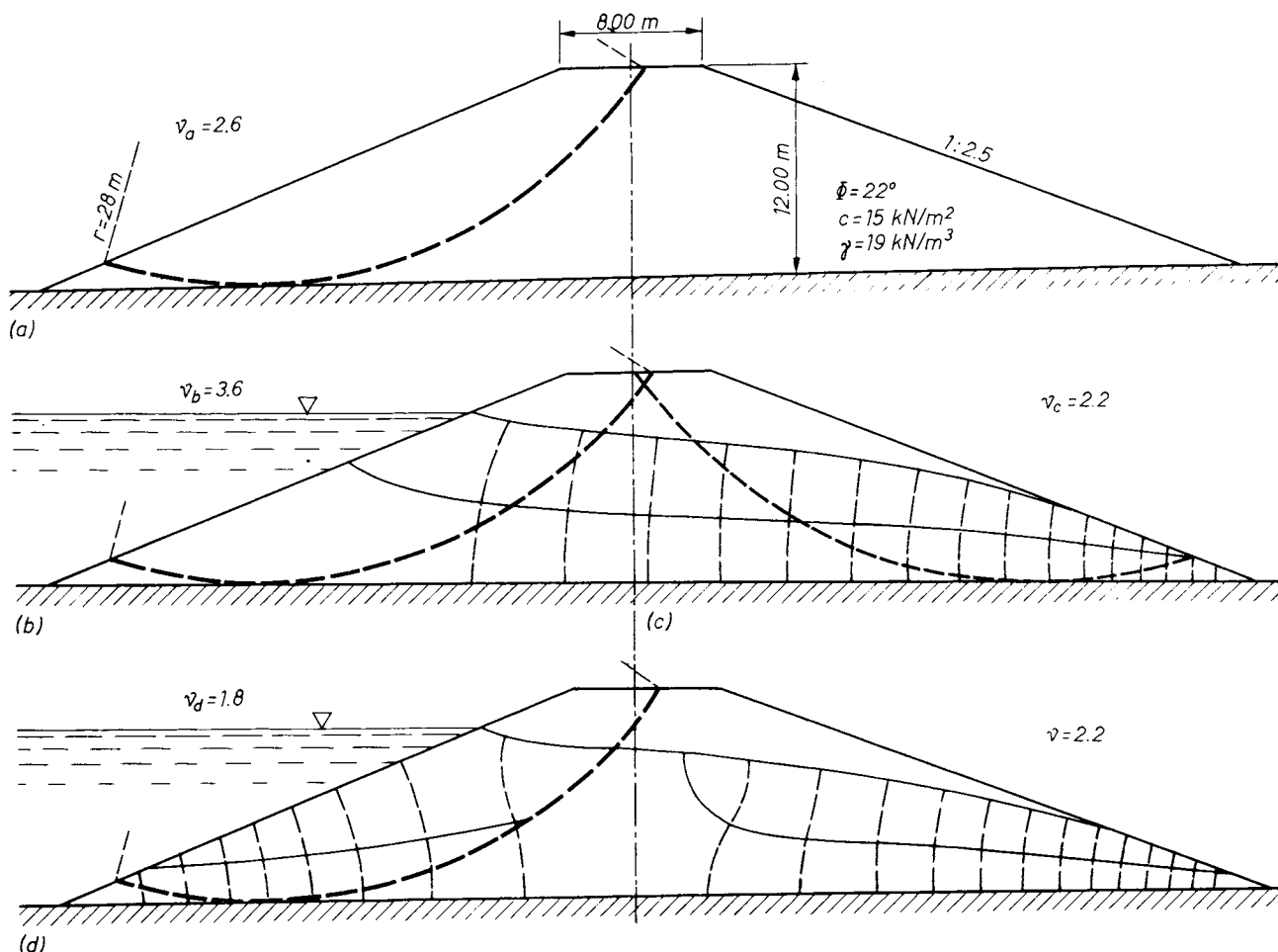


Fig. 96. Stability of dam slopes:
 a — seepage excluded; b — permanent seepage exists, upwater slope; c — permanent seepage exists, downwater slope; d — sudden lowering of the water level in the reservoir

By plotting the results in a $(\tan \Phi', c')$ coordinate system, we obtain the graph shown in Fig. 98. From this we may compute any combination of safety factors. Let, for example, the assumed friction angle be $\Phi' = 10^\circ$. The corresponding cohesion is $c' = 25.2 \text{ kN/m}^2$. The safety factor with respect to friction becomes $v_\Phi = \tan 15^\circ / \tan 10^\circ = 1.52$, and with respect to cohesion $v_c = 30 / 25.2 = 1.19$. Of the infinite possible values of the safety factor, two are of particular significance: v_c when $v_\Phi = 1$, and v_Φ when $v_c = 1$. The former represents the case where the frictional resistance is fully mobilized and the latter where the available cohesion is fully exhausted. These two extreme cases are interpreted in terms of Coulomb's shear envelope in Fig. 99. The friction circle method, as will be recalled, used the combination $v_\Phi = 1$ and $v_c = c'/c$. As was previously shown, in a homogeneous soil the value of cohesion necessary to maintain the stability of a slope is directly proportional to the height of the slope, i.e. when $v_\Phi = 1$, the safety factor v_c at the same time gives the safety factor with respect to height. If we plot corresponding values

of v_Φ and v_c in a coordinate system as shown in Fig. 100, the resulting curve will be a hyperbola. Its asymptotes can readily be determined, since

when $\Phi' = \beta, c' = 0$ and $v_c \rightarrow \infty$, and

when $\Phi' = 0, c' = \text{required } c$ and $v_\Phi \rightarrow \infty$.

It is obvious from the figure that there exists such a combination of the values v_Φ and v_c that the two are equal:

$$v_c = v_\Phi = v_s.$$

In this particular case, the Φ' and c' values corresponding to the limiting state of equilibrium define a straight line that passes through the same point at which the actual Coulomb envelope intersects the σ axis (Fig. 99). This value of v_s can also be determined from Fig. 98. If we plot the actual $\tan \Phi$ and c values on the graph, we obtain point A . A straight line joining this point with the origin of the coordinates O intersects the curve representing the limiting state of equi-

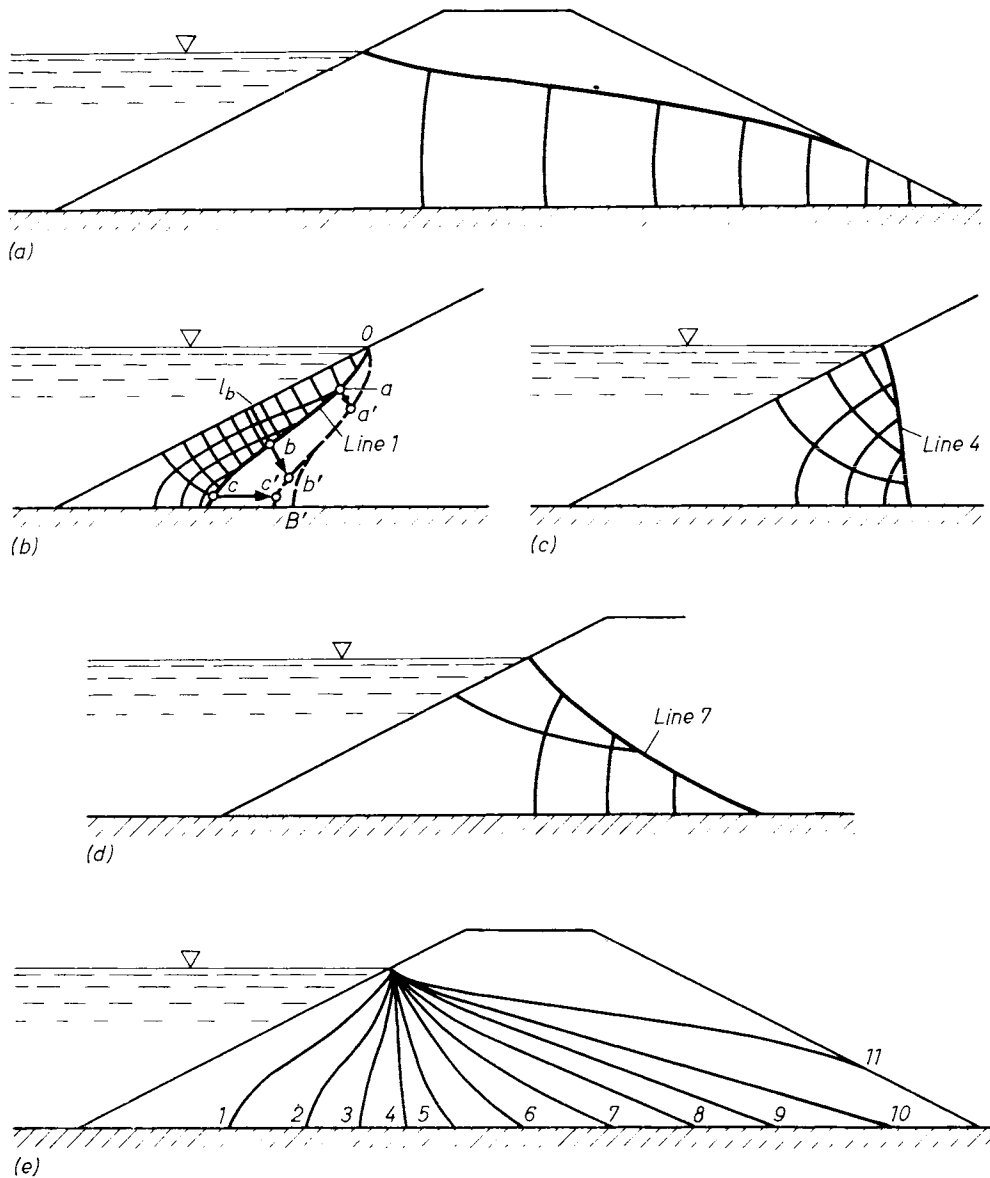


Fig. 97. Establishment of tentative flow net diagrams for various degrees of saturation:
 a — cross-section with flow lines in the fully saturated case; b — the first step in the design of a totally transverse seepage line;
 c — and d — intermittent positions of the progressing saturation line; e — sequence of progress

librium at point A' . By scaling off the distances \overline{OA} and $\overline{OA'}$, we obtain the safety factor:

$$v_s = \frac{\overline{OA}}{\overline{OA'}} = \frac{\tan \Phi}{\tan \Phi'} = \frac{c}{c'} \quad (75)$$

In the numerical example $v_s = 1.34$.

In an actual stability analysis, it must be taken into consideration that the available shear strength of the soil can be determined only with a limited accuracy; besides, it is likely to vary from point to point and also with time. Very often, there is a wide scatter of measured Φ and c values, and therefore the strength behaviour of the soil can be characterized by a region rather than by a single point in the c' versus $\tan \Phi'$ plot (Fig. 101).

The degree of safety can then be judged from the relative position of such a region and the $v = 1$ curve. A closer examination of the problem reveals that in view of the many uncertainties involved in the assumptions upon which our stability analyses are based, the $v = 1$ case cannot be characterized by a single curve. It should probably be replaced by a strip similar to that shaded in Fig. 101, which allows for possible variations in the assumptions, e.g. in the mode of distribution of stresses along the slip surface.

The possibility of interpreting safety in terms of $\tan \Phi$ and c coordinates was originally introduced by LAZARD (1961). The improved version of this approach, which has been presented above, aims to offer a better understanding of the

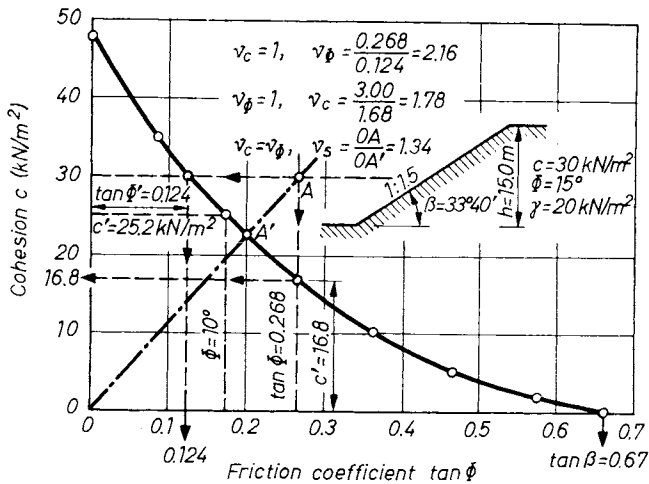


Fig. 98. Relationship between friction coefficient and cohesion under equilibrium limit conditions

relative to the $v = F = 1$ curve may in itself give an impression about the distribution of the safety factor, but true information about the actual situation can only be achieved when all curves of similar degrees of safety are duly established, as it has been done by SINGH (1970). With the help of such a set of curves, represented after Singh in Fig. 102, F -values can be determined at every pair of $\tan \Phi$ and c points, and then their distribution and the probability p_f of $v = 1$ value can be established (see Section 1.6.2). An advantage of this evaluation system is its independence from any stability method applied.

1.6.2 Applied probability theories for stability calculations

From the end of the nineteen-sixties, several researchers looked for possibilities as to which way probability theories could be applied to solve geotechnical problems. Early

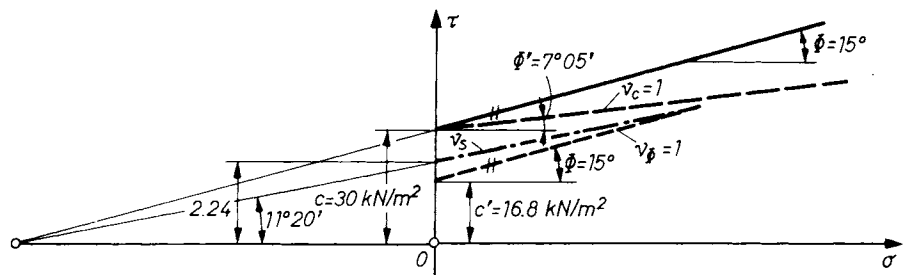


Fig. 99. Interpretation of the safety factor using Coulomb's relevant straight lines

reliability of deterministic methods. The same procedure can also be used for stochastic analyses. The position of the spread of $\tan \Phi$ and c points

studies dealt only with problems related to the safety factor, and even in that field only initial steps were reached. Parallel to this began the statistical investigation of the variability of soil characteristics which involved the problematics of numbers of samples too. A breakthrough in this respect in the field of geotechnics came in 1971 when an international conference was organized in Hong-Kong ("Applications of Statistics and Probability in Soil and Structural Engineering") where also slope stability problems appeared on the agenda.

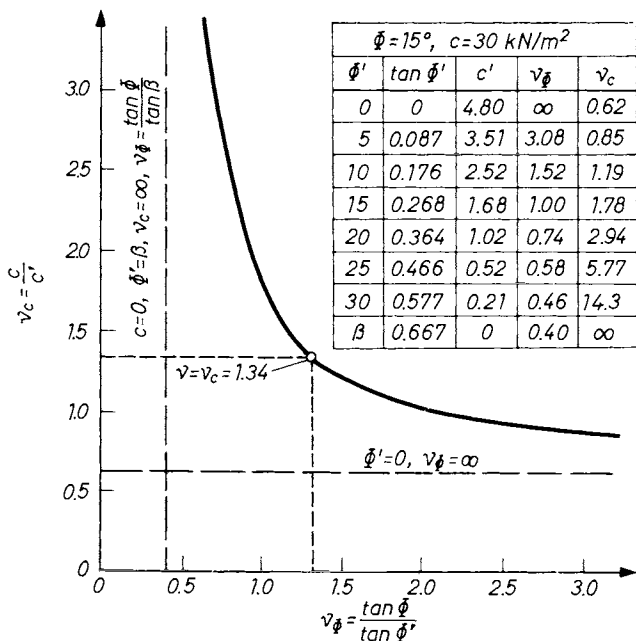


Fig. 100. Relationship between the various safety factors

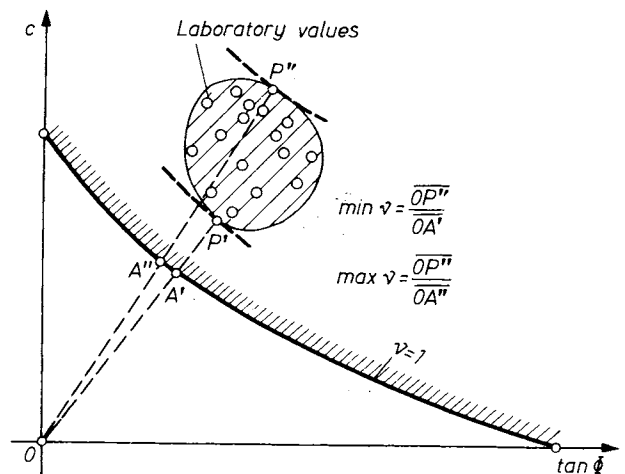


Fig. 101. Limiting values of the safety factor in the case of scattered test results

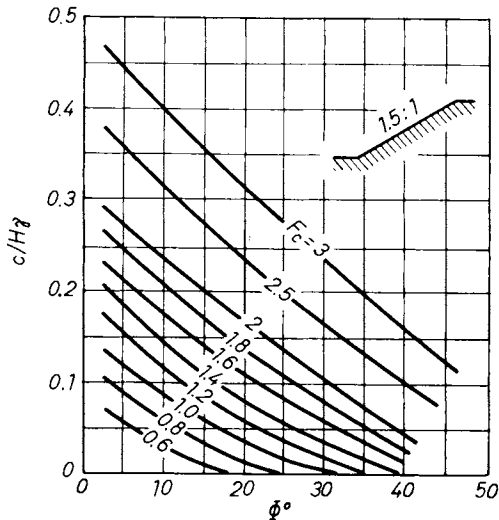


Fig. 102. The safety factor for various pairs of Φ and c/H values, after a numerical example given by SINGH (1971)

Following customary views, safety can be interpreted in two different ways.

The central safety factor is the ratio of the expected value of resistance (R) to the expected value of load (Q)

$$F_c = \frac{\bar{R}}{\bar{Q}} \tag{76}$$

The conventional safety factor differs from the above inasmuch as the resistance is assumed to be $R_N < \bar{R}$, and the load $Q_N > \bar{Q}$, and so the safety factor becomes:

$$F_N = \frac{R_N}{Q_N} < F_c \tag{77}$$

The safety factors defined in this way have three disadvantages:

- they do not give information about the probability of failure;
- probability levels assigned to the nominator and denominator (either identical or not) are rather arbitrary;
- their common effect mostly leads to the supposition of an event of unrealistically low probability, and thereby to uneconomical design.

These disadvantages can be eliminated by introducing the term “safety margin” (SM) which means the difference between “resistance” and “load”, i.e.:

$$SM = R - Q, \tag{78}$$

so it is also a random variable. The value

$$p_f = P [(R - Q) \leq 0] \tag{79}$$

is called the probability of failure.

The expected value of the safety margin is

$$\overline{SM} = \bar{R} - \bar{Q} \tag{80}$$

and its standard deviation (if R and Q are independent variables) is

$$s_{SM} = \sqrt{s_Q^2 + s_R^2}, \tag{81}$$

where s_R is the standard deviation of the resistance, and s_Q is the standard deviation of the load.

If Q and R are not independent variables, the standard deviation of the safety margin becomes:

$$s_{SM} = \sqrt{s_Q^2 + s_R^2 - 2rs_R s_Q}, \tag{82}$$

where r denotes the correlation coefficient for the relationship R, Q .

When the resistance can be described by a function $R(x_1, x_2, \dots, x_n)$, the expected value of the $R(x)$ function can be calculated from the expression:

$$\begin{aligned} \bar{R} = R(\bar{x}_1, \bar{x}_2, \dots, \bar{x}_n) &+ \frac{1}{2} \sum_1^n \frac{\partial^2 R}{\partial x_i^2} s_i^2 + \\ &+ \frac{1}{6} \sum_1^n \frac{\partial^3 R}{\partial x_i^3} C_{si} s_i^3 \end{aligned} \tag{83}$$

and its standard deviation from:

$$s_R^2 = \sum_1^n \left(\frac{\partial R}{\partial x_i} \right)^2 s_i^2 + \sum_1^n \frac{\partial R}{\partial x_i} \frac{\partial^2 R}{\partial x_i^2} C_{si} s_i^3 \tag{84}$$

where C_{si} is the coefficient of skewness of the variable x_i .

According to Eq. (83), the value R will only be equal to $R(\bar{x}_1, \bar{x}_2, \dots, \bar{x}_n)$ calculated with the substitution of the expected values, if every second grade calculus is zero! It can easily be envisaged that Eq. (84) will supply the term “mean error” used in surveying, if C_{si} is zero for every variable, i.e. if the distribution is symmetric.

As an example, the case of a vertical earth wall should be studied. Neglecting eventual tension cracks on the ground surface, the condition for equilibrium can be written as:

$$\frac{m_0^2 \gamma}{2} \tan^2 \left(45^\circ + \frac{\Phi}{2} \right) = 2c m_0 \tan \left(45^\circ - \frac{\Phi}{2} \right),$$

that is

$$\frac{m_0 \gamma}{2} \tan \left(45^\circ - \frac{\Phi}{2} \right) = 2c, \tag{85}$$

where the left side of the equation represents the load (Q) and the right side the resistance (R).

Suppose a wall of height $m_0 = 4$ m, and that the components of the shear resistances as measured in the soil have been found

Φ°	21.0	23.5	24.6	19.5	19.0	22.4	23.5	24.2	20.6	20.9	22.8
c (kN/m ²)	28.0	23.5	19.4	33.7	35.2	35.2	28.0	29.2	27.8	18.5	26.4

Then the expected values are

$$\bar{\Phi} = 22.0^\circ \text{ and } \bar{c} = 27.72 \text{ kN/m}^2,$$

and their standard deviations:

$$s_\Phi = 1.91^\circ \text{ and } s_c = 5.69 \text{ kN/m}^2.$$

The expected value and the standard deviation of $t = \tan\left(45^\circ - \frac{\Phi}{2}\right)$ terms are:

$$t = 0.6748 \text{ and } s_t = 0.02426.$$

Neglecting the standard deviation of the bulk density ($\gamma = 18.8 \text{ kN/m}^3$), the variance of the load becomes, according to Eq. (84) — when the distribution of t is assumed to be symmetric —

$$s_Q^2 = \left[\left(\frac{m_0 \gamma}{2} t \right)^2 \right] s_t^2 = 0.83$$

and that of the resistance:

$$s_R^2 = [(2c)^2 \cdot s_c^2 = 4 \cdot 5.69^2 = 129.5.$$

As both second grade calculi are zero, the expected values for load and resistance will be:

$$\bar{R} = 2 \cdot 27.72 = 55.48 \text{ kN/m}^2$$

and

$$\bar{Q} = 25.37 \text{ kN/m}^2.$$

Substituting these in Eq. (80), it results that:

$$\bar{SM} = 55.48 - 25.37 = 30.11 \text{ kN/m}^2.$$

As the relation between R and Q , i.e. between $\left(45^\circ - \frac{\Phi}{2}\right)$ and c , has an intermediate correlation coefficient ($r = -0.46$), the standard deviation of the safety margin (Eq. (82)) becomes:

$$s_{SM} = \sqrt{0.83 + 129.5 + 2 \cdot 0.46 \sqrt{0.83 \cdot 129.5}} = 11.83 \text{ kN/m}^2.$$

The probability of failure is then:

$$p_f = P \left[2c - \frac{m_0 \gamma}{2} \tan \left(45^\circ - \frac{\Phi}{2} \right) < 0 \right].$$

Supposing a normal distribution for SM , p_f can be calculated in the following manner. The standardized variable is:

$$\lambda = \frac{\bar{SM} - 0}{s_{SM}} = \frac{30.11}{11.83} = 2.545$$

for which the pertinent attributive is $\Phi(\lambda) = 0.9946$ and so

$$p_f = 1 - \Phi(\lambda) = 0.0054 = 0.54\%.$$

In accordance with the statements above, the possibility also exists of establishing pairs of H and β values when p_f is known (or prescribed). This type of analysis has been performed by GRIVAS (1981).

The probability of failure can also be expressed by using the coefficient of variation (standard deviation divided by mean) of R and Q . When these two variables are normally distributed, then

$$p_f = 1 - \Phi \left[\frac{F_c - 1}{\sqrt{F_c^2 C_{vR}^2 + C_{vQ}^2}} \right] \quad (86)$$

or with lognormal distribution

$$p_f = 1 - \Phi \left[\frac{\ln F_c \sqrt{\frac{1 + C_{vQ}^2}{1 + C_{vR}^2}}}{\sqrt{\ln(1 + C_{vQ}^2)(1 + C_{vR}^2)}} \right], \quad (87)$$

where F_c means the central safety factor.

It will be advantageous to examine here as an example, the case when $c = 0$. The safety factor

for a soil mass of granular material confined with a slope of β° to the horizontal can be described as

$$F_c = \frac{\overline{\tan \Phi}}{\tan \beta}. \quad (88)$$

This means that p_f can be determined by using the standard deviation or the coefficient of variation of $\tan \Phi$. As the standard deviation of β (uncertainties in construction of the slope) is negligible, the coefficient of variation on the load side is $C_{vQ} = 0$.

When earthworks are designed, data for $\overline{\tan \Phi}$ and C_{vR} are given (the latter is identical with the coefficient of variation of $\tan \Phi$). Wanted is the slope angle β which pertains to the probability of failure which is chosen. Transforming Eqs (86) and (87) new relations can be derived; with the assumption of a normal distribution:

$$\beta = \arctan [\overline{\tan \Phi} + (1 - C_{vR} \lambda_p)] \quad (89)$$

and with lognormal distribution:

$$\beta = \arctan [\exp(\ln \overline{\tan \Phi} + \ln A - \lambda_p B)], \quad (90)$$

where

$$A = \sqrt{\frac{1}{1 + C_{vR}^2}}, \quad (91)$$

$$B = \sqrt{\ln(1 + C_{vR}^2)} \quad (92)$$

and λ_p is the argument of the normal distribution available from the expression

$$p_f = 1 - \Phi(\lambda_p). \quad (93)$$

Example. The stability analysis is performed on a slope with an incline of 1.5 to 1 ($\beta = 33.7^\circ$) where $\overline{\tan \Phi}$ is 0.8185 and the coefficient of variation of $\tan \Phi$ is 0.05. As the central safety factor is

$$F_c = \frac{0.8185}{0.6667} = 1.228,$$

according to Eq. (86):

$$p_f = 1 - \Phi \left[\frac{0.228}{1.228 \cdot 0.05} \right] = 2.25 \cdot 10^{-5}.$$

The stability of slopes can also be examined by using the Monte Carlo method. An example for this application originates from SINGH (1971). The case of $\Phi \neq 0$, and $c \neq 0$ has been analysed on the basis of the following assumption:

- the two parameters are independent of each other;
- they are normally distributed.

The internal friction Φ has been chosen as one of the variables and the ratio $c/H\gamma$ as the other. Two hundred random numbers have been ordered to each of them. With reference to a numerical example the results are represented, in terms of F_c density and distribution functions, in Fig. 103. Varying the statistical characteristics of the shear

parameters SINGH (1971) tested different configurations. Concluding the calculations, he stated that:

- the distribution of F_c can be taken as normal;
- the coefficient of variation of F_c is in between those of Φ and c ;
- the value \bar{F}_c as determined by the application of the Monte Carlo method is almost similar to the one determined by the use of Φ and \bar{c} .

According to data collected and reported by Feld about 1800 earth dams were constructed in the USA before 1959, and thirty-three failures were registered therefrom. Having compiled these and Middlebrook's data, MEYERHOF (1970) concluded that one per cent of all earth dams which have been constructed on the basis of proper soil investigations in the last 30 years have failed, partially or totally. This fact confirms the statement — certified also by several other authors — that the probability of failure is around 0.01 to 0.02 when the customary central safety factor ($F_c = 1.3 - 1.6$) is used. A deviation (upwards or downwards) from this value of p_f can reasonably be made during the design work depending on certain characteristics of the earthwork: whether it is temporary or permanent, what would the requirements be with respect to enhancing the security in its lifetime or with respect to property conditions, what cost would be implied if a reconstruction were necessary, and so on. As the possibility exists of assigning the probability of failure to the geometry of the slope, there is also a possibility of making the assignment on the basis of an economic optimum (LANGEJAN, 1965).

The use of probability theory is also amenable to investigations as to the probability of the failure which might occur on a given length b of a linear construction. VANMARKE (1977) has presented a

suitable procedure by which the length $b = b_c$ having the maximal value of the probability of failure can be determined.

1.7 Drainage of earthworks

1.7.1 Dewatering by trench drains

The stability of earthworks may be widely affected by the manifold action of water originating from inside or outside a site. Indeed, problems of the stability of earthworks are inseparable from those of drainage. The practical implications of stability and drainage are dealt with in detail in a book by KÉZDI and MARKÓ (1969). In this section, some fundamental considerations, mainly of a theoretical nature, will be discussed.

Groundwater or water seeping through thin permeable layers may endanger the stability of earth slopes in many ways, and the practising engineer often faces the task of lowering the groundwater table on a construction site. This can be accomplished in many ways. Compact sites such as foundation pits are usually dewatered by filter wells. In the case where earthworks extend over a large area or great length, trench drains — deep and narrow slots filled with some free-draining material — can be more expedient. Their function is to collect and remove water from the adjacent soil by gravity, so that a permanent drawdown of the water table can be achieved. In this way the moisture content of the soil is reduced and its shear strength increased. Trench drains are often used in road and railway cuttings, along the edges of runways, etc., or as a remedial measure on unstable slopes and hillsides. In the latter case their buttressing effect also comes into play.

Trench drains consist of a bottom channel, a coarse-grained core, and an impervious seal on

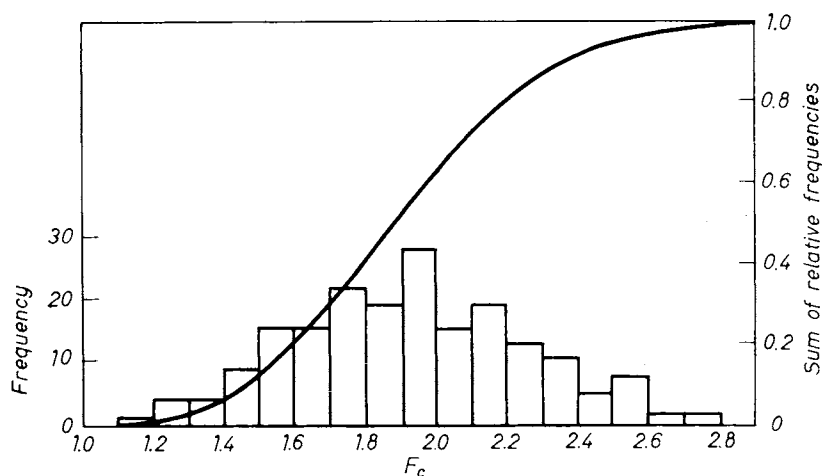


Fig. 103. Distribution of F_c as determined by the Monte Carlo method, after a numerical example from SINGH (1971)

the top (Fig. 104). The most important part is the core, which should be protected by graded filters on both sides to prevent fine material from being washed into the drain. Design details and the construction of drains are dealt with by KÉZDI and MARKÓ (1969). Only the drawdown effect of drains will be discussed here. But we must be aware that the methods of computation described in the following furnish dependable results only if the soil is fairly homogeneous and its coefficient of permeability is known with sufficient accuracy from laboratory or field tests.

Let us study first two typical cases of flow nets which may develop in the vicinity of drainage slots (Fig. 105). In case (a) there is a balance between the supply of water from the adjacent soil and the amount of water conveyed by the drain, so that a free water level will be formed in the trench, the elevation of which remains constant once a steady state of flow has been reached. In practical cases, a drop usually occurs between the breakout point of the top flow line (point *A*) and the water level in the trench (point *B*). If the rate of inflow is too low or the water is suddenly removed from the trench, the situation shown in Fig. 105b is likely to develop. There will be no free water level in the trench, since the small amount of water that drips from the soil and runs vertically along the sides *AC* is constantly removed before it can collect at the bottom of the drain. The neutral stress is therefore zero everywhere along the section *AC*. For the construction of flow nets, the following boundary conditions should be considered: the slot penetrates to the impervious base; the line *CD* and the drawdown curve *AE* are both flow lines. In case (a) the section *BC* of the vertical side is an equipotential line.

Let us consider first the case shown in Fig. 106. A vertical trench of infinite length fully penetrates a homogeneous, isotropic pervious stratum which contains free groundwater with a horizontal surface. It will be assumed that this stratum is supplied by a line source also of infinite length. Once a steady state of flow is reached, the quantity of flow through any vertical section such as *ab* is constant. We also assume that on this vertical section below the drawdown curve the hydraulic gradient is constant and equal to the slope of the drawdown curve at its point of intersection with the vertical line *ab*. This is known as the Dupuit-Thiem assumption. The quantity of flow through the shaded vertical element of unit width can be written as:

$$q = kiz.$$

Since $i \cong dz/dx$.

$$q = kz \frac{dz}{dx}.$$

Integrating and making use of the boundary conditions that at $x = l, z = h$ and at $x = 0,$

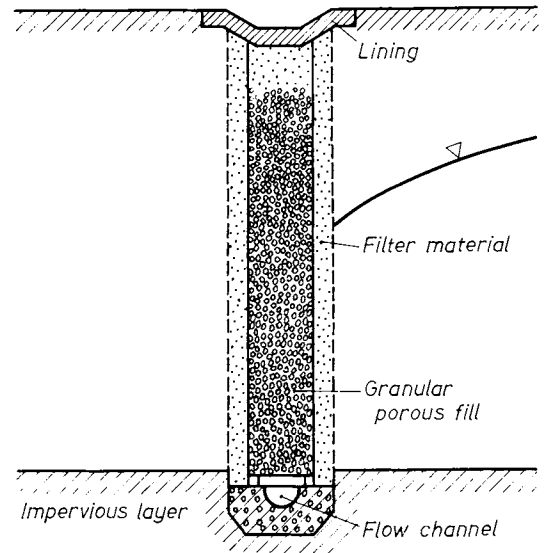


Fig. 104. Trench drain for depressing the groundwater level

$z = h_e$, gives

$$z^2 = \frac{2qx}{k} + h_e^2$$

and

$$q = \frac{k}{2l} (h^2 - h_e^2) \tag{94}$$

or

$$\left. \begin{aligned} z^2 &= \frac{x}{l} (h^2 - h_e^2) + h_e^2, \\ h^2 - z^2 &= \frac{2q}{k} (l - x) = \frac{l - x}{l} (h^2 - h_e^2) \end{aligned} \right\} \tag{95}$$

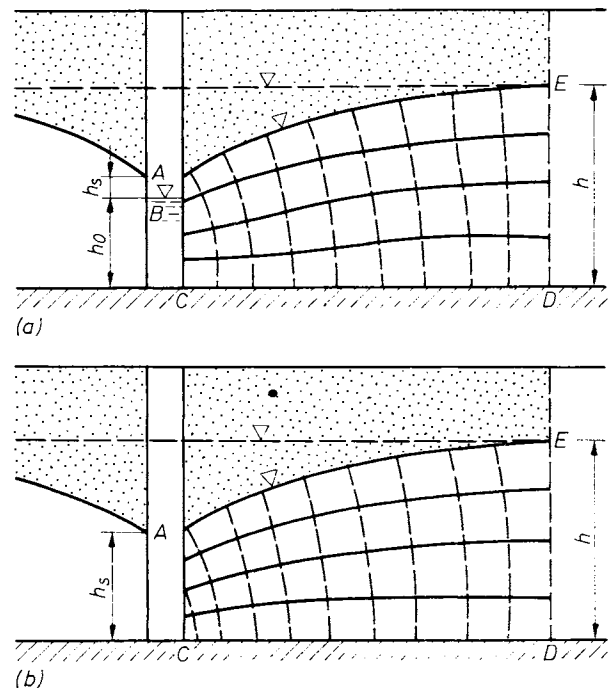


Fig. 105. Flow diagram in the vicinity of a trench drain: a — open free water level in the drain; h — immediate discharge

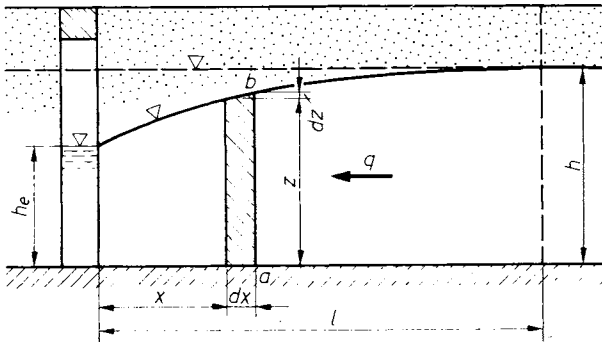


Fig. 106. Effect of a trench drain

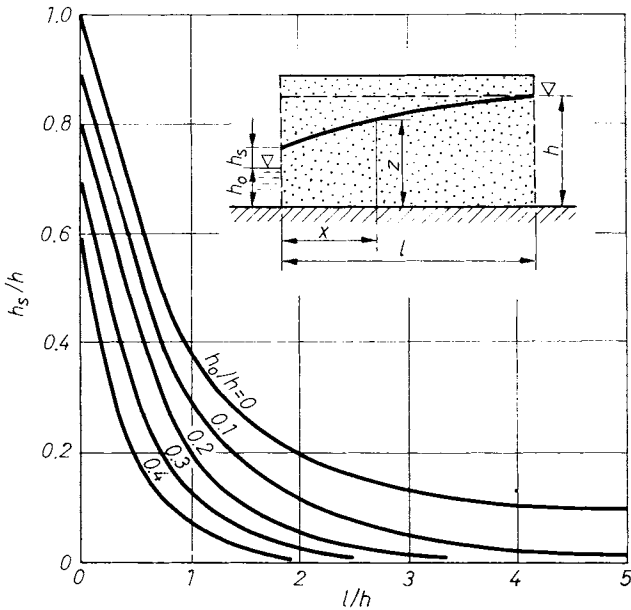


Fig. 107. Diagram for the determination of differences in the elevation of water table level and exit point of the upper seepage line

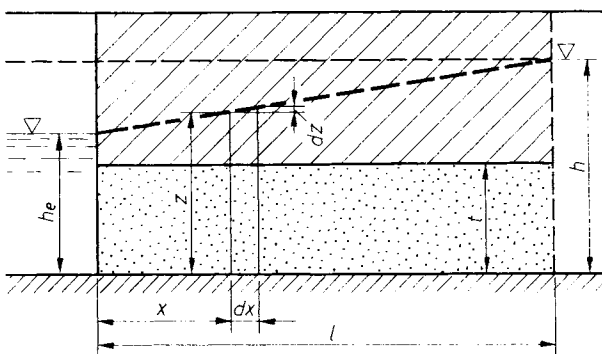


Fig 108. Flow diagram for seepage under pressure

Here, the expression h_e is the height of water in the trench (Fig. 106), and is equal to the height of the outbreak point of the top flow line above the impervious stratum. As was previously mentioned, this point is normally located on an eleva-

tion higher than the free water level in the trench so that water discharges freely on a part of the vertical surface (height h_s in Fig. 107). The height h_s of this surface can be estimated with the aid of the graph in Fig. 107, developed by CHAPMAN (1958). Except for small values of l/h or h_e/h , the shape of the drawdown curve can be determined from Eqs (95). In the vicinity of the trench, more accurate results can be obtained from the following expression:

$$h^2 - z^2 = \frac{l - x}{l} [h^2 - (h_0 + h_s)^2]. \quad (96)$$

As can be seen, to obtain Eq. (96), the height of the outbreak point ($h_0 + h_s$) should be substituted into Eq. (95) for the height of water h_0 at the trench.

The quantity of flow q from one side of the trench can be computed by the expression

$$q = \frac{k}{2l} (h^2 - h_0^2)$$

regardless of the height of the free discharge surface h_s .

In practice, it is often necessary to dewater a layer containing groundwater under pressure (artesian water). Figure 108 shows such a case; the water-bearing layer is overlain by an impervious layer. There is a steady supply of water by a line source located at a distance l . The trench fully penetrates the pervious layer. Water is continuously removed from the trench, but the water level in the trench stays above the top of the pervious layer even after a steady state of flow is reached, i.e. the flow occurs under pressure. The rate of flow q (for unit length) is given by the expression

$$q = k \frac{dz}{dx} t.$$

Integrating,

$$z = \frac{qx}{kt} + C.$$

The constant C can be determined from the boundary condition that $h = h_e$ where $x = 0$. Hence $C = h_e$.

Substituting, the expression for z becomes

$$z = \frac{qx}{kt} + h_e. \quad (97)$$

The discharge from one side of the trench can be obtained by inserting the boundary condition, $z = h$ at $x = l$ into Eq. (97). Hence

$$q = \frac{kt}{l} (h - h_e). \quad (98)$$

The drawdown at any distance x can be determined from the following equation:

$$h - z = \frac{q}{kt} (l - x) = \frac{l - x}{l} (h - h_e). \quad (99)$$

The formulas derived for flow rate and drawdown all contain the distance of the line source of seepage from the trench. This distance can be considered as the radius of influence of the drain. Its value is of little significance in the computation of seepage quantities, but may become an important factor in the design of drains where it is often required to determine, or to predict, the position of the drawdown surface. For this reason, the radius of influence should be determined as accurately as possible. If the drain is close to a river, the radius of influence is essentially determined by the distance between them. In the general case, Sichardt's empirical formula can be used:

$$l = C(h - h_v) \sqrt{k}.$$

Here the expression in parentheses is the maximum drawdown in metres and k is the coefficient of permeability in cm/s. A value of 3 was proposed by Sichardt for the constant C for gravity wells. This value was found to be valid in a number of field observations. For the case of a line source (two-dimensional flow) C values ranging from 1.5 to 2 were measured. Since the coefficient of permeability of coarse-grained soils is related to their grain-size distribution, the radius of influence l must also depend on grain size. On the basis of field investigations (U. S. Army Corps of Engineers), it was possible to develop an empirical relationship (Fig. 109) from which the value of l can readily be obtained for soils ranging from fine sand to sandy gravel.

The preceding formulas apply to the case where the trench fully penetrates the pervious layer. If the impervious base is located at a great depth, it may not be economical to lower the drain to that depth. We must therefore also investigate the case where a trench only partially penetrates the pervious layer. The quantity of gravity flow (Fig. 110) can be computed from an empirical formula derived from model tests by CHAPMAN (1956):

$$q = \left(0.73 + 0.27 \frac{h - h_0}{h} \right) \frac{k}{2l} (h^2 - h_0^2). \quad (100)$$

If the trench is supplied on one side only as in the case of interceptor drains, the water level on the opposite side does not rise above a maximum height given by

$$h_d = h_0 \left[\frac{1.48}{l} (h - h_0) + 1 \right]. \quad (101)$$

Equations (100) and (101) are valid only for values of $l/h \geq 3$. In the case of flow under pres-

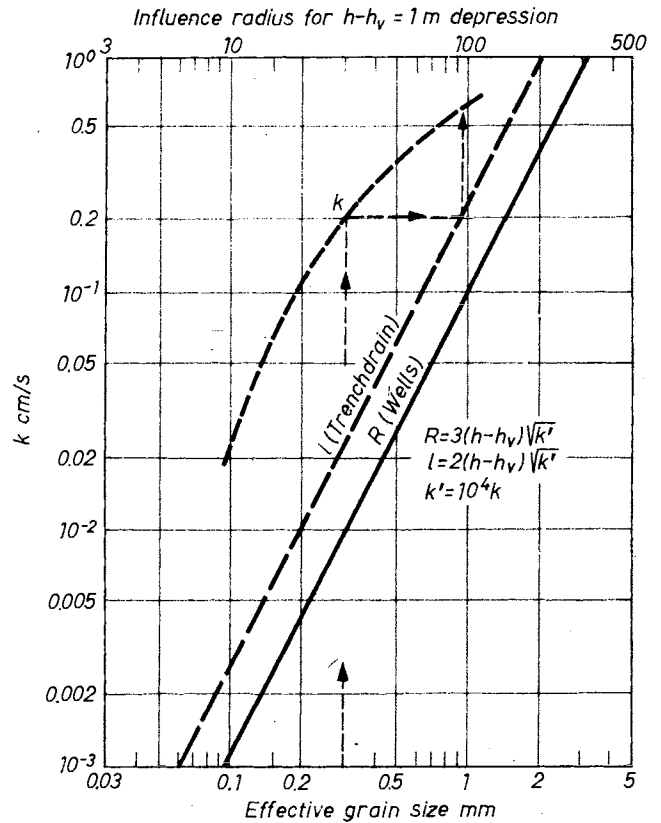


Fig. 109. Estimation of the radius of influence

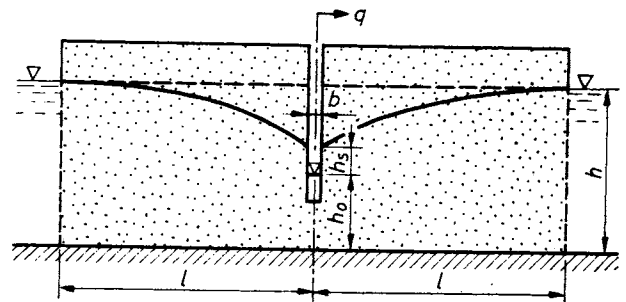


Fig. 110. Imperfect trench drain

sure (Fig. 111) the quantity of flow can be obtained from the following expression:

$$q = \frac{kt(h - h_e)}{l + l'}. \quad (102)$$

The distance l' depends on the penetration t_1 of the trench into the pervious layer and on the thickness t of the latter. Values of l' can be determined from the graph in Fig. 111 proposed by BARRON (1956). The maximum piezometric head h_d on the side opposite to the source is given by

$$h_d = \frac{l'(h - h_e)}{l + l'} + h_e. \quad (103)$$

In the following we shall deal with the case where a drain is supplied by line sources on both sides (Fig. 112). For a gravity flow, the quantities of seepage are simply doubled, but for flow under pressure the equation will be different. The quantity of flow can be computed by the formula

$$q = \frac{2kt(h - h_e)}{k_l(1 + \lambda_t)}, \quad (104)$$

where the factor λ is a function of the ratio t_1/t . Its value is obtained from Fig. 113.

For distance x greater than $1.3t$, the piezometric head z can be determined from the following equation

$$z = h_e + (h - h_e) \frac{x + \lambda t}{l + \lambda t}. \quad (105)$$

Finally, let us discuss the case where dewatering is carried out by means of two parallel drains (Fig. 114). In general, Chapman's empirical formula (Eq. (100)) can also be applied to this case. The top of the drawdown curve midway between the drains is located at a height

$$h_d = h_0 \left[\frac{c_1 c_2}{l} (h - h_0) + 1 \right]$$

above the impervious base, where c_1 and c_2 are obtained from Fig. 115. For flow under pressure, Eqs (101) and (102) are valid, in which case l' can be determined from Fig. 111.

It should be mentioned that a more accurate determination of neutral pressures and quantities of seepage is possible by means of flow nets, as was illustrated by Fig. 105. Figure 116 shows

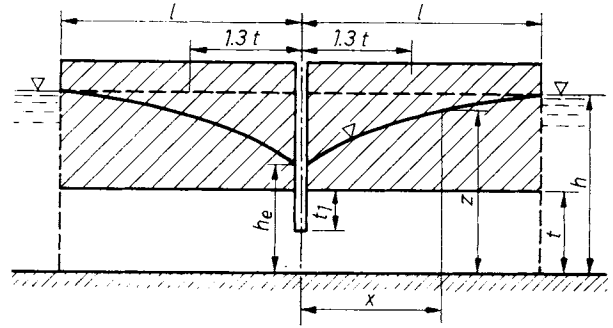


Fig. 112. Flow diagram for the seepage under pressure to an imperfect trench drain from both sides

a further example — a flow under pressure towards a partially penetrating (imperfect) drain from equidistant line sources of flow on both sides.

Making use of the computation formulas given in this section enables us to solve a number of practical problems. Usually, we have to answer the following questions.

1. What is the quantity of flow from a drain necessary to produce the required drawdown at a given point?
2. At what depth should the bottom of a slot drain be located, if it is required to keep the drawdown surface below a given level?
3. How far apart may two drains be located, if the required drawdown at a point between them is given?

In the following, numerical examples illustrate solutions to these problems.

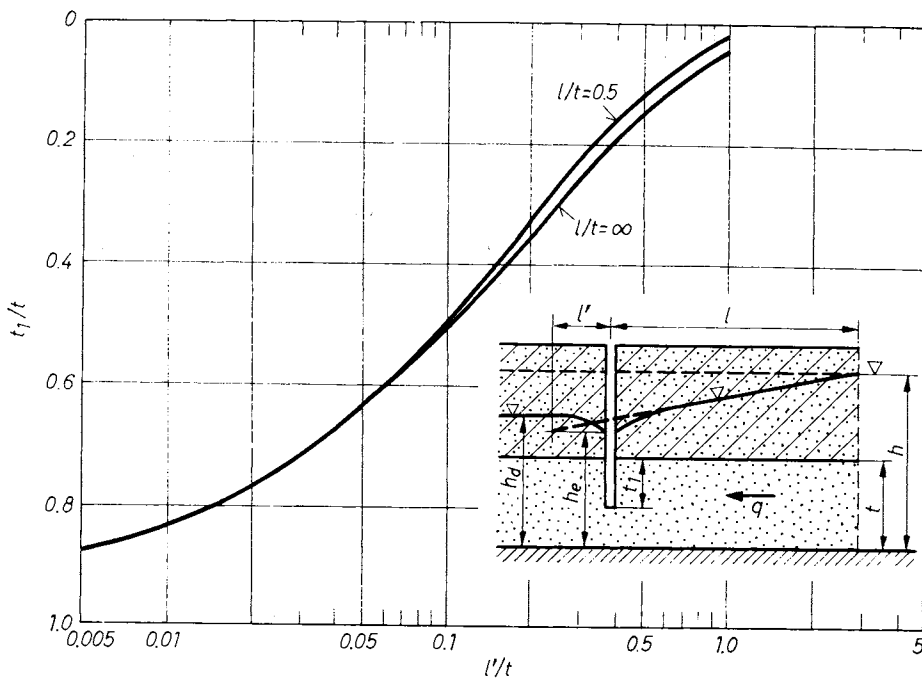


Fig. 111. Flow diagram for seepage under pressure to an imperfect trench drain

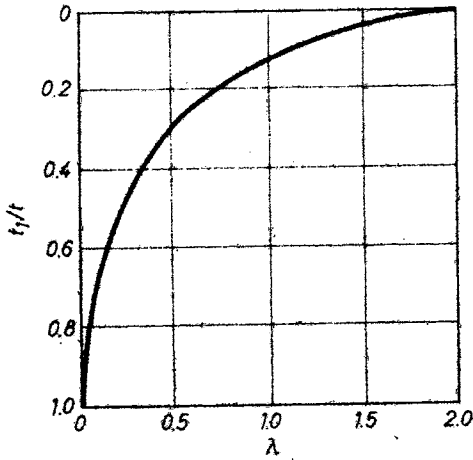


Fig. 113. Diagram for determination of coefficient λ

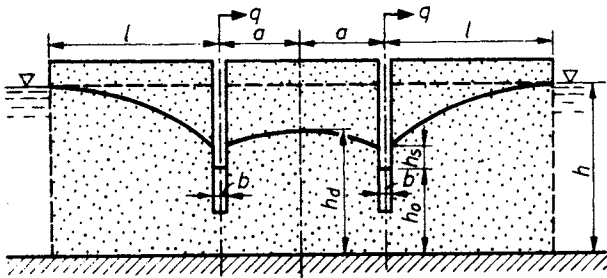


Fig. 114. Depression of the water table between two parallel deep drains

Example 1. What is the required discharge from a fully penetrating drain (Fig. 105) if the height of water in the trench is not to exceed $h_0 = 10$ cm? Given: $h = 400$ cm, $k = 2 \cdot 10^{-4}$ cm/s.

In the first approximation the radius of influence is assumed to be $l = 10$ m.

For flow from both sides, the discharge per length of 1 cm amount to $q = \frac{k}{l} (h^2 - h_0^2) = \frac{2 \cdot 10^{-4}}{1000} (400^2 - 10^2) = 0.032$ cm³/s.

For a total length of 100 m

$$Q = 10\,000 \cdot 0.032/1000 = 0.32 \text{ l/s.}$$

In order to compute the drawdown, the height of the free discharge surface h_s must first be determined with the aid of Fig. 107. For the ratios $l/h = 10/4 = 2.5$ and $h_0/h = 0.1/4 = 0.025$ we obtain $h_s/h = 0.13$. Hence $h_s = 0.13 \cdot 400 = 52$ cm. The elevation of the breakout point of the drawdown curve from the bottom of the drain is $h_e = h_0 + h_s = 62$ cm. The height of the water table at a distance $x = 3.0$ m as computed from the expression

$$h^2 - z^2 = \frac{l - x}{l} [h^2 - (h_0 + h_s)^2]$$

is $z = 2.24$ m.

To check this value we compute the radius of influence

$$l = 2[h - (h_0 + h_s)] \sqrt{k} = 2(4 - 0.62) \sqrt{2} = 9.60 \text{ m}$$

i.e., the first estimate was correct.

Example 2. An intercepting drain arranged as shown in Fig. 110 is made with the purpose of keeping the downstream section of the drawdown curve below the height $h_d = 5$ m from the impervious base. How deep should the trench be? The original water table is located at an elevation of $h = 8.0$ m above the base. The coefficient of permeability of the soil is $k = 10^{-3}$ cm/s.

The head of water in the trench should first be computed. The radius of influence is estimated to be $l = 25$ m. From Fig. 107 it is apparent that for the given ratios $l/h = 25/8 = 3.12$ and $h_0/h \approx 0.5$ (estimated value), $h_s/h \approx 0$, i.e.

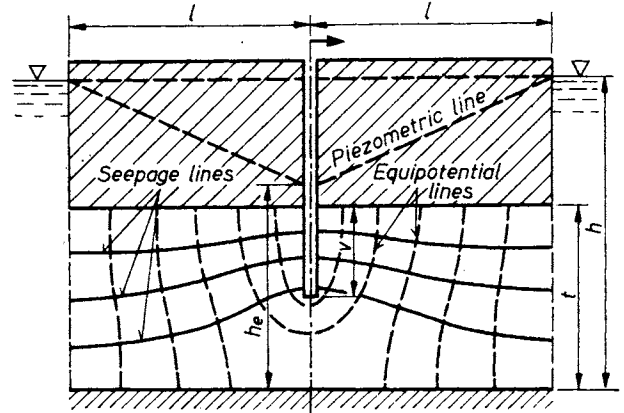


Fig. 116. Flow net diagram; flow under pressure to an imperfect drain from both sides

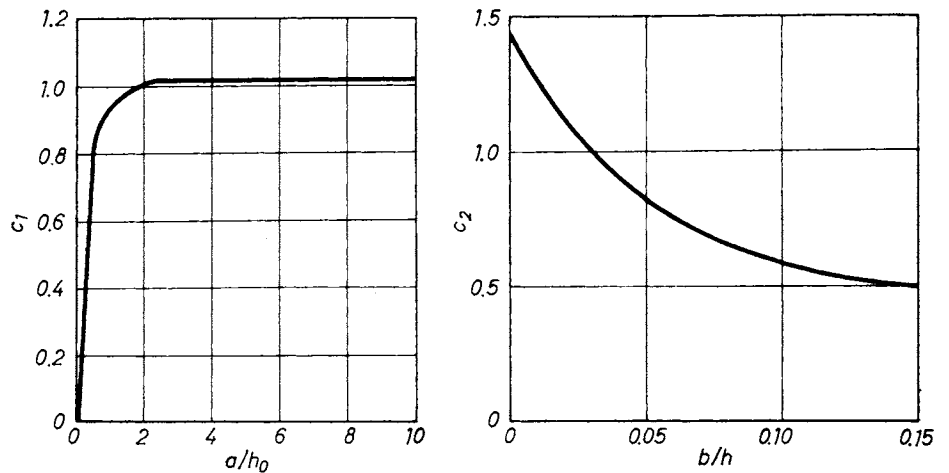


Fig. 115. Diagram for the determination of coefficients c_1 and c_2

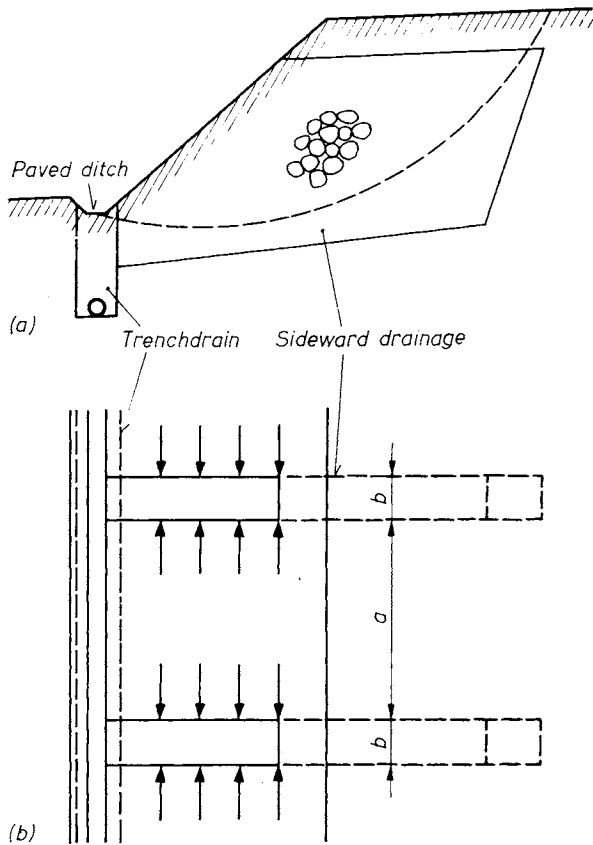


Fig. 117. Arrangement of stone ribs (draining trenches filled with crushed stones) in order to increase the stability of slopes:
a — cross-section; b — plan

the height of the free discharge surface is small enough to be neglected.

h_0 is obtained from Eq. (101):

$$h_d = h_0 \left[\frac{1.48}{l} (h - h_0) + 1 \right].$$

With $h_d = 5$ m, $h = 8$ m and $l = 25$ m,

$$5 = h_0 \left[\frac{1.48}{25} (8 - h_0) + 1 \right]$$

and

$$h_0^2 - 24.9 h_0 + 84.4 = 0.$$

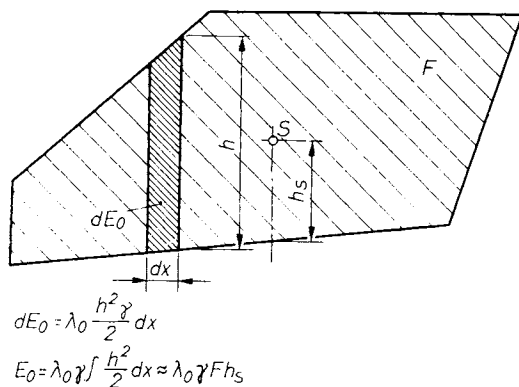


Fig. 118. Stability analysis of slopes reinforced by stone ribs, with respect to friction on the sides of the ribs

Solving the equation for h_0 gives $h_0 = 4.05$ m. The rate of discharge is given by Eq. (100).

$$q = \left(0.73 + 0.27 \frac{h - h_0}{h} \right) \frac{h}{2l} (h^2 - h_0^2),$$

$$q = \left(0.73 + 0.27 \frac{8 - 4.05}{8} \right) \frac{10^3}{2 \cdot 2500} (800^2 - 405^2),$$

$$q = 0.082 \text{ cm}^3/\text{s}.$$

For a total length of 100 m, $Q = 0.82$ l/s. Checking the radius of influence using Sichardt's formula

$$l = 2 (h - h_c) \sqrt{k} = 2(8 - 4.05) \sqrt{10} = 24.9 \text{ m} \approx 25 \text{ m}.$$

1.7.2 Buttress drains

Stone-filled drainage trenches are often used as a remedy in soft clays. They have a double effect. For a while after completion, their main function is to stabilize the adjacent soil masses by their buttress effect which is due to the action of frictional forces on the sides of the drains. Desiccation, the other beneficial effect, comes into play only later. With regard to their restraining effect, the spacing of buttress drains should be chosen so as to provide, immediately after construction, a sufficient degree of safety against sliding in cutting slopes or unstable hillsides.

The buttressing effect of drains can be assessed quantitatively as follows. An earth mass located between two parallel buttress drains (Fig. 117) exerts a horizontal pressure on the vertical sides of the drains. This pressure can be computed as an earth pressure at rest, since with the construction of the drains, the mass of soft soil between them becomes laterally confined. It can be seen from Fig. 118 that the resultant earth pressure acting on one side of a drain is proportional to the static moment of the contact surface between drain and soil with respect to the baseline of the drain. For clays, the coefficient of earth pressure at rest, K_0 , may have values ranging from 0.5 to 0.8, depending on the consistency of the soft material. As the earth mass tends to slip down from between the drains, a frictional resistance is mobilized on the surface between the soft soil and the coarse filter material of the drain. In the stability analysis of a slope, these frictional resistance acting on both sides must also be taken into account among the restraining forces. The magnitude of the resultant frictional force is $\mu_f E_0$. The coefficient of friction μ_f between clay and sand filter may have a value of 0.2 to 0.3. The stability analysis is illustrated by Fig. 119. The weight of the earth mass W is taken into consideration, with the width a between drains (Fig. 117). The construction shown in Fig. 119 is based on the assumption that $\Phi = 0$. The cohesion required for equilibrium can be determined from the polygon of forces.

With the aid of the analysis described, we can judge whether the spacing of buttresses, usually

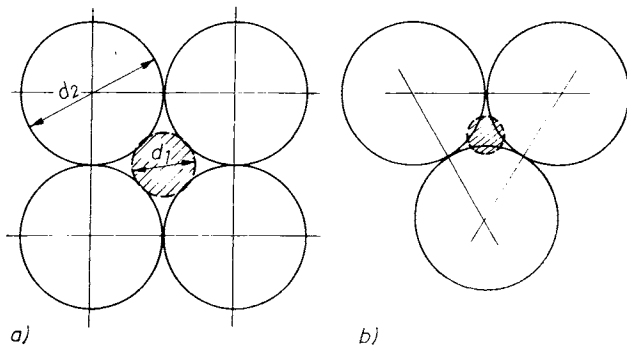


Fig. 121. Regular arrangement of spheres in the pore space: a — loosest disposition; b — densest disposition

In the densest packing (Fig. 121b), where the spheres form a tetrahedral array and each sphere touches twelve neighbouring spheres, the corresponding ratio is

$$f = \frac{d_2}{d_1} = 1 + 2\sqrt{3}.$$

The mean value of f , 3.43, is valid for irregular packing. For natural grain assemblies with non-uniform grading, a value of 4 to 5 can be adopted for the filter ratio. The validity of the relationship given by Eq. (106) was confirmed experimentally by BERTRAM (1940). Further tests were conducted by the U. S. Army Corps of Engineers (1941) and the U. S. Bureau of Reclamation (1955). The former stipulates that, in addition to the requirement

$$\frac{d_{15} \text{ of filter}}{d_{85} \text{ of soil}} \leq 5$$

the following criterion must also be satisfied:

$$\frac{d_{50} \text{ of filter}}{d_{50} \text{ of soil}} \leq 25.$$

In practice, protective filters are either made up of several layers (graded filters) or consist of a mixture of various grain sizes with favourable filtering properties (mixed filters). In cases where a greater thickness is required, the filter is usually constructed from several layers, each of which satisfy the filter rule with respect to the preceding layer. Such a multiple filter is shown in Fig. 122. Let the required filter ratio be denoted by f . Then, for successive layers the following relationships must be satisfied:

$$\begin{aligned} d_1 &= fd, \\ d_2 &= f^2d, \\ &\vdots \\ d_n &= f^n d, \\ D &= f^{n+1}d. \end{aligned}$$

For given values of d , D and f , the required number of layers can be obtained from the following equation:

$$n = \frac{\log D - \log d}{\log f} - 1. \quad (107)$$

Equation (107) can also be used to check the

actual value of f for a given number of layers n and given representative grain sizes d and D . Thus

$$f = \sqrt[n+1]{\frac{D}{d}}. \quad (108)$$

If the value of f computed by Eq. (108) is greater than 4.5, the number of layers should be increased.

It is also possible to construct a filter of a single material such that it contains a mixture of all the grain sizes that would be required for a graded filter. The grading of a mixed filter should be such that the voids in one component are just filled by the grains of the preceding component. For the design of such mixtures it can be assumed that the average porosity for each layer is equal to $n = 35\%$. A calculated example is given in Table 3.

Table 3. Data for producing mixed filters

Classification	Grain size (mm)	Volumetric proportion (m ³)	Percentage per mass
I	0 1	0.04	8
II	1 3	0.12	9
III	3 15	0.35	21
IV	15 50	1.0	62

The required thickness of a filter depends on the type of material to be protected, the intensity of seepage and the number of layers. The thickness of a single layer is seldom less than 50 cm, although in simple cases 30 cm may be practicable. Typical cases where the use of protective filters may be necessary are illustrated by Fig. 123.

The requirement upon which the design of mixed filters was based can also be applied to natural soils. If seepage is occurring in a soil, there is always a danger of fine particles being washed out. But any soil can be conceived as being made up of two components: one, being a relatively coarse component, serves as a filter for the rest of the soil. If the two components satisfy the filter criterion with respect to each other, the particles in the finer component are not likely to migrate through the void spaces in the coarser part. Such a condition is known as self-filtration. If any two components into which

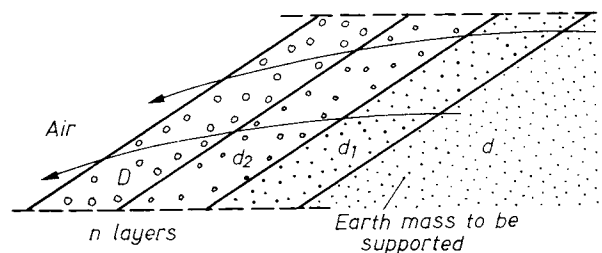


Fig. 122. Filter composed of several layers

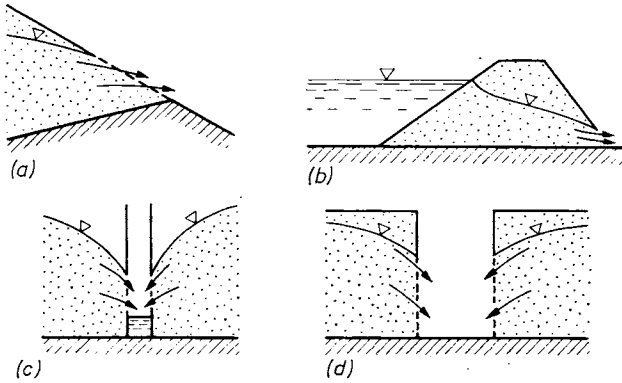


Fig. 123. Dotted areas show places where it is advised to incorporate filter layers:
a — slope; b — dike; c — trench; d — foundation pit

a given soil can be split satisfy the filter rule, the soil is said to be self-filtering.

Whether or not a soil shows this property can be ascertained by the following test. The grain-size distribution of the soil is given in Fig. 124a. We choose an arbitrary diameter d_0 and divide the material into two components. For the sake of better understanding, the grain-size distri-

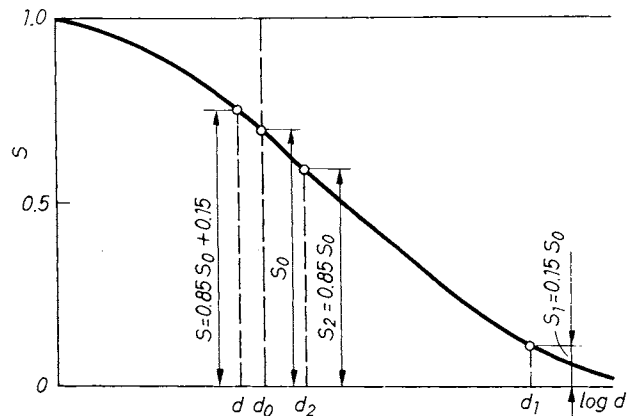
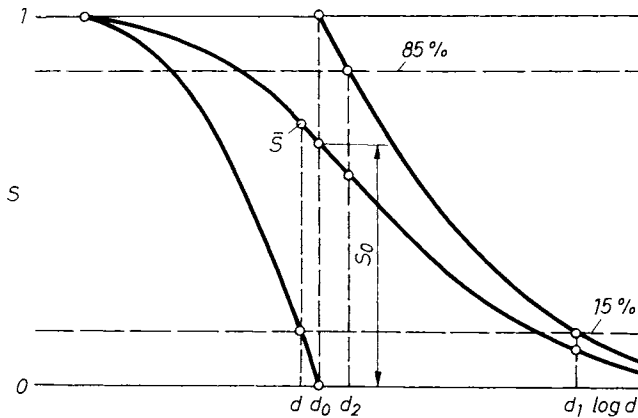


Fig. 124.
a — Investigation of the soil as to its own filtering capacity; division into components; b — establishment of the effective grain size

bution curves of these components are also shown in Fig. 124a. In an actual investigation only certain significant points of the curves need to be determined, as will be seen from the following.

The diameter d , representative of the component which is to serve as the filter, will be read off at $P' = 0.85 P_0 + 0.15$ from the original curve; for the component to be protected, the diameters d_1 and d_2 are taken at $P_1 = 0.15 P_0$ and $P_2 = 0.85 P_0$, respectively. The values d , d_1 and d_2 can be obtained directly from the original curve, as demonstrated by Fig. 124b.

Now we choose several other values for d_0 and repeat the calculation for each. If we plot the set of d , $4d_1$ and $4d_2$ values against d_0 , we can see at a glance whether the criterion

$$4d_2 > d > 4d_1$$

is satisfied or not.

The use of the method is shown in the following three examples. Figure 125 shows the grain-size distribution curves of three soils. Curve A represents a loess from Hungary, known to be very susceptible to surface erosion, but when water percolates through it, usually no fines are washed out and the water remains clear. The computation of the values d , $4d_1$ and $4d_2$ can conveniently be

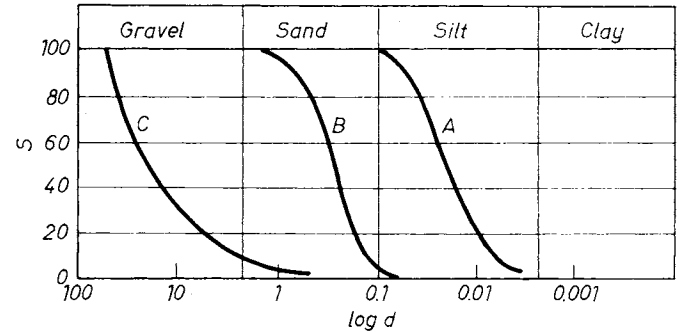


Fig. 125. Typical grain-size distribution curves of investigated soils

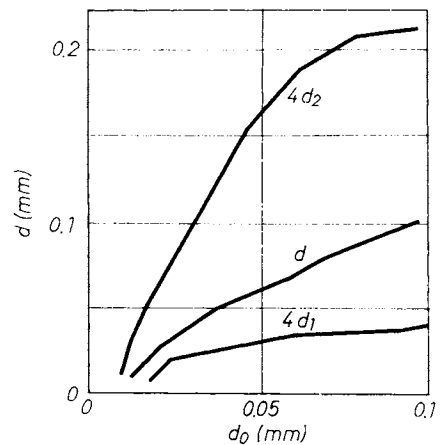


Fig. 126. Investigation of soil A

Table 4. Calculation of the critical grain-size diameter

	d_0	S_0	S_2	S'	S_1	d	$4d_1$	$4d_2$
A	0.10	1.00	0.850	1.000	0.150	0.100	0.038	0.210
	0.08	0.97	0.825	0.975	0.145	0.082	0.0375	0.208
	0.06	0.89	0.756	0.901	0.134	0.060	0.034	0.184
	0.04	0.72	0.612	0.762	0.108	0.044	0.029	0.132
	0.02	0.40	0.340	0.490	0.060	0.026	0.023	0.068
	0.01	0.18	0.153	0.333	0.027	0.017	0.009	0.038
	0.008	0.12	0.102	0.252	0.018	0.014	0.007	0.029
B	1.0	0.95	0.81	0.96	0.15	1.05	0.66	2.60
	0.9	0.93	0.80	0.95	0.13	1.00	0.62	2.44
	0.8	0.89	0.76	0.91	0.13	0.86	0.62	2.32
	0.7	0.85	0.72	0.87	0.125	0.76	0.61	2.04
	0.6	0.78	0.66	0.81	0.12	0.64	0.60	2.00
	0.5	0.70	0.60	0.75	0.10	0.56	0.56	1.60
	0.4	0.60	0.51	0.66	0.09	0.45	0.53	1.40
	0.3	0.40	0.34	0.49	0.06	0.34	0.44	1.06
	0.2	0.21	0.18	0.33	0.03	0.26	0.36	0.72
0.1	0.04	0.03	0.18	0.01	0.18	0.26	0.36	
C	50	1.00	0.850	1.000	0.150	50	10.0	176
	15	0.38	0.323	0.473	0.057	21.5	2.4	44
	3	0.17	0.144	0.294	0.026	8.6	0.8	9.6
	1	0.08	0.068	0.218	0.012	4.7	—	3.1

arranged in tabulated form (Table 4). The results are plotted in Fig. 126. It can be seen that the filter rule is fulfilled for the whole range of grain sizes.

Curve B in Fig. 125 shows a sand from the Sahara, which has never been subjected to water flow; no natural processes that would have led to the formation of a natural filter have occurred in it. It can be seen from the graphical representation of the test (Fig. 127) that for grain sizes smaller than 0.5 mm the filter rule is not fulfilled, so that movement of the fine particles may occur.

The third example (curve C) is an artificial mixture, made with the purpose of producing a good mixed filter, and according to experience it is indeed a good one. The test confirms this

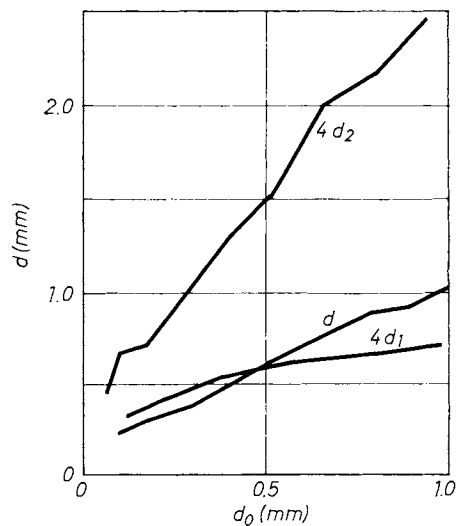


Fig. 127. Investigation of soil B

quality; the filter rule is fulfilled for the whole range (Fig. 128). The ratios of the respective grain sizes at every value of d_0 are approximately the same.

1.8.2 Filter design

Filters used on the discharge surface of the core in earth dams should be designed to meet certain hydraulic requirements. They must quickly intercept and remove seepage emerging from the core, without inducing high seepage forces or hydrostatic pressures. The permeability of granular materials was found to be approximately proportional to d_{15}^2 (TAYLOR, 1948). So if the filter rule is fulfilled, a filter is 16 to 25 times more permeable than the core material to be protected. Such a difference in permeability is usually sufficient to ensure that seepage is removed quickly, provided that adequate dimensions and hydraulic gradients are available in the drain, as is the case in the cross-section shown in Fig. 129. If, however, the hydraulic gradient is too small, it is advisable to make a check on the discharge capacity of the filter or, better still, to design it by applying hydraulic principles. For example, if the rate of infiltration q per unit length of drain is known, the required thickness h_r of the filter layer can be computed from Darcy's law as follows:

$$q = kiA = kih_r \cdot l.$$

Hence

$$h_r = \frac{q}{ki},$$

where i is the maximum allowable hydraulic gradient, determined by the allowable hydrostatic

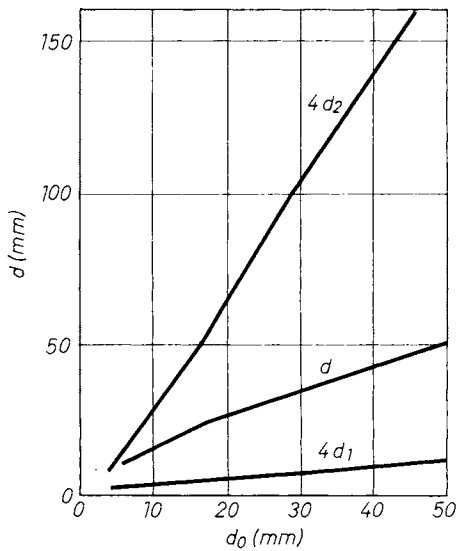


Fig. 128. Investigation of soil C

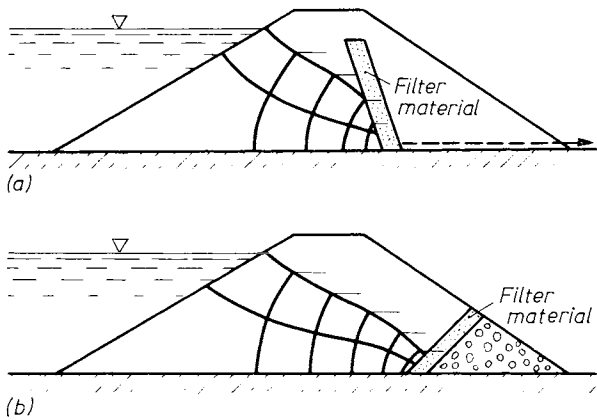


Fig. 129. Examples showing the arrangement of various filter layers:
a — slanting filter layer inside the dam; b — sand layer and stone base at the outer toe of the dam

pressures and seepage forces in the drain. On the other hand, i should not be too low lest saturation should spread into adjacent soil to an undesirable extent.

Example. It is required that a drain be designed for the composite dam cross-section shown in Fig. 130. The drain is to be made up of a steeply inclined section, called a chimney drain, and a horizontal blanket drain. The key dimension for both are given in Figs 130b and c.

First, we construct a flow net and, using the known coefficient of permeability of the core material, we compute the rate of discharge through the core. In addition, we should also estimate the quantity of seepage through the foundation into the horizontal blanket. Let us assume that seepage through the core per running meter of dam length is $q_1 = 0.2 \text{ m}^3/\text{day}$ and seepage into the horizontal filter is $q_2 = 1.0 \text{ m}^3/\text{day}$. On the basis of practical considerations, the chimney drain is to have a horizontal width of $b = 3.5 \text{ m}$. The required permeability of the filter k_F can be obtained as

$$k_F = \frac{q_1}{\frac{h_1}{l} b} = \frac{0.2}{\frac{90}{93} 3.50} = 0.059 \text{ m/day}.$$

A clean sand with no fines usually meets this requirement.

The horizontal outlet portion of the drain should be so designed as to be capable of discharging the total seepage $q = q_1 + q_2 = 1.2 \text{ m}^3/\text{day}$, without excess hydrostatic pressures being induced in the drain. In other words, the maximum head in the drain should not be greater than the thickness of the blanket drain: $h_d \leq d$. Therefore, the permeability of the filter material should not be smaller than

$$k_D = \frac{q}{id} = \frac{q_1 + q_2}{\frac{h_d}{l_d} d} = \frac{ql_d}{d^2}. \quad (109)$$

Substituting numerical values gives

$$k_D = \frac{198}{d^2} \text{ and } d = \sqrt{\frac{198}{k_D}}.$$

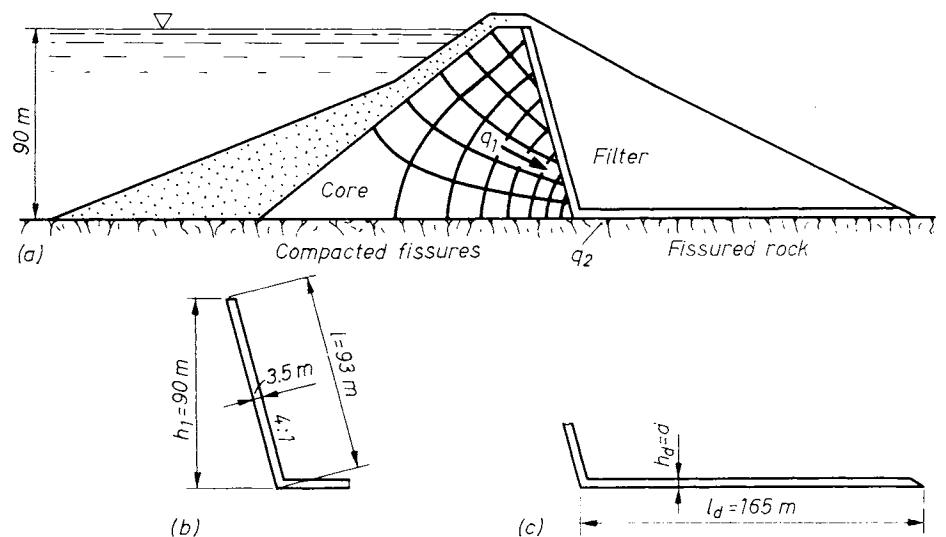


Fig. 130. Dimensions of the filtering system:
a — cross-section and flow net diagram; b — and c — filter units

For example, if we select a pea gravel with a permeability of $k_D = 100$ m/day (approximately 0.12 cm/s) as the filter material, the required thickness becomes

$$d = \sqrt{1.98} = 1.40 \text{ m}.$$

The best way to design a filter system is to use a composite flow net for dam and filter.

As is known from previous studies (see Vol. 1, Eq. (120)), when seepage occurs from an earth mass into a filter of higher permeability, the length-to-width ratio of the rectangles formed in the flow net within the filter must conform to the following relationship:

$$\frac{c}{d} = \frac{k_F}{k_E},$$

where k_F is the permeability of the filter and k_E is the permeability of the earth mass. In practice, either the dimensions of the filter are given and its required permeability should be determined, or, conversely, for an assumed permeability ratio the required dimensions should be found.

The design procedure will be demonstrated, after CEDERGREN (1967), by two examples shown in Fig. 131. The flow nets in either case were constructed on the assumption that the permeability of the filter is great enough to convey all of the seepage that enters straight into a gravel collector drain located at the toe. First we draw a flow net for the dam and determine the position of the point at which the top flow line emerges on the

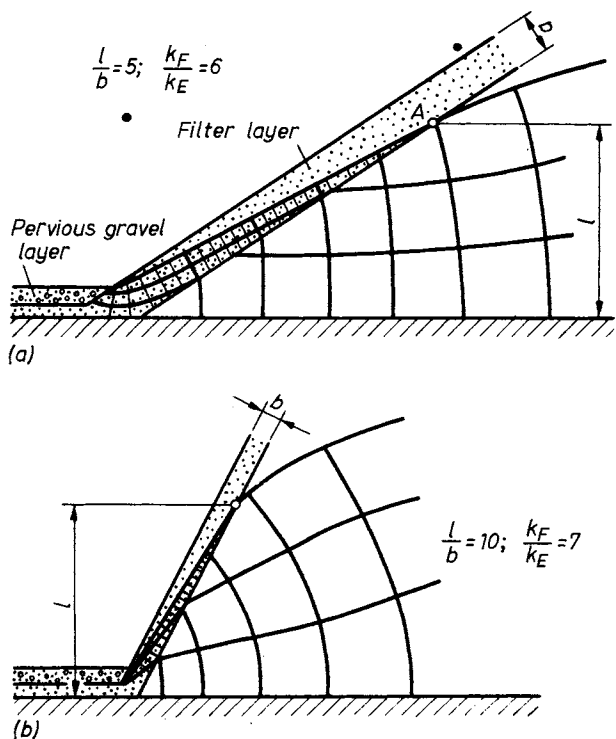


Fig. 131. Flow net diagrams for various filter layers of differently inclined slopes

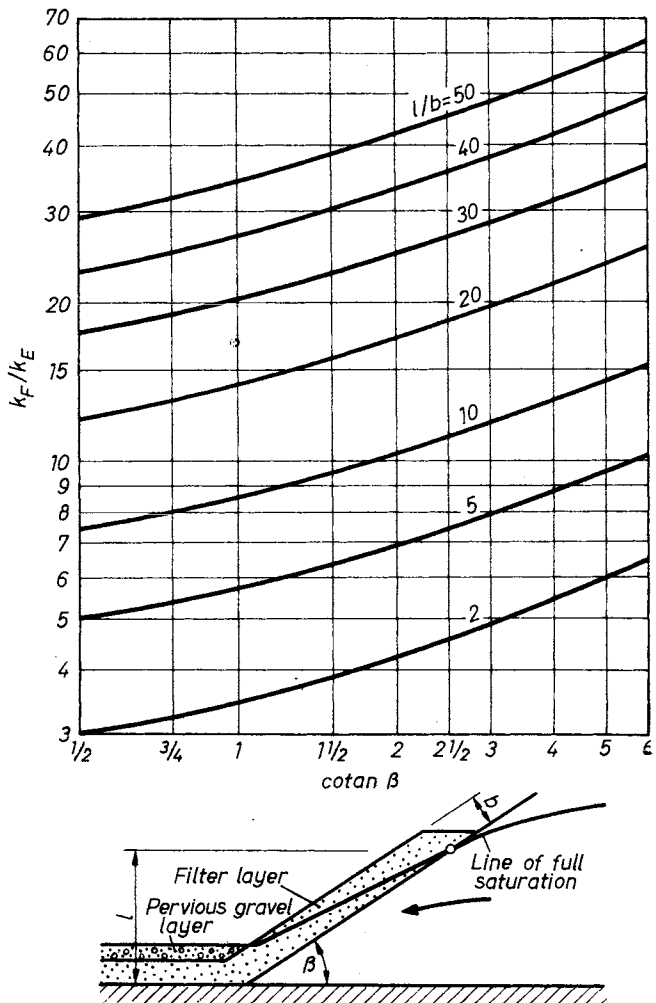


Fig. 132. Diagrams for dimensioning the filter layers in the case of differently inclined slopes

discharge surface (point *A*). Next we connect point *A* and the top of the gravel toe drain with a free-hand line and, in a similar manner, we draw the remaining flow lines. By continuing the equipotential lines already drawn within the dam, so that they deflect at the boundary, we can complete the flow net in the filter. The length-to-width ratio of the rectangles resulting from the construction can readily be determined and from this the required permeability ratio computed (Vol. 1, Eq. (120)). For the case shown in Fig. 131a this ratio is

$$\frac{c}{d} = \frac{l}{b} = \frac{k_F}{k_E} = 6$$

and for the flow net in Fig. 131b

$$\frac{l}{b} = \frac{k_F}{k_E} = 7.$$

As can be seen from the flow nets, the hydraulic gradients in the filters are fairly large.

For flow nets of the type illustrated by Fig. 131, CEDERGREN (1967) developed a design chart which is given in Fig. 132. It furnishes the required k_F/k_E ratios for various slopes and thicknesses of drain. It can be used to determine the required permeability ratio k_F/k_E for assumed dimensions l and b and vice versa.

References

- AAS, G. (1981): Stability of natural slopes in quick clays. *Proc. 10th ICSMFE*. Vol. 3, Stockholm.
- BALIGH, M. M., AZZOUZ, A. S. and LADD, C. C. (1977): Line loads on cohesive slopes. *Proc. 9th ICSMFE*. Vol. 2, Tokyo.
- BERNATZIK, W. (1947): *Baugrund und Physik*. Schweizer Druck- u. Verlagshaus, Zurich.
- BISHOP, A. W. (1955): The use of the slip circle in the stability analysis of slopes. *Géot.*, No. 1.
- CASAGRANDE, A. and SHANNON, W. L. (1948): Research on stress-deformation and strength characteristics of soils and soft rocks under transient loading. *Publ. Graduate School of Eng. Harvard Univ.*, Soil Mech. Series, No. 31.
- CEDERGREN, H. R. (1967): *Seepage, Drainage and Flow Nets*. Wiley, New York.
- FELD, J. (1965): The factor of safety in soil and rock mechanics. *Proc. 6th ICSMFE*. Vol. III, Montreal.
- FELLENIUS, W. (1927): *Erdstatische Berechnungen mit Reibung und Kohäsion und unter Annahme Kreiszyklindrischer Gleitflächen*. Ernst, Berlin.
- FELLENIUS, W. (1936): Calculation of the stability of earth dams. *Proc. 2nd Congress on Large Dams*. 4.
- FREDLUND, D. G. and KRAHN, J. (1977): Comparison of slope stability methods of analysis. *Can. Geot. J.*, No. 3.
- FRONTARD, M. (1922): Cycloïdes de glissement des terres. *Comptes Rendus*. Hebdom. Acad. Sci., Paris, 174.
- FRONTARD, M. (1954): Lignes de glissement et hauteur dangereuse d'un massif de terre limité par un talus plan. *Proc. Eur. Conf. on Stability of Earth Slopes*. Vol. 1, Stockholm.
- FRÖCHLICH, O. K. (1950): Sicherheit gegen Rutschung einer Erdmasse auf Kreiszyklindrischer Gleitfläche mit Berücksichtigung der Spannungsverteilung in dieser Fläche. *Federhofer und Girkman Festschrift*, Vienna.
- GREENWOOD, J. R. (1983): A simple approach to slopes stability. *Ground Eng.*, No. 4.
- GRIVAS, D. A. (1981): How reliable are present methods of slope failure prediction. *Proc. 10th ICSMFE*. Vol. 3, Stockholm.
- HUDER, J. (1977): Sicherheitsfaktor für eine geradlinige Böschung gegen Rutschen. *Die Bautechnik*, No. 12.
- JÁKY, J. (1925): The theoretical slope and engineering application thereof. (In Hungarian.) *MMÉÉ Közl.*, No. 7.
- JÁKY, J. (1944): *Soil mechanics*. (In Hungarian.) Egyetemi Nyomda, Budapest.
- JÁKY, J. (1948): Sur la stabilité des masses de terre complètement plastiques. *Műegyetemi Közlemények*, 1947/2 and 1948/1, Budapest.
- JANBU, N. (1957): Earth pressure and bearing capacity calculations by generalized procedure of slices. *Proc. 4th ICSMFE*. Vol. 2, London.
- JANBU, N., BJERRUM, L. and KJAERNSLI, B. (1956): Stabilitetsberegning for fyllinger skjaeringer og naturlige skraeringer. *Norw. Geot. Publ.*, No. 16. Oslo.
- KÉZDI, A. and MARKÓ, I. (1969): *Erdbauten, Schutz und Entwässerung*. Werner, Düsseldorf.
- LANGEJAN, A. (1965): Some aspects of the safety factor in soil mechanics, considered as a problem of probability. *Proc. 6th ICSMFE*. Vol. II, Montreal.
- LAZARD, M. (1961): Discussion. In: *Proc. 5th ICSMFE*. Vol. III, Paris.
- LEBUISSON, J. and RISSMAN, P. (1979): Earthflows in the Québec and Shawinigan areas. *Geol. Ass. of Canada Congress*. Québec, Brochure for field trip, B-11.
- LEONARDS, G. A. (1982): Investigation of failures. *Proc. ASCE*, GT 2.
- MANFREDINI, G., MARTINETTI, S., RIBACCHI, R., SANTORO, V. M., SCIOTTI, M. and SILVESTRI, T. (1981): An earthflow in the Siani Valley (Italy). *Proc. 10th ICSMFE*. Vol. 3, Stockholm.
- MEYERHOF, G. G. (1970): Safety factors in soil mechanics. *Can. Geot. J.*, No. 4.
- MORGENSTERN, N. R. and PRICE, V. E. (1965): The analysis of the stability of general slip surfaces. *Géot.*, No. 1.
- PAPADOPOULOS, D. D. and ANAGNOSTOPOULOS A. G. (1981): Factors affecting the stability of slopes. *Proc. 10th ICSMFE*. Vol. 3, Stockholm.
- RENDULIĆ, L. (1936): Porenziffer und Porenwasserdruck in Tonen. *Der Bauingenieur*, Vol. 17.
- SINGH, A. (1970): Shear strength and stability of man-made slopes. *Proc. ASCE*. SM 6.
- SINGH, A. (1971): How reliable is the factor of safety in foundation engineering? *Proc. 1st Int. Conf. on Application of Statistics and Probability in Soil and Structural Engg.* Hong-Kong.
- SKEMPTON, A. W.: (1948): The effective stresses in saturated clays strained at constant volume. *Proc. 7th. Int. Congr. Appl. Mech.* Vol. 1.
- SPENCER, E. (1967): A method of analysis of the stability of embankments assuming parallel inter-slices forces. *Géot.*, Vol. 1.
- TAVENAS, F., TRAK, B. and LEROUÉIL, S. (1980): Remarks on the validity of stability analysis. *Can. Geot. J.*, No. 1.
- TAYLOR, D. W. (1937): Stability of earth slopes. *J. Boston Soc. Civ. Eng.*, 24.
- TAYLOR, D. W. (1948): *Fundamentals of Soil Mechanics*. Wiley, New York.
- VANMARKE, E. H. (1977): Reliability of earth slopes. *Proc. ASCE*, GT 11.
- VIBERG, L. (1981): Mapping and classification of landslide conditions. *Proc. 10th ICSMFE*, Vol. 3, Stockholm.
- WRIGHT, S. G., KULHAWY, F. H., and DUNCAN, J. M. (1973): Accuracy of equilibrium slope stability analysis. *Proc. ASCE*. SM 10.

Chapter 2

Load-bearing capacity and settlement of shallow foundations

Foundations generally have to comply with three requirements:

- to transfer loads to the subsoil without causing failure therein;
- to confine deformations to such an extent that the components of movement do not surpass the acceptable level in the overstructure;
- to ensure the stability of the foundation system and the overstructure against sliding, tilting or floating.

In the early period of the development of soil mechanics, a number of researchers devoted their efforts to solve the problems related to the first item. Interest in the question has faded, however, during the last one or two decades, partly because no failures have been experienced (with the exception of a few cases where the cause could have been explained immediately by referring to the so-called “sudden loading”) and partly because the possibility of failure has been almost entirely eliminated by keeping deformations below the acceptable level. Similar considerations apply to the stability problems as well, mostly because few problems arise in this respect which concern the field of soil mechanics.

This book devotes separate chapters to shallow and pile foundation (Chapters 2 and 3). Owing to the widely different theoretical approaches which are needed to handle the problematic of these two branches. This difference arises mainly from the fact that in the case of pile foundations one cannot neglect

- the friction on the skin;
- the superimposed effect of the individual footings;
- the influence of the construction technology.

The topics of “Interaction between soil and superstructure” (Section 2.3.7) and “Settlement criteria” (Section 2.3.9) have been included in Chapter 2 because there is hardly any difference in practice between the two types of foundations. General validity should also be granted to the principle that the influence of the groundwater

should always be weighted beyond its instantaneous position, whichever of the three requirements is to be complied with (RÉTHÁTI, 1983).

2.1 Bearing capacity of shallow foundations

2.1.1 Mechanism of failure

If a rigid plate or a footing placed on or below the ground surface is acted upon by continuously increasing loads, the soil beneath the loaded area settles, and vertical and lateral displacements occur. Provided that the load is relatively small, the settlement is approximately proportional to the applied load; the soil is in a state of elastic equilibrium. The mass of soil located beneath the loaded area undergoes compression which results in an increase in the shear strength and hence in the bearing capacity of the soil. ТSYTOBИTCH (1951) termed this first stage of the loading process the phase of compression. As long as the applied load does not exceed the upper limit of phase *I*, the rate of deformation decreases with time and tends, in general, to zero (Fig. 133). In phase *I* the settlement of the footing is mainly due to vertical compression of the soil. The lateral displacements are negligibly small.

In phase *II*, plastic deformations become predominant in the soil. Plastic flow starts at the outer edge of the footing and then, under increasing loads, the plastic zone grows larger and larger. If the load exceeds a threshold value, the settlement no longer comes to an end, but continues at a steady rate without any further increase in the load. At this stage, lateral displacements also become significant. Within the plastic zones the shear strength of the soil is fully mobilized.

Phase *III* is characterized by a rapidly increasing rate of deformation as the load is increased, leading to excessive outward displacements in the soil until the soil support fails by shear along a curved surface of rupture.

Typical load–settlement curves are shown in Fig. 134. Two modes of failure are the most common. In the first case (curve *I*) failure occurs abruptly. After a very short transitional period, the load–settlement curve merges into a vertical

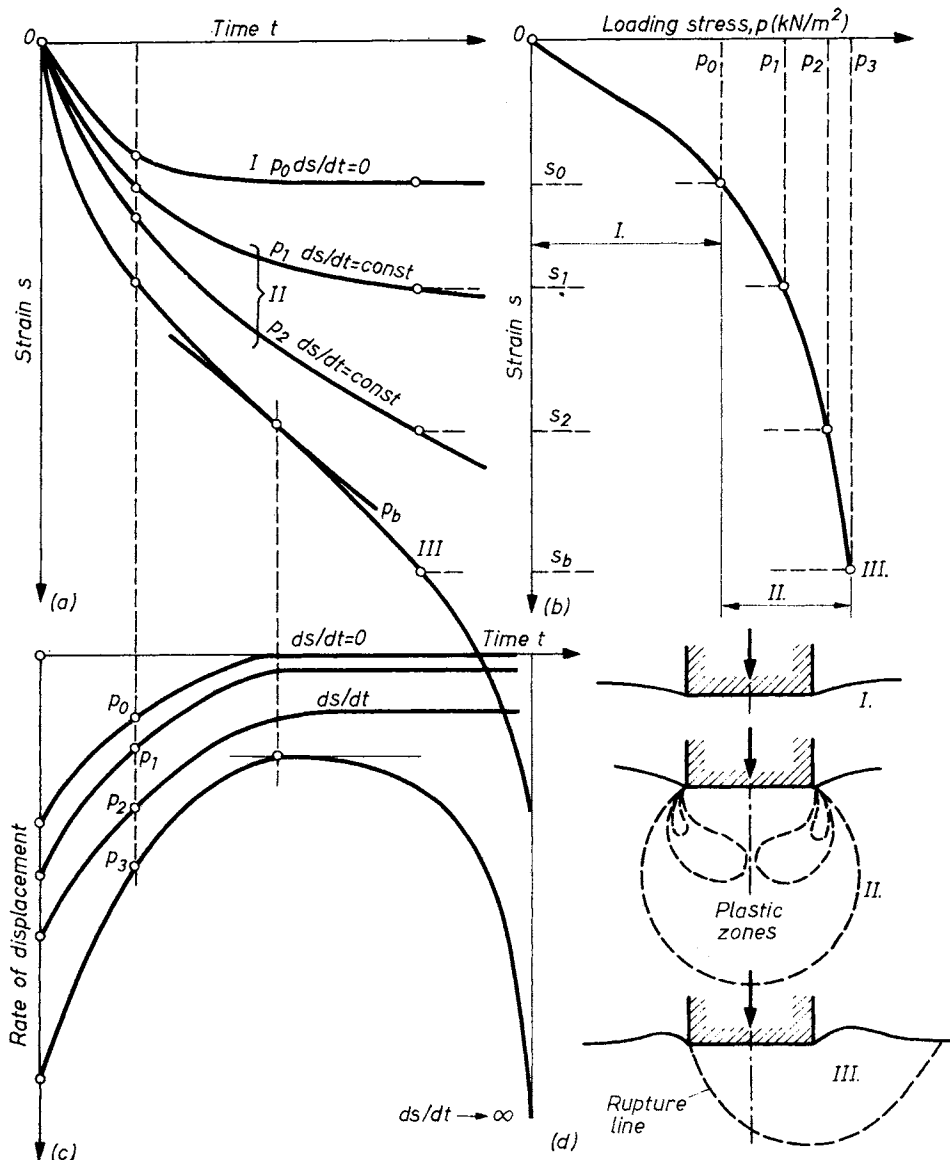


Fig. 133. Three phases in the underground after loading:

a — time-settlement curves; b — loading scheme; c — rates of settlement; d — generation of plastic zones

tangent. The surface of rupture is clearly defined, and well distinguishable. In the other case (curve 3), after an initial linear section, the settlement curve has a continuously steepening slope and finally passes into a slanting tangent. Curve 1 is typical of dense soil and curve 3 of loose soil. Curve 2 applies to dilating soils in which failure is accompanied by a substantial increase in volume. After failure is reached, the application of a load somewhat smaller than the ultimate load is sufficient to maintain a steady plastic flow, causing further settlement.

VEŠIĆ (1963) made an attempt to define the basic modes of the mechanism of foundation failure in sand and to determine the likely range of occurrence. On the basis of failure tests, he distinguished three characteristic types of failure (Fig. 135).

In the first case, known as a general shear failure (Fig. 135a), well-defined twin surfaces of rupture are formed, along which a part of the loaded mass moves outwards and upwards. It can be assumed, at least for the initial stage of failure, that this part of the soil mass moves as a rigid body in much the same way as a slope in a stiff soil fails. The shear resistance of the soil is uniquely determined by the shear deformations, and as the deformations under load continue, the shear strength becomes fully mobilized. This type of failure is the only one amenable to mathematical treatment. The failure of shallow foundations in dense sands usually follows this pattern.

In the second case (Fig. 135b), continuous surfaces of rupture cannot develop. The foundation sinks under increasing loads, deeper and deeper into the ground and causes compression in the

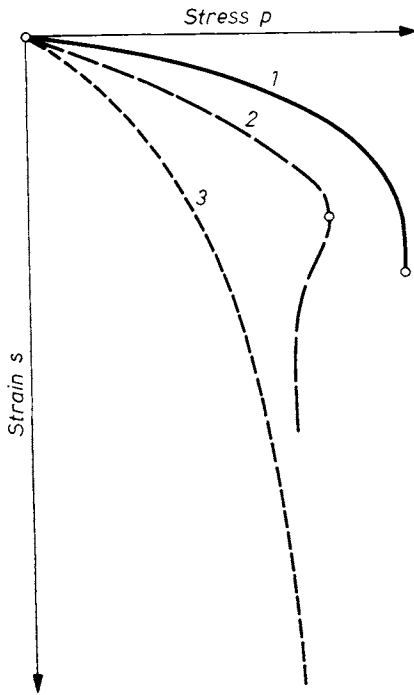


Fig. 134. Three different patterns of the loading diagram: 1 — total failure; 2 — failure accompanied by substantial loosening of the under ground; 3 — local failure

adjacent soil mass. This compression, however, may not be sufficient to produce a critical state of failure in the sand mass. Settlements are accompanied by increasingly large lateral displacements and, as a result, the load-settlement

curve tends to an inclined asymptote instead of a vertical one; the settlements increase steadily with increasing load. Radial cracks are formed at the edges of the footing as a sign of the spreading of a zone of radial shear. Such a pattern of failure, called a local shear failure, is characteristic of shallow foundations on sand of medium density.

In the third case (Fig. 135c), a shear failure in the strict sense of the word does not take place. Instead, the footing penetrates steadily into the ground under increasing load and pushes the soil aside, causing a local compression near the footing. The settlements increase almost linearly with increasing load. The compression due to penetration will extend only to a limited zone beneath and around the footing since the settlements, large as they may be, are not sufficient to produce such lateral displacements as would compress the surrounding soil to the state of critical density and thus mobilize the ultimate value of the shear strength. A wedge of compressed soil will be formed beneath the base of the footing and, together with the footing, it punches downward under increasing loads and continually forces the soil aside. This phenomenon was described by Vesic as a punching shear failure. Figure 136 after SCARLETT and FLEMING (1956), gives experimental evidence for this type of failure, showing deflections of dyed layers of sand under a loaded footing in a model test. A common feature of the tests is that a total shear failure is never reached and the load-settlement curve tends to an inclined asymptote. In the case of foundations located at greater depths, a general shear failure of the type shown in Fig. 135a is not likely to occur, even in dense sands, owing to lack of the required shear displacements. Therefore, the soil located near the ground surface may still be in a state of elastic equilibrium, while a local shear failure has actually taken place

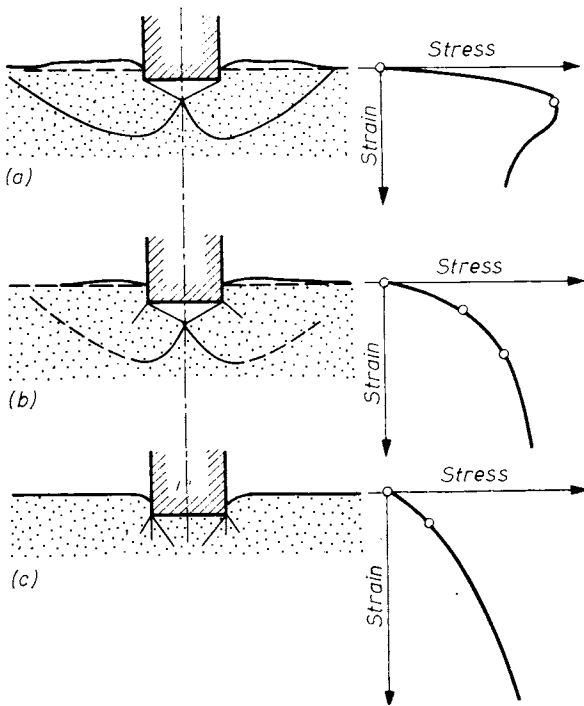


Fig. 135. Main types of failure: a — total shear failure; b — partial (local) shear failure; c — penetration failure

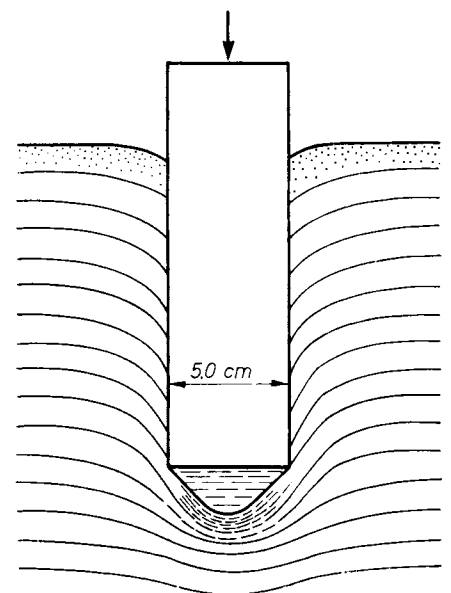


Fig. 136. Deformation below a model footing

under the base of the foundation. In cohesive soils, failure is indicated by the appearance on the surface of a set of irregular tension cracks instead of a clear shear pattern. Similar cracking may be observed in moist sands having a slight cohesion. The third type of failure can mainly be expected in cases where the depth to width ratio of the foundation is high.

The described phenomena of local shear cannot be taken into account adequately by existing failure theories. The main difficulty lies in the fact that in the case of local failure, no exact definition can be given of the state of failure. Therefore, instead of seeking some "limit value" of bearing capacity, a mathematical analysis of the whole process of failure under load seems to be a more promising future approach.

VEŠIĆ (1973) has carried out a large number of model tests in order to clarify the influence of the density of the sand and of the depth to width ratio of the foundation on the mechanism of failure. He found the approximate limits of the

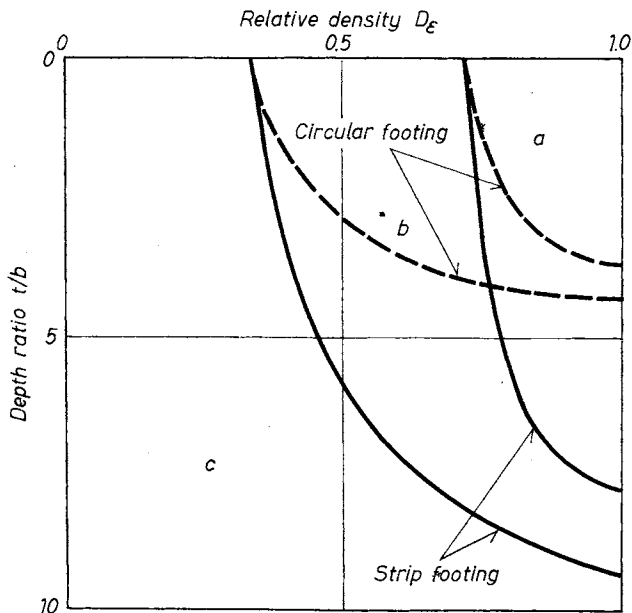


Fig. 137. Regions of the three different main types of failure after VEŠIĆ (1973)

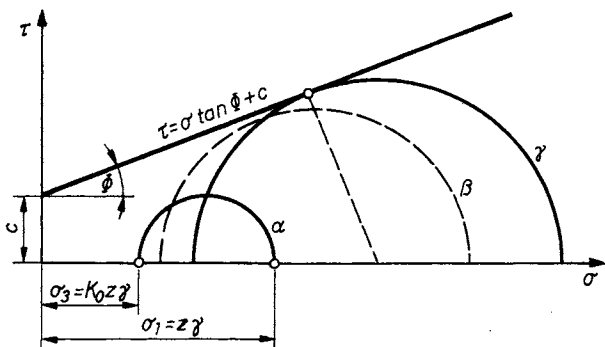


Fig. 138. Displacement and extension of the Mohr's circles when the load is increased

three types of failure to vary with the relative density of sand, D_{re} and the relative depth of foundation, t/b , as shown by Fig. 137. Type *a* occurs in the case of relatively shallow foundation on dense sand. If the relative depth is large enough, as in the case of pile or pier foundations, type *c* is always to be expected. In the light of these findings, any such theory of the bearing capacity of piles as would assume the formation of definite failure surfaces around the pile tip seems in general untenable.

In the following we shall use a different approach to the problem of failure by investigating the changes due to a surface load in the state of stress within a semi-infinite mass of soil. Figure 138 illustrates, by means of Mohr's circles, the variation in the state of stress at an arbitrary point *P* located at a depth *z* under an infinite strip load on the surface.

Before the application of load the entire mass of soil is in a state of rest, and at point *P* the principal stresses are $\sigma_1 = \sigma_z = z\gamma$; $\sigma_2 = \sigma_3 = K_0 z\gamma$ (circle α). As the intensity of the strip load *p* is increased, so are the principal stresses at point *P* and, at the same time, their directions rotate. The corresponding Mohr circles will be shifted to the right and their diameters will become larger. Successive phases of increase in strip load are represented by the Mohr circles β and γ . All these circles have a common envelope which is an approximately elliptical curve. At the moment this envelope touches the Coulomb line, the condition of failure is just reached at point *P*.

The changes in the state of stress under increasing load can be followed in Fig. 139, which shows σ_3 values plotted against the major principal stress σ_1 for several points located on a horizontal plane at a depth *z*. The failure condition

$$\sigma_3 = \sigma_1 \tan^2 \left(45^\circ - \frac{\Phi}{2} \right) - 2c \tan \left(45^\circ - \frac{\Phi}{2} \right)$$

is represented in this plot by a straight line which intersects the σ_3 axis at $\sigma_3 = -2c \tan (45 - \Phi/2)$ and has a gradient of $\tan \rho = \tan^2 (45 - \Phi/2)$. The curves *a* to *e* show the changes in the state of stress at the respective points. They all have a common starting point α which corresponds to the earth pressure at rest at a depth *z* below the surface. Failure condition at a point is reached when the corresponding curve intersects the failure line. It can be seen from the figure that the state of stress causing failure is different for each point. It follows that there may be a zone inside which the soil is already in a plastic state, whereas outside this zone the failure condition has not yet been reached. When a body of a brittle material, such as rock or concrete, is subjected to increasing loads, as soon as failure condition has been reached at any point within the body, the load cannot be further increased and a complete failure follows abruptly. For such materials, the "limit

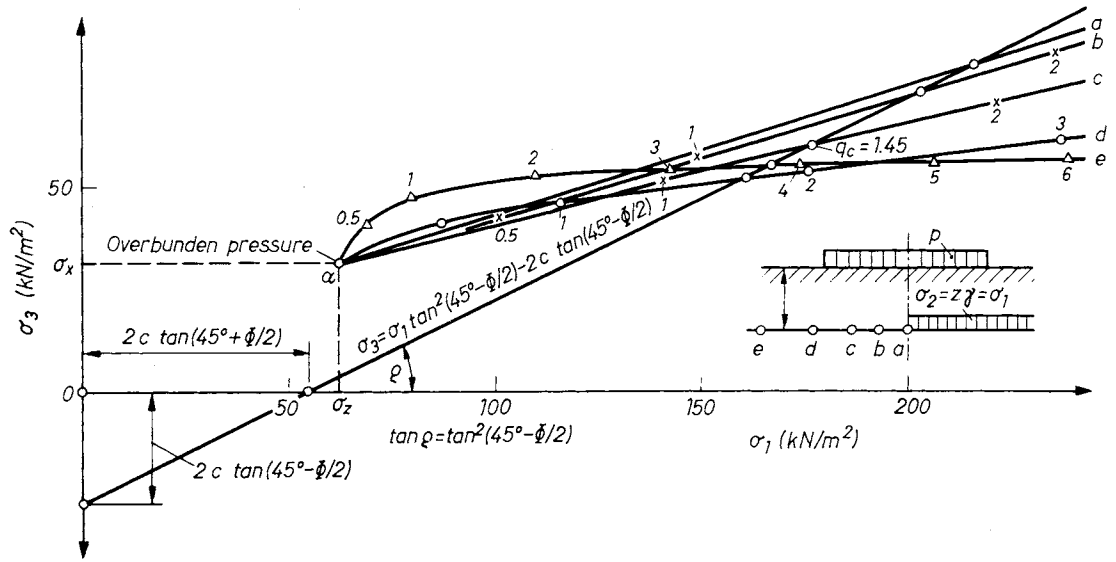


Fig. 139. Changes in the failure process according to the principal stresses

road” is essentially the same as the load required to produce failure condition at a single point anywhere in the loaded mass.

Plastic and semi-plastic materials exhibit an entirely different behaviour under load. Plastic yield usually starts at single points; for example, at the edges of a strip foundation, without the risk, however, of a complete and imminent failure of the entire mass. The foundation may still be capable of sustaining further increase in load while the plastic zone spreads over increasingly large masses of soil until finally failure takes place.

The failure of a shallow foundation usually follows the general fashion described in the foregoing paragraphs. Nevertheless, the mode of failure can be greatly influenced by various factors not mentioned so far. The distribution of stresses under a foundation, as well as the bearing capacity of the soil, depend not only on the physical properties of the soil, but also on the material, shape, size, rigidity, depth, etc., of the foundation. It is therefore one of the principal tasks of applied soil mechanics to define, by considering all the influencing factors, criteria for the failure of foundations and to predict the value of the allowable bearing pressure beneath a base.

2.1.2 Ultimate bearing capacity theories

As a fundamental case, we first discuss (Sections 2.1.2.1–2.1.2.3) the ultimate bearing capacity of an infinitely long strip foundation which is located at a shallow depth and is acted upon by a centric vertical load. The problem is thus two-dimensional (plane state of deformations).

When the base has a finite length (solitaire foundation, slab) the problem is a three-dimensional one (see Section 2.1.2.4).

During foregoing years, the requirements which the bearing capacity theories have to satisfy have been firmly established. The most important ones among them are:

- (a) Stresses developing on the shear surface have to comply with Coulomb’s failure conditions, and satisfy Kötter’s equation.
- (b) The shear surface should have a statically suitable shape (i.e. should, for example, fit the calculation of the equilibrium equations derived for both the vertical and horizontal components of forces acting and their moments).
- (c) The shear surface should kinematically accommodate a continuous displacement of the moving mass on the table one, so that the two masses should maintain an uninterrupted mutual contact, and the mass in motion should not evoke an additional resistance.
- (d) The shear surface should resemble the surfaces experienced during failure model-tests.
- (e) The theory applied should take account of the internal friction, cohesion and density of the earth mass in question.
- (f) The bearing capacity factors should always relate to the same shear surface.

None of the theories known up to the present are able to fulfil all these requirements completely, but the most up-to-date theories have succeeded in reflecting most of the test results experienced.

2.1.2.1 Determination of ultimate load for weightless soil

An exact solution for a weightless medium was given independently by PRANDTL (1920) and by CAQUOT (1934). If the footing has a perfectly smooth base, the shear pattern is similar to that

shown in Fig. 140. The central part *II* of the plastic zone is bounded by a logarithmic spiral. In zones *I* and *III* the soil is in the active and passive Rankine states, respectively.

The solution can be written in the following form:

$$p = t\gamma \tan^2\left(45^\circ + \frac{\Phi}{2}\right) e^{\pi \tan \Phi} + c \cot \Phi \left[\tan^2\left(45^\circ + \frac{\Phi}{2}\right) e^{\pi \tan \Phi} - 1 \right], \quad (110)$$

where t = the distance between foundation depth and ground level,
 γ = the bulk density of the soil mass above foundation level.

The multiplying factor referring to the own weight $t\gamma$ is marked by N_q and that of the cohesion c by N_c . These are the so-called bearing capacity factors. In Prandtl's theory, according to Eq. (110):

$$N_c = \cot \Phi (N_q - 1). \quad (111)$$

Prandtl's theory was first applied to soils by Caquot. In this application the problem has already been treated on the basis of the limiting equilibrium condition which exists between the active earth pressure in the soil beneath the foundation and the passive resistance of the earth mass on the sides. This demonstration has later been simplified by RAES (1941) and MANGEL, and the final form of the equation derived by these three authors is that shown as Eq. (110).

2.1.2.2 Theories of Buisman-Raes and Terzaghi

At the beginning insufficient emphasis was put on negligence of the soil's own weight, but it soon became obvious that this component of the bear-

ing capacity — the more so in granular soils — could not be neglected. Thus the Prandtl-Caquot-Magnel-Raes formula may only be used for practical purposes when the bearing capacity factor referring to the soil's own weight (designated as N_B or N_γ) is transported from another theory to the application on hand.

The first researcher to produce the relation for this case was BUISMAN (1940); his graphic solution was later condensed in an analytic form by RAES (1941). According to this procedure, the bearing capacity factor N_γ can be derived from the expression:

$$N_\gamma = \frac{1}{4} \left\{ 2K_p \exp(1.5 \pi \tan \Phi) - 2\sqrt{K_p} + \frac{1 + K_p}{1 + 9 \tan^2 \Phi} [(3 \tan \Phi \sqrt{K_p} - 1) \exp(1.5 \pi \tan \Phi) + 3 \tan \Phi + \sqrt{K_p}] \right\}, \quad (112)$$

where

$$K_p = \tan^2\left(45^\circ + \frac{\Phi}{2}\right).$$

Provided that the foundation depth is not greater than the width of the footing, the shear strength of the soil strata located above the foundation level can be neglected, since these strata normally consist of weak topsoil or loose backfill. For this case, TERZAGHI (1943) developed a general solution which, although not rigorously exact, furnishes dependable results in most practical cases. In this theory it is assumed that failure beneath the footing takes the form of a general shear failure characterized by the load-settlement curve of type *a* in Fig. 135.

Let us consider an infinite strip footing of width $2b$ at a depth t below surface level (Fig. 141). The shear strength of the layer located above the foundation level can, as was mentioned previously,

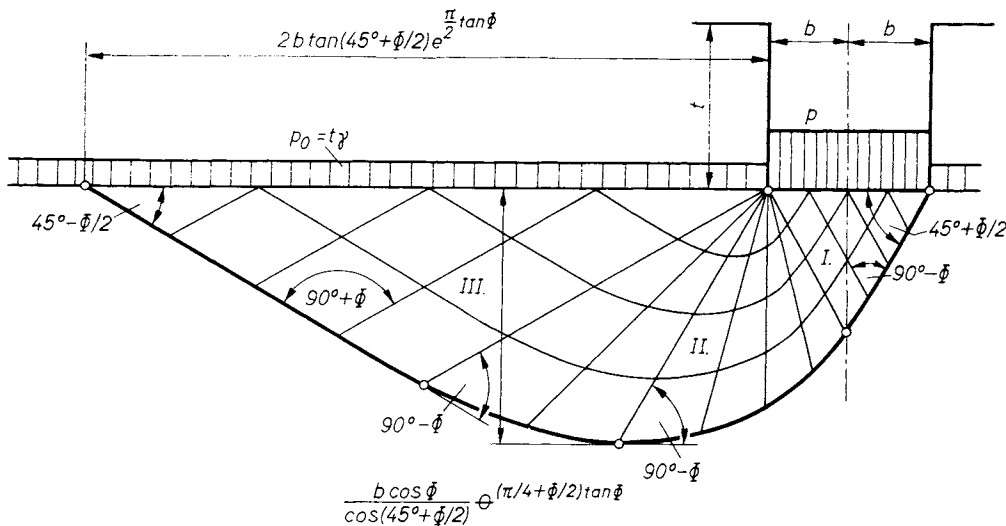


Fig. 140. Network of failure planes in a weightless mass

Hence

$$P_b + \gamma b^2 \tan \Phi - 2E_p - 2bc \tan \Phi = 0. \quad (113)$$

In this equation the first term represents the bearing capacity sought, the second is the weight of the wedge *ABD*, the third is the passive resistance, due to friction, on the sloping faces of the wedge, and the fourth is the vertical component of the cohesion force ($C \sin \Phi$).

The passive earth pressure E_p can be determined by a method which was described in detail in Vol. 1, Section 9.6 (cf. Fig. 434). There we also discussed, using simplifying assumptions, the computation of the distribution of stresses for the general case when $c \neq 0$, $\Phi \neq 0$ and $q \neq 0$ (cf. Fig. 435). Now we shall apply these methods to the case of a continuous footing in order to determine the passive resistance on the face *BD* (see Fig. 142). Having selected a trial slip surface, we perform the construction exactly in the same way as was illustrated by Fig. 435 in Vol. 1, the only difference being that instead of an adhesion force, a force of cohesion should be taken into account on the face *BD*. A worked-out numerical example is given in Fig. 142. The construction should be repeated for several trial surfaces in order to find the least value of the passive earth pressure, E_p .

The normal component of the passive earth pressure is, in general, given by the following expression (see Vol. 1, Section 9.6):

$$E_p = \frac{h}{\sin \beta} (cK_{pc} + qK_{pq}) + \frac{1}{2} \gamma h^2 \frac{K_{py}}{\sin \beta}. \quad (114)$$

For the case shown in Fig. 142, $h = b \tan \Phi$, $\beta = \delta = \Phi$, and $a = c$; thus the passive resistance can be written

$$E_{pn} = \frac{b}{\cos \Phi} (cK_{pc} + qK_{pq}) + \frac{1}{2} \gamma b^2 \frac{\tan \Phi}{\cos \Phi} K_{py}$$

and

$$E_p = \frac{E_{pn}}{\cos \delta} = \frac{E_{pn}}{\cos \Phi}.$$

Hence

$$E_p = \frac{b}{\cos^2 \Phi} (cK_{pc} + qK_{pq}) + \frac{1}{2} \gamma b^2 \frac{\tan \Phi}{\cos^2 \Phi} K_{py}.$$

Substituting this expression in Eq. (113) leads to

$$P_b = 2bc \left(\frac{K_{pc}}{\cos^2 \Phi} + \tan \Phi \right) + 2bq \frac{K_{pq}}{\cos^2 \Phi} + \gamma b^2 \left(\frac{K_{py}}{\cos^2 \Phi} - 1 \right). \quad (115)$$

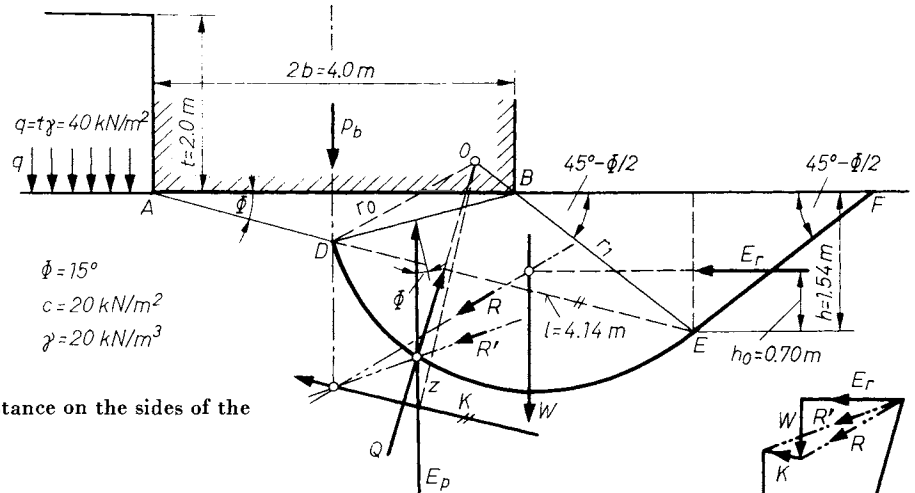


Fig. 142. Establishment of soil resistance on the sides of the elastic earth wedge

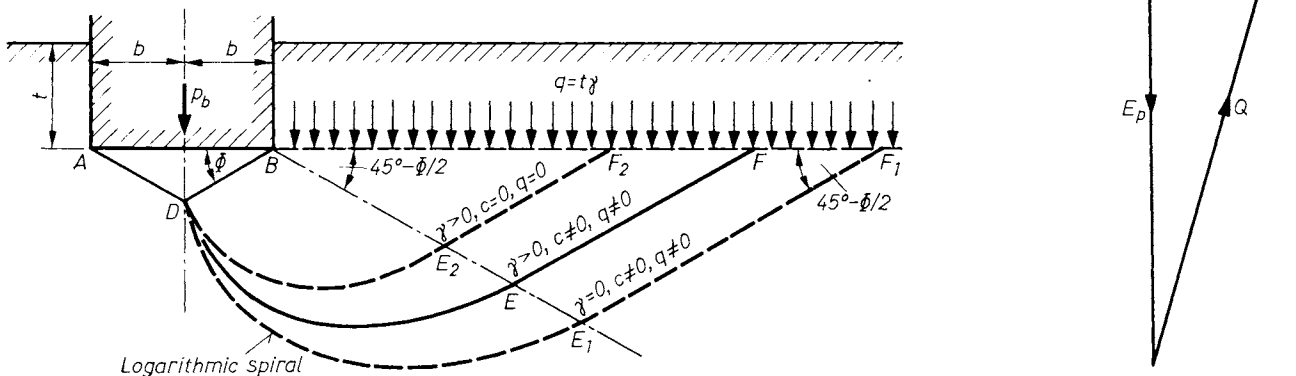
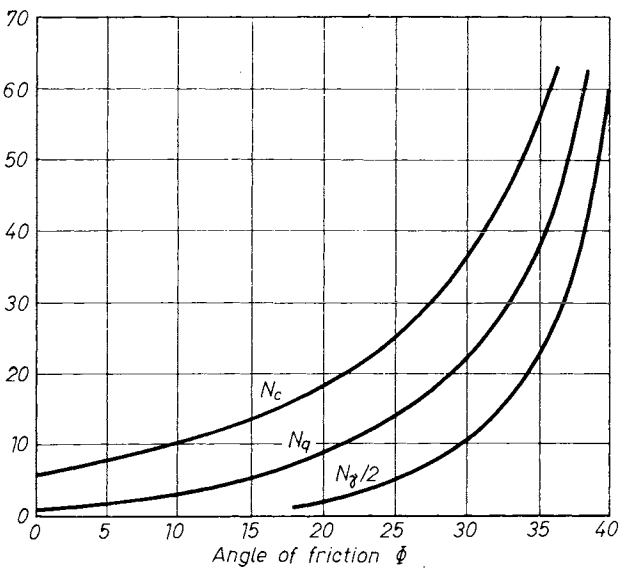
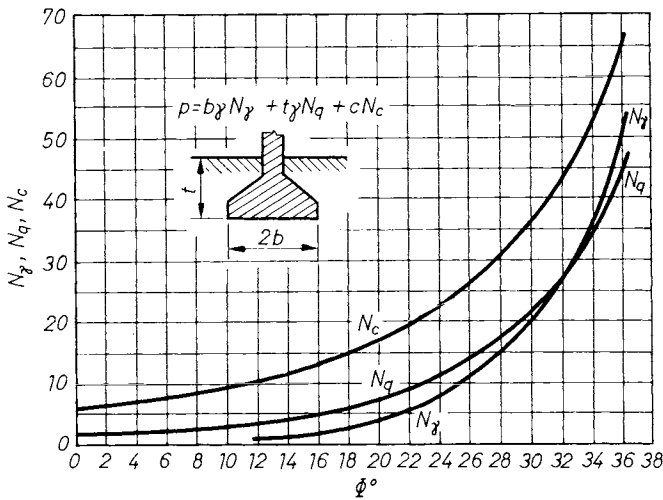


Fig. 143. Drawing the rupture planes for a strip foundation

The problem is thereby essentially solved. In practice, however, a further and rather tedious construction work is necessary to determine the coefficients K_{pc} , K_{pq} and $K_{p\gamma}$ for a definite sliding surface in Eq. (115). Therefore, TERZAGHI introduced another important simplifying assumption, namely that the values K_{pc} and K_{pq} can be computed with the aid of the critical slip surface that is valid for a weightless medium ($\gamma = 0$). For this theoretical case, a logarithmic spiral whose centre is located at the outer edge of the footing (point *B* in Figure 143) represents a rigorous solution. Theory supplies exact formulas for the coefficients K_{pc} and K_{pq} (PRANDTL, 1920 and REISSNER, 1924) and hence the following quantities can be derived:

$$N_c = \cot \Phi \left[\frac{e^{(3/2\pi - \Phi) \tan \Phi}}{2 \cos^2 (45^\circ + \Phi/2)} - 1 \right] = \cot \Phi (N_q - 1) \tag{116}$$



and

$$N_q = \frac{e^{(3/2\pi - \Phi) \tan \Phi}}{2 \cos^2 (45^\circ + \Phi/2)} \tag{117}$$

Introducing the above expressions into Eq. (115), we obtain the bearing capacity for a weightless medium $\gamma = 0$:

$$p_{bc} + p_{bq} = 2bc \left(\frac{K_{pc}}{\cos^2 \Phi} + \tan \Phi \right) + 2bq \frac{K_{pq}}{\cos^2 \Phi} = 2bcN_c + 2bqN_q \tag{118}$$

In a real cohesionless soil ($\gamma > 0, c = 0$) with no surcharge on the surface ($q = 0$), the critical slip surface (curve $D_2E_2F_2$, Fig. 143) is located well above that for the $\gamma = 0$ case (curve DE_1F_1). The rigorous equation for this slip surface is not yet known. The critical load required to bring about failure along this surface can be obtained from Eq. (115).

Terzaghi's final formula for the calculation of the ultimate bearing capacity is:

$$p = b\gamma N_\gamma + t\gamma N_q + cN_c \tag{119}$$

for which the bearing capacity factors (N) are given in Fig. 144a.

After having analyzed Terzaghi's bearing capacity factors, KRIZEK (1965) concluded that the ultimate bearing capacity could be determined for $\Phi = 0$ to 35° , with a maximum deviation of 15%, when the following expression is used:

$$p = \frac{(228 + 4.3 \Phi) c + (40 + 5\Phi) t\gamma + 6\Phi b\gamma}{40 - \Phi} \tag{120}$$

When the sand is loose, the footing may undergo very large settlements and yet no definite continuous surfaces of rupture are developed. The load-settlement curve passes into a steeply sloping final tangent (curve 3, Fig. 134), instead of a vertical one. Such a condition has been referred

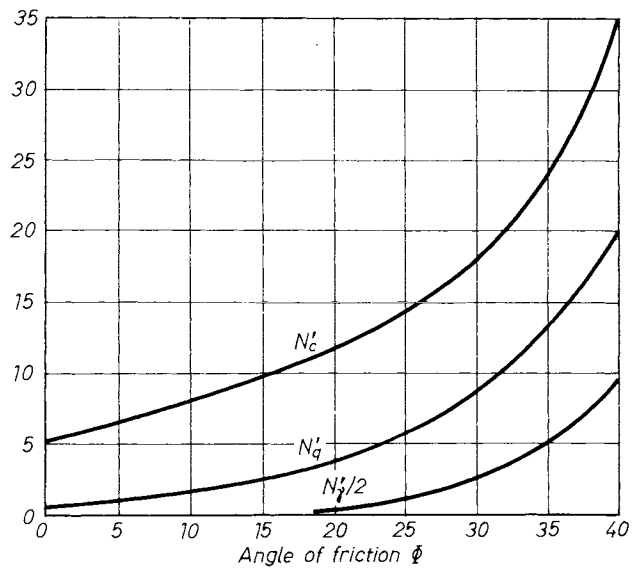


Fig. 144. Bearing capacity factors as functions of the internal friction (TERZAGHI):
 a — total failure; b — partial (local) failure

to as a local shear failure. TERZAGHI suggested that for this case the values of cohesion c and coefficient of friction $\tan \Phi$ should be divided by 1.5 and these reduced values used for the computation of the bearing capacity.

The corresponding bearing capacity factors N'_c , N'_q and N'_γ are given in Fig. 144b. For the case of local shear failure

$$p' = \frac{2}{3} cN'_c + t\gamma N'_q + b\gamma N'_\gamma. \quad (121)$$

2.1.2.3 Other theories for computing bearing capacity

As was pointed out in the foregoing, Terzaghi's method for computing the bearing capacity was based on a number of simplifying assumptions and, therefore, the solution obtained is not mathematically rigorous. One essential objection is that the exact solution of the surface of sliding is unknown. To overcome this difficulty, the curved portion of the actual slip surface is replaced by a circle or by a logarithmic spiral. Furthermore, the bearing capacity factors do not belong to one and the same surface of sliding. The superposition adopted in the derivation of the critical load is unjustified since the underlying equations are non-linear. The question of superposition of particular solutions for the limiting state of equilibrium was investigated by SOKOLOVSKII (1960). He found that the sum of the stresses required to produce failure in the three particular cases ($q = t\gamma \neq 0$, $\gamma = 0$; $c = 0$; $q = 0$, $\gamma \neq 0$, $c = 0$; $q = 0$, $\gamma = 0$, $c \neq 0$) satisfies the corresponding equations of equilibrium.

However, because of non-linearity, the numerical value of this sum does not agree with the value that would be furnished by an exact numerical analysis for a single critical slip surface. Superposition gives the lesser value. LUNDGREN and MORTENSEN (1953) carried out an exact numerical analysis for the case $\Phi = 30^\circ$ and found that the bearing capacity value obtained by superposition was lower by 17%. The error is, therefore, on the safe side.

Increasing emphasis has been laid in current research on the recognition that the critical slip surface must be not only statically and geometrically, but also kinematically admissible. If we further assume that the soil is incompressible, the kinematic conditions must also be satisfied everywhere within the zone of plastic equilibrium; this requirement is an equivalent of the compatibility condition in the theory of elasticity. In dilatant soil, volume changes which may take place during failure must also be taken into consideration — a fact often disregarded in theoretical approaches. So far, no such general solution as would simultaneously satisfy all the aforementioned requirements has been developed.

Most of the earlier theories assumed plane surfaces of rupture. Obviously, such an assumption is both geometrically and kinematically inadmissible. In addition, the solutions are often incompatible with the laws of statics.

MIZUNO's theory (1953) assumes the effect of the soil's own weight influencing not only the bearing capacity, but also the shape of the slip surface. Similarly to the theories which operate on the basis of plane slip surfaces, MIZUNO also assumes a configuration of zones. Purely active earth pressure prevails in the first zone and that is connected to the plane bounded Rankine's passive zone by a domain which is confined by a logarithmic helix. After having conducted a detailed stress analysis a graphical solution has been produced for deriving the $p/b\gamma$ value from $q/b\gamma$. Though the theory was originally elaborated for granular soils only, the cohesion can also be taken into account by adding the value $c \cot \Phi$ to the vertical stress q , or by taking $q + c \cot \Phi$ as the abscissa on the horizontal axis of the graph instead of q alone.

JÁKY has proved that in the range of $\Phi = 20-40^\circ$ the stress derived from Mizuno's diagram could also be described by Eq. (119), and that the bearing capacity p is approximately a linear function of the sum $(t + b)$. This latter observation has found its place in the Hungarian Code of Practice for Foundations inasmuch as one of the multiplying factors of the so-called limiting stress basic value is proportional to the sum $(t + b)$.

LUNDGREN and MORTENSEN (1953) also arrived at the same conclusion that the shape of the slip surface was a function of the load q , i.e. of the depth of foundation.

The failure theories discussed above were all based on the simplifying assumption that for a footing located at a shallow depth, the shear strength of the soil above the foundation level can be neglected and that the only contribution of this soil mass to bearing capacity is due to an overburden pressure $t\gamma$ at the depth of the footing.

A more realistic solution to the problem was developed by MEYERHOF (1951). He assumed that the slip surfaces extend to the ground surface (Fig. 145a) and that they consist of planar (AC) and curved (CDE) sections. As a first approximation, the base of the footing is assumed to be perfectly smooth. The area ACD represents a zone of radial shear with a set of plane slip surfaces radiating from the edge A of the footing, and $ADEF$ is a zone of composite — radial and plane — shear. The conditions for plastic equilibrium can be established from the boundary conditions on the base and sides of the footing. To simplify the analysis, the resultant of the forces acting on the side AF of the footing and the weight of the prism AEF are replaced by normal and tangential stresses acting on the plane AE . This plane can thus be regarded as an "equivalent ground surface" which is acted upon by the stresses σ_0 and τ_0 . The slope angle β of the equi-

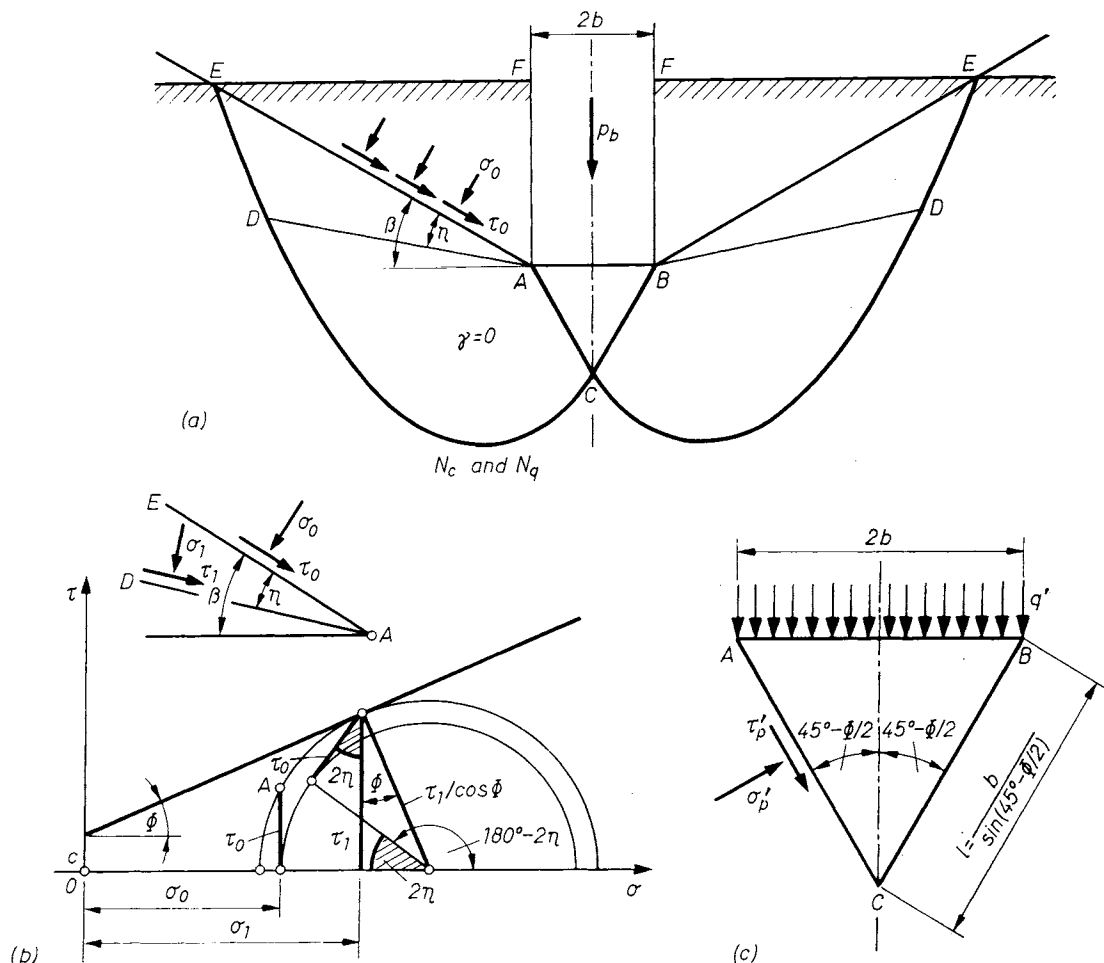


Fig. 145. Development of sliding surfaces according to Meyerhof's assumptions (1951)

valent ground surface increases with increasing depth.

The analysis leads to a general expression for bearing capacity which is of similar form to that derived by TERZAGHI:

$$p_b = cN_c + qN_q + b\gamma N_\gamma \quad (122)$$

N_c , N_q and N_γ are again bearing capacity factors, but with a more generalized meaning, in that they depend not only on the angle of internal friction, but also on the shape and depth of the footing and on the roughness of its base. The quantities N_c and N_q can be derived from the analysis of a weightless medium. N_γ is determined from the analysis of the case when $c = 0$ and $q = 0$. We find the critical slip surface, and, from the corresponding minimum passive earth resistance, we compute the value of N_γ . As can be seen, Meyerhof's solution contains the same inconsistency as Terzaghi's, namely that the bearing capacity factors in Eq. (122) do not correspond to one and the same critical slip surface.

In the zone ADE planar shear stress conditions prevail and limiting equilibrium conditions require

the fulfilment of the relation

$$\tau_1 = \sigma_1 \tan \Phi + c$$

between τ_1 and σ_1 which act on the plane AD and DE, respectively.

Should η mean the inclination of the failure plane to the horizontal, and

$$\theta = 45^\circ - \Phi/2 + 90^\circ + \beta - \eta = 135^\circ + \beta - \eta - \Phi/2$$

that of the plane AD, m should mean the ratio of the shear stress to the shear resistance on the substitutive ground level. As there is a radial shear in the domain ACD here the slip surface is a logarithmic helix (cf. Prandtl's theory). In this way it can be demonstrated that

$$p = c \cot \Phi \left[\frac{(1 + \sin \Phi) \cdot \exp(2\theta \tan \Phi)}{(1 - \sin \Phi) \cdot \sin(2\eta + \Phi)} - 1 \right] + p_0 \frac{(1 + \sin \Phi) \cdot \exp(2\theta \tan \Phi)}{(1 - \sin \Phi) \cdot \sin(2\eta + \Phi)} \quad (123)$$

In this expression the multiplier of c is identical with N_c and that of p_0 with N_q . Their values can be read in Fig. 145b.

The third bearing capacity factor, N_γ , can be derived from the particular curved slip surface giving the least passive earth pressure. The centre O of a trial slip surface can be chosen arbitrarily, and then the moment of equilibrium can be written as

$$E_p = \frac{E_{p1}l_1 + Wl_2}{l_3}, \quad (124)$$

where E_p = means the passive earth pressure on the plane BC ,

E_{p1} = is the passive earth pressure originating from the resistance of the prism DEG .

By repeating the procedure for a number of centres O , we can find the location of the critical slip surface and the minimum value of E_p . Finally, the ultimate bearing capacity of the footing is computed from the equilibrium of the soil wedge ABC :

$$p'' = \frac{b\gamma}{2} \left[\frac{4E_p \sin(45^\circ + \Phi/2)}{b^2\gamma} - \frac{1}{2} \tan(45^\circ + \Phi/2) \right] = \frac{b\gamma}{2} N_\gamma. \quad (125)$$

Values of N_γ are plotted in Fig. 145b as functions of β and Φ for the two limiting cases when $m = 0$ and $m = 1$.

As a next step, approximative values should be attributed to substitutive stresses τ_0 and σ_0 . These can be calculated from the forces acting on the sides of the footing, and the weight of the earth mass above the substitutive ground surface. The forces on the sides of the footing are combined from the adhesive force ($A = at$) and from the earth pressure in the direction of δ , i.e.:

$$E = K_a \frac{t^2\gamma}{2 \cos \delta}. \quad (126)$$

The weight of the earth mass is:

$$W = \frac{t^2\gamma}{2} \cot \beta.$$

Knowing the forces A , E and W , the components T and N acting in the plane of the substitutive ground surface can be calculated. Knowing them, we find:

$$\sigma_0 = \frac{N \sin \beta}{t} \quad (127)$$

and

$$\tau_0 = \frac{T \sin \beta}{t}. \quad (128)$$

To illustrate the significance of the angle β , Fig. 146 shows five typical cases. When $\beta = -90^\circ$,

the situation is equivalent to unconfined compression. When $-90^\circ < \beta < 0$, the ground surface slopes symmetrically downwards. The case when $\beta = 0$ and $m = 0$ corresponds to surface loading. The condition $0 < \beta \leq 90^\circ$ characterizes shallow foundation below the ground surface and deep foundations. Finally, the case when $\beta = 90^\circ$ and $m = 0$ is equivalent to that of a vertical slot for which a solution was also given by JÁKY.

Meyerhof's theory suggests that the critical load of a footing increases rapidly with increasing depths. This is, however, contrary to the results of loading tests. Therefore, MEYERHOF proposed in 1951 that for foundations with a ratio $t/b > 5$ a reduced value of the angle Φ should be used in the analysis.

MEYERHOF (1951, 1953, 1957) has subsequently extended his theory to circular and rectangular footings, and compared his results with those obtained from laboratory and field loading tests. For relatively shallow foundations he found a good agreement between computed and observed values. He also investigated the effect of the groundwater and of the roughness of the base on the load-bearing capacity and extended his analysis to eccentric and inclined loads. Some of these problems will be discussed in the following sections. Also, a general formula for the load-bearing capacity will be given in Section 2.1.2.5.

The problem of the load-bearing capacity of a continuous footing was also investigated by BALLA (1962). His solution differs in many respects

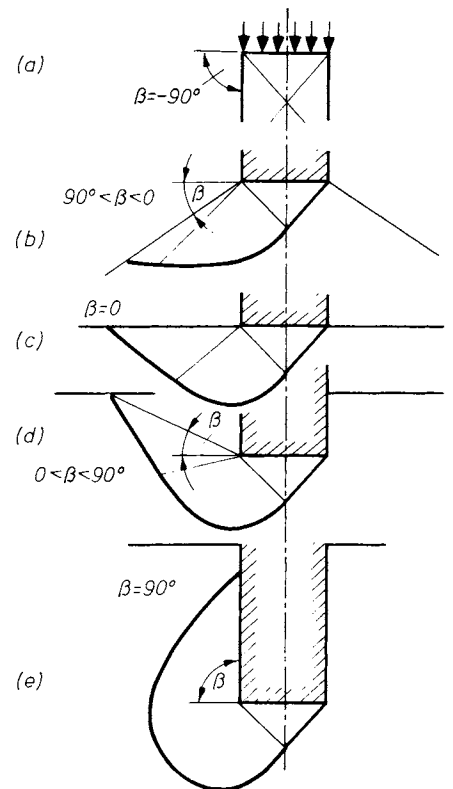


Fig. 146. Five various cases for the value of angle β

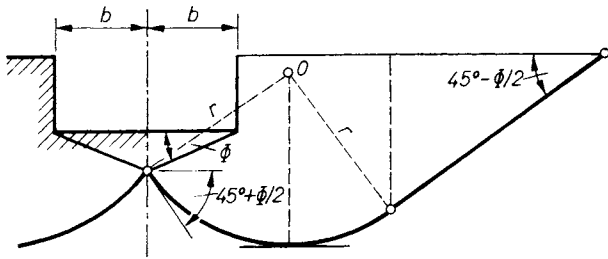


Fig. 147. Assumption of the sliding surface according to BALLA (1962)

from those previously discussed. The slip surface is assumed to be made up of circular and plane sections (Fig. 147). An elastic wedge is formed beneath the rough base of the footing. The twin

slip surfaces branch off from the centre line of the footing with an angle $45^\circ + \Phi/2$ to the horizontal, which is the statically correct value. BALLA used the Kötter equations (KÖTTER, 1882) to determine the distribution of the normal and tangential stresses on the slip surface. The parameters of the slip surface can be obtained from equilibrium conditions. Once the surface of rupture is established, the critical load on the footing can be determined by a limit state analysis which leads to a general formula similar in form to Eq. (119). In this case, however, the bearing capacity factors depend not only on the angle of internal friction of the soil, but also on its limit weight and cohesion; moreover, it depends on the width and depth of the footing. For the purpose of practical computations, BALLA has worked out a set of charts

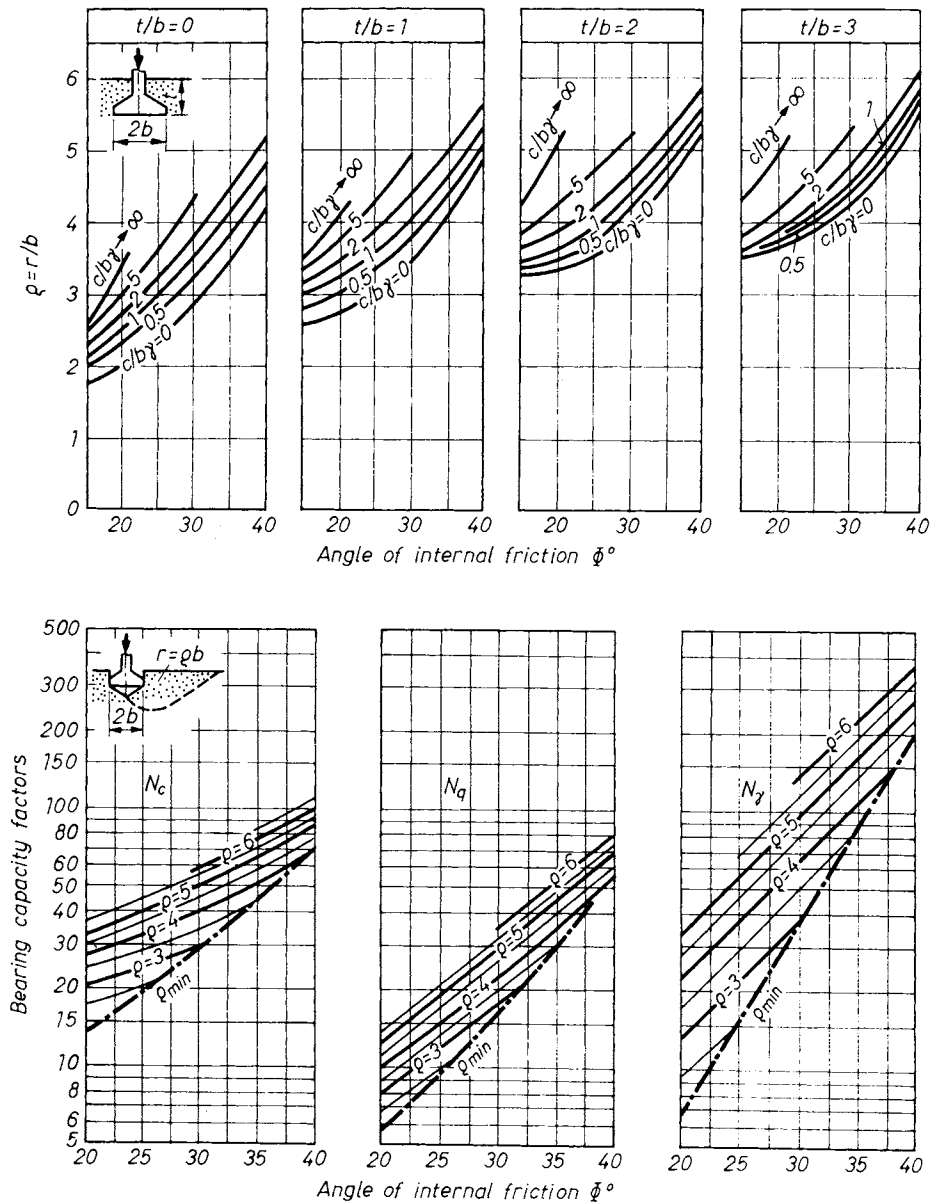


Fig. 148. Diagrams for finding the bearing capacity factors according to BALLA (1962)

giving values of bearing capacity factors for various geometrical conditions. These graphs are shown in Fig. 148. As a first step, the radius r of the critical slip surface has to be determined as a function of the quantities Φ , $c/b\gamma$ and t/b . Using the parameter $\rho = r/b$ thus obtained, we can find the factors N_c , N_q and N_γ from another set of graphs.

Balla's solution gives considerably greater values for N_γ than those obtainable by other theories; this implies a more significant influence of foundation width on the load-bearing capacity. On the other hand, the effect of depth appears to be less pronounced than suggested by the Meyerhof theory. These differences were found to be in close agreement with the results of loading tests and with full-scale observations. A detailed comparison of theoretical and measured data will be given in the next section.

An advanced view of the field of bearing capacity theories is presented by HU (1964). It is stated therein that the angle ψ between the horizontal and the side planes of the earth wedge below the footing depends on the density and the angle of internal friction of the soil, and on the load $t\gamma$ at the foundation level; its value ranges between Φ and $(45^\circ + \Phi/2)$. Consequently, the bearing capacity factors — in combination with the minimum principle relating thereto — should be selected on the basis of varying failure mechanism. Values of N_γ , N_q and N_c , as determined by this procedure, are illustrated in Fig. 149. The curve ψ_{\min} should be used in the case of $\Phi \neq 0$ and $c = 0$, when Φ is large and *vice versa*, and in the case of granular materials (when $c = 0$), as well as when the load $t\gamma$ is zero or negligible.

Some authors suggested using some relations among the bearing capacity factors (similar to Eq. (111)) for the calculations. BRINCH HANSEN draws attention to the fact that in the case of $\Phi = 0$

$$N_\gamma = N_q - 1 \quad (129)$$

and (with reference to the Prandtl-Caquot theory) Eq. (111) is valid, we can calculate with these theoretically correct relationships in their own realm. Substituting these relations into Eq. (119):

$$p = [b_\gamma + c \cot \Phi] (N_q - 1) + t\gamma N_q. \quad (130)$$

CAQUOT and KÉRISEL (1953) found the relation

$$N_\gamma = 2(N_q + 1) \tan \Phi \quad (131a)$$

and BIAREZ *et al.* (1961) the relation

$$N_\gamma = 1.8(N_q - 1) \tan \Phi \quad (131b)$$

acceptable for use.

2.1.2.4 Bearing capacity of finite size footings

The bearing capacity of limited-size footings can be estimated at present only from semi-empirical formulas. These have been derived as representa-

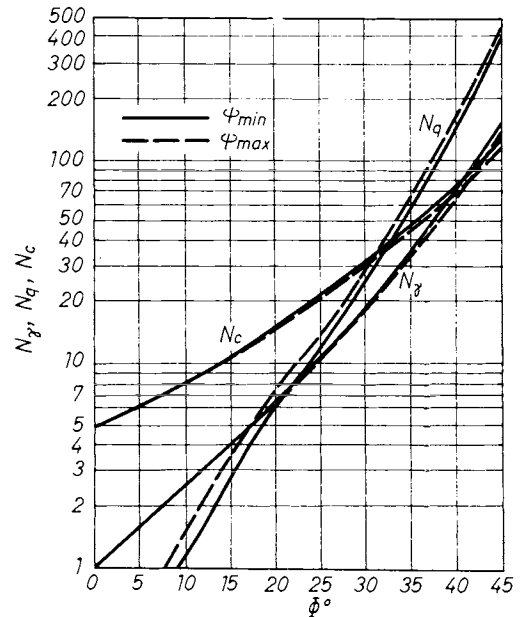


Fig. 149. Bearing capacity factors according to Hu's theory (1964)

tions of model test results conducted during the last decades.

The results of tests have proved that the bearing capacity below a footing becomes greater when the shape of the contact area becomes more closed, i.e. when the ratio of the periphery to the contact loading surface decreases. This phenomenon can be explained by the fact that by increasing the closeness of the foundation area a relative increase of the slip surface areas will be achieved which then adds to the resistance against failure, as in this way the magnitude of the earth mass involved in the bearing capacity increases. While the load might originate two slip surfaces only on the two sides of a strip foundation, the failure surface has to be developed on all four sides of a rectangular footing. In the latter case it obviously needs more effort to mobilize the shear resistance of the soil. As the length of the slip surface depends on the width of the footing, the sum of slip surface areas is substantially greater below a square shaped footing as it would be below a strip foundation of equal width. The test mentioned proved that this favourable effect can be anticipated only when the foundation submerges below the ground surface ($t \neq 0$).

Multiplying shape factors (f_i) are generally affixed to the basic form of the bearing capacity formulas — which were originally derived from experimental trial tests for strip foundations — to extend their suitability for the calculation of the bearing capacity beneath footings of limited sizes. The basic formula then takes the following form:

$$p = f_\gamma b\gamma N_\gamma + f_q t\gamma N_q + f_c c N_c. \quad (132)$$

Table 5. Shape factors recommended by some authors

Author		Shape factors		
		f_γ	f_q	f_c
TERZAGHI	circle	0.6	1.0	1.3
	square	0.8	1.0	1.3
SCHULTZE	circle	0.667	1.0	1.0
	rectangle	$1 - \frac{B}{3L}$	$1 + \frac{B}{3L}$	$1 + \frac{B}{3L}$
BRINCH HANSEN	I	$1 - 0.4 \frac{B}{L}$	$1 + 0.2 \frac{B}{L}$	—
	II	$1 - (0.2 + \tan^2\Phi) \frac{B}{L}$	$f_q = f_c$; for $\Phi = 0$ $f_q = 1$	$1 + (0.2 + \tan^2\Phi) \frac{B}{L}$
DE BEER		$1 - 0.4 \frac{B}{L}$	$1 + \frac{B}{L} \tan \Phi$	$1 + \frac{B}{L} \frac{N_q}{N_c}$
MUHS		$1 - 0.18 \frac{B}{L}$	$1 + 2 \frac{B}{L}$	—
Hungarian Standard		$1 - 0.1 \frac{B}{L}$	$1 + 0.2 \frac{B}{L}$	$1 + 0.2 \frac{B}{L}$

Some authors, as well as the Hungarian Code of Practice for Foundations, suggest the use of the shape factors listed in Table 5. The following conclusions can be deduced therefrom.

Shape factors depend solely on the geometry of the footing, with the exception of DE BEER's f_q and f_c factors (1970). Special attention should be attributed to the shape factors suggested by MUHS (1969) because these have been established on relatively large (0.5 to 2.0 m²) footings in the course of model tests. According to these results, the reduction in the first term of the original bearing capacity formula will be less than that inferred by other sources, while the increment of the second term becomes far more substantial.

In respect to the shape factors proposed by Schultze it can be proved that the bearing capacity — independently of the size of the footing, and of the values Φ , t and γ — decrease successively when the shape of the footing becomes more elongated. This can be proved as follows (RÉTHÁTI, 1976).

Failure stress below square footing of the width B is:

$$p = f_\gamma \frac{B}{2} \gamma N_\gamma + f_q t \gamma N_q + f_c c N_c. \quad (133)$$

Take β as the ratio of the width (B') to the length (L) of a quadrangle footing; it then follows from the equality of the loaded contact areas that

$$B' = B \sqrt{\beta}$$

and so the limiting stress becomes:

$$p = f'_\gamma \frac{B\sqrt{\beta}}{2} N_\gamma + f'_q t \gamma N_q + f'_c c N_c. \quad (134)$$

As $f_q > f'_q$ and $f_c > f'_c$, and the other terms remain identical, the last two terms in Eq. (133) are greater than in Eq. (134).

In respect to the first term it has yet to be proved that

$$f_\gamma \frac{B}{2} > f'_\gamma \frac{B\sqrt{\beta}}{2}$$

which means that

$$f_\gamma > f'_\gamma \sqrt{\beta}. \quad (135)$$

According to SCHULTZE

$$f_\gamma = \frac{2}{3} \text{ and } f'_\gamma = 1 - \frac{\beta}{3}.$$

Substituting these values into Eq. (135) we get

$$\frac{2}{3} > \left(1 - \frac{\beta}{3}\right) \sqrt{\beta}$$

which is:

$$2 > \sqrt{\beta}(3 - \beta). \quad (136)$$

β varies between zero and one; at the two extremes the right side term of the inequality may take the value zero or two, respectively. Thus it has yet to be proved that the term on the right side of the inequality function

$$y = \sqrt{\beta}(3 - \beta)$$

is nowhere greater than two, in the range of $\beta = 0$ and $\beta = 1$. This requirement is identical to having a monotony trend of y function in the

interval of $\beta = 0$ and $\beta = 1$, thus its calculus is positive in each point. This actual calculus is:

$$y' = \frac{1}{2\sqrt{\beta}}(3 - \beta) - \sqrt{\beta} = \frac{3 - \beta}{2\sqrt{\beta}} - \sqrt{\beta} = \frac{3(1 - \beta)}{2\sqrt{\beta}} \tag{137}$$

Owing to the postulatam that $0 \leq \beta \leq 1$, both the nominator and the denominator are positive for the whole interval, and so the monotony, and consequently the validity of the inequality (135), is duly proved.

The demonstration above therefore confirms that by using Schultze's shape factors an elongation of the footing — by keeping the contact area identical — causes a gradual decrease in the bearing capacity.

The same cannot be said when the shape factors proposed by BRINCH HANSEN (1955, 1961) are used. Namely, the term of the right side of the inequality is

$$(1 - 0.4\beta)\sqrt{\beta},$$

the calculus of which is

$$y' = \frac{1 - 1.2\beta}{2\sqrt{\beta}}; \tag{138}$$

this gives the zero result when $\beta = 0.833 < 1$. This means that the bearing capacity would not reach its maximum when the shape of the footing is square.

When the requirement is accepted that the bearing capacity of footings of identical contact areas has to decrease monotonously between $B/L = 1$ and $B/L = 0$, it can be demonstrated that A has to be equal to $1/3$ in the equation

$$f_y = 1 - A \frac{B}{L},$$

because the maximum can be achieved at the zero value of the expression

$$(1 - A\beta) \cdot \sqrt{\beta}, \tag{139}$$

i.e. where

$$\begin{aligned} [(1 - A\beta) \sqrt{\beta}]' &= \frac{-2A + 1 - A\beta}{2\sqrt{\beta}} = \\ &= \frac{1 - 3A\sqrt{\beta}}{2\sqrt{\beta}} = 0. \end{aligned}$$

And this condition is really only fulfilled when $A = 1/3$.

2.1.2.5 A general formula for the load-bearing capacity

A formula intended for general use was proposed by BRINCH HANSEN (1961). He retained the basic composition of the Terzaghi formula, but

by introducing various coefficients, he arrived at the following, more generalized equation:

$$p_b = b\gamma N_\gamma f_\gamma d_\gamma i_\gamma + qN_q f_q d_q i_q + cN_c f_c d_c i_c, \tag{140}$$

where N_γ, N_q and N_c = the usual bearing capacity factors,

- f = shape factor,
- d = depth factor,
- i = inclination factor.

By means of Eq. (140) we can determine the bearing capacity of a foundation of any shape, subjected to any load, centric or eccentric and vertical or inclined. The f factors, as proposed by BRINCH HANSEN can be read from Table 5. Here, therefore, only the suggestion made in respect of the d and i factors are dealt with.

The depth factors d can be obtained from the following equations proposed by BRINCH HANSEN:

$$d_c \approx 1 + \frac{0.35}{\frac{2b}{t} \frac{0.6}{1 + 7 \tan^4 \Phi}}, \tag{141}$$

$$d_q = d_c - \frac{d_c - 1}{N_q}; \quad (d_q \approx d_c \text{ when } \Phi \geq 25^\circ), \tag{142}$$

$$d_\gamma = 1. \tag{143}$$

The use of these factors is only permissible if the shear strength of the soil strata above foundation level is not smaller than that of the soil beneath the base of the footing.

The equations for obliquity factors are

$$\begin{aligned} i_q &= \frac{1 + \sin \Phi \sin (2\alpha - \Phi)}{1 + \sin \Phi} e^{-\left(\frac{\pi}{2} + \phi - 2\alpha\right) \tan \phi} \approx \\ &\approx \left[1 - \frac{H}{V + Ac \cot \Phi} \right]^2, \end{aligned} \tag{144}$$

$$i_c = i_q \frac{1 - i_q}{N_q - 1}, \tag{145}$$

$$i_\gamma = i_q^2. \tag{146}$$

Here H is the horizontal component and V is the vertical component of the resultant force R on the base of the footing, and A is the area of the base. Table 6 gives numerical values of the factor i .

Table 6. Coefficients of inclination, after BRINCH HANSEN (1961)

	t	δ°				
		0	10	20	30	40
i_γ	0	1.0	0.5	0.2	0	
	b	1.0	0.6	0.4	0.25	0.15
i_c	$0-b$	1.0	0.8	0.6	0.4	0.25

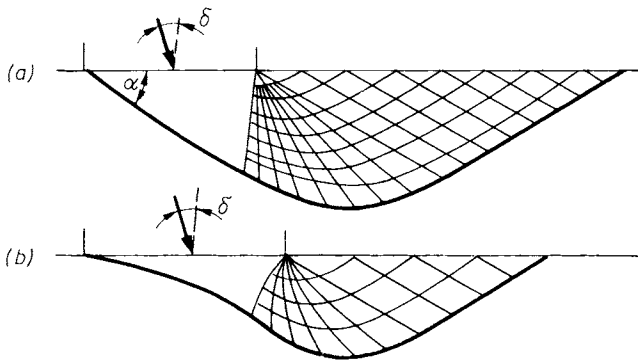


Fig. 150. Network of failure surface in the case of a leaning load:

a — in a weightless medium; b — in a heavy mass

The equation of i_q results from the theoretical analysis of a weightless medium (Fig. 150a). The slope angle α of the initial plane section of the slip surface can be computed from the following equation

$$\tan\left(\alpha - \frac{\Phi}{2}\right) = \frac{\sqrt{1 - (\tan \delta \cot \Phi)^2} - \tan \delta}{1 + \frac{\tan \delta}{\sin \Phi}}. \quad (147)$$

In a real soil with $\gamma > 0$, the failure pattern is similar to that shown in Fig. 150b.

In the case of a skew force, the shape of the active zone, and the set of slip surfaces in it, will be asymmetric. For the critical value of the force P with the incline δ , DUBROVA proposed the expression:

$$P_{cr} = B^2 \gamma N'_y + 2BqN'_q. \quad (148)$$

Taking the bearing capacity factor, N'_c , of a cohesive soil — according to Eq. (111) — as

$$(N'_q - 1) \cot \Phi$$

the failure stress can be written as:

$$p' = B\gamma N'_y + 2qN'_q + c(N'_q - 1) \cot \Phi, \quad (149)$$

where

$$\begin{aligned} B &= \text{the width of the footing,} \\ q &= \text{the overburden pressure on the foundation level (mostly } q = t\gamma). \end{aligned}$$

The bearing capacity factors can be taken from Fig. 151 as functions of δ and Φ .

In view of these considerations, the trial tests carried out at Degebo (Berlin) are really interesting, not only because of the impressive sizes of the test footings, but also because the loading events have been arranged in correspondence with the long or the short sides of the foundations.

The loaded contact area had a length of 2 m and a width of 0.5 m, and the foundation level was at 0.5 m below the ground surface. From the results the following conclusions can be drawn.

1. When the load was parallel to the long side and had an inclination of $\delta = 20^\circ$ to the vertical, the bearing capacity was 40% less than that for the vertical load. As $\tan 20^\circ = 0.37$, MUHS (1969) concluded that the reduction in the vertical projection of the force is in the range of $(1 - \tan \delta)$.

2. When the load acted parallel to the short side, the situation became even less favourable because in this case the force acted in the same direction in which — similarly to the case of a vertical loading — the slip surfaces would have developed anyhow.

Having analyzed the results of these tests (Fig. 152) MUHS and WEISS (1973) concluded that the ratio of the vertical component of the force to failure with incline δ (P_δ and P , respectively) to that of $\delta = 0$ can be written as:

$$\frac{P_\delta}{P} \cong (1 - \tan \delta)^2. \quad (150)$$

The problem of eccentrically loaded footings has been investigated by several authors. A common disadvantage of most theoretical solutions is that they lead to very complicated formulas. An approximate method, which is perhaps not very accurate but which is simple and on the safe side, was proposed by MEYERHOF (1963). He introduced the concept of effective base area — a portion of the actual base area on which the load is centric. Its internal boundary is constructed on the basis of axial symmetry as shown for a rectangular footing in Fig. 153. With this reduced area constructed, the computation of the load-bearing capacity proceeds as if the load on the base were centric. Note that the width and length of the effective base area should be entered into the relevant equations.

PRAKASH and SARAN (1971) elaborated a theory which is worth for attention on the ground that the pressure to failure has been determined according to conventional conditions — a failure mechanism in the wake of an eccentric load. The bearing capacity factors as suggested by the authors are illustrated in Fig. 154. After investigating the shape factors the authors found that for a dense sand

$$f_y = 1.0 + \left(\frac{2e}{B} - 0.68\right) \frac{B}{L} + \left(0.43 - \frac{3e}{2B}\right) \cdot \left(\frac{B}{L}\right)^2. \quad (151)$$

and for loose sand $f_y = 1$. Factor f_q was uniquely unity for both loose and dense sands. Hardly any variation with δ has been found in respect to the

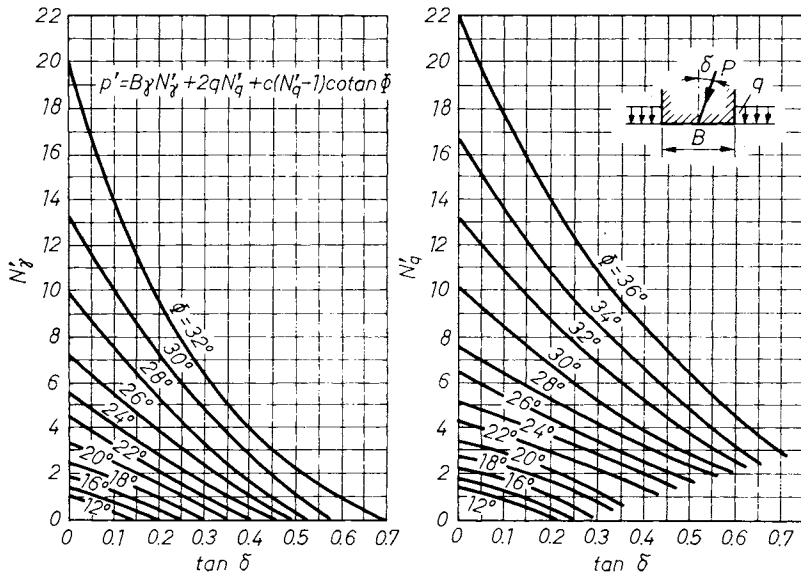


Fig. 151. Bearing capacity factors for a centrally acting leaning force (DUBROVA)

third bearing capacity factor f_c , so it was suggested that a constant value of $f_c = 1.2$ should be used for square and circular footings.

In the light of the trial tests at Degebo the p value calculated with the method of MEYERHOF is less than in reality (MUHS, 1969). The results of the model tests have been worked up to provide a single factor (ϵ) to express the reduction in respect of both the shape factors and eccentricity.

Pertinent proposals can be read from Fig. 155. In the formulas:

$$k_1 = \frac{a'}{a} \quad \text{and} \quad k_2 = \frac{b'}{b},$$

where

$$a' = a - 1.14e_a$$

and

$$b' = b - 1.14e_b.$$

	δ	P	$\frac{P_\delta}{P}$	P	$\frac{P_\delta}{P}$
		$D=0$		$D=0.2 \text{ m}$	
	0°	1900	1	2130	1
	10°	1340	0.71	1730	0.81
	20°	820	0.43	1040	0.49
	30°	320	0.17	360	0.17

Fig. 152. Model test results obtained under leaning loads (MUHS and WEISS, 1973)

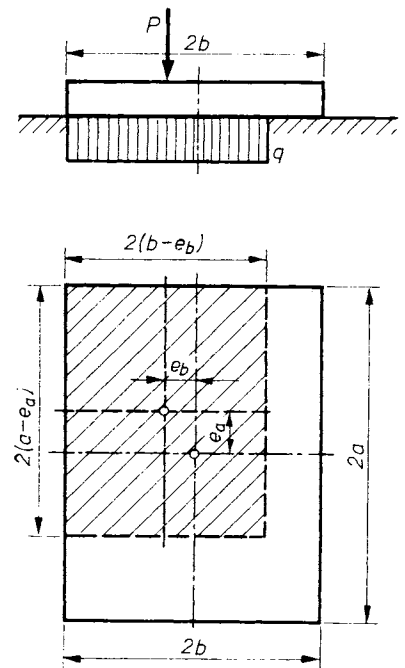


Fig. 153. Establishment of the effective load-bearing area under a force acting eccentrically

2.1.3 Bearing capacity of footings exposed to particular conditions

2.1.3.1 Foundations exposed to pulling forces

A shallow foundation might, in exceptional cases, be exposed to pulling forces which then should be accommodated with sufficient reliability. MORS (Baugrundtagung 1956, Köln) has conducted model tests in the interest of enabling comparison among three different design approaches (Fig. 156). One of them (insert in Fig. 156a) makes only use of the weight of the ripped prism to balance the pulling force (here β is a function of soil characteristics and the shape of the base). The second calculates the friction on the side walls of the prism of vertical wall (insert Fig. 156b). The third (insert Fig. 156c) applies the earth pressure at rest to the vertical walls of the prism (here the force $E_0 \tan \delta = E_0 \tan \Phi$ act against pulling).

The reaction against pulling might then be calculated in these cases as:

$$(a) Z_{\max} = W_b + W_1 + \tan \beta \gamma t^2 \left(2b + \frac{4}{3} t \tan \beta \right), \quad (152)$$

$$(b) Z_{\max} = W_b + W_1 + Uts, \quad (153)$$

$$(c) Z_{\max} = W_b + W_1 + U \frac{t^2 \gamma}{2} K_0 \tan \Phi, \quad (154)$$

- where W_b = the weight of the footing,
- W_1 = the weight of the earth prism above the footing,
- U = perimeter of the footing,
- s = average shear resistance,
- K_0 = factor of earth pressure at rest.

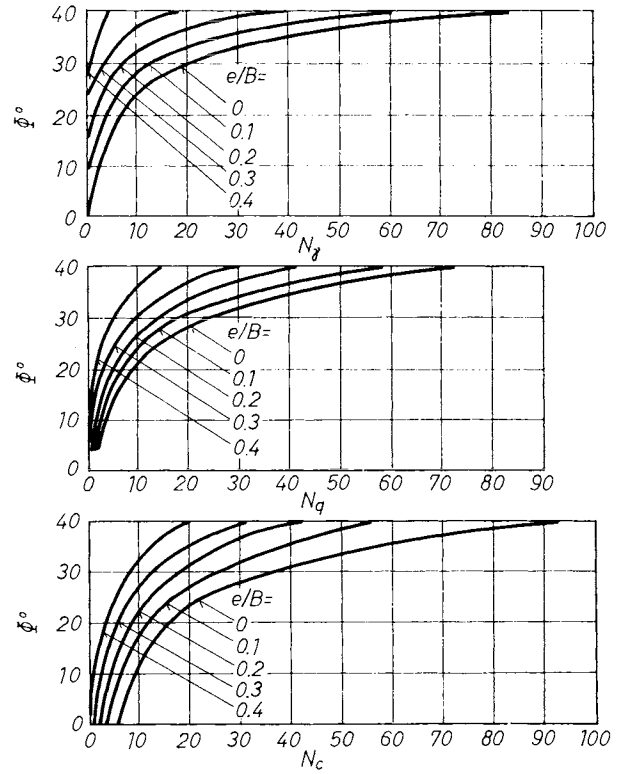


Fig. 154. Bearing capacity factors for eccentrically acting vertical forces (PRAKASH and SARAN, 1971)

MORS's suggestion was to apply the formulas in the following situations:

- (a) for greater depth in loose soils;
- (b) for shallow foundation in cohesive soils;
- (c) for dense, cohesionless soils.

Case		Reduction factors
Two-fold eccentricity	$a' \geq b'$	$\epsilon_{c,t} = \frac{1+0.3b'/a'}{1+0.3b/a} k_1 k_2$
		$\epsilon_B = \frac{1-0.4b'/a'}{1-0.4b/a} k_1 k_2^2$
	$a' < b'$	$\epsilon_{c,t} = \frac{1+0.3a'/b'}{1+0.3b/a} k_1 k_2$
		$\epsilon_B = \frac{1-0.4a'/b'}{1-0.4b/a} k_1 k_2^2$
Simple eccentricity	along the long side	$\epsilon_{c,t} = \frac{k_1 + 0.3b/a}{1+0.3b/a}$
		$\epsilon_B = \frac{k_1 - 0.4b/a}{1-0.4b/a}$
	along the short side	$\epsilon_{c,t} = \frac{1+0.3a/b k_1}{1+0.3b/a} k_1$
		$\epsilon_B = \frac{(1-0.4a/b k_1)}{1+0.3b/a} k_1$
	$a' = a$	$\epsilon_{c,t} = \frac{(1+0.3b/a k_2)}{1+0.3b/a} k_2$
		$\epsilon_B = \frac{1-0.4b/a k_2}{1-0.4b/a} k_2^2$

Fig. 155. Compounded shape factors for eccentric loads according to MUHS (1969)

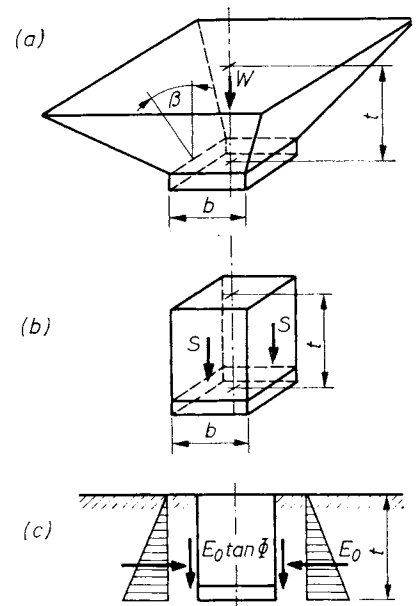


Fig. 156. Design of foundations exposed to tension according to the Mors method (1956)

2.1.3.2 Anchorages

When the footing has an anchoring function (Fig. 157) its bearing capacity can be estimated by using MARIUPOLSKII's (1965) formula:

$$P_{cr} = \frac{W_1 + \pi(R^2 - R_0^2)\gamma h}{1 - (R_0/R)^2 \cdot nh/R} + \xi \tan \Phi \cdot 4(R + 2ch)R \quad (155)$$

where the symbols — other than in Fig. 157 and the habitual ones — mean:

- W_1 = the weight of the anchoring base,
- ξ = coefficient of the side pressure (0.4–0.6),
- c = specific cohesion,
- n = coefficient which can be taken from Fig. 157 as a function of Φ .

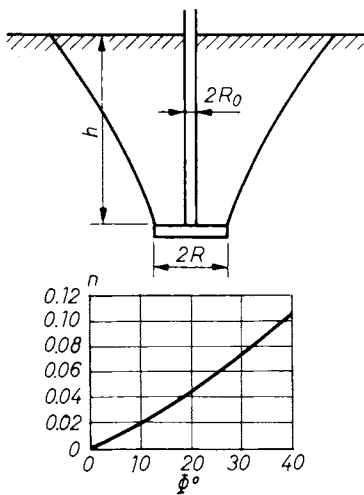


Fig. 157. Design of anchorages by using MARIUPOLSKII's method (1965)

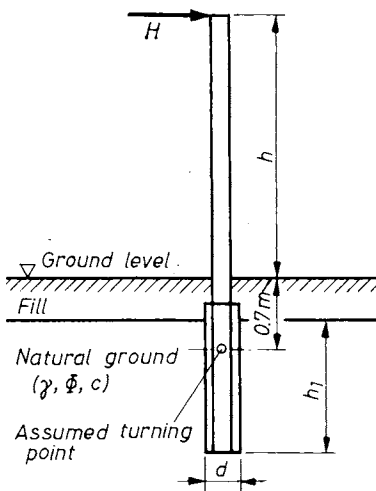


Fig. 158. Design of mast foundations

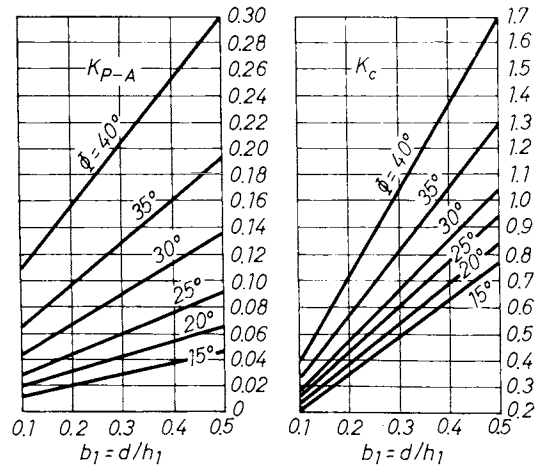


Fig. 159. Coefficients K_{p-A} and K_c for mast foundations

For square-shaped footings, the length of the side (B) should be used instead of the $(2R)$.

The formula is valid for relatively shallow pulled foundations only.

2.1.3.3 Mast foundations

The requirement that a foundation should reliably accommodate horizontal forces from wind pressure might be achieved in the simplest way by employing mast (column) foundation methods. In this case, piers are placed in boreholes and surrounded with concrete.

The design procedure of mast foundations is carried out in the following manner (see Fig. 158).

The horizontal force acting at the top of the pier, then the so-called "design moment" of that force at -0.70 m level at the fairly accurate turning point should be calculated. According to the trial test performed the turning point — which separates the zones of active and passive earth pressures — is generally in the depth of 0.7 m. The balancing moment originating from soil resistance can then be written as:

$$M_s = h_1^4 \gamma K_{p-A} + h_1^3 \tau K_c, \quad (156)$$

- where h_1 = effective height of the base (which is in contact with firm soil), m
- K_{p-A} = value taken from the diagram in Fig. 159,
- K_c = value taken from Fig. 159,
- γ = bulk density of the soil, kN/m^3 ,
- τ = shear resistance of the soil.

The following resistance of the soil can be used:

- in cohesionless soils: $\tau = 0.6h_1\gamma \tan \Phi$,
- in cohesive soils: as above, but with the addition of c , kN/m^2 .

The limiting horizontal bearing capacity of a mast foundation is then:

$$H_0 = \frac{1}{n} \frac{M_s}{h + h_1}, \quad (157)$$

where n = safety factor (≤ 2),
 h = the height of the pier, m.

The vertical bearing capacity should be determined as in the case of a conventional shallow foundation.

2.1.3.4 Foundation in the vicinity of slopes

MEYERHOF (1951) suggested calculating the bearing capacity of footings near to slopes of granular soil from the formula

$$p = 0.5\gamma BN_{\gamma q}, \quad (158)$$

where B = the width of the footing,
 $N_{\gamma q}$ = a factor depending on the depth, and on the distance of the nearest edge of the footing to the slope.

MEYERHOF (1957) and GIROUD and TRAN-VO-NHIEM (1971) published numerical values for the factor $N_{\gamma q}$. Those relating to $\Phi = 30^\circ$ are illustrated in Fig. 160. There is hardly any difference between the suggestion of the two authors for this case, but at $\Phi = 40^\circ$ the values proposed by MEYERHOF greatly surpass those given by GIROUD and TRAN-VO-NHIEM.

SCHIELDS *et al.* (1977) made trial tests in a 15 m long and 2 m wide model-box. The density of the dry sand employed in the box was 14.85 kN/m³ ("compact sand"), and 15.75 kN/m³ ("dense sand"), with relevant relative density values of 70 and 90%, respectively. The test results are shown in Fig. 161. On the basis of these tests, the authors concluded that the coefficients of GIROUD and TRAN-VO-NHIEM overestimate the actual bearing capacity. The same can be said in respect of Meyerhof's coefficients also, but in a more exaggerated manner.

2.1.4 Stability analysis of foundations

2.1.4.1 Safety against sliding

When a substantial horizontal force — due to the incline of the resultant force — is transferred onto the footing, consideration should be given to checking the possibility of sliding of the footing. According to classical suppositions, this would ensue when.

$$H > V \tan \varphi, \quad (159)$$

where φ represents the angle of friction between the material of the foundation and the soil. (With

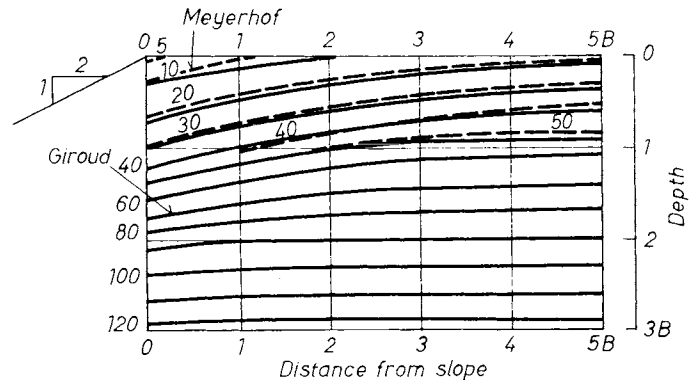


Fig. 160. Contours of theoretical $N_{\gamma q}$ values for $\Phi = 30^\circ$ (GIROUD and TRAN-VO-NHIEM, 1971; MEYERHOF, 1957)

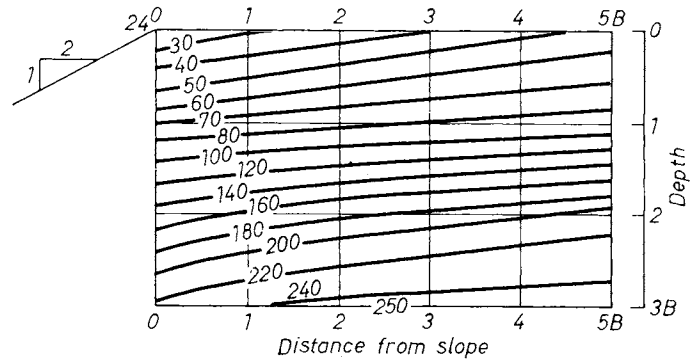


Fig. 161. Contours of experimental $N_{\gamma q}$ values in compacted sand (SCHIELDS *et al.*, 1977)

cohesive soils, both the cohesion and the adhesion should be taken into account.)

Applied tests which were conducted in the nineteen-sixties VARGA (1962) indicated that it is not sufficient to investigate this phenomenon solely on the basis of the above formula, as will be seen from the following.

Concrete cubes with 25 cm long sides were installed in the subsoil of the trial pits at the Elisabeth bridge in Budapest (VARGA, 1962). Iron blocks were applied measuring the force which was necessary to maintain a continuous creep of these blocks. These tests gave the surprising result that by increasing the vertical force V , the horizontal force H , required to maintain the continuous movement changed according to a concave curve — instead of a linear increase — and so was below the value which could have been expected from Eq. (159) (see Fig. 162).

The phenomenon can be explained by the fact that the applied skew load provoked failure along a slip surface in the underground. To prove this contention, a wooden plank was installed in the ground; thereafter the tests really did show a linear relation between the V and H components, as the development of a slip surface was obstructed (see the dashed straight line in the figure). The final conclusion has then been drawn beyond

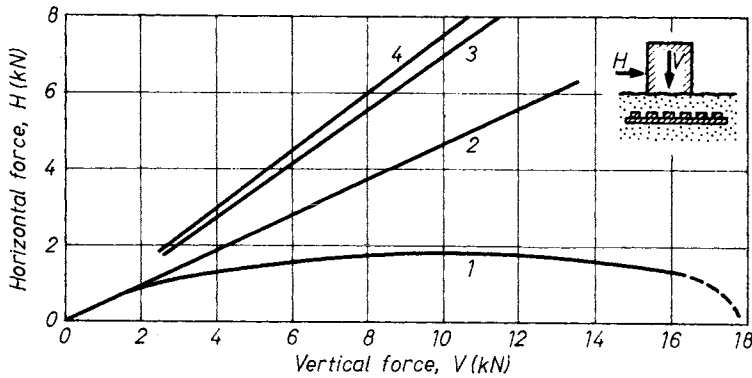


Fig. 162. The force $H = f(V)$ necessary to maintain continuous motion on the granular subsoil with or without the application of a grid plate below the concrete block (results of model tests carried out by KÉZDI and VARGA): 1 — concrete cube on the soil without grid plate; 2 — as in 1 but with plate; 3 — gravelly sand — smooth concrete $\phi \sim 35^\circ$; 4 — relationship corresponding to $\phi = 37^\circ$

a certain limit — in contradiction to the inequality in Eq. (159) — the normal force does not add to, but lessens the resistance against sliding. The validity of this concept can be felt extremely well in that range where the vertical force approaches the bearing capacity of the footing. A slight additional horizontal force would suffice in this case to destroy the stability of the footing. It can be proved theoretically that the tangent on the initial part of the curve is

$$\frac{dH}{dV} = \tan \phi,$$

while in the final section of the curve it is vertical, i.e.

$$\frac{dH}{dV} \rightarrow \infty.$$

Insufficient safety against sliding can be remedied by choosing one of several possible measures (greater depth or widening of the footing, anchorage, piling, etc.). In the case of a shale roofed hall in Belgium, for example, the floor slab was used to partially absorb horizontal forces from the structure, in the manner of a longitudinal joint inserted along the central axis of the building, to ensure the development of shear forces; in addition the floor slab was slightly reinforced and bars connected to the footings (HOMES, 1962).

2.1.4.2 Safety against tilt

This problem might emerge when the force is eccentric.

In the case of soils, the principle of mechanics is valid, inasmuch as a stiff body positioned on top of an other stiff and rigid mass will tilt off when the resultant of the forces acting intersects the interface outside the boundaries of the sup-

porting mass. The soil will be unevenly compressed and this process further accentuates the eccentricity (this can be exceptionally dangerous in the case of buildings with their centres of gravity located high).

Tension cannot build up between the soil and the footing, so there is no tensile section in the stress distribution diagram. When the line of the resultant force intersects the interface beyond the internal third core, the edge pressure (σ_p) starts to increase gradually. Its value can be determined from the supposition that the centre of gravity on the stress distribution diagram has to coincide with the line of action of the force, and the area of the diagram should equal the magnitude of the force (Fig. 163). In the case of a strip foundation the edge pressure can be found:

(a) when the acting line is inside the internal third core

$$\sigma_p = \frac{q}{B} \left(1 + \frac{6e}{B} \right), \quad (160)$$

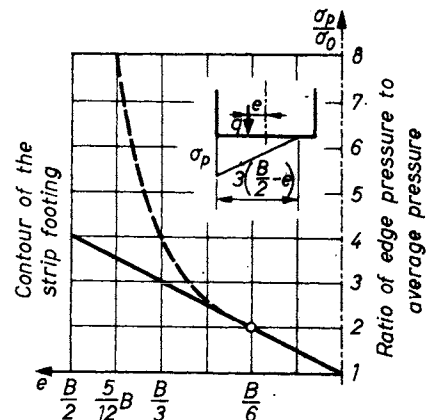


Fig. 163. Variation of average-, and edge-pressures as functions of eccentricity e

(b) when it is outside the internal third core

$$\sigma_p = \frac{4}{3} \frac{q}{B - 2e} \tag{161}$$

When the edge pressure due to an eccentric load has to be determined in any horizontal cross-section of a rigid body, it will be found that it increases linearly with the distance of excentricity. The same configuration exists with the pressure acting at the edge of the foundation, in so far as the force intersects in the internal third. As soon as it exceeds this boundary, Eq. (161) will be in force, and accordingly the edge pressure begins to increase hyperbolically with excentricity. In reality, the contact pressure distribution is not uniform, even in the case of a central force (usually it is not), and the formulas given above for rigid bodies will also not be valid in their original form. The graph indicates, however, how important it is to check the safety against tilting when e is greater than $B/6$.

There is no exact definition yet available in the literature in respect of safety against tilt. The general formula gives it as:

$$F = \frac{\text{the moment of forces preventing tilt}}{\text{the moment of forces evoking tilt}}$$

This concept is not quite universal, however, because the grouping of forces might be ambiguous. Some authors put all vertical forces in the nominator, and horizontal forces in the denominator of the formula. In this way, for example, reactive soil resistance as a force would be joined among the preventive forces, which is not the case in reality. Doubt arises similarly when there are oppositely directed horizontal forces involved in the problem. Suggestions can be found in the literature to form the groups of forces in such a way — and put them in the nominator or denominator accordingly — that their turning moment should be clockwise or anti-clockwise. Also this concept can be dubious because when the forces are divided into their components (or the opposite) this may change the value of calculated safety.

LESKE and KUSURELIS (1965) proposed using the formula below for the calculation of safety against tilt:

$$F = \frac{a}{a - c} \tag{162}$$

where: a = distance between the centre of gravity of the footing and the axis of tilt,
 c = distance between the acting point of the force and the axis of tilt.

According to this formula, for a centrally acting force, $F \rightarrow \infty$; and when the force acts at the contour line (i.e. on the axis of tilt), $F = 1$. This

interpretation complies with the commonly accepted principle that a definite $F = f(e)$ safety function has to be assigned to any eccentrically acting vertical force. Following the definition given by the authors, the value $F = 1.5$ can be attained when the resultant force intersects the base at 1/6th of the width.

Another question is where the axis of tilt has to be ordered. Field experiments have shown that the axis lies between the contour lines of the footing when the soil is soft. Neglecting this observation, disadvantageous consequences may effect the safety of the foundation.

To avoid uncertainties in relation with safety against tilt, the safety margin SM can be determined (see Section 1.6.2). This procedure has the advantage that also the probability of tilt can be anticipated.

2.1.5 Deformation theories

The basic idea in these theories is to find those points in the underground which — under the pressure of the load — attain a plastic condition. For shallow strip foundations, this condition would first be met at the two lower corners of the strip. At the beginning of the research it was said that the particular load would be the critical load which causes the plastic zone to develop only at these two points (PUZIRJEVSKII, 1929; FRÖHLICH, 1934). Later researchers found the development of larger plastic zones also acceptable.

The different deformation theories can be reduced to the following common formula:

$$q_0 = \frac{\pi(t\gamma + B + c \cot \Phi)}{\cot \Phi + \Phi - \pi/2} + t\gamma \tag{163}$$

where B is not the width of the footing but γ -times the distance between the foundation level and the depth to which the plastic zone extends.

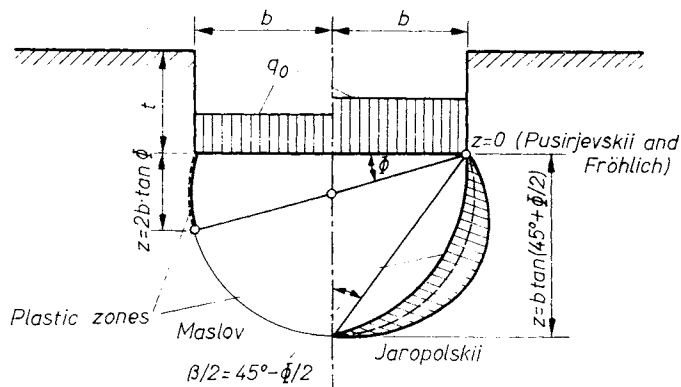


Fig. 164. Development and dimensions of the plastic zones according to presumptions made by PUZIRJEVSKII (1929), FRÖHLICH (1934), MASLOV (1949) and JAROPOLSKII (1929)

The formulas produced by individual authors might be derived from Eq. (163), with the following substitutions:

- JÁKY (1948a): $B = 0, t\gamma = 0$ (in the nominator only);
- PUZIRJEVSKII (1929)–FRÖHLICH (1934): $B = 0$;
- MASLOV (1949): $B = 2b\gamma \tan \Phi$;
- JAROPOLSKII (1929): $B = b\gamma \tan (45^\circ + \Phi/2)$,

were b = half the width of the base. (The above set is listed according to an increasing q_0 value when b, Φ, c and γ are kept as constants.)

The conditions postulated by the above authors in respect of the extension of the plastic zone are illustrated in Fig. 164.

The common expression of deformation theories (Eq. (163)) can be transformed into a configuration similar to Eq. (119). So, for example, the Maslov-formula can be written as:

$$q_0 = b\gamma N_\gamma^M + t\gamma N_q^M + cN_c^M, \quad (164)$$

where $N_\gamma^M = 2N \tan \Phi, \quad (165)$

$$N_q^M = N + 1, \quad (166)$$

$$N_c^M = N \cot \Phi, \quad (167)$$

$$N = \frac{\pi}{\cot \Phi + \Phi - \pi/2} \text{ respectively.} \quad (168)$$

From Eq. (165) to (167) the conclusion can also be drawn that

$$N_c^M = (N_q^M - 1) \cot \Phi \quad (\text{for any } \Phi) \quad (169)$$

and

$$N_\gamma^M = N_q^M - 1 \quad (\text{for } \Phi = 0 \text{ and } \Phi = 26.3^\circ). \quad (170)$$

From expressions (164) — which were transformed to resemble the failure stress formulas — the desired allowable stress can be found by help of similar diagrams as have been used for failure stresses. Maslov's bearing capacity factors are, for example, illustrated in Fig. 165; Puzirjevskii's and Fröhlich's final values are gained from Maslov's formula when the first term is eliminated ($N_\gamma = 0$).

When $\Phi = 0, q_0$ can be calculated in the following manner (RÉTHÁTI, 1966). Dividing the nominator and the denominator in the first term in Eq. (163), by $\cot \Phi$, it becomes:

$$q_0 = \frac{\frac{\pi t\gamma}{\cot \Phi} + \frac{\pi B}{\cot \Phi} + \pi c}{1 + \frac{\Phi}{\cot \Phi} - \frac{\pi}{a \cot \Phi}} + t\gamma. \quad (171)$$

When $\Phi = 0$, the first two terms in the nominator become zero (B should be substituted from whichever theory), and the second and third terms in the denominator would be zero as well (in

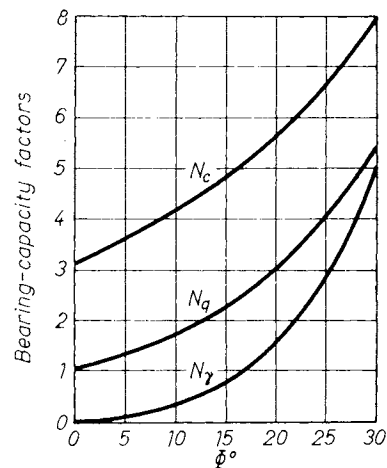


Fig. 165. Bearing-capacity factors according to MASLOV (1949)

respect of the second term becoming zero, the proof can be given by the l'Hospital-rule), and so:

$$q_0 = \pi c + t\gamma. \quad (172)$$

In the Soviet praxis deformation theories are also used to find the approximate value of the proportionality limit of the deformation curve (σ, s)

2.2 Distribution of stresses in soils

2.2.1 Introduction

One important task of soil mechanics is to predict the movements, especially settlements, that buildings founded on a soil are likely to undergo. If the foundation is properly designed, the stresses induced in the soil by the load of the structure are small enough not to give rise to plastic deformations. Under such conditions, it can reasonably be assumed that the soil is a perfectly elastic material and so the stresses in the soil can be estimated by the theory of elasticity. As is well known, the equations of elastic theory are rigorously correct only for materials in which stresses and strains are proportional. When these equations are used for determining stresses in soils, inaccuracies of unknown magnitude can occur. But if we consider that there is normally a two- or threefold margin of safety against the occurrence of plastic failure, it can well be assumed that a constant ratio exists between stresses and the corresponding strains, and therefore the elastic theory based on Hooke's law is applicable. If the requirement of proportionality is not fulfilled, the equation of the theory of plasticity must be used. This means that we have to satisfy ourselves with an analysis of the failure state in the place of an elastic stress-strain analysis.

If a soil specimen is subjected to unconfined compression or to triaxial compression, the stress-strain curve will be similar to that shown in

Fig. 166. Up to a certain stress value (marked by point *A* on the curve), strains appear to be proportional to the corresponding stresses even if the test is performed with the utmost care. This apparent linearity, however, is only due to imperfections in laboratory testing techniques and apparatus, since the deformations of disperse systems such as soils must inherently be governed by a law different from Hooke's law.

Nevertheless, within the stress range previously mentioned, the approximation of linearity is permissible provided the stresses are kept within these limits everywhere in a soil mass. This is the case, for example, when the stresses acting on a layer at a great depth are to be estimated for the computation of settlements.

The stress-strain diagram in Fig. 166 can be divided into three characteristic sections. For section *I* (*OA*) it can be assumed that Hooke's law holds. The vast arsenal of the theory of elasticity is then at our disposal to compute stresses in soils. For the equations of elastic theory to be applied, only the Young's modulus and the Poisson number of the soil need be determined. Past the limit of proportionality (point *A*), very little if anything is known about the law governing the stress-strain relationship (see Section *II*, *AC*). Even approximate solutions for practical problems are lacking. This fact in itself would be of minor importance if it were possible to determine the upper limit of proportionality with a reasonable accuracy. A definite criterion for this, however, remains to be found.

As the stresses are further increased, a limit is reached at which continuous deformations occur under constant load (Section *III*). This condition constitutes the fundamental criterion of plastic flow; the soil is said to be in the plastic state. Unlike state *II*, the plastic state should by no

means be regarded as terra incognita, and in fact it has been the subject of extensive research. Rigorous theoretical solutions are available for special cases such as ideally plastic and weightless soil masses and also for a semi-infinite mass, both cohesive and frictional, with or without a uniform surcharge on the surface. For more complicated practical cases, approximate solutions or semi-empirical methods are in use.

Rigorous solutions for a variety of boundary conditions are available only in the theory of elasticity. This fact has to some extent biased the theoretical approach to problems encountered in soil mechanics. Theoretical solutions which were developed in the 19th century have been applied indiscriminately to practical problems in which the boundary conditions were anything but identical with those upon which the original solution was based. A blatant example is the attempt to derive the stresses induced in a soil mass by frictional forces acting on the shaft of a pile from Boussinesq's fundamental formula for stresses due to a point load on the surface of a semi-infinite mass. The application of elastic theory has also been encouraged by the fact that Boussinesq's formula (and all those derived from it) for vertical stresses does not contain the elastic constants. Young's modulus and Poisson's number of the material are difficult to determine experimentally for soils.

It should also be noted that in soil mechanics it is the equations from elastic theory that are primarily used for estimating stresses under loads, whereas deformations, especially settlements, are generally determined by entirely different methods.

Yet another aspect is worth noting.

Since a study of the mathematical theory of elasticity is beyond the scope of undergraduate civil engineering courses, soil engineers often use the equations from elastic theory without being fully aware of the specific conditions upon which their derivations were based. Furthermore, the relatively complicated formulas of elastic theory produce the illusion that they are capable of furnishing accurate results. The applicability of a formula should not, however, be judged on the ground of its complexity or on the multitude of the factors involved, but by the degree to which the assumptions upon which its derivation was based are fulfilled in the given case.

The numerous pitfalls involved explain why, from the very beginning of the application of elastic theory to soils, there has been a tendency to make use only of the simplest formulas in practical computations. But if one accepts, subject to certain conditions, the applicability of the theory of elasticity to soils, one must be consistent and find solutions that satisfy all the boundary conditions of the problem in question. Unfortunately, even if some of the actual boundary conditions are fulfilled, the resulting solution may be too complicated for practical use. Nevertheless,

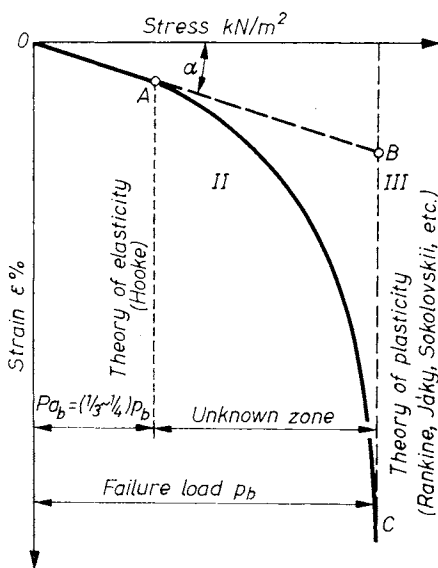


Fig. 166. Loading curve on the underground

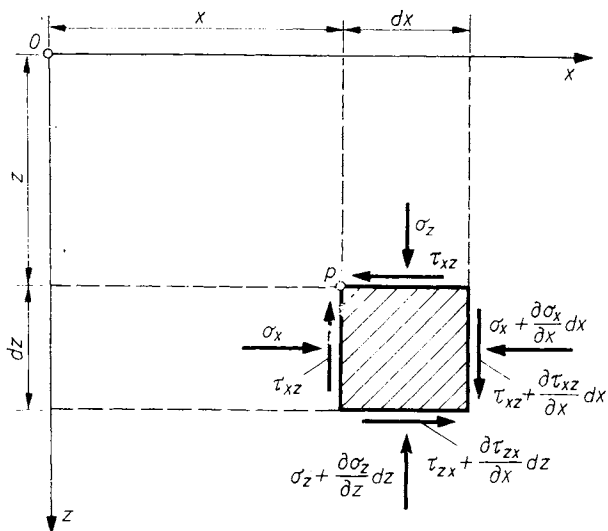


Fig. 167. Equilibrium on a volumetric soil element in the plane case

it is often imperative, from both scientific and practical viewpoints, to use exact formulas, no matter how complicated they may be; for example, in order to assess the relative significance of certain factors influencing the distribution of stresses in soils or to ascertain whether or not certain simplifications made in the computation of settlements lead to tolerable errors. When such an analysis is performed, it is possible to develop approximate methods of calculation which are easy to handle and at the same time accurate enough for most practical purposes.

After these preliminary remarks on the applicability of elastic theory to soils, we shall briefly discuss the fundamental relationships of the theory of elasticity. After that we shall deal with some common problems of the distribution of stresses in soils.

2.2.2 Fundamental equations of the theory of elasticity in the plane state

Many civil engineering problems associated with the distribution of stresses are two-dimensional. These can be defined as either a plane state of stress, when all the stresses acting on a structure or on a mass of soil are parallel to a given plane, or a plane state of strain, and this is more common, when the body considered is of infinite extent in one direction whereby the strains in that direction are equal to zero (retaining walls, embankments, continuous footings, etc.). The basic equations for these two kinds of plane state are closely related and can be dealt with together. In either case, the determination of three stress components σ_x , σ_z and τ_{xz} is required for the state of stress to be defined completely. The strains and deformations are obtained in both cases as linear combinations of stresses.

In order to describe the state of stress, let us consider the equilibrium of the elementary prism shown in Fig. 167. The coordinated stresses acting on the sides of the prism are assumed to be continuous and differentiable functions of the coordinates x and z of point P . Hence, the difference between the stresses on opposite faces in one direction is obtained, as the elementary change in the coordinates multiplied by the rate of change, is given by the partial derivative with respect to the variable considered. Provided the dimensions of the prism are sufficiently small, the elementary force on one of its faces can be obtained as the product of the width of the face and the average stress (the stress acting at the mid-point) on the face. In soils, a body force — the weight of the prism — must also be taken into account since it is of the same order of magnitude as the forces acting on the boundaries of the prism. By making use of the condition for equilibrium that the sums of elementary forces parallel to directions x and z , respectively, must be equal to zero, we obtain the following equations

$$\left. \begin{aligned} \sigma_z dz - \left(\sigma_x + \frac{\partial \sigma_x}{\partial x} dx \right) dz + \tau_{xz} dx - \\ - \left(\tau_{xz} \frac{\partial \tau_{xz}}{\partial z} dz \right) dx = 0, \\ \sigma_z dx - \left(\sigma_z + \frac{\partial \sigma_z}{\partial z} dz \right) dx + \tau_{xz} dz - \\ - \left(\tau_{xz} + \frac{\partial \tau_{xz}}{\partial x} dx \right) dz + \gamma dx dz = 0. \end{aligned} \right\} \quad (173)$$

After simplifying and rearranging terms, we obtain

$$\left. \begin{aligned} \frac{\partial \sigma_x}{\partial x} + \frac{\partial \tau_{xz}}{\partial z} = 0, \\ \frac{\partial \sigma_z}{\partial z} + \frac{\partial \tau_{xz}}{\partial x} = \gamma. \end{aligned} \right\} \quad (174)$$

The above system of equations, also known as the Cauchy equations, represents the conditions for equilibrium in a two-dimensional problem. These conditions must be satisfied at every point within the mass subjected to stresses. In addition, the stresses must satisfy the boundary conditions.

It should be pointed out that Eqs (174) are valid also for the case where the stresses on the sides of the elementary prism are not uniform as assumed, but change linearly. In this case a third equation, the moment equation of equilibrium should be involved to obtain Eqs (174).

As was previously stated, in a two-dimensional problem three stress components, which are functions of the coordinates, are required to define the state of stress in the vicinity of a point. The two equilibrium conditions expressed by Eqs (174) are, however, insufficient to find the three un-

knowns. The problem is thus statically indeterminate and a third equation is needed. In a stability analysis, the missing equation is provided by the requirement that in a limiting state of equilibrium the stresses must satisfy the condition of failure. As regards strains and deformations, the problem remains indeterminate. In a problem of deformation, the strains caused by the stresses must be compatible with the laws of geometry; this requirement, linked with a physical relationship between strains and stresses, will furnish the third equation required to solve Eqs (174).

In the theory of elasticity we are concerned with very small deformations. We also assume that the supports — the boundary forces — are sufficient to prevent the body from being moved as a rigid body. This means that an element within the mass cannot undergo any displacement without being deformed.

Let the components parallel to the axes x and z of the displacement of a point O be denoted by u and v , respectively (Fig. 168). The point A , located at a distance dx from O on the axis x , will be shifted to a new position A' . Its displacement parallel to x is given by

$$u + \frac{\partial u}{\partial x} dx.$$

The change in the horizontal component of the distance between points O and A is equal to $\frac{\partial u}{\partial x} dx$ and hence the horizontal strain is $\frac{\partial u}{\partial x}$.

In a similar manner, the strain in the vertical direction is found to be equal to $\frac{\partial v}{\partial z}$.

As a result of the displacements, the directions of the straight lines OA and OB will also change so that the lines $O'A'$ and $O'B'$ deflect by angles $\frac{\partial v}{\partial x}$ and $\frac{\partial u}{\partial z}$, respectively. The change in the angle AOB , which is originally a right angle, is determined by

$$\frac{\partial v}{\partial x} + \frac{\partial u}{\partial z}.$$

This quantity is denoted by γ and called the shear strain.

The deformations in the two-dimensional case are thus determined by the following expressions:

$$\epsilon_x = \frac{\partial u}{\partial x}; \epsilon_z = \frac{\partial v}{\partial z}; \gamma_{xz} = \frac{\partial u}{\partial z} + \frac{\partial v}{\partial x}. \quad (175)$$

Since the three components of strain were derived of two components of displacement, u and v , they cannot assume any arbitrary value, but are inter-related. Differentiating the first expression twice with respect to z , the second twice with respect to x and the third once with respect to x and once with respect to z , leads to the following expression:

$$\frac{\partial^2 \epsilon_x}{\partial z^2} + \frac{\partial^2 \epsilon_z}{\partial x^2} = \frac{\partial^2 \gamma_{xz}}{\partial x \partial z}. \quad (176)$$

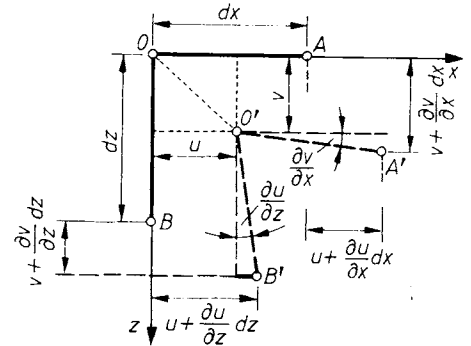


Fig. 168. Modifying components

This is known as the equation of compatibility and implies the requirement that the deformations must be in harmony with the laws of geometry.

The relation between stresses and strains can be established experimentally. In the theory of elasticity it is postulated that the stress-strain relation is linear, as is stated by Hooke's law, and that the principle of superposition is valid. The latter statement means that the strain, in one direction, produced by a composite state of stress, is equal to the sum of strains, in the same direction, produced by each one of the stresses individually.

In the three-dimensional case, the linear strain components are given by the following expressions:

$$\begin{aligned} \epsilon_x &= \frac{1}{E} [\sigma_x - \mu(\sigma_y + \sigma_z)], \\ \epsilon_y &= \frac{1}{E} [\sigma_y - \mu(\sigma_x + \sigma_z)], \\ \epsilon_z &= \frac{1}{E} [\sigma_z - \mu(\sigma_x + \sigma_y)]. \end{aligned} \quad (177)$$

In the plane state of stress $\sigma_y = 0$, and therefore from Eq. (177) we obtain

$$\begin{aligned} \epsilon_x &= \frac{1}{E} (\sigma_x - \mu\sigma_z), \\ \epsilon_z &= \frac{1}{E} (\sigma_z - \mu\sigma_x), \\ \gamma_{xz} &= \frac{2(1 + \mu)}{E} \tau_{xz} = \frac{1}{G} \tau_{xz}. \end{aligned} \quad (178)$$

Here the constant G is the shear modulus.

Substituting these components of strain into the equation of compatibility, Eq. (176), leads to

$$\begin{aligned} \frac{\partial^2}{\partial z^2} (\sigma_x - \mu\sigma_z) + \frac{\partial^2}{\partial x^2} (\sigma_z - \mu\sigma_x) &= \\ &= 2(1 + \mu) \frac{\partial^2 \tau_{xz}}{\partial x \partial z}. \end{aligned} \quad (179)$$

Differentiating the first of the Cauchy equations (174) with respect to x , and the second with respect to z and adding the two, we obtain

$$2 \frac{\partial^2 \tau_{xz}}{\partial x \partial z} = - \left(\frac{\partial^2 \sigma_x}{\partial x^2} + \frac{\partial^2 \sigma_z}{\partial z^2} \right).$$

Substituting into Eq. (179) gives

$$\left(\frac{\partial^2}{\partial x^2} + \frac{\partial^2}{\partial z^2} \right) (\sigma_x + \sigma_z) = 0. \quad (180)$$

Using Laplace's operator

$$\nabla = \frac{\partial^2}{\partial x^2} + \frac{\partial^2}{\partial z^2}.$$

Equation (180) becomes

$$\nabla (\sigma_x + \sigma_z) = 0. \quad (181)$$

This is an equivalent to the equation of compatibility, expressed in term of stresses.

In the plane state of strain $\epsilon_y = 0$. From Eqs (177) we obtain

$$\left. \begin{aligned} \epsilon_x &= \frac{1}{E} [(1 - \mu^2) \sigma_x - \mu(1 + \mu) \sigma_z], \\ \epsilon_z &= \frac{1}{E} [(1 - \mu^2) \sigma_z - \mu(1 + \mu) \sigma_x], \\ \gamma_{xz} &= \frac{2(1 + \mu)}{E} \tau_{xz}. \end{aligned} \right\} \quad (182)$$

By substituting Eqs (182) into Eq. (176) and making use of the Cauchy equations of equilibrium, we can verify that Eq. (180) holds also for the plane state of strain.

To sum up, the solution of a two-dimensional problem of the theory of elasticity amounts to solving the following simultaneous partial differential equations:

$$\left. \begin{aligned} \frac{\partial \sigma_x}{\partial x} + \frac{\partial \tau_{xz}}{\partial z} &= 0, \\ \frac{\partial \sigma_z}{\partial z} + \frac{\partial \tau_{xz}}{\partial x} &= -\gamma, \\ \left(\frac{\partial^2}{\partial x^2} + \frac{\partial^2}{\partial z^2} \right) (\sigma_x + \sigma_z) &= 0. \end{aligned} \right\} \quad (183)$$

A workable method of solution is to introduce a stress function, known as the Airy function. AIRY (1862) showed that the first two equations, signifying equilibrium conditions, in Eqs (183) are satisfied by a function $F(x, z)$ such that the three components of stress are defined as

$$\sigma_x = -\frac{\partial^2 F}{\partial z^2}, \quad \sigma_z = \frac{\partial^2 F}{\partial x^2} \quad \text{and} \quad \tau_{xz} = -\frac{\partial^2 F}{\partial x \partial z} - \gamma z. \quad (184)$$

The correct stress function will also satisfy the equation of compatibility. By substituting the expressions of stresses from Eqs (184) into the third of Eqs (183), we obtain the following partial differential equation for the Airy stress function:

$$\frac{\partial^4 F}{\partial x^4} + 2 \frac{\partial^4 F}{\partial x^2 \partial z^2} + \frac{\partial^4 F}{\partial z^4} = 0, \quad (185)$$

with which the usual notation becomes

$$\nabla \nabla F = 0. \quad (186)$$

The solution of a problem in two dimensions consists in finding a biharmonic function F which satisfies Eq. (185) and whose partial derivatives, representing components of stresses (Eqs (184)) satisfy the boundary conditions of the problem. Once such a function $F(x, z)$ is found, the components of stresses can be obtained by differentiation. The components of strain are determined by the following expressions:

$$E\epsilon_z = \sigma_z - \mu\sigma_x; \quad E\epsilon_x = \sigma_x - \mu\sigma_z; \quad G\gamma_{xz} = \tau_{xz}. \quad (187)$$

In soil mechanics, it is often expedient to treat problems of stress distribution in cylindrical coordinates (Fig. 169). For such cases, neglecting the unit weight of the soil, the equations of equilibrium are

$$\left. \begin{aligned} \frac{\partial \sigma_r}{\partial r} + \frac{1}{r} \frac{\partial \tau_{r\theta}}{\partial \theta} + \frac{\sigma_r - \sigma_\theta}{r} &= 0, \\ \frac{1}{r} \frac{\partial \sigma_\theta}{\partial \theta} + \frac{\partial \tau_{r\theta}}{\partial r} + \frac{2\tau_{r\theta}}{r} &= 0. \end{aligned} \right\} \quad (188)$$

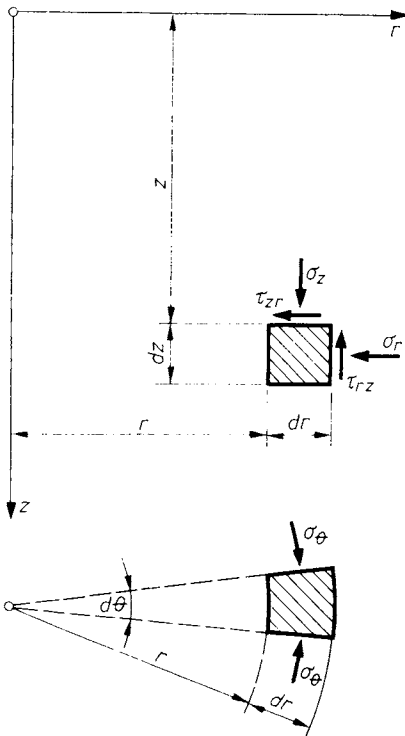


Fig. 169. Volumetric soil element in the cylindrical coordinate system

The solution is again obtained in the form of a stress function $f(r, \theta)$ whose partial derivatives furnish the components of stress:

$$\left. \begin{aligned} \sigma_r &= \frac{1}{r} \frac{\partial f}{\partial r} + \frac{1}{r^2} \frac{\partial^2 f}{\partial \theta^2}, \\ \sigma_\theta &= \frac{\partial^2 f}{\partial r^2}, \\ \tau_{r\theta} &= \frac{1}{r^2} \frac{\partial f}{\partial \theta} - \frac{1}{r} \frac{\partial^2 f}{\partial r \partial \theta} = -\frac{\partial}{\partial r} \left(\frac{1}{r} \frac{\partial f}{\partial \theta} \right). \end{aligned} \right\} (189)$$

It can be verified by substitution that Eqs (189) satisfy Eqs (188). In order that the solution be geometrically admissible, the stress function must also satisfy the equation of compatibility. With

$$r^2 = x^2 + z^2 \text{ and } \tan^{-1} \theta = \frac{z}{x}.$$

Equation (180) can be transformed into the following polar form

$$\left(\frac{\partial^2}{\partial r^2} + \frac{1}{r} \frac{\partial}{\partial r} + \frac{1}{r^2} \frac{\partial^2}{\partial \theta^2} \right) (\sigma_r + \sigma_\theta) = 0. \quad (190)$$

By substituting the stress components derived from the Airy stress function $f(r, \theta)$, we obtain

$$\left(\frac{\partial^2}{\partial r^2} + \frac{1}{r} \frac{\partial}{\partial r} + \frac{1}{r^2} \frac{\partial^2}{\partial \theta^2} \right) \left(\frac{\partial^2 f}{\partial r^2} + \frac{1}{r} \frac{\partial f}{\partial r} + \frac{1}{r^2} \frac{\partial^2 f}{\partial \theta^2} \right) = 0 \quad (191)$$

or using Laplace's operator

$$\nabla \nabla f = 0. \quad (192)$$

A special difficulty in solving problems of the theory of elasticity arises from the fact that apart from Eq. (185) or (191) there is no guidance whatsoever as to how to find the stress function. We only know that this function must be of the biharmonic type. A correct solution can normally only be found after laborious experimentation. Among the available solutions we have polynomials, trigonometric functions, Fourier series and Fourier integrals.

2.2.3 Stresses in a semi-infinite mass; plane strain

2.2.3.1 Line load on the surface

The problem is set out in Fig. 170. We have to determine the stresses in a semi-infinite soil mass with a horizontal surface $a-a$ due to a uniform load of intensity p acting on a line of infinite length which passes through point O at right angles to the section considered. The stresses due to the body force — the weight of the soil mass itself — will be neglected and only those caused by the surface load will be computed.

Let the stress function be of the form

$$f = Ar\theta \sin \theta. \quad (193)$$

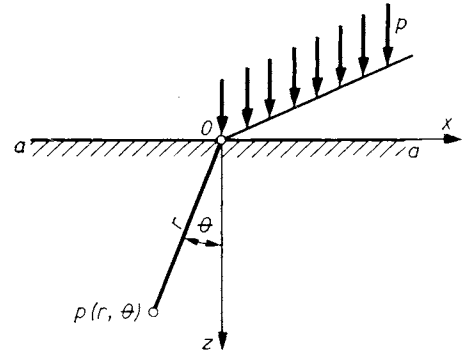


Fig. 170. Vertical line load on the surface of the half-space

By substituting the corresponding partial derivatives of this function in Eq. (191), we can verify that it is indeed a biharmonic function. The components of stress can be obtained from Eqs (189):

$$\begin{aligned} \sigma_r &= \frac{2A \cos \theta}{r}, \\ \sigma_\theta &= 0, \\ \tau_{r\theta} &= 0. \end{aligned}$$

The state of stress is found to be very simple; the distribution of stresses is radial. Any element of the soil mass is subjected only to a radial compression. At any point such as P , the direction of the major principal stress σ_r is coincident with that of radius vector OP , while the minor principal stress is zero.

The constant A in Eq. (193) still needs to be determined. To this end we consider the equilibrium of a half-cylinder of radius r with its axis passing through O (Fig. 171). The sum of the vertical components of the elementary radial forces $\sigma_r r d\theta$ on the cylindrical surface must be equal to the line load per unit of length, i.e.

$$\begin{aligned} -p &= 2 \int_0^{\pi/2} \sigma_r \cos \theta r d\theta = 4A \int_0^{\pi/2} \cos^2 \theta d\theta = \\ &= 4A \left[\frac{1}{4} \sin 2\theta + \frac{1}{2} \theta \right]_0^{\pi/2} = A\pi, \end{aligned}$$

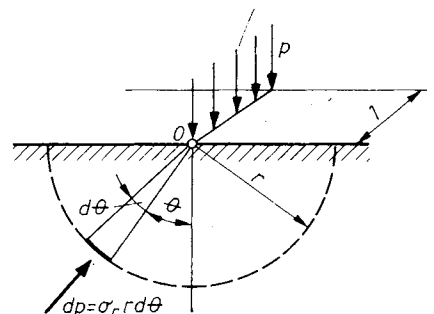


Fig. 171. Equilibrium conditions

whence

$$A = -\frac{P}{\pi}$$

After substituting in Eq. (193), the stress function becomes

$$f = -\frac{P}{\pi} r\theta \sin \theta \tag{194}$$

and the radial stress is

$$\sigma_r = -\frac{2p}{\pi} \frac{\cos \theta}{r} \tag{195}$$

The boundary condition that on the surface ($\theta = \pm\pi/2$) the stress must be zero is also satisfied at every point except O which is a point of singularity.

In rectangular coordinates the stress function becomes

$$F = -\frac{P}{\pi} x \tan^{-1} \frac{z}{x}$$

Hence the components of stress in polar and rectangular coordinates, respectively, are

$$\left. \begin{aligned} \sigma_z &= -\frac{2p}{\pi} \frac{\cos^3 \theta}{r} = -\frac{2p}{\pi} \frac{z^3}{r^4}, \\ \sigma_x &= -\frac{2p}{\pi} \frac{\cos \theta \sin^2 \theta}{r} = -\frac{2p}{\pi} \frac{x^2 z}{r^4}, \\ \tau_{xz} &= -\frac{2p}{\pi} \frac{\cos^2 \theta \sin \theta}{r} = -\frac{2p}{\pi} \frac{x z^2}{r^4}. \end{aligned} \right\} \tag{196}$$

For the case of a horizontal line load on the surface, the solution is similar to that for a vertical load. The expressions of components of stress are identical with those in Eqs (196), except that the angle θ is meant to be measured from the direction of the line load as shown in Fig. 172.

If the direction of the load is inclined at an angle α to the vertical (Fig. 173), the solution can be obtained by combining the equations for vertical and horizontal loads. After resolving the load p into the vertical and horizontal components $p \cos \alpha$ and $p \sin \alpha$, respectively, the radial stress

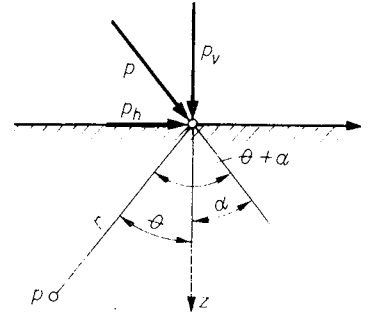


Fig. 173. Slanting line load

at any point P can be obtained by superposition. From Eq. (195) we obtain

$$\begin{aligned} \sigma'_r &= -\frac{2p}{\pi r} [\cos \alpha \cos \theta + \sin \alpha \cos (90^\circ + \theta)] = \\ &= -\frac{2p}{\pi r} \cos (\alpha + \theta). \end{aligned} \tag{197}$$

Thus we see that Eq. (195) is valid for any inclination of load, only the angle θ should always be measured from the direction of the line load.

The σ_r isobars, lines of equal radial stress, are defined by the equation

$$\sigma_r = -\frac{2p}{\pi} \frac{\cos \theta}{r} = \text{constant}.$$

In the case of a vertical load, these lines are found to be ellipses, with their centres on the vertical axis z , having the equation

$$\frac{z}{x^2 + z^2} = \text{constant}.$$

The σ_z isobars for a vertical line load are curves of the fourth order, defined by the following equation

$$\frac{z^3}{(x^2 + z^2)^2} = \text{constant}.$$

2.2.3.2 Strip load on the surface of a semi-infinite mass

The case of loading discussed in the preceding section is mainly of theoretical interest since, in reality, a line load is always distributed over a finite width. In a state of plane strain, this is called a strip load. Supposing the slab through which the load is transmitted onto the soil is perfectly flexible, the strip load acting on the surface of an elastic semi-infinite mass can be divided into an infinite number of elementary line loads, from which the equations of stresses can be derived by integration, making use of the principle of superposition.

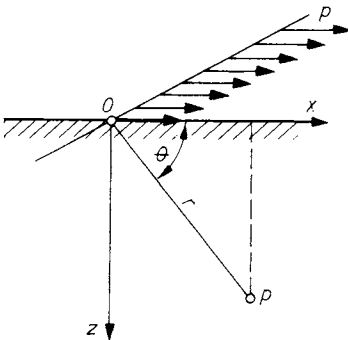


Fig. 172. Horizontal line load on the surface of the half-space

Beneath the base of a real footing, the contact pressures may be distributed in different fashions. The character of the distribution of stress is influenced by a number of factors. In the simplest case the load can be assumed to be uniformly distributed across the base of the footing. This case can be treated, after TIMOSHENKO (1957), as follows (Fig. 174).

Let the Airy stress function be of the form

$$f = Ar^2\theta.$$

The components of stress are obtained by successive derivations:

$$\sigma_r = \frac{1}{r} \frac{\partial f}{\partial r} + \frac{1}{r^2} \frac{\partial^2 f}{\partial \theta^2} = 2A\theta,$$

$$\sigma_\theta = \frac{\partial^2 f}{\partial r^2} = 2A\theta,$$

$$\tau_{r\theta} = -\frac{\partial}{\partial r} \left(\frac{1}{r} \frac{\partial f}{\partial \theta} \right) = -A.$$

If we apply this state of stress to a semi-infinite mass, the situation shown in Fig. 174a results, with normal stresses of intensity $A\pi$ and shear stresses of intensity $-A$ acting on the surface. The normal stresses change sign at the origin O of the polar coordinates.

If we now move the point O into a new position O_1 and change the sign of the stress function, we obtain the surface loading shown in Fig. 174b. By superimposing loading b on loading a , we

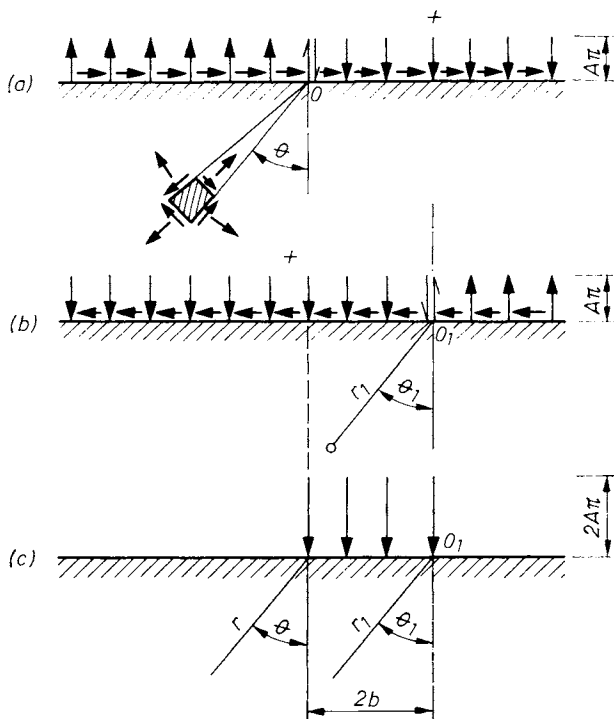


Fig. 174. Derived regular distribution of a line load: a — and b — surface stresses; c — transformation of loads from a and b

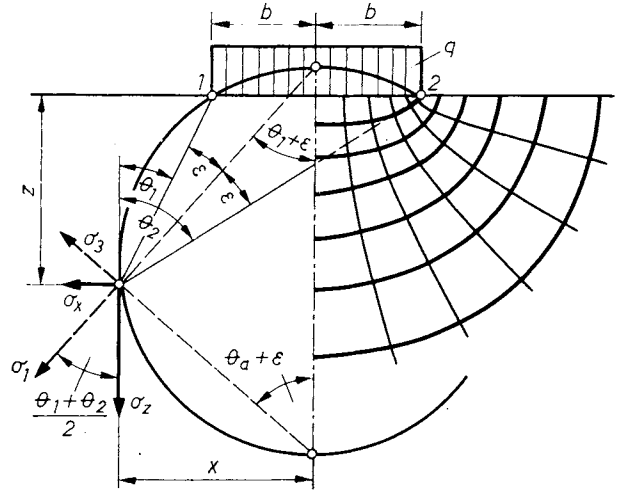


Fig. 175. Direction of principal stresses: isobar and trajectory stress lines

obtain a uniform finite load acting on a strip of width $2b$ on the surface. If the intensity per unit of area of this strip load be q , then $2A\pi = q$ and, hence, $A = q/2\pi$. The stress function for the combined case c can be written as

$$f = \frac{q}{2\pi} (r^2\theta - r_1^2\theta_1). \tag{198}$$

The components of stress, with the notation of Fig. 175 are determined by the following equations:

$$\left. \begin{aligned} \sigma_z &= \frac{q}{\pi} [\sin(\theta_2 - \theta_1) \cos(\theta_2 + \theta_1) + (\theta_2 - \theta_1)] = qF(\theta_1, \theta_2), \\ \sigma_x &= \frac{q}{\pi} [-\sin(\theta_2 - \theta_1) \cos(\theta_2 + \theta_1) + (\theta_2 - \theta_1)], \\ \tau_{xz} &= \frac{q}{\pi} [\sin^2 \theta_2 - \sin^2 \theta_1]. \end{aligned} \right\} \tag{199}$$

It is noteworthy that for a uniform strip load the principal stresses can be computed from the following expressions:

$$\left. \begin{aligned} \sigma_1 &= \frac{q}{\pi} (2\epsilon + \sin 2\epsilon), \\ \sigma_2 &= \frac{q}{\pi} (2\epsilon - \sin 2\epsilon). \end{aligned} \right\} \tag{200}$$

The meaning of angle ϵ is shown in Fig. 175. According to Eqs (200), the principal stresses depend solely on angle ϵ . It follows that the principal stress isobar for a given angle ϵ is a circle which passes through the edges 1 and 2 of the footing and for which the circumferential angle subtended by the chord $2b$ is equal to 2ϵ . The major principal stress makes an angle $(\theta_1 +$

Table 7. Influence factors of vertical stresses σ_z/q below a strip load of uniform distribution

z/b \ x/b	0	0.5	1.0	1.5	2.0
0	1.000	1.000	0.500	0.000	0.000
0.5	0.959	0.902	0.497	0.089	0.019
1.0	0.818	0.735	0.480	0.214	0.075
1.5	0.668	0.607	0.448	0.270	0.146
2.0	0.550	0.510	0.409	0.288	0.185
2.5	0.462	0.437	0.370	0.285	0.205
3.0	0.396	0.379	0.334	0.273	0.211
3.5	0.345	0.334	0.302	0.258	0.216
4.0	0.306	0.298	0.275	0.242	0.205
4.5	0.274	0.268	0.251	0.226	0.197
5.0	0.248	0.244	0.231	0.212	0.188
6.0	0.209	0.206	0.198	0.186	0.171
7.0	0.180	0.178	0.173	0.165	0.154
8.0	0.158	0.156	0.153	0.147	0.140
9.0	0.140	0.139	0.137	0.133	0.128
10.0	0.127	0.126	0.124	0.122	0.117

$+\theta_2)/2$ with the vertical. The principal stress trajectories are confocal ellipses and hyperboles as shown on the right-hand side of Fig. 175.

To facilitate computation of stresses, influence values for the vertical stresses due an infinite strip load are given in Table 7. For notation see Fig. 175.

BRINCH HANSEN (1955) approximates the calculation of stresses below the center line of a strip foundation, using the equations:

$$\sigma_1 = \sigma_z = \frac{p B}{B + z} \tag{201}$$

and

$$\sigma_3 = \sigma_h = \frac{p B^2}{(B + z)^2} \tag{202}$$

It should be noted that Eqs (199) can also be obtained by integration from the expression of stresses for a vertical line load (Eqs (196)). In the same way, formulas can be derived for any other type of distribution of strip load: linearly increasing, triangular, trapezoidal, etc. Those cases for which solutions are available in the literature are compiled in Fig. 176. The corresponding equations for the computation of stresses are given in the following. All stress components are referred to rectangular coordinates x, z .

Case 1

Uniform loading over one half of the surface of a semi-infinite mass

Principal stresses:

$$\sigma_{1,2} = \frac{P}{\pi} (\beta \pm \sin \beta)$$

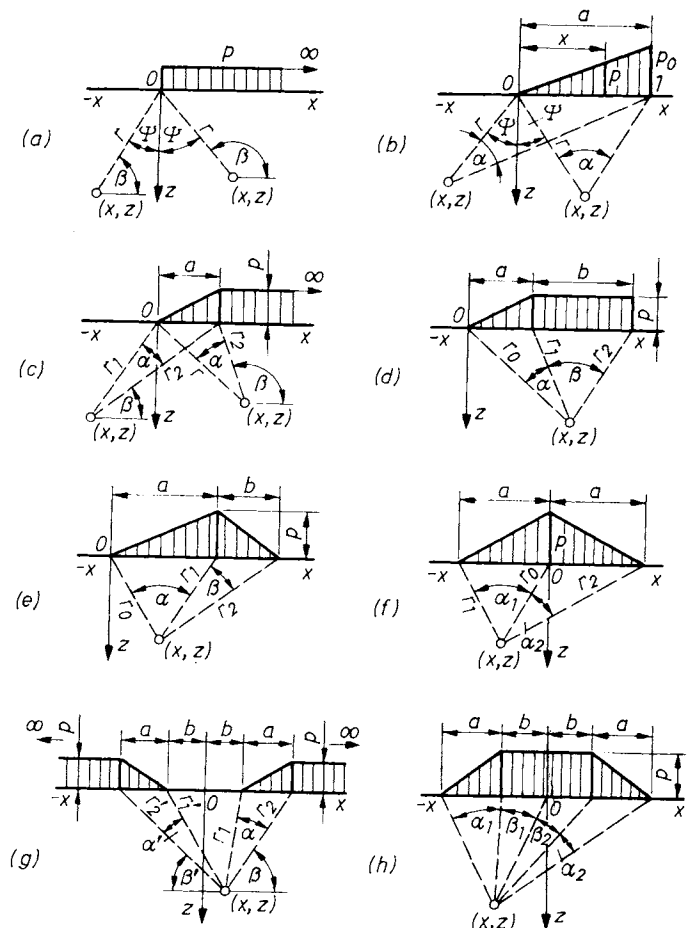


Fig. 176. Different formations of strip loads

Stress components:

$$\sigma_x = \frac{P}{\pi} \left(\beta - \frac{xz}{R^2} \right), \quad \sigma_z = \frac{P}{\pi} \left(\beta + \frac{xz}{R^2} \right),$$

$$\tau_{xz} = -\frac{P}{\pi} \sin^2 \beta.$$

Case 2

Triangularly distributed finite load

Vertical stress:

$$\sigma_z = \frac{P}{a\pi} \left\{ x\alpha \frac{az}{(x-a)^2 + z^2} (x-a) \right\}.$$

Case 3

Triangular load combined with semi-infinite uniform loading

Principal stresses:

$$\sigma_{1,2} = \frac{P}{a\pi} \left[\left(a\beta + x\alpha + z \ln \frac{R_2}{R_1} \right) \pm \right. \\ \left. \pm z \sqrt{\ln^2 \frac{R_2}{R_1} + a^2} \right].$$

Stress components:

$$\sigma_x = \frac{P}{a\pi} \left[a\beta + x\alpha + 2z \ln \frac{R_2}{R_1} \right],$$

$$\sigma_z = \frac{P}{a\pi} [a\beta + x\alpha],$$

$$\tau_{xz} = -\frac{P}{a\pi} z\alpha.$$

Case 4

Triangular load combined with finite uniform load

Principal stresses:

$$\sigma_{1,2} = \frac{P}{a\pi} \left[\left[a\beta + x\alpha + z \ln \frac{R_1}{R_2} \pm \right. \right. \\ \left. \left. \pm z \sqrt{\left\{ \frac{a}{R_2^2} (x-b) + \ln \frac{R_1}{R_2} \right\}^2 + \left(a - \frac{az}{R_2^2} \right)^2} \right] \right].$$

Stress components:

$$\sigma_x = \frac{P}{a\pi} \left[a\beta + x\alpha + \frac{az}{R_2^2} (x-b) + 2z \ln \frac{R_1}{R_2} \right],$$

$$\sigma_z = \frac{P}{a\pi} \left[a\beta + x\alpha - \frac{az}{R_2^2} (x-b) \right],$$

$$\tau_{xz} = \frac{P}{a\pi} \left[z\alpha - a \frac{z^2}{R_2^2} \right].$$

Case 5

Asymmetrically distributed triangular load

Principal stresses:

$$\sigma_{1,2} = \frac{P}{\pi} \left[\frac{x}{a} \alpha + \frac{a+b-x}{b} \beta + \frac{z}{a} \ln \frac{R_1}{R_2} + \right. \\ \left. + \frac{z}{b} \ln \frac{R_1}{R_2} \right] \pm \\ \pm \frac{Pz}{\pi} \sqrt{\left(\frac{1}{a} \ln \frac{R_1}{R_0} + \frac{1}{b} \ln \frac{R_1}{R_2} \right)^2 + \left(\frac{\alpha}{a} - \frac{\beta}{b} \right)^2}.$$

Stress components:

$$\sigma_x = \frac{P}{\pi} \left[\frac{x}{a} \alpha + \frac{a+b-x}{b} \beta + \frac{2z}{a} \ln \frac{R_1}{R_0} + \right. \\ \left. + \frac{2z}{b} \ln \frac{R_1}{R_2} \right],$$

$$\sigma_z = \frac{P}{\pi} \left[\frac{x}{a} \alpha + \frac{a+b-x}{b} \beta \right],$$

$$\tau_{xz} = \frac{Pz}{\pi} \left[\frac{\alpha}{a} - \frac{\beta}{b} \right].$$

Case 6

Symmetrically distributed triangular load

Principal stresses:

$$\sigma_{1,2} = \left[\frac{P}{a\pi} a(\alpha_1 + \alpha_2) + x(\alpha_1 - \alpha_2) - z \ln \frac{R_1 R_2}{R_0^2} \right] \pm \\ \pm \frac{Pz}{a\pi} \sqrt{\ln^2 \frac{R_1 R_2}{R_0^2} + (\alpha_1 - \alpha_2)^2}.$$

Stress components:

$$\sigma_x = \frac{P}{a\pi} \left[a(\alpha_1 + \alpha_2) + x(\alpha_1 - \alpha_2) - 2z \ln \frac{R_1 R_2}{R_0^2} \right],$$

$$\sigma_z = \frac{P}{a\pi} [a(\alpha_1 + \alpha_2) + x(\alpha_1 - \alpha_2)],$$

$$\tau_{xz} = \frac{Pz}{a\pi} [\alpha_1 - \alpha_2].$$

Case 7

Symmetrical combination of triangular finite loads and semi-infinite uniform loads

Principal stresses:

$$\sigma_{1,2} = \frac{P}{a\pi} \left[a(\beta + \beta') - b(\alpha + \alpha') + x(\alpha - \alpha') + \right. \\ \left. + z \ln \frac{R_2 R_2'}{R_1 R_1'} \right] \pm \frac{Pz}{a\pi} \sqrt{\ln^2 \frac{R_2 R_2'}{R_1 R_1'} + (\alpha - \alpha')^2}.$$

Stress components:

$$\sigma_x = \frac{P}{a\pi} \left[a(\beta + \beta') + b(\alpha + \alpha') + x(\alpha - \alpha') + 2z \ln \frac{R_2}{R_1} \frac{R'_2}{R'_1} \right]$$

$$\sigma_z = \frac{P}{a\pi} [a(\beta + \beta') - b(\alpha + \alpha') + x(\alpha - \alpha')],$$

$$\tau_{xz} = -\frac{Pz}{a\pi} (\alpha - \alpha').$$

Case 8

Symmetrical trapezoidal load (embankment)

Vertical stress:

$$\sigma_z = \frac{P}{a\pi} [a(\beta_1 + \beta_2) + (a + b)(\alpha_1 + \alpha_2) + x(\alpha_2 - \alpha_1)].$$

2.2.3.3 Some remarks on the computation of stresses due to line and strip loads

1. In the literature one often encounters the view that the equations of stresses for an infinite line load, (Eqs (196)), are strictly valid only when Poisson's number is $m = 2$ (OHDE, 1939; FRÖHLICH, 1934). For other values of m , FRÖHLICH (1934) developed an entirely independent stress distribution theory. He started from the principle that the propagation of stresses is radial, but the intensity of the radial stress is proportional to the $(\nu - 1)$ th negative power of the radius vector drawn from the point of application of the load and not to its (-1) th power as stated in the theory of elasticity. However, in the light of the fact that in the theory of elasticity the equations of stresses are derived from a stress function satisfying the equation of compatibility, $\nabla \nabla F = 0$ — which implies that the internal forces are in equilibrium while both geometrical compatibility and boundary conditions are also satisfied — there is no reason to suggest why the validity of the solution obtained should be confined to certain m values only. The simple rule of the distribution of stresses, being radial, is found to be valid up to any m value. Also, by deducing expressions for the strains, we can easily verify the correctness of the solution based on the theory of elasticity (KÉZDI, 1947). The usual argument raised against the general validity of the elastic solution, namely that the equations of stress components do not contain the elastic constants, E and m , of the material, does not hold either, since so long as the load acts on the surface of a semi-infinite mass and the boundary conditions refer only to stresses, the material constants should not appear in the

equations. FRÖHLICH developed his equations from an analogy with an isotropic semi-infinite mass, and he determined the unknown coefficients from equilibrium conditions. In this way, he obtained a set of possible stress distributions which differ by a parameter termed by FRÖHLICH the stress concentration factor, ν . He did not, however, go into analyzing what the implications are of the arbitrary choice of a factor ν concerning the elastic properties of the material of the semi-infinite mass. It can be shown that each ν value corresponds to a unique function that describes the variation of Young's modulus of the soil with the depth from the surface, a function which, however, may not always be realistic. It is only when $\nu = 0$ that Fröhlich's generalized theory furnishes a practicable solution. This assumption applies to a semi-infinite medium whose modulus of elasticity increases linearly with depth, which is often the case with real soils.

2. An exact theoretical solution can only be developed for the infinite line load (Eqs (196)). But if, making use of the principle of superposition, we extend the solution from line load to a strip load by integration, the result contains a serious error, notably that there is a discontinuity in the distribution of stresses at the edges of the strip.

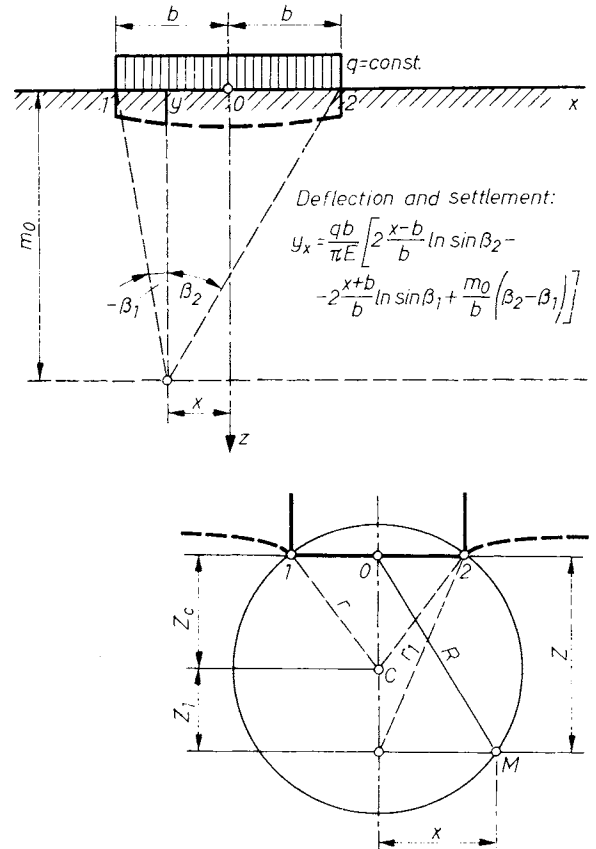


Fig. 177. a — Settlement analysis in the case of an assumed depth limit; b — rigid footing on the surface of the half-space

For the stress σ_z just beneath the surface, as computed from Eqs (199), different values will be obtained depending on whether the points 1 and 2 are approached from within or from outside the loaded area. The result is q in the first case and $q/2$ in the second. The explanation for this discrepancy lies in the nature of partial differential equations. Although this error has no practical significance, it still points out the imperfection of stress distribution theory.

3. In the analysis of a strip load we assumed a uniform distribution of contact pressures on the base of the footing. If we now determine the settlement y of the surface at any vertical by integrating elastic vertical strains in that section, taking infinity as the upper limit of integration, we obtain the embarrassing result that the settlement is infinitely large. For example, in the centre line of the strip load (Fig. 177a):

$$\begin{aligned}
 y &= \frac{1}{E} \int_0^\infty \sigma_z dz = \frac{q}{\pi E} \int_0^\infty (\sin 2\beta + 2\beta) dz = \\
 &= \frac{2q}{\pi E} \int_0^\infty \left(\frac{bz}{b^2 + z^2} + \tan^{-1} \frac{b}{z} \right) dz = \quad (203) \\
 &= \frac{2qb}{\pi E} [\beta \cot \beta - 2 \log_e \sin \beta] \Big|_{\beta=\pi/2}^{\beta=0} \longrightarrow \infty.
 \end{aligned}$$

The result is obviously absurd. But if we assume, to be realistic, that compression of the soil is confined to a certain limiting depth or else we compute the differential settlements of the surface, which unlike total settlements are found to be finite quantities, we obtain a characteristic bowl-shaped depression of the surface. Assuming some value m_0 for the limiting depth, we obtain the

following equation, with the notation shown in Fig. 177a, for the settlement:

$$\begin{aligned}
 y &= \frac{qb}{\pi E} \left[2 \frac{x-b}{b} \sin \beta_2 - \right. \\
 &\quad \left. - 2 \frac{x+b}{b} \ln \sin \beta_1 + \frac{m_0}{b} (\beta_2 - \beta_1) \right]. \quad (204)
 \end{aligned}$$

The settlement profile computed by Eq. (204) is also shown in Fig. 177. It follows from this result that the assumption of a uniform strip load is tenable only if the surface, or rather the structure transmitting the load to the soil, is sufficiently flexible. Otherwise, if the footing is rigid, the distribution of contact pressures must have an entirely different character. An advanced theory of elasticity offers a rigorous solution for the computation of stresses in a semi-infinite mass in the case where the footing is perfectly rigid (HRUBAN, 1944). The equations of stress components, with the notation shown in Fig. 177b, are

$$\left. \begin{aligned}
 \sigma_z &= \frac{q}{4\pi r} \left[3 - \frac{(z-z_1)(r-2z_1)}{r^2} \right] \sqrt{\frac{r+z_1}{z}}, \\
 \sigma_x &= \frac{q}{4\pi r} \left[1 + \frac{(z-z_1)(r-2z_1)}{r^2} \right] \sqrt{\frac{r+z_1}{z}}, \\
 \tau_{xz} &= \frac{qx}{4\pi r^3} \frac{r^2 + (z-z_1)(r+2z_1)}{\sqrt{z(r+z_1)}}.
 \end{aligned} \right\} (205)$$

The character of stress distributions obtainable from Eqs (205) is visualized in Fig. 178. Like the solution derived for a flexible footing (Eqs (199)), this solution also satisfies the equation of both equilibrium and compatibility, without containing the absurdities inherent in the former. Its use should, therefore, be preferred in the computation of settlements under rigid footings.

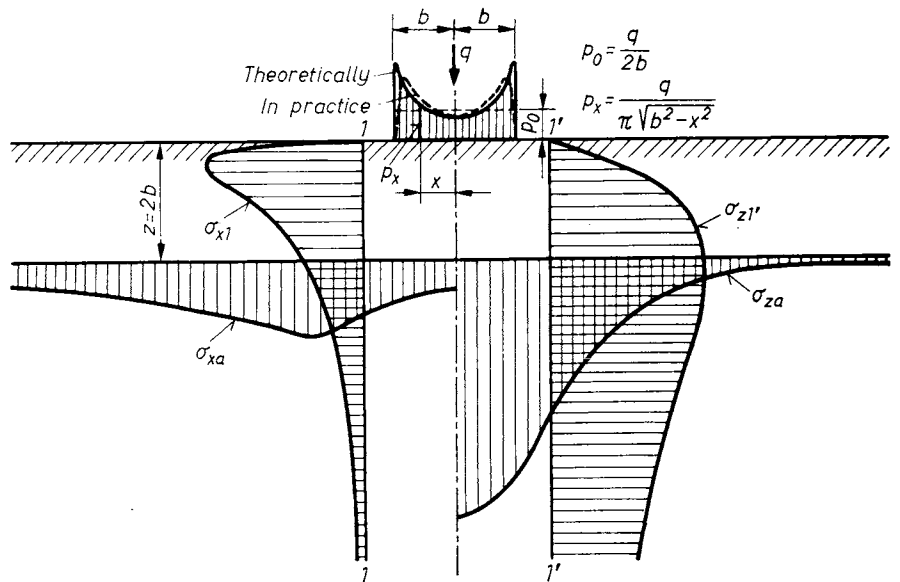


Fig. 178. Stresses in the half-space and distribution of contact pressures below a stiff footing

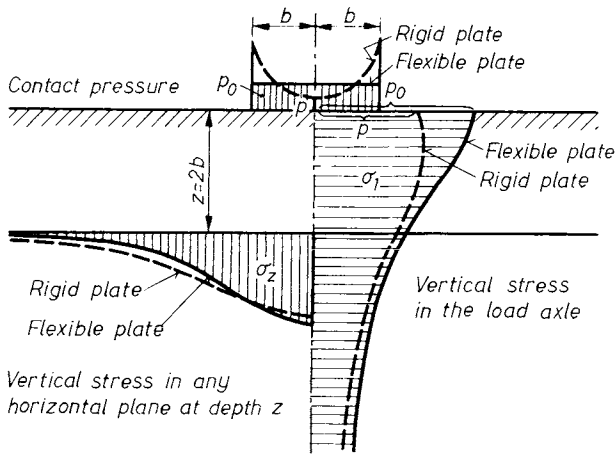


Fig. 179. Comparison of vertical stress distributions in the case of flexible and rigid slabs

Equations (205) also lead, however, to discontinuity in that the magnitude of the contact pressure at the edges of the rigid footing tends to infinity (Fig. 178). This is obviously in conflict with reality, since plastic deformations that occur in the vicinity of the edges prevent contact pressures from exceeding a critical finite value. A realistic assumption for the distribution of contact pressures is that shown by the dashed line in Fig. 178. The principal stresses for a rigid footing are

$$\sigma_{1,2} = \frac{q}{2\pi r} \left(\sqrt{\frac{r+z_1}{z}} \pm \sqrt{\frac{R}{2rz}} \right). \quad (206)$$

The stress components in the centre line of the loaded area are:

$$\left. \begin{aligned} \sigma_z &= \frac{q}{\pi} \frac{r_1^2 + z^2}{r_1^3}, \\ \sigma_x &= \frac{q}{\pi} \frac{b^3}{r_1^3}, \\ \tau_{xz} &= 0, \end{aligned} \right\} \quad (207)$$

where

$$r_1^2 = b^2 + z^2.$$

For comparison, Fig. 179 shows the distribution of contact pressures and of σ_z stresses for both flexible and rigid footings. At the centre line of the loading, the rigid footing produces smaller stresses (SCHLEICHER, 1926).

2.2.3.4 The effect of shear stresses in the contact plane on the stress pattern

The shear stresses invariably arising in the contact plane between footings with a rough base and the subsoil will to a certain extent, prevent the latter from being displaced laterally from under the footing. These shear stresses are responsible for the fact that a soil wedge will retain its

elastic state during the process of failure. They are further responsible for the concentration of stresses in the center line of the footing, provided that the load is an axial one. In other words, the stresses about the center line are higher than the value which would result from uniformly distributed vertical bearing pressures. This circumstance has been verified by stress measurements, inducing FRÖHLICH (1934) to modify the Boussinesq formulae by a concentration factor, in order to obtain stress values corresponding to actual conditions. Under axial loads, these shear stresses are directed towards the center line. Concerning their distribution, a linear variation may be assumed from zero in the axis of symmetry towards the edges of the footing. There, the tendency for the soil to yield laterally and thus the magnitude of displacements and, in turn, the shear stresses mobilized, are higher. The resulting stresses acting in the contact plane are illustrated in Fig. 180. The vertical stress due to shear can be written in the form

$$\sigma_z = \frac{2p}{\pi z} \sin \epsilon \cos^3 \epsilon.$$

The surface shear stress at the distance x (see Fig. 181) is

$$s_x = c(x_i + b - x) \quad [x_1 \leq x \leq x_1 + 2b]$$

and the elementary stress

$$d\sigma = \frac{2dS_x}{\pi z} \sin \epsilon \cos^3 \epsilon,$$

$$dS_x = s_x dx,$$

$$dx = \frac{z}{\cos^2 \epsilon} d\epsilon,$$

so that

$$\sigma_z = -\frac{c}{\pi} \cdot [(x_1 + b) \sin(\epsilon_2 + \epsilon_1) \sin(\epsilon_2 - \epsilon_1) + z(\sin \epsilon_2 \cos \epsilon_2 - \sin \epsilon_1 \cos \epsilon_1) - z(\epsilon_2 - \epsilon_1)]. \quad (208)$$

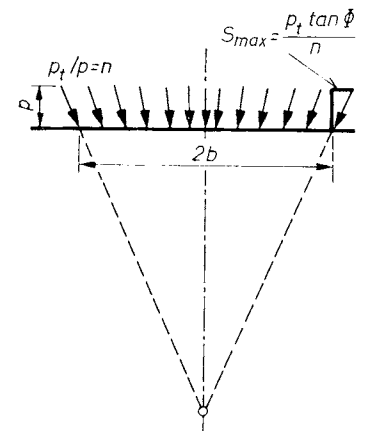


Fig. 180. Contact pressure below a rough footing

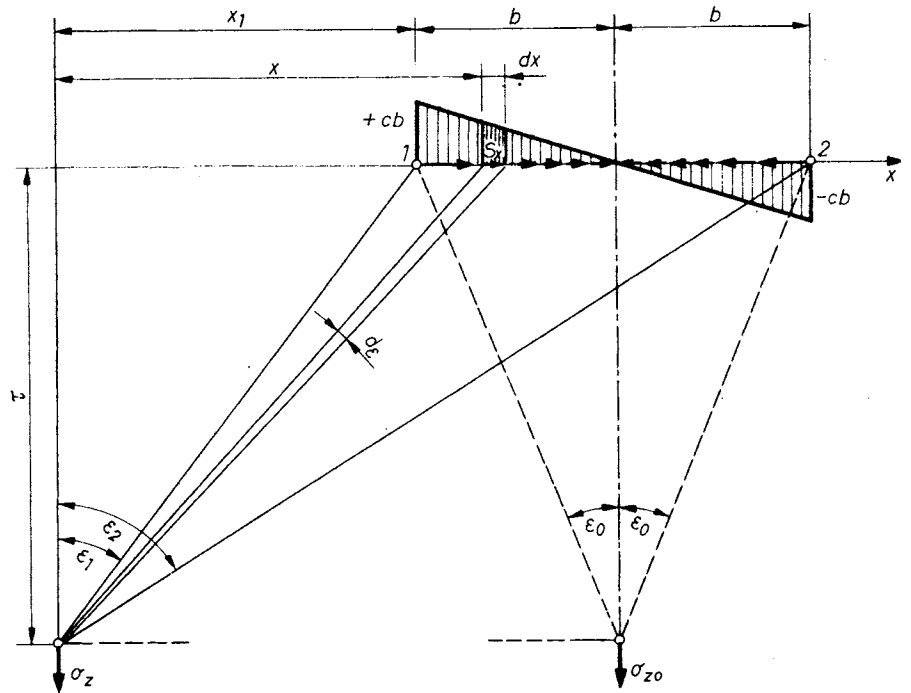


Fig. 181. Vertical stresses generated by tangential stresses at the bottom of the footing

The vertical stress in the center line of the footing is

$$\sigma_{z0} = \frac{2bc}{\pi} (\epsilon_0 \cot \epsilon_0 - \cos^2 \epsilon_0). \quad (209)$$

The potentially highest value of these shear stresses at the edge of the footing remains to be determined. As the vertical load p is increased up to the limit of plastic deformation, s_{max} may attain the value $p \tan \varphi$ (where φ is the angle of friction between the soil and the footing). Though this value is well below the plastic yielding value — and this has been mentioned as the criterion for the application of the theory of elastic-

ity — it is necessarily smaller than the $p \tan \Phi$ value, but no positive statement can be made concerning its magnitude. A fair approximation of actual conditions is likely to result, however, from assuming the same margin of safety relative to the sliding value $p \tan \varphi$ as that available against failure in the magnitude of the vertical load p .

The influence of the shear stress on the stress distribution is substantially greater in the case of footings subjected to overturning, and occasionally even to horizontal forces. Concerning the distribution of the shear stress along the contact plane, the cases shown in Fig. 182 may be assumed:

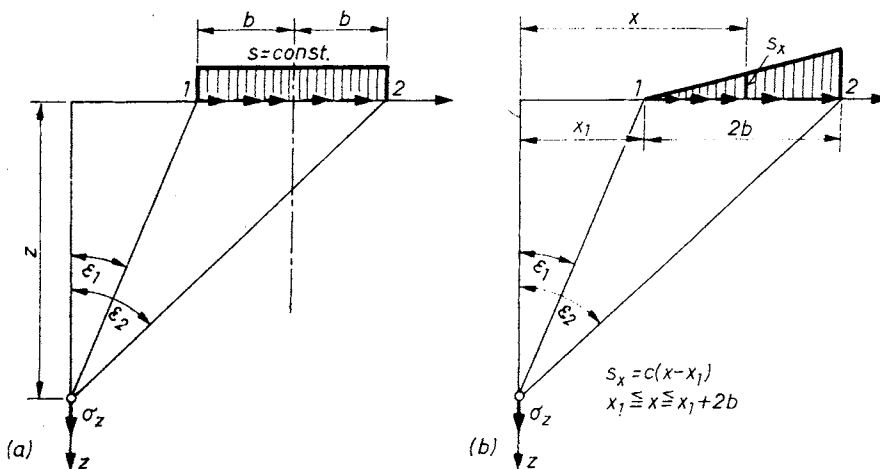


Fig. 182. Distribution of tangential stresses at the bottom of the footing:
a — constant; b — linearly increasing

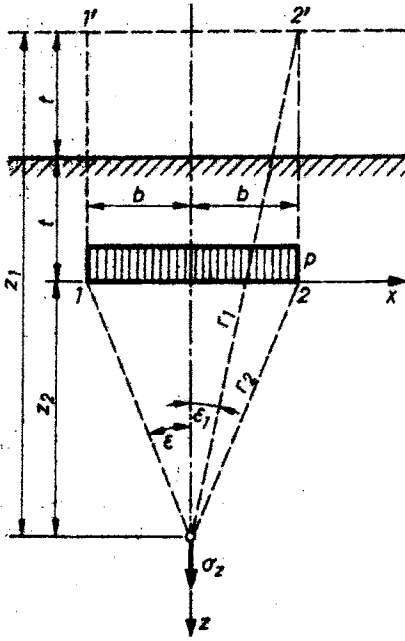


Fig. 184. Strip load acting at some depth

The existence of tensile stresses is thus theoretically conceivable in any kind of soil as long as the values thereof remain smaller than the magnitude of compressive stresses due to dead weight.

In the application of Eqs (213), (214) and in particular of Eq. (215), additional difficulties are encountered on account of the fact that in constructing the load-transmitting footing the foundation pit is usually excavated with sloping sides, with a consequent reduction in loading. Moreover, the backfill over the completed footing is in a disturbed condition; it does not interact with the original soil as assumed for the unloaded half space and it usually has a lower bulk density than the surrounding soil (Fig. 186). An approximate solution

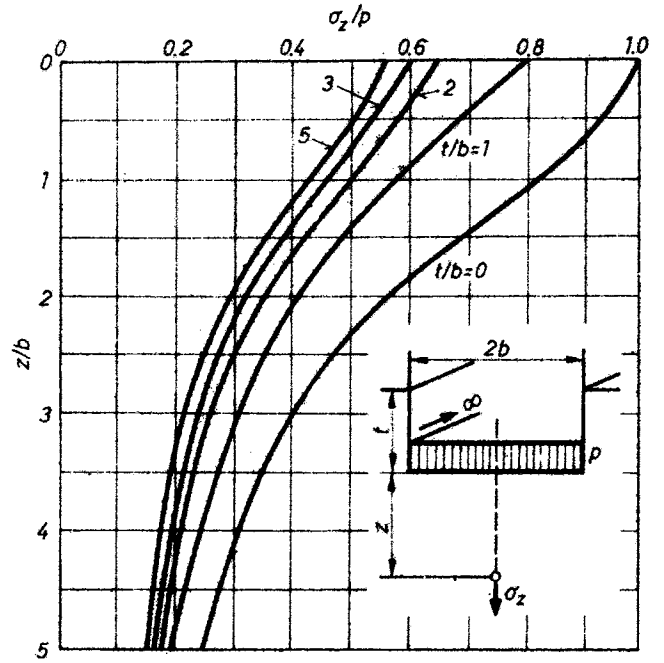


Fig. 185. Vertical stresses below a strip load acting at some depth

for the case of line loads has been suggested by JELINEK (1951).

The three-dimensional case is treated briefly in Section 2.2.4.2.

2.2.4 Three-dimensional stress distribution

2.2.4.1 Concentrated load

The general three-dimensional equations of the theory of elasticity are too complicated and cumbersome to handle to be used in normal practice. However, in most problems of practical interest the stress distribution is symmetrical

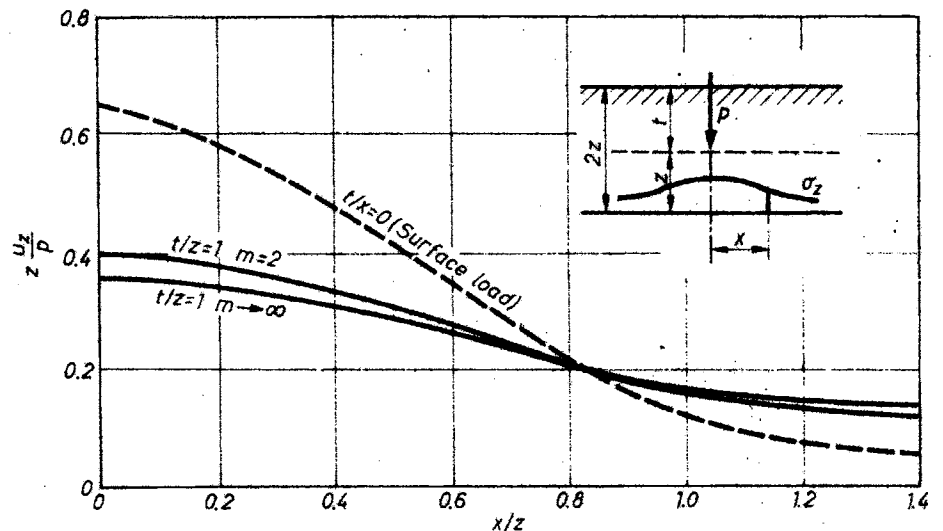


Fig. 186. Vertical stresses below a line load at some depth

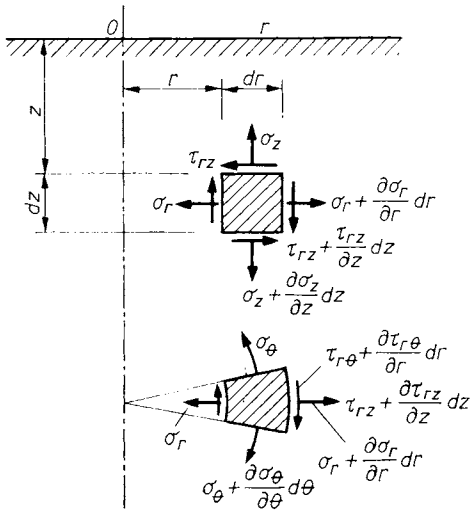


Fig. 187. Cylindrical coordinate system for a singular force: a — stresses; b — deformations

about an axis and the formulae applying to such cases are substantially simplified. Such problems are expediently written in a system of cylindrical coordinates, as shown in Fig. 187.

In the axial-symmetrical case, the stresses are independent of the angle θ and thus their differentials with respect to θ are zero as also are $\tau_{r\theta}$ and $\tau_{\theta z}$, because of symmetry.

The equation of equilibrium are thus (Fig. 188)

$$\left. \begin{aligned} \frac{\partial \sigma_r}{\partial r} + \frac{\partial \tau_{rz}}{\partial z} + \frac{\sigma_r - \sigma_\theta}{r} &= 0, \\ \frac{\partial \tau_{zr}}{\partial r} + \frac{\partial \sigma_z}{\partial z} + \frac{\tau_{zr}}{r} &= 0. \end{aligned} \right\}$$

The solution is again obtained by introducing a stress function. The foregoing equations can be shown to be satisfied if the stresses are computed by substitution from the stress function F as follows:

$$\left. \begin{aligned} \sigma_r &= \frac{\partial}{\partial z} \left(\frac{1}{m} \nabla^2 F - \frac{\partial^2 F}{\partial r^2} \right), \\ \sigma_\theta &= \frac{\partial}{\partial z} \left(\frac{1}{m} \nabla^2 F - \frac{1}{r} \frac{\partial F}{\partial r} \right), \\ \sigma_z &= \frac{\partial}{\partial z} \left(\frac{2m-1}{m} \nabla^2 F - \frac{\partial^2 F}{\partial z^2} \right), \\ \tau_{rz} &= \frac{\partial}{\partial r} \left(\frac{m-1}{m} \nabla^2 F - \frac{\partial^2 F}{\partial z^2} \right). \end{aligned} \right\} \quad (216)$$

In the foregoing expressions, ∇^2 is the operator

$$\nabla^2 = \frac{\partial^2}{\partial r^2} + \frac{1}{r} \frac{\partial}{\partial r} + \frac{1}{r^2} \frac{\partial^2}{\partial \theta^2} + \frac{\partial^2}{\partial z^2}.$$

It will be observed that in the axial-symmetrical case the third term in the above expression vanishes.

For the displacements to develop in conformity with the geometrical conditions, the strain components are required to be interrelated. This requirement is represented here again by a compatibility equation, which, converted to stresses according to Hooke's law and in combination with Eqs (216), gives the differential equation for the stress function F :

$$\left(\frac{\partial^2}{\partial r^2} + \frac{1}{r} \frac{\partial}{\partial r} + \frac{\partial^2}{\partial z^2} \right) \left(\frac{\partial^2 F}{\partial r^2} + \frac{1}{r} \frac{\partial F}{\partial r} + \frac{\partial^2 F}{\partial z^2} \right) = \nabla^2 \nabla^2 F = 0 \quad (217)$$

from which the stress function will again be seen to be biharmonic.

The fundamental problem consists, as shown in Fig. 188, of finding the stresses induced in the infinite half-space by a concentrated force acting on its surface. The formulae of stresses in the half space due to pressures distributed over a finite area are then derived therefrom by applying the principle of superposition. The problem was solved by BOUSSINESQ (1885). According to BEREZANTSEV (1952) the stress function

$$F = C_1 z \ln r + C_2 R + C_3 z \ln \frac{R-z}{R+z} \quad (218)$$

$$(R = \sqrt{r^2 + z^2})$$

is applicable, yielding the stress components

$$\left. \begin{aligned} \sigma_z &= \frac{3P}{2\pi z^2} \cos^5 \psi = \frac{3P}{2\pi r^2}, \quad \cos^3 \psi = \frac{3P}{2\pi} \frac{z^3}{r^5}, \\ \sigma_r &= \frac{P}{2\pi z^2} \left[3 \cos^3 \psi \sin^2 \psi - \frac{m-2}{m} \frac{\cos^2 \psi}{1 + \cos \psi} \right], \\ \sigma_\theta &= -\frac{m-2}{m} \frac{P}{2\pi z^2} \left[\cos^3 \psi - \frac{\cos^2 \psi}{1 + \cos \psi} \right], \\ \tau_{rz} &= \frac{3P}{2\pi z^2} \cos^4 \psi \sin \psi. \end{aligned} \right\} \quad (219)$$

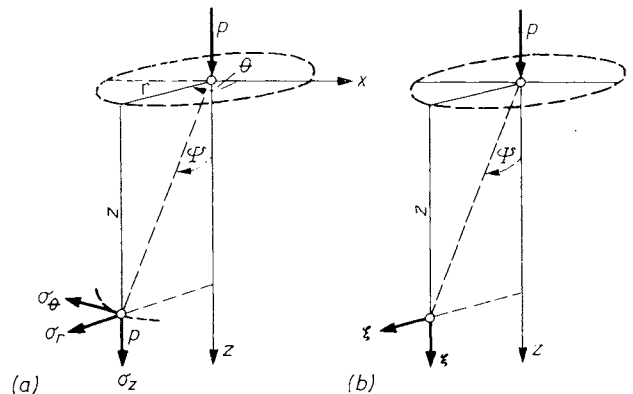


Fig. 188. Equilibrium conditions for a volumetric element in axle-symmetric situation

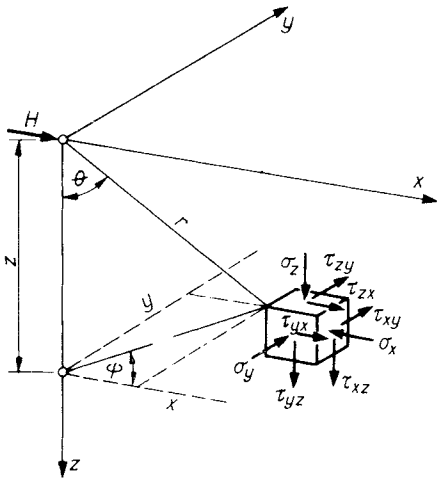


Fig. 189. Horizontal singular force (*H*) on the surface

In the case of comparable stress-distribution problems — e.g., concentrated force and line load on the surface — the corresponding *f* and *F* stress functions of the plane and axial-symmetrical states of stress have been demonstrated by WEBER (1925) to be interrelated and obtainable from each other by differentiation, or integration. It should be noted in this context that the stress distribution formulae of line load can also be found by integration from the expression of the Bousinesq load, as determined by the senior author (1946), in contrast to the findings of OHDE (1939).

A similar solution has been developed for the case of a horizontal, concentrated force acting at

a point on the surface (Fig. 189). The vertical stress is

$$\sigma_z = \frac{2H}{2\pi z^2} \cos \psi \sin \psi \cos^4 \psi. \quad (220)$$

An example for the case of a vertical load is presented in Fig. 190, in which the curves of equal stress have also been plotted. In the majority of practical problems it is the vertical stresses that are of interest; for the rapid estimation of these the influence coefficient

$$N_B = \frac{3}{2\pi \left[1 + \left(\frac{r}{z} \right)^2 \right]^{5/2}} \quad (221)$$

involved in the expression

$$\sigma_z = \frac{3P}{2\pi z^2} \cos^5 \psi = \frac{P}{z^2} N_B \quad (222)$$

is found from Table 8.

In three-dimensional-states of stress, the effect of embedment is even greater than in their plane counterparts, in that the contact planes of piles, shafts, sunk caissons, etc., are at depths corresponding to several times the diameter of the load-bearing element (pile, shaft, etc.) so that the use of formulae applying to surface loads is completely unwarranted in such cases. Using notations in Fig. 191, the senior author (1952) has developed formulae giving the stress components induced by embedded loads. He has

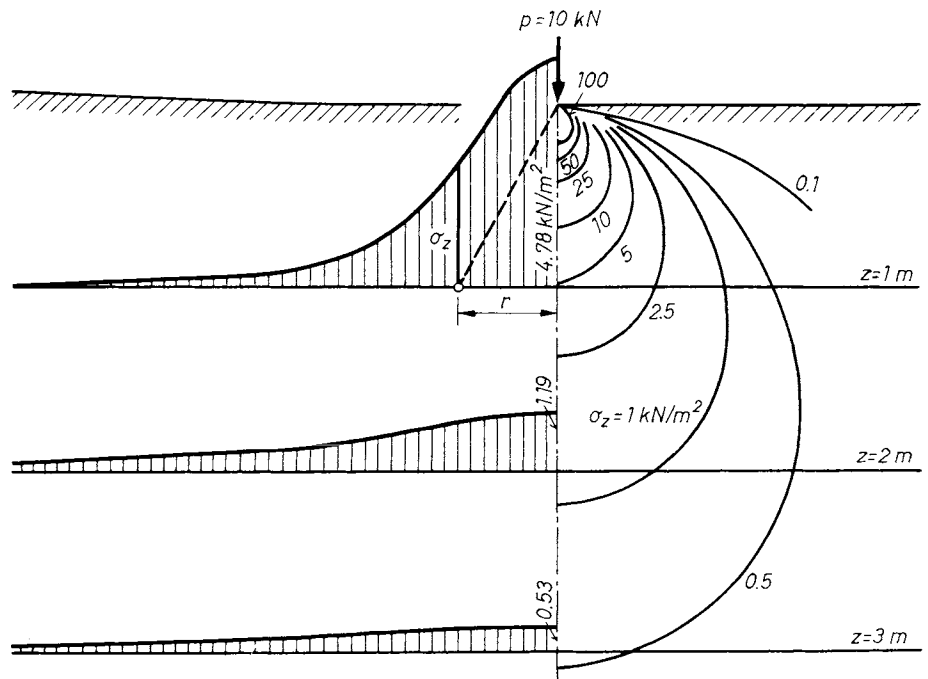


Fig. 190. Stresses in the half-space due to a vertical load

Table 8. Influence factors of stresses due to a vertical singular force, after BOUSSINESQ (1885)

r/z	N _B	r/z	N _B	r/z	N _B	r/z	N _B	r/z	N _B	r/z	N _B
0.00	0.4775	0.50	0.2733	1.00	0.0844	1.50	0.0251	2.00	0.0085	2.50	0.0034
0.02	0.4770	0.52	0.2625	1.02	0.0803	1.52	0.0240	2.02	0.0082	2.52	0.0033
0.04	0.4756	0.54	0.2518	1.04	0.0764	1.54	0.0229	2.04	0.0079	2.54	0.0032
0.06	0.4732	0.56	0.2414	1.06	0.0727	1.56	0.0219	2.06	0.0076	2.56	0.0031
0.08	0.4699	0.58	0.2313	1.08	0.0691	1.58	0.0209	2.08	0.0073	2.58	0.0030
0.10	0.4657	0.60	0.2214	1.10	0.0658	1.60	0.0200	2.10	0.0070	2.60	0.0029
0.12	0.4507	0.62	0.2117	1.12	0.0626	1.62	0.0191	2.12	0.0068	2.62	0.0028
0.14	0.4548	0.64	0.2024	1.14	0.0595	1.64	0.0183	2.14	0.0065	2.64	0.0027
0.16	0.4482	0.66	0.1932	1.16	0.0567	1.66	0.0175	2.16	0.0063	2.66	0.0026
0.18	0.4409	0.68	0.1846	1.18	0.0539	1.68	0.0167	2.18	0.0060	2.68	0.0025
0.20	0.4329	0.70	0.1762	1.20	0.0513	1.70	0.0160	2.20	0.0058	2.70	0.0024
0.22	0.4242	0.72	0.1681	1.22	0.0489	1.72	0.0153	2.22	0.0056	2.72	0.0023
0.24	0.4151	0.74	0.1603	1.24	0.0466	1.74	0.0147	2.24	0.0054	2.74	0.0023
0.26	0.4054	0.76	0.1527	1.26	0.0443	1.76	0.0141	2.26	0.0052	2.76	0.0022
0.28	0.3954	0.78	0.1455	1.28	0.0422	1.78	0.0135	2.28	0.0050	2.78	0.0021
0.30	0.3849	0.80	0.1386	1.30	0.0402	1.80	0.0129	2.30	0.0048	2.80	0.0021
0.32	0.3742	0.82	0.1320	1.32	0.0384	1.82	0.0124	2.32	0.0047	2.84	0.0019
0.34	0.3632	0.84	0.1257	1.34	0.0365	1.84	0.0119	2.34	0.0045	2.91	0.0017
0.36	0.3521	0.86	0.1196	1.36	0.0348	1.86	0.0114	2.36	0.0043	2.99	0.0015
0.38	0.3408	0.88	0.1138	1.38	0.0332	1.88	0.0109	2.38	0.0042	3.08	0.0013
0.40	0.3294	0.90	0.1083	1.40	0.0317	1.90	0.0105	2.40	0.0040	3.19	0.0011
0.42	0.3181	0.92	0.1031	1.42	0.0302	1.92	0.0101	2.42	0.0039	3.31	0.0009
0.44	0.3068	0.94	0.0981	1.44	0.0288	1.94	0.0097	2.44	0.0038	3.50	0.0007
0.46	0.3055	0.96	0.0933	1.46	0.0275	1.96	0.0093	2.46	0.0036	3.75	0.0005
0.48	0.2843	0.98	0.0887	1.48	0.0263	1.98	0.0089	2.48	0.0035	4.13	0.0003

adopted the stress function

$$\left. \begin{aligned} \zeta &= \frac{P}{2\pi r} \frac{m+1}{mE} \left[\frac{2(m-1)}{m} + \cos^2 \psi \right] \sin \psi, \\ \xi &= \frac{P}{2\pi r} \frac{m+1}{mE} \left[\frac{m-2}{m} + \cos \psi + \right. \\ &\quad \left. + \cos^2 \psi \right] \sin \psi \tan \frac{\psi}{2}, \end{aligned} \right\}$$

using which the vertical stress of greatest practical interest was obtained in the form

$$\sigma_z = \frac{m}{m-1} \frac{3P}{4\pi} \left[\frac{m-2}{6m} z_1 \left(\frac{1}{r_1^3} - \frac{1}{r_2^3} \right) + \frac{z_1^3}{2r_1^5} + \left\{ \frac{3m-4}{2m} z_2 \frac{m-2}{m} t \right\} \frac{z_2^2}{r_2^5} - tz_2(z_2-t) \frac{3r^2-2z_2^2}{r_2^7} \right]. \quad (223)$$

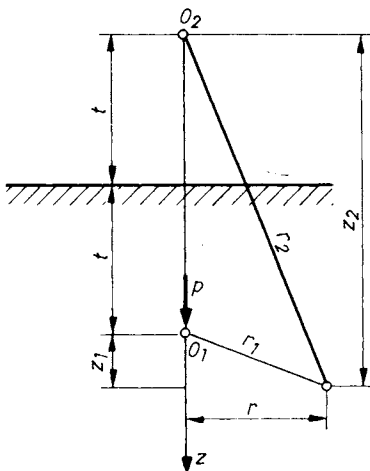


Fig. 191. Singular force inside the half-space

The first term of the expression within the brackets yields the stresses induced by the forces *P*, of equal magnitude, acting at the points *O*₁ and *O*₂ in the infinite space. Since the quantity *r*₂ figures in the denominator of this term at the third power and in the denominators of the other terms at the fifth and seventh powers, the effect of these terms is considered negligible in all cases where *z*₁ > *t*. Thus for instance, the stresses induced by the force *P*, acting at depth *t* below the surface in a clay layer situated at greater depth, can be computed with the foregoing simplification, as if the infinite space were acted upon by two concentrated forces of the same direction and magnitude at the points *O*₁ and *O*₂.

For estimating the stresses induced in the infinite half-space by embedded, concentrated vertical and horizontal forces, detailed tables have been compiled by TAKEO MOGAMI (1957), who has also published the formulae for all Cartesian stress components.

2.2.4.2 Surface load distributed over a finite area

The stresses at a particular point in the half space, due to pressure transmitted to the soil at the surface of the infinite half-space, are obtained by integrating the Boussinesq formulae. In the case shown in Fig. 192 the pressure distributed according to the function *p*_{*x,y*} = *f*(*x,y*) acts on the area *F*. The elementary force on the area element *dF* is *f*(*x,y*) *dF* and the resulting stress at the point *P* becomes

$$\sigma_z = \int_F d\sigma_z = \frac{3z^3}{2\pi} \int_F \frac{f(x,y)}{R^5} dF. \quad (224)$$

The expression in Eq. (224) is rather difficult to integrate, even in relatively simple cases. Thus for instance, no explicit expression is available for the stress at a general point under a circular plate subjected to a uniformly distributed load. For this case a rather slowly converging series was published by BABKOV and BUKOWSKI (1950). For the stresses induced in the vertical center line of the circular plate, on the other hand, extremely simple formulae are obtained; thus the vertical stress under the uniformly distributed pressure (Fig. 193a) is

$$\sigma_z = q_0(1 - \cos^3 \theta), \quad (225)$$

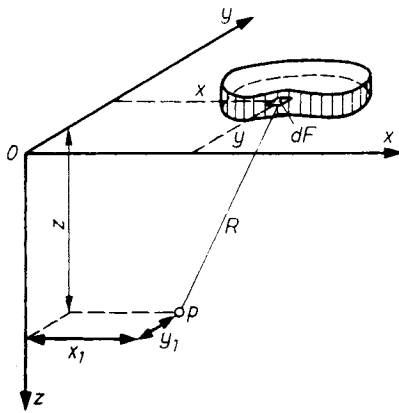


Fig. 192. Effect of uniformly distributed pressure acting on any likely contact area

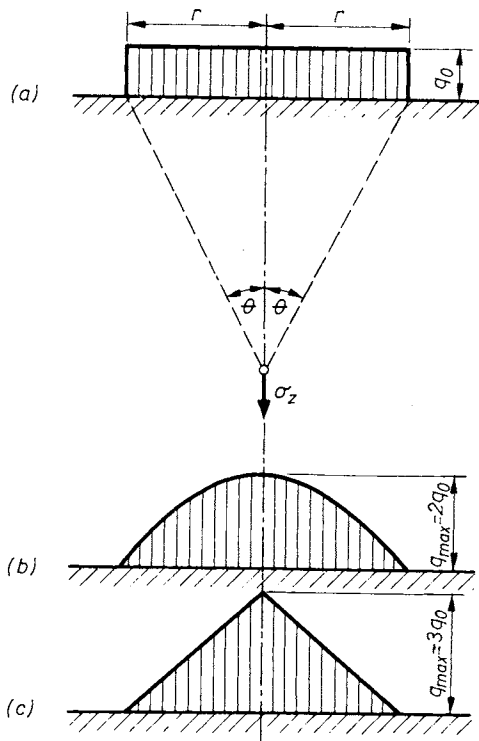


Fig. 193. Three different forms of contact pressure distributions on a circular plate

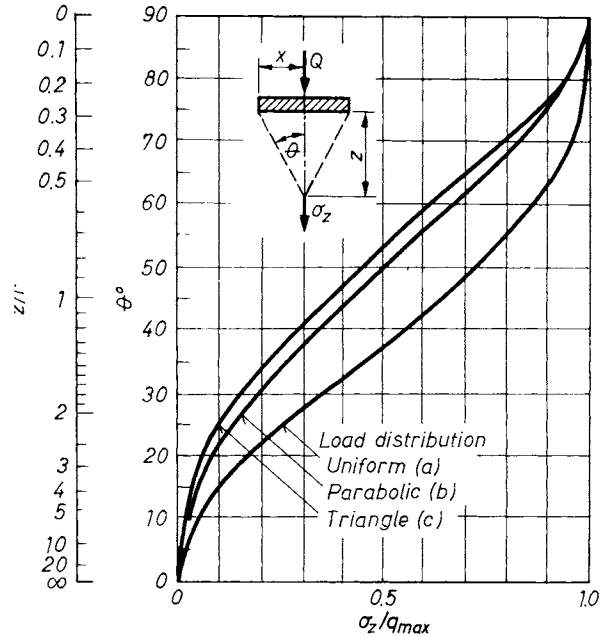


Fig. 194. Vertical stresses in the axis of a loaded circular plate

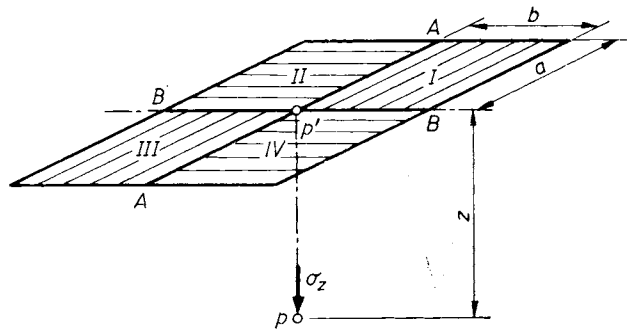


Fig. 195. Determination of the vertical stress below an internal point of a loaded rectangle

under the paraboloidic distribution (Fig. 193b)

$$\sigma_z = 2q_0[1 - 2 \cot^2 \theta(1 - \cos \theta)] \quad (226)$$

and under the conical distribution (Fig. 193c)

$$\sigma_z = 3q_0(1 - \cos \theta). \quad (227)$$

In Eqs (225)–(227) $q_0 = Q/F$ is the average unit pressure transmitted by the circular plate.

The curves in Fig. 194 can be used to advantage in rapid stress estimations according to Eqs (225)–(227). The influence coefficients σ_z/q_0 compiled in Table 9 will permit the stresses induced by a uniformly distributed load to be computed more accurately in the center line of the load, as well as in the verticals corresponding to quarter-points of the radius and further to points around the perimeter (LORENZ and NEUMEUER, 1953).

The stresses due to a load distributed uniformly over a rectangular area at the surface of the infinite half-space are computed by the formula of STEINBRENNER (1934) and NEWMARK (1935). The case

Table 9. Stresses below a uniformly loaded circular plate

(a) Vertical stresses in the axle

r/z	I	r/z	I	r/z	I	r/z	I	r/z	I
0.00	0.00000	0.50	0.28446	1.00	0.64645	1.50	0.82932	2.00	0.91056
1	0.00015	1	0.29304	1	0.65171	1	0.83167	2	0.91267
2	0.00060	2	0.30162	2	0.65690	2	0.83397	4	0.91472
3	0.00135	3	0.31019	3	0.66200	3	0.83624	6	0.91672
4	0.00240	4	0.31875	4	0.66703	4	0.83847	8	0.91865
4	0.00374	5	0.32728	5	0.67198	5	0.84067	10	0.92053
6	0.00538	6	0.33579	6	0.67686	6	0.84283	15	0.92499
7	0.00731	7	0.34474	7	0.68166	7	0.84495	20	0.92914
8	0.00952	8	0.35272	8	0.68639	8	0.84670	25	0.93301
9	0.01203	9	0.36112	9	0.69104	9	0.84910	30	0.93661
								35	0.93997
0.10	0.01481	0.60	0.36949	1.10	0.69562	1.60	0.85112	40	0.94310
1	0.01788	1	0.37781	1	0.70013	1	0.85312	45	0.94603
2	0.02122	2	0.38609	2	0.70457	2	0.85507	50	0.94877
3	0.02483	3	0.39431	3	0.70894	3	0.85700	55	0.95134
4	0.02870	4	0.40247	4	0.71324	4	0.85890	60	0.95374
5	0.03283	5	0.41058	5	0.71747	5	0.86077	65	0.95599
6	0.03721	6	0.41863	6	0.72163	6	0.86260	70	0.95810
7	0.04184	7	0.42662	7	0.72573	7	0.86441	75	0.96009
8	0.04670	8	0.43454	8	0.72976	8	0.86619	80	0.96194
9	0.05181	9	0.44240	9	0.73373	9	0.86794	90	0.96535
								95	0.96691
0.20	0.05713	0.70	0.45018	1.20	0.73763	1.70	0.89966		
1	0.06268	1	0.45789	1	0.74147	1	0.87136	3.00	0.96838
2	0.06844	2	0.46553	2	0.74525	2	0.87302	10	0.97106
3	0.07441	3	0.47310	3	0.74896	3	0.87467	20	0.87346
4	0.08057	4	0.48059	4	0.75262	4	0.87628	30	0.97561
5	0.08692	5	0.48800	5	0.75622	5	0.87787	40	0.87753
6	0.09346	6	0.49533	6	0.75976	6	0.87944	50	0.97927
7	0.10017	7	0.50259	7	0.76324	7	0.88098	60	0.98083
8	0.10704	8	0.50976	8	0.76666	8	0.88250	70	0.98224
9	0.11408	9	0.51685	9	0.77003	9	0.88399	80	0.98352
								90	0.98468
0.30	0.12126	0.80	0.52386	1.30	0.77334	1.80	0.88546		
1	0.12859	1	0.53079	1	0.77660	1	0.88691	4.00	0.98573
2	0.13605	2	0.53763	2	0.77981	2	0.88833	20	0.98757
3	0.14363	3	0.54439	3	0.78296	3	0.88974	40	0.98911
4	0.15133	4	0.55106	4	0.78606	4	0.89112	60	0.99041
5	0.15915	5	0.55766	5	0.78911	5	0.89248	80	0.99152
6	0.16706	6	0.56416	6	0.79211	6	0.89382		
7	0.17507	7	0.57058	7	0.79507	7	0.89514	5.00	0.99246
8	0.18317	8	0.57692	8	0.79797	8	0.89643	20	0.99327
9	0.19134	9	0.58317	9	0.80083	9	0.89771	40	0.99396
								60	0.99457
								80	0.99510
0.40	0.19959	0.90	0.58934	1.40	0.80364	1.90	0.89897		
1	0.20790	1	0.59542	1	0.80640	1	0.90021		
2	0.21627	2	0.60142	2	0.80912	2	0.90143	6.00	0.99556
3	0.22469	3	0.60734	3	0.81179	3	0.90263	50	0.99648
4	0.23315	4	0.61317	4	0.81442	4	0.90382		
5	0.24165	5	0.61892	5	0.81701	5	0.90498	7.00	0.99717
6	0.25017	6	0.62459	6	0.81955	6	0.90613	50	0.99769
7	0.25872	7	0.63018	7	0.82206	7	0.90726		
8	0.26729	8	0.63568	8	0.82448	8	0.90838		
9	0.27587	9	0.64110	9	0.82694	9	0.90948		

(b) Vertical stresses below a quarter point

r/z	I	r/z	I	r/z	I	r/z	I	r/z	I	z/r	I
0.00	1.000	0.40	0.894	0.80	0.664	1.20	0.480	1.60	0.351	2.00	0.262
1	1.000	1	0.889	1	0.658	1	0.476	1	0.348	2	0.259
2	0.999	2	0.883	2	0.653	2	0.472	2	0.345	4	0.255
3	0.999	3	0.878	3	0.648	3	0.468	3	0.343	6	0.251
4	0.998	4	0.873	4	0.642	4	0.465	4	0.340	8	0.248
5	0.998	5	0.867	5	0.638	5	0.461	5	0.338	10	0.244
6	0.997	6	0.861	6	0.632	6	0.457	6	0.335	15	0.236
7	0.997	7	0.856	7	0.627	7	0.454	7	0.333	20	0.228
8	0.996	8	0.850	8	0.622	8	0.450	8	0.331	25	0.221
9	0.996	9	0.845	9	0.617	9	0.446	9	0.328	30	0.214
										35	0.208

Table 9 (cont.)

z/r	I	z/r	I	z/r	I	z/r	I	z/r	I	z/r	I
0.10	0.995	0.50	0.840	0.90	0.612	1.30	0.443	1.70	0.326	40	0.201
1	0.994	1	0.836	1	0.607	1	0.439	1	0.324	45	0.195
2	0.992	2	0.828	2	0.602	2	0.435	2	0.321	50	0.189
3	0.991	3	0.822	3	0.597	3	0.432	3	0.319	55	0.184
4	0.989	4	0.816	4	0.593	4	0.428	4	0.317	60	0.178
5	0.988	5	0.810	5	0.588	5	0.425	5	0.314	65	0.173
6	0.986	6	0.806	6	0.583	6	0.421	6	0.312	70	0.168
7	0.983	7	0.798	7	0.579	7	0.418	7	0.310	75	0.163
8	0.981	8	0.792	8	0.574	8	0.414	8	0.308	80	0.158
9	0.979	9	0.786	9	0.569	9	0.411	9	0.305	85	0.154
										90	0.149
										95	0.145
0.20	0.977	0.60	0.780	1.00	0.565	1.40	0.408	1.80	0.303		
1	0.974	1	0.774	1	0.560	1	0.405	1	0.301		
2	0.971	2	0.768	2	0.556	2	0.402	2	0.299	3.00	0.141
3	0.966	3	0.762	3	0.551	3	0.399	3	0.297	10	0.133
4	0.962	4	0.755	4	0.547	4	0.396	4	0.294	20	0.126
5	0.960	5	0.749	5	0.543	5	0.393	5	0.292	30	0.119
6	0.956	6	0.743	6	0.538	6	0.388	6	0.290	40	0.113
7	0.952	7	0.737	7	0.534	7	0.387	7	0.288	50	0.107
8	0.949	8	0.731	8	0.530	8	0.384	8	0.286	60	0.101
9	0.945	9	0.724	9	0.525	9	0.381	9	0.284	70	0.096
										80	0.091
										90	0.086
0.30	0.941	0.70	0.718	1.10	0.521	1.50	0.378	1.90	0.282		
1	0.936	1	0.712	1	0.517	1	0.375	1	0.280		
2	0.932	2	0.706	2	0.512	2	0.372	2	0.278	4.00	0.082
3	0.927	3	0.700	3	0.508	3	0.369	3	0.276		
4	0.923	4	0.695	4	0.504	4	0.367	4	0.274		
5	0.918	5	0.690	5	0.500	5	0.364	5	0.272		
6	0.913	6	0.684	6	0.496	6	0.361	6	0.270		
7	0.908	7	0.679	7	0.492	7	0.359	7	0.268		
8	0.903	8	0.674	8	0.488	8	0.356	8	0.266		
9	0.899	9	0.669	9	0.484	9	0.353	9	0.264		

(c) Vertical stresses below an edge point

z/r	I	z/r	I	z/r	I	z/r	I	z/r	I	z/r	I
0.00	0.500	0.30	0.447	0.60	0.395	0.90	0.346	1.20	0.298	1.50	0.254
1	0.498	1	0.445	1	0.393	1	0.344	1	0.296	1	0.252
2	0.496	2	0.443	2	0.392	2	0.342	2	0.295	2	0.251
3	0.494	3	0.441	3	0.390	3	0.340	3	0.293	3	0.250
4	0.492	4	0.440	4	0.388	4	0.339	4	0.292	4	0.248
5	0.490	5	0.438	5	0.386	5	0.337	5	0.290	5	0.247
6	0.488	6	0.437	6	0.385	6	0.335	6	0.288	6	0.246
7	0.486	7	0.435	7	0.383	7	0.334	7	0.287	7	0.245
8	0.484	8	0.433	8	0.381	8	0.332	8	0.285	8	0.243
9	0.482	9	0.431	9	0.380	9	0.330	9	0.284	9	0.242
0.10	0.481	0.40	0.430	0.70	0.378	1.00	0.329	1.30	0.283	1.60	0.241
1	0.480	1	0.428	1	0.377	1	0.327	1	0.282	1	0.240
2	0.478	2	0.426	2	0.375	2	0.325	2	0.280	2	0.239
3	0.476	3	0.424	3	0.373	3	0.324	3	0.278	3	0.237
4	0.474	4	0.423	4	0.371	6	0.322	4	0.277	4	0.236
5	0.472	5	0.421	5	0.370	5	0.321	5	0.275	5	0.235
6	0.470	6	0.419	6	0.369	6	0.319	6	0.273	6	0.234
7	0.469	7	0.417	7	0.367	7	0.317	7	0.272	7	0.233
8	0.467	8	0.416	8	0.365	8	0.316	8	0.271	8	0.231
9	0.465	9	0.414	9	0.363	9	0.315	9	0.269	9	0.230
0.20	0.464	0.50	0.412	0.80	0.362	1.10	0.313	1.40	0.268	1.70	0.229
1	0.462	1	0.410	1	0.360	1	0.311	1	0.267	1	0.228
2	0.460	2	0.408	2	0.358	2	0.310	2	0.265	2	0.226
3	0.458	3	0.407	3	0.357	3	0.308	3	0.264	3	0.225
4	0.457	4	0.405	4	0.355	4	0.307	4	0.262	4	0.224
5	0.455	5	0.403	5	0.353	5	0.305	5	0.261	5	0.223
6	0.453	6	0.402	6	0.352	6	0.304	6	0.259	6	0.221
7	0.452	7	0.400	7	0.350	7	0.302	7	0.258	7	0.220
8	0.450	8	0.398	8	0.349	8	0.301	8	0.257	8	0.219
9	0.449	9	0.397	9	0.347	9	0.299	9	0.255	9	0.218

Table 9 (cont.)

z/r	I	z/r	I	z/r	I	z/r	I	z/r	I	z/r	I
1.80	0.217	1.90	0.206	2.00	0.195	40	0.158	95	0.123	90	0.080
1	0.216	1	0.204	2	0.193	45	0.154	3.00	0.119	4.00	0.077
2	0.214	2	0.203	4	0.191	50	0.150				
3	0.213	3	0.202	6	0.189	55	0.147	10	0.114	20	0.071
4	0.212	4	0.201	8	0.187	60	0.143	20	0.109	40	0.065
5	0.211	5	0.200	10	0.185	65	0.140	30	0.105	60	0.060
6	0.210	6	0.199	15	0.180	70	0.137	40	0.100	80	0.056
7	0.209	7	0.198	20	0.176	75	0.134	50	0.096	5.00	0.052
8	0.208	8	0.197	25	0.171	80	0.131	60	0.092		
9	0.207	9	0.196	30	0.167	85	0.128	70	0.088		
				35	0.163	90	0.125	80	0.084		

Table 10. Influence factors of vertical stresses below the corner of a uniformly loaded rectangle

b/z	a/z										
	0.1	0.2	0.3	0.4	0.5	0.6	0.7	0.8	0.9	1.0	1.2
0.1	0.00470	0.009171	0.01323	0.01678	0.01978	0.02223	0.02420	0.02576	0.02698	0.02794	0.02926
0.2	0.00917	0.01790	0.02585	0.03280	0.03866	0.04348	0.04735	0.05042	0.05283	0.05471	0.05733
0.3	0.01323	0.02585	0.03735	0.04742	0.05593	0.06294	0.06858	0.07308	0.07661	0.07938	0.08323
0.4	0.01678	0.03280	0.04742	0.06024	0.07111	0.08009	0.08734	0.09314	0.09770	0.10129	0.10631
0.5	0.01978	0.03866	0.05593	0.07111	0.08403	0.09473	0.10340	0.11035	0.11584	0.12018	0.12626
0.6	0.02223	0.04348	0.06294	0.08009	0.09473	0.10688	0.11679	0.12474	0.13105	0.13605	0.14309
0.7	0.02420	0.04735	0.06858	0.08734	0.10340	0.11679	0.12772	0.13653	0.14356	0.14914	0.15703
0.8	0.02576	0.05042	0.07308	0.09314	0.11035	0.12474	0.13653	0.14607	0.15371	0.15978	0.16843
0.9	0.02698	0.05284	0.07661	0.09770	0.11584	0.13105	0.14356	0.15371	0.16185	0.16835	0.17766
1.0	0.02794	0.05471	0.07938	0.10129	0.12018	0.13605	0.14914	0.15978	0.16835	0.17522	0.18508
1.2	0.02926	0.05733	0.08323	0.10631	0.12626	0.14309	0.15703	0.16843	0.17766	0.18508	0.19584
1.4	0.03007	0.05894	0.08561	0.10941	0.13003	0.14749	0.16199	0.17389	0.18357	0.19139	0.20278
1.6	0.03058	0.05994	0.08709	0.11135	0.13241	0.15028	0.16515	0.17739	0.18737	0.19546	0.20731
1.8	0.03090	0.06058	0.08804	0.11260	0.13395	0.15207	0.16720	0.17967	0.18976	0.19814	0.21032
2.0	0.03111	0.06100	0.08867	0.11342	0.13496	0.15326	0.16856	0.18119	0.19152	0.19994	0.21335
2.5	0.03138	0.06155	0.08948	0.11450	0.13628	0.15483	0.17036	0.18321	0.19375	0.20236	0.21512
3.0	0.03150	0.06178	0.08982	0.11495	0.13684	0.15550	0.17113	0.18407	0.19470	0.20341	0.21633
4.0	0.03158	0.06194	0.09007	0.11527	0.13724	0.15598	0.17168	0.18469	0.19540	0.20417	0.21722
5.0	0.03160	0.06199	0.09014	0.11537	0.13737	0.15612	0.17185	0.18488	0.19561	0.20440	0.21749
10.0	0.03162	0.06202	0.09019	0.11544	0.13745	0.15622	0.17196	0.18502	0.19576	0.20457	0.21769
∞	0.03162	0.06202	0.09019	0.11544	0.13745	0.15623	0.17197	0.18502	0.19577	0.20458	0.21770
	1.4	1.6	1.8	2.0	2.5	3.0	4.0	5.0	6.0	10.0	∞
0.1	0.03007	0.03058	0.03091	0.03111	0.03138	0.03150	0.03158	0.03160	0.03161	0.03162	0.03162
0.2	0.05894	0.05994	0.06058	0.06100	0.06155	0.06178	0.06194	0.06199	0.06201	0.06202	0.06202
0.3	0.08561	0.08709	0.08804	0.08867	0.08948	0.08982	0.09007	0.09014	0.09017	0.09019	0.09019
0.4	0.10941	0.11135	0.11250	0.11342	0.11450	0.11495	0.11527	0.11537	0.11541	0.11544	0.11544
0.5	0.13003	0.13241	0.13395	0.13496	0.13628	0.13684	0.13724	0.13737	0.13741	0.13745	0.13745
0.6	0.14749	0.15028	0.15207	0.15326	0.15483	0.15550	0.15598	0.15612	0.15617	0.15622	0.15623
0.7	0.16199	0.16515	0.16720	0.16856	0.17036	0.17113	0.17168	0.17185	0.17191	0.17196	0.17197
0.8	0.17389	0.17739	0.17967	0.18119	0.18321	0.18407	0.18469	0.18488	0.18496	0.18502	0.18502
0.9	0.18357	0.18737	0.18986	0.19152	0.19375	0.19470	0.19540	0.19561	0.19569	0.19576	0.19577
1.0	0.19139	0.19546	0.19814	0.19994	0.20236	0.20341	0.20417	0.20440	0.20449	0.20457	0.20458
1.2	0.20278	0.20731	0.20132	0.21512	0.21633	0.21722	0.21749	0.21760	0.21760	0.21769	0.21770
1.4	0.21020	0.21510	0.21836	0.22058	0.22364	0.22499	0.22600	0.22623	0.22644	0.22654	0.22656
1.6	0.21510	0.22025	0.22372	0.22610	0.22940	0.23088	0.23200	0.23236	0.23249	0.23261	0.23263
1.8	0.21836	0.22372	0.22736	0.22986	0.23334	0.23495	0.23617	0.23656	0.23671	0.23684	0.23686
2.0	0.22058	0.22610	0.22986	0.23247	0.23614	0.23782	0.23912	0.23954	0.23970	0.23985	0.23987
2.5	0.22364	0.22940	0.23334	0.23614	0.24010	0.24196	0.24344	0.24392	0.24412	0.24429	0.24432
3.0	0.22499	0.23088	0.23495	0.23782	0.24196	0.24394	0.24554	0.24608	0.24630	0.24650	0.24654
4.0	0.22600	0.23200	0.23617	0.23912	0.24344	0.24554	0.24729	0.24791	0.24817	0.24842	0.24846
5.0	0.22632	0.23236	0.23656	0.23954	0.24392	0.24608	0.24791	0.24857	0.24885	0.24914	0.24919
10.0	0.22654	0.23261	0.23684	0.23985	0.24429	0.24650	0.24842	0.24914	0.24946	0.24981	0.24989
∞	0.22656	0.23263	0.23686	0.23987	0.24432	0.24654	0.24846	0.24919	0.24952	0.24989	0.25000

under consideration is illustrated in Fig. 195. It is desired to find the stress at point P on the vertical through point P' . For this purpose the full rectangle is divided by straight lines through point P' and parallel to the sides into four similar rectangular areas. The full stress at point P is obtained as the sum of the stresses induced by the part-loads acting on each of the four rectangles thus formed. The formula mentioned above yields the magnitude of stress produced in the vertical through the corner point of a loaded rectangular area. The stress due to the load I is, e.g.

$$\sigma_z = \frac{q}{4\pi} \left[\frac{2 \ln \sqrt{l^2 + n^2 + 1}}{l^2 + n^2 + 1} \frac{l^2 + n^2 + 2}{l^2 + n^2 + 1} + \text{arc sin} \frac{2 \ln \sqrt{l^2 + n^2 + 1}}{l^2 + n^2 + 1 + l^2 n^2} \right], \quad (228)$$

where $l = a/z$ and $n = b/z$ are the ratios of the length of the sides of the rectangle to the depth of the point P under consideration, while q is the intensity of the uniformly distributed load. The formula is too complicated for direct computations and, therefore, a number of tables and charts have been published in the relevant literature for rapid stress estimations. The table compiled by NEWMARK (1935) is reproduced here as Table 10 from which the stress influence coefficients σ_z/p are found in terms of the ratios a/z and b/z .

The stress in the vertical through a point outside the rectangle is found by composing the loaded area of rectangles, the corners of which are above the point examined. For example, if it is desired to compute the stress under point A shown in Fig. 196, induced by the rectangular load $BCDE$, the rectangles used for computations are

$$AHBF - AHEG + AJDG - AJFC.$$

The common corner point of the above rectangles is A and so the stresses can be obtained from Eq. (228), or from the corresponding tables. The full stress is then found by summing the values obtained, with due regard to their sign.

According to BRINCH HANSEN (1955), the vertical stresses below the centre of a rectangular footing are well approximated by using the equation:

$$\sigma_1 = \frac{P}{(A+z)(B+z)}. \quad (229)$$

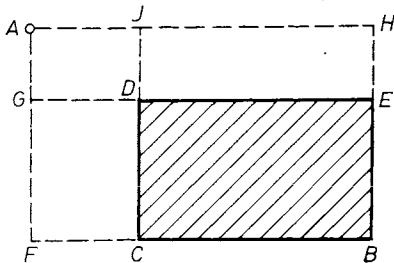


Fig. 196. Determination of stresses below an outstanding point of the loaded area

q*

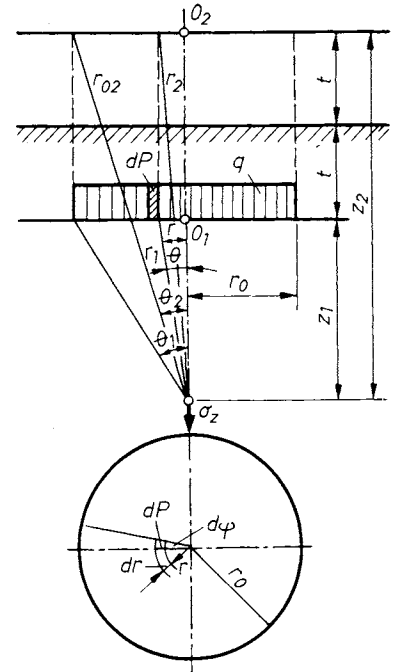


Fig. 197. Uniformly distributed pressure on a circular plate founded at depth t

Horizontal stresses parallel to B and A , respectively, can be estimated from the following formulas, in which B and A mean the width and length of the footing:

$$\sigma_{hB} = \frac{PA^2}{(B-z)^2(A-z)} \quad (230)$$

and

$$\sigma_{hA} = \frac{PA^2}{(A+z)^2(B+z)}. \quad (231)$$

To take the effect of embedment into account in the case of loads acting over a finite area, an expression is available for the stress induced in the center line of a uniformly loaded circular plate only. This is obtained by integrating Eq. (223). With the notations of Fig. 197,

$$\sigma_z = \int_{r=0}^{r_0} \int_{\psi=0}^{2\pi} d\sigma_z,$$

whence, after integration and simplification (KÉZDI, 1958)

$$\sigma_z = \frac{m}{m-1} \frac{3q}{2} \left\{ \frac{m-2}{6m} z_1 \left(\frac{1}{R_{02}} - \frac{1}{R_{01}} - \frac{1}{z_2} + \frac{1}{z_1} \right) + \frac{1}{6} - \frac{z_1^3}{6R_{01}^3} + \left[\frac{3m-4}{2m} z_2 - t \frac{m-2}{m} \right] \left(\frac{1}{3z_2} - \frac{z_2^2}{3R_{02}^3} \right) - tz(z-t) \left[\frac{z_2^2}{R_{02}^5} - \frac{1}{R_{02}^3} \right] \right\}. \quad (232)$$

For loads acting on the surface of the infinite half-space the expression is greatly simplified, since

$$t = 0, \quad z_1 = z_2 = z, \quad R_{01} = R_{02} = R_0, \quad \vartheta_2 = \vartheta_1 = \theta. \quad (233)$$

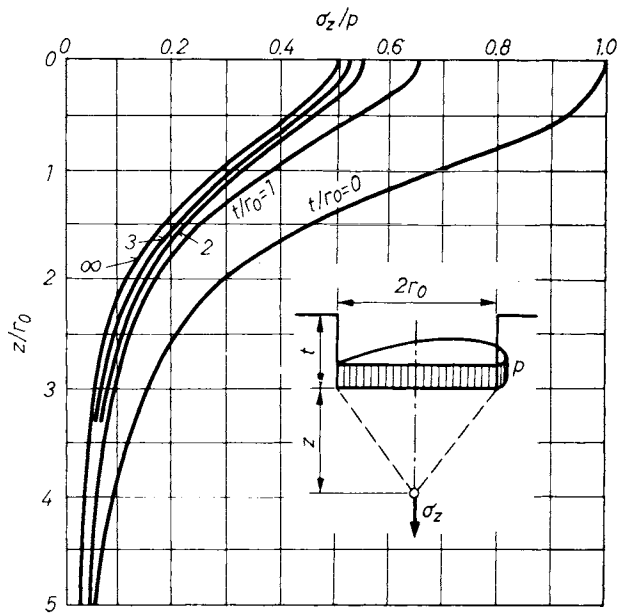


Fig. 198. Diagram for the calculation of vertical stresses in the axis of a uniformly loaded circular plate founded at depth t

and thus in agreement with Eq. (225) the stress becomes

$$\sigma_z = q (1 - \cos^3 \theta).$$

The charts in Fig 198 have been plotted in order to facilitate practical computations by Eq. (232).

The influence coefficients have been computed by assuming a Poisson's number $m = 3$. Detailed computations have shown the magnitude of stresses to change by no more than 8% if m is varied between 3 and 6. The use of $m = 3$ is thus justified in the majority of cases.

In Fig. 198 curves have also been plotted for loads acting on the surface of the infinite half space, as well as for the case of the infinite space (the curves $t/b = 0$ and $t/b = \infty$).

The vertical stresses will be seen to diminish rapidly as the footing is embedded, and at the depth corresponding to about 2.5 times the diameter of the disc, the difference related to the stresses in the infinite space is no more than 2%.

EWERT (1969) proposed a solution for the calculation of stresses below the corners of a quadrangle flexible footing. The expression is composed of two parts: the first term refers to the values of the STEINBRENNER (1934) formula for surface load; the second term reckons with the depth of the footing. Poisson's ratio is also included in the second term, but it has a slight influence on the value of σ_z . EWERT pointed out that, according to his calculations, the result deviated by max. 10% between the assumptions of $m = 2$ and $m = 5$. A significant difference resulted, however, in settlement forecast, when the calculation took account of, or dismissed, the influence of foundation depth, as it can be seen from Fig. 199.

2.2.5 Stresses below the characteristic point

When the compression of a soil slice, bounded by horizontal parallel planes in the underground, is calculated, it will be found that its value varies from point to point in compliance with the vertical stress which also varies from point to point over the slice. It is obvious that the maximum vertical stress develops in the centerline of the load, but this does not evoke the same compression to which the base as a whole would be subjected. For the calculation of settlements, it is not the maximal, but the average stress inside the proper lines of the foundation that should be taken as effective. It is rather complicated to calculate its actual value, especially below surfaces of limited size. Making use of the advantageous situation that for a given load distribution the particular point of the footing under which (at any depth) just the desired average vertical stress can be known beforehand, the elaboration of influence diagrams is possible. The location of the characteristic point is at a distance $0.7 b$ from the central axis of a strip foundation, and at $0.7 b$ from the longitudinal and $0.74 a$ from the perpendicular axis of a quadrangle footing (b is the half-width, a is the half-length of the footing).

The stresses in the vertical line of the characteristic point of a quadrangle footing are shown in Table 11 after KANY (1959).

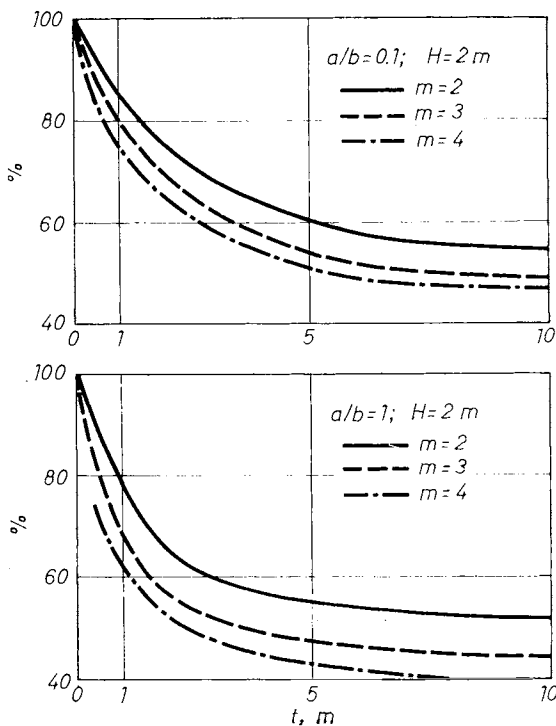


Fig. 199. Comparison of settlements calculated with or without respect to depth of foundation (EWERT, 1969)

Table 11. Stresses below the characteristic point of rectangular footings: *a* — half-length of the footing; *b* — half-width of the footing; *z* — depth

<i>z/b</i>	<i>a/b</i>						
	1	1.5	2	3	5	10	∞
0.1	0.98	0.98	0.99	0.99	0.99	0.99	0.99
0.2	0.90	0.93	0.94	0.94	0.94	0.94	0.94
0.3	0.79	0.84	0.86	0.88	0.88	0.88	0.88
0.4	0.69	0.76	0.79	0.81	0.82	0.83	0.83
0.6	0.56	0.62	0.66	0.71	0.73	0.74	0.74
1.0	0.41	0.46	0.50	0.56	0.60	0.63	0.63
1.4	0.32	0.37	0.40	0.45	0.51	0.55	0.56
2.0	0.23	0.28	0.31	0.35	0.40	0.45	0.47
3.0	0.14	0.18	0.21	0.24	0.28	0.30	0.36
4.0	0.09	0.13	0.15	0.17	0.21	0.25	0.29
6.0	0.05	0.07	0.08	0.10	0.13	0.16	0.20
10.0	0.02	0.03	0.03	0.05	0.06	0.08	0.13
14.0	0.01	0.01	0.02	0.03	0.04	0.05	0.09
20.0	0	0.01	0.01	0.01	0.02	0.03	0.06
40.0	0	0	0	0	0.01	0.01	0.03

2.2.6 Location of the depth limit

Stresses are principally calculated with the aim of enabling the forecasting of settlements in the underground. As a consequence of the structure of the formulas for the calculation of stresses a minute additional increment with depth will increase the calculated settlement even at very large depths. (Not to speak of the fact that the settlement, when calculated for a strip foundation according to Section 2.2.3.3 would have an infinitely huge value.) Surveys carried out on actual buildings have shown, however, that the yielding of a compressed earth mass is vertically restricted to a depth, say, of 2 or 3 times the width of the footing. This can be easily understood because:

- in saturated soils only a gradient above some threshold value i_0 would be able to initiate the movement of the pore water;
- the skeleton structure of the soil (whether saturated or not) may undergo a deformation only when the applied stress exceeds a critical value of p_0 .

The latter statement has been interpreted by FEDA *et al.* (1977) in the following manner. The position of contact forces between the grains of an undisturbed soil is quite random (Fig. 200). With increasing load, these contact forces gradually reach their limit position *A*, inclined to the normal of the contact plane at the angle of the intergranular friction Φ_u . (An additional increment of contact strength may arise between the particles by cementation.) The soil will be considerably deformed only if a statistically significant number of particles start to slide (i.e. $K \rightarrow A$). Beneath the footing, the vertical stress decreases with depth, and so does the number of contact forces that have reached their limit position. This is manifested by the non-linear behaviour of the mass. At the same time, owing to the increase of the geostatic pressure, the number of contacts in a volumetric soil unit increases, and therefore the soil becomes more and more deformation resistant with depth.

The aforesaid considerations find their solution in practice by taking the underground as compressible

to a depth limit of m_0 only. Most countries have decided to allow a depth limit z in their Codes of Practice where

$$\sigma_z = \beta \sigma_g, \tag{234}$$

i.e. that particular depth where the stress from external forces equals β times the overburden pressure, σ_g , with an assigned value of 0.1 or 0.2 for β .

In Hungary, the formula proposed by JÁKY is still in use for estimating the settlement. It states that

$$m_0 = 4 \frac{ab}{a + b}, \tag{235}$$

where a and b are the half-width and -length of the footing, respectively.

There are two suitable ways to select the appropriate value for the depth limit:

- measured settlements of existing buildings are back-analyzed, and when sufficient data have been obtained a regression analysis is performed; or
- gauges are incorporated in the soil and the deformation of each slice is determined.

ALTES (1976) chose the first method for analyzing the measured settlements of 132 buildings. With the data a multiple regression analysis was then performed to find the relationship $m_0/B = f(p, F, E, B/L)$.

These calculations produced the following formula:

$$\frac{m_0}{B} = 5.04 B 10^5 q^{0.47} \left[1 + \frac{1}{1 + 5 F^{-0.05}} \right]^{-17.7} \cdot \left[0.333 + \frac{1}{1 + 0.075 E_s^{-0.1}} \right]^{-40.8} \cdot \left[\frac{1}{1 + 0.02 B/L} \right]^{10.2}, \tag{236}$$

where

- B = width of the base, m,
- L = length of the base, m,

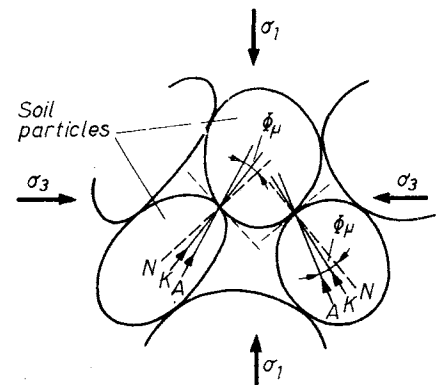


Fig. 200. Contact forces between soil particles: K — initial random position; A — limit position; N — normal position (FEDA *et al.*, 1977)

F = surface area of the base, m^2 ,
 p = contact pressure, kp/cm^2 ,
 E_s = modulus of compressibility, kp/cm^2

(The correlation index was $I = 0.82$ for his calculation.)

Based on this formula, Fig. 201 has been composed for three different F , and two different E_s values each. The following conclusions can be drawn therefrom:

- the depth limit decreases when E_s increases;
- the ratio m_0/B decreases when B increases;
- the depth limit as calculated by the supposition $\sigma_z = 0.2 t\gamma$ will deviate more and more from the result of the above formula when the footing is elongated, and/or the surface area becomes larger.

A study performed by FEDA *et al.* (1977) presented another possibility. Four loading tests were carried out using a 138 cm diameter plate on three different soils (silty sand, loess, and dense clayey sand). The relationship between s and z for one of the trial tests is shown in Fig. 202. The following values were obtained for the relative depth of the compressible zone m_0/D as a function of the load:

Load					
$\epsilon(\%)$	0.05	0.1	0.2	0.4	0.75
5	0.7	0.9	1.1	1.3	1.7
0	1.2	1.6	1.9	2.2	2.6

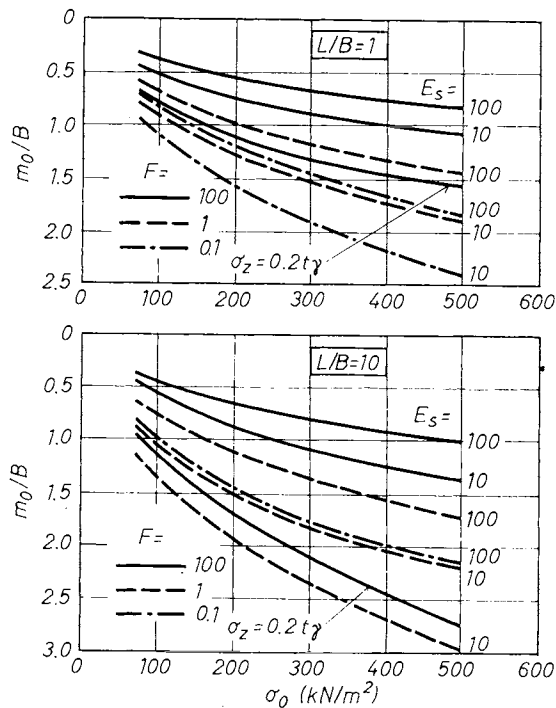


Fig. 201. Determination of the depth limit (m_0) after ALTES (1976)

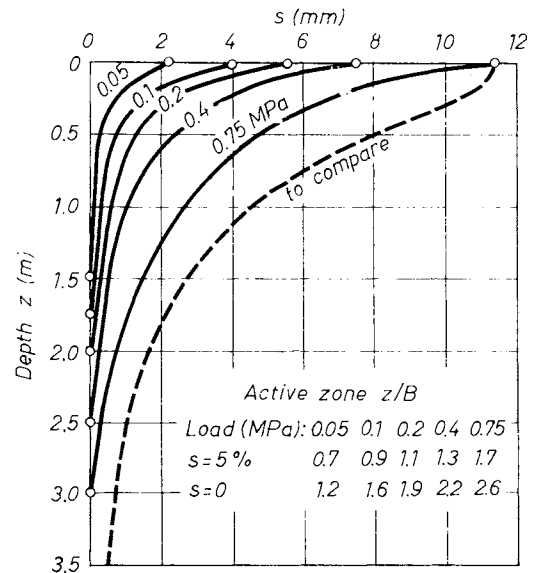


Fig. 202. Depth limit as determined by model tests (FEDA *et al.*, 1977)

The authors proposed accepting the depth over which 95% of the settlement occurs as m_0 .

The observation of these authors that m_0 does not depend on E_s contradicts the observations made by ALTES (1976), JEGOROV and POPOVA (1971) and others, and this might be attributed to the small number of tests.

2.2.7 Stresses in layered systems

Throughout the foregoing considerations, the medium in which the stresses are induced has been assumed to be uniform and to extend to infinity. However, cases are often encountered in practice where a layer — solid rock, dense sand, or gravel — is situated at a certain depth below the footing which is virtually incompressible and completely rigid for all practical purposes. At the interface of the two layers shear stresses will ensue which will modify the whole stress pattern. A solution to this problem was presented by MARGUERRE (1931), the results being reproduced after JELINEK (1951) in Fig. 203. As will be noted the effect of the rigid layer is to concentrate the stresses around the centerline of the load.

Another case of practical interest is that where the layer closer to the surface is relatively stiff and is underlain by weaker layers of considerable thickness. This situation is often created artificially, when the poor subsoil is excavated and replaced by a desirable material, e.g. to support the footing on a well compacted base of sand or gravel. The compressibility of the upper soil layer is then considerably lower than that of the underlying layer, so that owing to the higher resistance to deformation, the stresses are concentrated in the upper layer, only a lower stress being transmitted to the soft layer.

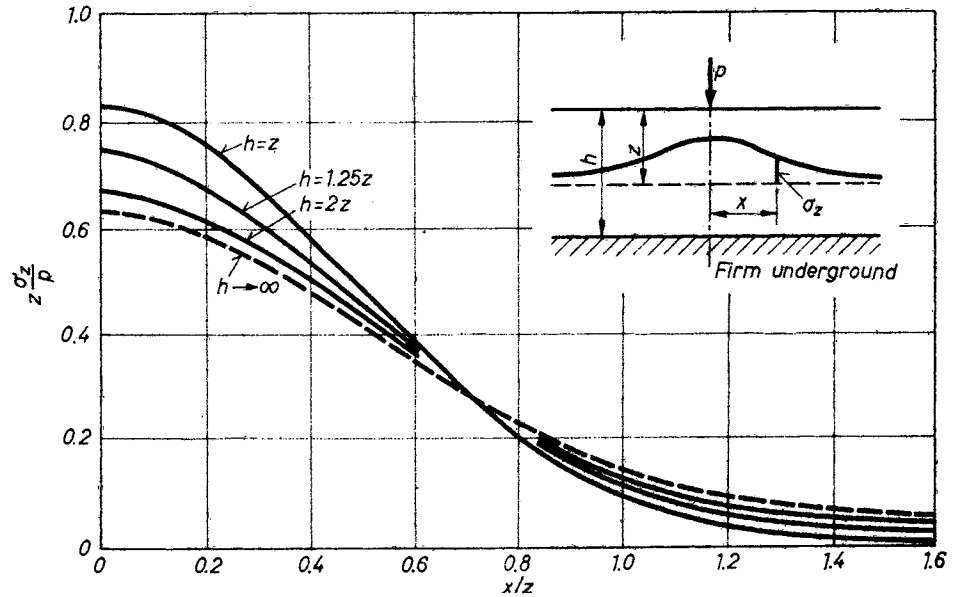


Fig. 203. Vertical stresses in the elastic layer resting on a stiff subbase material

For estimating the stresses in two-layer systems, with special regard to pavement design, a method has been suggested by BURMISTER (1945).

The stresses induced in a lower layer of reduced strength may be found by using the method developed by the senior author (KÉZDI, 1958). In essence, this approximate approach consists of introducing an equivalent layer thickness.

The principle underlying the determination of the equivalent layer thickness h' is that the unit load p acting on the surface of this layer should induce the same vertical stress, at the bottom of the layer in the case of a homogeneous soil, as the original load at the same depth (Fig. 204). The value of h' is found with the help of the curves in Fig. 205. It should be emphasized that the applicability of this method is restricted to cases where the upper layer is cohesive and thus has a certain tensile strength, since according to the theory, the radial stresses developed at the interface of the two layers cause tension which granular soils are incapable of withstanding.

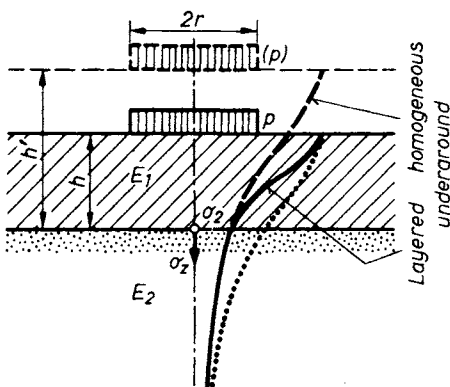


Fig. 204. Concept of the equivalent layer thickness

The method is thus also unsuited for estimating the settlement of foundations on imported fill. Such problems will yield to the theory advanced by POKROVSKII (1937). The assumption underlying this theory is that the extent to which a material is capable of resisting stresses is dependent upon the value of its modulus of elasticity. The velocity at which vibrations are propagated also depends on the modulus of elasticity. Let us now denote the velocities in the upper and lower layers by v_1 and v_2 , respectively. If $E_1 > E_2$, then $v_1 > v_2$. A beam of energy emanating from a center of vibration will retain its direction in the upper layer, but will be refracted (Fig. 206) at the boundary between the two layers. The radial distance which the wave has attained at the bottom of the lower layer is

$$T = h \tan \alpha_1 + H \tan \alpha_2 \approx h \alpha_1 + H \alpha_2. \quad (237)$$

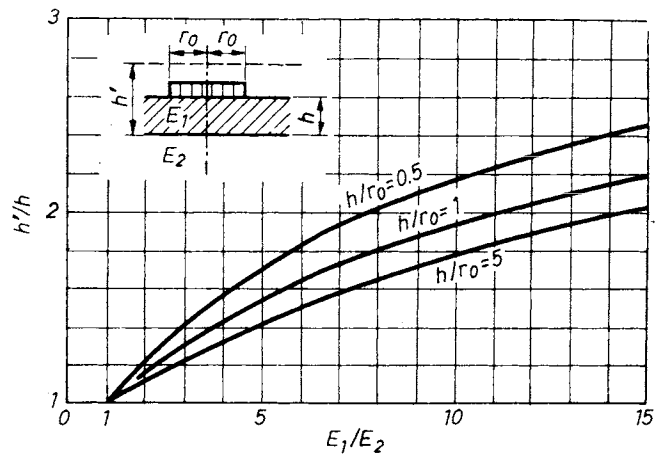


Fig. 205. Determination of the equivalent layer thickness

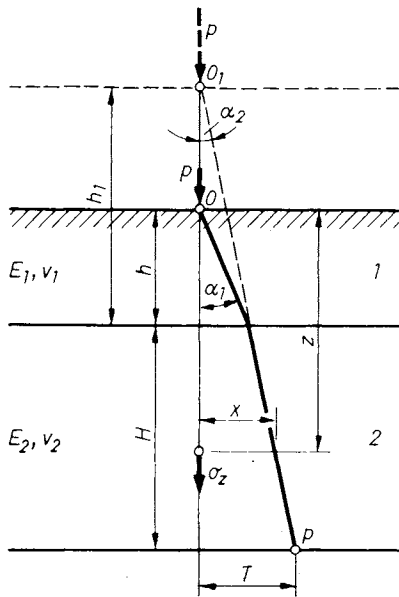


Fig. 206. POKROVSKII's method (1937) for the investigation of the two layer system

Introducing the imaginary layer of thickness h' and postulating that in the uniform layer of thickness $(h' + H)$ the wave should attain the same point as in the original layer of thickness $(h + H)$, we have

$$T \cong (h' + H) \alpha_2 \tag{238}$$

or

$$h' = h \frac{\alpha_1}{\alpha_2} \tag{239}$$

Now according to the theory of vibrations

$$\alpha_2 = \alpha_1 \frac{v_1}{v_2}, \text{ so that}$$

$$h' = h \frac{v_1}{v_2}$$

NEWTON found the velocity of propagation in uniform media to be

$$y = A \sqrt{\frac{E}{\delta}}, \tag{240}$$

where E = Young's modulus of elasticity of the medium,

δ = the density of the medium,

A = a constant whose magnitude depends on the lateral elasticity of the medium and on the direction of propagation.

Combining Eqs (238) and (239):

$$h' = h \sqrt{\frac{E_1 \delta_2}{E_2 \delta_1}} \tag{241}$$

Consequently, the stresses induced in the lower layer of a two-layer system by a concentrated force P acting on the surface of the upper layer may be computed by the formulae of BOUSSINESQ, but the depth is to be measured from the surface of the equivalent layer of thickness h' , as if the load acted at point O_1 , rather than at point O (Fig. 206).

Accordingly, in the centerline of the load

$$\sigma_z = \frac{3P}{2\pi \left(z + h \sqrt{\frac{E_1}{E_2}} \right)^2} \tag{242}$$

Another well-known solution is connected with the name of ODEMARK (1949). Making use of the slab theory it is possible to deduce the substitutive thickness (H_e) of the upper layer which gives the same bending strength in both the upper and the lower layer. It can namely be written that

$$\frac{E_2}{1 - \mu_2^2} H_e^3 = \frac{E_1}{1 - \mu_1^2} n^3 H_1^3, \tag{243}$$

where E_1 and E_2 = modulus of elasticity in the upper and the lower layer, respectively,

μ_1 and μ_2 = Poisson's ratio relating to the upper and the lower layer, respectively.

Using Burmister's theory, we can take the n factor as 0.9, and supposing that μ_1 is equal to μ_2 , the substitutive layer thickness will be found as:

$$H_e = 0.9 H_1 \sqrt[3]{\frac{E_1}{E_2}} \tag{244}$$

Another possibility of finding H_e is offered by using optical analogy (BRANDL, 1970). The velocity v of a light beam depends on E and γ . When the beam reaches the interface with a material of lower modulus of elasticity it breaks toward the normal of the plane (Fig. 207), complying with the law

$$\frac{\sin \alpha_1}{\sin \alpha_2} = \frac{v_1}{v_2},$$

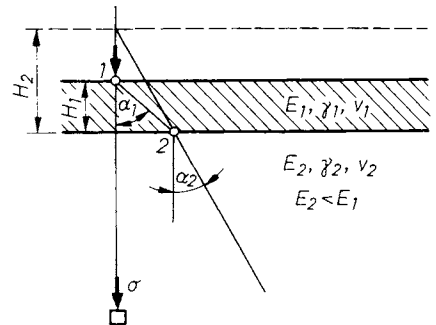


Fig. 207. Calculation of stresses in the two layer system by using optical analogy (BRANDL, 1970)

where in reference to the figure $\tan \alpha_1 = s/H_1$ and $\tan \alpha_2 = s/H_e$, and so:

$$H_e = H_1 \frac{\tan \alpha_1}{\tan \alpha_2}. \tag{245}$$

As here the angles and angle differences are small, it can be said that:

$$H_e \cong H_1 \frac{\sin \alpha_1}{\sin \alpha_2} = H_1 \frac{v_1}{v_2}.$$

Newton's law postulates that

$$v = A \sqrt{\frac{E}{\delta}},$$

where δ is the density of the material, A is a constant depending on Poisson's ratio, and so, by changing δ to γ :

$$H_e = H_1 \sqrt{\frac{E_1 \gamma_2}{E_2 \gamma_1}}, \tag{246}$$

which is congruent with the formula proposed by POKROVSKII.

Indications can be found in the literature that Eq. (244) is closer to reality.

Problems related to the distribution of stresses in two-layer and multi-layer systems will be dealt with in Chapter 4.

2.2.8 Stresses in anisotropic media

The stresses dealt with in the foregoing sections were invariably based on the assumption of uniform, isotropic soils with identical elastic properties in all directions. In the case of sedimentary soils, this assumption is, in general, not valid. Thus in typical marine clay deposits thin coarse-grained layers are usually interbedded. On the surface thereof a higher shear may be developed and thus the resistance to lateral displacement may be appreciably greater than in uniform soils. Loess soils also display anisotropic properties, in that owing to the minute vertical, lime-encrusted canals, the soil is of a columnar structure with widely differing compressibilities in the vertical and horizontal directions. On the other hand, the modulus of compressibility will usually be observed to increase with depth in sands. The distribution of stresses is necessarily influenced by such anisotropy, prompting a number of researchers to find a solution to this problem. Some of the relevant theories are described below.

The method suggested by BABKOV and BUKOWSKI (1950) for anisotropic soils provides a fair degree of approximation and is supported by experimental evidence. In the case of a line load acting on an anisotropic infinite half-space, the Young's moduli of elasticity will be denoted by E_1 and E_2 in the horizontal and vertical directions,

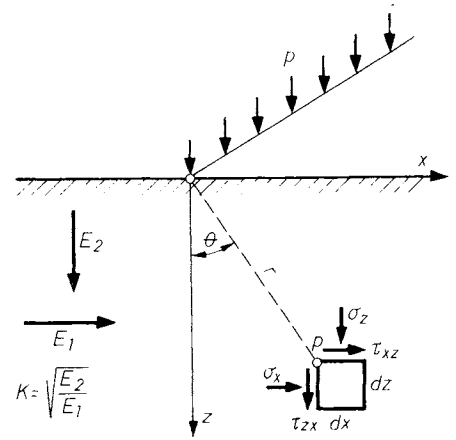


Fig. 208. Stresses in the anisotropic half-space generated by a vertical line load on the surface

respectively, and the stresses are given approximately by the following expressions:

$$\left. \begin{aligned} \sigma_z &= \frac{2p}{\pi} \frac{Kz^3}{r^4}, \\ \sigma_x &= K \frac{2p}{\pi} \frac{x^2z}{r^4}, \\ \tau &= K \frac{2p}{\pi} \frac{xz^2}{r^4}. \end{aligned} \right\} \tag{247}$$

The notations are explained in Fig. 208 while K denotes the ratio

$$K = \sqrt{\frac{E_2}{E_1}}.$$

Under a concentrated force the stresses are given as

$$\sigma_z = \frac{P}{\pi} \frac{z^3 (1 + K + K^3)}{R^5 K (1 + K)}. \tag{248}$$

With $K = 1$ the expressions reduce to the form given for uniform soils. Applying the foregoing expressions to frozen soils, TSYTOVICH has shown the stresses under concentrated loads to exceed those after thawing by as much as 70%.

The problem of stress distribution has been solved by WESTERGAARD (1938) for clay soils with interstratified thin horizontal layers. These have been assumed to be present in great numbers, closely spaced and of negligible thickness, but of infinite rigidity, thereby preventing the soil mass from undergoing lateral strain. For a concentrated vertical load on the surface of the half-space, the vertical stresses are given as

$$\sigma_z = \frac{P}{2\pi} \frac{1}{z^2 \left[\frac{m+2}{2m-2} + \left(\frac{r}{z} \right)^2 \right]^{3/2}}. \tag{249}$$

Regarding the Poisson's number to be infinitely large — in agreement with the starting assumption:

$$\sigma_z = \frac{P}{\pi} \frac{1}{z^2 \left[1 - 2 \left(\frac{r}{z} \right)^2 \right]^{3/2}} \quad (250)$$

The notations are the same as those in Fig. 191, Under a rectangular footing with sides a and b the stresses are found by integrating Eq. (249) thus

$$\sigma_z = \frac{q}{\pi} \arccot \sqrt{\left(\frac{m-2}{2m-2} \right) \left(\frac{1}{l^2} + \frac{1}{n^2} \right) + \left(\frac{m-2}{2m-2} \right)^2 \frac{1}{l^2 n^2}} \quad (251)$$

For $m = \infty$

$$\sigma_z = \frac{q}{2\pi} \arccot \sqrt{\frac{1}{2l^2} + \frac{1}{2n^2} + \frac{1}{4l^2 n^2}} \quad (252)$$

The stresses obtained by Westergaard's equations and for the isotropic half-space are compared in Fig. 191.

In cases where the load is concentrated and $r/z < 0.8$ and further for surface loads with both l and n smaller than about unity, Westergaard's formulae give lower values, viz. about two-thirds of those computed with Boussinesq's equation.

There is not enough evidence available to indicate positively which of the two formulae gives the more reliable results in general practice. In sedimentary soils the assumptions underlying Westergaard's solution seem to be more realistic. This appears to be supported by the fact that the settlements estimated using the formulae applying to isotropic soils were generally found to be smaller than those actually observed, although this may be due to a variety of other factors as well.

In the case of anisotropy considered by Fröhlich, the compressibility, i.e. compression-, or elastic modulus of the soil, varies according to a certain relationship with depth. The reduction of compressibility with depth is observable, particularly in sands.

The reason for this is that the criterion of superposition does not hold true for soils, as can be readily demonstrated by the triaxial compression tests described in Part I. In the case of perfectly elastic bodies acted upon by an initial hydrostatic pressure, the vertical deformation would be found to be independent of the magnitude of the initial pressure. The same test performed with sand would yield deformations which are the smaller, the greater the initial pressure may be. In a natural sand deposit subject to geostatic pressure, the vertical and horizontal stresses increase with depth, so that the strains induced by a given external stress will decrease correspondingly.

An exact theoretical solution for the conditions described above was given by BOROWICZKA (1943) in the form of slowly converging infinite series, which is thus of but little practical interest.

For the case of a Young's modulus of elasticity increasing in linear proportion with depth, the following formulae have been derived by FRÖHLICH (1934):

$$\left. \begin{aligned} \sigma_z &= \frac{3}{4} q \left\{ \sin \theta_2 - \sin \theta_1 - \frac{1}{3} \sin^3 \theta_2 + \frac{1}{3} \sin^3 \theta_1 \right\}, \\ \sigma_x &= \frac{1}{4} q [\sin^3 \theta_2 - \sin^3 \theta_1], \\ \tau_{xz} &= \frac{1}{4} q [\cos^3 \theta_2 - \cos^3 \theta_1]. \end{aligned} \right\} \quad (253)$$

(for the notations cf. Fig. 175).

In the example shown in Fig. 209, the stresses computed by assuming $E = \text{constant}$ and $E = az$ are compared. The latter will be seen to be more concentrated in the centerline of the load.

Concerning the propagation of stresses in anisotropic soils, the name of JELINEK (1948) should be mentioned; rigorously observing the laws of the mathematical theory of elasticity, he has succeeded in developing relationships for the case of media having different moduli of elasticity in the horizontal and vertical directions. The computation formulae for concentrated and line loads are rather simple, especially for the case of $m = \infty$. Since the stresses obtained in the case that $k^2 = E_2/E_1 > 1$ are concentrated about the centerline, he has suggested making allowance for the effect of shear stresses in the contact plane, as well as of the increase of the compression modulus with

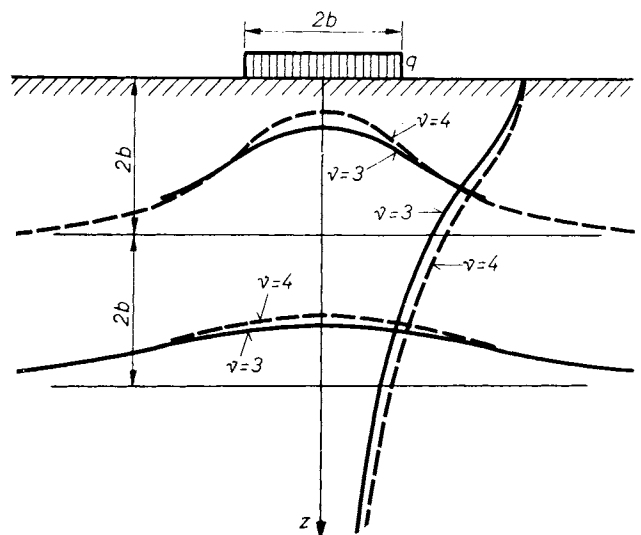


Fig. 209. Vertical stresses in the elastic half-space: a — constant modulus of elasticity ($\nu = 3, E = \text{constant}$); b — modulus of elasticity increases linearly with depth ($\nu = 4, E = az$)

depth by the appropriate choice of the value k^2 , the effects of these factors on the stress distribution being of the same sense.

2.3 Settlement of foundations

Total settlement of a footing is, in general, composed of three parts. The first of these is the instantaneous, or initial settlement. This is not accompanied by a volume change and is due principally to the effect of shear stresses. This settlement frequently remains unobserved during the construction of a building as it occurs within a very short time and is small relatively to the two other parts. It assumes significance in the analysis of deformations produced by transient loads, or when processing and evaluating the results of loading tests of short duration. This initial settlement will be dealt with in Section 2.3.2.1.

The second part comprises the settlement due to consolidation, caused by the displacement of air, or water from the soil under the load. Consequently, this part of settlement is accompanied by a change in volume. The process is delayed over a certain period of time, the length of which is controlled by the air- and water permeability of the soil, while its magnitude may be estimated from the compression curve, or another load-deformation diagram.

The third part is called the secondary settlement and is due to secondary compression. The shear stresses cause plastic flow in the soil skeleton, the particles being slowly displaced relative to each other. This part of the settlement becomes great enough to be of importance in specific soil types only, namely fat clays, peat and other organic soils.

The settlements under a particular structure, and even more so the differential settlements under the diverse parts thereof depend, however, not on the compressibility of the soil alone, or of the individual soil layers, but also — to a considerable extent — on the structure itself. The individual supports of statically determinate structures may settle to a certain extent independently from each other without affecting the distribution of forces in the entire structure, whereas differential settlement will produce internal forces in statically indeterminate structures. These, in turn, will bring about changes in the bearing loads responsible for the settlements, the resulting interaction, as a rule, being very difficult to investigate analytically. This is the reason for the common practice in settlement computations of regarding the footings — spread and continuous alike — as independent elements and of estimating, more or less in the light of past experience, the probable behaviour of the structure from the differential settlement thus computed. In some cases, more accurate computations are also possible, as will be shown in Section 2.3.7.

The application of the theory of elasticity to settlement computation problems will first be demonstrated and then followed by a description of conventional settlement computation. These problems are commonly encountered with foundations on clay soils, while footings on sand are usually dimensioned for the load-bearing capacity of the soil. Once the margin of safety with respect to soil failure is wide enough, the settlements — on sand soils — are usually small enough to be neglected. Nevertheless, settlements must be examined as well in such cases.

2.3.1 Settlement computations by the theory of elasticity

The theory of elasticity is used in soil mechanics exclusively for the determination of stresses. In general, this is actually the case and explicit formulae for particular problems are available, which can be used to advantage. The literature in this field has grown in volume considerably over the past years. The fundamental problem encountered when trying to apply the formulae derived in the theory of elasticity is concerned with the numerical value to be introduced for the modulus of elasticity. According to one approach, the modulus value corresponding to the total stress is used for computing the initial settlement, whereas that determined on the basis of effective stresses is adopted for estimating the final value of consolidation settlement.

Let us first consider two fundamental cases, namely those of the circular plate and of the rigid strip footing, both loaded at their centerline (FISCHER, 1957).

Under a concentrated vertical load acting in its centerline, the infinitely rigid circular plate will settle uniformly. In such cases, the bearing pressures in the contact plane are not distributed evenly but according to the expression (BOUSSINESQ, 1885):

$$\sigma = \frac{1}{2} \frac{qr}{\sqrt{r^2 - x^2}} = \frac{1}{2} \frac{q}{\sqrt{1 - \rho^2}} \quad (254)$$

(cf. Fig. 210).

The distribution of the vertical and horizontal principal stresses in the centerline is found by integration, whence the compression along z of a cylindrical element in the centerline can be computed, thus

$$\sigma_z = \frac{1}{E} \left[\sigma_z - \mu(\sigma_x + \sigma_y) \right] = \frac{1}{E} [\sigma_z - 2\mu\sigma_x] \quad (255)$$

and the compression of a layer extending from $z = 0$ to $z = z$ becomes

$$y = \frac{1}{E} \int_0^z (\sigma_z - 2\mu\sigma_x) dz. \quad (256)$$

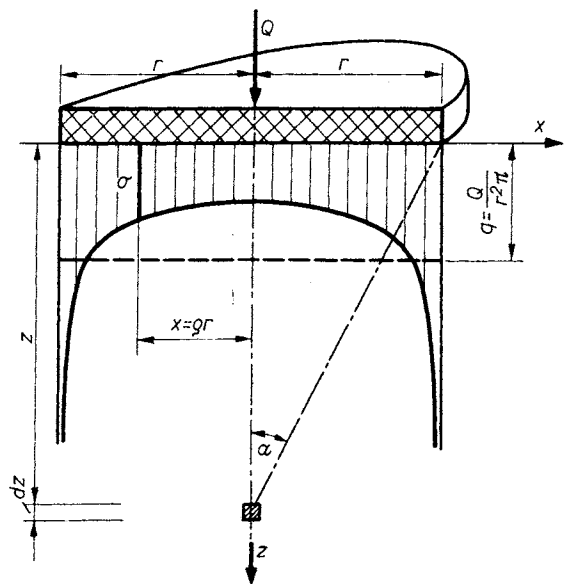


Fig. 210. Contact pressure distribution (σ) below a rigid circular plate loaded by a vertical singular force (Q) at the centre

Since in the case of a rigid, circular plate

$$\sigma_z - 2\mu\sigma_x = \frac{1}{2} (1 + \mu)q \sin^2\alpha(1 - 2\mu + 2 \cos^2\alpha)$$

and

$$z = r \cot \alpha ,$$

$$dz = - r d\alpha / \sin^2 \alpha ,$$

whence

$$y = \frac{1}{2} (1 + \mu) \frac{qr}{E} \int_{\alpha}^{\pi/2} (1 - 2\mu - 2 \cos^2\alpha) d\alpha =$$

$$= (1 - \mu) \frac{qr}{2E} \left[2(1 - \mu) \left(\frac{\pi}{2} - \alpha \right) - \sin \alpha \cos \alpha \right] =$$

$$= \frac{Q}{rE} f(\alpha) . \tag{257}$$

For $z \rightarrow \infty$ also $\alpha \rightarrow 0$, the total settlement becomes

$$y_0 = (1 - \mu^2) \frac{r\pi q}{2E} . \tag{258}$$

With the help of Eq. (257) the settlement can be found for layered soils as well. To this end, the settlements y are computed for each layer, always using the appropriate value of the E modulus. Values of the function $f(\alpha)$ can be found from Eq. (257) or from Fig. 211. The component settlements are thus

$$\Delta y_i = \frac{Q}{rE_i} [f_i(\alpha) - f_{i-1}(\alpha)] \tag{259}$$

producing the total settlement

$$y = \Sigma \Delta y .$$

If the load on the circular disc is distributed uniformly, implying a flexible plate, the settlement in the centerline is given by the expression

$$y = (1 - \mu^2) \frac{2qr}{E} = 1.28 y_0 . \tag{260}$$

Problems related to the settlement of strip footings will yield to a similar approach. The distribution of the contact pressure is described here by the expression

$$\sigma = \frac{2}{\pi} \frac{qb}{\sqrt{b^2 - x^2}} = \frac{2}{\pi} \frac{q}{\sqrt{1 - \xi^2}} \tag{261a}$$

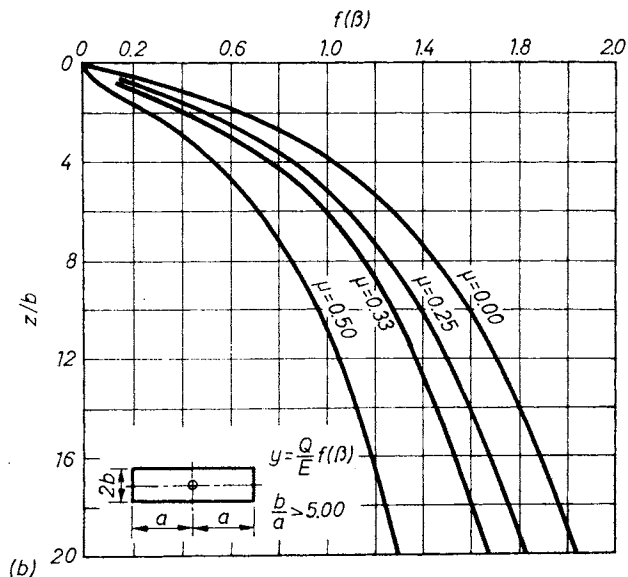
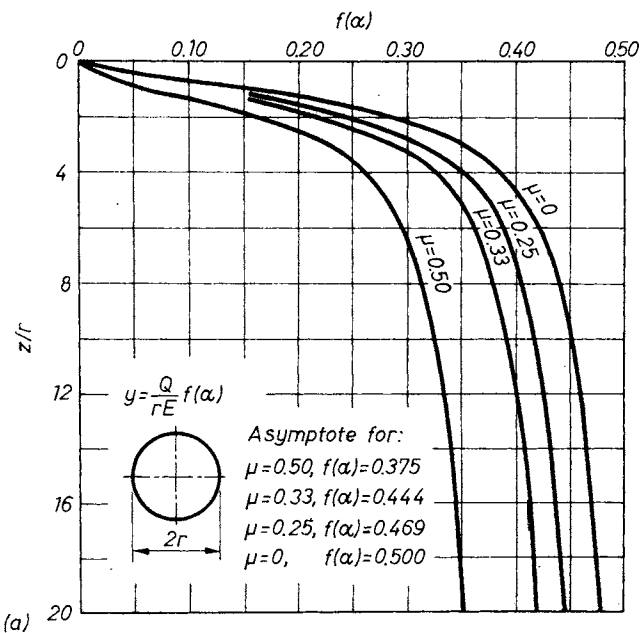


Fig. 211. Diagram for the calculation of partial settlements (y):
 a — for a rigid circular plate loaded by a vertical singular force in the centre; b — for a rigid centrally loaded beam

(cf. Fig. 212), the resulting compression of the layer down to depth z being

$$y = (1 - \mu^2) \frac{Q}{\pi E} \left[2 \ln \cot \frac{\beta}{2} - \frac{1}{1 - \mu} \cos \beta \right] = \frac{Q}{E} f(\beta). \tag{261b}$$

The values of $f(\beta)$ are plotted in Fig. 211. The partial settlements resulting from compression of single layers are computed from Eq. (259). It should be noted that for $z \rightarrow \infty$ again $y \rightarrow \infty$, so that the anomaly described before is again encountered.

2.3.2 Calculation of the three phases of settlement

The procedures for calculating the settlement have been elaborated for cohesive soils (Sections 2.3.2.1–2.3.2.3) because present laboratory testing technology can only cover the deformation analysis of these types of soils. Problems relating to granular soils will be dealt with, therefore, in Section 2.3.2.4.

2.3.2.1 Initial settlement

When a load is applied rapidly to a saturated clay, the soil deforms at constant volume ($\nu = 0.5$) to accommodate the imposed shear stresses. The settlement associated with these deformations, that occurs without significant dissipation of excess pore pressures, is called the initial (or undrained, or shear) settlement.

Appraising the initial settlement separately is important for the following reasons.

1. Initial settlement may constitute a large portion of the total settlement, depending on the nature of the soil, the geometry of loading, and the thickness of the compressible layer.
2. Analysis of the initial settlement is an integral part of the analysis of the overall time vs. settlement behaviour of foundations (cf. Section 2.3.2.2).
3. Initial settlement is closely related to the undrained stability of foundations of both buildings and dams (cf. Section 2.4). Excessive initial settlement may be a warning of impending failure.

Commonly used methods for computing the initial settlement employ various integrations of Boussinesq's solution for the settlement under a point load on the surface of a homogeneous, isotropic, linearly-elastic half-space. Thus

$$s_i = pB \frac{1 - \nu^2}{E} I, \tag{262}$$

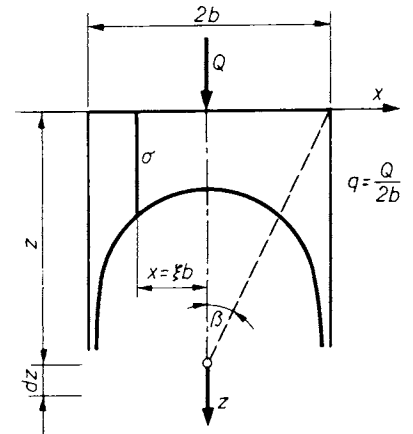


Fig. 212. Contact pressure distribution (σ) below a rigid beam

- where s_i = initial settlement,
 p = average contact pressure,
 B = characteristic dimension of the loaded area,
 E = Young's modulus,
 I = influence factor that is dependent upon the problem geometry.

If Poisson's ratio is incorporated in the influence factor, expression (262) can be re-written as

$$s_i = \frac{pB}{E_u} I, \tag{263}$$

where E_u means the undrained modulus of elasticity.

D'APPOLONIA *et al.* (1971) proposed taking the initial *in situ* shear stress also into account and to modifying the value gained from expression (263) as a function thereof. Three characteristic sections can be identified on the idealized q vs. s_i curve (Fig. 213):

1. a linear segment OA where s_i is proportional to load (elastic settlement);

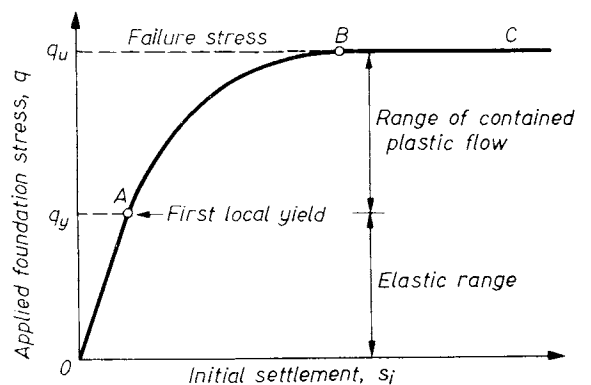


Fig. 213. Idealized load–initial settlement curve (D'APPOLONIA *et al.*, 1971)

2. a non-linear segment *AB* commencing when the shear stress becomes equal to the shear strength at some point in the soil mass (local yield);

3. a horizontal segment *BC*, representing the failure of the foundation at the ultimate bearing stress, q_u .

The linear portion of the curve can be obtained from an elastic analysis, requiring only the E_u modulus and the problem geometry to be known. The point *A* at which the first yield occurs can be estimated by determining the applied foundation stress required to induce failure at some point within the soil mass. To evaluate the segment *AB*, an analytical method is required that considers the plastic flow in the soil mass. Finally, the ultimate bearing stress q_u can be obtained from a stability analysis using the average undrained shear strength. For simple problem geometries and soil conditions, an explicit expression is available for q_y . The safety factor f beyond which local yield first occurs below a strip footing is plotted in Fig. 214 as a function of an initial *in situ* shear stress before any external load is applied and of the undrained shear strength s_u .

$$f = \frac{\bar{\sigma}_{vo} - \bar{\sigma}_{ho}}{2s_u} = \frac{1 - K_0}{\frac{2s_u}{\bar{\sigma}_{vo}}}, \quad (264)$$

where $\bar{\sigma}_{vo}$ = the initial vertical effective stress,
 $\bar{\sigma}_{ho}$ = the initial horizontal effective stress,
 K_0 = the coefficient of lateral earth stress at rest.

Further on the authors suggested to use an S_R settlement ratio which has been validated for various q/q_u and H/B ratios (H being the thickness of the layer) by means of the finite element method (Fig. 215). In this sense the calculation will proceed in the following steps:

1. Estimate the value E_u and f from laboratory or field tests.
2. Perform an undrained stability analysis to obtain the ultimate bearing capacity and hence the applied stress ratio q/q_u at the working load.
3. Estimate the elastic initial settlement s_i from conventional elasticity theories.
4. For the computed values of q/q_u and f , use Fig. 215 to obtain the settlement ratio S_R .

The initial settlement is then computed as:

$$q_i = s_i/S_R. \quad (265)$$

The validity of Eqs (262) and (263) has also been commented by other researchers. The influence of the safety factor on the initial settlement of an embankment on clay has been recognized by Pusch, who suggested the introduction of a correcting factor equal to

$$1 + \frac{1}{F} \quad (266)$$

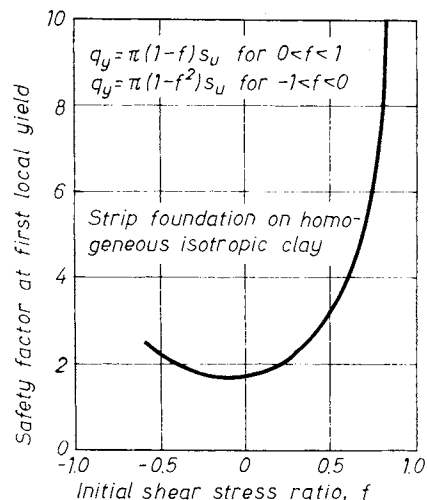


Fig. 214. Safety factors at which local yield first occurs under strip foundations (D'APPOLONIA *et al.*, 1971)

and by MÉNARD, who suggested a factor in the form of

$$\beta = \frac{2}{3} \frac{F}{F - 1}, \quad (267)$$

which implies that the computed elastic settlement has to be increased when the safety factor is less than 3.0.

Some authors point it out that observed initial settlement was beyond that calculated and infer that the cause was probably the pore water which had already begun to dissipate in this phase.

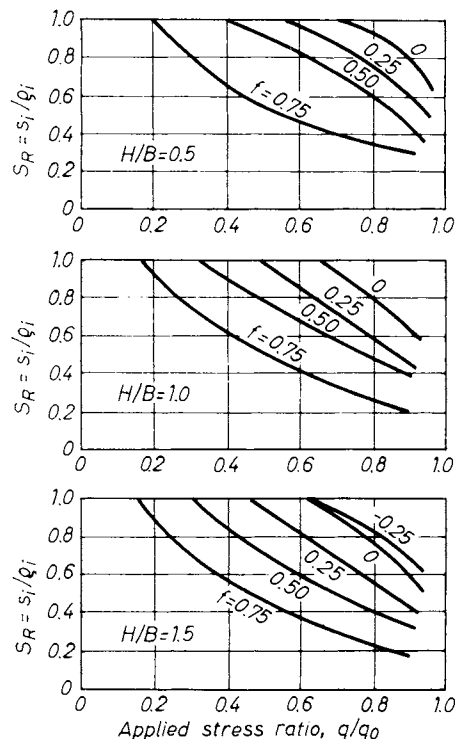


Fig. 215. Relationship between settlement ratio and applied stress ratio for strip foundations on homogeneous isotropic elastic layer (D'APPOLONIA *et al.*, 1971)

TAVENAS and LEROUËIL (1980) call attention to overconsolidated clays which — beyond a certain load — begin to behave like normally consolidated clays, whereby the process of consolidation is not “homogeneous”.

DAVIS and POULOS (1968) — similarly to the calculation of the primary settlement, cf. Section 2.3.2.2 — suggest involving σ_x and σ_y stresses in the calculation. In this way the initial settlement might be calculated from the formula:

$$s_i = \sum \frac{\sigma_z + 0.5 (\sigma_x + \sigma_y)}{E_u} \Delta z. \quad (268)$$

Several authors express the opinion that s_i is identical to the settlement which occurs during construction. SIMONS and SOM (1970) analyzed 12 case records of settlement of major structures on over-consolidated clays and quote a range of values for the ratio of settlements at the end of construction to the total settlements as 0.32 to 0.74, with an average of 0.58. MORTON and AU (1974) have studied eight case records of buildings on London clay and quoted a range of 0.4 to 0.82 with an average of 0.63. BRETH and AMANN (1974) reported similar results for Frankfurt clays. Fig. 216 shows the results of settlement surveys on Hungarian buildings; the diagram is plotted as a function of q/t_c , where t_c means the time period of the construction.

A quick loading may introduce serious problems in the case of silos, as it has demonstrated the analysis of measured settlements of 19 Hungarian silos (RÉTHÁTI, 1977). These objects were founded on slabs of 300 to 670 m² surface area (four of them on 1200 to 4160 m²). The average contact pressure was 127 kN/m² for dead load rising to 311 kN/m² when the silos were fully loaded (the ratio is 1 : 2.45). Registered average settlement under the dead load was 3.48 cm, and it rose 21.14 cm when the live load was effective. Here the ratio is 1 : 6.07, indicating an extremely great deviation from the previous ratio of contact pressures. This cannot be attributed to the sole fact that in higher ranges of pressures the relation between q and s ceases to be linear. The cause of this phenomenon should be clear when the ratio of total load (s_t) to dead load (s_c) is grouped by soil types:

Soil type	n	$\bar{\sigma}_c$	$\bar{\sigma}_t$	$(s_t/s_c)_{av}$
Granular (and mixed)	6	1.32	4.53	3.88
Transitional	4	1.95	16.03	7.79
Cohesive	9	5.61	34.30	6.97

The different behaviour of granular and cohesive soils can be recognized also from the curves s and t in Fig. 217. In every case when the subsoil consisted of cohesive layers the settlement vs. time curve shows a characteristic break not far behind the instant when the transfer of loads begins. A similar event appears in the case of transitional

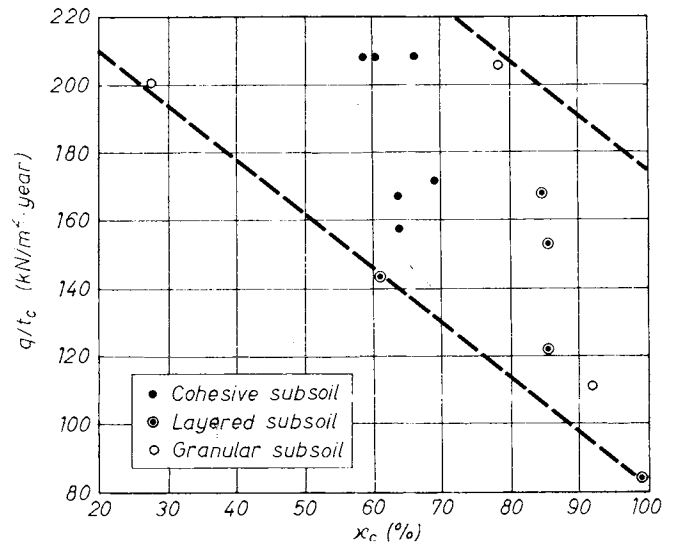


Fig. 216. Degree of consolidation up to the end of construction (K_c), according to surveys made in Hungary

soils as well, but none of these features is manifested on granular soils. (These surveys call attention to the need of keeping the rate of loading at an acceptable level, and of arranging a schedule of loading in advance and adhering to it.)

2.3.2.2 Primary compression

Primary compression (consolidation) is understood to be a process in which the pore-water dissipates from the soil mass continuously under the effect of the loading pressure until equilibrium — governed by hydraulic boundary conditions — is restored. During the process the effective stress ($\bar{\sigma}$) increases uninterruptedly at the expense of the neutral stress (u), so that at every minute and at every point of the compressed mass the equality $\sigma = \bar{\sigma} + u$ prevails.

The problem of one-dimensional compression (consolidation) has been solved by TERZAGHI (1923). The settlement in this case can be found from the equation:

$$s = \int_0^z m_v \Delta u dz,$$

where Δu = the excess pore-water pressure, identical with the effective vertical pressure, on the layer.

m_v = the coefficient of volumetric compressibility (the invert of the modulus of compressibility E_s). It can be determined by an oedometer, i.e. in a device in which sideward displacement of the sample is restricted.

The settlement for a given situation can be determined by dividing the stress diagram (σ_z) into

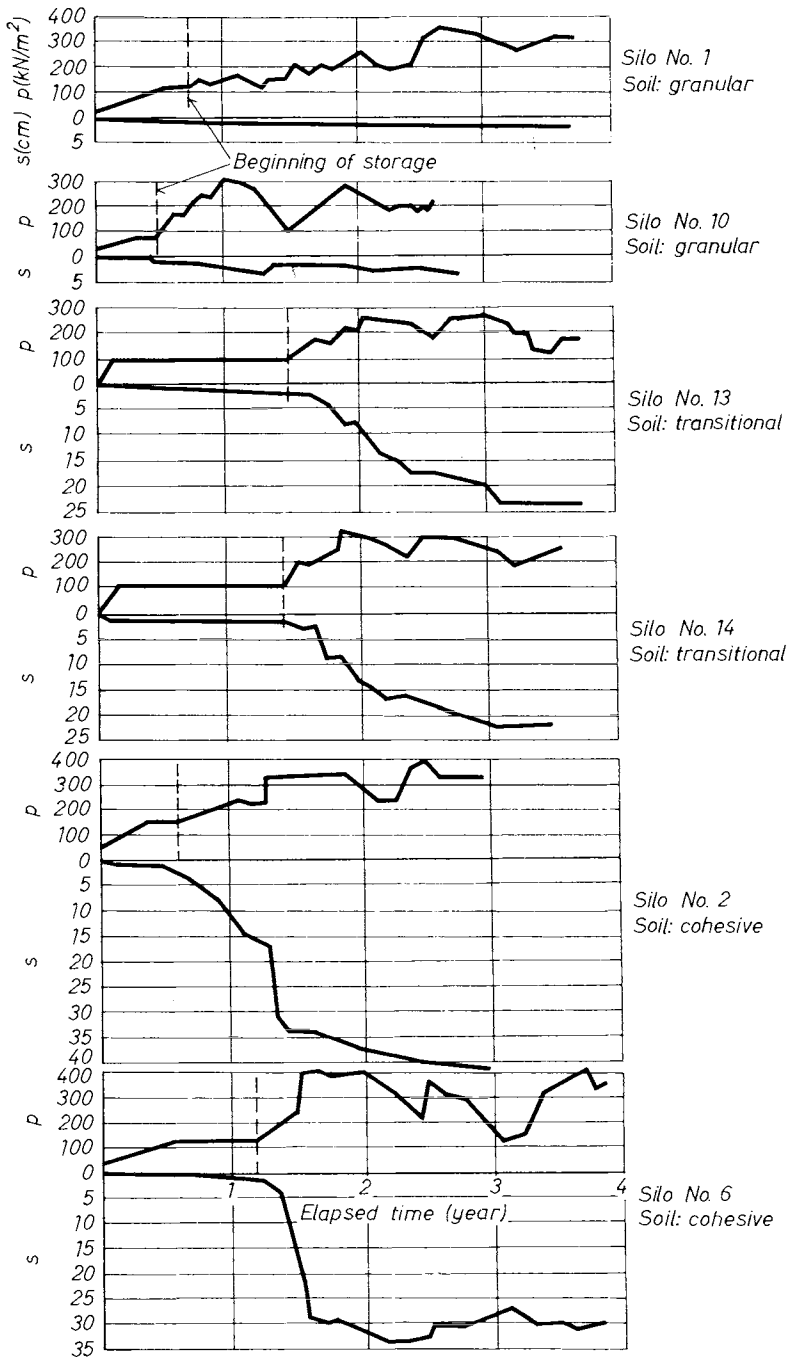


Fig. 217. Time-settlement curves as measured at silos on various soils (RÉTHÁTI, 1977)

n parts, and computing the sum given by:

$$\sum_{i=1}^n \sigma_{zi} \cdot m_{vi} \cdot \Delta z_i, \quad (269)$$

where Δz_i = means the thickness of the i -th slice,
 σ_{zi} = the vertical stress at the centerline of the i th slice,
 m_{vi} = the coefficient of volume compressibility in that point.

(As the relation between σ and ϵ is not linear m_v varies according to the stress applied — increasing with the stress — because the sideward movement

is obstructed.) The vertical stress — i.e. its influence — should be counted up to the level of the stiff layer, or to the depth limit mentioned in Section 2.2.6.

Terzaghi's procedure gives acceptable results only when

- the thickness of the compressible layer is small in relation to the size of the footing, and/or it is at a great depth; and
- a reliable sample can be tested in the oedometer, or the test can be substituted by some other suitable method.

Since the 1950's many authors have remarked that the use of one-dimensional methods for thick beds of compressible soils is inaccurate since substantial lateral displacement can occur. SKEMPTON, PECK and MACDONALD (1955) recognized that the undrained settlement $s_v (= s_i)$ can be significant and by accepting that the total settlement s_t is equal to s_{od} they suggested that the consolidation settlement was given by

$$s_c = s_{od} - s_u \tag{270}$$

SKEMPTON and BJERRUM (1957) proposed a new method for estimating s_c by applying a correction factor μ to s_{od} to take account of the magnitude of the pore pressure set up beneath the foundation during undrained loading and which is dissipated during consolidation. The total settlement is therefore given by

$$s_t = s_u + \mu s_{od} \tag{271}$$

The authors suggested to introduce

$$\mu = [A + I(1-A)], \tag{272}$$

where A is the pore-water parameter as suggested by SKEMPTON, and I is a function of L/B in the following sequence:

L/B	0	0.25	0.5	1	2	4	10	∞
I	1.0	0.75	0.53	0.37	0.26	0.20	0.14	0

SKEMPTON (1957) suggested that in due course settlement analysis would probably be carried out by means of triaxial tests in which appropriate principal stresses are applied first under undrained conditions and then allowing for drainage. This is the basis of the stress path method of LAMBE (cf. Section 2.3.3) and a variation of this method has been proposed by DAVIS and POULOS (1968) with similar approach to that by KÉRISEL and QUATRE (1968).

Following the procedure suggested by the latter authors, the first step to be taken is to let the sample reconsolidate, this means that the stresses $\sigma_1 = \sigma_g$ and $\sigma_x = K_0 \cdot \sigma_1$ should be applied to imitate the original (*in situ*) condition of the sample. The next step is to apply the deviator stress $\sigma_1 - \sigma_3$ to the sample (which correlates with the external load) and record the relative deformation, the volume of expelled water, and the pore-water pressure. When these data are known, the three phases of settlement can be separated from each other. As can be observed in Fig. 218 the rate of settlement and that of the squeezing water are not congruent, which is a consequence of the initial settlement. In the case of a rectangular footing, two tests are needed (as $\sigma_2 \neq \sigma_3$), one with the deviator stress $\sigma_1 - \sigma_2$, and the other with $\sigma_1 - \sigma_3$. The true relative deformation might be expected between the two values.

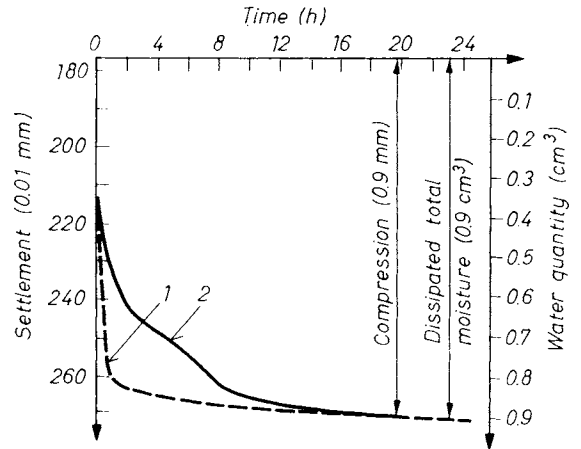


Fig. 218. Distinction between settlements relating to initial and primary consolidations during the evaluation of triaxial test results (KÉRISEL and QUATRE, 1968): 1 — settlement; 2 — dispelled water

By using the formula below the Poisson ratio is also predictable from the Kérisel-Quatre theory

$$\nu = \frac{\epsilon_3 \Delta\sigma_1 - \epsilon_1 \Delta\sigma_3}{2 \epsilon_3 \Delta\sigma_3 - \epsilon_1 (\Delta\sigma_1 + \Delta\sigma_3)} \tag{273}$$

where $\Delta\sigma_1$ and $\Delta\sigma_3$ = are the increments of principal stresses,
 ϵ_1 and ϵ_3 = deformations as activated by the above (the value of ϵ_3 can be calculated from ϵ_1 and the volume of water expelled).

The problem can only be solved by using sequential iteration. An initial value should be assumed for ν — the authors suggested taking $\nu = 0.25$ at the beginning — to enable the calculation of σ_3 from σ_1 . Should the ν assumed deviate substantially from that which can be calculated from Eq. (273), the test should be repeated using the stress σ_3 calculated from latter ν -value.

DAVIS and POULUS (1968) proposed for the three-dimensional situation, calculating the total settlement $s = s_{TF}$ from the formula:

$$s_{TF} = \sum \frac{1}{E'} [\sigma_z \nu' (\sigma_x + \sigma_y)] dz \tag{274}$$

where E' and ν' relate to the soil skeleton. As the calculation of the one-dimensional settlement s_{od} corresponds to the case of $\nu = 0$, and the relation of E — the modulus of compressibility which was used for its calculation — to E' can be described as

$$E = \frac{1}{m_v} = \frac{E' (1 - \nu')}{(1 + \nu') (1 - 2\nu')} \tag{275}$$

it can be seen that the ratio s_{od}/s_{TF} depends primarily on the Poisson ratio. This proportionality is represented on Fig. 219 (insert a) for a uniformly loaded circular footing which rests on an elastic underground. Thus, the one-dimensional approach

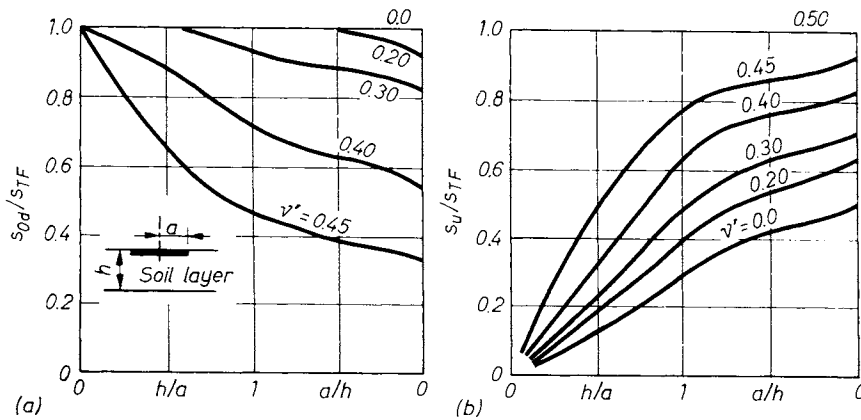


Fig. 219. Error incurred (a) by estimating the settlement from the one-dimensional approximation (s_{0d}), (b) the ratio of the initial (s_u) to the total (s_{TF}) settlement as a function of POISSON'S ratio (DAVIS and POULOS, 1968)

is allowable when $v' \leq 0.25$ but begins to diminish essentially thereafter, and the more so as the thickness of the layer becomes greater in relation to the diameter of the circular footing.

DAVIS and POULOS (1968) analyzed the initial settlement as well (cf. Section 2.3.2.1). The value s_u will be defined by using the elastic displacement theory by putting

$$E = E_u = 3 E' \frac{1}{2(1 + v')} \text{ and } v = v_u = 0.5.$$

The ratio s_u/s_{TF} is plotted in Fig. 219b for the same conditions as in Fig. 219a. Two expected trends are apparent: the initial settlement contributes to the total final settlement to a much higher proportion when v' is high, and the initial settlement is relatively small for shallow layers. The authors' original article also describes a procedure for the determination of E_u .

2.3.2.3 Secondary settlement

Secondary compression (consolidation) due to viscous deformations can be described according to experimental result by the logarithmic function:

$$s_{sec} = \frac{H}{1 + e_0} C_\alpha \log \frac{t_i + t}{t_i}, \quad (276)$$

where C_α = coefficient of secondary consolidation,
 H = thickness of the layer,
 t_i = time when the secondary consolidation begins.

It has not yet been made clear when the secondary consolidation begins: should it be at the instant at which the primary compression settlement terminated, or should it be placed before that time?

ZEEVAERT and VOGEL (1953) combined Eq. (276) with the primary settlement in the form:

$$s = \left[m_{va} + m_t \log \frac{t}{t_a} \right] \cdot H \Delta p, \quad (277)$$

where $m_{va} \cdot H \cdot \Delta p = s_a$ represents the primary compression settlement which occurred up to time t_a . As the curves describing the two sections of consolidation have to share a common tangent at their meeting point, i.e.

$$\frac{\partial s_1}{\partial t} = \frac{\partial s_2}{\partial t}, \quad (278)$$

the process of secondary compression settlement has to begin before the primary process has ended (i.e. while $\alpha < 100\%$).

After having scrutinized the data from several settlement surveys, JEGOROV and BUDIN (1981) suggested propagating the use of the relationship:

$$s = s_0 + A \ln(1 + Bt), \quad (279)$$

where s_0 means the settlement measured at the end of construction.

The reality implied in Eqs (276) and (279) is further supported by two other circumstances:

(a) the one-dimensional consolidation can be described, in the realm of $\alpha = 0.526$ to 1 by the expression

$$k = 1 - 10^{-\delta_i - \beta}; \quad (280)$$

(b) according to experimental observations, the measured settlement might be successfully extrapolated by using exponential functions (cf. Section 2.3.4.3).

The coefficient C_α can be determined from long-term oedometric laboratory tests. It is also customary to accept C_α as a given portion of C_c . COX (1981), for example, made the suggestion to take $C_\alpha = 0.045 C_c$ for virgin consolidation and $C_\alpha = 0.015 C_c$ in the overconsolidation range.

2.3.2.4 Settlement of bases on granular underground

Deformation of granular soils cannot be properly determined on the basis of laboratory tests. Investigation and testing procedures made *in situ* can provide some information, first of all the Plate Loading Test, the Standard Penetration Test and the Static Cone Test, but useful information can also be acquired from settlement survey data of nearby buildings as well. Forecasting methods are described in Section 2.3.4. but it can be emphasized already at this point that really reliable methods have as yet not been developed.

2.3.3 Allowance for the state of stress

Vertical deformations of the soil and consequent settlements of the structures supported by it depend not only on the magnitude of the stresses transmitted, but also on the method by which these are imposed. As a means of visualizing this method, "stress-paths" have been advanced by LAMBE (1964) and the stress-path curves permit this effect to be studied (cf. Vol. 1, Section 7.6.3). The stress-path curve is understood as a sequence of Mohr's circles describing the variation of the state of stress. Any Mohr's circle of stress is defined by two coordinates (Fig. 220), namely

$$\left. \begin{aligned} p &= \frac{\sigma_1 + \sigma_3}{2}; \bar{p} = \frac{\bar{\sigma}_1 + \bar{\sigma}_3}{2} \\ q &= \frac{\sigma_1 - \sigma_3}{2}; \bar{q} = q. \end{aligned} \right\} \quad (281)$$

As can be seen, total and effective stresses may equally well be used. An example is given in Fig. 220a. The soil sample was first under hydrostatic pressure (point 1), then the first principal stress was increased (line 1-2-3) and finally the third principal stress was reduced (line 3-4). The stress-path 1-2-3-4 is a single-line substitute for the number of circles and presents a clear picture of the changes.

Let us now trace the stress-path for an oedometer test (LAMBE, 1964). The stress circles are shown in Fig. 221a. The initial condition is represented by point A, where the neutral stresses are zero. Increasing the load, the total stress will also increase and as long as there is no volume change, the shear stress will remain unchanged. For this reason, the line AB is horizontal and the diameter of the circle remains the same. The total stress increment $\Delta\sigma_1$ is thus reflected in the neutral stress.

After the load is applied (compression) consolidation starts and the diameter of the Mohr's circles of total stress increases (points C and D). The total vertical stress remains constant. The line A-B-C-D is thus the stress-path traced on the basis of total stresses. The line AFD is the path of effective stresses, as will be readily perceived. The line OD

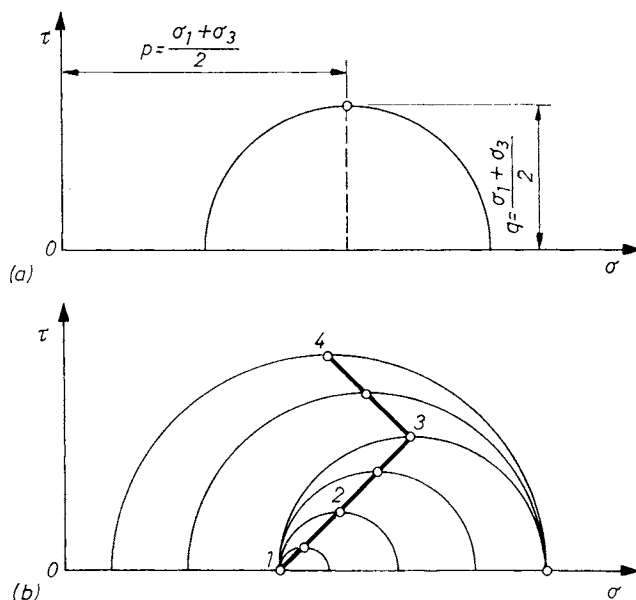


Fig. 220. a — Drawing the Mohr's circle of principal stresses for two values p and q ; b — stress-path of an experiment

is that of static pressure. The angle β is given by the expression

$$\tan \beta = \frac{1 - K_0}{1 + K_0} \quad (282)$$

The deformations can be plotted on the same (σ, τ) diagram. A series of triaxial tests of the consolidated, undrained type will yield compression curves resembling those shown in Fig. 222. If the coefficient of static pressure is available from other tests, the lines pertaining to identical deformations can be traced from the curves and used in settlement calculations. Before describing the process involved, attention is called to Fig. 223, in which the deformations produced by different loads have been plotted, assuming that the increment of the first principal stress was the same in each case. In the case where the hydrostatic pressure was the initial condition (point E), the

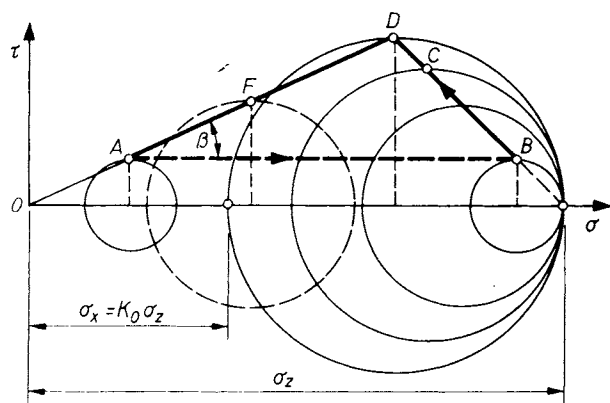


Fig. 221. Stress-path from an oedometer test

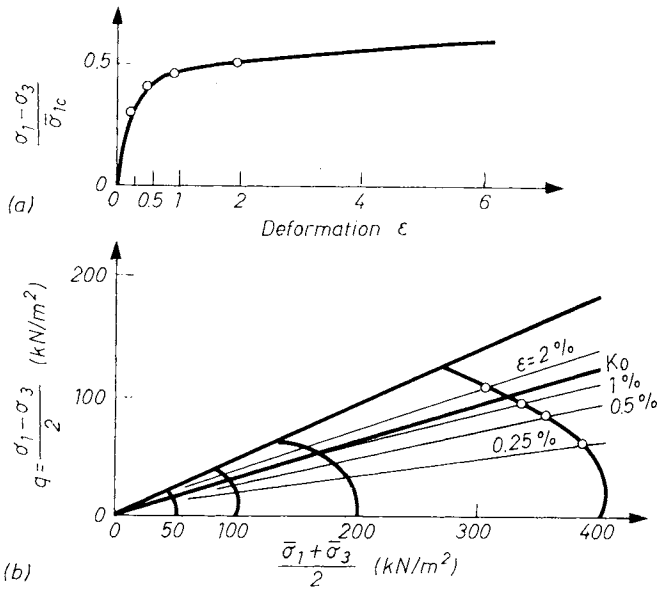


Fig. 222. a — Deformations; b — representation of equal deformations in the coordinate system p, q

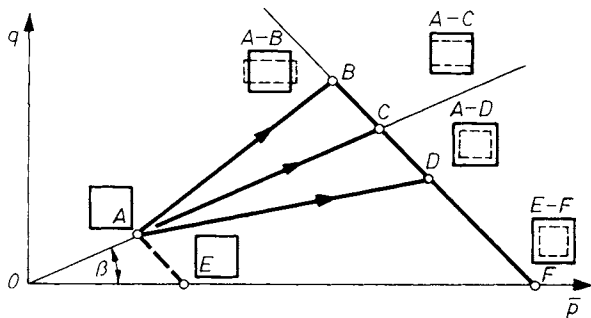


Fig. 223. Deformation patterns for various compressive testing methods

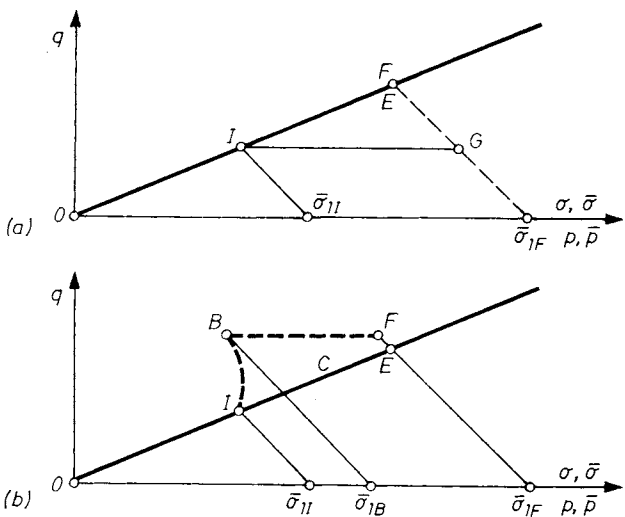


Fig. 224. Procedure for settlement calculations: a — assumption of one-dimensional consolidation; b — calculation using triaxial test results following the stress-path (LAMBE, 1964; 1967)

increase in hydrostatic pressure will cause uniform compression ($E-F$). A soil sample consolidated in the oedometer (or an element of a normally consolidated clay layer) is in the state of static pressure (point A). A stress-path following the line of static pressure produces compression (line $A-C$) in the vertical direction. In the case of the stress-path $A-D$, the lateral displacement is compression, while in that of AB it is expansion.

The question arises as to how these graphs can be used in settlement calculations. Two methods will be demonstrated (Fig. 224), the first of which is substantially already known. Settlement is assumed here to result from one-dimensional consolidation and the initial value of excess pore-water pressure to equal the increment vertical stress. The initial settlement is then zero, whereas the consolidation settlement is found from the deformation curves (see Fig. 222b) along the line K_0 , from the section IF (Fig. 224a). The initial value of excess pore-water pressure is given by the section IG . This is thus the simple, familiar approximate method.

Before the second method can be applied (Fig. 224b), a triaxial test is performed in the laboratory, according to the stress-path IBF , where BF represents the excess pore-water pressure. The initial settlement depends on IB , while its consolidation counterpart depends on BF .

The total settlement is found by multiplying the corresponding total strain obtained on the sample by the thickness of the clay layer.

Allowance for the actual spatial stress distribution around a foundation can also be made in a settlement computation using the method suggested by SKEMPTON and BJERRUM (1957), in which the pore-water pressure coefficients of SKEMPTON are involved (cf. Vol. I, Section 5.3, Eq. (5.3)).

A load placed on the surface of a soil layer will produce excess pore-water pressure at various points within the soil. The total principal stresses will be increased by $\Delta\sigma_1, \Delta\sigma_2$ and $\Delta\sigma_3$. Assume the soil to be saturated, i.e. B equals unity. The state of plain strain will be considered first, followed by the axial-symmetrical strain, i.e. the settlement of the centerline of a strip footing and of the center of a circular plate will be determined.

The effective vertical stress is increased due to the load by

$$\Delta\bar{\sigma}_1 = \Delta\sigma_1 - u.$$

The effective stress acting in the vertical plane of symmetry is

$$\Delta\bar{\sigma}_{2,3} = \Delta\sigma_{2,3} - u.$$

At the center, the consolidation settlement due to the gradual decrease of pore-water pressure is given as

$$y_k = \int_0^z u \frac{a_s}{1 + e_0} dz. \quad (283)$$

The pore-water pressure is found with the help of the pore-water pressure coefficients. The soil being saturated, $B = 1$ and thus for the case of a circular plate, where $\Delta\sigma_2 = \Delta\sigma_3$, we have

$$u = \Delta\sigma_3 + A(\Delta\sigma_1 - \Delta\sigma_3) = A \Delta\sigma_1 + (1 - A) \Delta\sigma_3. \tag{284}$$

In the case of a strip of infinite length, in plain strain, $\sigma_2 = \frac{1}{2}(\sigma_1 + \sigma_3)$, so that

$$u = \Delta\sigma_3 + \left[\frac{\sqrt{3}}{2} \left(A - \frac{1}{3} \right) + \frac{1}{2}(\sigma_1 - \sigma_3) \right] = N\Delta\sigma_1 + (1 - N)\Delta\sigma_3, \tag{285}$$

where

$$N = \frac{\sqrt{3}}{2} \left(A - \frac{1}{3} \right) + \frac{1}{2} = 0.866 A + 0.211. \tag{286}$$

If the settlement is calculated from the results of a compression test (from the compression curve), then assuming one-dimensional consolidation, the settlement becomes

$$y'_k = \int_0^z \Delta\sigma_1 \frac{a_v}{1 + e_0} dz. \tag{287}$$

The value of u is introduced from Eqs (284) or (285) into Eq. (283) to obtain y_k . The ratio of y_k to y'_k is μ , so that

$$y_k = \mu y'_k. \tag{288}$$

μ is a dimensionless number, a function of A and of the basic dimension related to the thickness of the compressible layer. For a circular plate

$$\mu_{\text{circle}} = \frac{\int_0^z [A\Delta\sigma_1 + (1 - A)\Delta\sigma_3] \frac{a_v}{(1 + e_0)} dz}{\int_0^z \Delta\sigma_1 \frac{a_v}{(1 + e_0)} dz}. \tag{289}$$

The value of μ_{strip} is found from the above expression if A is replaced in Eq. (289) by N , cf. Eq. (286).

In the cases where the compressibility of the soil and the coefficient A are constant, from Eq. (289)

$$\mu_{\text{circ}} = A + \alpha(1 - A) \tag{290}$$

or

$$\mu_{\text{strip}} = N + \alpha(1 - N), \tag{291}$$

where

$$\alpha = \frac{\int_0^z \Delta\sigma_3 dz}{\int_0^z \Delta\sigma_1 dz}.$$

The magnitude of α is thus seen to be dependent on the geometrical dimensions alone. Once the stresses have been calculated with the help of the theory of elasticity, α can be determined and the correction factor can be plotted against A . The resulting diagram is shown in Fig. 225. The settle-

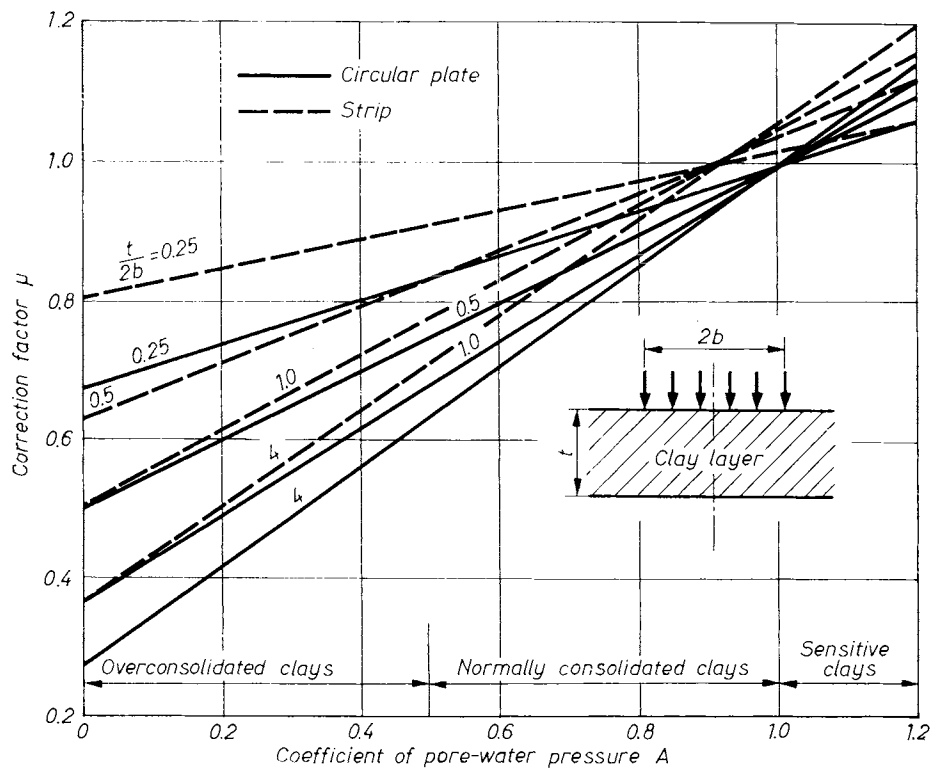


Fig. 225. Correction factor for consolidation settlement as a function of the pore-water pressure coefficient

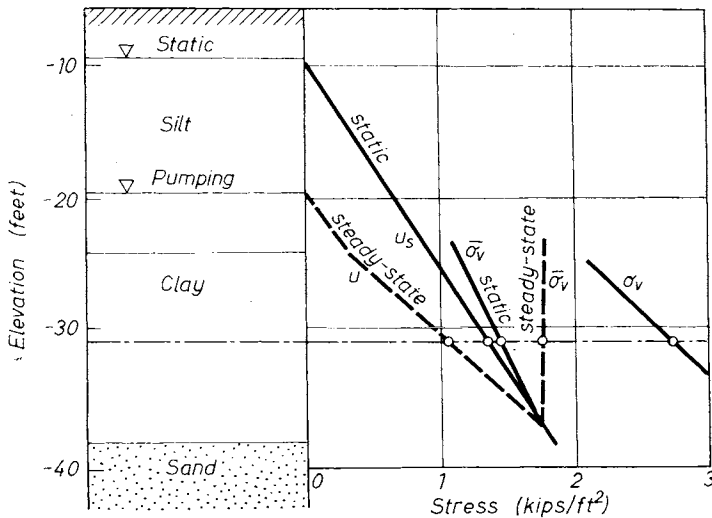


Fig. 226. Stresses associated with lowering and raising the water table (LAMBE, 1967)

ments of strip- and circular footings transmitting a uniformly distributed pressure to the soil, which thus cause two- and three-dimensionally stressed states, can thus also be found on the basis of the compression curve of an oedometer test. To do this, the values obtained by assuming unconfined conditions must merely be multiplied by the correction factor μ found from Fig. 225. Of course, μ cannot be found unless the value of A is known.

This correction should, however, be applied with care, since A is difficult to determine and the estimate of preconsolidation may be very inaccurate. In unsaturated soils the significance of the correction is but imperfectly understood.

The principle and the advantage connected with the use of the "stress-path" method are well demonstrated on an example given by LAMBE (1967).

Figures 226 and 227 show the stresses and strains associated first with the lowering and then the raising of the water table in the profile shown. Initially, the phreatic surface is at -9.5 ft. It is then lowered over a large lateral area to -19.5 ft and kept at that depth until vertical steady-state flow exists. Pumping is then stopped and groundwater conditions gradually returned to static. The distributions of pore pressures for these two equilibrium conditions are shown in Fig. 226.

Mid-depth of the clay has been taken as the "average" point. Actually this is slightly above mid-depth since the stress versus strain curve of the clay is not a straight line. In other words, slightly larger strains occur in the upper part of the clay for a given stress increment than would

occur in the lower part, because the initial effective stress in the upper part is less.

The distribution of pore pressures shown in Fig. 226 is based on the following conditions:

1. no total head is lost in the silt above the clay or the sand below the clay,

2. the permeability of the clay is constant with depth, thereby giving a constant gradient and straight line distribution of pore pressure at the equilibrium condition.

The dewatering causes a reduction in pore pressure and, therefore, an equal increase in effective stress, because the total vertical stress remains constant. Since the dewatering occurs over a large lateral area, the horizontal strains must be equal to zero, i.e. a K_0 condition exists. As shown in Fig. 227, the effective stress-path lies along the loading K_0 line going from A to B for the dewatering, and along the unloading K_0 line from B to F when groundwater conditions again become static. The total stress path lies along a line of constant vertical stress, going from C to D with the dewatering and from D to E when groundwater conditions return to static. As can be seen from Fig. 227 the vertical total stress remains constant and the lateral total stress drops during the dewatering. The horizontal distance AC equals FE , which equals the static pore pressure at the centre of the clay, and BD is equal to the pore pressure under steady-state vertical flow.

At the right in Fig. 227, the results are shown of a stress-strain test along the stress-path for the field conditions. Since the loading and unloading

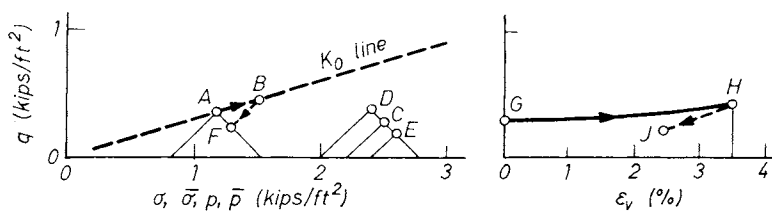


Fig. 227. Effective stress-path and strain for lowering then raising the water table (LAMBE, 1967)

is K_0 , the oedometer test is appropriate for this problem. The vertical strain during groundwater lowering is from G to H , i.e. 3.5%, and HJ for the return to static conditions, i.e. -1%. Multiplying the compressive strain of 3.5% by the thickness of the clay of 14 ft gives a component of settlement from compression in the clay equal to 0.49 ft. The clay expands $14 \times 1\%$ equal to 0.14 ft.

2.3.4 Prediction of settlement on the basis of field observations and surveys

2.3.4.1 Settlement analysis on the basis of loading tests

Some version of model rule or the modulus of compressibility as calculated from the deformation curve can be used to determine anticipated settlement from the results of loading tests.

U.S. Standard Load Bearing Tests are performed on a square plate of 30 cm sides. TERZAGHI and PECK presented the following empirical relationship for use in the case of sands:

$$s = s_p \left(\frac{2B}{B + \sqrt{0.3}} \right)^2, \tag{292}$$

- where B = length of the footing, m,
- s = expected settlement of the footing, cm,
- s_p = registered settlement during the loading test under the design pressure, cm.

In recent years the validity of this formula has been criticized by scientists. BJERRUM and EGGESTAD (1963) after the detailed examination of test results of 46 loading tests described in the literature — which were supported by settlement surveys — reduced each loading surface to 0.1 m², and concluded that the points representing dense sands fell well below the boundary line in the diagram with the coordinates s/s_p and B/B_0 (as defined in Eq. (292)), but that the plots of loose sands were above that line.

According to BARATA (1973) Eq. (292) gives uncertain results because the variation with E_s is

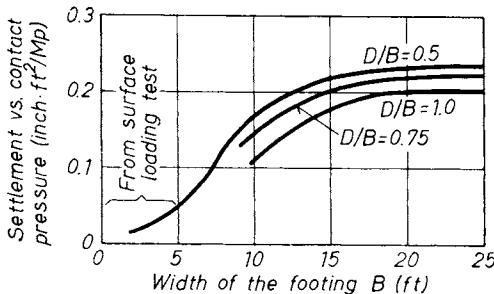


Fig. 228. Settlement of footings in sand as a function of width (B) and depth of the foundation (D'APPOLONIA and BRISETTE, 1968) (1 ft = 0.3048 m, 1 in = $25.4 \cdot 10^{-3}$ m)

neglected. To give way to this concept, namely that generally E_s varies according to depth, the use of the HOUSEL (1929) and BURMISTER (1947) formula would be amenable

$$\frac{s}{s_p} = \frac{B}{B_0} \cdot \frac{E_{00} + CB_0}{E_{00} + CB}, \tag{293}$$

- where E_{00} = modulus of compressibility at the foundation level,
- C = depth increment of the above modulus per cm.

Should the soil be homogeneous, i.e. $C = 0$, the formula becomes:

$$\frac{s}{s_p} = \frac{B}{B_0} \tag{294}$$

and so the settlement will increase linearly according to the side length of the footing which is naturally in full coincidence with the expression deduced on the basis of the theory of elasticity which states:

$$s = \frac{\pi(1 - \nu^2) \sigma D}{4 E}, \tag{295}$$

where D is the diameter of the circular footing.

D'APPOLONIA and BRISETTE (1968) presented the relation illustrated in Fig. 228, which has been conceived on the basis of settlement surveys on about 300 buildings. The main conclusions to be drawn therefrom, are:

- (a) if $B \geq 4.5$ m, an increase of the width of the footing will not increase the settlement;
- (b) increasing the depth of the foundation (i.e. the ratio D/B) a slight decrease in s would result; for example, when $B = 4.5$ m, the ratio of the settlement relating to $D = 0$ and $D = B$ attains 1 : 0.75;
- (c) the increase of soil compressibility with B is greater between $B = 3$ to 6 m, as was supposed by TERZAGHI and PECK (1948).

RUDNICKII (1968) measured the settlements of strip foundations of 20 and 30 cm width lying on sand and deduced the following correlation:

$$\text{for } D = 0 \quad s = 0.013 B \left(\frac{P}{B\gamma} \right)^{1.62}, \tag{296}$$

$$\text{for } D = B \quad s = 0.008 B \left(\frac{P}{B\gamma} \right)^{1.44}. \tag{297}$$

2.3.4.2 Settlement analysis on the basis of penetration tests

Both static and dynamic probing (penetration) procedures are suitable for the prediction of expectable settlements.

Using static probes, the settlement can be estimated from the expression:

$$s = \sum \frac{h}{C} \log \frac{\sigma_g + \sigma_z}{\sigma_g} \quad (298)$$

The coefficient of compressibility C can be taken from the experimental formula:

$$C = 1.5 \frac{C_{kd}}{\sigma_g} \quad (299)$$

where C_{kd} represents the cone-resistance (in $\text{kp/cm}^2 = 100 \text{ kN/m}^2$).

From among the dynamic penetration methods, empirical formulas have been deduced for the calculation of the expectable settlement when the Standard Penetration Method is used. That given by TERZAGHI and PECK (1948) is written as:

$$s = C_w C_d \frac{3P}{N} \left(\frac{2B}{B+1} \right)^2, \quad (300)$$

where N = number of blows,
 B = width of the footing
 C_w = depends on the depth of the groundwater below the footing (D_w) and its value is
 $C_w = 1$ when $D_w \geq 2B$, or
 $C_w = 2$ when $D_w \leq B$,
 C_d = coefficient of depth, obtained from the formula:

$$C_d = 1 - \frac{D}{4B} \quad (301)$$

Field observations have revealed that Eq. (300) gives overestimated values for s . Therefore, MEYERHOF suggested that 2 should be written in the nominator, instead of 3, and $C_w = 1$ should be applied uniquely, because, as the author emphasizes, the result of the penetration test (the number of blows) includes in itself the influence of the groundwater.

PECK and BAZARAA further refined the procedure, mainly by suggesting affixing modifying factors to the number of blows (N) and to put these modified values in the formula.

SCHULTZE and SHERIF (1973) compared the measured settlement of 48 buildings (all founded on sand) with those predicted on the basis of Standard Penetration Test results. Multiple regression analysis (where the multiple correlation coefficient of 0.938 was achieved!) resulted in the following expression for the prediction of the settlement s :

$$s = \frac{pf}{1.71 N^{0.87} \cdot \sqrt{B/B_1}} \cdot \frac{1}{(1 + 0.4t/B)} B, \quad (302)$$

where p = contact pressure, kp/cm^2 (but do not deduct $t\gamma$),

f = influence factor of the settlement,
 $B_1 = 1 \text{ cm}$,
 t = depth of foundation level.

The interesting feature in this expression is the linear relation between s and p which means that given identical underground conditions and footing geometry the modulus of subgrade reaction (k) does not vary with the load.

Measured settlements compared to those calculated by using Eq. (302) have shown a 40% standard deviation, which is a fair agreement. The authors pointed out that according to their calculation the settlement as calculated by the Terzaghi-Peck formula is overestimated.

2.3.4.3 Settlement analysis using the pressiometer method

By using Ménard's pressiometer, the total settlement is calculated as the sum of two partial deformations:

$$\frac{s}{p} = \frac{\alpha \lambda_1 r}{4.5 E_1} + \frac{1 + \nu}{3 E_2} r_0 \left(\lambda_2 \frac{r}{r_0} \right)^2, \quad (303)$$

where p = contact pressure,
 r = radius of the footing,
 r_0 = reference radius (30 cm)
 E_1 = modulus of deformation to the depth r ,
 E_2 = modulus of deformation in the realm of deviator stresses,
 λ_1 and λ_2 = shape factors,
 ν = Poisson's ratio.

This evaluation method is based on the supposition that the settlement is composed of two components: (a) volumetric change in the half sphere corresponding to the diameter of the footing; (b) shear displacement without volumetric change outside the half sphere.

The coefficient α is the indicator representing the influence of the width of the footing on the settlement:

$$\frac{s_2}{s_1} = \left(\frac{B_2}{B_1} \right). \quad (304)$$

For sands $\alpha = 0.25$, and for clays $\alpha = 0.67$ (according to the theory of elasticity it would be $\alpha = 1.0$).

MÜLLER (1972) evaluated the settlement of 11 buildings and experienced $\pm 20\%$ deviation between measured and pressiometer-predicted settlements.

2.3.4.4 Back-analysis of E_s from measured settlements

The method of calculation should be selected by taking the soil conditions and the method of measurement of the settlement into account. This latter may be realized by: (a) continuous instrumental measurements, or (b) a single levelling of

an originally horizontal structural part. In the following a few examples are shown to demonstrate the methodology of the calculations (RÉTHÁTI, 1981).

(a) Homogeneous stratification.

In the case when the load and the surface area of the foundations are identical, the procedure is the following, as described in this example. The mean settlement measured on 21 pillars of a hall was $\bar{s} = 27.0$ mm and the standard deviation $\sigma = 4.22$ mm. Therefore, the confidence limits for the settlement were (at a probability level of $\alpha = 0.05$)

$$s = 27 \pm 2.086 \frac{4.22}{\sqrt{20}} = 27 \pm 1.92 \text{ (mm)}$$

and for the modulus of compressibility:

$$\frac{F}{27 + 1.92} \leq E_s \leq \frac{F}{27 - 1.92},$$

wherein F is the area of the stress diagram. By replacing F , the probability by which the value of E_s falls between 10.3 and 11.9 MN/m² is 95%.

In the case of footings of different loadings and/or surfaces, one may proceed according to one of the following two methods.

1. The values of E_s should be calculated for each footing, and their mean value characterized by the standard deviation.

2. A correlation should be established between F and s (see later).

(b) Presence of one highly compressible layer.

In this case, the settlement should be brought into relation with the stresses aroused in the layer in question, and the deformation of the other layers should be neglected. The calculation will depend on how many equations to exhibit E_s can be written.

The strip foundation of the damaged building represented in Fig. 229 is 0.45 m wide and transfers a load of 146 kN/m. The strips rest on sand in the section along the cellars, and on a peaty clay ($w = 53\%$, $w_p = 38\%$) in the other sections. Levelling has shown $\Delta s = 2.7$ cm, and so:

$$E_s = \frac{F}{s} \approx \frac{F}{\Delta s} = \frac{0.0848}{0.027} = 3.14 \text{ MN/m}^2.$$

In Fig. 230 the schematic borehole profiles around a building which suffered a significant settlement ($\Delta s = 15$ cm) are illustrated. The location was on an abandoned bed section of the Danube which has been filled up with fine grained sand but veins of peat were merged with it. By having levelled the footings a relative settlement of Δs has been determined for each bore profile, and to them an F -value is assigned obtained from

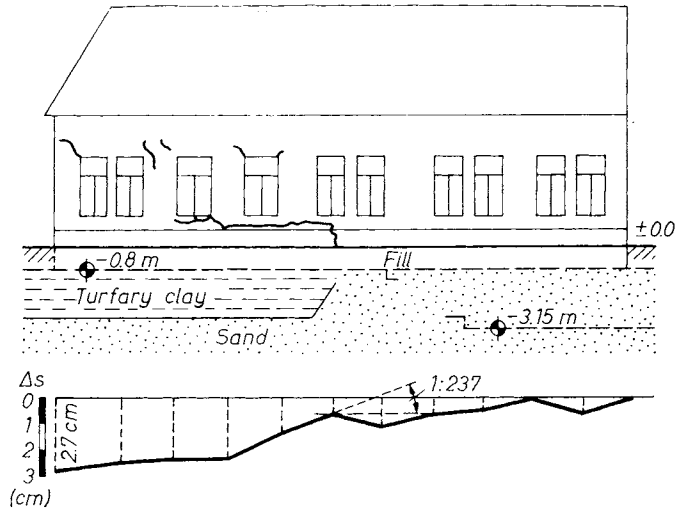


Fig. 229. Example on back analyzing the E_s -value from measured relative settlements; one of the layers is of high compressibility (RÉTHÁTI, 1981)

the summation of the areas in the stress diagram which were associated with the organic layers:

Borehole No.	F (kN/mm)	Δs (mm)	$E_s = F/\Delta s$
1	135.4	60	2.26
2	184.1	150	1.23
5	109.7	120	0.91
6	105.6	60	1.76

The equation of the regression line obtained for the two variables was:

$$\Delta s = 0.792 F - 8.4 \quad (r = 0.64).$$

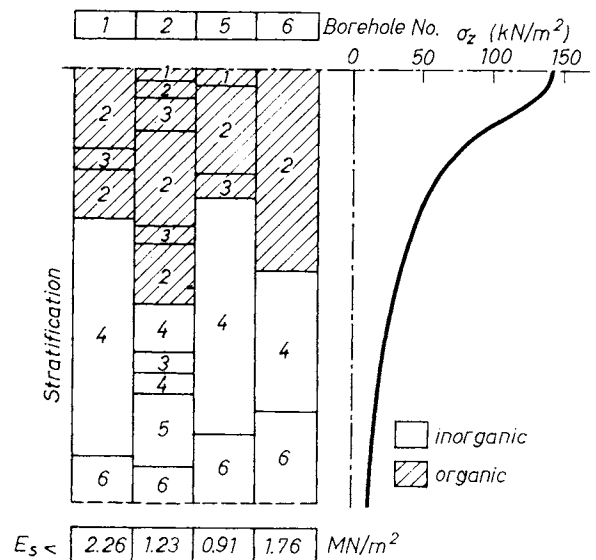


Fig. 230. Example on back analyzing the E_s -value from measured relative settlements; one of the layers is of high compressibility; four boreholes (RÉTHÁTI, 1981)

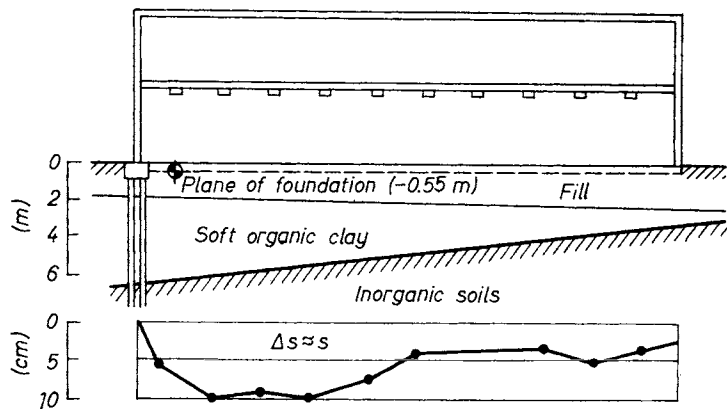


Fig. 231. Example on back analysing the E_s -value from measured relative settlements; two compressible layers (RÉTHÁTI, 1981)

Nos of the pillar	1	2	3	4	5	6	7	8	9	10
$\Delta s \approx s$ (mm)	107	98	103	82	42	41	49	56	41	30
v_1 (m)	1.3	1.35	1.35	1.35	1.4	1.4	1.45	1.5	1.55	1.6
v_2 (m)	3.1	2.85	2.6	2.4	1.95	1.7	1.45	1.15	0.9	0.8
F_1 (kN/mm)	58.7	59.7	59.7	59.7	60.7	60.7	61.7	62.7	63.7	64.7
F_2 (kN/mm)	37.2	34.7	32.8	31.1	26.6	23.6	20.6	16.7	13.4	11.9

From the intercept (-8.4) it can be stated with a probability of 90%, that it does not differ significantly from zero, wherefore $\Delta s \approx s$, i.e. the ratios $F/\Delta s$ may be considered to represent the E_s values of the organic layers. The average value and standard deviation for the four boreholes were obtained as:

$$E_s = 1.54 \text{ MN/m}^2 \text{ and } \sigma_E = 0.59 \text{ MN/m}^2.$$

The reciprocal of the slope of the regression line is 1.26, which is identical with the E_s defined with the aid of the least-square method.

(c) Two or more compressible layers

In this case there are two questions to be answered:

- which layer produces the decisive effect on the settlement (damage)?
- what is the characteristic modulus of compressibility of these layers?

Two examples will be shown to demonstrate how the model of the calculation can be selected.

The strip foundation supporting 12 pillars and the floor beams of a hall failed in about a year after construction, and rather wide cracks appeared in the partition walls. The foundation ($B = 0.50 \text{ m}$, $q = 100 \text{ kN/m}^2$) had been connected at one end to an old pile head, but the further sections of the foundation rested on a sandy brick back-fill of 1.2 to 1.8 m thickness which was underlain by an organic clay 0.8 to 3.8 m thick (Fig. 231 explains). The properties of the latter layer have shown: $w = 76\%$, $w_p = 42\%$, $I_{om} = 11\%$.

The relative settlements of the pillars, the thickness of the fill and the organic layer, as well as the

areas of the corresponding parts on the stress diagram are represented in the following table. (The equality $\Delta s \approx s$ is intended to express that the pile head supporting pillar No. 1 is assumed to be motionless.)

The behaviour of the two compressible layers might be investigated by utilizing regression analysis where s (or Δs) is the dependent and F the independent variable. The following equation has been obtained for the regression line of the fill

$$\Delta s = -12.1 F_1 + 806 \quad (r = -0.80).$$

The negative sign of the correlation coefficient (r) shows that the differential settlement was not generated by deformation of the fill. (Note that Δs and F change their values in an opposite sense.)

The equation of the regression line for the organic material was found to be

$$\Delta s = 2.85 F_2 - 5.9 \quad (r = 0.88)$$

which indicates a rather close agreement. (Remember that the heterogeneity of the layer, the restricted accuracy of the measurement, and the marking of the boundaries of the layers all constituted a source of error). For the intercept ($b = -5.9$) it can be proved that this does not differ significantly from zero, thus, the assumption $\Delta s \approx s$ was real.

The relation between v_2 and s has also been found to be as close as the above one ($r = 0.90$); here v_2 means the thickness of the organic layer.

The modulus of compressibility of the organic layer might be calculated by using three different methods.

1. As the inverse of the slope:

$$E_{s2} = \frac{1}{2.85} = 0.35 \text{ MN/m}^2.$$

2. As the average of the quotients $E_{s2} = F_2/\Delta s$ calculated separately for each pillar:

$$\bar{E}_{s2} = 0.40 \pm 0.112 \text{ MN/m}^2.$$

3. By analysing the standard deviation in the following way. By definitely assuming the quotient of the moduli of compressibility in the two layers $\alpha = E_{s1}/E_{s2}$, at each measuring point a value of E_{s2} may be calculated. The mean of the 10 values (\bar{E}_{s2}) and their standard deviation (σ_E) should then be determined and the coefficient of variation

$$C_v = \frac{\sigma_E}{\bar{E}_{s2}}$$

to the given α should be coordinated. By varying the value of α the parameters investigated obtain the following values:

α	\bar{E}_{s2}	σ_E	C_v	E_{s1}
2	0.98	0.30	0.309	1.97
3	0.79	0.23	0.294	2.37
4	0.69	0.19	0.280	2.77
5	0.63	0.17	0.273	3.17
10	0.52	0.13	0.258	5.20
∞	0.41	0.11	0.265	∞

It is a justifiable assumption that the real value of E_{s2} will be approximated most closely by \bar{E}_{s2} where C_v is minimum. According to the table this extreme value exists, and it falls between $\alpha = 10$ and $\alpha \rightarrow \infty$. This means that

$$0.41 < E_s < 0.52 \quad (\text{MN/m}^2).$$

The second example deals with a case where the building tilted as a stiff body.

In the second month after finishing the panel-mounting of a 10-storey building, it was discovered that the elevator shaft has tilted 12 cm to the lead line. Borings made at the four corners of the building revealed that under the raft foundation there was a fill, 0.15 to 1.35 m thick which was underlain by a layer of sandy silt 2.5 to 3.0 m thick (Fig. 232). The fill consisted of fine sand, slack and rubble of a very loose structure. The void ratio of the silt was $e = 0.80$ to 0.92 which is also an indication of loose layers.

From the angles of inclination determined at the edges of the building, the relative settlements (Δs , mm) have been calculated. From the borehole profiles, the thicknesses v_1 and v_2 of the fill and the sandy silt, respectively, as well as the partial areas F_1 and F_2 (in kN/mm) on the vertical

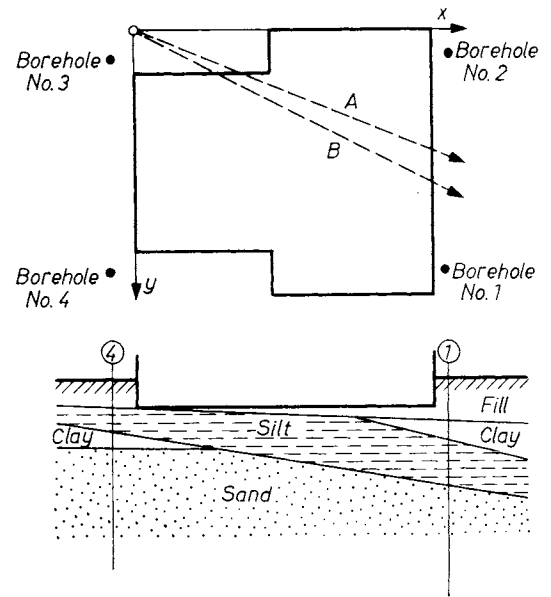


Fig. 232. Example of back analyzing the E_s -value from tilt; two compressible layers (RÉTHÁTI, 1981)

stress diagram were established. The values acquired are summarized in the table below:

Bore-hole	Δs	v_1	v_2	F_1	F_2
3	0	1.35	0.00	224.1	0
4	24.3	0.15	1.75	24.9	290.5
2	87.9	0.30	2.85	49.8	473.1
1	124.8	0.90	3.20	149.4	531.2

The influence of the two loose layers on the development of the tilt may be determined by a regression analysis. The equation of the regression line obtained for the fill was:

$$\Delta s = -0.115 F_1 + 72.2$$

and the correlation coefficient $r = -0.19$. The negative sign cannot be defined from a physical point of view; consequently, the fill did not play any part in the development of the tilt.

The equation of the regression line for the silt was

$$\Delta s = 0.233 F_2 - 13.0$$

and the correlation coefficient $r = 0.93$. This extraordinarily high value unequivocally proves that the grade of damage caused by the tilt was the consequence of the uneven thickness of the silt.

Thereafter the question arises as to with what accuracy the main direction of the tilt can be predicted on the basis of the variation in the thickness of the silt. This investigation can be carried out with the aid of a tervariable correlation. In plotting the coordinates x and y according

to Fig. 232, the following equation will be obtained for the regression plane:

$$v_2 = 0.1169 x + 0.0611 y + 0.348.$$

If $v_2 = 0$,

then $y = -1.915 x - 5.704$

which is the equation of the intersecting line between the plane fitted to the values v_2 and the plane x, y . The negative inverse of the slope of the straight line is $m' = 0.5223$, therefore, the angle of inclination of the plane v_2 is:

$$\alpha = \arctan 0.5223 = 27.6^\circ.$$

Since according to surveys the principal direction of the inclination subtends an angle 23.3° with the x -axis, it can be stated that the change in the thickness of the layer defines the angle of inclination of the building very accurately.

This example shows that the direction and degree of the tilt to be expected may be calculated with a good approximation even in the design phase. Mathematical statistics not only give the expected value of these parameters, but also the standard deviation, i.e. the accuracy of the prediction.

2.3.4.5 Extrapolation of measured settlements

The gradual reduction of safety makes it necessary to know, in many cases, the final values of the components of the motion in order to take the appropriate measure in due time.

The two methods to be described hereafter, and especially the first one (RÉTHÁTI, 1981), might be used, strictly speaking, only in a case when one-dimensional consolidation predominates.

By proceeding according to the first method, the final value of the settlement s_u should be estimated on the basis of the survey, then the quo-

tients associated with the different moments t_i are calculated:

$$\alpha_i = \frac{s_i}{s_u}.$$

The T_i time factors corresponding to the boundary conditions should be read from Fig. 233 and then the quotients established:

$$\alpha_i = \frac{t_i}{T_i}.$$

The reliability of the settlement s_u may be characterized by the coefficient of variation of α_i , i.e. by the ratio $C_v = \sigma_{\alpha}/\bar{\alpha}$. In varying s_u those values will be considered as the most probable at which C_v is minimum.

Assume that the distribution of the vertical stresses corresponds to case No. 5 in Fig. 233 and $\xi = p_f/p_a = 2$, that is

$$\alpha_i = \alpha_1 - \frac{\xi - 1}{\xi + 1} (\alpha_1 - \alpha_2) = \frac{2}{3} \alpha_1 + \frac{1}{3} \alpha_2.$$

Let us assume further that the time series s_i measured at moments t_i (in months) since the beginning of the construction is as shown in Table 12. In the lines 3 to 7 of the table the α_i values are related to $s_u = 6.6$ to 7.2 cm; their standard deviations and coefficients of variation are also readable in the table. Accordingly, $s_u = 6.8$ cm might be considered as the most probable value.

The second method is based on the fact that in one-dimensional case the second stretch of the curve may be approximated by an exponential function. Thus, it might be rightly expected that the settlements are well described by the expression:

$$s = s_u (1 - e^{-At}). \tag{305}$$

Since this function cannot be linearized, the procedure is again to estimate the value of s_u and calculate the A_i values belonging to the pairs of values t_i and s_i with the help of the formula:

$$A = - \frac{\ln(1 - s/s_u)}{t}. \tag{306}$$

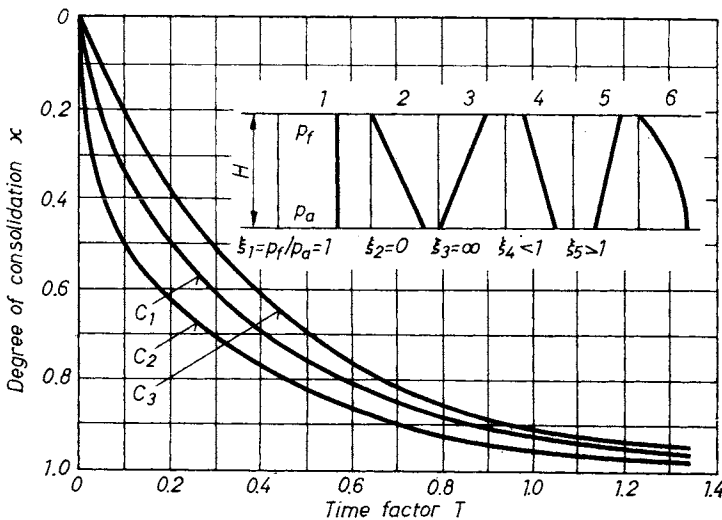


Fig. 233. Correlation between α and T_i for one-dimensional consolidation

Table 12. Determination of the final settlements (numerical example)

s_u (cm)	t_i (month): s_i (cm):	3 1.8	4.7 2.7	7.5 4.0	9.5 4.4	12 4.8	σ_α, σ_A	$C_{\sigma\alpha}, C_{\sigma A}$
6.0	$\alpha =$	24.0	21.4	17.6	18.6	19.0	2.58	0.128
6.6		27.3	25.4	22.1	22.4	23.5	2.20	0.091
6.8		27.3	26.1	22.1	23.8	25.5	2.05	0.082
7.0		30.0	27.6	24.2	24.7	26.7	2.34	0.088
7.2		31.6	27.7	25.0	26.8	28.2	2.42	0.087
6.0	$A =$	0.1189	0.1272	0.1465	0.1391	0.1341	0.0106	0.0799
6.8		0.1025	0.1076	0.1183	0.1096	0.1020	0.0066	0.0614
7.0		0.0991	0.1037	0.1130	0.1043	0.0965	0.0063	0.0611
7.2		0.0959	0.1000	0.1081	0.0994	0.0916	0.0061	0.0618

Then, on the basis of the corresponding coefficients of variation associated with the different s_u 's, that settlement should be accepted at which C_v is minimum.

According to the data entered in lines 8 to 11 of Table 12 the most probable value is $s_u = 7.0$ cm in fair agreement with the value obtained by the first method.

Knowing s_u and A , the settlement at any optional time t , or that time at which a certain degree of consolidation (α) ensues might be determined. Using these, the reliability of the calculation might also be characterized; thus, for example, in the case of the second method the measured settlements (s_m) and those calculated (s_c) can be arranged in the following order:

s_m	1.80	2.70	4.00	4.40	4.80
s_c	1.86	2.68	3.76	4.36	4.96

Accordingly, the correlation coefficient is $r = 0.993$, and the residual standard deviation only $\sigma_r = 0.15$ cm.

SHERIF (1970) approximated the consolidation curve with a hyperbola and attempted also to trace the variation of loading patterns (contact pressure). The procedure can be seen in Fig. 234. Choosing the time (t) as the abscissa, and the product

$$\frac{t}{s} \cdot \frac{p_t}{p} \quad (307)$$

as ordinata, the final settlement to be expected is:

$$s_u = \cot \beta.$$

An advantage of this procedure is that a problem can be solved by using the linear regression.

A comparative study between the exponential and the hyperbolic approximation of the consolidation curve showed that the correlation indices of the two methods are similar (near to 1.0), the total settlement differs, however, by 15 to 20%. (In most cases the hyperbolic approach gives the higher value.)

2.3.5 Settlement due to water absorption

It often occurs that the moisture content of the soil below the foundation increases compared to the conditions experienced during the investigation period. The cause might be attributed to an increasing groundwater table or to the infiltration of surface water, eventually to the seepage from a broken conduit. Whatever the reason, it might be seriously perilous for the building. The variation of the groundwater level and its consequences can well be forecasted (RÉTHÁTI, 1983), but it is rather difficult to exclude the impact of seepage and it requires installation of a number of preventive measures (prevention of run-off water, arrangement for intermittent inspection and overhaul of facilities, etc.). Recollection of statistical data will reveal the magnitude of the danger, because 64.2% of damage on buildings was caused

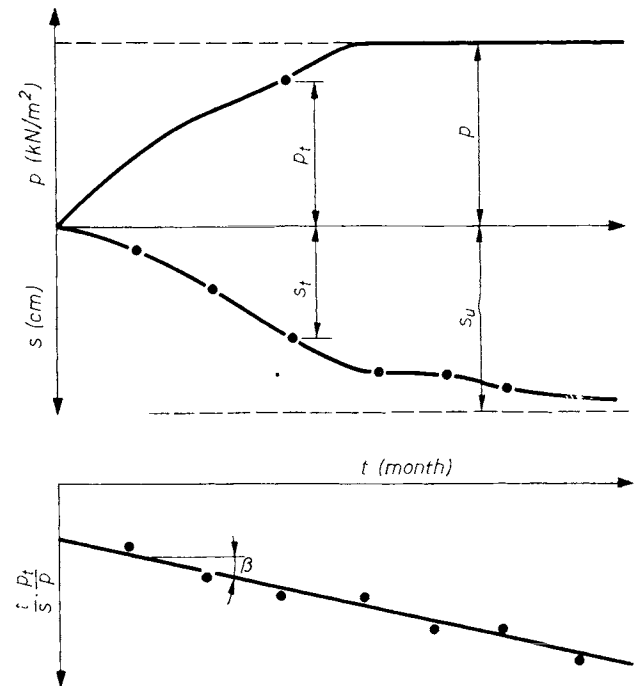


Fig. 234. Extrapolation of measured settlements by using SHERIF's method (1970)

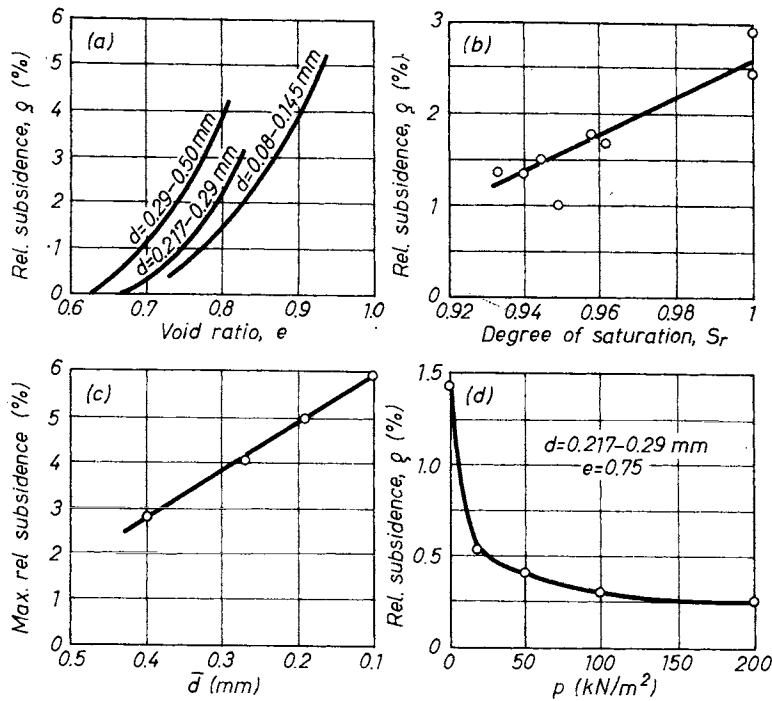


Fig. 235.

Specific subsidence (ρ) resulting from absorption of capillary water as a function of the void ratio (a); the degree of saturation (b); the grain size (c); and load (d); (RÉTHÁTI, 1963; 1965)

by water seeping below the foundation, while only 14.2% was caused by static compression (by differential settlement) (RÉTHÁTI, 1977).

How severely the building is exposed to harm by water infiltrating below the foundation depends on the physical and chemical properties of both the water and the soil. The character of the impact is mainly determined by flow velocity; some phenomena may only appear where the velocity is relatively high while others do not have this requisite.

Effects in the first group might be characterized as to whether compaction or loosening in the soil has been involved therefore in both cases, the rearrangement of soil particles, is essential. Compaction may be caused, for example, by the seepage pressure, by subsidence (due to the effect of surface tension, or by silting due to gravitational flow). Loosening, on the other hand, may be caused by leaching of fine grains and subsequent internal erosion or development of cavities in the soil.

Effects in the second group may include reduced consistency and swelling due to water uptake, harmful influence of chemical substance either on the soil or on the foundation material.

In respect of the stability of the building it is important to know which of the phenomena (physical or chemical) was caused by water in initiating the damage because they not only differ in the character and magnitude of deformation but also in the mathematical sign (heave or shrinkage) and its rate. Immediate or sudden displacements are mostly perilous for the structure itself (cf. Section 2.3.8) while the mathematical sign of the deformation plays a role in a gradual rearrangement of internal stresses or moments.

By all means the most perilous events include the subsidence of the soil or the leaching of fine particles; these can be exceptionally devastating when they occur suddenly, say as a consequence of a breakage of a water main.

Subsidence may occur principally in two types of soils: macroporous loess, and loose granular soils. As the subsidence of loess has been dealt with in detail in Vol. 1, only the deformation of granular soil materials — under the influence of water — will be treated here.

ERLENBACH and later JÁKY (1948b) were the first scientists to point out how serious subsidence might be in loose granular materials under the influence of gravitational water flow. Soaking tests, carried out on sands, have proved (RÉTHÁTI, 1963, 1965) that subsidence might also be provoked by absorption of capillary water. Pertinent test results are briefly summarized below (Fig. 235).

1. Displacement — due to water uptake — ensues immediately; this indicates that subsidence is the “*in statu nascendi*” result of surface stresses (capillary pressure) contrary to shrinkage which is caused by the lasting effect of surface stresses.

2. So called “specific subsidence” (ρ) — the strain expressed in percentage of the height of the sample — increases rapidly with the porosity of the soil.

3. Fine grained soils show swelling beyond a critical density when the access of capillary water is allowed.

4. Keeping the porosity constant, the subsidence varies sensibly according to the degree of saturation in the course of water uptake.

5. Specific subsidence increases gradually when d decreases. A measured $\rho_{\max} = 2.65\%$ was for a

soil of grain size $d = 0.4$ mm, and $\rho_{\max} = 5.7\%$ for $d = 0.1$ mm.

6. Specific subsidence has a maximum value when there is no surcharge on the soil mass, and it diminishes rapidly when the smallest overburden is applied.

There is a substantial difference between characteristic subsidence curves of granular soils and loess. The p, ρ curve of the latter has a pronounced maximum at ~ 300 kN/m² and the subsidence is practically zero when $p = 0$, i.e. where the subsidence of a granular soil is maximum. The reason for this feature probably lies in the special physical and chemical properties of loess (macroporosity, inhomogeneous structure, cementation caused by calcareous films around the grains), while the behaviour of granular soils is governed by the mechanical properties of the mass. The load imposed on granular soils simultaneously increases the magnitude of inter-granular forces which press the particles together and obstructs their free movement (the reason for this phenomenon can be attributed to the homogeneous structure of the material). Thus by increasing the load beyond a critical limit, the water can — in a statistical sense — only produce a random displacement among the particles, which is practically independent from density of the soil.

The findings of these tests can mostly be utilized when foundations on fill or indoor earth fill are made or designed. Selecting the suitable material and compacting it properly brings the risk of subsidence to a minimum or even to zero (Fig. 235b). In the figure, attention is called to the slightly loaded floor slabs and partition walls which are the most exposed elements because their static rigidity is by itself of a low grade.

2.3.6 Settlement in regional extension

There are certain human activities which may cause substantial displacement over huge areas (up to 10 or even 100 km²). Such activities most frequently include among others: mining operations, landscaping, and permanent pumping of the groundwater.

Two branches of mining activities are mostly susceptible to cause displacement on the ground surface: slope facing and subsequent caving, or permanent pumping of groundwater. (Tunnelling of urban subways might also be classified in this range.)

Large, horizontally extended and high embankments or dumping areas may be perilous if (a) there are shallow or pile foundations in or on them, (b) the underlying subsoil consists of thick soft layers. In respect of both alternatives it makes an important difference whether the works are 1 or 2 years old, or older.

Permanent pumping of the groundwater may have two consequences: (a) it increases the effective stress over the soft layer, (b) it increases the "layer pressure" in the aquifer.

Though the magnitude of motion on the terrain due to mining largely depends also on the physical properties of the overburden; soil mechanics and its methodology are mainly applied to investigat-

ing the influence of large embankments and of permanent pumping.

An embankment, even if it is not high but is extensive, may cause considerable displacement in its surrounding. LACY (1981) gives an account, for example, of a fill 1.5 to 4.5 m deep in the vicinity of the Omondoga Lake which caused 1 m of consolidation settlement in the soft underground. INOUE *et al.* (1977) investigated the impact of an embankment construction of 2.5 m height over a loose sand; here the case was worsened due to the water uptake by the regional water works which resulted in a yearly 10 cm displacement on the terrain.

Permanent pumping of aquifers and groundwater reservoirs frequently causes unavoidable problems in town areas. The St. Paul's cathedral is said to have settled 1 cm between 1920 and 1970 due to the gradual loss of the water level. The cathedral in Milan has settled 1.5 cm between 1961 and 1969 because the groundwater level had sunk from 16 m to 40 m below ground surface (KÉRISEL, 1975).

At Long Beach a bowl shaped depression with a 20 mile diameter and 7.8 m maximal depth has developed up to the end of 1959 (FELD, 1968). This movement was caused partly by dredging and landscaping operations in the region, but a major role can be attributed to the uptake of industrial and drinking water and the lowering of the water table for construction sites, and partly to oil pumping.

At present, the case of Mexico City is reckoned among the classical examples in this field. In the extremely porous clay which developed from the volcanic tuff (void ratios up to $e = 7.0$ have been measured in the upper strata) the deep pumping of the groundwater has caused settlements in the range of 7 to 8 m at some locations. Downtown Tokyo also suffers a considerable (6 to 12 cm) settlement per year.

Regional settlements may evoke the following damage to constructions:

(a) Absolute and relative (differential) settlement of buildings. For example, according to Lacy's article a large number of edifices suffered damage around Lake Onondoga, not to speak about that experienced in Mexico City.

(b) Settlement of road and railway embankments. Cox (1981) reports on the 150 cm settlement of the roads in the neighbourhood of Bangkok in the last 12 years (partly under the dead load of embankments but mostly because of the yearly 10 to 15 cm general settlement of the terrain caused by the pumping of the groundwater). As a consequence of the movement, rice irrigation ponds flood the settled pavements, locally and temporarily.

(c) Negative skin friction on pile foundations (cf. Chapter 3). In Tokyo, for example, due to the general settlement of the ground surface, piles were

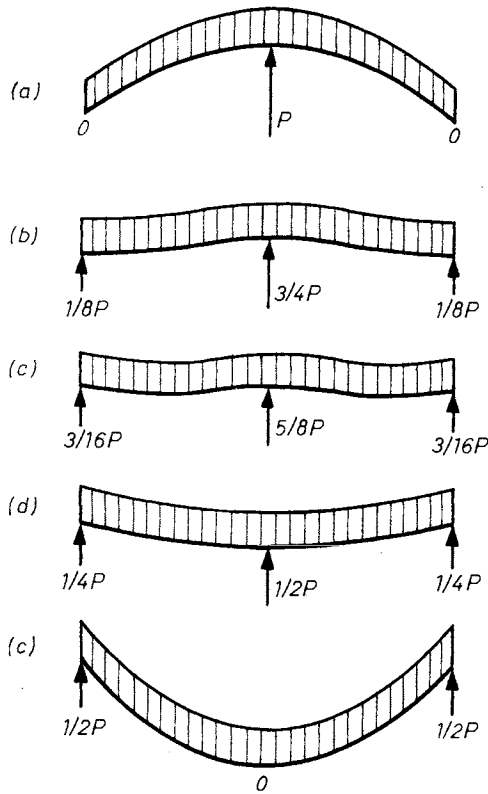


Fig. 236. Variation of supporting forces in the case of differential settlements

dragged downwards through the grip of the subsoil on them (negative skin friction). Because of the difference between the two movements, gaps de-

veloped between the ground level and pile head which very often caused the failure of utility conduits (KISHIDA and TAKANO, 1976).

(d) Decay and rotting of wooden piles. Such damages have been experienced, for example, in the Grand Palais in Paris and in the museum at Grenoble (LOGEAS, 1971). Similarly the same type of damage has been found on an 11 storey building in New York City and in the town of Kearny (MCKINLEY, 1964).

2.3.7 Soil-structure interaction

In settlement computations the individual footings are assumed to settle as if the others did not exist. In some cases, where the footings are close to each other, allowance is made also for the superposition of stresses. The same attitude is adopted in estimating the load-bearing capacity of foundations. However, actual structures are as a rule redundant, namely continuous beams, fixed arches, frame structures, etc. For this reason, any differential settlement within the structure will affect the overall stress pattern. Structures made of timber, brick, or stone may often suffer differential settlement of considerable magnitude without any major change in the support reactions, whereas in structures of steel, or reinforced concrete designed for monolithic behaviour, differential settlement results in a rearrangement of forces. The change in support reactions is illustrated by the example in Fig. 236 showing the case of a beam continuous over two spans. In case (c) the

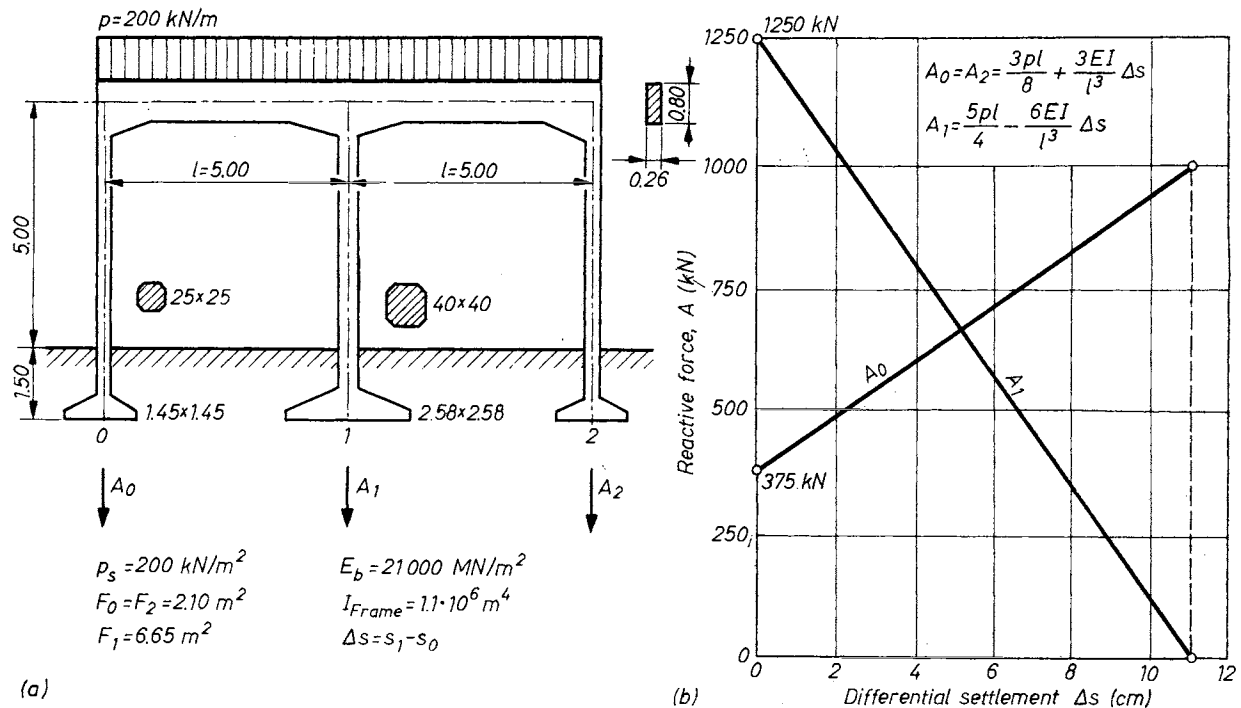


Fig. 237. Reactive forces in a frame structure: a — dimensions of the structure; b — changes in the supporting forces when differential settlement occurs

three supports are in the same plane. Under the load the central support suffers a greater settlement as a consequence of which the reaction under the central support decreases, whereas that under the lateral supports increases. The support reactions are found from the differences in settlement, by Clapeyron's theorem as

$$A_0 = A_2 = \frac{3pl}{16} + \frac{3EI}{l^3} \Delta s$$

and

$$A_1 = \frac{5pl}{8} + \frac{6EI}{l^3} \Delta s.$$

The change in support reactions for a specific case is shown in Fig. 237.

In reality, however, the process takes a much more complicated course. Once the three columns are completed and loaded, the soil starts to consolidate. The central column will again settle at a faster rate and the process is repeated. The bearing pressures will continue to change as long as an ultimate state is not reached.

An analytical solution is also available for the case of a frame on three supports (RÉTHÁTI, 1955). Using the symbols in Fig. 238, it has been demonstrated that the differential settlement at the end of the consolidation (η_m) can be calculated from the expression

$$\eta_m = \frac{P}{R} (1 - U), \quad (308)$$

where

$$P = \frac{hG}{1.234 E_s} \frac{pl(10 F_0 \xi_1 - 3 F_1 \xi_0)}{8 F_1 \cdot F_0}, \quad (309)$$

$$R = \frac{hG}{1.234 E_s} \frac{EI(6 F_0 \xi_1 + 3 F_1 \xi_0)}{l^3 F_1 F_0}, \quad (310)$$

$$G = 2.468 \frac{c}{H^2}, \quad (311)$$

$$U = \frac{\exp(-D\sqrt{t_h})}{\exp\left(\frac{R}{G} e^{-Gt_h}\right)}. \quad (312)$$

The key for the symbols above is the following:

- F_0 = contact area of the footings on the sides,
- F_1 = contact area of the central footing,
- ξ_0 = the ratio σ_z/σ_0 , where σ_z is the vertical pressure at depth z (ξ_1 is the same in respect to σ_1),
- c = coefficient of consolidation,
- t_h = time relating to $\kappa = 0.526$.

The variation of reaction forces A_0 and A_1 , i.e. the relative difference between the initial stage (\bar{A}_0 and \bar{A}_1) referring to $\eta = 0$, and the final stage

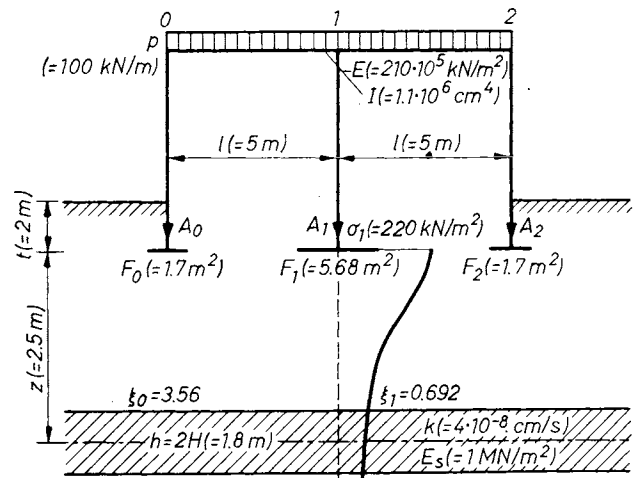


Fig. 238. Calculation of differential settlements for a frame structure on three supports — in brackets the numerical values from the example (RÉTHÁTI, 1955)

(A_0 and A_1) referring to $\eta = \eta_m$, can be determined from the following expressions:

$$\alpha_0 = \frac{A_0 - \bar{A}_0}{\bar{A}_0} = \frac{5}{3} \varphi (1 - U) = (1 - U) \frac{10 F_0 \xi_1 - 3 F_1 \xi_0}{6 F_0 \xi_1 + 9 F_1 \xi_0} \quad (313)$$

and

$$\alpha_1 = \frac{A_1 - \bar{A}_1}{\bar{A}_1} = -\varphi (1 - U) = (1 - U) \frac{10 F_0 \xi_1 - 3 F_1 \xi_0}{10 F_0 \xi_1 + 5 F_1 \xi_0}. \quad (314)$$

The terms U , φ , α_0 and α_1 refer to the case when the compressible layer of $h = \text{constant}$ is equally present below the three supports. Other cases can be solved by using the expression given in Fig. 239.

	Position of the compressible layer		
	I	II	III
$\ln U$	$\frac{0.736 h E I}{E_s} \frac{6 F_0 \xi_1 + 3 F_1 \xi_0}{l^3 F_1 F_0}$	$\frac{0.736 h}{E_s} \frac{6 E I \xi_1}{l^3 F_1}$	$\frac{0.736 h}{E_s} \frac{3 E I \xi_0}{l^3 F_0}$
φ	$\frac{3}{5} \frac{10 F_0 \xi_1 - 3 F_1 \xi_0}{6 F_0 \xi_1 + 3 F_1 \xi_0}$	1	-0.6
α_0	$\frac{5}{3} \varphi (1 - U)$	$\frac{5}{3} (1 - U)$	$U - 1$
α_1	$-\varphi (1 - U)$	$U - 1$	$0.6 (1 - U)$

Fig. 239. Reactive forces and differential settlement at time $t = \infty$ for the three support frames (RÉTHÁTI, 1955)

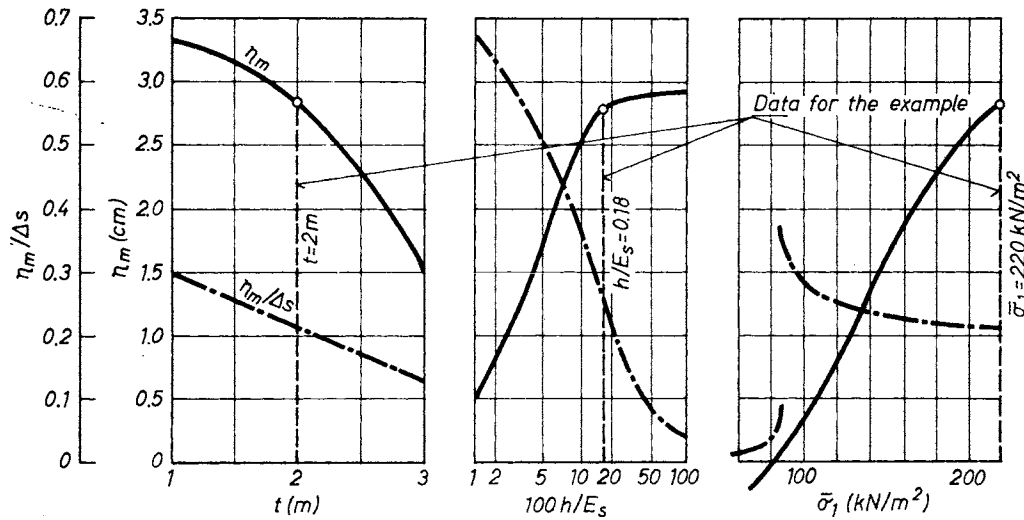


Fig. 240. Effect of parameters t , h/E_s and $\bar{\sigma}_1$ on η_m and $\eta_m/\Delta s$ (RÉTHÁTI, 1955)

Using the numerical values in Fig. 238, and loading all supports with a pressure of 220 kN/m², the differential settlement $\Delta s = 13.3$ cm will be found if the calculation is related to independent foundations (without being coupled into a frame). When Eq. (308) is used, a value only of $\eta_m = 2.8$ cm will be obtained ($\alpha_0 = +42\%$ and $\alpha_1 = -25.2\%$). Interesting results would be obtained if the influence of each term were investigated separately on η_m and α_0 .

From Fig. 240 the following conclusions can be drawn.

(a) η_m will progressively decrease when t is increased; it is therefore questionable whether it is economical to place the foundation level at a high elevation, remote from the compressible layer.

(b) The relative settlement increases with the ratio h/E_s and approaches the limit at $\eta_m = P/R = 2.9$ cm. An interesting consequence of this statement is that e.g. in the case $h = 200$ cm the differential settlement of a given girder will only by 0.7 mm be greater when the assumption $E_s = 1$ MN/m² is changed to 0.3 MN/m².

(c) Varying the contact pressure of the central support ($\bar{\sigma}_1 = 80$ N/m²) $\eta_m = \theta$ can be achieved; but this would — as a consequence — increase the size of the footing enormously ($F_1 = 15.64$ m²). This fact implies therefore that there necessarily exists a relation with an economic optimum between the designed differential settlement and the material requirement of the structure.

An important conclusion may be arrived at from the foregoing. From Clapeyron's theorem it follows that the rearrangement of stresses and the equalization of settlements are the more pronounced, the greater the rigidity of the structure; i.e. the greater the product EI . If the compressibility of the soil is greater under some supports of a conventional structure than under the others, differential settlements will occur. If, however, the structure is a very rigid one, the reactions are modified in magnitude and rearranged already in the early stages of the consolidation process and, as a consequence of this, the differential settlements are reduced. For this reason, on highly compressible soils, either a rigid structure should be built for reduced differential settlement, or a flexible structure should be envisaged, which is capable of withstanding even major differences in settlement without suffering damage.

A visual demonstration of the foregoing is presented, after Terzaghi, in Fig. 241, showing the foundation of a structure involving a tower and

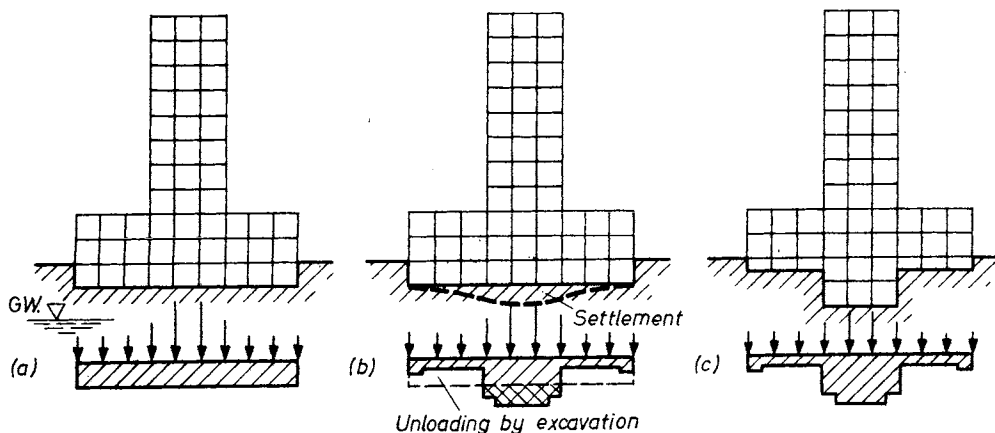


Fig. 241. Methods to avoid harmful effects of differential settlement: a — rigid raft; b — flexible raft; c — different foundation depths in relation to the height of the building

two wings. Three potential alternative designs to avoid differential settlement from occurring are illustrated. Since the groundwater table is below the base of the foundation, no hydrostatic uplift force will act and the total load is transmitted to the soil. Settlement will, however, be caused only by the load remaining after the weight of the soil excavated for the basement is deducted. In case (a), the structure is founded on a completely rigid raft which, being incapable of deformation, will prevent differential settlements from developing. The loads are concentrated under the tower and to make the slab truly rigid it must be made strong enough to withstand the very severe bending moments developed. Consequently, this design would be rather expensive. In case (b), on the other hand, the structure is completely flexible and the soil reaction acting on every part of the foundation base is roughly equal to the load acting on it. Owing to the high load at the center, the tower will suffer greater settlement than the two wings and the structure will deflect. To accommodate this deflection without injury to the building construction joints must be provided to resolve the structure into several parts. The design and execution thereof all along the foundation is again rather expensive. In case (c), finally, almost uniform settlement has been attained by founding the component parts of the building at different levels, i.e. by removing soil masses of different weights from the subgrade. This method should, however, be applied with caution. It should be ascertained that the excavation is not extended to the vicinity of an underlying soft layer, since this would induce greater settlements.

The effect of rigidity has been illustrated clearly by WINDGATE (1938), who determined the column loads and the settlements for the columns of the building shown in Fig. 242 for three cases, namely: 1. a reinforced concrete frame designed in the conventional manner, 2. a completely rigid structure (a grid of heavy beams encasing the column heads), and 3. a completely flexible structure. The results obtained are shown in Table 13. The great change in the load carried by the columns Nos 1 and 3 is especially conspicuous.

The magnitude of the total settlement is of interest insofar as it affects the design of connections and the destination of the building only, but it is

Table 13. Reactive forces and settlements for a reinforced concrete structure (WINDGATE, 1938)

No. of columns	Designed structure		Very stiff structure		Flexible structure	
	P (Mp)	s (cm)	P (Mp)	s (cm)	P (Mp)	s (cm)
1	133	4.8	237	5.3	85	4.5
2	125	6.9	77	5.3	161	6.6
3	261	7.4	127	5.3	296	8.1
4	144	6.1	131	5.3	154	6.3
Means		6.4		5.3		6.4

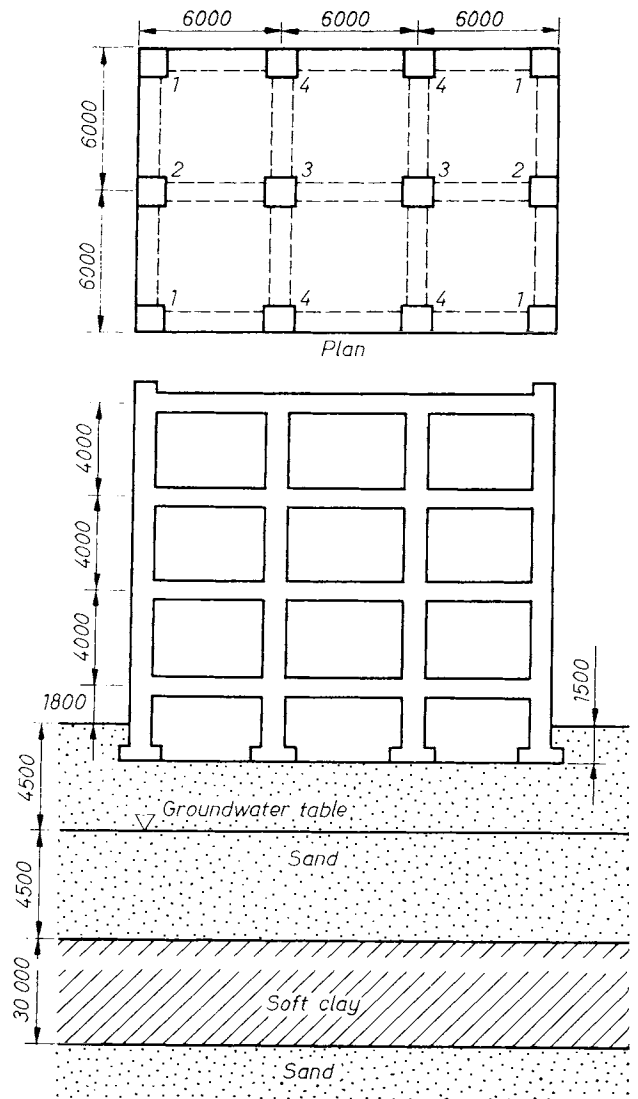


Fig. 242. Structure and underground conditions for the case in the example to interpret the interaction between them

not influenced by the rigidity of the structure. Thus, it is but rarely involved in dimensioning design problems. The magnitude of differential settlements depends not only on the factors influencing total settlement, but also on the arrangement and rigidity of the structure, as well as on differences in the compressibility of the soil under the building. The value thereof is, therefore, much more difficult and yet at the same time much more important to estimate; the differential settlements affect even the behaviour of the structure under normal operating conditions.

The load intensities commonly adopted for the differential settlement under framed structures built on clay roughly equals one-half of the total movement, but the curvature of the deflection line is very mild, so that the relative settlement between two adjacent columns is only a fraction of the total differential settlement within the whole

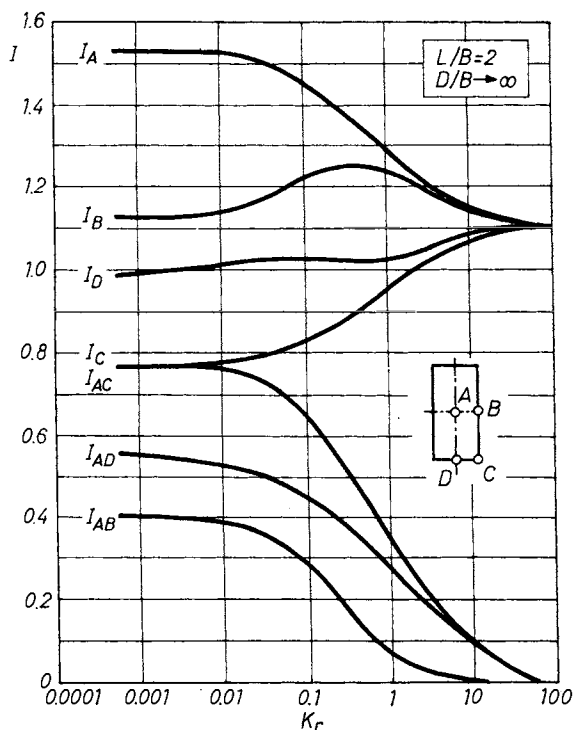


Fig. 243. Factors influencing settlement and differential settlement for a rectangular raft on an elastic half-space (FRASER and WARDLE, 1976)

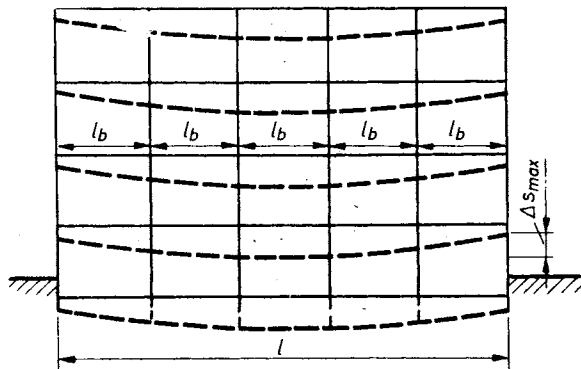


Fig. 244. Deflection lines on a multistorey frame building

structure. The differential settlement under uniformly loaded strip footings and column footings of largely identical size and carrying the same load rarely exceeds three-quarters of the greatest settlement. In the case of frames built on sand the relative settlement between two adjacent columns may attain as much as the entire difference over the frame, i.e. about 40% of the total movement.

Once the total probable settlement has been estimated, the practical experience mentioned before may be relied upon in estimating the differential settlement under structures on raft foundations. No such rule of general validity is believed to be acceptable concerning the allowable relative displacements. In cases of major importance, the magnitude thereof should be determined by struc-

tural analysis, in the course of which the super- and substructure, together with the supporting soil, should be treated as an integral system, as a statically indeterminate structure, allowing for the stiffness of each component.

An important factor is the stiffness of the raft (or strip) in relation to the stiffness of the ground (this ratio is generally denoted as \$K_r\$). It can be shown that for a simple rectangular raft with the length \$L\$ and the width \$B\$, standing on a homogeneous elastic half space,

$$K_r = \alpha \frac{E_r I_r (1 - \nu_s^2)}{E_s B^3} \tag{315}$$

or

$$K_r = \alpha \frac{E_r}{E_s} \cdot \left(\frac{t}{B}\right)^3 \cdot (1 - \nu_s^2) \tag{316}$$

is valid. Here the subscripts \$r\$ and \$s\$ refer to the raft and the soil, respectively, \$I_r\$ is the inertia of the raft per unit length, and \$t\$ is the thickness of the raft. The two expressions for \$K_r\$ differ in the choice of the proportionality constant. In general, \$B\$ might be thought of as a characteristic dimension.

FRASER and WARDLE (1976) examined the behaviour of smooth uniformly loaded rafts resting on a homogeneous elastic layer underlain by a rough rigid base. Graphical solutions were presented for the vertical displacement in the centre, mid-edge and corner points of the raft and for the maximum bending moment in the raft. Some typical results on the relative deflections are reproduced in Fig. 243 for a raft of \$L/B = 2\$. The stiffness factor is defined by:

$$K_r = \frac{4}{3} \cdot \frac{E_r (1 - \nu_s^2)}{(1 - \nu_r^2)} \cdot \frac{t^3}{B^3} \tag{317}$$

The settlement is given by

$$s = qB \frac{1 - \nu_s^2}{E_s} I$$

where \$I\$ is an influence factor (Fig. 243). \$A, B, C\$ and \$D\$ are associated with \$s\$ of the point, \$AB, AC\$, etc., with the differential settlement between the related two points.

It can be seen from Fig. 243 that the most rapid change in performance is in the range of \$0.05 < K_r < 1\$ for \$I_{AB}\$, and \$0.1 < K_r < 10\$ for \$I_{AC}\$ and \$I_{AD}\$. Charts were also included in the article by these authors to allow for the depth of the elastic layer.

The stiffness of the superstructure can also be included in this type of simple analysis using the approximative method outlined by MEYERHOF (1953) to estimate the equivalent flexural rigidity of a frame containing panels and shear walls. (This method was later endorsed by the American Concrete Institute in the report "Suggested procedures for combined footings and mats".) The Meyerhof-method is the following.

Consider an open, multistorey frame structure with approximately uniform spans, in which the greatest relative vertical displacement between adjacent legs is uniformly Δy over each storey (Fig. 244). Since the beams and slabs may be considered stiff relative to the columns, the points of counterflexure in the latter may be assumed, as a first approximation, to be situated at mid-height between the individual stories. The first step consists of determining the magnitude of the product EI which is representative for the rigidity of the overall structure. Let us sever from the structure the part shown in Fig. 245 and denote the moment of inertia of the horizontal beam by I_b that of the upper column by I_f and that of the lower one by I_a . The corresponding stiffnesses are

$$K_g = \frac{I_g}{l}; \quad K_a = \frac{I_a}{h_a}; \quad K_f = \frac{I_f}{h_f}.$$

The differential settlement between adjacent frame legs will produce — as will be recalled from structural analysis — the fixed-end moment at the end of the beam

$$M_g = 6EK_g \frac{K_a + K_f}{K_g + K_a + K_f} \frac{\Delta l}{l},$$

where E is the actual Young's modulus of elasticity.

A beam of length l and stiffness EI_g , subject to the pair of moments $+M_0$ and $-M_0$, suffers the deflection at mid-span

$$\Delta y_{\max} = \Delta_0 - \Delta_g,$$

where

$$\Delta_0 = \frac{M_0 l^2}{8EI_g}$$

is the deflection caused by the moment M_0 ,

$$\Delta_g = M_g l^3 / 12EI_g$$

is the deflection caused by the moment $2M_g$ at all joints.

Introducing these values and M_g into the expression for Δy_{\max} , we have

$$y_{\max} = \frac{M_0 l^2 / 8EI_g}{1 + \left(\frac{K_a + K_f}{K_g + K_a + K_f} \right) \frac{l^2}{l_g^2}} = \frac{M_0 l^2}{8EI_g'}$$

where I_g' is the actual bending stiffness of the beam:

$$EI_g' = EI_g \left[1 + \left(\frac{K_a + K_f}{K_g + K_a + K_f} \right) \frac{l^2}{l_g^2} \right].$$

This is thus the contribution of the frame structure to the rigidity of the foundation. The ratio K_r should now be introduced to characterize the relative stiffnesses of the soil and the structure as $K_r = EI_g' / E_t b^3 l$, where E_t is the Young's modulus

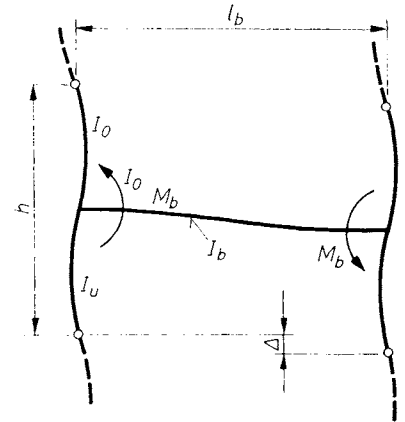


Fig. 245. Details on a frame structure building when differential settlement occurs

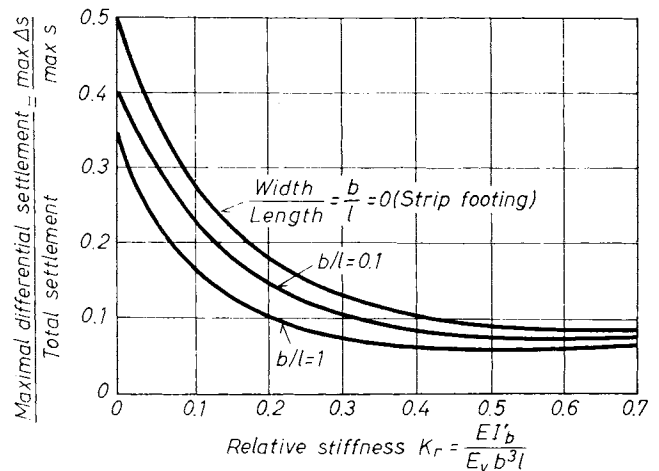


Fig. 246. Relation of max. differential settlement to max. settlement as a function of rigidity in the structure (after Meyerhof)

of elasticity of the soil, while h and l are the width and length of the foundation, respectively. The ratio of the greatest differential settlement — deflection — along the full length of the continuous or strip footing to the greatest settlement can hereafter be determined in terms of K_r . The results of such computations have been plotted in Fig. 246. The greatest deflection has been shown to decrease rapidly at the increasing value of K_r , and to increase slightly at a constant K_r value as the ration l/b is increased.

Once the resulting differential settlements have been determined, the forces induced thereby in the structure can be computed. In the case of a uniform load intensity the bending moments in the base slab can be related directly to the relative stiffness K_r , by the analysis described before. This relationship is illustrated in Fig. 247, demonstrating the greatest bending moments to increase rapidly from the value, $K_r = 0$, corresponding to a

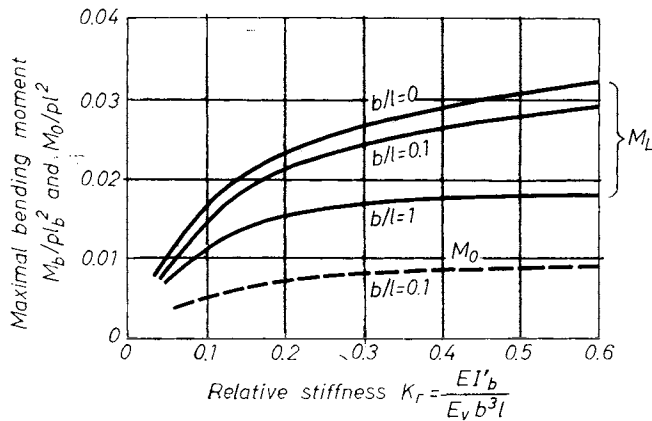


Fig. 247 Bending moments as functions of relative rigidity (MEYERHOF, 1953)

perfectly flexible structure, as K_r is increased, and to increase together with the ratio l/b , i.e. it tends to be greater for long and narrow footings.

Comparing the bending strength of the foundation system and the overstructure, KRSMANOVIČ (1955) distinguishes four basic situation (Fig. 248), and proposes the following methods for their calculation.

In the first case, the inertia can be taken as $I = I_t + I_k$, and the moment should be divided in proportion I_t/I_k . First the reactive forces of the superstructure should be determined — assuming

motionless conditions — then solving this condition, the differential settlements are found. The modification of the reactive forces follows with the calculated settlement differences; earlier and new reactive forces are distributed in the ratio of I_t/I_k between the foundation and the superstructure and generate additive moments. (KANY, 1959, published a more accurate method for this case.) The situation is slightly more complicated when I_t is so small that secondary effects due to the pressure distribution have to be taken into account.

In the second case, the initial assumption is to take the overstructure as flexible and to calculate the reactive forces as for motionless supports. After having found the deflection line of the base slab, the reactive forces should be newly determined from the differential settlements. Relating the new forces to the previous ones, calculated differences should be split between the two systems, and the additive moments calculated accordingly. In the second step, the overstructure is really considered as stiff, and the contact pressure distribution should be calculated as such; the difference between this and the calculated contact pressure results an addition to the moment, so the load of the difference between the original and the latter reactive forces has to be charged to the overstructure.

In the third case — if I_t is rather large — the footing is conceived as a stiff slab and the influence of the overstructure can be neglected.

In the fourth case, the reactive forces are calculated both downwards, and — on the basis of Boussinesq's contact pressure distribution — upwards. The difference should be split up in proportion of the two inertiae, and moments calculated accordingly.

It is easy to conceive that a unanimous relation has to exist among the compression of the soil, the distribution of the contact pressures, and the stiffness of the foundation and the overstructure. Several methods have been elaborated which take account of these interactions and solve the problem with all these parameters in a single run of calculations, without using iterations. These procedures can be divided into two main groups:

- (a) the so-called "C-methods" which make use of the modulus of subgrade reaction, and
- (b) the so-called "E-methods" which calculate on the basis of the elastic half-space theory.

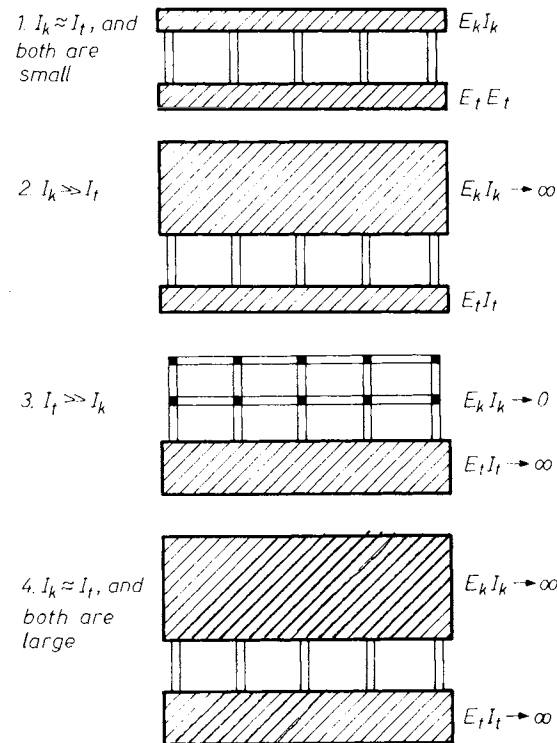


Fig. 248. Bending strength of the foundation system related to that of the overstructure (four fundamental cases mentioned by KRSMANOVIČ, 1955)

The well-known procedures which apply the "C-method" are, among others, connected with the names KÖGLER and SCHEIDIG (1938), HETÉNYI (1946). The "E-method" has been used by: OHDE (1942), GRASSHOF (1951, 1955), KANY (1959) DENINGER (1965), GORBUNOV-POSADOV (1953), and more recently by SHERIF and KÖNIG (1975). The combination of the two theories has been attempted by REPNIKOV (1967) and by SCHULTZE (1969).

2.3.8 Settlement criteria

Procedures have been elaborated during the past decades which are suited to take account of the interactions among the underground, the foundation system and the overstructure (cf. Section 2.3.7). These are alike in their characteristic of the tiresome calculations required, even in the simplest case, not to mention the complexity of the mathematical apparatus which a practical engineer has to face when any of the initial conditions have to be changed.

It is also questionable how close the calculated stresses and deformations will approach the actual ones. Measured stresses and strains indicate that the reaction of the overstructures is almost always more favourable than could have been supposed. MEYERHOF, for example, pointed out, after investigation of a five-storey reinforced concrete frame building, that the 75 m-long girders which suffered a differential settlement of $\Delta s = 8$ cm, and therefore were exposed to an additional 75% moment-increment, were able to carry this extra load without showing any sign of deformation (SKEMPTON and MACDONALD (1956)). Only 50 to 75% of the anticipated (calculated) stresses in the steel frame of two warehouse built in America, and only 30% in the elements of an other steel structure was detected. SKEMPTON and MACDONALD (1956) disclosed this discrepancy with the comments that: (a) the designer is extremely cautious in the assumption of live loads, (b) calculation methods are not suitable for taking into consideration the statical cooperation of the skeleton (of the load-bearing elements) and the other elements (partition walls, floors, etc.).

Essentially, the pressing conditions listed motivated the researchers to find the limiting values of allowable movements in the overstructure, mostly on a statistical basis, acquired by surveys and observations on actually existing buildings. The data referring to the allowable deformation limits in different structures have been condensed in the form of settlement criteria. The purpose was to characterize clearly in a relatively simple manner, the line of deformation causing additional stresses in the structure. The procedure is similar to that which was followed in the case of the consistency limits: the condition (property) is first defined, then a numerical value is ordered to it (these are the limiting values).

2.3.8.1 Settlement criteria for buildings

After BURLAND and WROTH (1974), the criteria usually applied for buildings can be summarized as follows (Fig. 249).

1. Settlement (s) and differential (or relative) settlement (Δs).
2. Rotation (θ) as the change in gradient of a line joining two reference points.

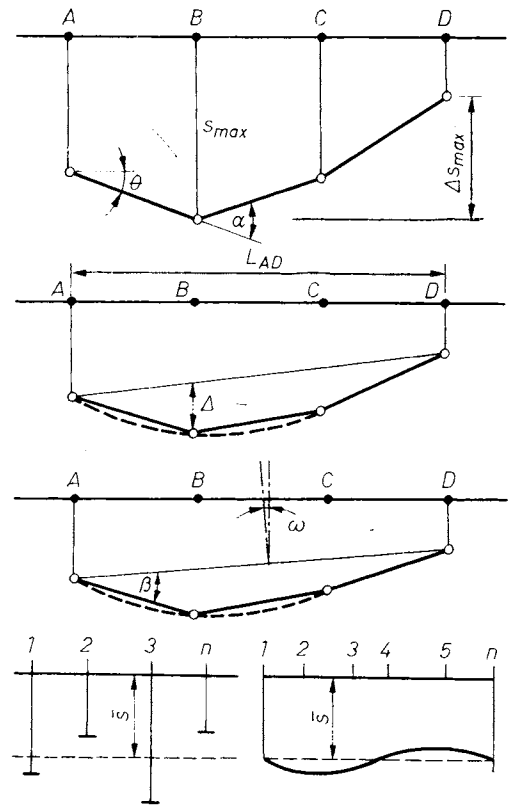


Fig. 249. Settlement criteria (BURLAND and WROTH, 1974)

3. Angular strain, denoted by α , and given (at B) by

$$\alpha_B = \frac{\Delta s_{BA}}{L_{AB}} + \frac{\Delta s_{BC}}{L_{BC}} \quad (318)$$

It is positive if it produces “sag” or upward concavity, and negative if it produces “hog” or downward concavity. Angular strain is particularly useful for predicting crack widths in buildings in which movement occurs at existing cracks or at lines of weakness.

4. Relative deflection (relative sag or hog) Δ is the displacement relative to the line connecting two reference points a distance L apart. The sign convention is the same as in case 3.

5. Deflection ratio (sagging ratio or hogging ratio) is denoted by Δ/L . When a smooth profile is drawn between a number of reference points, considerable judgement is often needed in estimating the maximum value of Δ/L .

6. When the deformed profile is approximately circular, the curvature radius is given by

$$R = \frac{L^2}{8 \Delta} \quad (319)$$

7. Tilt is denoted by ω and describes the rigid body rotation of the structure or a well-defined part of it. Figure 249 shows how the tilt might be estimated if the points were located on a raft

foundation. (This might be quite inappropriate for a frame building on separate footings.)

8. Angular distortion (relative rotation) β is the rotation of the line joining two reference points relative to the tilt. The term was defined by SKEMPTON and MACDONALD (1956) and is now widely used.

9. Horizontal displacement u can be of importance. A change of length ΔL over a length L gives rise to an average strain $\varepsilon = \Delta L/L$.

The last item in Fig. 249 defines the average settlement in the case of separate footings, for strip or slab foundations.

There are basically three criteria concerning limiting movements which have to be satisfied: (a) visual appearance, (b) serviceability or function, (c) stability.

Several authors have made propositions in respect of limiting values. TERZAGHI (1938) observed that conventionally built buildings 20 to 50 m long always suffered harm when the differential settlement exceeded 2.5 cm, but houses 12 to 30 m long did not show the sign of deformation when Δs was less than 1.9 cm.

TSHEBOTARIOFF (1951) remarked that most buildings preserve their intact condition when $s < 5.0$ to 7.5 cm and Δs is below 2.5 cm. BOZOUK (1962) surveyed 574 two and a half-storey houses and experienced that a relative rotation of 1 : 180 did not cause damage, 1 : 120 caused slight, 1 : 80 medium, and 1 : 50 serious damages. MEYERHOF (1953) recommended limiting relative rotations of 1 : 300 for open frames, 1 : 1000 for infilled frames and $\Delta/L = 1 : 2000$ for load-bearing walls or continuous brick cladding.

Following TERZAGHI and PECK (1948), foundations on sand should be treated differently from those on clayey soils because of the following:

(a) In sands, settlement develops rapidly under the load. Hence, for frame buildings, where often a significant proportion of the load is applied prior to the application of the cladding and finishes, some guides may be conservative.

(b) Constructions can bear greater differential settlement (or any other type of movement) when it occurs over an extended time period.

According to the literature, hardly any problem arises in respect of buildings founded on sand. TERZAGHI (1956) stated that he did not know of a building which settled more than 75 mm. Of the settlement survey of 37 buildings reported on by BJERRUM (1963) only one exceeded 75 mm and the majority were below 40 mm. None of the cases reported by MEYERHOF (1965), or SCHULTZE and SHERIF (1973) exceeded 35 mm. Difficulties occur only when vibration takes place due to machinery, traffic or nearby construction work.

One of the best known selection of criteria is connected with the names of SKEMPTON and

MACDONALD (1956). These limiting values are reprinted in Table 14. The authors appended the following remarks to the table:

Table 14. Settlement criteria of SKEMPTON and MACDONALD (1956)

		Solaire	Raft
		foundation	
Angular distortion (β)		1/300	
Max. differential settlement (Δs_{max})	clay	4.5 cm	
	sand	3.2 cm	
Max. settlement (s_{max})	clay	7.6 cm	7.6–12.7 cm
	sand	5.1 cm	5.1– 7.6 cm

- the criteria refer to customary structures (like houses with load-bearing structural walls, or buildings with habitual steel or reinforced concrete frames);
- damage to structural parts might be anticipated when the angular distortion exceeds the ratio 1 : 150;
- the second and the third criteria have been deduced from the first one, and are less reliable.

Combining the above criteria with the statistical data published by LEUSSINK (cf. Section 2.4.2), also critical values for the average settlement (\bar{s}) can be defined (RÉTHÁTI, 1969). If the distribution of settlements is supposed to be symmetric, and the values suggested by SKEMPTON and MACDONALD are used (for clays: $s_{max} = 7.6$ cm and $\Delta s_{max} = 4.5$ cm);

$$\bar{s} = s_{max} - \frac{\Delta s_{max}}{2} = 7.6 - 4.5/2 = 5.35 \text{ cm}$$

and

$$\frac{\Delta s_{max}}{\bar{s}} = 4.50/5.35 = 0.84 .$$

In the case of sands of quick consolidation — on the ground of similar considerations — the result is 0.92. As all buildings surveyed by SKEMPTON and MACDONALD (1956) rested immediately on a compressible layer, and LEUSSINK (1955), determined a ratio 0.9 for this case, the agreement is rather favourable.

On the basis of the two sets of statistical data the critical value of \bar{s} can be determined. In the case, for example, of singular footings on clay:

LEUSSINK gives the value: $\Delta s_{max} = 0.9 \bar{s}$;

SKEMPTON and MACDONALD give the value $\Delta s_{max} = 4.5$ cm and therefore the desired criterion can be found as:

$$\bar{s} = 5.2 \text{ cm} .$$

Extending these considerations to the case of sand, it can be said that a foundation system emplaced immediately on a compressible layer — on which the calculations predicted a uniform settlement — should not be trusted to accept more than 5.0 to 5.2 cm settlement when the consolidation process is slow, or not more than 3.5 to 3.6 cm when the consolidation is rapid. When the compressible layer is lying at a greater depth, these values can be increased.

POLSCHIN and TOKAR (1957) take account also of the ratio of length to height L/H . Depending on it, the allowable Δ/L deflection ratio — as experience has proved — is:

$$\begin{aligned} \Delta/L &= 0.0003 && \text{when } L/H \leq 2 \text{ and} \\ \Delta/L &= 0.0010 && \text{when } L/H = 8 . \end{aligned}$$

The Soviet Code of Practice allows the following values:

	for sand	for clay
(a) for multi-storey buildings and civil dwellings		
when $L/H \leq 3$	0.0003	0.0004;
$L/H \geq 5$	0.0005	0.0007;
(b) for one storey mills	0.0010	0.0010.

Statistical data reveal that the critical limiting values depend also on the stiffness of the building, which in first approximation can be characterized by the number of storeys. Figure 250 shows (RÉT-HÁTI, 1969) that for conventional buildings the critical angular strain is 1 : 350 for one-storey, 1 : 285 for three-, and 1 : 180 for six-storey buildings.

2.3.8.2 Limiting tensile strain

With these limitations in mind, BURLAND and WROTH (1974) suggested that a more fundamental criterion for damage was required and they put forward the idea that a criterion related to visible cracking would be useful since tensile cracking is often associated with settlement damage. Following the work of POLSHIN and TOKAR (1957), they assumed the onset of visible cracking at a limiting tensile strain of $\epsilon_{lim}(= \epsilon_{crit})$.

BURLAND and WROTH (1974) pursued the following idea. If the bottom plane of a girder of rectangular cross-section becomes bent under the influence of a moment the radius can be calculated from Eq. (319). The maximal specific deflection will be $\epsilon = H/2R$ at a distance of $H/2$ from the neutral line (H is the height of the girder). Making the two expressions equal:

$$\frac{\Delta}{L} = \frac{L}{4H} \epsilon. \tag{320}$$

Reckoning with the actual deformation line of the girder the following expressions can be obtained (Fig. 251, insert a):

for uniformly distributed load:

$$\frac{\Delta}{L} = \frac{L}{4.8H} \epsilon \tag{321}$$

and for a singular force acting in the center:

$$\frac{\Delta}{L} = \frac{L}{6H} \epsilon.$$

In a case of pure shear, the diagonal deflection is $\epsilon = \alpha\Delta/L$, where α can be taken, with good approximation, as unity (independently from the type of load). (see Fig. 251 insert b).

For the case of combined shear and bending, the relations can be deduced from the TIMOSHENKO

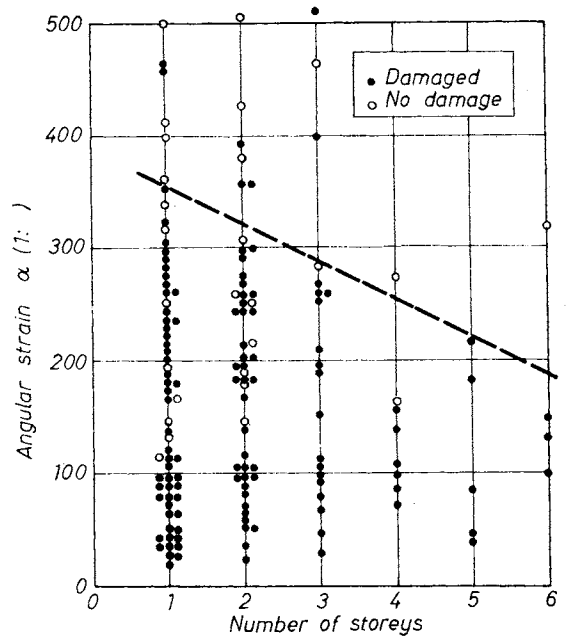


Fig. 250. Relationship between number of stories in a building and the critical angular strain (RÉT-HÁTI, 1969)

formulas (1957). These are illustrated graphically in Fig. 251 insert c, and the following conclusions can be drawn therefrom:

- the value $\Delta/L \epsilon$ is almost independent of the type of loading;
- deformation due to bending in comparison to shear, is always determinant when L/H exceeds 6.

When a reinforced concrete structure is designed the neutral line must not be taken in the symmetrical axis but near to the bottom. Thus, the following expressions should be applied: (see insert d, Fig. 251).

for deformation from moment

$$\frac{\Delta}{L} = \left(0.083 \frac{L}{H} + 1.3 \frac{H}{L} \right) \epsilon \tag{322}$$

and for diagonal elongation due to shear

$$\frac{\Delta}{L} = 0.064 \left(\frac{L^2}{H^2} + 1 \right) \epsilon. \tag{323}$$

Equation (322) is only valid for the case of hogging (the curve of deformation is convex when seen from above), because in the case of sagging $\epsilon = 0$.

Up to this point, it was supposed that the ratio of the elastic to the shear modulus – in line with the isotropic case in the theory of elasticity – is $2(1 + \nu)$. This assumption is rarely valid in reality. There are constructions which are rigid in longitudinal direction but they are much less rigid against shear forces (walls with several doors or windows, for example), or the reverse. The in-

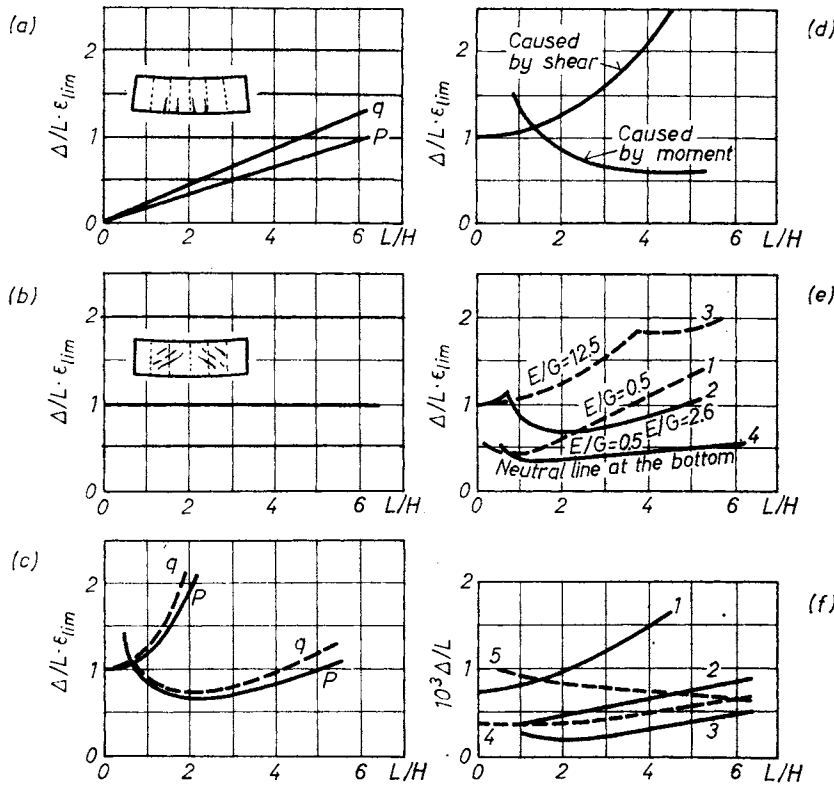


Fig. 251. The quotient $\Delta/L\epsilon$ as a function of L/H for the case of uniform loading pressure p and a singular force P :
 a — moment; b — shear; c — strain caused by moment and shear; d — as in c, but the neutral line is close to the bottom of the beam; e — effect of E/G on ϵ_{lim} ;
 f — 1 — diagonal strain is determinant; 2 — bending strain is determinant (neutral line in the middle, sagging); 3 — same as 2, but neutral line is at the bottom, hogging; 4 — the POLSHIN-TOKAR criterion (1957); 5 — the SKEMPTON-MACDONALD criterion (1956) (BURLAND and WROTH, 1974)

fluence of E/G can be found in Fig. 251c, and from this it appears that:

- to keep the specific strain at a minimum, a construction is advantageous in which the ratio E/G is large (curve 3);
- if the construction is rigid against shear (curve 1) the strain due to bending will predominate, therefore the relation can be approximated by the straight line in Fig. 251a.

The critical value of the specific strain (namely, that which will be visible by the naked eye in the form of fissures) is in the range of 0.05 to 0.10. If $\epsilon_{lim} = 0.075$ is accepted as the average, the relations 1 to 3 illustrated in Fig. 251f can be derived as allowable values for Δ/L . Curve 1 (compare with insert d) relates to the case when diagonal strain predominates, i.e. when the rigidity against shear is small in relation to the longitudinal rigidity, or when the resistance against tension stress is fairly large (frame, reinforced concrete load-bearing walls). Curve 2 refers to the case when — due to small resistance against tension — bending deformation is prevalent (customary brick walls), assuming that the neutral line coincides with the central axis. Curve 3 applies to similar structures to those above, with the restriction that hogging is

presumed (according to the assumptions E/G is small, and the neutral line lies close to the lower part of the structure). Curve 4 corresponds to the criterion described by POLSHIN and TOKAR (1957), and Curve 5 to that of SKEMPTON and MACDONALD (1956), when $\beta = 1 : 150$ is postulated. (The latter had to be transformed to fit the coordinates chosen.)

Having analysed the relationships in Fig. 251, and the observations published in the literature BURLAND and WROTH (1974) announced their findings as follows.

(a) The Skempton-MacDonald criterion ($\beta = 1 : 500$) is convenient for conventional and modern frame structures, but a stricter requirement is needed in respect of buildings with load-bearing walls.

(b) The Polshin-Tokar criterion gives values which are fairly close to reality in the case of buildings with load-bearing walls and of reinforced concrete panel buildings, with the exception of when hogging ensues, because in this case the authors recommend using the half of the critical ratio Δ/L_1 suggested by POLSHIN and TOKAR (1957).

The authors lay stress on the fact that in the case of identical Δ/L ratios the hogging causes substantially greater harm than does sagging, because noth-

Table 15. Classification of visible damage to walls with particular reference to case of repair of plaster and brickwork or masonry

Degree of damage	Description of typical damage ⁺	Approximate crack width (mm)
1. Very slight	Hairline cracks of less than about 0.1 mm are classed as negligible. Fine cracks which can easily be treated during normal decoration. Perhaps isolated slight fracture in building. Cracks in external brickwork visible on close inspection.	max. 1*
2. Slight	Cracks easily filled, re-decoration probably required. Several slight fractures showing inside of building. Cracks are visible externally and some re-pointing may be required externally to ensure weathertightness. Doors and windows may stick slightly.	max. 5*
3. Moderate	The cracks require some opening up and can be patched by a mason. Recurrent cracks can be mashed by suitable linings. Repointing of external brickwork and possibly a small amount of brickwork to be replaced. Doors and windows sticking. Service pipes may fracture. Weathertightness often impaired.	5 to 15* or a number of cracks ≥ 3
4. Severe	Extensive repair work involving breaking-out and replacing sections of walls, especially over doors and windows. Windows and door frames distorted, floor sloping noticeably. Walls leaning or bulging noticeably, some loss of bearing in beams. Service pipes disrupted.	15 to 25* but also depends on the number of cracks
5. Very severe	This requires a major repair job involving partial or complete re-building. Beams lose bearing, walls lean badly and require shoring. Windows broken with distortion. Danger of instability.	usually 25* but depends on the number of cracks

⁺ In assessing the degree of damage account must be taken of its location in the building or structure.

* Crack width is only one aspect of damage and should not be used on its own as a direct measure of it.

ing can resist cracking of the wall down to the foundation. Hogging has to be assumed in any of the following cases: swelling or shrinking of the soil, mining beneath the foundation, settlement of the terrain due to tunneling, displacement of the support due to undercutting, deep foundation next to the existing one, permanent pumping of the groundwater in the neighbourhood.

In appreciating the damage an important role should be attributed to the width of the crack. MACLEOD and LITTLEJOHN (1974) proposed a classification which is based on the U.K. National Coal Board's recommendations reprinted in Table 15. Approximate crack widths are listed and are intended merely as an additional indicator rather than as a direct measure of the degree of damage.

2.3.8.3 Critical movement components at oil tanks

An ever-increasing number of reservoir tanks has been constructed during the past decades for fluids, mostly for the storage of oil. In respect to the stability of these structures there are some characteristic features to be taken into account such as:

- substantial dead load and large dimensions (40 to 50 m diameters are not rare);
- alternating fill and discharge which gives a cyclic character to the live load;
- great flexibility (which can lead to errors when deformations are considered);
- eventually considerable operating temperature (70 to 80 °C);
- preloading tests by using water.

Tanks are expensive projects and any failure may cause enormous harm. A tank which was built in 1974 in the vicinity of Mizushima, Japan, failed 7 months after its installation and discharged 50 thousand m³ of hot oil into the nearby fishing lake, causing a loss of 150 million dollars in property (BELL and IWAKIRI, 1980).

A storage tank consists of four main structural elements: shell, bottom plate, connection of shell to bottom plate and roof. Each settlement pattern may influence any of these components. Figure 252 describes detrimental settlement patterns that may develop at the foundation of a tank. Each of these patterns may produce one or more modes of failure. Failures of most concern include: 1. distortion of the shell to such extent that the floating roof malfunctions, 2. rupture of the shell or the bottom plate or shell-bottom plate connection.

Figure 252 summarizes the principal criteria for unequal settlements. After MARR *et al.* (1982) the criteria in respect of storage tanks can be summarized as follows.

(a) Criteria for shell

Uniform settlement would not cause harm in the tank but may damage adjoining ducts.

Using statistics and geometrical considerations, the maximum tilt which a tank can sustain without overstressing the shell equals

$$\delta_{\max} \leq \frac{4\sigma_f(t_{\max} - CA)}{FS \cdot \gamma_w \cdot G_s D} - 2(H - \Delta h_d), \quad (324)$$

where H = tank height,

Δh_d = design freeboard,

δ_f = rupture stress of the steel in the shell,

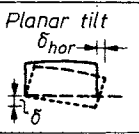
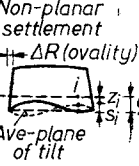

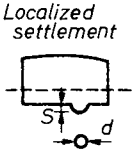
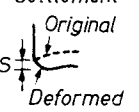
		Settlement criteria and recommendations					
		Lambe et al. (1961)	Langeveld (1974)	Hayashi (1973) Gruber (1974)	Greenwood (1974)	Others	Japanese Fire Defense Ag.
Shell	Planar tilt 	No problem	$\delta \leq 50 \text{ cm}$ $\delta_{hor} \leq 30 \text{ cm}$	Little problem	$\delta \leq D/200$ for aesthetics	Little problem	$\delta \leq D/100$
	Non-planar settlement ΔR (ovality) 	$SAG \leq D/267$ excess stress $SAG \leq 0.25 \frac{D}{H} \Delta R_t$ ovality	$S \leq (0.2L^2/HD)\Delta R_t$ ovality	$\Delta g/l \leq 1/180$	For $D < 50 \text{ m}$ $S_{max} \leq 4 \text{ cm}$ For $D \geq 50 \text{ m}$ $S_{max} \leq 6 \text{ cm}$ ovality	De Beer $\Delta S/l < 1/450$ Sullivan-Nowicki $S \leq 3.0-4.5 \text{ cm}$ Malik $\Delta S \leq (l^2/HD)\Delta R_{tot}$ Penman $SAG \leq (D/4H)\Delta R_t$	$\Delta g \leq D/100$
Bottom plate	Dish-type settlement 	No problem	$W \leq D/100$	$W < D/90$ to $D/50$	Little problem	Rinne $W \leq D/90$	$W \leq D/100$
	Localized settlement 	$(S/d) < 1/30$	Visual inspection of tank bottom after water test	$S < d/90$ to $d/50$	Little problem	Not considered	$S \leq D/100$
Shell-bottom plate connection	Non-planar settlement Original Deformed 	Use prepared foundation pad to prevent		$S \leq d/50$ to $d/30$	Not considered	Not considered	Use prepared foundation pad to prevent $S \leq D/100$

Fig. 252. Differential settlement criteria for tanks (MARR et al., 1982)

t_{max} = thickness of the shell,
 CA = corrosion allowance on shell thickness,
 FS = safety factor against rupture of shell,
 D = diameter of tank.

Non-planar settlement may radially distort or overstress the shell. Radial distortion, called ovality, may cause malfunction of the floating roof. Overstresses may produce rupture and consequently the spillage of the content of the tank. In respect to ovality the criterion proposed by MALIK et al. (1977) can be accepted, it states that

$$\Delta S \leq \frac{l^2}{H \cdot D} \Delta R_{tot}, \quad (325)$$

where $\Delta S = S_i - 0.5(S_{i+1} + S_{i-1})$, and l is the distance between two reference points. This expression has been modified by MARR et al. (1982) as:

for $n = 8$ $S_{max} \leq 0.154 \frac{D}{H} \Delta R_{tot}$,
 and
 for $n = 16$ $S_{max} \leq 0.132 \frac{D}{H} \Delta R_{tot}$, (326)

where n = the number of reference points,
 S_{max} = the max. deviation beyond the average.

In respect of overstresses MARR et al. (1982) suggested using the following criterion

$$\Delta S_i \leq \frac{Kl^2}{HE} \sigma_f, \quad (327)$$

where ΔS_i = the differential settlement between two points,
 σ_f = the rupture stress of the shell,
 K = a constant that covers the non-elastic behaviour of the shell material, secondary effects of the tank geometry, and other factors (evaluation of failed tanks has shown the max. value of K to be of 12).

(b) Criteria for the bottom plate

Uniform settlement and tilt would not cause a problem, but a non-planar settlement does. Two important modes of deformation may occur: disk-shaped settlement, and local depressions. For the former MARR et al. (1977) suggested the following

criterion

$$W \leq \left(W_0^2 + \frac{0.37}{FS} \cdot \frac{\sigma_f}{E} \cdot D^2 \right)^{0.5}, \quad (328)$$

where W = the max. deflection,
 W_0 = the initial maximum camber of the bottom plate,
 σ_f = the ultimate stress of the particular weld used to construct the bottom plate.

The camber which has to be maintained is defined in U.K. regulations as a grade of 0.83% toward the centre. A tank is able to sustain a substantial deflection when s_{max} develops at its midpoint, but major deflections mostly ensue around the rim, so damage and impairment occur quite frequently (PENMAN, 1978).

(c) Criteria for shell-bottom plate connections.

Uniform settlement would not cause a problem, and the criterion to limit planar tilt of the shell seems sufficient to ensure that additional stresses in the connection are kept within allowable limit. Concerning non-planar settlement, no criterion is yet available to evaluate the condition of the connection.

2.3.8.4 Settlement criteria for miscellaneous engineering structures

The composition of the previous paragraphs indicates that both criteria and assigned limiting values are dependent on the type of the structure and on the character of the event which evoked the damage.

Crane tracks are exposed to a perilous effect, not so much when the track settles unequally but when it tilts; the Hungarian Code of Practice allows a grade of max. 0.004 for longitudinal displacement of the rails, and max. 0.03 for tilt.

Agricultural buildings resting on column piles are discussed by ZHUKOV *et al.* (1979). Allowed tilt is (x)

$$x = s h_p / 2 L_0 \quad (329)$$

where s = settlement at the supports,
 h_p = height of the panel,
 L_0 = length of the panel.

Unequal settlement is the more dangerous when the link between the panels is stiff, and the gap (d) between them is narrow. Usually d is 20 to 50 mm, and so, for the case of $h_p = 1.2$ m and $L_0 = 6$ m the allowable differential settlement would be $\Delta s = 6$ cm. Experience on model tests suggests taking $\Delta s/L = 0.01$, and for the gap between the panels $d = 40$ to 50 mm.

In mining areas relative expansion or contraction (ϵ , mm/m) of the ground surface is also monitored (as the depression bowl exhibits tension in some regions, and compression in others). It is also

usual in Hungarian practice to calculate the radius of the depression bowl (R , km), and the relative differential settlement ($\Delta s/l$, mm/m) which are then taken as design values in relation to the sensitivity of the buildings. Four categories were chosen:

	I	II	III	IV
R^*	20	12	6	2
$\Delta s/l$	3	7	10	20
ϵ	1	2	3	6

During construction of underground (metro) tunnels, it has been observed that various buildings are differently sensitive for given movement components, and so it can be stated that quite unlike movement components are determinant for various types of constructions. For example, single buildings are more sensitive to deflection; roads, railways and utility ducts are sensitive to deflection and relative elongation, but block buildings react severely when the radius of the depression is small or the elongation on the terrain is great.

2.4 Reliability of calculations and the safety factor

2.4.1 Bearing capacity of foundations

Similarly to the case of the stability analysis of slopes, the reliability of calculations can also be treated on the basis of deterministic or stochastic methods.

2.4.1.1 Deterministic methods

We must face the fact that our investigations, the data used, the conclusions drawn, etc., may be incorrect. For example, when computing the ultimate bearing capacity of a footing we are aware that both the design loads and the shear-strength parameters can be inaccurate. In order to rectify the situation, we have to introduce safety factors. This can be done in three different ways.

In the first method the ultimate bearing capacity is divided by an assumed or prescribed safety fac-

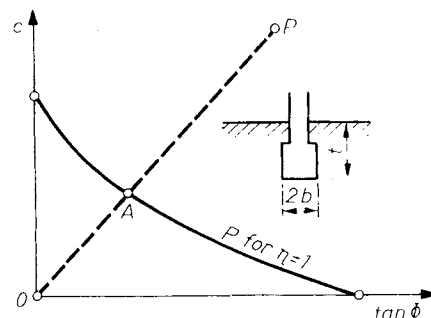


Fig. 253. Establishment of failure safety factors for a strip foundation

tor and thus an “allowable bearing pressure” is obtained. A footing is then said to be designed correctly if the “actual” pressure on its base, which itself is computed from more or less uncertain design loads does not exceed the “allowable” value. Formerly, this concept was in general use. Using Eq. (119), the allowable bearing pressure of a footing can be written in the following from

$$P_{\text{allowable}} = \frac{P_b}{\nu} = \frac{1}{\nu} (cN_c + t\gamma N_q + b\gamma N_\gamma). \quad (330)$$

Hence the required area A of the base of the footing is

$$A = \frac{P}{P_{\text{allowable}}}, \quad (331)$$

where p is the total load on the footing. To obtain the required width of a continuous or a rectangular footing calls for the solution of an equation of second or third order, respectively. A value of $\nu = 2$ to 3 for the safety factor is usually chosen.

This method is now regarded as obsolete since it makes no allowance for uncertainties other than those resulting from the soil conditions not having been adequately investigated.

Nevertheless, in a modified form this method can still be very useful since it permits variations in both shear strength and design loads and their

effect on bearing capacity to be assessed by means of a graphical representation.

The basic idea of the method is the same as that used in the stability analysis of slopes (see Section 1.6.1). Since the fundamental factor in a limit state analysis is shear strength, it is appropriate to express the safety factor in terms of this. To this end, for a given load we determine a set of those simultaneous values of Φ and c for which the safety factor against failure is $\nu = 1$. We then plot these c values against $\tan \Phi$ as shown in Fig. 253, and compute the safety factor in the same way as in the case of slopes

$$\nu = \frac{\overline{OP}}{OA}. \quad (332)$$

It is of interest to compare the safety factor defined by Eq. (332) with that used in Eq. (330), $\nu_p = P_b/P_{\text{allowable}}$.

Numerical examples to show the difference between the two sets of values, are given in Fig. 254. The safety factors referred to bearing pressures are $\nu_p^a = 4$, $\nu_p^b = 8.2$ and $\nu_p^c = 11.8$.

If we perform the computation for the smallest and greatest probable values of c , the condition $\nu = 1$ will be represented by a strip instead of a single curve in the c versus $\tan \Phi$ plot (Fig. 255). If we again plot the measured shear strength parameters in this graph, the margin of safety against failure can be judged by simple visual inspection.

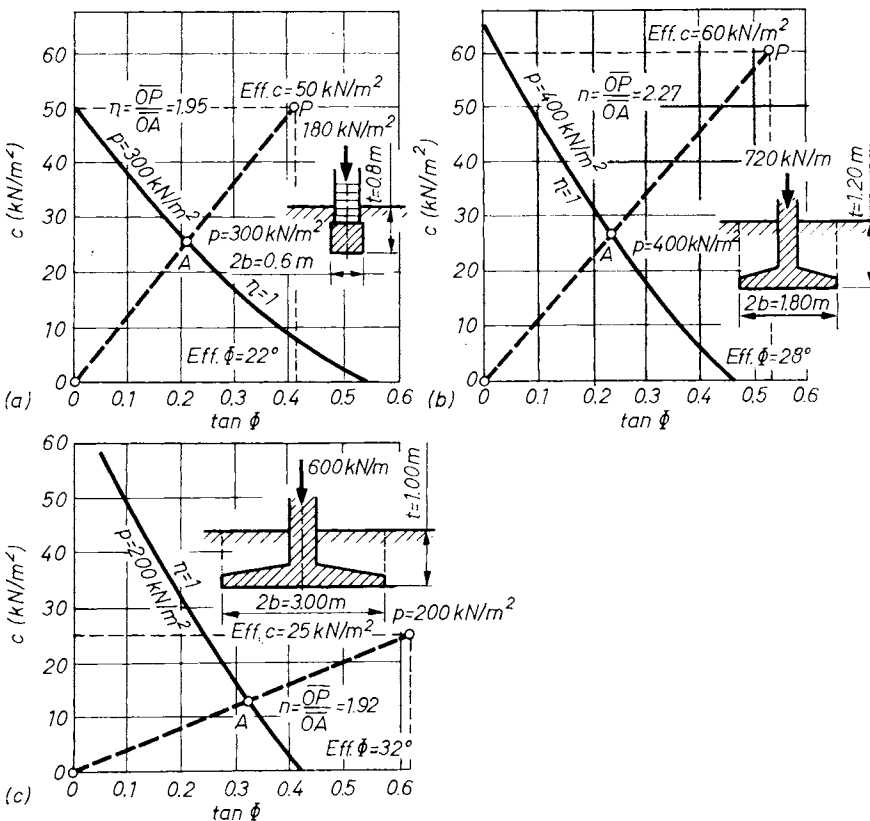
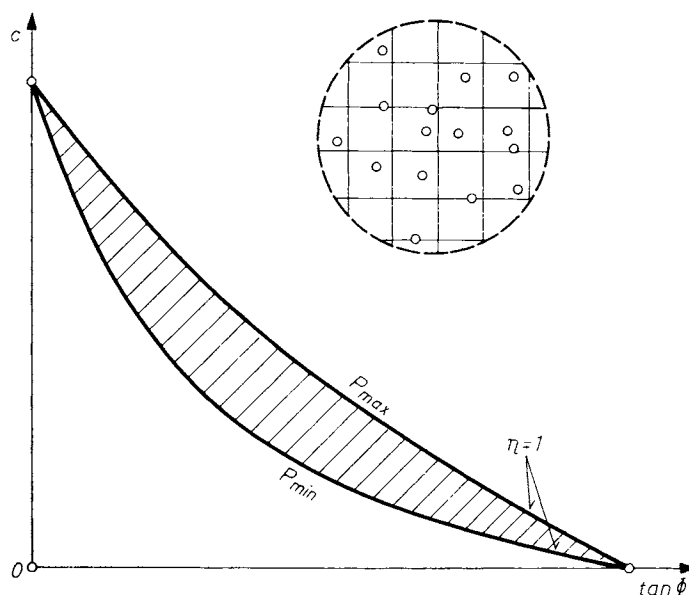


Fig. 254. Examples of how to estimate safety factors

Fig. 255. Exploration of the spreading zone of safety factors



The $\nu = 1$ curves can be determined by various theories and thus the differences in the results can be studied.

In the second method, the dead and live loads on the structure are multiplied by a factor f which is greater than 1. In this way we can allow for the uncertainties in the estimation of design loads. The footing is then said to be correctly designed if the ultimate bearing pressure is greater than or just equal to, the bearing pressure computed from the increased loads on the base:

$$p_b \geq \sigma = \frac{P_d f_d + P_l f_l}{A} \quad (333)$$

The subscripts d and l refer to dead loads and live loads, respectively.

The shortcoming of this method is that it makes no allowance for possible variations in soil characteristics (especially in Φ and c).

The third method consists in using partial coefficients. The method was proposed by BRINCH HANSEN and LUNDGREN (1960). According to this method we reckon with a nominal state of failure. The loads acting on a footing are multiplied by a set of partial coefficients greater than 1, while the strength parameters of both the material of the footing and the soil are divided by another set of partial coefficients. The structure is said to be correctly designed if the conditions of equilibrium are just satisfied in the nominal state of failure. Moreover, the critical nominal stress in the structure itself must not exceed the nominal compressive strength of the material. In mathematical terms:

$$\frac{f_1 P_1 + f_2 P_2 + \dots + f_n P_n}{A} \leq \sigma \left(\frac{\tan \Phi}{f'}, \frac{c}{f''} \dots \right) \quad (334)$$

A choice of the partial coefficients is based on the following principles:

- the greater the uncertainty in the determination of the quantity considered, the greater should be the numerical value of the relevant partial coefficients;
- the coefficients should be so chosen that the resulting dimensions of the footing do not differ too much from those obtained by formerly used conventional methods.

The numerical values proposed by BRINCH HANSEN and LUNDGREN are the following

Dead weight	f_d	= 1.00 to 1.05,
Water pressure	f_w	= 1.0,
Water pressure if water level changes unpredictably	f_w	= 1.2,
Live load	f_l	= 1.5,
Live load, special cases (silos, etc.)	f_l	= 1.2,
Wind thrust	f_g	= 1.5,
Earth pressure at rest	f_0	= 1.3.

The computed, or assumed loads must be multiplied by the relevant coefficients. On the other hand, the shear strength parameters Φ and c must be divided by the following numbers:

Coefficient	Bearing capacity of footings	Earth pressure and stability computations
Cohesion f_c	2.0	1.5
Friction f_ϕ	1.2	1.2

These values are valid for the case where the shear strength parameters are determined by the best possible method.

2.4.1.2 Stochastic methods

An up-to-date design procedure views every term in Eq. (119), so also the ultimate bearing capacity itself, as a random variable. Basic principles are the same as in Section 1.6.2 and their methodics similar to that applied in the case of slope stability analyses.

The terms b and t on the right hand side in Eq. (119) can be taken as constants, and the standard deviation of γ_1 and γ_2 can be neglected. Just the opposite has to be said about the cohesion and the argument of the bearing capacity factors, the internal friction of the soil.

As the statistical parameters of cohesion are given, we have to deal principally with the variability of the N_i factors. The standard deviation of the bearing capacity factors can be determined by using one of two methods: the Monte Carlo simulation or by the help of Eq. (163) which expresses the law of propagation of errors.

Choosing the first alternative, SINGH (1971) examined the variability of the factors

$$N_q = \tan^2(45^\circ + \Phi/2) \exp(\pi \tan \Phi) \quad (335)$$

and

$$N_c = (N_q - 1) \cot \Phi. \quad (336)$$

The results of this consideration are condensed in Table 16 from which the following can be deduced:

- (a) the variance of N_q exceeds that of N_c ;
- (b) with increased internal friction, also the coefficient of variation of the bearing capacity factors increases gradually;
- (c) the relationship between the coefficients of variation for the bearing capacity factors and that of the angle of internal friction is not linear; the ratio of the two terms decreases when the coefficient of variation of Φ ($C_{v\Phi}$) increases.

Singh's data revealed that the variability of q is rather significant. Similar observations originate from other researchers as well, for example, LUMB (1966) and SCHULTZE (1975, 1977).

Using the law of error propagation, and assuming that the variance of b , t and γ is negligible in relation to that of Φ and c , the variance of q can be

written as

$$s_q^2 = \left(b\gamma_1 \frac{\partial N_\gamma}{\partial \Phi} s_\Phi \right)^2 + \left(t\gamma_2 \frac{\partial N_q}{\partial \Phi} s_\Phi \right)^2 + \left(c \frac{\partial N_c}{\partial \Phi} s_\Phi \right)^2 + (N_c s_c)^2 \quad (337)$$

when Φ and c are assumed to be independent variables.

The calculi of the bearing capacity factors defined by the expressions Eq. (335) and (336), and of that given by CAQUOT and KÉRISSEL (1953) as

$$N_\gamma = 2(N_q - 1) \tan \Phi, \quad (338)$$

are (HARR, 1977):

$$\frac{\partial N_q}{\partial \Phi} = \frac{N_q \pi}{\cos^2 \Phi} + \frac{\tan(45^\circ + \Phi/2)}{\cos^2(45^\circ + \Phi/2)} e^{\pi \tan \Phi}, \quad (339)$$

$$\frac{\partial N_c}{\partial \Phi} = \frac{\partial N_q}{\partial \Phi} \cot \Phi - \frac{N_q - 1}{\sin^2 \Phi}, \quad (340)$$

$$\frac{\partial N_\gamma}{\partial \Phi} = \frac{2(N_q + 1)}{\cos^2 \Phi} + 2 \tan \Phi \frac{\partial N_q}{\partial \Phi}. \quad (341)$$

Example. The allowable load Q_h (kN/m²) should be found for a building on which an additional storey is desired. The existing strip foundation is $2b = 1.2$ m wide, made at -1.3 m ($= t$) depth below ground level. The desired probability of failure is $p_f = 0.005$. Assume $\gamma_1 = \gamma_2 = 19$ kN/m³, $\bar{c} = 25$ kN/m² cohesion with $s_c = 5.2$ kN/m² and $\Phi = 20^\circ$ with $s_\Phi = 2.2^\circ$ ($= 0.0384$).

Using Eqs (335), (336) and (338), the expected value of the failure stress would be:

$$\bar{q} = 0.6 \cdot 19 \cdot 5.39 + 1.3 \cdot 19 \cdot 6.40 + 25 \cdot 14.93 = 590 \text{ kN/m}^2.$$

Substituting the values calculated from Eqs (339) to (341) in Eq. (337), the variance of q is:

$$s_q^2 = (0.6 \cdot 19 \cdot 43.3 \cdot 0.0384)^2 + (1.3 \cdot 19 \cdot 36.4 \cdot 0.0384)^2 + (25 \cdot 53.8 \cdot 0.0384)^2 + (14.83 \cdot 5.2)^2 = 10\,166,$$

and so $s_q = 100.8$ kN/m².

From the table of normal distribution function we can find $\lambda = 2.57$ to $p_f = 1 - \Phi(\lambda) = 0.005$, and so the desired value of the allowable stress is:

$$q - \lambda s_q = 590.3 - 2.57 \cdot 100.8 = 331.2 \text{ kN/m}^2$$

and the allowed load on the strip:

$$Q_h = 1.2 \cdot 331.2 = 397 \text{ kN/m}.$$

The conventional safety factor is

$$FS = 590.3/331.2 = 1.78.$$

Table 16. Coefficients of variation for the bearing capacity factors defined in Eqs (335) and (336) as the functions of Φ and $\sigma_{v\Phi}$ (SINGH, 1971)

	$C_{v\Phi}$	$\Phi = 15^\circ$		$\Phi = 25^\circ$		$\Phi = 35^\circ$	
		\bar{N}_t	C_{vN}	\bar{N}_t	C_{vN}	\bar{N}_t	C_{vN}
N_q	0.10	3.983	0.143	11.081	0.268	37.242	0.474
	0.20	4.037	0.216	11.645	0.419	43.439	0.820
	0.30	4.115	0.291	12.515	0.590	55.763	1.380
N_c	0.10	11.029	0.086	21.147	0.180	49.357	0.342
	0.20	11.096	0.130	21.712	0.278	54.197	0.575
	0.30	11.192	0.175	22.563	0.388	63.123	0.940

2.4.2 Reliability of predicted settlement

It is not habitual to require a safety factor for the calculated settlement, despite the fact that several errors may aggravate the calculations.

Concluding the treatment on settlement calculations, analytical- and observational data for some structures will be compared. Unfortunately, these data are of but limited value for a number of reasons. One of them is that such reports are, as a rule, published after an extended period of observation only, and in some instance even the "analytical" results are only subsequently obtained, using the "best" method available. The results of soil explorations and laboratory tests are almost invariably incomplete. Moreover, often different methods of computation are applied; for this reason only a few reports will be mentioned.

The results of settlement observations published in the relevant literature and observed by himself for 103 structures have been compiled and evaluated by LEUSSINK (1953). The observations are summarized in Fig. 256 where the values of "restricted validity" are shown in diagram (a), while those considered "perfect" are given in diagram (b). In the first case, the settlement values processed

are not the ultimate-, but intermediate settlements, or were such where the magnitude of settlement was influenced by lateral yielding as well. The number of "perfect" values was 40.

The arithmetic mean of the ratio of the settlements observed (y) to those computed (y') was $y/y' = 85.2\%$ with all data included, whereas it was 93.3% using the perfect data only. The frequency curve in Fig. 256 does not reveal a normal distribution, but rather one of a complex type. The presumable partial normal distributions have also been plotted on the diagram. This distinction has been attributed by LEUSSINK to differences between the soil types, in that for silt soils, where sampling is more liable to cause disturbances, the computed settlements are excessive, whereas in clay soils the agreement is, in general, closer.

The distribution curves of the "perfect" values are steep, the settlements observed ranging from 75 to 125% of the theoretical values. In the case of slightly cohesive and granular soils, the distribution curve is much flatter, indicative of reduced accuracies.

Various settlement calculation models have been compared in a study made by SCHULTZE and SIEVERING (1977), evaluating the settlement of 148 buildings. There were 112 buildings on slab, 29 on single footings and 7 on strip foundations on the list. The size of the foundations ranged between $1 \cdot 1$ m and $60 \cdot 100$ m, and their contact pressure between 20 and 1263 kN/m^2 . The E_s was based on the Standard Penetration Test and Static Penetration Test results, or on the basis of oedometric tests, depending on which of these was mentioned in the literature as the pertinent case. The depth limit of the compressible zone was taken as the width of the slab or as double the width of a rectangular footing. Settlements were calculated using ten different methods. In the first three cases E_s was assumed to be constant and the settlement influence factor was taken in the following combinations of Fröhlich's concentration factor (ν) and the Poisson ratio (μ): $\mu = 0, \nu = 3$; $\mu = 0, \nu = 5$; $\mu = 0.3, \nu = 3$. In the next three cases the procedure was the same, but E_s was assumed to increase with depth. The last four cases (Nos 7 to 10) were calculated by the following expressions:

$$s = 3.5 \frac{pR_H}{E_s}, \tag{342}$$

$$s = \frac{LBp}{E_s(L + B)}, \tag{343}$$

$$s = 2.3 \frac{N}{2E_s(L - B)} \log \frac{2B + z}{2E_s + z} \cdot \frac{L}{B}, \tag{344}$$

$$s = \frac{0.6 pB}{E_s}. \tag{345}$$

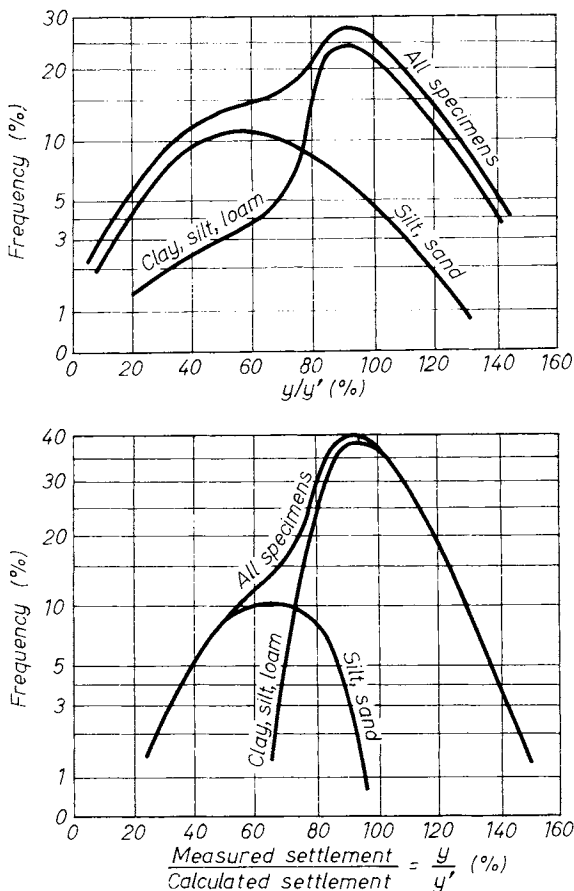


Fig. 256. a — Relation between measured and calculated settlements plotted in Beckel's frequency system; all 103 values with restricted validity; b — the same, of which 40 data are unanimously valid

Table 17. Ratio of calculated (with methods 1 to 10) and measured settlements (SCHULTZE and SIEVERING, 1977)

Calculation	All values (148)			Raft foundation (112)			Single footing (29)			Strip footing (7)		
	mean	standard deviation	coefficient of variation	mean	standard deviation	coefficient of variation	mean	standard deviation	coefficient of variation	mean	standard deviation	coefficient of variation
1	1.82	1.43	0.79	1.99	1.54	0.78	1.51	0.79	0.52	0.52	0.35	0.67
2	2.16	1.66	0.77	2.28	1.78	0.78	2.07	1.05	0.51	0.57	0.38	0.67
3	1.49	1.15	0.77	1.60	1.24	0.78	1.31	0.69	0.52	0.40	0.27	0.67
4	1.41	1.12	0.79	1.56	1.21	0.77	1.05	0.52	0.50	0.40	0.27	0.67
5	1.63	1.27	0.78	1.78	1.37	0.77	1.36	0.66	0.49	0.44	0.29	0.67
6	1.13	0.89	0.78	1.24	0.96	0.77	0.89	0.44	0.50	0.31	0.20	0.67
7	3.71	3.37	0.91	4.30	3.64	0.85	2.05	1.05	0.51	1.26	0.82	0.66
8	1.70	1.45	0.85	1.52	1.58	0.82	1.06	0.49	0.46	0.72	0.47	0.66
9	0.55	0.49	0.90	0.64	0.53	0.82	0.35	0.16	0.46	0.005	0.006	1.19
10	2.02	1.75	0.87	2.31	1.90	0.82	1.27	0.59	0.46	0.47	0.31	0.67

The means of the ratios between differently calculated and measured settlements ranged between $\mu = 0.55$ and $\mu = 3.71$. The coefficient of variation of these μ -values decreased when the foundations were classed by type (Table 17). For the linear relationships established between calculated and measured settlements the correlation coefficients were 0.81 to 0.87. As the intercept of the regression lines was close to zero, it was possible to order a corrective factor to any one of the methods used (Table 17).

Experience has confirmed that differential settlement may also develop among footings which

rest on an underground qualified as homogeneous. LEUSSINK (1955) studied the settlements of foundations rested on soils which were classified as homogeneous in the laboratory and were equally loaded. He found that the measured max. differential settlement of the footings under the same building attained 30 or 90% of the average settlement, depending on the position of the compressible layer. 30% refers to the case when the compressible layer was at a depth of more than half the width of the strip, or in the case of singular footings, at a depth $B/2$ or $L/4$, whichever was less.

The study allows to draw the following conclusions.

(a) It is wise to confine also the average settlement, to avoid unwanted differential settlement among the footings (see Section 2.3.8).

(b) The assumption — made on the basis of probability theories — that a random differential settlement or tilt may ensue due to the variability of E_s and other parameters seems to be really acceptable (RESENDIZ and HERRERA, 1969).

(c) There exists definite relationship among the components of movement. Let give an example here to prove the validity of this statement. Figure 257 reflects the variation of some components of movement in a reinforced concrete silo as a function of time (loading). Shown are:

- the angle of the chute to the axle α ;
- the mean \bar{s} of the settlements (s_i) measured at the valves;
- the tilt, δ .

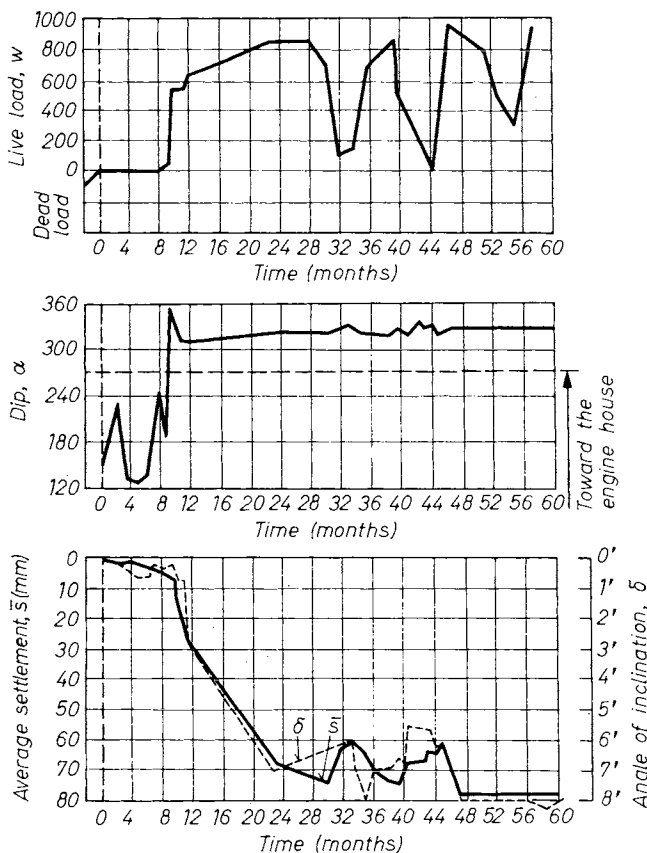


Fig. 257. Movement components of a silo, synoptic drawing

The figure reveals the very close relation between \bar{s} and δ , namely, with increasing load, not only the average settlement but also the tilt increases gradually. After evaluating the case of 14 silos the average correlation coefficient for the relationship \bar{s}, δ has been found as $\bar{r} = 0.73$ (four values were above 0.90). The figure indicates also the phenomenon that the dead load generally causes the silos to tilt toward the elevator (machine shop), which is the result of an initial excentricity.

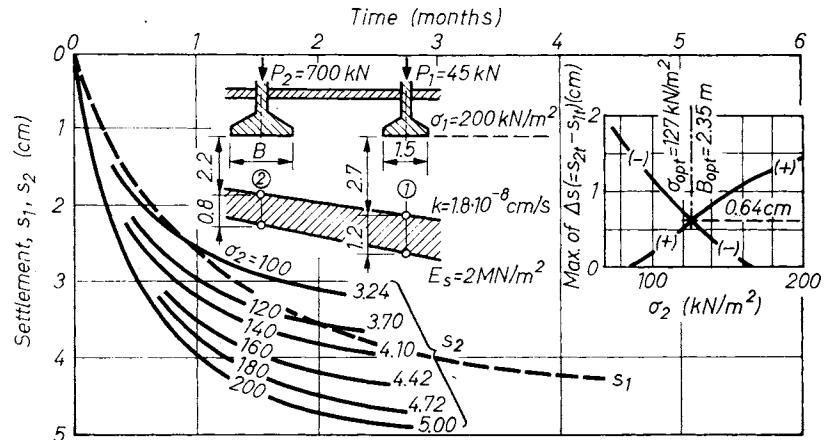


Fig. 258. Maximum settlements deduced from the consolidation process when the width of one footing is varied (RÉTHÁTI, 1955)

The case of the frame mentioned in Section 2.3.7 indicates that it is convenient to examine the development of movement components as a function of time. Even if the stratification is not uniform, the soil is inhomogeneous and/or the loads on the footings are different, it can be achieved that the calculated settlement attain the same value at each footing, but this will be valid at one single instant only. Let us examine, for example, the differential settlement of the two footings in Fig. 258 as a function of time (RÉTHÁTI, 1955). Even if the final settlements at time $t \rightarrow \infty$ are identical, there are appreciable differences during the consolidation period. The time-settlement curve for footing 1 is drawn using numerical values (see figure). If the width of footing 2 is widened, various final settlements and different time-curves are produced. Take for example $\sigma_2 = 140 \text{ kN/m}^2$ and $B = \sqrt{700/140} = 2.23 \text{ m}$, then the pressure in the center of the compressible layer will be 103 kN/m^2 , and the settlement (at $t \rightarrow \infty$) is $s_2 = 4.10 \text{ cm}$ [the time-settlement curve has been derived from the consolidation curve s_1 by reducing it at the rate of $(1.2/0.8)^2 = 2.25$]. Taking the largest differences between the ordinatae of time-curves s_1 and s_2 the relationship between stress σ_2 and maximal differential settlements $\Delta s_m = s_2 - s_1$ is obtained (the Δs changes its sign, so most of the σ_2 -s have both a positive and a negative maximal value). The calculation shows (see the right upper corner of the figure):

$$\begin{aligned} \Delta s_m &= 1.4 \text{ cm when } \sigma_2 = \sigma_1, \\ \Delta s_m &= 1.1 \text{ cm when } s_{2\infty} = s_{1\infty}, \\ \Delta s_m &= 0.64 \text{ cm when } \sigma_2 = 127 \text{ kN/m}^2. \end{aligned}$$

In a practical case, that particular contact pressure has to be found by which Δs_m is minimal; but no combination exists which could reduce the differential settlement to absolute zero.

The reliability of predicted settlements can be calculated on the basis of the probability theory, similarly to the case of slope stability analysis

(Section 1.6.2) or for the ultimate bearing capacity (Section 2.4.1.2).

Should we suppose for example that the following set of E_s values has been established — at distance d from each other — in the axis of a loaded strip foundation:

14.2 — 13.8 — 16.3 — 14.9 — 9.5 — 11.3 — 12.4 — 8.1. Then the regression line defined for the s_i value will have the following equation

$$s = 0.346 d + 3.01$$

and the value of the correlation coefficient is $r = 0.73$.

According to the equation above, the settlement to be expected at point 1 is $s_1 = 3.36 \text{ cm}$, and at point 8, $s_8 = 5.78 \text{ cm}$; thus the expected value of the differential settlement will be $\Delta s = 2.42 \text{ cm}$.

The standard deviation of the regression coefficient is:

$$\sigma_a = \sqrt{\frac{\sigma_r^2}{(n-1)\sigma_d^2}} = \sqrt{\frac{0.792^2}{(8-1)2.45^2}} = 0.122$$

considering that the residual standard deviation σ_r is:

$$\sigma_r = \sigma_s \sqrt{1 - r^2} = 1.159 \sqrt{1 - 0.73^2} = 0.792.$$

Accordingly, it may be stated with 90% probability that the regression coefficient cannot be greater than

$$0.346 + 1.28 \cdot 0.122 = 0.502$$

and Δs is not more than

$$(8 - 1) 0.502 = 3.52 \text{ cm}.$$

References

AIRY, G. B. (1862): *Brit. Assoc. Advancement, Sci. Rept.*
 ALTES, J.; (1976): *Die Grenztiefe bei Setzungsberechnungen. Bauingenieur*, No. 3.
 BABKOV, V. F. and BUKOWSKI, N. I. (1950): *Gruntovedenie i mehanika gruntov*. Moscow.

- BALLA, Á. (1962): Bearing capacity of foundations. *Proc. ASCE*, No. SM 5.
- BARATA, F. E. (1973): Prediction of settlements of foundations on sand. *Proc. 8th ICSMFE*, Vols 1,3, Moscow.
- BELL, R. A. and IWAKIRI, J. (1980): Settlement comparison used in tank-failure study. *Proc. ASCE*, Vol. GT 2.
- BIAREZ, J., BUREL, M. and WACK, B. (1961): Contribution à l'Étude de la Force Potante des Fondations. *Proc. 5th ICSMFE*, Vol. 1, London.
- BJERRUM, L. (1963): Discussion. *Proc. Eur. Conf.* Vol. 2, Wiesbaden.
- BJERRUM, L. and EGGESTAD, A. (1963): Interpretation of loading tests on sand. *Proc. Eur. Conf.* Vol. 1, Wiesbaden.
- BOUSSINESQ, J. (1885): *Applications des potentiels à l'étude de l'équilibre et du mouvement des solides élastiques*. Paris, Gauthier — Villars.
- BOROWICZKA, H. (1943): Die Druckausbreitung im Halbraum bei linear zunehmendem Elastizitätsmodul. *Ing. Archiv*, No. 2.
- BOZOUK, M. (1962): Soil shrinkage damages of shallow foundations at Ottawa. *Engg. J., (Canada)*, No. 7.
- BRADL, H. (1970): Die Spannungsermittlung in Mehrschichtsystem. *Der Bauingenieur*, No. 2.
- BRETH, H. and AMMANN, P. (1974): Time settlement and settlement-distribution with depth in Frankfurt clay. *Proc. Conf. on Settlement of Structures*, Cambridge.
- BRINCH HANSEN, J. (1955): Simpel beregning of fundamenters bæreevne. *Ingeniøren*, 4;.
- BRINCH HANSEN, J. (1961): A general formula for bearing capacity. *Ingeniøren*, Vol. 5.
- BRINCH HANSEN, J. and LUNDGREN, H. (1960): *Hauptprobleme der Bodenmechanik*. Springer, Berlin.
- BUISMAN, A. S. K. (1940) *Groundmechanica*, Waltman, Delft.
- BURLAND, J. B. and WROTH, C. P. (1974): Settlement of buildings and associated damage. *Proc. Conf. on Settlement of Structures*, Cambridge.
- BURMISTER, D. M. (1945): The general theory of stresses and displacements in layered systems. *J. Appl. Physics*, Vol. 16.
- BURMISTER, D. M. (1947): Discussion. *Symposium on load tests of bearing capacity of soils*, ASTM. No. 79.
- CAQUOT, A. (1934): *Équilibre des massifs à frottement interne*, Paris, Gauthier — Villars.
- CAQUOT, A. and KÉRISEL, J. (1953): Sur le terme de surface dans le calcul des fondations en milieu purvérulent. *Proc. 3rd ICSMFE*. Vol. 1, Zurich.
- COX, J. B. (1981): The settlement of a 55 km long highway on soft Bangkok clay. *Proc. 10th ICSMFE*. Vol. 1, Stockholm.
- DAVIS, E. H. and POULOS, H. G. (1968): The use of elastic theory for settlement prediction under three dimensional conditions. *Géotechnique*, No. 1.
- D'APPOLONIA, D. J. and BRISETTE, R. F. (1968): Settlement of spread footings on sand. *Proc. ASCE*. No. SM 3.
- D'APPOLONIA, D. J., POULOS, A. G. and LADD, CH. C. (1971): Initial settlement of structures on clay. *Proc. ASCE*. No. SM 10.
- DE BEER, E. E. (1970): Proefondervindelijke bijdrage tot de studie van het gransdraagvermogen van zand onder funderingen op stall. *Geotechnique*, No. 4.
- DENINGER, A. (1965): Neue Möglichkeiten der Berechnung von Gründungsplatten durch Benützung elektronischer Rechengerate. *Bautechnik*, No. 10.
- EGEROV, K. E. and BUDIN, A. YA. (1981): Stress-strain behaviour of soil bases related to time. *Proc. 10th ICSMFE*. Vol. 2, Stockholm.
- ERLENBACH, L. (1946): Über das Verhalten des Sandes bei Belastungsänderungen und Grundwasserbewegung. *Degebo*, Rep. 2.
- EWERT, R. (1969): Spannungen und Setzungen im Baugrund unter Berücksichtigung der Gründungstiefe. *Bauplanung-Bautechnik*, No. 7.
- FEDA, J., HAVLIČEK, J., SEYČEK, J. and SKOPEK, J. (1977): Active zone beneath foundations. *Proc. 9th ICSMFE*, Vol. 1, Tokyo.
- FELD, J. (1968): *Construction Failure*. Wiley, New York.
- FISCHER, K. (1957): Zur Berechnung der Setzung einer starren, mittig belasteten Kreisplatte auf elastischer Unterlage. *Beton und Stahlbetonbau*.
- FRASER, R. A. and WARDLE, L. J. (1976): Numerical analysis of rectangular rafts on layered foundations. *Géotechnique*, No. 4.
- FRÖHLICH, O. K. (1934): *Druckverteilung im Baugrunde*. Springer, Berlin.
- GIROUD, J. P. and TRAN-VO-NHIEM (1971): Force portante d'une fondation sur une pente. A.I.T.B.T.P. No. 283-284.
- GORBUNOV-POSADOV, M. J. (1953): *Raschet konstrukcii na uprugom osnovanii*, Izd. Stroit. i Arhitekturi, Moscow.
- GRASSHOF, H. (1951): Ein einfaches Näherungsverfahren zur Berechnung elastisch gebetteter Balken. *Bautechnik*.
- GRASSHOF, H. (1955): Die Berechnung einachsiger ausgesteifter Gründungsplatten. *Bautechnik*.
- HARR, M. E. (1977): *Mechanics of Particulate Media — a Probabilistic Approach*. McGraw-Hill, New York.
- HETÉNYI, M. (1946): *Beams on Elastic Foundations*. University of Michigan Press.
- HOMES, A. (1962): Équilibre des effort obliques sur les fondations au moyen de dalles de frottement.
- HOUSEL, W. S. (1929): A practical method for the selection of foundations based on fundamental research in soil mechanics. Univ. of Michigan, *Ann. Arbour*, Bull. 13.
- HRUBAN, K. (1944): A semi-infinite solid subjected to the pressure of a rigid body. *Bull. Int. de l'Ac. Tech. des Sc.*, No. 6.
- HU, G. C. Y. (1964): Variable-factors theory of bearing capacity. *Proc. ASCE*. Vol. SM 4.
- INOUE, V., TAMAOKI, K. and OGAI, T. (1977): Settlement of building due to pile downdrag. *Proc. 9th ICSMFE*. Vol. 1, Tokyo.
- JÁKY, J. (1948a): Sur la stabilité des masses de terre complètement plastiques. *Műegy. Közl.*
- JÁKY, J. (1948b): Influence of groundwater level oscillation on subsidence of structures. *Proc. 2nd ICSMFE*. Vol. 2, Rotterdam.
- JAROPOLSKII, I. V. (1929): O primenimosti teorii uprugnosti k rascheti estestvenih osnovanij. *Sbornik LIIPS*, No. XCIX.
- JEGOROV, K. E. and POPOVA, O. V. (1971): Osadki fundamentov soorushenij bashennovo tipa. III. Vsesayuznoe soveshshaniye. *Osnovaniya fundamenti i mekhanika gruntov*, Kiev.
- JELINEK, R. (1948): *Die Kraftausbreitung im Halbraum für querisotrope Böden*. Abh. Bodenmechanik und Grundbau, Bielefeld.
- JELINEK, R. (1951): Der Einfluss der Gründungstiefe und begrenzter Schichtmächtigkeit auf die Druckausbreitung im Baugrund. *Bautechnik*, 28.
- KANY, M. (1959): *Die Berechnung von Flächengründungen*. W. Ernst, Berlin.
- KÉRISEL, J. (1975): Old structures in relation to soil conditions. *Géotechnique*, No. 3.
- KÉRISEL, J. and QUATRE, M. (1968): Settlements under foundations. *Civ. Engg. and Public Works Rev.* No. 5, 6.
- KÉZDI, Á. (1947): Investigation of plane stress state (in Hungarian). Manuscript, Budapest.
- KÉZDI, Á. (1951): Einige Probleme der Spannungsverteilung im Boden. *Acta Techn. Acad. Sci. Hung.* Tom. II, fasc. 2-4.
- KÉZDI, Á. (1958): Beiträge zur Berechnung der Spannungsverteilung im Boden. *Bauingenieur*.
- KÉZDI, Á. (1961): Shallow foundations — Discussion of Section 3A. *Proc. of the 5th ICSMFE*, Vol. 3, Paris.
- KISHIDA, H. and TANKANO, H. (1976): Protrusion of piles out of ground surface due to ground subsidence. *Proc. 5th Budapest Conf. SMFE*. Akadémiai Kiadó, Budapest.
- KÖCLER, F. and SCHEIDIG, A. (1938): *Baugrund und Bauwerk*. W. Ernst, Berlin.
- KRIZEK, R. J. (1965): Approximation for Terzaghi's bearing capacity. *Proc. ASCE*. Vol. SM 2.
- KRŠMANOVIČ (1955): Influence de la continuité et de la rigidité sur le calcul des constructions et des poutres continues de fondation. *Ann. Trav. Publ. Belg.* 108.
- LACY, H. S. (1981): Pile integrity and capacity determined by re-driving. *Proc. 10th ICSMFE*. Vol. 2, Stockholm.
- LAMBE, T. W. (1964): Methods of estimating settlement. *Proc. ASCE Settl. Conf.* Northwest. Univ.
- LAMBE, T. W. (1967): Stress path method. *Proc. ASCE*. Vol. SM 6.
- LESKE, W. and KUSURELIS, D. (1965): Zur Definition der

- Kippsicherheit von Bauwerken. *Bauplanung-Bautechnik*, No. 4.
- LEUSSINK, H. (1953): Die Genauigkeit von Setzungsbeobachtungen. *Vorträge der Baugrundtagung*, 1953, Hannover.
- LEUSSINK, H. (1955): Über die Gleichmässigkeit von Bauwerksetzungen. *Vorträge der Baugrundtagung* 1954. Hamburg.
- LOGEASIS, L. (1971): Pathologie des fondations. *Ann. de l'Inst. Techn. du bâtiment et des travaux publics*, No. 280.
- LORENZ, H. and NEUMEUER, H. (1953): Spannungsrechnung infolge Kreislasten unter beliebigen Punkten innerhalb und ausserhalb der Kreisfläche. *Bautechnik*.
- LUMB, P. (1966): The variability of natural soils. *Canadian Geotechn. J.*, No. 2.
- LUNDGREN, H. and MORTENSEN, K. (1953): Determination by the theory of plasticity of the bearing capacity of continuous footing on sand. *Proc. 3rd ICSMFE*. Vol. 1, Zurich.
- MACLEOD, I. A. and LITTLEJOHN, G. S. (1974): Discussion on Session 5. *Proc. Conf. on Settlement of Structures*. Cambridge.
- MALIK, Z., MORTON, J. A. and RUIZ, C. (1977): Ovalization of cylindrical tanks as a result of foundation settlement. *J. of Strain Analysis*. No. 4.
- MARGUERRE, K. (1931): Druckverteilung durch eine elastische Schicht auf starrer-ruher Unterlage. *Ingenieur-Archiv*, Vol. 2.
- MARIUPOLSKII, L. G. (1965): Nasuschaya sposobnosty ankerh fundamentov. *Osnov, fund. i mekh. gruntov*, No. 1.
- MARR, W. A., RAMOS, J. A. and LAMBE, T. W. (1982): Criteria for settlement of tanks. *Proc. ASCE*. No. GT 8.
- MASLOV, N. N. (1949): *Prikladnaya mekhanika gruntov*. Mashstroizdat, Moscow.
- MCKINLEY, D. (1964): Field observation of structures damaged by settlement. *Proc. ASCE*. Vol. 90.
- MELAN, E. (1918): Die Druckverteilung durch eine elastische Schnitt. *Österr. Wochenschr. öff. Baudienst*. p. 83.
- MEYERHOF, G. G. (1951): The ultimate bearing capacity of foundations. *Géotechnique*.
- MEYERHOF, G. G. (1953): The bearing capacity of foundation under eccentric and inclined loads. *Proc. 3rd ICSMFE*. Vol. 1, Zurich.
- MEYERHOF, G. G. (1957): The ultimate bearing capacity of foundations on slopes. *Proc. 4th ICSMFE*. Vol. 3, London.
- MEYERHOF, G. G. (1963): Some recent research on the bearing capacity of foundations. *Can Geot. J.* No. 1
- MEYERHOF, G. G. (1965): Shallow foundations. *Proc. ASCE*. No. SM 2.
- MIZUNO, T. (1953): On the bearing power of soil under a uniformly distributed circular load. *Proc. 3rd ICSMFE*. Vol. 1, Zurich.
- MORTON, K. and AU, E. (1974): Settlement observations on eight structures in London. *Proc. Conf. on Settlement of Structures*. Cambridge.
- MUHS, H. (1969): Neue Erkenntnisse über die Tragfähigkeit von flachgegründeten Fundamenten aus Grossversuchen und ihre Bedeutung für die Berechnung. *Bautechnik*, No. 6.
- MUHS, H. and WEISS, K. (1973): Inclined load tests on shallow strip footings. *Proc. 8th ICSMFE*. Vol. 1.3, Moscow.
- MÜLLER, H. (1972): Setzungsprognosen nach dem Pressiometerverfahren von Ménard. *Bautechnik*, No. 9.
- NEUBER, H. (1961): Setzungen von Bauwerken und ihre Vorhersage. *Mitt. der deutschen Forschungsges. für Bodenmechanik*, No. 15.
- NEWMARK, N. M. (1935): Simplified computation of vertical pressures in elastic foundations. *Univ. Ill. Eng. Exper. Sta.*, Circular 24.
- ODEMARK, N. (1949): Investigations as to the elastic properties of soils and design of pavements according to the theory of elasticity. *Statens Väginstut*, No. 77.
- OHDE, J. (1939): Zur Theorie der Druckverteilung im Baugrund. *Der Bauingenieur*, No. 33/34.
- OHDE, J. (1942): Die Berechnung der Sohldruckverteilung unter Gründungskörpern. *Der Bauingenieur*.
- PENMAN, A. D. M. (1978): Soil-structure interaction and deformation problems with large oil tanks. *Ground Engg.*, No. 2.
- POKROVSKII, G. I. (1937): *Isledovaniya po fizike gruntov*. ONTI.
- POLSHIN, D. E. and TOKAR, R. A. (1957): Maximum allowable non-uniform settlement of structures. *Proc. 4th ICSMFE*. Vol. 1, London.
- PRAKASH, SH. and SARAN, S. (1971): Bearing capacity of eccentrically loaded footings. *Proc. ASCE*. No. SM 1.
- PRANDTL, L. (1920): Über die Härte plastischer Körper. *Nachr. Kgl. Ges. Wiss., Göttingen*, Math. Phys. Klasse.
- PUZIRJEVSKII, N. P. (1929): *Rascheti fundamentov*. Izd. Inst. Putej soobscheniya. Teoria Naprochennosti zemlistykh gruntov. Sbornik LIIPSZ. XCIX.
- RAES, P. E. (1941): Het opersingvraagstuk bej een strookvormig fundament. *Technisch Wetensgappolijk Tijdschrift*.
- RANKINE, W. J. M. (1857): On the stability of loose earth. *Transactions Royal Society London*, Vol. 147.
- REISSNER, H. (1924): Zum Erddruckproblem. *Proc. 1st Int. Congr. Appl. Mech.*, Delft.
- REPNIKOV, L. N. (1967): Raschet balok na uprugom osnovanii, obediniyuschem deformativnye svoistva osnovaniya Vinklery i lineino — deformiruemoy sredy. *Osnov., fundam. i mekh. gruntov*, No. 4.
- RESENDIZ, D. and HERRERA, I. (1969): A probabilistic formulation of settlement-controlled design. *Proc. 7th ICSMFE*, Vol. 2, Mexico.
- RÉTHÁTI, L. (1955): Relative Setzungen, als Funktion der Zeit. *Gedenkbuch für Prof. dr. J. Jáky*. Akadémiai Kiadó, Budapest.
- RÉTHÁTI, L. (1963): Die Sackung von rölligen Böden infolge der Aufnahme von Kapillarwasser. *Europäische Baugrundtagung*, Wiesbaden.
- RÉTHÁTI, L. (1965): The subsidence of granular soils from the combined effect of water absorption and loading. *Proc. of the 6th ICSMFE*. Vol. 1, Montreal.
- RÉTHÁTI, L. (1966): Theoretische Untersuchungsmethoden der im Erdboden entstehenden Plasticitätsbereiche. *Acta Techn. Acad. Sci. Hung.*, Tom. 53.
- RÉTHÁTI, L. (1969): Soil mechanics evaluation of building movements. *Hydrotechniki*, No. 1.
- RÉTHÁTI, L. (1976): On the shape factor ξ_y of the bearing-capacity equation. *Proc. of the 5th Budapest Conf. on SMFE*. Akadémiai Kiadó, Budapest.
- RÉTHÁTI, L. (1977): Building damages caused by subsoil (in Hungarian). Akadémiai Kiadó, Budapest.
- RÉTHÁTI, L. (1981): Statistical evaluation of calculated and measured settlements. *Acta Techn. Acad. Sci.* Tom. 93, fasc. 3—4.
- RÉTHÁTI, L. (1983): *Groundwater in Civil Engineering*. Elsevier — Akadémiai Kiadó, Amsterdam — Budapest.
- RUDNICKII, M. JA. (1968): K raschetu osadok fundamentov na rykhlyh peskhoh. *Osnov., fundam. i mekh. gruntov*, No. 2.
- SCHIELDS, D. H., SCOTT, J. D., BAUER, G. E., DESCHEMES, J. H. and BARSVARY, A. K. (1977): Bearing capacity of foundations near slopes. *Proc. 9th ICSMFE*. Vol. 1, Tokyo.
- SCHLEICHER, F. (1926): *Kreisplatten auf elastischer Unterlage*. Springer, Berlin.
- SCHULTZE, E. (1969): The combination of modulus of subgrade reaction and modulus of compressibility methods. *Int. Symp. "Civ. eng. structures resting on soil and rock," Sarajevo*.
- SCHULTZE, E. (1975): Some aspects concerning the application of statistics and probability to foundation structures. *Proc. of the 2nd Int. Conf. on Appl. of Statistics and Probability in Soil and Structural Engineering*. Vol. II, Aachen.
- SCHULTZE, E. (1977): The probabilistic approach to soil mechanics design. *Proc. 9th ICSMFE*. Vol. 3, Tokyo.
- SCHULTZE, E. and SHERIF, G. (1973): Prediction of settlements from evaluated observation for sand. *Proc. 8th ICSMFE*, Vol. 1.3, Moscow.
- SCHULTZE, E. and SIEVERING, W. (1977): Statistical evaluation of settlement observations. *Proc. 9th ICSMFE*. Vol. 1, Tokyo.
- SHERIF, G. (1970): Zur Auswertung von Zeitsetzungslinien von Hoch- und Industriebauten. *Mitt. VGB* 46.
- SHERIF, G. and KÖNIG, G. (1975): *Platten und Balken auf nachgiebigem Baugrund*. Springer, Berlin.
- SIMONS, N. E. and SOM, N. N. (1970): Settlement of structures on clay with particular emphasis on London clay. *Ciria Report*, 22.
- SINGH, A. (1971): How reliable is the factor of safety in found-

- ation engineering? *Proc. 1st Int. Conf. on Appl. of Statistics and Probability in Soil and Structural Engineering*, Hong Kong.
- SKEMPTON, A. W. (1957): Discussion — Session 5. *Proc. 4th ICSMFE*. Vol. 3, London.
- SKEMPTON, A. W. and BJERRUM, L. (1957): A contribution to the settlement analysis of foundations on clay. *Géotechnique*, No. 4.
- SKEMPTON, A. W. and MACDONALD, D. H. (1956): Allowable settlement of buildings. *Proc. Int. Civ. Engrs., part 3*. Vol. 5, London.
- SKEMPTON, A. W., PECK, R. and MACDONALD, D. H. (1955): Settlement analyses of six structures in Chicago and London. *Proc. Inst. Civ. Engrs.* Vol. 4, No. 4, London.
- SOKOLOVSKII, V. V. (1960): *Statika sypuchii sredi*. Izd. AN SSSR.
- STEINBRENNER, W. (1934): Tafeln zur Setzungsberechnung. *Strasse*, p. 121.
- TAKEO MOGAMI (1957): Numerical tables for calculation of stress components induced in a semi-infinite elastic solid, when force is applied at a point in the interior of the body. *Kajima Constr. Techn. Research Inst.*
- TAVENAS, F. and LEROUÉIL, S. (1980): The behaviour of embankments on clay foundations. *Canad. Geotechn. J.*, No. 2.
- TERZAGHI, K. (1923): Die Berechnung der Durchlässigkeit-ziffer des Tones aus dem Verlauf der hydrodynamischen Spannungserscheinungen. *Akad. Wissenschaft*, Vienna.
- TERZAGHI, K. (1938): Settlement of structures in Europe and methods of observation. *Trans. ASCE*, Vol. 103.
- TERZAGHI, K. (1943): *Theoretical Soil Mechanics*. Wiley, New York.
- TERZAGHI, K. (1956): Discussion on paper by Skempton and MacDonald "The allowable settlement of buildings". *Proc. Inst. Civ. Engrs. Part 3*, Vol. 5.
- TERZAGHI, K. and PECK, R. B. (1948, 1967): *Soil Mechanics in Engineering Practice*. Wiley, New York.
- TIMOSHENKO, S. (1957): *Strength of materials*. Part 1, D. von Nostrand, London.
- TSHEBOTARIOFF, G. P. (1951): *Soil Mechanics, Foundations and Earth Structures*. McGraw-Hill, New York.
- TSYTOVICH, N. A. (1951, 1963): *Mekhanika gruntov*. Stroizdat, Moscow.
- VARGA, L. (1962): The sliding of footings (in Hungarian). *Mélyép. Szemle*, No. 6.
- VEŠIĆ, A. (1963): Bearing capacity of deep foundations in sand. *Highway Research Record*. No. 39.
- VEŠIĆ, A. (1973): Analysis of ultimate loads of shallow foundations. *Proc. ASCE*. SM 1.
- WESTERGAARD, H. M. (1938): A problem of elasticity suggested by a problem in soil mechanics. In: *Contributions to the Mechanics of Solids*. MacMillan, New York.
- WINDGATE, R. H. (1938): *A settlement study interrelating building frame stresses and soil stresses*. Massachusetts Inst. of Techn. M. S. Thesis. (Manuscript.)
- ZAHARESCU, J.: Contribuții la studiul capacitii portante a fundațiilor. *Acad. Rep. Pop. Romine*.
- ZEEVAERT, L. and VOGEL, H. (1953): Discussion in the *Proc. 3rd ICSMFE*. Vol. III, Zurich.
- ZHUKOV, N. Y. et al. (1979): Ustanovlenie znachenih predelno¹ — dopustimyh neravnomernyh osadok selskokoziastvennyh zdanih. *Osnov., fundamenti i meh. gruntov*, No. 5.

Chapter 3.

Bearing capacity and settlement of pile foundations

3.1 General remarks

Foundation types outlined in Chapter 2 are not necessarily and under all conditions appropriate to transfer the loads from superstructures to the soil. If the shear resistance is small and/or the compressibility is large in the upper strata, the load has to be transmitted to more radiable strata at greater depths. A compound word for foundations complying with this aim is deep foundation. Their widespread application may have several reasons:

- increasingly heavily loaded structures (high buildings, silos, etc.);
- structures sensitive to settlements are required nowadays;
- deep foundation methods are fairly simple to mechanize (to economize in time and labour);
- tiresome work is eliminated (for example dewatering and supporting of foundation pits) when deep foundation is applied.

In respect to soil mechanics, there are two major features which constitute the difference between the two foundation methods:

(a) The side walls of a deep foundation do provide a considerable friction to the bearing capacity (which in some cases may practically attain its totality).

(b) There is a profound difference in the failure mechanism with the two types of foundation methods.

Several deep foundation methods are known (well foundations, caisson, diaphragm walls, etc.) but piling has always been the most widely applied version. This may partly explain why the literature deals predominantly with this type of deep foundation method, but a contributive factor might also be that the other types do not raise so serious problems.

The main differences between pile and shallow foundation can be condensed in the points below.

(a) In a different form — and generally more intensively — the difference between granular and cohesive soils appears.

(b) Bearing capacity and settlement are affected not only by the soil below but also by the soil around the foundation, with the latter sometimes being the determinant.

(c) Construction technology (driving, boring, pressing, prefabrication, casting, etc.) and also the shape of the pile (extended foot, taper, tube, etc.) have an important weight in considerations.

(d) Group action (superposition) has a significant influence on both the bearing capacity and the settlement of the foundation.

(e) The construction technology may cause difficulties not only in the existing buildings but also in the neighbouring piles.

(f) Both in respect to statics and to soil mechanics there are sharp differences between axially and laterally loaded piles.

(g) In searching for the best technical and economical solution very often a loading test is performed which differs basically from that made for shallow foundations, including its evaluation.

(h) Piles are usually not designed for limiting stability conditions (slide, tilt, buoyancy) and very seldom for buckling.

3.2 Performance of single piles

Two major problems arise during the design of individual (single) piles: what will be the bearing capacity of a pile (Section 3.2.3) and what will be the settlement of the pile (Section 3.2.4)? These two questions are closely interrelated, partly because in restricting the settlement a means is simultaneously introduced against failure, and partly because the bearing capacity of a pile is very often decided upon its settlement.

A strong influence is exercised on the performance of a pile by the processes which develop in the surrounding soil (Section 3.2.1) and by the type of the pile which will be defined — among others — by its stiffness (Section 3.2.2).

In respect to the surrounding soil the main factor is the density when it is a case of sand, or the degree of overconsolidation when it is a clay, but homogeneity has an influence in both cases.

3.2.1 **The properties of the soil around a pile**

The changes in the strength and deformation properties that occur during the excavation for bored piles and the driving of prefabricated piles can have a pronounced effect on both the ultimate bearing capacity and the settlement of piles.

For bored piles it is mainly the soil in a narrow zone just around the shaft that is affected. MEYERHOF (1976) estimates the disturbed zone around a pile as not more than 25 mm. The disturbance can be large if a casing with oversized shoe is used.

The process of installing a displacement pile into clay is not easily modelled analytically. Figure 259 shows schematically the main movements which occur in the soil. Their most common idealisation has been attempted by assuming the expansion of a cylindrical cavity (e.g. SÖDEBERG, 1962). This idea neglects, however, such local effects as heave of the ground surface around the pile and does not attempt to model the precise detail of the soil movement near the advancing pile tip. It has been shown, however (RANDOLPH *et al.*, 1979a) that over most of the pile length, the radial soil displacement due to the installation of a displacement pile is well described when the installation is considered as the expansion of a cylindrical cavity under the conditions of plane strain.

In investigating the impact of a driven pile on the surrounding soil mass, two questions require an answer:

- to what extent with the stress condition and the strength of the surrounding soil be affected, and
- how large displacement has to be presumed, and at what distance from the pile will this deformation diminish to zero?

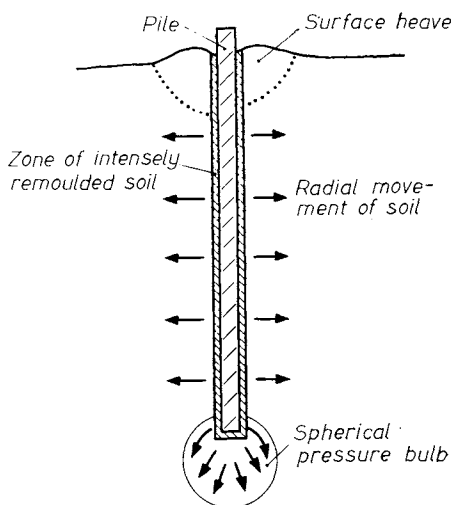


Fig. 259. Soil movements due to installation of pile (RANDOLPH, 1983)

The first question depends on the excess pore pressure (Δu) to be anticipated. STEENFELT *et al.* (1981) stated, on the basis of model tests on jacked piles, that the relation between Δu and the distance from the axis of the pile (r) is well described by the formula:

$$\frac{d(\Delta u)}{d(\ln r)} = -2c_u, \quad (346)$$

where c_u is the undrained shear strength of the soil.

Discussing the same problem in general, RANDOLPH and WROTH (1982) came to the following conclusion. The excess pore pressure arises partly from the increase in the mean total stress that accompanies cavity expansion, and partly as a result of changes in the mean effective stress as the soil is sheared and remoulded. For normally or lightly overconsolidated clay the mean effective stress will decrease during undrained shearing to failure, while for heavily overconsolidated clay there will be an increase in the mean effective stress (as the soil attempts to dilate). It may therefore be expected that higher excess pore pressure will be generated in a lightly overconsolidated clay than in a heavily overconsolidated clay. RANDOLPH *et al.* (1979b) suggest an approximate expression for estimating the excess pore pressure generated adjacent to a driven pile:

$$\Delta u = 4c_{u0} - \Delta p', \quad (347)$$

where $\Delta p'$ is the change in mean effective stress due to shearing the soil to a critical state condition. For normally consolidated soil $\Delta p'$ will be negative and will typically be in the range of one to one and half c_{u0} . At increasing values of the overconsolidation ratio (OCR) $\Delta p'$ will increase, becoming positive for values of OCR greater than 2–3.

This trend of decreasing excess pore pressure with increasing OCR has been found in model pile tests reported on by FRANCESCON (1982). Figure 260 shows some of his experimental results where the excess pore pressure generated at the pile shaft during installation has been plotted against OCR. (The value Δu has been normalised by the initial undrained shear strength, c_{u0} , and also by the effective overburden pressure, σ'_{v0} .)

The excess pore-water pressure can locally be so high that the soil fractures radially around the pile (hydraulic fracturing). These radial cracks impede the subsequent reconsolidation of the soil (BROMS, 1981).

STEENFELT *et al.* (1981) after having analysed the displacement of the soil around a driven pile, produced the formula

$$\frac{\xi}{r_0} = \sqrt{\left(\frac{r}{r_0}\right)^2 + \varrho^2} - \frac{r}{r_0} \quad (348)$$

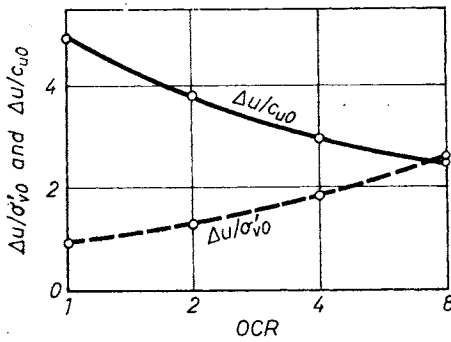


Fig. 260. Excess pore pressures generated close to a model jacked pile during installation (FRANCESCON, 1982)

for the calculation of the radial displacement ξ of an elementary soil particle, on the basis of the model of undrained cylindrical cavity expansion. Here

$$\rho = 1 - \left(\frac{\rho_i}{\rho_0} \right)^2$$

is the so-called displacement ratio, r is the distance from the central axis of the pile, r_i is the internal and r_0 the external radius of the pile.

In evaluating their model tests, carried out on jacked piles, the authors found that an assumption of $\rho = 0.8$ would have given a better fit of the test results to the curve calculated by using Eq. (348), despite the fact that the actually applied closed ended pile required the substitution of $\rho = 1$. In the wake of this discrepancy the authors inferred that about 20% of soil particles did not move laterally but took a vertical direction.

RANDOLPH (1977) proposed finding the influence radius (r_m) around a driven pile from the formula

$$r_m = 2.5 \rho l (1 - \nu), \quad (349)$$

in which

$$\rho = \frac{G_{1/2}}{G_l};$$

$G_{1/2}$ and G_l are the values of the shear modulus at pile mid and pile base depths, respectively.

A group of piles is going to have a more extensive zone of influence than a single pile of the same length. It has been found (RANDOLPH, 1977) that r_m should be increased by an amount of r_g related to the dimension of the pile group. Thus

$$r_m = 2.5 \rho l (1 - \nu) + r_g. \quad (350)$$

For rectangular groups of pile r_g may be taken as the radius of the circle of area equivalent to that covered by the pile group.

3.2.2 Definition of pile stiffness

Similarly to shallow foundations, there exists a measure for piles also which characterizes the interrelation between the pile and the surrounding soil (eventually deterministic for the performance

of the pile). Thus, the flexibility of the pile can be described by the expression

$$K_R = \frac{E_p I_p}{E_s L^4}, \quad (351)$$

which is the so-called "relative pile flexibility ratio". E_p denotes the modulus of elasticity of the pile, I_p is the moment of inertia, and L is the length of the pile.

BANERJEE and DAVIES (1978) define a pile as very stiff (rigid) when $K_R < 0.1$, and $K_R = 10^{-4}$ corresponds to piles commonly encountered in practice (flexible piles). POULOS (1971a) considers a pile as perfectly stiff when $K_R \geq 1.0$, and absolutely flexible when $K_R \leq 10^{-5}$. (The case $K_R = 0$ corresponds to an infinitely long pile.)

The stiffness of piles has a significant effect on the soil-pile structure interaction. Laterally loaded piles are classified according to their stiffness into the following groups (BROMS, 1972):

1. rigid or short piles;
2. semi-rigid or intermediate piles;
3. flexible or long piles.

The long pile is defined as one whose lateral deflection at the ground surface is independent of the pile length when a lateral load is applied to the pile head. In other words, a structure supported on long piles has natural periods of translational modes that are not affected by the pile length, L . From the same point of view FLORES-BERRONES (1977) has classified the long pile by $\lambda > 0.5$ where

$$\lambda = (\beta L)^4 \quad (352)$$

and

$$\beta = \left(\frac{k_h B}{4 E_p I_p} \right)^{0.25}, \quad (353)$$

where k_h is the subgrade reaction.

The performance of a pile can also be related to the so-called "relative pile compressibility ratio" (see for example BANERJEE and DAVIES, 1978):

$$K_A = \frac{E_p}{E_s}. \quad (354)$$

When $K_A > 10^4$ the pile is stiff but when $K_A < 10^2$ the pile is exposed to strain (compressible).

3.2.3 Load-bearing capacity of single piles

The ultimate bearing capacity at failure Q_u is composed of the point resistance Q_p (Section 3.2.3.2) and the side resistance Q_s (Section 3.2.3.1), i.e. it is:

$$Q_u = Q_p + Q_s. \quad (355)$$

This does not mean, however, that the two components can be summarized without any condi-

tion, because both Q_p and Q_s reach their maximal value only after having attained a critical settlement (displacement) which is not the same for the two terms. Thus, the ratio Q_p/Q_s depends on several factors: the type of the pile and of the soil, the magnitude of the load, and also on time (Section 3.2.3.3). Time is predominant in cohesive soils (Section 3.2.3.4) and may have a deterministic influence not only on the ratio mentioned but on the ultimate bearing capacity as well.

3.2.3.1 *Load-bearing capacity due to skin friction*

The vertical displacement of an axially loaded pile gradually mobilizes the friction between the side of the pile and the surrounding soil. Its specific unit is usually denoted by f_s (or c_a) and is given in kN/m². The bearing capacity from side friction on a pile is defined, therefore, by the formula

$$Q_s = U_s \sum_{i=1}^n f_{si} \Delta z_i, \quad (356)$$

where U_s is the perimeter of the pile and Δz_i is the height of that section. If we use \bar{f}_s as the mean of specific side frictions, then

$$Q_s = \bar{f}_s A_s, \quad (357)$$

in which A_s means the surface area of the pile.

Two main models are available for the estimation of the specific skin friction for design purposes: one reckons with the total stresses and the other calculates effective stresses.

The total stress method defines c_a as a function of the undrained shear strength (c_u). Experience has shown that

$$c_a = \alpha c_u, \quad (358)$$

where α is the so-called adhesion factor, which depends on

- the nature (e.g. the plasticity index) and strength of the soil;
- the dimensions and the method of installation of the pile and
- on time.

The values of α vary within wide limits (0.3–1.0) and decrease rapidly as shear strength increases. For driven piles, the values of α range from unity for soft clay to one and half or less for stiff clay, while for bored piles α is around 0.5 in stiff clay (TOMLINSON, 1957 and 1971; WOODWARD and BOITANO 1961).

Some source claim that for piles of various types or shapes the formula

$$f_s = S \alpha c_u \quad (359)$$

takes hold, where S is the shape factor.

BALASUBRAMANIAM *et al.* (1981) assume, for example, $S = 1$ for vertical plain shafts and $S = 1.2$ for tapered shafts.

VESIĆ (1967) suggested calculating c_a from the following formula (instead of Eq. (358)):

$$c_a = 50(1 - 17 - 0.01c_u). \quad (360)$$

The effective stress method, proposed by BURLAND (1973), relates the shaft resistance to the effective stress produced by the overburden pressure $\bar{\sigma}_v$ through the equation

$$f_s = K_s \bar{\sigma}_v \tan \Phi'_a, \quad (361)$$

where the coefficient

$$K_s \tan \Phi'_a = \beta \quad (362)$$

takes care of the coefficient of the shaft pressure K_s , and the roughness of the pile surface (Φ'_a is the angle of friction along the pile shaft).

The coefficient K_s is affected by the coefficient of lateral earth pressure at rest

$$K_0 = 1 - \sin \Phi', \quad (363)$$

the type (displacement or non-displacement pile) and shape of the pile (straight sides or tapered). For bored piles and for piles driven into saturated soft clay the coefficient K_s may be expected to be close to that of the earth pressure at rest K_0 (BURLAND, 1973 and others), as has been found in loose sand too. Analysis of piles driven into soft and medium clays shows that the factor β decreases with the length of the pile in a range of about 0.25 to 0.50 for short piles to about 0.1 to 0.25 for very long (25–30 m) piles. This may be explained by the progressive mobilization of the maximum skin friction due to the compression of long piles (MEYERHOF, 1976).

The specific skin friction varies substantially with the density in sands. MEYERHOF (1976) has found, for example, $K_s \approx K_0$ for bored piles or piles jacked into loose sand, and $K_s \geq 4K_0$ for piles driven into dense sand — due to dilatancy effects and other factors. KÉRISEL *et al.* (1965) conducted trial tests and disclosed the following relation between f_s and the dry bulk density of the sand:

γ_d (kN/m ³)	1.58	1.685	1.75
f_s (kN/m ²)	5–10	30	70

Suggestions in respect to β have been made by several other authors as well.

VIJAVERGIYA and FOCHT (1972) included the undrained shear strength in their expression:

$$f_s = \lambda(p'_v + 2s_u), \quad (364)$$

where λ is a function of length.

JANBU (1976) proposed to use

$$f_s = S_v(p'_v + a), \quad (365)$$

where $a = c \cdot \cot \Phi$ is the attraction, and S_v is a function of the friction angle and length.

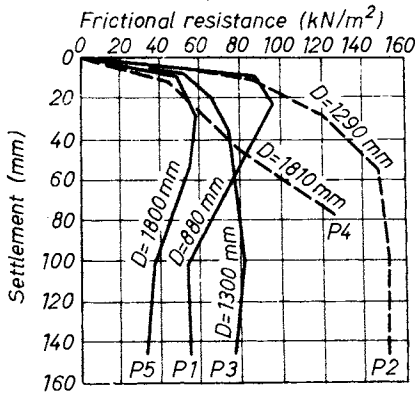


Fig. 261. Changes in frictional resistance with settlement (JELINEK *et al.*, 1977)

ZEEVAERT (1973) presented the formula:

$$f_s = \sigma_z \frac{1 - \sin^2 \Phi}{1 + \sin^2 \Phi} \tan \Phi. \quad (366)$$

BJERRUM'S (1973) suggestion was:

$$f_s = \mu_L [(0.3 - 0.001 I_p) \sqrt{R_0} p'_v + 0.008 I_p c_u], \quad (367)$$

where μ_L is a function of the pile length, R_0 is the overconsolidation ratio (OCR).

MEYERHOF (1976) would prefer to involve the OCR in the factor K_s , and so, instead of Eq. (362), he writes:

$$K_s = (1 - \sin \Phi) \sqrt{R_0} \tan \Phi_a. \quad (368)$$

Surveys made *in situ* revealed that K_s depends also on the depth. Trial tests conducted in sand prompted MEYERHOF (1976) to propose that the local coefficient K_z decreases with depth along the pile from a maximum near the top, where K_s may approach the passive earth pressure coefficient, to a minimum near the pile point where K_z may be less than K_0 , the average ultimate value of K_z being denoted by K_s .

A great practical importance can be attributed to the question: what is the displacement (settle-

ment) of the pile which produces the maximal skin friction? Figure 261 illustrates (after JELINEK *et al.*, 1977) measured f_s values as a function of s for five large diameter piles in clay. Thus, for piles without enlarged bases (Nos 1, 3, 5), full mobilization of frictional resistance is reached at a settlement of approximately 20 mm and for piles with enlarged bases (Nos 2, 4) at 50 mm or more. As the settlement increases beyond the point of full mobilization, the friction resistance either remains constant or decreases. Similar results have also been reported by other authors; for small diameter piles the critical displacement was found around 8 to 10 mm.

The so-called transfer curve f_s, s (or τ, s) can be approximated with an exponential expression or with a hyperbola.

In the theory of elasticity the relationship between stress and strain is assumed to be linear. This assumption is invalid here, the aim being to investigate the ultimate condition as well. For this reason, allowing also for the results of experiments performed for determining the angle of surface friction, the following formula has been developed (KÉZDI, 1957):

$$\tau = \sigma \tan \Phi \left[1 - \exp \left(-k \frac{s}{s_0 - s} \right) \right]. \quad (369)$$

In the formula

- $\tau = \sigma \tan \Phi$, the equation describing Coulomb's line in the ultimate condition (shear failure at the pile surface),
- s = the relative displacement between the pile and the soil,
- k = a constant,
- s_0 = shear deformation at which the full shear resistance is mobilized.

The magnitude of s_0 was found during the experiments to depend only little on the normal stress. The result of surface friction test (shear of sand on a concrete surface) is shown in Fig. 262.

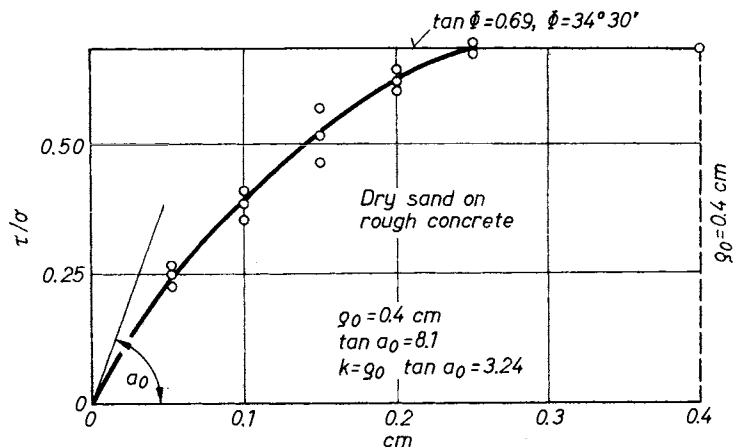


Fig. 262. Determination of friction coefficients between concrete and sand

All boundary conditions are satisfied by Eq. (369) in that

1. $\tau = 0$ at $\sigma = 0$;
2. $\tau = 0$ for $s = 0$;
3. $\tau = \sigma \tan \Phi$ for $s = s_0$ (Coulombs' line);
4. $\partial\tau/\partial s = 0$ for $s = s_0$.

The constants involved in the equation are simple to determine. The magnitude of φ is obtained as the slope of Coulomb's line at failure, s_0 is found reliably from the diagram of the load-penetration curves, while k is computed from the slope of the tangent to the curve $\tau/\sigma = \tan \Phi f(s)$ at the origin. In fact (see Fig. 263):

$$\tan \alpha_0 = (\partial\tau/\partial s)_{s=0},$$

$$\frac{\partial\tau}{\partial s} = \sigma \tan \Phi \left[ke^{-k \frac{s}{s_0-s}} \frac{s_0}{(s_0-s)^2} \right]$$

so that

$$\tan \alpha_0 = k/s_0$$

whence

$$k = s_0 \tan \alpha_0.$$

An approximation with hyperbola has been presented by SABINI and SAPIO (1981) in the form;

$$\tau = \frac{s}{a + bs}. \tag{370}$$

Plotting the experimental points in the plane s/τ , a straight line can be fitted to them:

$$\frac{s}{\tau} = a + bs$$

thus allowing the determination of the parameters a and b of the hyperbola as the intercept and slope of the straight line. The asymptotic value of τ is given by

$$\tau = \lim_{s \rightarrow \infty} \frac{s}{a + bs} = \frac{1}{b}. \tag{371}$$

During the last 10-15 years, some authors have called the attention to the finding that the skin friction increases only to a critical depth (D_{cr}) and

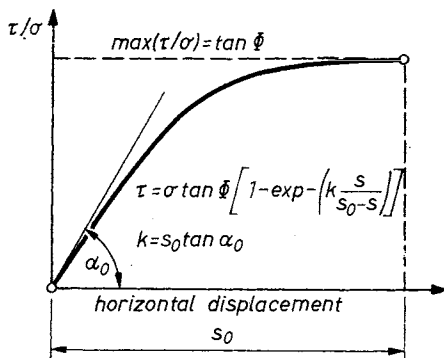


Fig. 263. Shear-path curve

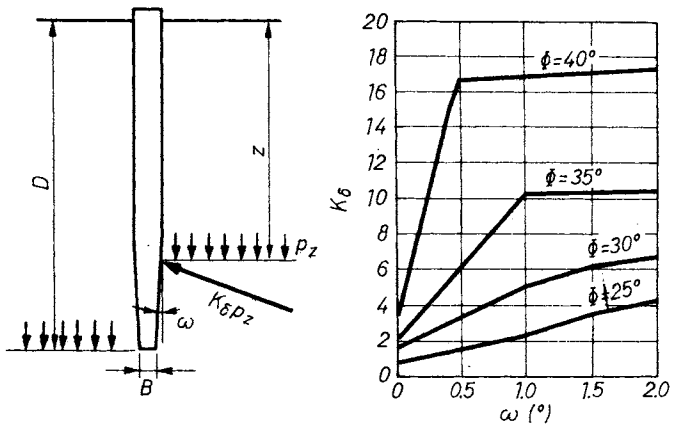


Fig. 264. Relationship between taper (ω) and K_δ (LINDQUIST and PETAJA, 1981)

remains constant below this depth. MEYERHOF (1976) states that the depth can be taken as identical with the critical depth given for the point resistance (Section 3.2.3.2).

It was mentioned before that f_s depends also on the shape of the pile. Figure 264 (after NORLUND, 1963) represents the factor $K_s = K_\delta$ relating to conical piles as a function of the angle ω . Trial tests and experimentation conducted by LINDQUIST and PETAJA (1981) on such piles revealed how important it was to find and apply the proper value of Φ .

3.2.3.2 Load-bearing capacity due to point resistance

The point resistance of piles implies the same concept as the ultimate load-bearing capacity with shallow foundations. The so-called static formulas assume that below the pile tip and around the shaft sliding surfaces develop, and the point resistance is provided by the shear strength in acting against failure. Thus the formula presented for its calculation resembles the one used to design a shallow foundation:

$$Q_p = q_p A_p = A_p (p_0 N_q + c N_c), \tag{372}$$

where p_0 is the overburden pressure at the elevation of the pile-point, and A_p is the cross-section area of the pile.

Several authors made proposals for the calculation of the point resistance. As an example, the following one is re-called here.

BEREZANTSEV (1952, 1960) assumed failure to occur under the pile tip only and a compacted zone to develop around the pile (BEREZANTSEV et al., 1961). This zone settles together with the pile as the latter is loaded (Fig. 265). The development of failure surfaces under the pile tip is prevented by the soil mass $b c d a - b_1 c_1 d_1 a_1$, the weight of which is reduced, however, by frictional forces induced along the cylindrical surface. These frictional forces are found in terms of the

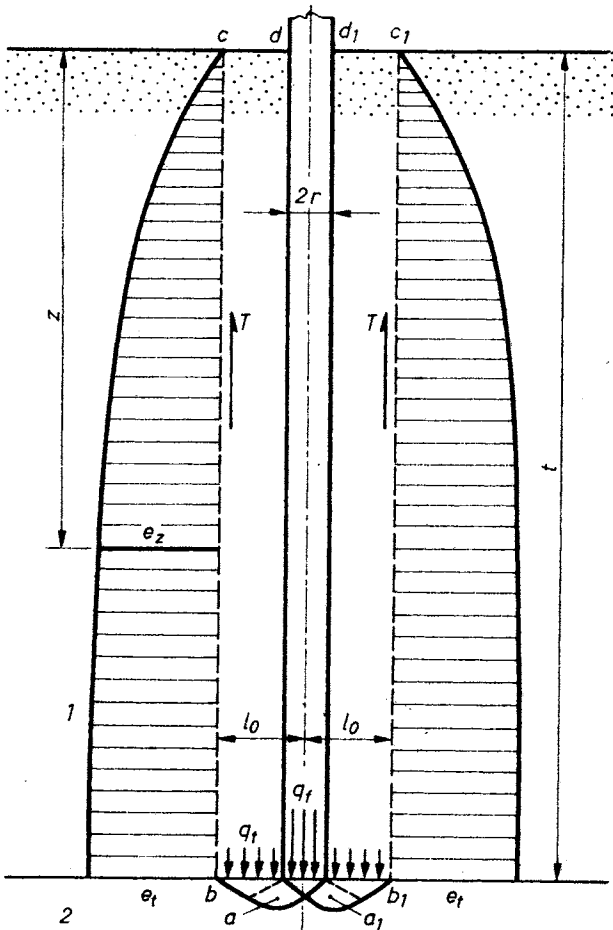


Fig. 265. Failure mechanism in the Berezantsev theory

normal stresses acting on the cylindrical surface $b c$, or $b_1 c_1$. The normal stresses, in turn, are found by solving the axial-symmetrical problem of limit equilibrium with the help of Berezantsev's earth pressure theory (1952). The magnitude of the horizontal pressure intensity at depth z is accordingly

$$e_2 = \frac{\tan(45^\circ - \Phi_1/2)}{\lambda - 1}$$

$$\left\{ 1 - \left[\frac{1}{1 + \frac{z}{l_0} \tan(45^\circ - \Phi_1/2)} \right]^{\lambda-1} \right\} \gamma_1 l_0,$$

where Φ_1 and γ_1 are characteristics of the soil layer around the pile tip and

$$\lambda = 2 \tan \Phi_1 \tan \left(45^\circ + \frac{\Phi_1}{2} \right).$$

The failure surface under the pile tip is, according to the theory of Prandtl-Caquot

$$l_0 = r \left[1 + \frac{\sqrt{2} \exp^{(45^\circ - \Phi) \tan \Phi/2}}{\sin \left(45^\circ - \frac{\Phi_2}{2} \right)} \right],$$

Table 18. Values of α_t

$t/2r$	Φ_1	26°	30°	34°	37°	40°
5		0.75	0.77	0.81	0.83	0.85
10		0.62	0.67	0.73	0.76	0.79
15		0.55	0.61	0.68	0.73	0.77
20		0.49	0.57	0.65	0.71	0.75
25		0.44	0.53	0.63	0.70	0.74

where Φ_2 is the angle of internal friction in the soil under the pile tip.

The vertical stress q_t acting in the plane of the pile tip is computed hereafter. The sum of frictional resistance obtained from the expression $e_2 \tan \Phi_1$ is deduced from the weight of the soil mass $cb - b_1 c_1$ and the residual is divided by the base area of the cylinder. The result is written into the form

$$q_t = \alpha_t \gamma_1 t.$$

The coefficient α_t is a function of the ratio $t/2r$ and of the friction angle Φ . For numerical values see Table 18.

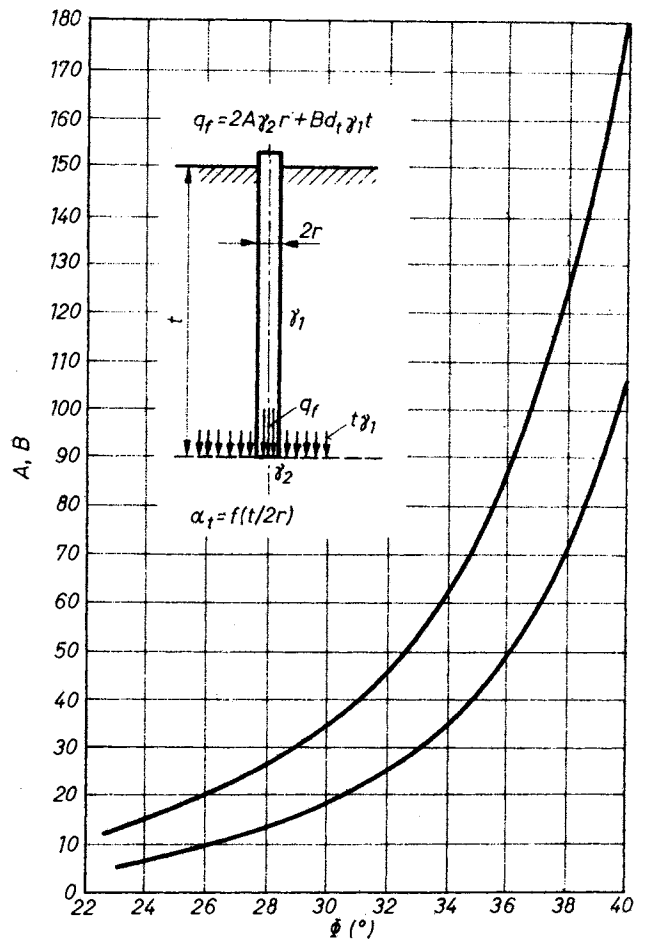


Fig. 266. Factors for calculating the bearing capacity of a pile, after Berezantsev

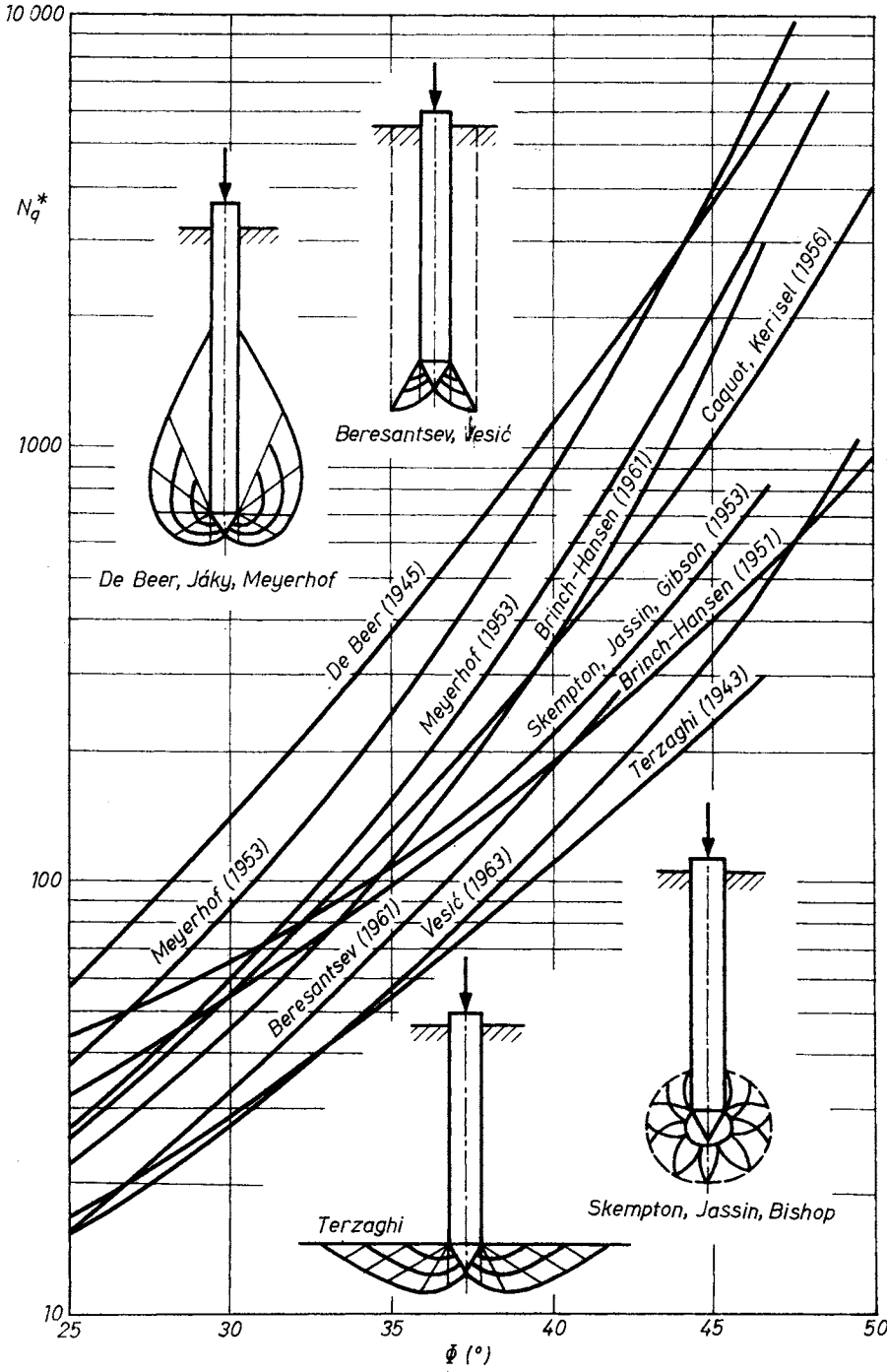


Fig. 267. Bearing capacity factors N_q for a deeply founded circular plate ($N_q^* = N_q \xi_q$)

The vertical stress q_f bringing about the failure condition depicted in Fig. 265 is found on the basis of the limit equilibrium theory of the axisymmetrical state of stress from the expression

$$q_f = 2A\gamma_2 r + B\alpha_1 \gamma_1 t.$$

The constants A and B are obtained from Fig. 266. The end-bearing resistance of the pile is thus

$$P_s = r^2 \pi q_f.$$

No side friction is commonly assumed to act in combination with this mechanism of failure.

Starting from different failure mechanisms, other authors have suggested different load-bearing coefficients. A review thereof is presented in Fig. 267 (VESIĆ, 1967), indicating also the essential features of the failure pattern assumed. The theoretical formulae have the general form

$$q_p = c N_c \xi_c + q_t N_q \xi_q,$$

where N_c and N_q are the bearing capacity factors, while ξ_c and ξ_q are the shape coefficients. The following expressions are derived:

$$N_c = (N_q - 1) \cot \Phi,$$

$$\xi_c = \frac{\xi_q N - 1}{N - 1}.$$

The values of $N^*_q = N_q \xi_q$ are shown in Fig. 267. Recently carried out research has proved that Eq. (372) can only be used with some restrictions.

One of the most important results of pertinent investigations disclosed, namely, that the ultimate unit point pressure remains constant beyond a certain depth (and so does not depend on the overburden pressure). One of the first such observations will be presented here after KÉRISEL *et al.* (1965), in Fig. 268. The authors concluded therefrom that

(a) the q_p — independently from the density of the sand — remains constant beneath a certain depth;

(b) in loose sand, q_p is significantly smaller than had been calculated from the Prandtl-theory (for 2 MN/m² the real value of $N_q = 18$ has been found as correct instead of the value of formula 33.3).

The authors also deduced that in loose sand q_p does not depend on the diameter of the pile. In

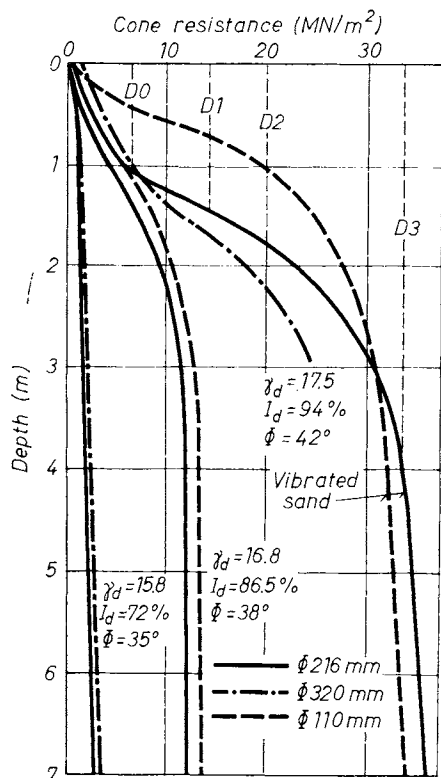


Fig. 268. Changes of the unit point pressure with depth (KÉRISEL *et al.*, 1965)

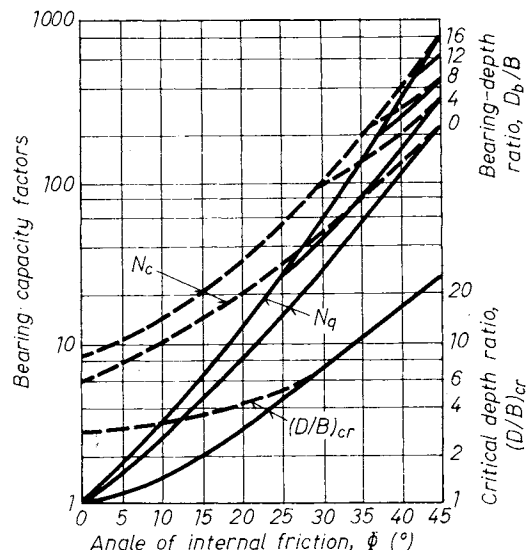


Fig. 269. Bearing capacity factors and critical depth ratios for driven piles (MEYERHOF, 1976)

medium dense and dense sand the critical depth does depend on this diameter, and so, in this case there exists a definitive ratio of

$$\left(\frac{D}{B}\right)_{cr} \tag{373}$$

due to effects of soil compressibility, crushing, arching, and other factors.

Making use of the previously mentioned findings, MEYERHOF (1976) proposed calculating Q_p in the following manner.

In sand the presumption has to be true that

$$q_p = p_0 N_q \leq q_l, \tag{374}$$

where q_l is the limiting value of unit point resistance for $D/B \geq (D/B)_{cr}$. The semi-empirical relationship between N_q for driven circular or square piles with various depth ratios D_b/B in the bearing stratum and the angle of internal friction Φ of the soil before pile driving is shown in Fig. 269. It has been found (CAQUOT and KÉRISEL, 1966; MEYERHOF, 1963) that the factor N_q increases roughly linearly with D_b/B and reaches its maximum value at a depth ratio of roughly one-half of the critical depth ratio $(D/B)_{cr}$ beyond which conventional bearing capacity theory no longer applies. The approximate depth ratio $(D/B)_{cr}$ after DE BEER (1971) is also shown in Fig. 269, and at full sized piles it depends mainly on the friction angle, the compressibility of the soil, and groundwater conditions. The relation of q_l to Φ can be approximated by using the formula:

$$q_l [100 \text{ kN/m}^2] = 0.5 N_q \tan \Phi. \tag{375a}$$

So, its range is between 25 and 50 kN/m², in loose sand and dense sand, respectively.

The values of N_q and q_l are also influenced by the compressibility of the soil, the method of pile

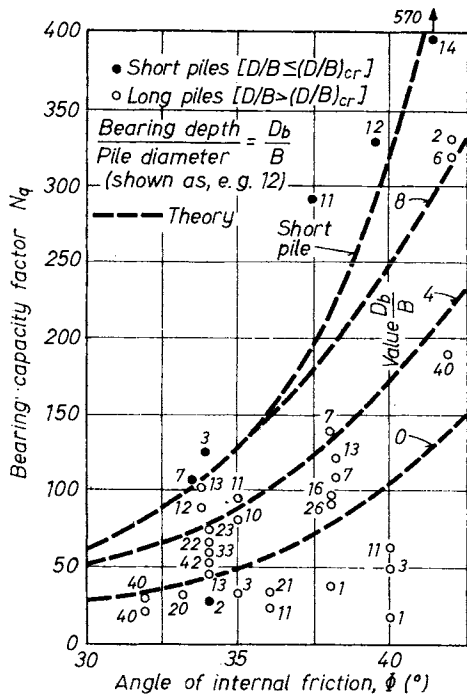


Fig. 270. Bearing capacity factors for driven piles in sand (MEYERHOF, 1976)

installation, and other factors. Thus, for a given initial Φ , bored piles have a unit point resistance of only about one-third to one-half of that of driven piles (DE BEER, 1964; KÉRISEL, 1961; VEŠIĆ, 1967), and bulbous piles driven with great impact energy have up to about twice the unit point resistance of driven piles of constant A_p (MEYERHOF, 1959).

If piles are driven into homogeneous soil to more than the critical depth, or if they penetrate through compressible material into a thick bearing stratum which is located below the critical depth of the stratum, the unit point resistance cannot be estimated by conventional bearing capacity theory in terms of N_q . The corresponding value of q_p becomes practically independent of p_0 at the pile point and it depends on the value of q_l . This is shown by an analysis of the results of pile load tests (MEYERHOF, 1976) which roughly support the semi-empirical bearing capacity factors, N_q , for short piles in sand above the critical depth but not for piles longer than about 15 to 20 pile diameters (Fig. 270).

In clay Eq. (374) can be written in the following form:

$$q_p = p_0 N_q + c N_c \leq q_m, \quad (375b)$$

where q_m is the limiting value of the point resistance below the critical depth. The semi-empirical factor N_c can be read from Fig. 269.

In saturated homogeneous clay under undrained conditions both theory and observation show that the value of N_c below the critical depth varies

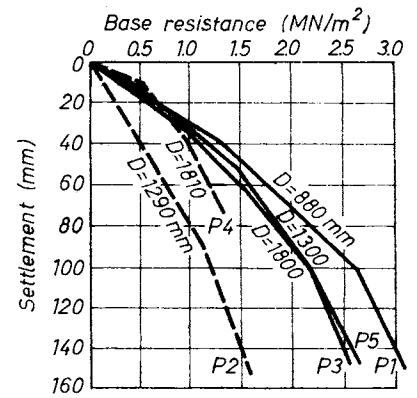


Fig. 271. Base resistance of straight piles and piles with enlarged base (JELINEK *et al.*, 1977)

with the sensitivity and deformation characteristics of the clay, from about 5 for very sensitive brittle normally consolidated clay (LADÁNYI, 1973; ROY *et al.*, 1974) to about 10 for insensitive stiff overconsolidated clay (MEYERHOF, 1951; SKEMPTON, 1951), although a value of 9 is frequently used for driven and bored piles. Any disturbance of the clay by pile installation mainly affects the initial point resistance and subsequent consolidation will normally lead to a bearing capacity exceeding the undrained value at the end of the construction of the foundation.

Large diameter bored piles have shown during tests (JELINEK *et al.*, 1977) that the q_p of piles without enlarged base (1, 3, 5) is considerably greater than for these with enlarged base (2, 4), particularly when the settlement exceeds 20 mm (see Fig. 271).

The displacement needed to produce the maximal point resistance depends on the type of the soil and the pile. The literature gives this dis-

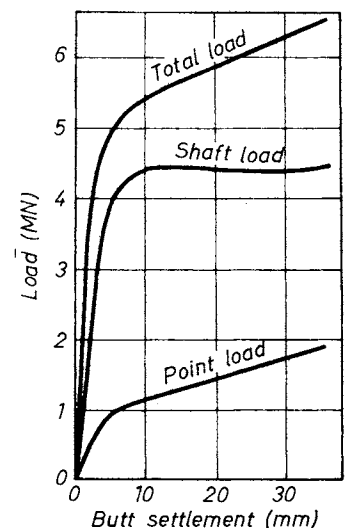


Fig. 272. Development of shaft and point resistance with settlement (PROMBOON and BRENNER, 1981)

placement as $0.1D$ to $0.3D$, but in loose sand it may reach over $1D$. All authors agree in assuming that s_{cr} has to be greater for point resistance than for skin friction. Figure 272 tries to interpret this feature for the case of a 1.2 m diam. pile, bored in clay (PROMBOON and BRENNER, 1981).

3.2.3.3 The ratio of point resistance to skin friction

Figure 272 indicates that the ratio Q_p/Q_s changes its value continuously during settlement. This is a generally valid phenomenon and is the result of two causes:

- (a) various displacements are needed to mobilize either Q_p or Q_s .
- (b) Q_s attains a constant value (or even decreases slightly) well before it reaches the Q_u (see Fig. 261).

Thus, because s is a function of Q , for the same pile the ratio Q_p/Q_s is also a function of load Q . For large diameter ($D = 0.88$ m) bored pile in clay JELINEK *et al.* (1977) obtained the following relationship:

s (mm)	10	30	50	100	150
Q_p (kN)	220	630	990	1625	1925
Q_s (kN)	590	630	550	365	375
Q_p/Q_s	0.73	0.50	0.36	0.18	0.16

BALASUBRAMANIAM *et al.* (1981) examined the ratio Q_p/Q_u for driven piles and summarized their finding as:

- the end bearing capacity contributed approximately 15% to the total bearing capacity in the case of concrete piles in stiff clay, with the exception of one pile of large cross-section area (0.45×0.45 m²) where the contribution was nearly 30%;
- for driven steel piles embedded in stiff clay the contribution from end bearing was nearly 25%;
- the end bearing contributed approximately 45% to the total bearing capacity when the concrete piles were bearing in the sand layer.

Also from these experiments it appears that the ratio Q_p/Q_s depends on both the material and the sizes of the pile (including its shape), and on the characteristics of the soil.

There is a wide difference whether the pile is of a displacement or a non-displacement type: the ratio Q_s/Q_p is much larger for the former type than for the latter.

The ratio varies also with time as the two components (mostly the Q_s) also change in time.

3.2.3.4 Changes of the bearing capacity with time

The bearing capacity of piles passing through clay changes to a considerable extent after installation. The ratio of the initial to the ultimate bearing capacity is largely influenced by the width of the disturbed zone. It follows therefore that this phenomenon is markedly experienced in the case of driven piles (see Section 3.2.1).

Figure 273 reflects an example (after FLAATE and SELNES, 1977) showing the variation of the bearing capacity of friction piles in clay. It appears that 1 to 3 months (at pile even 3 more) are needed to achieve the final value. Similar findings were reported by BURLAND *et al.* (1977) with the addition that (a) reconsolidation is faster in an over-consolidated clay than in normal clays and (b) the time is around one month for timber piles.

BARTOLOMEY *et al.* (1981) mention 40 to 50 days as being sufficient for the development of the final bearing capacity. According to the T versus P curves in Fig. 274 there is no difference in this respect between single piles and pile groups, but other researchers (e.g. FLAATE and SELNES, 1977) claim that pile groups need a longer time for reconsolidation. The figure reveals that a rather substantial ratio (2.5 to 2.6) develops between initial and final bearing capacities.

The undrained shear strength of the clay around driven piles increases gradually with time as the water content gradually decreases. Piles in soft, normally consolidated clay will with time be surrounded by a shell of medium to stiff clay. This strength increase can be traced in the calculation by the application of the effective stresses when the final skin friction is determined.

Equation (361) also illustrates that the earth-pressure parameter K_s is higher than the earth pressure at rest, K_0 , by about 50% (see Section 3.2.3.1).

The phenomenon of reconsolidation draws attention to the fact that it is wise to note that any loading test — which is intended to acquire information on the bearing capacity of piles as foundations of a building — may only provide reasonable results if the test is carried out about two-three months later than the installation of the

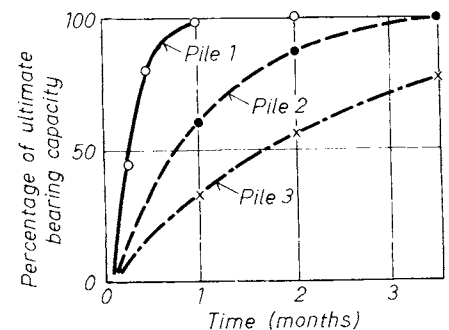


Fig. 273. Variation of bearing capacity of piles in clay with time after driving (FLAATE and SELNES, 1977)

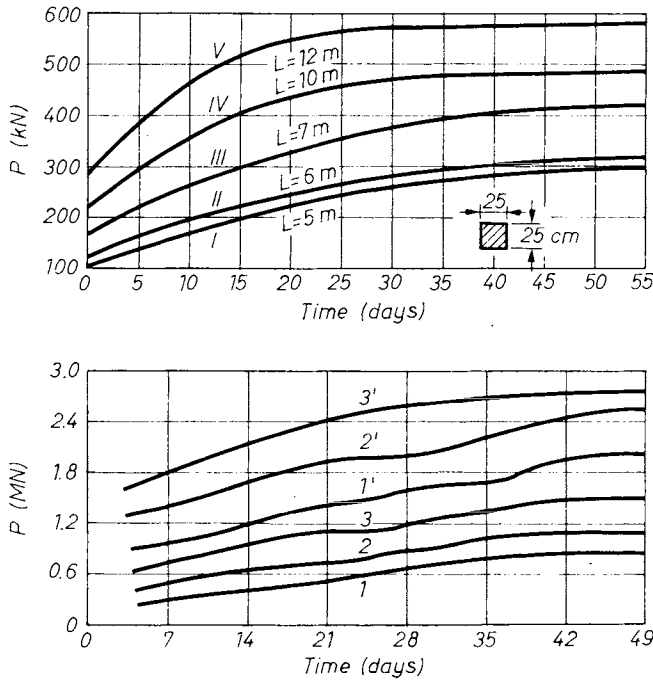


Fig. 274. Increase in the bearing capacity of piles (I) and pile group (II-V) with time (BARTOLOMEY *et al.*, 1981): 1, 2, 3—groups of 4 piles (L = 5, 7 and 9 m); 1', 2', 3'—groups of 9 piles (L = 5, 7, and 9 m)

piles. The influence of reconsolidation should also be accounted for when the design uses other parameters for the determination of the bearing capacity of piles (for example, skin resistance or cone resistance of penetration or probing tests).

3.2.3.5 Bearing capacity of piles in the case of cyclic loading

This problem is rarely treated in the literature, despite the fact of how important it is to detect the influence of cyclic loading from both theoretical and practical view points.

STEENFELT *et al.* (1981) carried out model tests on piles jacked into clay. The overconsolidation ratio in the clay was $OCR = 1$ in test runs Nos 01 and 02, but $OCR = 8$ has been used in run No. 03. In test No. 01, two-way cycling of the pile was arranged to attain failure. This led to a dramatic reduction in shaft adhesion, over 18 cycles, by a factor of ~ 10 cm compression and ~ 6.3 cm in tension, giving a final shaft adhesion of $\tau_s \sim 10$ kN/m².

Calculated values of $\alpha = 0.24$ according to Eq. (358), and $\beta = 0.05$ according to Eq. (362) have been attained in these tests. A comparison with Fig. 275 would reveal — this figure represents the values of α and β for static load— how small indeed the value of β was.

The drop in shaft adhesion was accompanied by a gradual rise in excess pore-water pressure at the pile shaft of between 30 and 35 kN/m².

In test runs Nos 02 and 03 the pile was two-way cycled between limits of 1/2 to 1/3 of the failure loads in compression and tension, respectively. In over 50 cycles no significant pore-water pressure change was noted, and load tests performed directly after the cyclic loading showed no evidence of a reduction in shaft capacity.

3.2.4 Settlement of single piles

3.2.4.1 Prediction of settlement

Three methods are available to predict the expected settlement of piles:

1. loading tests;
2. *in situ* investigations (penetration tests, probing, pressiometer test, etc.);
3. analytical calculation.

Item 1 is discussed in Sections 3.6.1 to 3.6.3 and item 2 is treated in Section 3.6.4.

In respect to item 3, presented analytical methods are all based on the principles of elasticity theories. A pile is considered as a point load in the infinite half-space which generates stresses in its surrounding. There is a difference, however, in comparison to the classical case, inasmuch as load transfer occurs in the soil mass at both the peak and the shaft, instead of at the ground surface. This is why the settlement calculated from the Boussinesq formula

$$s = pB \frac{1 - \nu^2}{E_s} I_w \tag{376}$$

generally gives larger values than would occur in reality (e.g. KOERNER and PARTOS, 1974). (I_w is

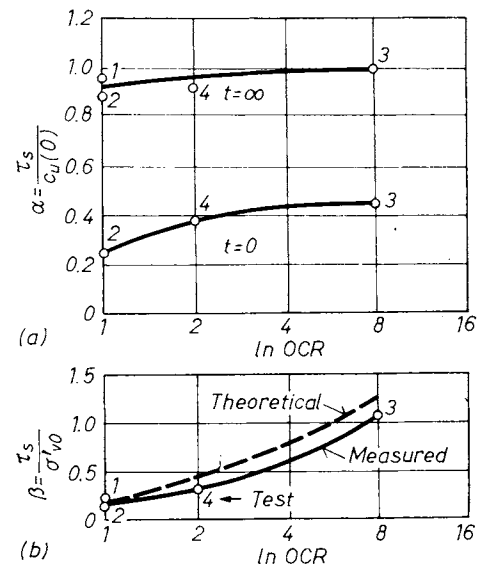


Fig. 275. a — Values of α at $t = 0$ and $t = \infty$; b — values of β at $t = \infty$ (STEENFELT *et al.*, 1981)

an influence factor reflecting the shape and stiffness of the pile.)

GEDDES (1966) evaluate in detail the difference between the two types of load transfer. Three basic situations were assumed:

- a point load P , at depth D ;
- a total load of P , applied along a vertical axis in uniform increments from the surface to depth D (the case of uniform skin friction);
- a total load of P , applied along a vertical axis in uniform increments varying linearly with depth, from zero at the surface to a maximum at depth D (the case of linear variation of the skin friction).

The first situation was investigated by MINDLIN (1936) who produced a set of equations giving the stresses due to a vertical point load. The second and third items were solved by GEDDES (1966) who gave the influence factors in a tabular form in functions of ν , r/D and z/D . In respect to items 2 and 3, the pile load is assumed to be delivered as a shear, but according to St. Venant's principle a small error will occur in the estimated stresses at some distance from the pile shaft as a consequence of the assumption of a series of incremental point loads. According to the calculations completed by GEDDES the Boussinesq equation leads to an overestimation of the vertical stresses in the vicinity of the line of action of the load and an underestimation of the stresses at greater radial distances.

The methods based on the theory of elasticity can be categorized into the following four groups.

1. In the elastic methods based on Mindlin's equations it is assumed that the soil behaves as an ideal elastic material with constant E_s and a high tensile strength. This approach has been used by D'APPOLONIA and ROMUALDI (1963), POULOS and DAVIS (1968), MATTES and POULOS (1969). These methods normally do not take into account the slip that can ensue along the shaft even at relatively low load levels, or the low tensile strength of the soil.

2. The step integration method (or "boundary element method") introduced by SEED and REESE (1957) and by COYLE and REESE (1966) is based on the assumption that the movement of a point at the surface of the pile depends only on the shear stress at that particular point, and that the stresses elsewhere do not affect the movement.

3. In the finite element method (FEM), non-linear and time-dependent stress-strain relationships are considered.

4. Analytical methods considering the load-deformation characteristics of the pile shaft separately from those of the pile base (RANDOLPH, 1977; RANDOLPH and WROTH, 1978, 1979).

The POULOS and DAVIS (1968) method in the first category gives the settlement of the pile head for an incompressible pile $L \leq 50d$ long, as:

$$s = \frac{PI_1}{E_s d}, \tag{377}$$

in which P is the total applied load on the pile, E_s is Young's modulus of the soil, and d is the diameter of the pile. The influence factor I_1 can be read from Fig. 276.

The influence of pile compressibility on the behaviour of a floating pile has been investigated by MATTES and POULOS (1969). The compressibility of the pile relative to the soil (see Section 3.2.2) is conveniently expressed in terms of a pile stiffness factor, K :

$$K = \frac{E_p}{E_s} R_A, \tag{378}$$

in which R_A is the area ratio, i.e. the area of a pile section per gross area of the pile ($R_A = 1.0$ for solid piles). The lower the value of K , the more compressible is the pile relative to the soil. The influence factor of K on pile head displacement is plotted in Fig. 277 in terms of a correction factor R_K , where

$$R_K = \frac{\text{settlement of the compressible pile}}{\text{settlement of an incompressible pile}}$$

(It has been found that R_K does not vary greatly with d_b/d and might therefore be used for both uniform piles and for piles with an enlarged base.)

The "step integration method" is discussed in Section 3.2.4.2.

To introduce the FEM method, an applied example is presented here as the solution given by RANDOLPH and WORTH (1979). The program used by the authors was based on six-noded iso-

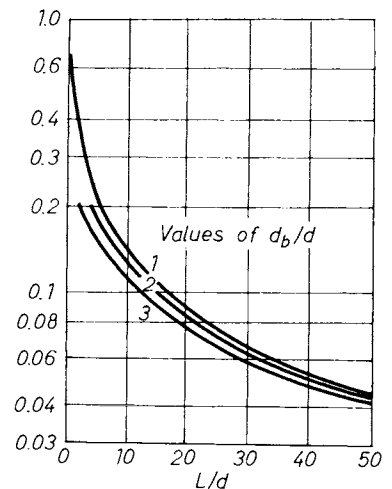


Fig. 276. Displacement influence factor I_1 for incompressible piles (POULOS and DAVIS, 1968)

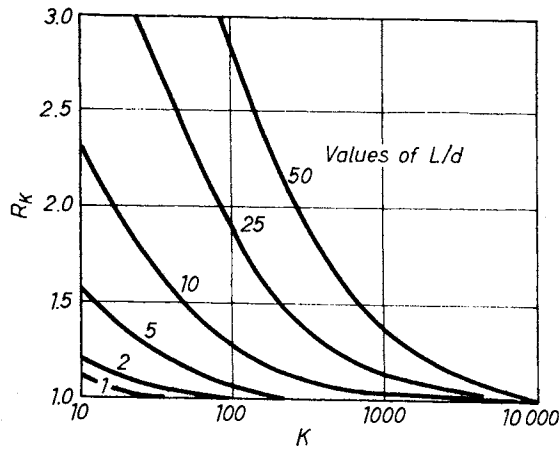


Fig. 277. Compressibility correction factor for settlement R_K (MATTEI and POULOS, 1969)

parametric triangular elements in an axi-symmetric mode, which allows a linear variation of strain across each element. The method of solution was the Gaussian elimination of a banded matrix, the bandwidth being restricted to 100. The pile and surrounding soil were divided into 267 elements (580 nodes) with a rigid horizontal boundary imposed at a depth h , where $h = 2.5l$. (This is close enough to affect the solution for a pile in an elastic half-space, but only by less than 5%; see BANERJEE, 1970.) The outer vertical boundary was at a radius of $50r_0$ ($= d/2$) and care had to be taken to ensure that this did not effect the solution. For piles longer than $l = 40r_0$, it was found that the method of fixing these boundary nodes affected the pile settlement. Fixing the nodes in the radial direction only, produced a good compromise, but for very long piles ($l > 80r_0$) the mean of the settlements for totally fixed and totally free vertical boundary nodes gave the best agreement with equivalent analyses supplied by integral equations. Ideally, the outer vertical boundary should be at a radius of a least twice the length of the pile.

The substance of the solution of category 4 was presented by RANDOLPH and WROTH (1978, 1979). The analysis is based on an elastic soil characterized by the shear modulus G , which may vary with depth, and the Poisson's ratio, ν . (Using the shear modulus is preferred to Young's modulus E , since soil deformation is produced primarily by shear, and because the shear modulus is usually assumed to be unaffected whether the loading is drained or undrained.) The soil surrounding the pile is divided into two layers by a line AB drawn at the level of the pile base (Fig. 278). Initially it is assumed that the soil above AB will be deformed solely by the stresses at the pile base. Some modification of this assumption is necessary in order to take account of the interaction between the upper and lower layers of soil; the interaction will serve to limit the defor-

mation of the upper layer, reducing the deformations to a negligible size at some radius r_m .

From considerations of vertical equilibrium, it may be shown (e.g. COOKE, 1974) that the shear stress in the soil around the pile shaft decreases inversely with the radial distance from the pile. This leads to a logarithmic variation of the deformation w with radius r . The deformation may then be:

$$w(r) = \frac{\tau_0 r_0}{G} \ln \frac{r_m}{r} \quad r_0 \leq r \leq r_m \quad (379)$$

$$w(r) = 0 \quad r \geq r_m.$$

τ_0 here means the shear stress at the pile shaft; r_0 is the radius of the pile, and r_m is the limiting radius of influence of the pile, in correspondence with Eq. (350).

The deformation of the pile shaft can be written:

$$w_s = \xi \frac{\tau_0 r_0}{G}, \quad (380)$$

where

$$\xi = \ln \frac{r_m}{r_0}.$$

The pile base acts as a rigid punch on the surface of the lower layer. The deformation of the pile base (Boussinesq) is:

$$w_b = \frac{P_b(1 - \nu)}{4r_0 G}. \quad (381)$$

At some distance from the pile base, the load will appear as a point load. The settlement around

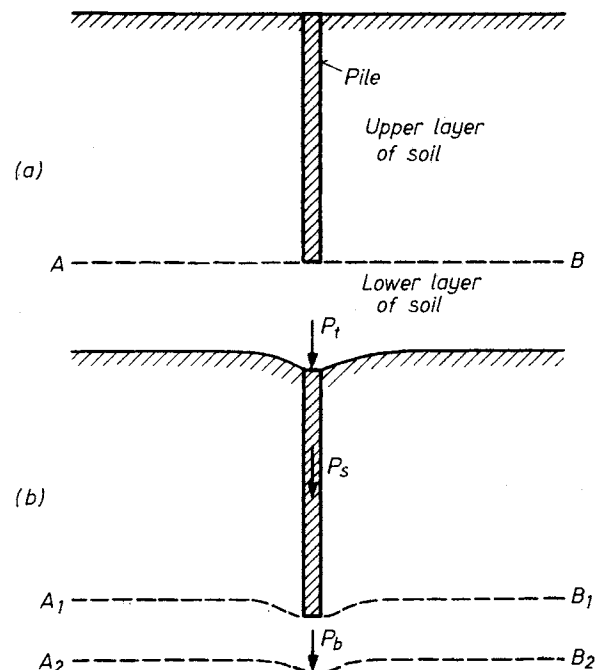


Fig. 278. Decoupling of effects due to pile shaft and base: a — upper and lower soil layers; b — separate deformation patterns of upper and lower layers (RANDOLPH and WROTH, 1979)

a point load decreases inversely with the radial distance and is given by:

$$w(r) = \frac{P(1 - \nu)}{2 \pi r G} \tag{382}$$

The ratio of settlements in Eqs (381) and (382) for a given load is:

$$\frac{w(r)}{w_b} = \frac{2}{\pi} \frac{r_0}{r} \tag{383}$$

Following St. Venant's principle, the settlement caused by the pile base should, at large distances, equal that of a point load. Thus the settlement profile at the top of the lower layer of soil in Fig. 278 may be approximated by

$$w(r) = w_b \frac{2}{\pi} \frac{r_0}{r} \tag{384}$$

For a rigid pile, the shaft settlement is constant down the pile and equals the settlement of the pile base. Assuming that the shear strain in the soil next to the pile shaft is constant with depth, the shear stress τ_0 will be proportional to G at that depth. The total load transferred to the soil from the pile shaft may be written using Eq. (380)

$$\begin{aligned} P_s &= 2\pi r_0 l (\tau_0)_{av} = 2\pi l \frac{w_s}{\xi} G_{1/2} = \\ &= \frac{2\pi}{\xi} l w_s \rho G_l, \end{aligned} \tag{385}$$

where ρ is the homogeneity index (see Eq. (349)).

Thus, the overall load vs. settlement ratio for a rigid pile might be written in a dimensionless form

$$\begin{aligned} \frac{P_t}{G_l r_0 w_t} &= \frac{P_b}{G_l r_0 w_b} + \frac{P_s}{G_l r_0 w_s} = \\ &= \frac{4}{1 - \nu} + \frac{2\pi \rho}{\xi} \frac{l}{r_0}. \end{aligned} \tag{386}$$

The authors emphasized that the settlement as calculated from their method was in good agreement with that of method 1 and 3. The authors provided a solution also for the case when the compressibility of the pile was not negligible (RANDOLPH and WROTH, 1978).

The reliability of any solution based on the theory of elasticity depends primarily on the accurate estimation of E_s (method 4 partly avoids the difficulties arising from this fact).

The disadvantage of these methods is that it is, in general, not possible to take into account the difference in the elastic modulus on loading and unloading, the effect of the loading rate and the creep at different load levels, the disturbance of the soil caused by the pile driving, or the reconsolidation of the soil after the driving and

installation of the piles (BROMS, 1981). These consequences are also implied in the findings of POULOS (1972) who concluded that

- for soft to medium clays ($c_u < 117 \text{ kN/m}^2$) the E_s for driven piles is greater than that for bored piles, but for stiff clays the E_s becomes greater with bored piles;
- for stiff clays it seemed that E_s reached a limiting value which was about 40 MN/m^2 for driven piles, and about 80 MN/m^2 for bored piles.

The shape of a pile affects its settlement. A bored pile with an enlarged base will settle more, under the same relative load (Q/Q_{ult}) than a pile without enlarged base (WITHAKER and COOKE, 1966). The settlement for bored piles with enlarged bases can be estimated from the following semi-empirical relationship:

$$s = \frac{0.02 q_b D_b}{q_{ult}}, \tag{387}$$

where q_b is the contact pressure at the base, and D_b is the base diameter (BURLAND and COOKE, 1974).

Some observations indicate that — similarly to shallow foundations — a secondary consolidation (creep) also takes place with pile foundations. Surveys made by BARTOLOMEY *et al.* (1981) have disclosed, for example, that about 15% of the total settlement occurred later than one year after the completion of the construction.

3.2.4.2 The load–settlement curve

A method to establish the relationship between load and settlement has been provided by REESE based on the following considerations (COYLE and REESE, 1966).

Figure 279 shows an axially loaded pile divided into four segments with the forces acting on each segment. It is desired to compute the load, Q_0 , at the top of the pile and the settlement, δ , at the top of the pile. The procedure has to begin at the bottom by assuming a small tip movement, computing the forces and movement at each segment upwards on the pile. For differently assumed tip movements, different values will be obtained at the top for Q_0 and δ , and a load–settlement curve can be plotted. The steps involved in this procedure proceed in the following manner

1. Assume a small tip movement, y_T .
2. Compute the tip load, T , corresponding to the movement y_T . This can be done by making use of a method such as that proposed by SKEMPTON (1951).
3. Divide the pile into several segments (e.g. into four segments, as can be seen in Fig. 279).

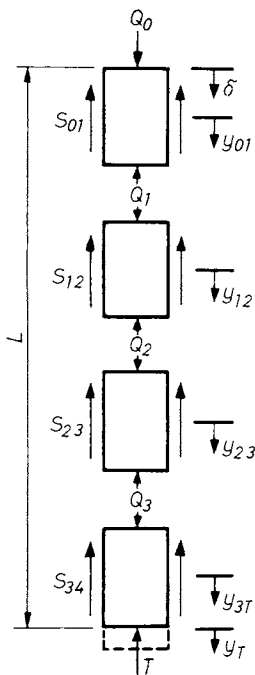


Fig. 279. Axially loaded pile showing forces acting on segments (COYLE and REESE, 1966)

4. Estimate a midpoint movement of the segment at the bottom. For the first trial, the midpoint movement is assumed equal the movement at the tip.

5. Using the estimated midpoint movement, refer to a curve showing the ratio of load transfer to soil shear strength versus pile movement. Figure 280 is a curve developed by SEED and REESE (1957) based on measured load transfer in an instrumented pile and vane shear test. (For example, with a simulated pile movement of 7.5 mm, the ratio is 1.0; therefore, the full shearing resistance is assumed to be developed.)

6. Using the ratio determined in step 5, refer to a curve of soil shear strength versus depth. A load transfer is the product of the value read from this curve and the ratio obtained in step 5.

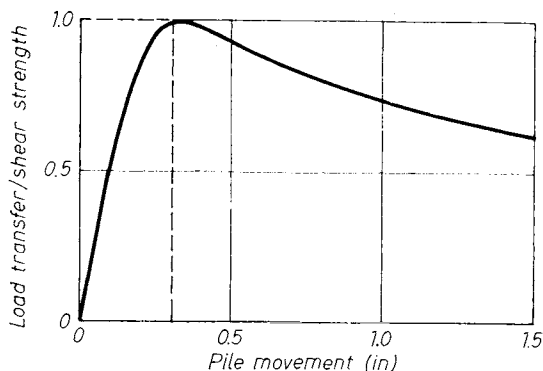


Fig. 280. Ratio of load transfer to soil shear strength vs. pile movement (1 in = 25.4 · 10⁻³ m)

7. Using the value of load transfer computed in step 6, compute the load Q_3 at the top of the bottom segment as

$$Q_3 = qT + S_{3T}, \quad (388)$$

in which

$$S_{3T} = s_{3T}CL_{3T} \quad (389)$$

and Q_3 is the load at the top of the segment, T is the load at the tip from step 2, s_{3T} is the load transfer in the bottom segment from steps 4, 5 and 6, C is the circumferential area of the segment, πD , and L_{3T} is the length of the bottom segment ($= L/4$).

8. Compute the elastic deformation in the lower half of the bottom segment by

$$y_{3T} = \frac{\frac{Q_{\text{mid}} + T}{2} \frac{L_{3T}}{2}}{AE} \quad (390)$$

Assuming a linear variation on the load distribution for small segments

$$Q_{\text{mid}} = \frac{Q_3 + T}{2} \quad (391)$$

9. Compute the new midpoint movement of the bottom segment by

$$y_{3T} = \Delta y_{3T} + y_T \quad (392)$$

10. Compare the computed midpoint movement from step 9 with the estimated midpoint movement from step 4.

11. If the computed movement does not agree with the assumed movement within a specified tolerance, repeat steps 2 through 10 and compute a new midpoint movement.

12. When convergence is achieved, go to the next segment above the bottom segment and work up the pile to compute a value of Q_0 and δ at the top.

The procedure is then repeated using a different assumed tip movement, until a series of Q_0 and δ values is obtained. These values can then be used to plot a computed load-settlement curve. For the calculations used in their paper, the authors assumed that the tip load was equal to zero, but any tip load can be included in the calculation, if desired. For carrying out the study in this manner, an assumed tip movement is required, but then step 2 can be omitted.

3.3 Performance of pile groups

3.3.1 Load-bearing capacity of pile groups

Due to superposition of stresses transferred into the soil, there is a substantial difference between the performance of a single pile and a pile group. This difference appears also in respect of bearing

capacity, namely the interaction influences the ultimate shaft load and the ultimate point resistance to a different extent and in various manners. The interaction of piles depends mainly on

- the distance between the piles;
- the properties of the soil;
- the type of the piles and the technology.

Problems arising can be usually condensed to the question: what will be the relationship between the bearing capacity of a pile group (Q_{ug}) to the summarized bearing capacities Q_{ui} of the single piles in the group or — since each pile in the group is assumed to have the same load-bearing capacity — to the sum nQ_{ui} ?

Since several difficulties had to be faced in using the theoretical approach, at present we have mostly to rely on experience acquired by *in situ* surveys or investigations. An important role is also attributed in this field to model tests, since loading tests of pile groups would be extremely tiresome and expensive due to the enormous load involved.

MEYERHOF (1976) stated, on the basis of experimental results, that for piles driven into sand,

$$Q_{ug} > \Sigma Q_{ui}$$

if the distance between the piles is not more than $4d$. The greater group capacity is due to the overlap of the individual soil compaction zones near the piles, increasing mainly the skin resistance, which may produce equivalent pier shear failure at small pile spacings, while the point resistance is practically unaffected by the group action, even at small pile spacings (VESIĆ, 1967).

The senior author conducted a series of trial tests with 2 m long $A = 10 \cdot 10 \text{ cm}^2$ piles (KÉZDI, 1957). Four piles were driven in a row and at the corners of a square, and loading diagrams were made at different pile spacings. The relation between ultimate load of the group and the pile centres is shown in Fig. 281; the horizontal line denotes the fourfold bearing capacity of a single pile. Both in the case of piles driven in a row and at the corners of a square, the group capacity is substantially higher than that; only at $d = 6D$ does the group capacity diminish to the value of the single piles. At $d = 2D$ the increase is more than 100%.

According to VESIĆ (1981) in the case of piles driven into soft clay the ultimate shaft load of the group is less than nQ_i .

The ultimate load of a pile group with the piles being bored in sand is smaller than the sum of the single bored pile capacities, due to the overlap of the individual shear zones in the soil near the piles without soil compaction (MEYERHOF, 1976). Interference of the individual pile-point shear zones would theoretically lead to a reduction of the individual ultimate point loads by roughly

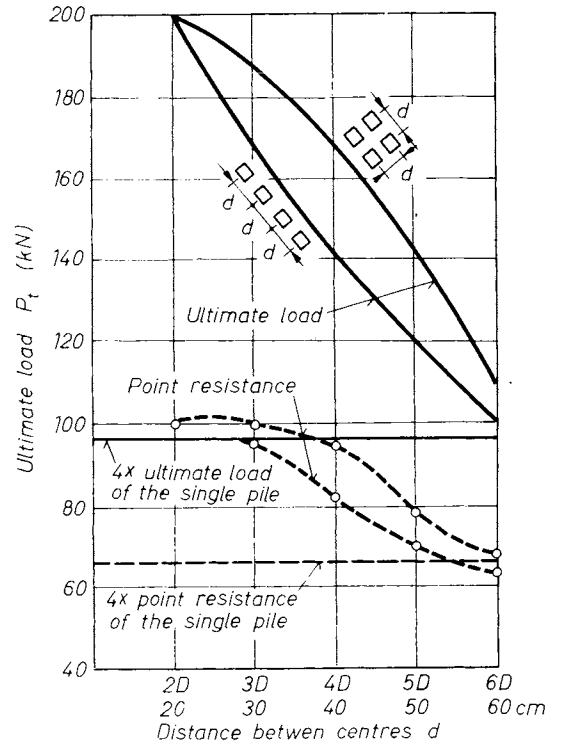


Fig. 281. Ultimate load of pile groups (KÉZDI, 1957)

one-half for a pile spacing of about 3 pile diameters, and some reduction of the skin resistance must also be expected. It may, therefore, be suggested that the ultimate group capacity of bored pile groups in sand, not underlain by a weak deposit, should be taken as about two-third of the sum of the single pile capacities at customary pile spacings.

The ultimate load of pile groups in clay can be estimated from the smaller value from either a block failure of an equivalent pier consisting of the piles and enclosed soil mass, or from the ultimate bearing capacities of the individual piles (MEYERHOF, 1976).

The ultimate group load for block failure of an equivalent pier of driven or bored piles in saturated clay should be based on the initial undrained shear strength of the clay for both side and base resistance. If the pile caps are not resting on the ground, the group capacity will usually be governed by the sum of the ultimate loads of the single piles, with some reduction due to the overlapping zones of shear deformation in the surrounding soil (MEYERHOF, 1976). This has been confirmed by full-scale load tests of friction piles driven into soft and medium clays (e.g. SCHLITT, 1951) and by similar model tests (WITHAKER, 1957) which have shown that at customary pile spacings of 3 to 4 pile diameters the ultimate group capacity may be only about two-thirds of the sum of the single pile capacities, using the drained remolded shear strength of the clay for the skin friction.

In making a comparison between the effective load Q to be carried by the piles and the ultimate load capacity, Q_u , it should be also considered that the stiff raft on the pile heads may transfer various loads on to the individual piles (see Section 3.2.2).

The process of reconsolidation goes on more slowly in the case of pile groups than with single piles (VESIĆ, 1981). This may be partly the result of the differences in the influence zone, as can also be seen from Eqs (349) and (350) (Section 3.2.1).

3.3.2 Settlement of pile groups

3.3.2.1 Rules derived from surveys and observations

Figure 274 indicates that pile groups settle substantially more than individual piles do under the same load. The figure refers to piles driven into cohesive soil but the results might be generalized for whatever type of soil or pile (VESIĆ, 1981).

BEREZANTSEV *et al.* (1961) explained that pile foundations with an equal load transmitting area at the level of the pile ends, but with a different number of piles, have practically equal settlements under equal loads (Fig. 282).

If the distance between piles driven into sand is reduced, the influence of compaction gains more and more space, as has been proved by the model tests carried out by the senior author (KÉZDI, 1957). Figure 283 shows the magnitude of loads causing given pile settlements. The less the distance between pile centres, the smaller will be the settlement under a given load: at $d = 6D$ the loading diagram approaches the line giving the four-fold loading capacity of an individual pile as a function of its settlement. The groups thus behaved very favourably from the point of view of settlement, most probably due to soil compaction caused by driving.

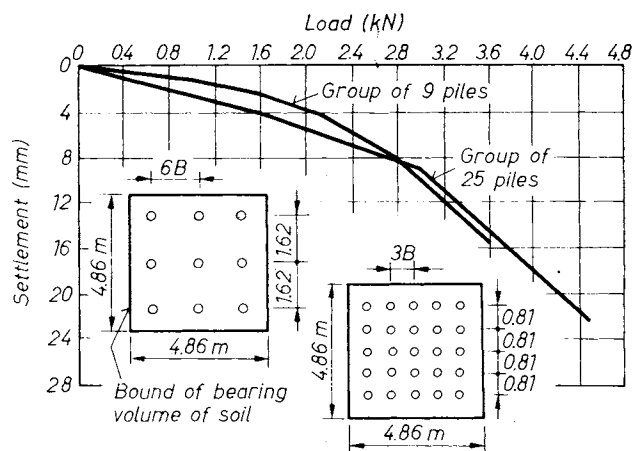


Fig. 282. The relationship between loading and settlement of piles and the role of the number of piles (BEREZANTSEV *et al.*, 1961)

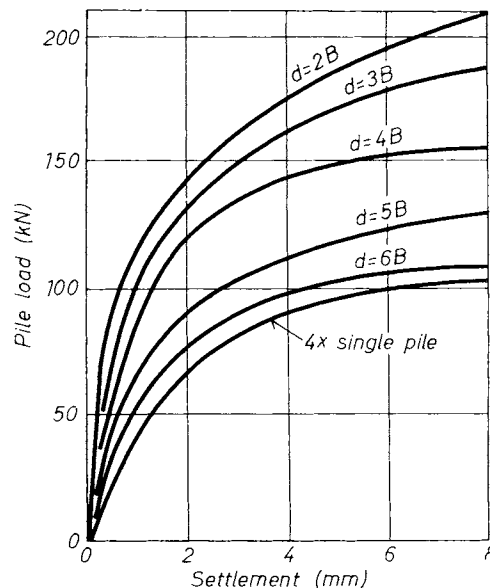


Fig. 283. Settlement of pile groups (KÉZDI, 1957)

The pertinent soil strain parameters being known, the settlement of a pile group is usually calculated after TERZAGHI and PECK as if it were a shallow foundation of the area $A = B \cdot L$. (B is the width and L is the length of the external contour line of piles, respectively.) The level of load transfer can be taken to the tips of the piles for end-bearing piles, or to two-thirds of the length of friction piles. TONG *et al.* (1981) suggested assuming the level of load transfer to be at the tips of the piles when the surrounding soil is a soft clay and the load acting on the pile group is greater than the load-bearing capacity of the multiple individual piles. In this case the difference $Q - nQ_{u1}$ will be carried by the soil through totally mobilizing both the peak resistance and the skin friction. BURLAND *et al.* (1977) also considered this solution as an appropriate means of lessening settlement.

There are several semi-empirical methods available to calculate the settlement of a pile group.

BEREZANTSEV *et al.* (1961) suggest that the settlement of the group increases in proportion to the square root of the area enclosed by the piles.

VESIĆ (1968) holds that the settlement is in proportion to $\sqrt{B/D}$, where B is the width of the pile group and D is the diameter of the pile.

SKEMPTON (1953) offered a formula for the calculation of the settlement of a pile group in sand (relative to that of an individual pile, s_{si}):

$$\frac{s_{gr}}{s_{si}} = \left(\frac{4B + 3}{B + 4} \right)^2, \quad (393)$$

where B is the width of the pile group in metres.

MEYERHOF (1959) produced the formula:

$$\frac{s_{gr}}{s_{st}} = \frac{s \left(5 - \frac{s}{3} \right)}{\left(1 + \frac{1}{r} \right)^2}, \quad (394)$$

where s is the ratio of spacing to diameter; r is the number of rows for a square group.

3.3.2.2 Settlement analysis on the basis of elastic theories for piles of unrestricted settlement

Similarly to single piles the settlement of pile groups can also be determined by using the principles of the theory of elasticity. At present there are three such solutions known: one was elaborated by POULOS, DAVIS and MATTES, the second by RANDOLPH and WROTH, and the third by COOKE.

POULOS *et al.* (POULOS and DAVIS, 1968; POULOS, 1968) based the solution on the Mindlin theory, as was done in the case of single piles. The behaviour of each pile may be examined by dividing it into a number of cylindrical elements, each loaded by a uniform load acting around the periphery of the element and a circular uniformly loaded base. Referring to Fig. 284, the displacement q_i of the soil adjacent to the centre of the periphery of an element i on pile 1 due to pile 1 itself and the adjacent pile 2, is

$$q_i = \sum_{j=1}^n p_j ({}_1I_{ij} + {}_2I_{ij}) + p_b ({}_1I_{ib} + {}_2I_{ib}), \quad (395)$$

- where ${}_1I_{ij}$ = is the displacement influence factor at element i due to a uniform ring load on element j on pile 1,
- ${}_2I_{ij}$ = is the displacement influence factor at element i due to a uniform ring load on element j on pile 2,
- ${}_1I_{ib}$ = is the displacement influence factor at element i due to a uniform load on the base of pile 1,
- ${}_2I_{ib}$ = similarly as above, for pile 2.

A similar expression may be obtained for the displacement q_b of the soil directly beneath the base of the pile

$$q_b = \sum_{j=1}^n p_j ({}_1I_{bj} + {}_2I_{bj}) + p_b ({}_1I_{bb} + {}_2I_{bb}), \quad (396)$$

- where ${}_1I_{bj}$ = is the displacement factor for the pile base due to a uniform ring load on element j on pile 1, and similarly for ${}_2I_{bj}$,
- ${}_1I_{bb}$ = is the displacement factor for the pile base due to a uniform load on the base of pile 1, and similarly for ${}_2I_{bb}$.

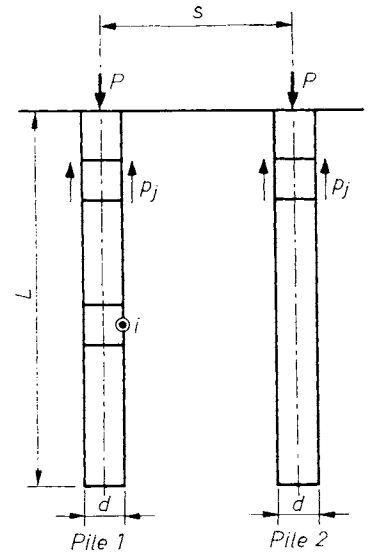


Fig. 284. Analysis of a group of two piles (POULOS and DAVIS, 1968)

The displacement factors ${}_1I_{ij}$ and ${}_2I_{ij}$ may be obtained by integration of the Mindlin equation for vertical displacement, over the cylindrical ring elements j on piles 1 and 2, respectively, for the appropriate points i on pile 1. The factors ${}_1I_{ib}$ and ${}_2I_{ib}$ may similarly be obtained by integrations of the Mindlin equation over the circular base of pile 1 and 2 (POULOS and DAVIS, 1968). For all the elements on pile 1, the vertical displacement of the soil adjacent to the pile may be expressed in a matrix as

$$[q] = ({}_1I + {}_2I) [p] + p_b ({}_1I_b + {}_2I_b). \quad (397)$$

(Since the two piles are identical, this equation applies to pile 2 as well.)

The soil displacement at each element may now be equated to the displacement of each element of the pile. If this displacement is assumed to be unity, then for the pile elements

$$[q] = [1]. \quad (398)$$

Equating Eqs (397) and (398) the new equation may be solved to obtain the distribution of shear stresses along each pile and the stress on the base for unit displacement of the pile, whence the displacement of each pile for a unit load may be calculated. In this manner the influence of an adjacent pile on the displacement of a pile may be determined for various spacings between the piles. The additional displacement of a pile in a semi-infinite mass due to an equally loaded identical adjacent pile is expressed in terms of an interaction factor α where:

$$\alpha = \frac{\text{additional settlement due to adjacent pile}}{\text{settlement of pile under its own load}}.$$

For two piles α ranges between 1 for a zero spacing between the piles, and zero for an infinite spacing.

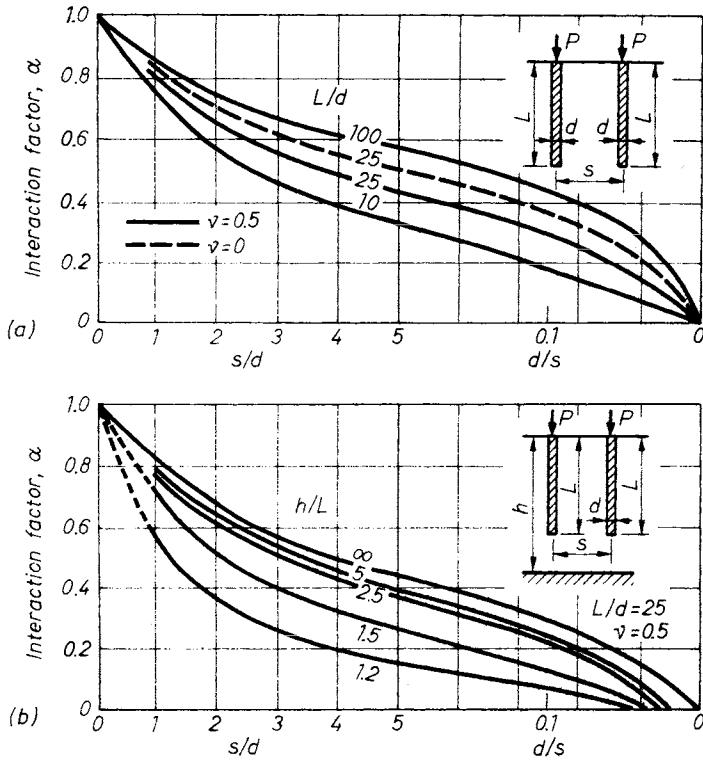


Fig. 285. a — Settlement interaction between two piles in a semi-infinite mass; and b — in a finite layer (POULOS, 1968)

In Fig. 285a α is plotted against the centre to centre spacing between the piles for various values of L/d for the case $\nu = 0.5$. We can see that

- the values of α at large spacings are surprisingly large;
- the relative length L/d has an important influence with any given spacing (this effect becomes more pronounced as the spacing between the piles increases);
- the role of ν is negligible.

The effect of an underlying rigid base is shown in Fig. 285b. The effect of the rigid base is to “damp” the interaction, particularly at large spacings where the value of α for a finite layer is considerably less than that for a semi-infinite mass.

The analysis applied for two piles can be extended to any symmetric pile groups and a matrix similar to Eq. (397) can be written.

For the case $L/d = 25$ and $\nu = 0.5$, solutions have been established for groups of three and four piles. In Fig. 286 the interaction factor α is plotted against the spacing s/d for the above groups and also for a group of two piles. This figure shows that the additional settlement of each pile in the group due to the adjacent piles is almost exactly equal to the sum of the displacement increases due to each of the adjacent piles in turn. Thus, for a group of three piles the value of α is twice the value for a group of two piles with the same spacing, while for a group of four

piles the value of α is

$$\alpha = 2\alpha_1 + \alpha_2, \tag{399}$$

where α_1 is the value of α of two piles at a spacing of s diameters, α_2 is the value of α for two piles

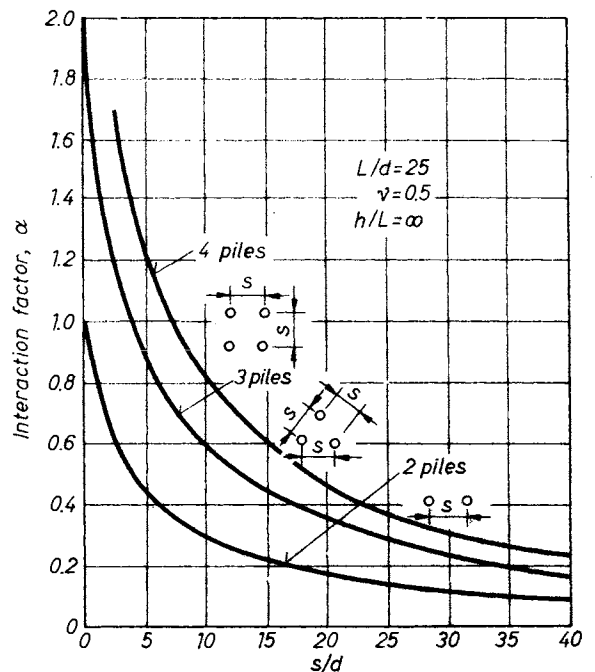


Fig. 286. Settlement interaction—symmetrical pile groups (POULOS, 1968)

at a spacing of $s\sqrt{2}$ diameters. The corresponding displacement of each pile in the group due to equal loads Q_1 in each pile is thus

$$\rho = Q_1 \rho_1 (1 + 2\alpha_1 + \alpha_2), \quad (400)$$

where ρ_1 is the displacement of a single pile under unit load.

RANDOLPH and WROTH (1979) extended their method presented in Section 3.2.4.1 to cover the case of pile groups as well.

The authors assumed that Eq. (379) gives the settlement profile at the pile mid-depth and Eq. (383) that at the pile base. Considering two rigid piles, the overall settlement of one pile may be written as the sum of the settlement due to its own load plus that due to the displacement field of neighbouring piles. Thus

$$w = w_1 + w_2. \quad (401)$$

At the mid-depth of the pile:

$$w_s = w_1 + w_2 = \frac{\tau_0 r_0}{G} \left[\ln \frac{r_m}{r} + \ln \frac{r_m}{s} \right], \quad (402)$$

where s is the pile spacing. Thus s is the average radius of one pile as seen from the other pile. The load-settlement ratio for each pile shaft is now:

$$\frac{P}{G r_0 w_s} = \frac{2\pi \rho}{\xi + \ln(r_m/s)} \frac{l}{r_0}. \quad (403)$$

Similarly, the settlement of the pile base is

$$w_b = w_1 + w_2 = \frac{P_b(1 - \nu)}{4r_0 G} \left(1 + \frac{c r_0}{s} \right), \quad (404)$$

whence

$$\frac{P_b}{G r_0 w_b} = \frac{4}{1 - \nu} \frac{s}{c r_0 + s} \quad (405)$$

(c is equal to $2/\pi$).

Thus, the overall load-settlement ratio for each of two similarly loaded piles is

$$\left(\frac{P_t}{G r_0 w_t} \right)_2 = \frac{4}{1 - \nu} \frac{s}{c r_0 + s} + \frac{2\pi \rho}{\xi + \ln(r_m/s)} \cdot \frac{l}{r_0}. \quad (406)$$

The expression for piles in a group of three (at the corners of an equilateral triangle of side s) and a group of four piles (at the corners of a square of side s) are respectively:

$$\left(\frac{P_t}{G r_0 w_t} \right)_3 = \frac{4}{1 - \nu} \frac{s}{2r_0 c + s} + \frac{2\pi \rho}{\xi + 2 \ln\left(\frac{r_m}{s}\right)} \frac{l}{r_0} \quad (407)$$

and

$$\left(\frac{P_t}{G r_0 w_t} \right)_4 = \frac{4}{1 - \nu} \frac{s}{2.707 r_0 c + s} + \frac{2\pi \rho}{\xi + \ln \frac{r_m^3}{s^3 \sqrt{2}}} \frac{l}{r_0}. \quad (408)$$

It is possible to use Eq. (406) to obtain the interaction factors between two piles, in the manner of POULOS (1968). Thus the increased settlement for a given load may be written as

$$\left(\frac{G r_0 w_t}{P_t} \right)_2 = (1 + \alpha_v) \left(\frac{G r_0 w_t}{P_t} \right)_1 \quad (409)$$

where α_v is the interaction factor.

Included in their presentation RANDOLPH and WROTH also treated the case when the compressibility of the pile was not negligible, i.e. $w_s \neq w_b$.

In one of their articles, POULOS and RANDOLPH (1983) compared the results of their methods and concluded that the agreement was very close, the maximal deviation being not more than 15 to 18%.

COOKE *et al.* (1980) performed trial tests using 17 cm diam. piles jacked in clay, and proved that the interference between the piles can be calculated on the basis of superposition principles. Beside the factor α from the Poulos theory, they introduced the ratio:

$$\Omega = \frac{\text{the induced settlement of a pile 1 due to the loading of another pile 2}}{\text{the settlement of the loaded pile}}$$

Beside this, another useful term was presented by the authors, namely the settlement ratio (R_s) which is defined as the ratio of the mean settlement of the pile group to the settlement of a single pile carrying a load equal to the mean load

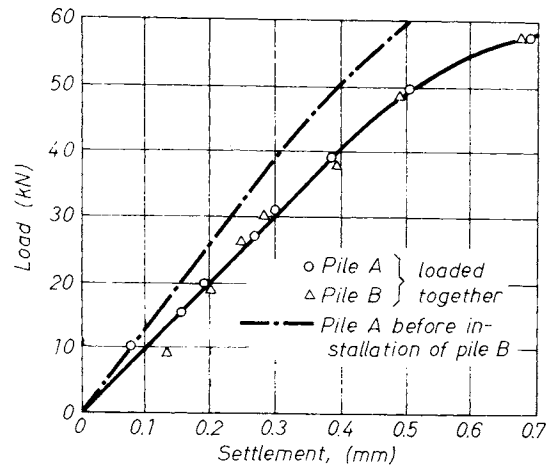


Fig. 287. The load-settlement curve for piles A and B loaded together compared with the load-settlement curve for pile A before B was installed (COOKE *et al.*, 1980)

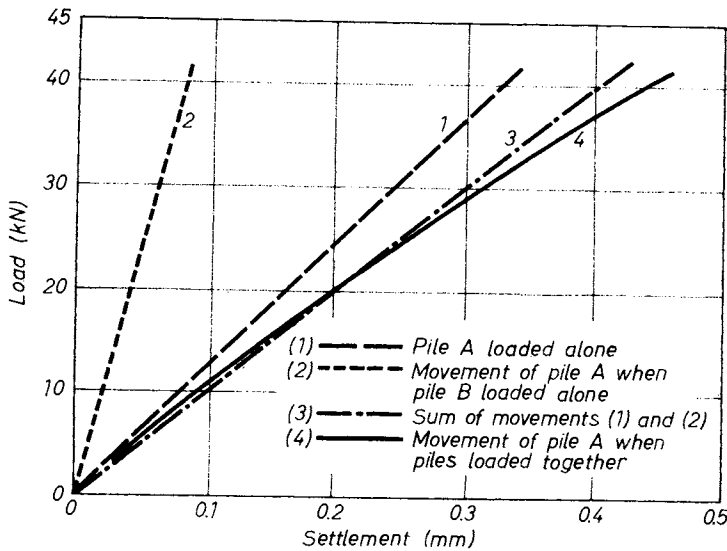


Fig. 288. Comparison of the load-settlement curve for pile A when piles A and B were loaded together with the sum of the components of movement of pile A when the piles were loaded separately (COOKE *et al.*, 1980)

carried by the piles in the group. In the case of two similar, equally loaded piles in the same soil, the displacement or additional settlement of both piles due to interaction are equal. Thus, $R_s = 1 + \Omega_s$, where Ω_s is the value of the interaction factor at a given spacing s .

The results of differently performed test runs were as follow.

Test 1. A load-settlement curve for piles A and B loaded together is presented in Fig. 287 and compared with the curve obtained in the final test of pile A before pile B was installed.

When the two piles were loaded together, their settlements were approximately equal at all loads and both were 25% greater than the settlement of pile A loaded alone. The value Ω_s for a spacing of three pile diameters was therefore 0.25 and R_s was 1.25.

Test 2. Here the two piles were loaded separately. A tiny settlement was experienced only on the unloaded pile. Figure 288 illustrates four various patterns of movement on piles A and B. The figure shows how the settlement of pile A — when both piles were loaded together (curve 4) — could

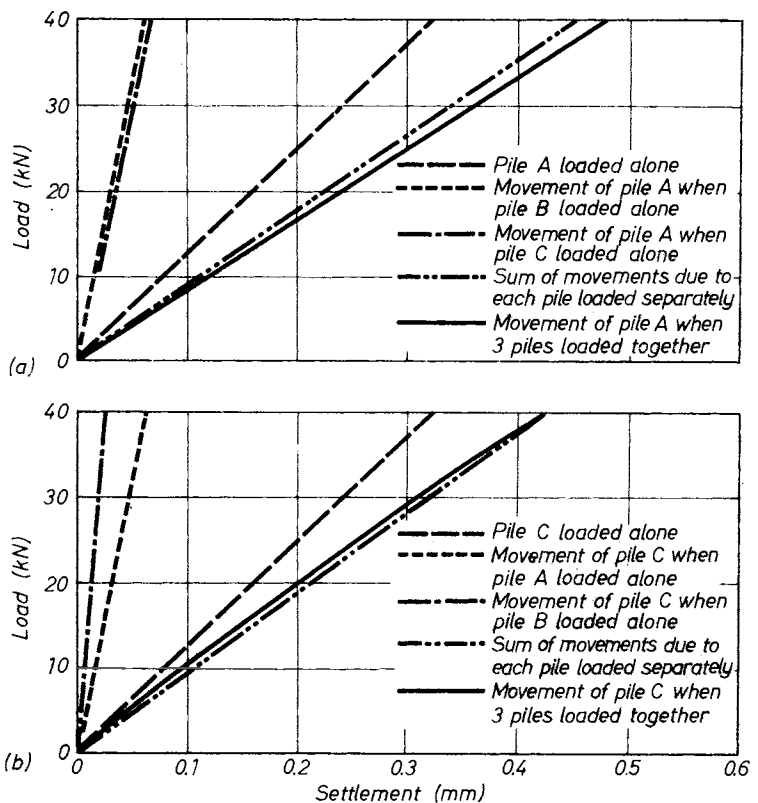


Fig. 289. a — Comparison of the load-settlement curve for pile A when equally loaded with piles B and C with a curve given by the sum of the components of movement of pile A when the three piles were loaded separately; b — corresponding comparison for pile C (COOKE *et al.*, 1980)

be predicted with considerable accuracy from the sum of the movements observed when it was loaded alone (curve 3), and when only pile B was loaded. The factor Ω_s is 0.24, almost the same as that observed for both piles in Test 1.

This survey confirmed also that the idea of superposition prevails also in respect of both the skin friction and of the settlement of the ground surface around the piles.

Test 4 and 5 (piles in three rows). Figure 289a presents the load-settlement curve for pile A loaded alone together with curves showing the movement of this pile when pile B and C were loaded alone under similar load increments. The figure shows that the sum of the three components of movement of pile A, due to loading the piles separately is in good agreement with the movement of this pile when all the piles were loaded. The movement of the centre pile, due to the separate loading of piles B and C, the three pile diameters are shown to be very similar. As expected, the separate loadings of piles A and B did not have equal effects on the movement of pile C situated at one end of the row. Figure 289b shows how the sum of the components of the movement of pile C compares with its movement when the three piles were loaded together.

3.3.2.3 Settlement analysis on the basis of elastic theories for pile groups with a rigid cap

When the piles are clamped together with a perfectly rigid cap, two questions arise:

- what will be the settlement of the foundation;
- what load will be carried by each of the piles?

To render the solution more easy, POULOS (1968) introduced two factors. The settlement

ratio, R_s , is defined as the ratio of the settlement of the pile group to the settlement of a single pile carrying the same average load as a pile in the group. The reduction factor, R_G , is the ratio of the settlement of the group to the settlement of a single pile carrying the same total load as the group. For a group of m piles the settlement ratio, R_s , is related to the reduction factor, R_G , as

$$R_G = R_s/m. \tag{410}$$

The value of R_G represents the reduction in settlement which results from using a pile group instead of a single pile to carry a given load.

The actual settlement of the group is given by

$$\dot{S}_G = R_s S_1 = R_G m S_1, \tag{411}$$

where S_1 is the settlement of a single pile carrying the same average load as a pile in the group. From the analysis of a single pile carried out by POULOS and DAVIS (1968) S_1 may be expressed by applying Eq. (377). Since the total load on the group $P_G = mP$, the settlement of the group is:

$$S_G = \frac{P_G}{Ed} R_G I_1. \tag{412}$$

Values of the single pile influence factor I_1 obtained by POULOS and DAVIS (1968) are shown in Fig. 276 and in Table 19 for a range of values

Table 19. Settlement influence factors I_1 for single pile (POULOS and DAVIS, 1968)

h/L	L/d	$\nu = 0.5$			$\nu = 0$		
		10	25	100	10	25	100
∞		1.41	1.86	2.54	1.16	1.47	1.95
5		1.91	1.76	2.44	1.07	1.37	1.86
2.5		1.20	1.64	2.31	0.96	1.27	1.75
1.5		0.98	1.42	2.11	0.80	1.11	1.58
1.2		0.72	1.18	1.89	0.62	0.94	1.44

Table 20. Values of R_G , pile group with rigid cap; L/d 25, $\nu = 0.5$ (POULOS, 1968)

s/d	h/L	2^2					3^2				
		∞	5	2.5	1.5	1.2	∞	5	2.5	1.2	1.2
1		0.839	0.819	0.815	0.745	0.621	0.715	0.677	0.670	0.593	0.464
2.5		0.672	0.638	0.629	0.550	0.443	0.541	0.495	0.479	0.387	0.283
5		0.547	0.519	0.501	0.422	0.348	0.415	0.363	0.339	0.256	0.195
10		0.425	0.408	0.385	0.323	0.291	0.303	0.245	0.220	0.165	0.141
20		0.366	0.317	0.297	0.267	0.258	0.214	0.157	0.142	0.122	0.116
40		0.307	0.260	0.254	0.250	0.250	0.159	0.117	0.114	0.111	0.111

s/d	h/L	4^2					5^2				
		∞	5	2.5	1.5	1.2	∞	5	2.5	1.5	1.2
1		0.643	0.599	0.590	0.500	0.371	0.584	0.538	0.525	0.432	0.309
2.5		0.460	0.409	0.388	0.296	0.206	0.403	0.349	0.325	0.235	0.160
5		0.334	0.277	0.250	0.176	0.128	0.281	0.220	0.194	0.129	0.091
10		0.227	0.166	0.143	0.100	0.083	0.180	0.119	0.100	0.067	0.055
20		0.148	0.093	0.083	0.069	0.066	0.112	0.062	0.054	0.045	0.042
40		0.105	0.066	0.064	0.063	0.063	0.070	0.041	0.041	0.040	0.040

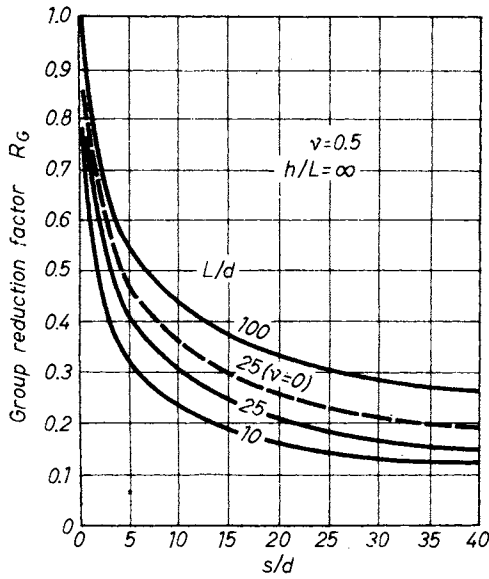


Fig. 290. Effect of L/d on settlement — 3^2 group with rigid cap (POULOS, 1968)

of h/L and L/d . For 2^2 , 3^2 , 4^2 and 5^2 groups, values of the group reduction factor R_G are tabulated in Table 20 for the case $L/d = 25$ and $\nu = 0.5$.

From Table 20 it can be seen that as h/L decreases, the value of R_G decreases at any given spacing because of the damping effect of the rigid base. The smaller the value of h/L , the closer the spacing at which the limiting value of R_G for no interaction of $1/m$ (corresponding to a settlement ratio R_S of 1) is reached.

The effect of the value of L/d is shown in Fig. 290, where R_G is plotted against s/d for a 3^2 group in a semi-infinite mass. As L/d increases, the settlement for any given spacing increases. The effect of the number of piles in the group on the value of R_G is shown in Fig. 291. The reduction in settlement with an increasing number of piles in the group, for a given spacing, is clearly shown in this figure. However, at relatively close spacings ($s/d < 5$) the use of an increased number of piles to reduce settlement becomes increasingly ineffective if the same spacing is maintained. For example, the settlement of a 5^2 group of piles at a spacing of $5d$ is only about 20% less than that of a 4^2 group of piles at the same spacing. It is interesting to note that for the group of 5 piles, S is identical with that of a 2^2 group for spacings up to about $10d$, i.e. the additional centre pile has no effect in reducing the settlement.

For a given size of pile cap the pile spacing will vary with m . The variation of R_G with foundation breadth (centre-to-centre spacing between the outermost piles) is shown in Fig. 292. For the groups 3^2 , 4^2 ... the value of R_G for all groups is identical up to a breadth of about $16d$. Beyond this breadth, R_G tends to decrease as the number of piles increases. Figure 292 therefore suggests

that over a considerable range of breadths S_G is primarily dependent on the breadth rather than the number of piles. The results of full-scale field tests carried out by BEREZANTSEV *et al.* (1961), and data collected by SKEMPTON (1953) confirm this conclusion. Thus in the design, the use of a small m at a relatively large spacing is generally to be preferred to a larger number of piles at a closer spacing on the grounds of economy.

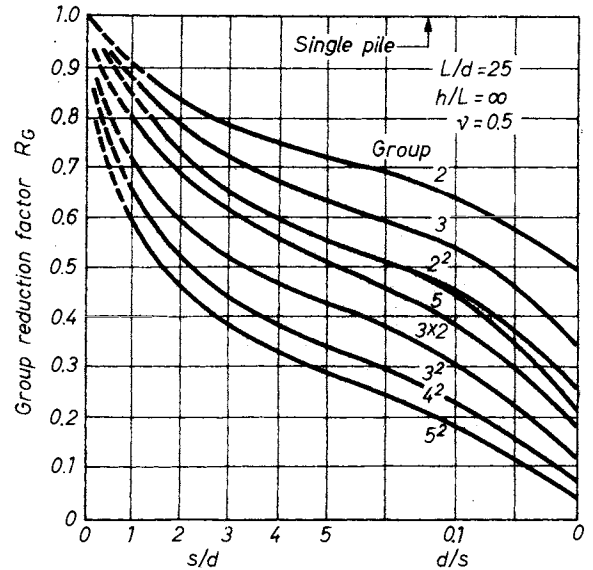


Fig. 291. Influence of type of group on settlement — groups with rigid cap (POULOS, 1968)

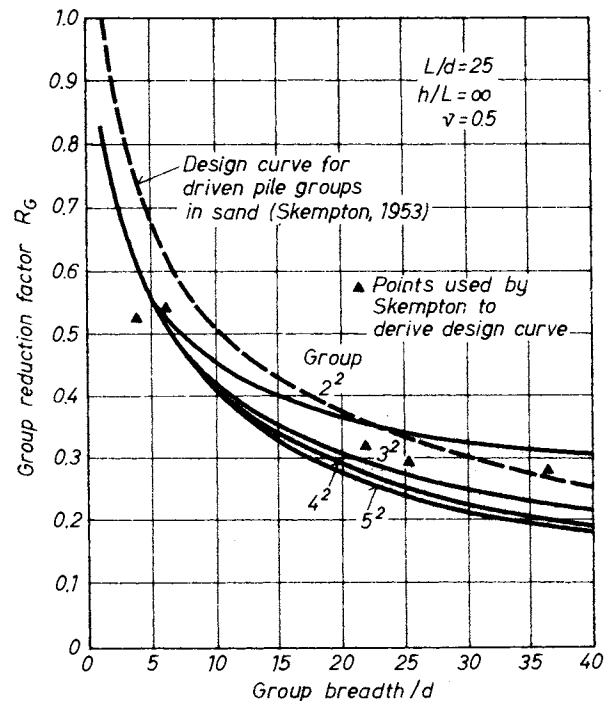


Fig. 292. Settlement against breadth of group — rigid pile cap (POULOS, 1968)

Table 21. Values of P/P_{av} ; group with rigid cap; $L/d = 25$, $\nu = 0.5$, $h/L = \infty$ (POULOS, 1968)

Group	3 ²			4 ²			5 ²					
	Pile			Pile			Pile					
	s/a	1	2	3	1	2	3	1	2	3	4	5
1	2.31	0.33	-1.57	2.99	0.75	-0.49	4.12	0.75	1.87	-1.56	0.03	1.16
2.5	1.52	0.74	-0.05	2.02	0.96	0.05	2.58	1.18	1.16	0.01	0.10	0.19
5	1.32	0.84	0.34	1.71	0.99	0.31	2.11	1.20	1.08	0.35	0.27	0.22
10	1.22	0.89	0.55	1.49	1.00	0.50	1.74	1.16	1.07	0.56	0.47	0.37
20	1.13	0.94	0.72	1.26	1.00	0.43	1.40	1.09	1.05	0.75	0.71	0.67
40	1.06	0.98	0.88	1.03	0.99	0.98	1.27	1.07	1.02	0.84	0.80	0.75

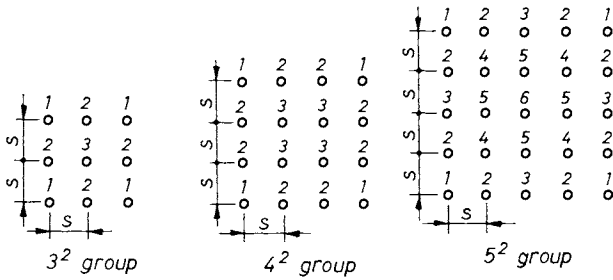


Fig. 293. Identification of piles in square groups (Key to Table 21)

As the settlement of each pile in the group is identical — due to the rigid cap — the influence of superposition will be transferred to another aspect, namely having different portions of the total load carried by each of the piles. The ratio P/P_{av} of the load to the average pile load in the group for 3², 4² and 5² groups is tabulated in Table 21 for the cases $L/d = 25$ and $h/L \rightarrow \infty$. (The key for the identification of the piles is given in Fig. 293.) For close spacings, the load in the outer piles of each group is considerably more than P_{av} , while the load in the centre piles is less than P_{av} , and may even theoretically be negative. As the pile spacing increases the load distribution becomes more uniform. From Table 21 it will be seen that the load distribution is considerably influenced by the number of piles in the group, the major influence being that the load on the outer piles increases as the number of piles increases.

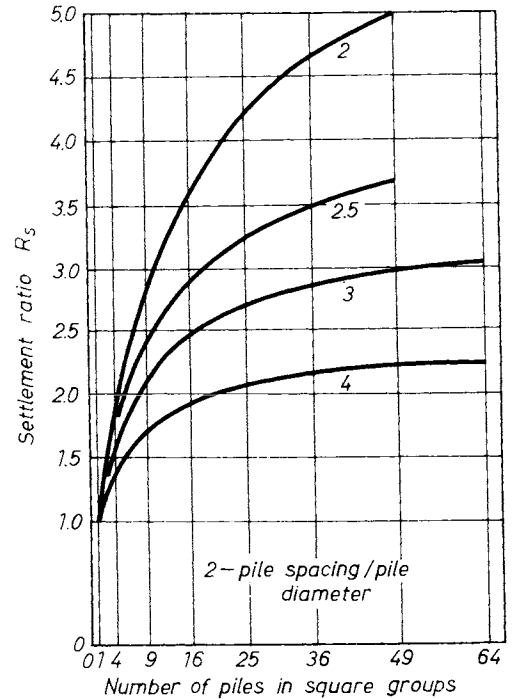


Fig. 294. The variation of settlement ratio with the number of piles in square groups for a range of common pile spacings (COOKE *et al.*, 1980)

Confirming the validity and making use of the principle of superposition (Section 3.3.2.2), COOKE *et al.* (1980) presented a method also for the case when the piles are clamped with a rigid cap or raft. The results obtained for some cases are shown in Figs 294 and 295.

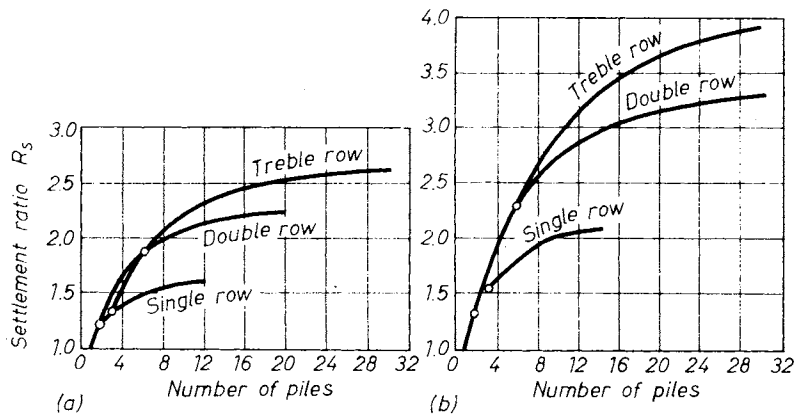


Fig. 295. The variation of settlement ratio with the number of piles in single, double and treble rows at pile spacing of:

a — 3 pile diameters; b — 2 pile diameters (COOKE *et al.*, 1980)

3.3.3 Pile groups in heterogeneous soil

The most intensive study in this respect has been made by BANERJEE and DAVIES (1977). The authors applied the “boundary element” method in their calculations. They investigated the so-called Gibson-type soils. The particularity of this soil is that its Young’s modulus varies with depth according to the formula

$$E(z) = E(0) + mz. \quad (413)$$

Investigating cases with single piles the authors found that the ratio Q_b/Q_u is hardly greater than in homogeneous soils. This condition changes, however, in the case of pile groups. Figure 296 shows the interaction factors (α) for various spacing to diameter ratios and pile compressibility ratios (E_p/mL). It can be seen that

- for pile groups with spacing to diameter ratios greater than 3, the interaction factors are much smaller than those reported by POULOS (1968);
- for short piles ($L/D < 20$) the presence of another pile beyond spacing to diameter ratios of about 8 to 10 may help to reduce the settlement of the pile under consideration.

Figure 297 shows the plots of the settlement ratios (defined as the ratio of the settlement of a group under a load of nP to that of a single pile under a load P) for various pile groups with rigid caps. It can be seen that these ratios are considerably smaller for groups with $S/D > 3$ than those predicted by POULOS (1968).

The authors have also determined the loads to be carried by each pile in the group under a rigid cap and the distribution of these loads. They found that with spacing of $6D$ to $8D$ the distribution becomes uniform. (Note that this condition

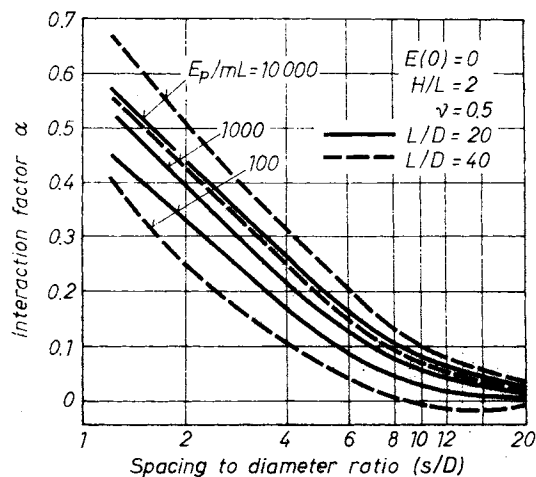


Fig. 296. Interaction factors for pile groups in Gibson soil (BANERJEE and DAVIES, 1977)

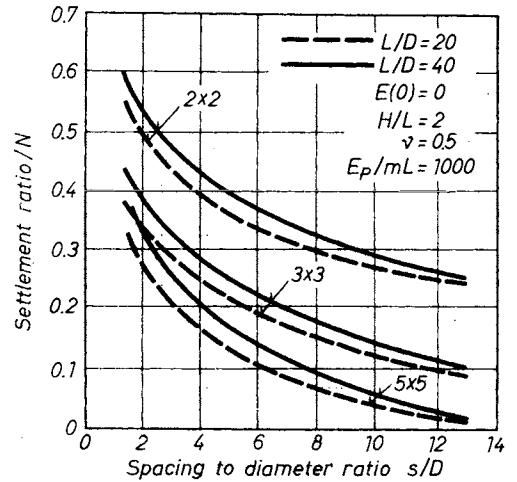


Fig. 297. Settlement ratios for pile groups in Gibson soil (BANERJEE and DAVIES, 1977)

arises only with greater distances in the case of homogeneous soils, as was demonstrated in Section 3.3.2.3.)

3.4 Piles under horizontal load

3.4.1 Horizontally loaded single piles

VESIĆ (1975) considered that a distinction has to be made between the following two branches:

- piles which are expected to transmit lateral loads to the soil (“active piles”), and
- piles which are subjected to lateral loading along their shafts by horizontal movements of the surrounding soil (“passive piles”).

The designer is mostly interested in finding out the lateral displacement of the pile, and the maximal moment developing in the pile. Comparison is then made versus the allowed limiting movement of the superstructure, and the allowable bending moment in the pile, respectively, and finally the design has to comply with both conditions.

3.4.1.1 Conclusions derived from observations

In respect to the design parameters mentioned above the following generalization can be accepted (BROMS, 1981). The lateral displacement and the ultimate resistance of a laterally loaded pile is primarily governed by the properties of the soil close to the ground surface down to a depth of three to four pile diameters. The installation procedure (driving or drilling) thus has a large effect as well as the loading conditions (cyclic and sustained). Generally, the lateral displacement of a pile is much more affected than the maximum bending moment or the ultimate lateral resistance.

Time also plays an important role, inasmuch as the total ultimate horizontal displacement does not — especially not in clays — take place instantaneously.

Several lessons can be learned from experience gained during *in situ* investigations and model tests, but only three cases will be mentioned here.

LU (1981) monitored the performance of bored, 1.04 m diameter reinforced concrete piles. Six piles, including two vertical (Nos 1 and 6) two inward battered (Nos 2 and 4), and two outward battered (Nos 3 and 5) piles were tested. The soil consisted of sandy clay. The following findings were recorded.

(a) Measured earth-pressure distribution along the three different piles is illustrated in Fig. 298.

(b) It can be conceived from the figure that it is most probable that the maximum bending moment would be less in inward battered piles than in the outward battered ones under the same loading condition.

(c) Failure occurred after 40 to 50 mm of lateral displacement, the end of the proportionality limit was at 3 mm. (Note that up to this point only 3 to 7% of the ultimate failure load, or 0.16 to 0.28% of the diameter pertain.)

(d) The maximum stress (and so the bending moment) in the steel bars fixed along the circumference of the piles developed at a depth of $z = 2.0$ m.

Summarizing his findings, the author concluded that a laterally loaded pile might be designed only to a force H which can be read at the breaking point on the graph plotted with $\log H$ and $\log y$ coordinates.

REESE and WELCH (1975) investigated piles standing in stiff clay. Their findings are summarized below.

(a) Displacement is not a linear function of the lateral force.

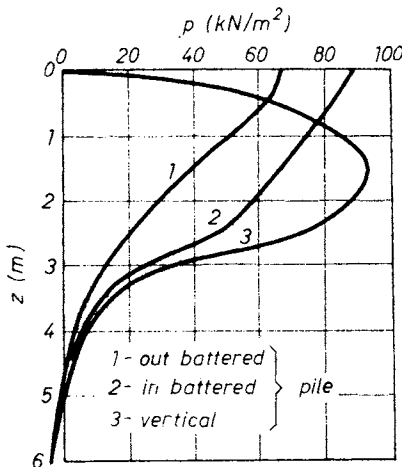


FIG. 298. Earth pressure vs. distance (LU, 1981)

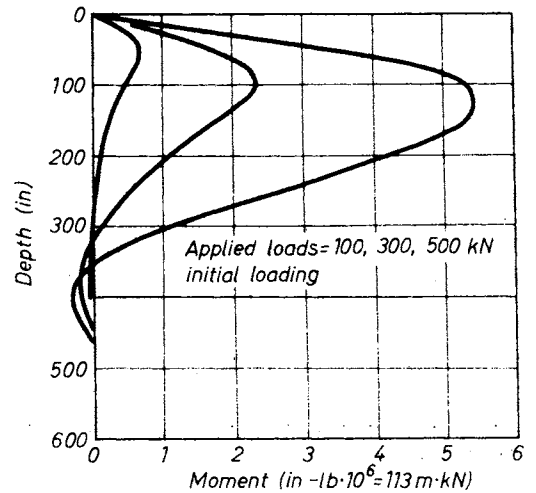


Fig. 299. Effects of increasing loads on moment (REESE and WELCH, 1975) (1 in = 25.4 · 10⁻³ m)

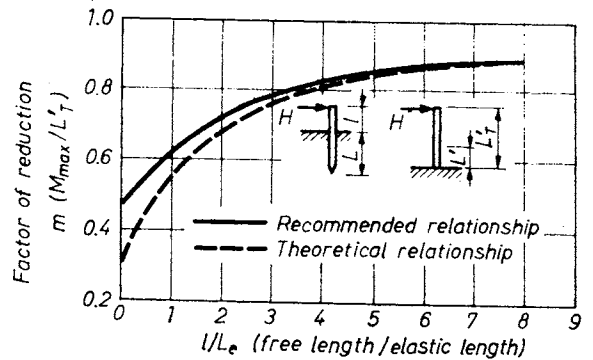


Fig. 300. Reduction factor of the maximum bending moment (OTELO and VALERIO, 1981)

(b) The depth to the point of maximum moment increases with load.

(c) The magnitude of the maximum moment is a non-linear function of the load (Fig. 299).

The maximum bending moment can be found from the semi-empirical formula:

$$M_{\max} = mHL'_T, \tag{414}$$

where m = correction factor,
 H = lateral force,
 $L'_T = l + L'$, in which l means the free length of the pile (not confined in the soil), and L' can be estimated in the case of a homogeneous soil from the formula:

$$L' = 1.2L_e = 1.2 \sqrt[4]{\frac{E_p I_p}{G}}, \tag{415}$$

where G is the “transversal modulus”.

The reduction factor m can be found in Fig. 300, where the “recommended relationship” complies

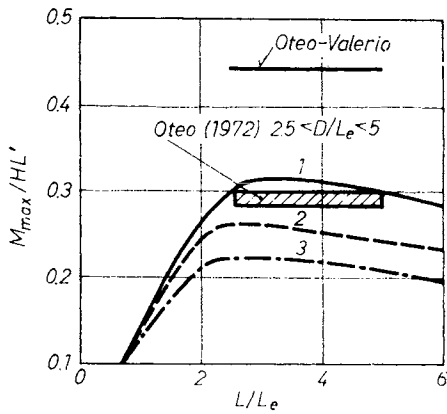


Fig. 301. Variation of maximum bending moment with pile length (OTE0 and VALERIO, 1981)

with the suggestion of OTE0 and VALERIO (1981). When the whole length L of the pile is surrounded with earth (i.e. $l = 0$), the maximum bending moment is given in Fig. 301.

3.4.1.2 Design of laterally loaded piles on the basis of elasticity theories

The differential equation for the problem of the laterally loaded deep foundation is:

$$EI \frac{d^4y}{dx^4} + P_x \frac{d^2y}{dx^2} - p = 0, \quad (416)$$

$$p = -E_s y,$$

where P_x = the axial load,

- y = the deflection,
- x = the length along the foundation,
- EI = the flexural stiffness of the foundation and
- p = the soil reaction.

For the problem solution of a laterally loaded pile, it is necessary to predict a set of p - y curves. The procedure to obtain experimental p - y curves involves field tests. From sets of experimental bending-moment curves (Section 3.6.3) the values of p and y at points along the pile can be obtained by solving

$$y = \iint \frac{M(x)}{EI} \quad (417)$$

and

$$p = \frac{d^2M(x)}{dx^2}. \quad (418)$$

When it is not possible to acquire local data, we have to turn to other — not so reliable — sources.

POULOS (1971a) suggested calculating the displacement of the pile by using the Mindlin equation. The pile is divided into $n + 1$ segments of

the length δ , except at the top and bottom segments where the length is $\delta/2$. Displacement is related to the midpoints of the segments, except at the top and bottom, where the reference points are the two ends of the pile.

Two types are differentiated during the discussion: (1) a pile, the head of which is free to turn, and (2) a pile with fixed head.

For pile (1) the horizontal displacement at ground level is given by:

$$e = I_{eH} \frac{H}{E_s L} + I_{eM} \frac{M}{E_s L^2}, \quad (419)$$

where H and M are the horizontal force acting on the pile, and the moment, respectively, L is the length of the pile.

Influence factors I_{eH} and I_{eM} can be read from Figs 302 and 303, as functions of K_r and L/d , respectively. K_r is the flexibility ratio defined in Eq. (351) and d is the diameter of the pile.

For pile (2):

$$e = I_{eF} \frac{H}{E_s L}; \quad (420)$$

the influence factor I_{eF} can be found in Fig. 304.

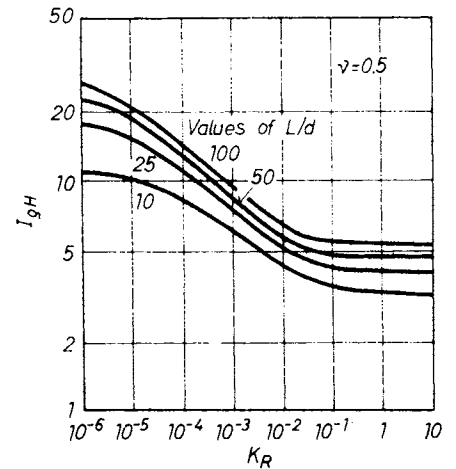


Fig. 302. Influence factors I_{eH} — free-head pile (POULOS, 1971a)

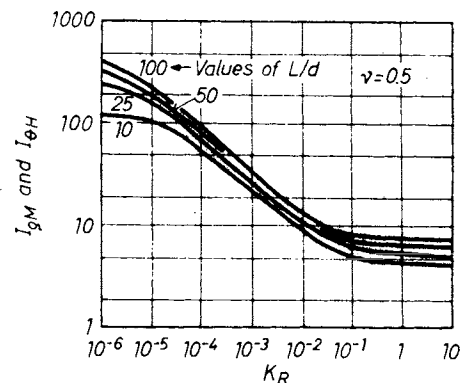


Fig. 303. Influence factors I_{eM} and I_{eH} — free-head pile (POULOS, 1971a)

The rotation of pile (1) at the ground level is given by:

$$\theta = I_{\theta H} \frac{H}{E_s L^2} + I_{\theta M} \frac{M}{E_s L^2} \quad (421)$$

From the reciprocal theorem $I_{\theta H}$ should be identical with the values of I_{eM} in Fig. 303. The influence factor is given in Fig. 305.

For a free-head pile subjected to load H at distance e above the surface, the displacement at the point of application of the load, is given by:

$$e = \frac{H}{E_s L} I_{eH} + 2 \frac{He}{E_s L^2} I_{\theta H} + \frac{He^2}{E_s L^2} I_{\theta M} + \frac{He^3}{3E_p I_p} \quad (422)$$

The maximum moment in a free-head pile subjected to a horizontal load is shown in Fig. 306 as a function of K_R and L/d . This moment typically

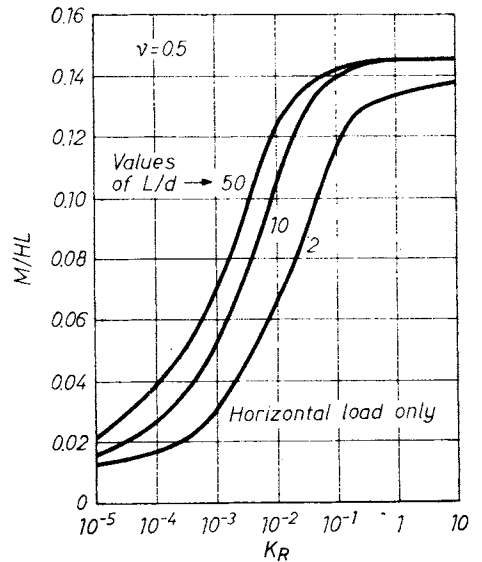


Fig. 306. Maximum moment in free-head pile (POULOS, 1971a)

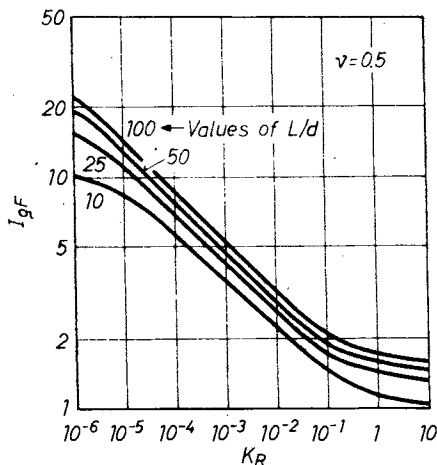


Fig. 304. Influence factors I_{qF} — free-head pile (POULOS, 1971a)

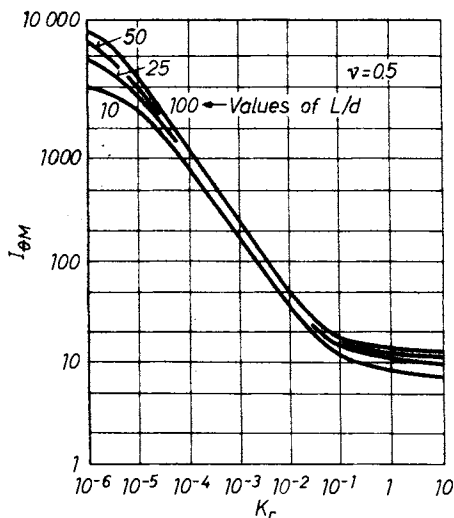


Fig. 305. Influence factors $I_{\theta M}$ — free-head pile (POULOS, 1971a)

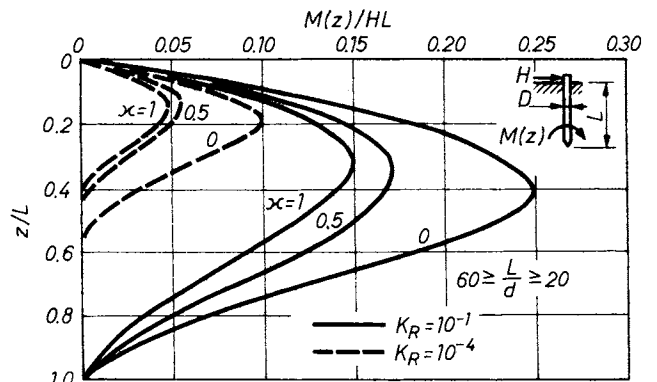


Fig. 307. The distribution of moments along a free-head pile due to lateral loads (BANERJEE and DAVIES, 1978)

occurs at a depth of between $0.1L$ and $0.4L$ below the surface, the lower depth being associated with stiffer piles.

3.4.1.3 Performance of laterally loaded piles in heterogeneous soils

BANERJEE and DAVIES (1978) discuss the conditions in the so-called Gibson-type soil for which the formula Eq. (413) applies. The authors introduce the term “non-homogeneity index” as:

$$\kappa = E(0)/E(L) \quad (423)$$

The most interesting finding among their test results relates to maximum bending moments. Figure 307 illustrates the pronounced influence of the dimensionless bending moment parameter $M(z)/HL$ referring to lateral loads and, most importantly, the considerable increase of the moment in non-

homogeneous cases in comparison to homogeneous underground conditions. The maximum bending moment develops between $0.1L$ to $0.3L$, where the higher value refers to piles of elevated stiffness. If the pile is submitted to a moment load instead of a horizontal force, the two conditions $\kappa = 1$ and $\kappa = 0$ will only differ from each other slightly.

OTEO and VALERIO (1981) pointed out that the calculation can also follow the method shown in Section 3.4.1.1. The length L' indicated in Eq. (415) has to be written in this case as:

$$L' = 1.2f \sqrt[4]{\frac{I_p E_p}{E(L)/3}} \quad (424)$$

in which for $\kappa = 0, f = 1.70,$
 $\kappa = 0.5, f = 1.25,$
 $\kappa = 1.0, f = 1.00.$

3.4.2 Horizontally loaded pile groups

SCHMIDT (1981) indicated that distinction should be made between two situations in respect of the pile-soil interaction in the case of laterally loaded pile groups.

(1) Long piles penetrating through a very soft layer and keying into a very hard rock. The pile tips are then rigidly fixed in the rock and the contact pressure is far below the strength of the material; load transfer in the upper layer is negligible. In this case any individual pile in the group will behave as a single pile.

(2) Short piles that rotate rather than deflect under horizontal loads, embedded in a uniform soil. Interference will be the greatest in this case and it is likely to depend on the pile length, on the pile spacing, on the type and strength of the subsoil, and on the amount of the lateral load.

Appraisal of any individual pile in the group should start with calculating the horizontal displacement of a single pile at the ground level and assuming the same for a pile in the group. The group efficiency, E_{gr} , is then defined as the allowable load of the pile group divided by the number of piles, and related to the corresponding load of the single pile.

Figure 308 shows the results of a trial test which has been carried out on two pairs of bored piles (SCHMIDT, 1981). As is seen, in spite of small interspaces between the piles, the group efficiency is about 0.8 and apparently nearly independent of the amount of load in either case. Nevertheless, SCHMIDT remarked that the group action was not so drastic as it is usually supposed to be.

OTEO and VALERIO (1981) applied the semi-empirical approach for this case again (refer to Sections 3.4.1.1 and 3.4.1.3) and conceived that the pile behaved as if the equivalent fictitious

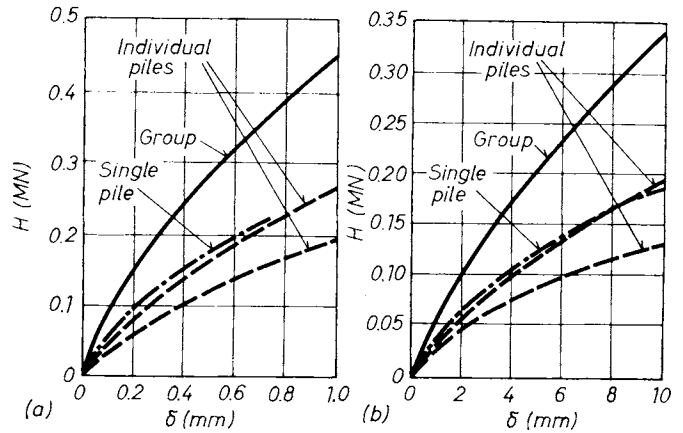


Fig. 308. Efficiency of two 1.2 m diameter piles: a — 28 m long piles in weathered gneiss, clear distance 1.7 m; b — 16 m long piles in silt and marl, clear distance 0.4 m (SCHMIDT, 1981)

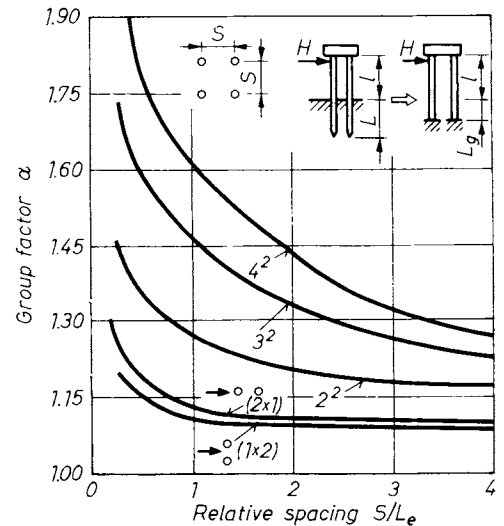


Fig. 309. Group effect for static loads vs. relative spacing (OTEO and VALERIO, 1981)

fixed point were at a greater depth than the estimated for a single pile, that is:

$$L'_g = \alpha L', \quad (425)$$

where L'_g denotes the depth of the equivalent fixed point for a pile group, and α is the factor of the group effect. Considering average characteristics for a problem [L/L_e of 2.5 to 5, and $D/L_e \approx 0.3$] the parameter (S/L_e) has been determined according to the type of group and the relative spacing between pile centres. This parameter is represented in Fig. 309. This way it will be easy to determine the displacement, Y_{Hg} , of a pile group:

$$Y_{Hg} = \frac{H(l + L'_g)^3}{3E_p I_p} \text{ (hinged head),} \quad (426)$$

where l is the free length of the pile. The maximum bending moment for a pile group can be taken as 10% more than that of a single pile, with equal loads at the head (OTEO and VALERIO, 1981).

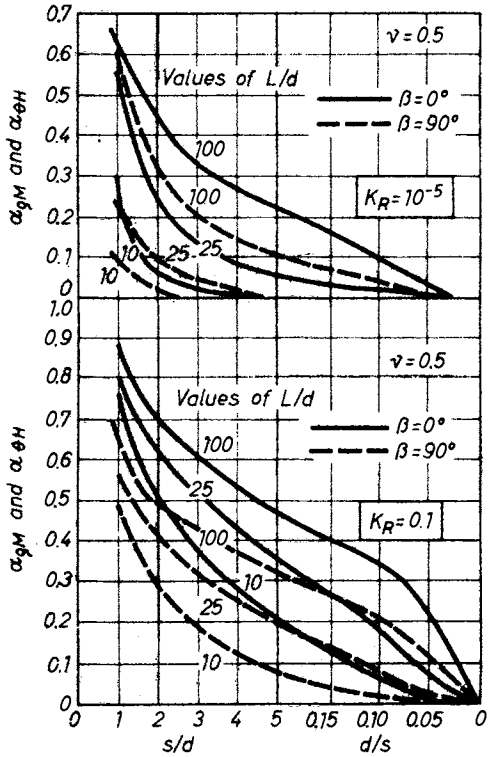


Fig. 310. Interaction factors $\alpha_{\theta H}$ for free-head piles subjected to horizontal load: a — for $K_R = 10^{-5}$; b — for $K_R = 0.1$ (POULOS, 1971)

POULOS (1971b) treats the case of a pile group as the generalization of a single pile (see Section 3.4.1.2). Beside the influence factor, α_{θ} , introduced by the author, another such factor is defined for this case as:

$$\alpha_{\theta} = \frac{\text{additional rotation due to the adjacent pile}}{\text{rotation of the pile due to its own loading}}$$

Both factors are dependent also on the mode of loading, be it either a horizontal force H , or a moment M .

The interaction factors for free-head piles, $\alpha_{\theta H}$ and $\alpha_{\theta M}$, are given as functions of s/d and L/d for two different K_r -s in Fig. 310 and Fig. 311 (the same relations can be found in the article cited for the case of fixed-head piles as well).

POULOS (1971b) emphasizes the following aspects from among his test results.

1. All α values decreases with increasing spacing and are greater for $\beta = 0$ than for $\beta = 90^\circ$ (β is the departure angle between the piles).
2. All α values increase with increasing L/d .
3. All α values increase with increasing pile stiffness (i.e. increasing K_r).
4. For a free-head pile, the interaction factors for moment loading, $\alpha_{\theta M}$, are less than the corresponding values for horizontal loading, $\alpha_{\theta H}$.
5. The displacement interaction factors for fixed head piles are greater than those for a free-head pile.
6. The interaction factors for deflection, $\alpha_{\theta H}$ and $\alpha_{\theta M}$, are greater than those for rotation $L_{\theta H}$ and $\alpha_{\theta M}$.

POULOS (1971b) established that for practical purposes the distributions of pressure and moment obtained for a single pile can be used for the case of two interacting piles. The article cited deals also with cases of generally arranged and unlimited number of piles.

3.4.3 Piles submitted to horizontal cyclic loading

Section 3.2.3.5 has demonstrated to what extent the axially loaded piles are sensitive to cyclic loading. The same can be stated in respect to horizontal loading as well.

REESE and WELCH (1975), after investigating the influence of repeated loading on piles embedded in stiff clay, produced the following conclusions.

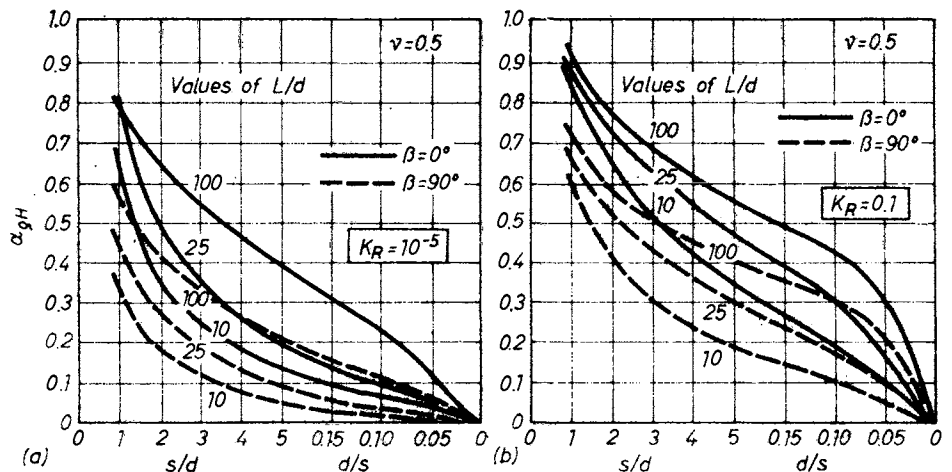


Fig. 311. Interaction factors $\alpha_{\theta M}$ and $\alpha_{\theta H}$ for free-head piles subjected to moment, for $K_R = 10^{-5}$ and 0.1, respectively (POULOS, 1971b)

1. The rotation of a pile will be increasingly greater under repeated loading; 20 repetitions produce a 20 to 25% increase.

2. The maximum moment increases with each application of the load (10–20% increase over 20 cycles) but the depth to the point of maximum moment increases very little.

When a soil is judged sensitive to liquefaction, a great reduction of lateral resistance must be considered in the design of piles. Although liquefied soil is often considered as air, or a heavy liquid, such an assumption would result in prohibitively expensive design. However, once liquefied, the soil cannot transfer shear waves and consequently shows quite reduced motions. Hence, it is probable that the soil and pile might reach their maximum amplitude of motion prior to liquefaction rather than after its onset (TAJIMI, 1977).

Many reports have been presented on model tests, full-scale field tests and seismic observations of pile foundations, although they are restricted to small vibrations. Some already confirmed findings may be summarized as follows (TAJIMI, 1977).

1. It is difficult to get a significant increase in horizontal stiffness of foundations by applying vertical piles.

2. For small size piles, the increase of damping is produced more effectively by making backfill around the pile cap, because the soil–pile interaction may produce only a slight damping effect during horizontal vibration.

3. When the bottom surface of a pile cap (or raft) is only in loose contact with the soil, as in the case of end-bearing piles, the horizontal stiffness and the damping of a pile foundation decrease considerably with increased lateral loads, because the contribution of the pile cap in the total resistance is reduced. This condition alters also the dynamic behaviour of a building on end-bearing piles, depending on the intensity of the earthquake.

4. Piles contribute to increasing the rocking stiffness characteristics of foundations. They result in reducing the earthquake response in the upper stories of buildings.

5. Usually, horizontal motions of piles are controlled by the surrounding soil. However, large diameter piles filter out the high-frequency components of earthquake motions.

3.5 Negative skin friction

The friction along a pile shaft that acts downward, i.e. increasing the load and the settlement of the pile, is called negative skin friction.

This phenomenon is always provoked by some vertical deformation in the surrounding soil. The reason for such compression may include:

- the consolidation of a recently made loose fill around the pile;
- the compressive action of a substantial fill being brought on the ground;
- regional water uptake from the underground on which the piles are standing.

Though the load may approach or even reach the ultimate bearing capacity of the pile (OKABE, 1977), the harmful effect of negative skin friction mostly appears in the following forms:

- settlements and/or differential settlements beyond the acceptable level;
- overstresses beyond the allowable level in the material of the pile (HORVAT and VAN DER VEEN, 1977).

INOUE *et al.* (1977) gave an account about a building founded on steel piles which failed completely four years after construction due to differential settlement evoked by negative skin friction. (The surrounding area had been filled up with an embankment 2.5 m high, and beside that the regional water uptake caused a deflection of the ground surface at the rate of 10 cm/year.) Reproducing this case schematically in Fig. 312 an example can be seen of how dangerous an uneven stratification can be: the line of the differential settlement is in good agreement with the top line of the load-bearing layer.

3.5.1 Development and amount of negative skin friction

To enable observation of the phenomenon, many researchers conducted full-scale experiments which may shed light on the nature of this occurrence.

OKABE (1977) investigated the performance of three driven steel piles of 60 cm diameter in the vicinity of Tokyo. The subsoil consisted of very loose sands and silts down to 40 m depth below ground surface. The region was submitted to deep pumping for water uptake and suffered a yearly 10 cm subsidence. This unwanted situation was further aggravated by the construction of an embankment in the neighbourhood of the piles. (This action lasted for 150 days after the installation of the piles.) During the tests, the axial forces in the piles, the earth- and pore-water pressure in the subsoil, and the elevation of the ground level were measured (refer to Section 3.7).

The time-dependent pattern of axial force and friction distribution is shown in Fig. 313. Maximum axial forces at each stage were 4.4 MN at the end of embankment work, 5.3 MN 460 days after pile driving, and 1660 days after driving the force attained 7.0 MN. The negative skin friction at depths of 29 to 35 m was derived from the measurements as 200 kN/m². The pile head settled 7 cm, of which compression of the pile itself accounted for 1 cm.

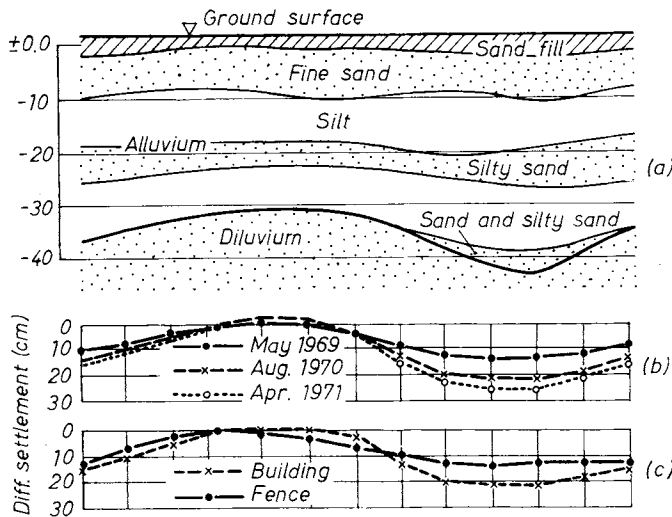


Fig. 312. Soil profile and differential settlement from negative skin friction (INOUE *et al.*, 1977)

A neutral point, defined as the transition point between negative and positive friction zones, is supposed here to exist at the depth where the settlement of the pile equals that of the surrounding soil, at about 8 m distant from the pile. The neutral point of pile 1 developed near its lower end, or at the point 0.9 times the pile length.

Pile 2 was loaded somewhat later. It was observed that the neutral point developed at depth 0.8L when the load was 0.7 MN; when the load was increased to 1.7 MN, this point was elevated in the beginning but later sunk again to a greater depth.

Specific negative skin friction (F_i) has been calculated by using three different methods:

$$F_1 = q_u/2,$$

$$F_2 = \text{in situ vane shear resistance},$$

$$F_3 = K_0\sigma \tan \Phi \text{ } (\Phi \text{ was taken from a CU test}).$$

Comparison of calculated to measured values showed a fair agreement for all three alternatives when very loose condition existed in the soil ($z = 0-15$ m, $N < 5$), but at greater depths $q_u/2$ supplied a much lower value than would have been reasonably estimated on the basis of the measurements.

AUVINET and HANELL (1981) monitored the performance of 30.5 and 32.0 m long piles driven in the subsoil in the Mexico Valley during four years. Due to deep-water uptake, the extremely porous ($e = 6$ to 10) clay suffered a sompression of 21 cm during the first two years. Two months later, when pumping was stopped in all but four wells (out of 140), the process of consolidation ceased and, moreover, a small expansion ensued.

Figure 314 shows the variation of axial load in a point-bearing pile as a function of time. The vertical load generated by the negative skin friction achieved 0.32 MN at the maximum. A periodic behaviour was observed as the downdrag loads increased during the dry seasons and decreased during the rainy seasons. After pumping stopped, the downdrag loads disappeared progressively or turned to tension as the clay layer expanded. (The behaviour of a friction pile was rather similar; the measured max. vertical load attained 0.21 MN.)

Defining as the neutral point the elevation at which there is no relative movement between soil

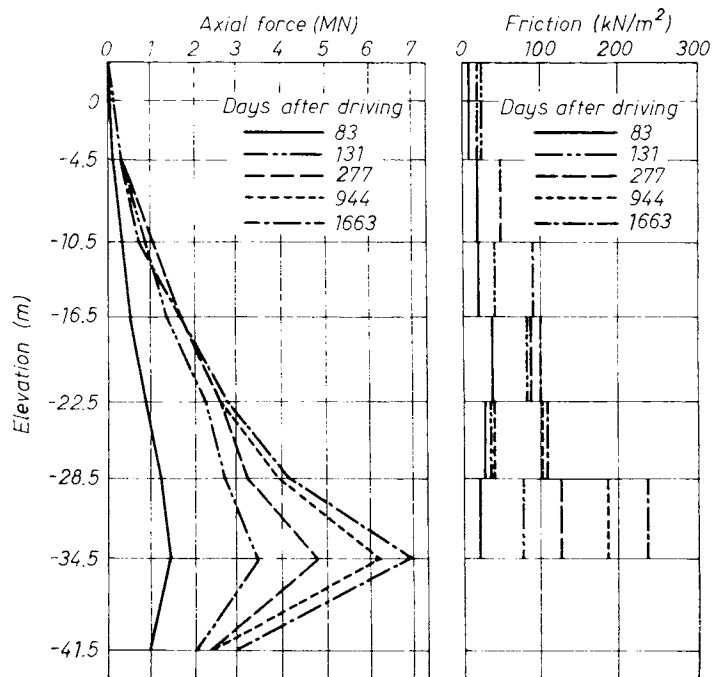


Fig. 313. Axial force and friction of Pile No. 1 (OKABE, 1977)

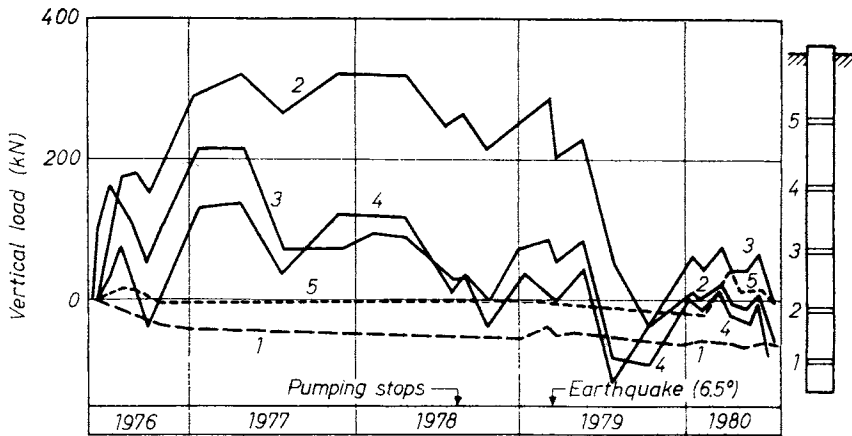


Fig. 314. Downdrag load of point-bearing piles (AUVINET and HANELL, 1981)

and pile, it may be concluded that for the point-bearing pile this point was located at 23 m (for the friction pile it was slightly higher). It was observed that during the rainy season the soil moved upward in relation to the upper part of the piles. A second neutral point may then develop and affect the negative skin friction distribution. Two different friction distributions, such as those shown in Fig. 315 may then be expected — depending on the period of the year.

AUVINET and HANELL (1981) concluded after the evaluation of measured and calculated data from these tests that the formula presented by KÉRISEL (1976)

$$s(z) = 1.5c_u \tan \Phi$$

is the most reliable one for the calculation of the specific skin friction, but a good approach is also achieved by using the value $0.8c_u$.

HORVAT and VAN DER VEEN (1977) observed that already a few mm of settlement is able to provoke a substantial skin friction. The authors observed also that the vertical force produced on the pile grows at a higher rate at the beginning than later; they related this fact to the reconsolidation process.

3.5.2 Elimination of negative skin friction

Bitumen is used in Scandinavia and Canada to reduce the negative skin friction on piles in clay. The bitumen is either brushed on, or the piles are dipped into it. CLEMENTE (1981) described a case in Hawaii where bitumen coating reduced the negative skin friction by 60 to 80%; the effect increased with the thickness and with decreasing softness of the bitumen layer. VELLOSO *et al.* (1981) reported that a bituminous coating of 3 mm thickness decreased the skin friction by 75%.

HORVAT and VAN DER VEEN (1977) investigated three piles next to each other. One was surface treated with bitumen, the other with bentonite,

and the third was the control. Measured reduction in vertical forces was between 30 to 60% for the treated piles, respectively.

OKABE (1977) proposed protecting the load-bearing pile by putting it in a steel tube. The outer pipe can then easily slide on the inner pile owing to the steel spacers installed. An elastic epoxy resin is additionally poured into the circular space between the pile and the tube on the upper 5 m section of the pile to prevent soil from entering into the gap.

3.6 Pile heave due to driving of neighbouring piles

Pile driving generates substantial stresses in the surrounding soil mass which may then give rise to various vertical and horizontal forces on neighbouring objects under the ground level. In a given case it may then happen that the upward

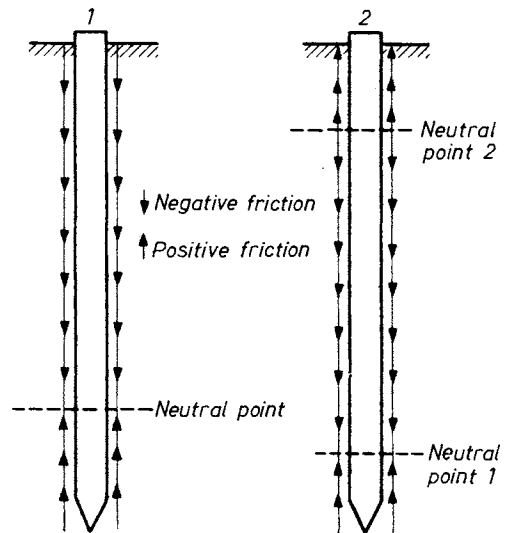


Fig. 315. Skin friction distribution(1) in dry season and (2) in rainy season (AUVINET and HANELL, 1981)

vertical component of the force attains a critical value that is sufficient to lift up a mass in the vicinity of driving, including a previously embedded pile. This phenomenon may be especially dangerous — according to observed situations — in cases of:

- point-bearing piles which are not sufficiently keyed into the load-bearing stratum (KOUTSOFTAS, 1982), or
- piles with enlarged footings (CLARK, 1981).

It might be interesting to note, in respect of the extent of heave, that TONG *et al.* (1981) measured 12 cm of heave and 5 cm of lateral displacement on 30.7 m long piles which were driven in at 1.9 m distances from each other.

A very intensive investigation has been completed in this respect by KOUTSOFTAS (1982). H-profile piles were driven in a cluster of 5 × 8, with 1.07 m centre-to-centre distance. The piles in the cluster were driven row by row, starting at the south end of each row and proceeding northward until all the piles in each row were driven (see Fig. 316).

29 piles (out of 40) heaved 10.2 to 17.8 mm, 3 piles heaved more than 20 mm, and one pile suffered 25.4 mm upward movement. Each pile underwent a small but distinct heave when an additional pile was driven. Levelling during the 9 days after completion of driving showed that the heave remained constant after the driving operation stopped. (The lateral distribution of the vertical displacements can be seen in Fig. 316.)

Figure 317 shows the heave of piles keyed with lengths of 1.5 to 6.1 m into the load-bearing layer as a function of distances from later driven piles. The incremental heave appears to decrease exponentially with increasing distance from the driven piles. The data indicate a radius of influence between 4.6 and 9.1 m. Similar behaviour for other types of piles was reported by COLE (1972). OLKO (1963) found an influence radius of 12.2 m when he investigated friction piles; he experienced that the impact of driving one row of piles extended to a distance of 10.7 m.

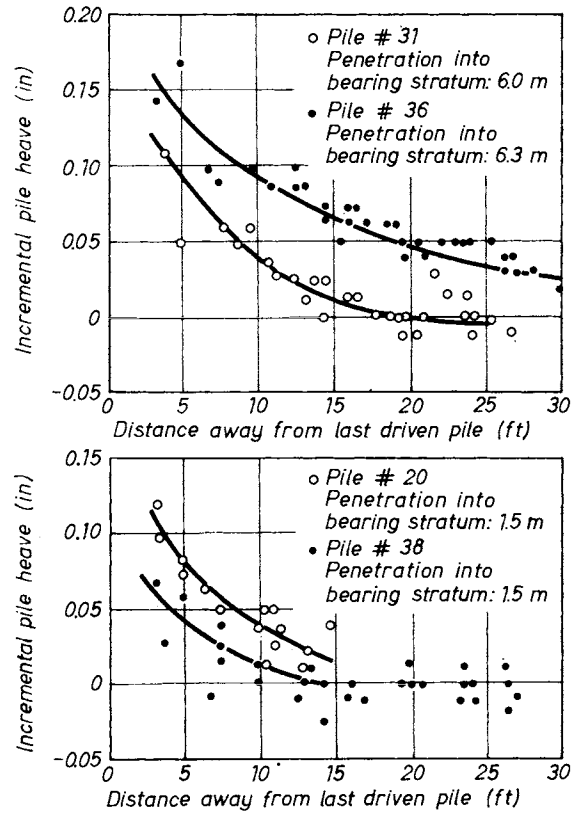


Fig. 317. Incremental pile heave vs. distance from last driven pile with different penetration into bearing stratum (KOUTSOFTAS, 1982) (1 ft = 0.3048 cm— 1 in = 25.4 · 10⁻³ m)

The range of heave depends also on the number of piles being driven later. In the example referred above (KOUTSOFTAS, 1982), the heave at the end of driving was about twice that recorded after the first four rows of piles were driven. This effect is demonstrated in Fig. 318 which is a plot of max. and average recorded heave within the cluster versus the number of driven piles. (A further extension of the cluster would cause the straight line to transform into a curve with horizontal asymptote.)

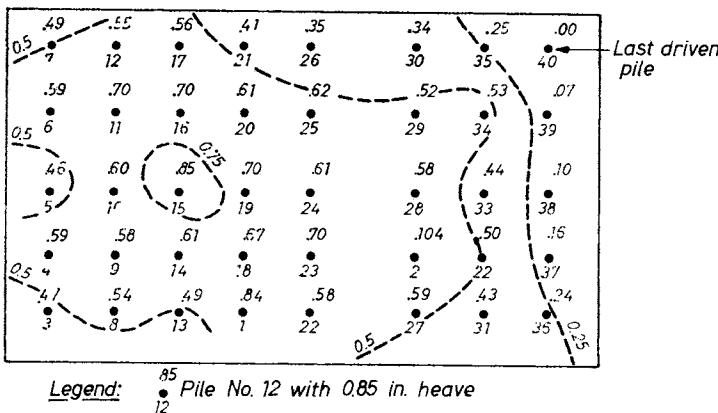


Fig. 316. Distribution of heave within test cluster, in inches (KOUTSOFTAS, 1982) (1 in = 25.4 · 10⁻³ m)

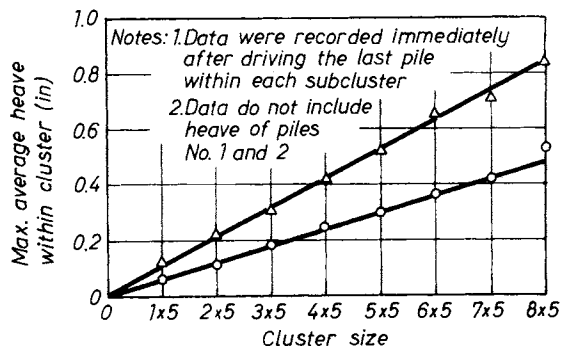


Fig. 318. Effects of cluster size (number of driven piles) on average and maximum pile heave within cluster (KOUTSOFTAS, 1982) (1 in = 25.4 · 10⁻³ m)

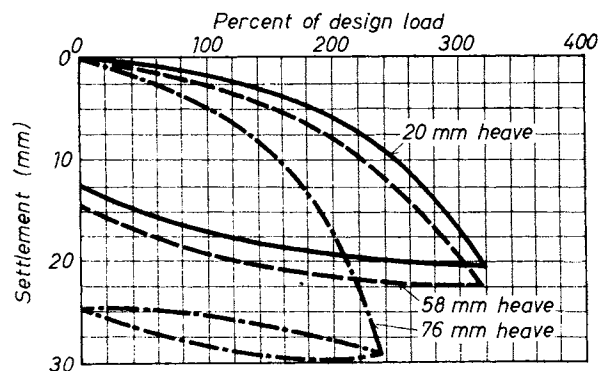


Fig. 319. Load test results for piles with different heaves (CLARK *et al.*, 1981)

OLKO (1963) reported the heave of some 244HP piles driven within an area of approximately 15.2 × 17.3 m at a spacing of 1.02 m. Heave as large as 280 mm was recorded, while the arithmetic average of all recorded heaves was 116 mm. This further demonstrates that under certain circumstances, H-piles may experience large heaves.

Pile driving may cause a heave that tears off the enlarged base from the pile, or may harmfully influence the quality of the newly cast concrete.

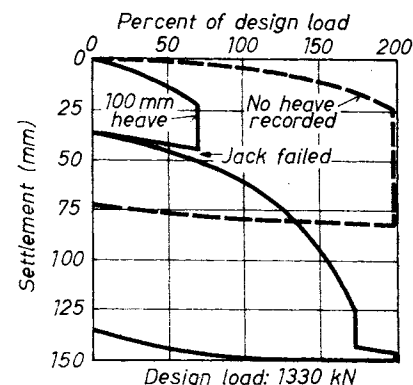


Fig. 320. Load test results of piles with heaves of 0 and 100 mm, respectively (CLARK *et al.*, 1981)

This relates mostly to piles cast *in situ* without casing, as can be shown from the three case-studies of CLARK *et al.* (1981).

In the middle of a cluster of 132 piles (at the centre of a building being built) 810 mm of heave has been measured (as the maximum), while the eight piles at the contours heaved by 250 mm. In this case the investigation proved that 200 piles out of the 292 driven, turned out to be useless, on the ground of two types of deteriorations:

- if the neighbouring pile was driven on the same day, the shaft declined in quality, because — as ultrasonic testing proved — the bond had not yet matured in the concrete, or
- if driving occurred some days later, the enlarged foot separated from the trunk of the pile.

No harmful effect has been experienced — even if the piles were driven on the same day — when the distance between the piles exceeded 9D.

In the second case measured heave was 25 to 75 mm, 90 mm as the maximum, the distance between the piles was 3D. Figure 319 shows the results of loading tests completed of three differently heaved piles. According to the figure the piles with less than 25 mm of heave behaved as normal piles, while the others showed the features of friction piles.

The third example deals with two cement container silos. Here, it was previously agreed that piles with distances less than $t = 9D$ should not be driven on the same day. Heave measurements started only after the installation of 30 piles and, surprisingly, heaves of 70 to 250 mm were experienced. A load test was carried out on one of the last piles driven (with no recorded uplift) and on a pile which heaved by at least 100 mm. The results are shown in Fig. 320. It can be seen that the pile which heaved 100 mm failed in friction before being jacked to where the shaft returned to contact with the base. These heaved piles were later excavated down to base level and clearly showed the signs of rupture between the base and the shaft, with separations of 250 and 125 mm, corresponding very closely to the heave recorded.

Both data and theory indicate that the effect of uplift decreases when the depth of driving increases. For the 500 to 600 mm shaft diameters commonly used in Canada, the critical depth has been determined by observation, and has been found in the range of 8 to 12 pile diameters. This corresponds to the critical depth as described by MEYERHOF (1976) for maximum pile shaft resistance. It can be said, as a first approximation, that if the critical depth is less than twice the length of the shaft there will be no significant separation of the pile shaft from the base.

CLARK *et al.* (1981) also pointed out that the rehabilitation costs in the first example mentioned before equalled the cost of construction. This is

why great respect should be attributed to the methodology of investigation and rehabilitation as it was stipulated earlier by CLARK (1978).

3.7 Prediction of pile performance on the basis of *in situ* measurements

3.7.1 Loading tests under axial loads

Loading tests are primarily carried out to find out the following characteristics:

- the Q - s (load-settlement) curve;
- the ultimate bearing capacity, Q_u ;
- the value of the skin friction;
- the displacement necessary to mobilize skin friction and point resistance;
- the ratio of skin friction capacity to point-resistance capacity;
- the amount of negative skin friction and the depth to the neutral point.

In some cases even the simplest measurements, the determination of the load-settlement curve may provide valuable information. So, for example, having made tests with micro-piles, it has been found that the Q - s curves of friction and of point bearing piles, acquired at the same working site, were identical. From this result it was easy to deduce that the bearing capacity of the point-bearing piles originated also from the skin friction alone (SABINI and SAPIO, 1981).

An investigation can be either a static or a dynamic loading test, depending on the character of loading and type of measurement.

With respect to static loading tests, two different loading procedures are used (BROMS, 1981): maintained loading (*ML*) and constant rate of penetration (*CRP*). In maintained loading the load is applied in increments. Up to the estimated allowable load, the increments are normally 25% of this load. Thereafter the increments are reduced. At the allowable load, the load is normally maintained for 24 hours. The time can be reduced by keeping the time for each load increment constant (20 to 30 minutes). In the *CRP*-method, the penetration rate of the pile is kept constant, normally 0.5 mm/min, and the applied load is measured. A relatively large total penetration is normally required to reach failure with a friction pile. A load test on a point-bearing pile is normally stopped when the ultimate bearing capacity has been reached, or when the applied load is two to three times the design load.

In the case of pile groups or large-diameter single piles it often occurs that the size of the loading frame restricts the application of sufficient load to attain the ultimate bearing capacity of the pile. The hyperbolic approach can be used in such cases to find the estimate of the Q_u value (CHIN, 1970).

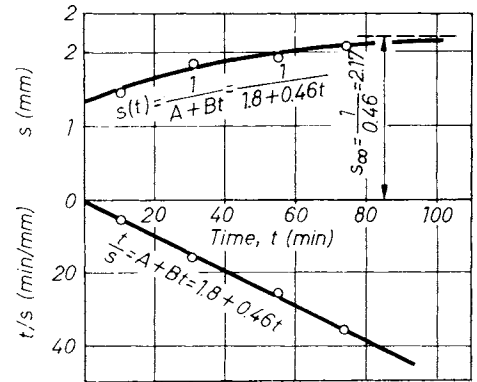


Fig. 321. Determination of settlement from pile load test — evaluation of final settlement in a load increment (PROMBOON and BRENNER, 1981)

The load-settlement relationship is approximated here by a hyperbolic curve. In a plot of the settlement ratio, s/Q , versus settlement, s , the inverse slope, $1/b$, of the fitted straight line would then correspond to the ultimate load of the pile, i.e.:

$$\frac{s}{Q} = a + b s \text{ and } Q = \frac{1}{b}. \quad (427)$$

The settlement, s_n , which corresponds to a load step, Q_n , can be evaluated by a procedure proposed by ROLLBERG (1977). This is illustrated in Fig. 321. The end settlement, $s_{\infty, n}$, is obtained from the inverse slope of the fitted straight line in a t/s versus t plot.

The methodology of loading tests has been perceptibly improved in the last 20 to 25 years. Instrumentation incorporated in the piles may shed light on several questions:

- what is the elastic compression of the pile material;
- what type of axial forces appear in the pile material, and what is their distribution;
- what is the value of the skin friction at different sections of the pile (vertical distribution of f_s);
- what is the earth pressure on the pile shaft (vertical distribution of the earth-pressure);
- what kind of pore-water distribution develops in the vicinity of the pile owing to the installation of the pile?

The instruments being installed in respect of the above questions include: electric strain gages, strain rods (tell-tales), load cells, earth pressure cells and pore-water pressure cells.

The elastic compression of the pile material will be established from the vertical displacements measured at the head and at the point of the pile. (Note that this displacement causes some skin friction even if the displacement is zero at the point of the pile.)

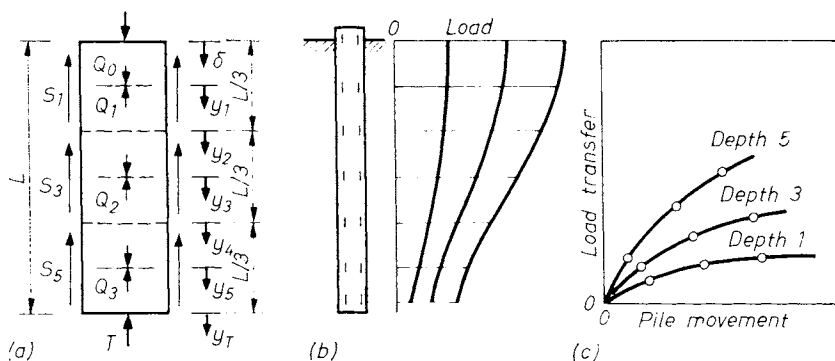


Fig. 322. a — Axially loaded pile divided into three segments; b — typical curves showing load distribution vs. depth; c — typical curves showing load transfer vs. pile movement (COYLE and REESE, 1966)

By measuring the axial forces in the pile it will be possible to establish

- the variation of forces with depth (for example, the load produced by negative skin friction, as has been mentioned in Section 3.5.1);
- the distribution of the skin friction along the shaft.

For the calculation of the latter item, we can use the procedure proposed by COYLE and REESE (1966).

In their example the authors divide the pile into three segments (Fig. 322a). Each segment is then divided into two equal parts and the value of load transfer and pile movement can be obtained at the midpoint of each segment. The settlement, δ , at the top is obtained from a load–settlement curve. The Q values for different depths are obtained from a load distribution curve (Fig. 322b). The procedure for computing the load transfer is to subtract the load at the bottom of the segment from the load at the top and divide by the circumferential area. This gives the load transfer in kN/m^2 . For the top segment in Fig. 322a the load transfer is

$$s_1 = \frac{Q_0 - Q_1}{\pi D_1 L/3} \tag{428}$$

The load transfer s_3 and s_5 can be computed in a similar manner.

The procedure for computing the pile movement at the midpoint of a segment is to subtract the elastic deformation in the pile, first from the settlement at the top, and then from midpoint to midpoint at each segment. The pile movement y_1 is:

$$y_1 = \delta - \frac{\frac{Q_0 + Q_1}{2} \frac{L}{3} \frac{L}{2}}{AE_0 + AE_1} \tag{429}$$

and the pile movement y_3 is:

$$y_3 = y_1 - \frac{\frac{Q_1 + Q_3}{2} \frac{L}{3}}{AE_1 + AE_3} \tag{430}$$

In a similar manner y_5 can also be established. After the load transfer and pile movement have been computed at different depths along the pile for different loads at the top, the results can be plotted as a family of curves. A typical family of curves of load transfer versus pile movement is shown in Fig. 322c.

As loading tests are rather expensive manoeuvres it is highly desirable to make use of earlier performed loading test results. One such method comprises the application of the Bayes-theorem (KAY, 1976, 1977). Using this method any parameter can be determined which is in correlation with the bearing capacity of the pile (Q_u, f_s , etc.). The idea is that (by preferably using data from earlier nearby loading test results) the *a priori* distribution is first determined. Having completed the loading test, the parameters of the *a posteriori* distribution are determined by help of the Bayes-theorem. The same procedure is then followed after the 2nd, 3rd, . . . , loading test. Eventually the expected value and standard deviation of the desired parameter can be produced, and so, their value to any desired probability level can also be established. This procedure is also useful when a decision is needed about the optimal number of necessary loading tests (KAY, 1976, 1977).

Dynamic methods might also be applied to determine the allowable bearing capacity of piles. The simplest method is “trial ramming” where the penetration is measured as a function of the number of blows (n). Though during the past 40 to 50 years several researchers attempted to make this procedure more reliable, its accuracy is still rather limited.

Another dynamic testing method is the “case method” which measures the acceleration of the

pile (SANTOYO and GOBLE, 1981). The method uses electronic measurements made during pile driving to predict pile bearing capacity. Pile top acceleration, a , and pile top force, \bar{F} , are measured. The pile is originally assumed to be a rigid body of mass, m . The resistance force of the soil, using Newton's law, is calculated as

$$R = F(t) - ma(t), \quad (431)$$

where F and a are functions of time.

Studies including longer piles ($L > 18$ m) showed that their elasticity could not, in general, be neglected. Assuming a uniform pile and ideal soil behaviour the following equation was derived (GOBLE *et al.*, 1970).

$$R = 0.5 [F(t_1) - F(t_2)] + \frac{mc}{2L} [v(t_1) - v(t_2)], \quad (432)$$

where $t_2 = t_1 + 2L/c$ and t_1 is a selected time during blow; L is the pile length, v is the velocity of the pile top, and c is the wave propagation velocity through the pile. The soil resistance, R , can be considered to be the sum of the static, S , and a dynamic component, D ; so,

$$R = R_S + D. \quad (433)$$

The "damping force", D , is obtained approximately:

$$D = Jv_{toe} \quad (434)$$

where J is a damping constant dependent on soil type. It can be shown from wave theory (GOBLE *et al.*, 1975) that the pile toe velocity can be calculated as

$$v_{toe} = 2v_{top} - \frac{L}{mc} R, \quad (435)$$

where v_{top} is the velocity at time t_1 .

Equation 435 is approximately correct for the first $2L/c$ seconds, after the initial arrival of the stress wave at the toe. The static soil resistance, R_S is then obtained by subtracting the calculated damping force, D , from the total driving resistance. Thus, the final expression becomes:

$$R_S = R - j_c [2F(t_1) - R], \quad (436)$$

where j_c is the dimensionless form of J (after dividing it by mc/L). In Eq. (436) all quantities except j_c can be derived from measurements.

3.7.2 Loading tests under horizontal loads

The simplest method consists of measuring the lateral displacement of the pile under the influence of gradually increased horizontal force increments. Correlating coherent P_h and y values, the resulting graph may reveal one of the desired design values. (The crushing force (P_{ho}) can also be determined if the load really reaches the amount required to

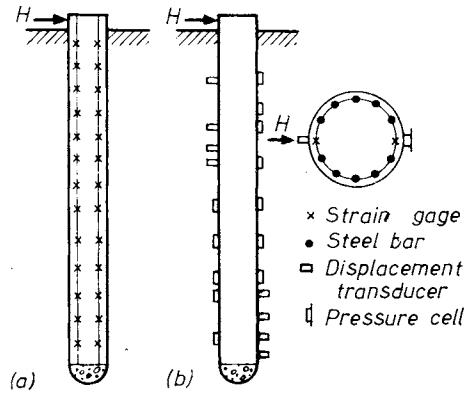


Fig. 323. Lay-out of measuring devices for a bored pile laterally loaded (LU, 1981):

a — strain gages; b — displacement transducers and pressure cells

cause failure.) The other important design information, namely the distribution of soil resistance (p), will not be provided by this test, and so the maximum bending moment in the pile cannot be determined in this way. This testing method can therefore only be accepted as satisfactory when it proves that a given pile does not break under the influence of the design load and/or the horizontal displacement remains within the allowable range.

Substantially more information on the presumed performance of piles can be gained when various instruments are installed in the set up. Such a situation is illustrated in Fig. 323 after LU (1981). These devices were mounted manually after the completion of boreholes made for bored piles. During the test, carried out by REESE and WELCH (1975) the quantities measured were: applied load, top deflection, top slope, and bending strains along the length of the shaft. The load applied to the shaft was measured with a strain gage load cell in the loading system, and by a pressure transducer connected to the hydraulic jack. A dial indicator and a linear potentiometer were used to measure the deflection of the top of the shaft. The slope of the top was measured by a specially constructed slope measuring device (pivot, micrometer screw on a rigid horizontal beam). For measuring the bending strain (and hence the bending moment), an instrument column was used.

Evaluation of loading tests carried out with applied instrumentation can be made by using Eqs (417) and (428); when the variation of the bending moment according to depth is known, y and p , i.e. the p versus y curve can be plotted. This calculation can make use of a graphic integration and differentiation, but can also be solved by analytical methods. AKÖZ *et al.* (1981) proposed the following procedure.

Figure 324 shows a section through a pile which has been driven into the soil and loaded with a horizontal load P , with excentricity e above the

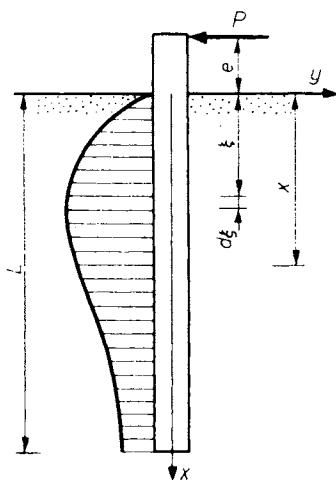


Fig. 324. Generalized pile-soil system (Aköz *et al.*, 1981)

soil surface, producing a soil reaction distribution $p = p(x)$ along the embedded length of the pile, L . At a depth x below the ground surface, the following equation can be written between measured bending moment and soil reactions:

$$M(x) = P(e + x) - \int_0^x p(\xi)(x - \xi)d\xi. \quad (437)$$

Writing this in the form

$$F(x) = P(e + x) - M(x) \quad (437a)$$

the value of $F(x)$ will be known from measured pile moments; $p(\xi)$ is the soil reaction to be determined. $F(x)$ is a Volterra-type integral equation; the soil reaction function $p(x)$ can be expressed in a series form;

$$p = \sum_{n=0}^{\infty} a_n x^n = a + a_1 x + a_2 x^2 + \dots \quad (438)$$

which it is wise to transform to a non-dimensional form ($\bar{p} = pL/P$, $\bar{x} = x/L$). The solution can be found by using Galerkin's method (Aköz *et al.*, 1981).

3.7.3 Forecast of pile behaviour from results of exploratory probings

The static cone penetrometer is a model pile and, when pushed into the soil, its penetration resistance can be correlated with a similarly installed full-size pile. When the pile point is above the critical depth in the bearing stratum (see Section 3.2.3.2), the unit point resistance has to be reduced from the limiting static cone resistance, q_c , in proportion to the embedment ratio, D_b/B , in this stratum. For sands it was suggested (MEYERHOF, 1956) that the approximate equation

$$q_p = \frac{q_c D_b}{10B} \leq q_l \quad (439)$$

should be used.

Using standard penetration tests, the ultimate unit point resistance, in t/ft^2 ($= 108 \text{ kN/m}^2$), might be taken approximately as

$$q_p = \frac{0.4ND_b}{B} \leq 4N. \quad (440)$$

The average ultimate skin friction of driven displacement piles in sand, in t/ft^2 , is roughly:

$$f_s = \frac{\bar{N}}{50}, \quad (441)$$

in which \bar{N} is the average standard penetration resistance in blows per 0.3 m; one-half of this value may conservatively be used for piles with small soil displacement, such as H -piles. From the analysis of pile load tests it is found that the observed unit point resistance is generally in fair agreement with Eq. (440), except with greater overburden pressure at the point when the ratio of q_p/N decreases (Fig. 325).

There is no universally accepted formula in respect of clays. Some progress might be achieved by compiling relationships between loading test results and characteristic soil properties on extended regions. This approach has been used e.g. by TONG *et al.* (1981) who provided $f_s(q_c)$ functions for the clays encountered in the Eastern Provinces of China. Accordingly, for normally consolidated or lightly overconsolidated clays at depths of not less than 6–8 m below ground level, and for overconsolidated soils of medium to stiff consistency not less than 20 m below ground level, the authors established the following expressions:

$$\begin{aligned} f_s &= 0.05q_c \text{ (for } q_c \leq 1000 \text{ kN/m}^2\text{),} \\ f_s &= 25 + 0.025q_c \text{ (for } 1000 < q_c < 3000 \text{ kN/m}^2\text{),} \\ f_s &= 100 \text{ kN/m}^2 \text{ (for } q_c \geq 3000 \text{ kN/m}^2\text{).} \end{aligned}$$

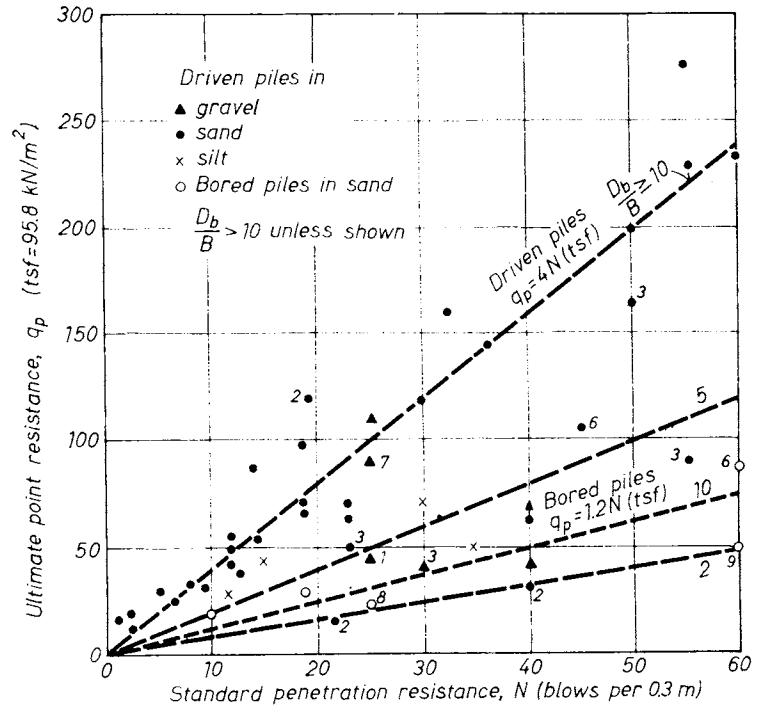
From empirical correlations between standard penetration resistance and settlement observations on structures on spread foundations, MEYERHOF (1974) derived the following conservative expression, in inches ($= 25 \text{ mm}$), for the total settlement, s , of shallow foundation on saturated sand and gravel:

$$s = \frac{2p\sqrt{B}}{N}, \quad (442)$$

in which B is the width of the pile group, in feet (0.3 m), p is the net foundation pressure, in t/ft^2 ($= 108 \text{ kN/m}^2$). For silty sand a factor of 2 should be used at the right-hand side of Eq. (442).

It has also been proposed to use Eq. (442) with a 50% reduction for estimating the settlement of deep spread foundations, which may be taken at an effective depth in a bearing stratum of more than about four times the width of the pile group. In other cases, s can be interpolated roughly in direct proportion to the ratio of the effective depth to D'/B of the pile group. Accordingly,

Fig. 325. Empirical relation between ultimate point resistance of piles and SPT resistance in cohesionless soil (MEYERHOF, 1976)



Eq. (442) can be rewritten, in inches (= 25 mm), as:

$$s = \frac{2p\sqrt{B} \cdot I}{N}, \quad (443)$$

in which I is an influence factor relating to the effective group embedment, approximately given by

$$I = 1 - \frac{D'}{8B} \geq 0.5. \quad (444)$$

Using static cone penetration tests,

$$s = \frac{pBI}{2q_c}, \quad (445)$$

in which q_c is the average static cone resistance within the seat of settlement (MEYERHOF, 1974).

3.7.4 Quality control of piles

For checking the integrity of locally made concrete deep foundations, a frequently used possibility is to incorporate tubes in their interior through which the whole depth can later be monitored by the use of isotopic probing devices.

RAUSCHE and GOBLE (1979) elaborated a dynamic testing method for the investigation of the soundness of piles. This procedure has been applied by LACY (1981) to the investigation of piles driven to depth of 62 to 70 m. Tests were performed several weeks after the piles were initially driven

using a pile hammer for re-driving. The testing procedure consisted of attaching two accelerometers and two strain transducers at opposite sides near the top of the pile. These gauges were connected to a pile-driving analyzer for immediate evaluation, with signals recorded on an analog magnetic tape for further processing. This equipment records strain and acceleration waves as they pass through the pile following the impact of a pile hammer, plus returning waves that rebound from the pile tip. The strain and acceleration waves are usually integrated and presented as force and velocity waves. These waves pass through the concrete at a known constant speed. Completely broken piles reflect downward velocity waves in a much shorter time than longer unbroken piles. A broken pile within a clay layer reflects a markedly reduced return force wave or even a tension wave, as there is little tip resistance to pile penetration and a high reflected positive or downward velocity. Figure 326 shows a pile broken at 22 m depth; this depth has been established on the basis of measuring the distance between positive peaks and a force wave that drops to zero.

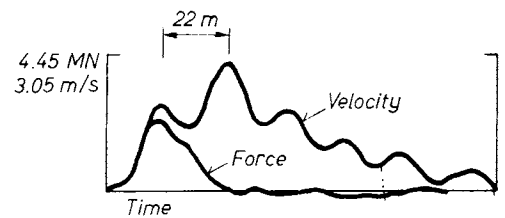


Fig. 326. Record from completely broken pile (LACY, 1981)

3.8 Economy and safety

In the course of design decisions are needed about the type of the piles to be used, their length and diameter, and the reasonable spacing between them. Several aspects have to be weighed in this process: stratification of the subsoil, properties of the layers encountered, location and aggressiveness of the groundwater, the sensitivity to movements of the building to be constructed, the condition and distance of nearby structures, etc. Any mature decision naturally has to comply with economic and safety requirements.

Interesting conclusions have been drawn by RANDOLPH (1983) in respect of the length L , and the slenderness ratio L/r_0 (r_0 being the radius of the pile). Ideally, the cost of installing the pile (inclusive of material costs) should be minimized for a given required capacity. As an approximate guide, the embedded volume of a pile will be taken as an indication of cost. The problem is then to optimize the ratio L/r_0 in order to maximize the pile capacity for a given volume of pile. The ultimate capacity of the pile may be written as

$$Q = r_0^2 \pi q_b + 2 \pi r_0 \bar{\tau}_s, \quad (446)$$

where q_b and $\bar{\tau}_s$ represent the bearing pressure at the pile base and the average skin friction, respectively. For a gross volume of $V = \pi r_0^2 L$, the capacity per volume is then:

$$\frac{Q}{V} = \left[\frac{\pi}{V(L/r_0)^2} \right]^{0.5} \left[q_b + 2 \frac{L}{r_0} \bar{\tau}_s \right]. \quad (447)$$

For a relatively homogeneous soil deposit, where q_b and $\bar{\tau}_s$ are not significantly affected by L , the above expression has a minimum at

$$\frac{L}{r_0} = \frac{q_b}{\bar{\tau}_s}$$

and maxima as L/r_0 approaches either zero or infinity. This indicates that the longer and thinner the pile is, the more efficient it will be in terms of capacity per embedded volume. In cases where the strength of the soil increases with depth, the advantage to be gained from a long slender pile is perhaps more obvious, since both $\bar{\tau}_s$ and q_b will increase with its length.

In practice, of course, there are physical limitations in respect of length or slenderness.

For bored piles, the length may be limited by the drilling rig, while for driven piles, the directional stability of the advancing pile tip becomes a problem. Another factor to be considered is the effect of pile compressibility on shaft capacity:

- long piles have a proportionally smaller shaft capacity;
- the skin friction is reduced to a residual value in the upper part of the pile, before the lower part has reached its limiting resistance (MEYERHOF, 1976).

In respect of pile spacing, aspects of techniques and economy are more than often congruent. For example, assessing horizontally loaded piles Poulos (1971b) mentioned that in regard to displacements, considerable economy can be achieved by using a relatively small number of piles at relatively large spacings.

Another problem to be considered is the number of loading tests which ought to be performed. These are very expensive manoeuvres, thus attempt should be made to depress the number of tests as far as possible. The following guidelines might be useful in this context:

- earlier loading test results should be utilized;
- relationships should be established between penetration test results and anticipated pile performance (see Section 3.7.3);
- it is reasonable to calculate the bearing capacity on the basis of the Bayes-theorem using earlier data (see Section 3.7.1);
- it will be useful to determine the bearing capacity of large diameter piles from results of loading test conducted on small diameter piles (FRANKE, 1981);
- the economic ratio of implementation costs should be weighed against the number of desired loading test results (JAEGER and BAKHT, 1983).

(Remark: to provide an economic design, it is a prerequisite to perform the trial tests after the development of reconsolidation processes.)

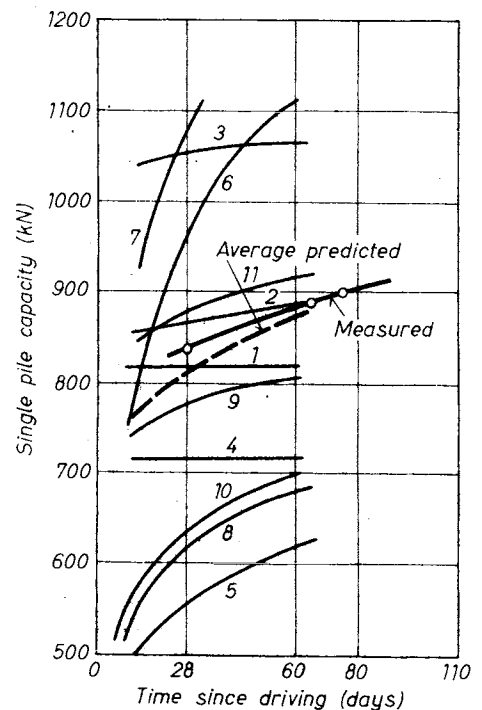


Fig. 327. Comparison of single pile predictions made by 11 specialists (VESIĆ, 1981)

In relation to safety the same principles apply as in the case of shallow foundations. Some "uncertainty" may, however, arise in the complexity of several contributive factors. Among them:

- differences peculiar to the applied technologies;
- inhomogeneity of the soil;
- eventual slanting position or excentricity of the pile (VESIĆ, 1981);
- gap between the pile-head and the soil, mostly in cases of vibrated piles in stiff clays (COYLE and REESE, 1966).

Such and similar factors may cause the bearing capacity not to be the same for individual piles, even in the same surrounding. The literature does not at present provide confirmatory data to determine how wide the scatter may be. KAY (1977) concluded, partly from loading test results evaluated by him, and partly from the variance of shear strength values, that an acceptable coefficient of variation for Q_u might be assumed to be 0.2, or even higher.

The reliability of predictions is further substantially influenced by the uncertainties inherent in various theories ("scattering of the model"). An interesting experiment has been reported by VESIĆ (1981) in this respect. Eleven individual experts were invited to calculate and forecast the performance of a single pile and of a pile group. All pertinent data were duly provided. The summary of predicted single pile capacities is shown in Fig. 327, where the measured capacities are also given. It can be seen that, in spite of great scatter of predictions, the average of the predictions, i.e. the average of all predicted capacities agrees quite well with the measured values.

References

- AKÖZ, Y., ÖNTUNA, K. A. and SAGLAMER, A. (1981): A new approach to the analysis of laterally loaded piles. *Proc. 10th ICSMFE*. Vol. 2, Stockholm.
- AUVINET, G. and HANELL, J. J. (1981): Negative skin friction on piles in Mexico City clay. *Proc. 10th ICSMFE*. Vol. 2, Stockholm.
- BALASUBRAMANIAM, A. S., PHOTA-YANUVAT, C., GANESHANANTHAN, R. and LEE, K. K. (1981): Performance of friction piles in Bangkok subsoils. *Proc. 10th ICSMFE*. Vol. 2, Stockholm.
- BANERJEE, P. K. (1970): *A contribution to the study of axially loaded pile foundations*. Ph. D. thesis, Univ. of Southampton.
- BANERJEE, P. K. and DAVIES, T. G. (1977): Analysis of pile groups embedded in Gibson-soil. *Proc. 9th ICSMFE*. Vol. 1, Tokyo.
- BANERJEE, P. K. and DAVIES, T. G. (1978): The behaviour of axially loaded and laterally loaded single piles embedded in non-homogeneous soils. *Géot.*, No. 3.
- BARTOLOMEY, YUSHKOV, B. S., DOROSHKEVITCH, N. M., LESHIN, G. M., KHANIN, R. F., KALESNIK, G. S. and MUYLUKOV, E. I. (1981): Pile foundation settlements. *Proc. 10th ICSMFE*. Vol. 2, Stockholm.
- BEREZANTSEV, V. G., KHRISTOFOROV, V. and GOLUBKOV, V. (1961): Load-bearing capacity and deformation of piled foundations. *Proc. 5th ICSMFE*. Vol. 2, Paris.
- BJERRUM, L. (1973) Problems of soil mechanics and construction on soft clays. *Proc. 8th ICSMFE*. Vol. 3, Moscow.
- BROMS, B. B. (1972): Stability of flexible structures. *Proc. Eur. Conf. SMFEE*. Madrid.
- BROMS, B. B. (1981): Pile foundations. General report. *Proc. 10th ICSMFE*. Vol. 4, Stockholm.
- BURLAND, J. B. (1973): Shaft friction on piles in clay — A simple fundamental approach. *Ground Engg.*, No. 3.
- BURLAND, J. B. et al. (1977): Behaviour of foundations and structures — state of the art. *Proc. 9th ICSMFE*. Vol. 2, Tokyo.
- BURLAND, J. B. and COOKE, R. W. (1974): The design of bored piles. *Ground Engg.*, No. 4.
- CAQUOT, R. J. and KÉRISSEL, J. (1966): *Traité de Mécanique des Sols*. Gauthier — Villars, Paris.
- CHIN, F. K. (1970): Estimation of the ultimate, load of piles from tests not carried out to failure. *Proc. 2nd. S. E. Asian Conf. Soil Eng.* Singapore.
- CLARK., J.;I. (1978): Failure during construction and subsequent rehabilitation and performance of a dynamically cast-in-place concrete pile foundation. A. S. T. N. STP 670.
- CLARK, J. I., HARRIS, M. C. and TOWNSEND, D. L. (1981): Heave of compacted expanded base concrete piles. *Proc. 10th ICSMFE*. Vol. 2, Stockholm.
- CLEMENTE, F. M. (1981): Downdrag on bitumen coated piles in a warm climate. *Proc. 10th ICSMFE*. Vol. 2, Stockholm.
- COLE, K. E. (1972): Uplift of piles due to driving displacement. *Civ. Eng. and Publ. Works. Review*, March.
- COOKE, B. W. (1974): The settlement of friction pile foundations. *Proc. Conf. Tall Buildings*. Kuala Lumpur.
- COOKE, R. W., PRICE, G. and TARR, K. (1980): Jacked piles in London clay: interaction and group behaviour under working conditions. *Géot.*, Vol. 2.
- COYLE, H. M. and REESE, L. C. (1966): Load transfer for axially loaded piles in clay. *Proc. ASCE*. SM 2.
- D'APPOLONIA, E. and ROMUALDI, J. P. (1963): Load transfer in end-bearing steel H-piles. *Proc. ASCE*. SM 2.
- DE BEER, E. E. (1964): Some considerations concerning the point bearing capacity of bored piles. *Proc. Symp. on Bearing Capacity of Piles*. Roorkee.
- DE BEER, E. E. (1971): Méthods de déduction de la capacité portante d'un pieu à partir des résultats des essais de pénétration. *Ann. des Travaux Publics de Belgique*. Nos 4-6.
- FLAATE, K. and SELNES, P. (1977): Side friction of piles in clay. *Proc. 9th ICSMFE*. Vol. 1, Tokyo.
- FRANCESCONI, M. (1982): Discussion in *2nd Int. Conf. on Num. Methods in Offshore Piling*. Austin.
- FRANKE, E. (1981): Point pressure versus length and diameter of piles. *Proc. 10th ICSMFE*. Vol. 2, Stockholm.
- GEDDES, J. D. (1966): Stresses in foundation soils due to vertical subsurface loading. *Géot.*, Vol. 3.
- GOBLE, G. G., RAUSCHE, F. and MOSES, F. (1970): Dynamic studies on the bearing capacity of piles. Phase III. *Division of Solid Mech., Struct. and Mech. Design*. Univ. Cleveland, Report No. 48.
- GOBLE, G. G., LIKINS, G. E. and RAUSCHE, F. (1975): Bearing capacity of piles from dynamic measurements. *Report submitted by Dept. of Civ. Engg.*, Univ. Cleveland.
- HORVAT, E. and VAN DER VEEN (1977): Negative skin friction and safety analysis of piles. *Proc. 9th ICSMFE*. Vol. 1, Tokyo.
- INOUE, V., TAMAOKI, K. and OGAI, T. (1977): Settlement of building pile downdrag. *Proc. 9th ICSMFE*. Vol. 1, Tokyo.
- JAEGER, L. G. and BAKHT, B. (1983): Number of tests versus design pile capacity. *Proc. ASCE. J. of Geot. Engg.*, Vol. 6.
- JANBU, N. (1976): Static bearing capacity of friction piles. *Eur. Conf. SMFE*. Vols 1-2, Vienna.
- JELINEK, R., KORECK, H. W. and STOCKER M. (1977): Load tests on five large-diameter bored piles in clay. *Proc. 9th ICSMFE*. Vol. 1, Tokyo.
- KAY, J. N. (1976): Safety factor evaluation for single piles in sand. *Proc. ASCE*. GT 10.
- KAY, J. N. (1977): Factor of safety for piles in cohesive soils. *Proc. 9th ICSMFE*. Vol. 1, Tokyo.
- KÉRISSEL, J. (1961): Fondations profondes en milieux sableux. *Proc. 5th ICSMFE*. Vol 2, Paris.
- KÉRISSEL, J. (1976): Contribution. *3rd N. Carrillo Lecture*, Soc. Mexicana de Mec. de Suelos, Guanajato.

- KÉRISSEL, J., L'HERNINIER and TSCHENG, Y. (1965): Résistance de pointe en milieux pulvérulants de serrages divers. *Proc. 6th ICSMFE*. Montreal.
- KÉZDI, Á. (1957): Bearing capacity of piles and pile groups. *Proc. 4th ICSMFE*. London.
- KOERNER, R. M. and PARTOS, A. (1974): Settlement of building on pile foundation in sand. *Proc. ASCE*, GT 3.
- KOUTSOFTAS, D. C. (1982): H-pile heave: a field test. *Proc. ASCE*, GT 8.
- LACY, H. S. (1981): Pile integrity and capacity determined by re-driving. *Proc. 10th ICSMFE*. Vol. 2, Stockholm.
- LADÁNYI, B. (1973): Bearing capacity of deep footings in sensitive clays. *Proc. 8th ICSMFE*. Vol. 2, 1, Moscow.
- LINDQUIST, L. and PETAJA, J. (1981): Experiences of tapered friction piles. *Proc. 10th ICSMFE*. Vol. 2, Stockholm.
- LU, S. S. (1981): Design load of bored pile laterally loaded. *Proc. 10th ICSMFE*. Vol. 2, Stockholm.
- MATTES, N. S. and POULOS, H. G. (1969): The settlement of a single compressible pile. *Proc. ASCE*. SM 1.
- MEYERHOF, G. G. (1951): The ultimate bearing capacity of foundations. *Géot.*, Vol. 2.
- MEYERHOF, G. G. (1956): Penetration tests and bearing capacity of cohesionless soils. *Proc. ASCE*. SM 1.
- MEYERHOF, G. G. (1959): Compaction of sands and bearing capacity of piles. *Proc. ASCE*. SM 6.
- MEYERHOF, G. G. (1963): Some recent research on the bearing capacity of foundations. *Can. Geot. J.*, Vol. 1.
- MEYERHOF, G. G. (1974): Ultimate bearing capacity of footings on sand layer overlying clay. *Can. Geot. J.*, Vol. 11.
- MEYERHOF, G. G. (1976): Bearing capacity and settlement of pile foundations. *Proc. ASCE*, GT 3.
- MINDLIN, R. D. (1936): Force at a point in the interior of a semi-infinite solid. *Physics*, 7.
- NORLUND, R. L. (1963): On piles in cohesionless soils. *Proc. ASCE*, SM 3.
- OKABE, T. (1977): Large negative friction and frictionfree pile methods. *Proc. 9th ICSMFE*, Vol. 1, Tokyo.
- OLKO, S. M. (1963): Discussion of "Pile heave and re-driving", by E. J. Klobn. *Trans. ASCE*, Vol. 128.
- OTEO, C. S. and VALERIO, J. (1981): A simplified analysis of piles with lateral loads. *Proc. 10th ICSMFE*. Vol. 2, Stockholm.
- POULOS, H. G. (1968): Analysis of the settlement of pile groups. *Géot.*, Vol. 4.
- POULOS, H. G. (1971a): Behaviour of laterally loaded piles: I - single piles. *Proc. ASCE*. SM 5.
- POULOS, H. G. (1971b): Behaviour of laterally loaded piles: II - pile groups. *Proc. ASCE*. SM 5.
- POULOS, H. G. (1972): Load-settlement prediction for piles and piers. *Proc. ASCE*. SM 9.
- POULOS, H. G. and DAVIS, E. H. (1968): The settlement behaviour of single, axially loaded, incompressible piles and piers. *Géot.*, Vol. 18.
- POULOS, H. G. and RANDOLPH, M. F. (1983): Pile group analysis: a study of two methods. *Geot. Engg.*, No. 3.
- PROMBOON, S. and BRENNER, R. P. (1981): Large diameter bored piles in Bangkok clay. *Proc. 10th ICSMFE*. Vol. 2, Stockholm.
- RANDOLPH, M. F. (1977): *A theoretical study of the performance of piles*. Thesis, Cambridge Univ.
- RANDOLPH, M. F. (1983): Settlement considerations in the design of axially loaded piles. *Ground Engg.*, No. 4.
- RANDOLPH, M. F. and WROTH, C. P. (1978): Analysis of deformation of vertically loaded piles. *Proc. ASCE*, GT 12.
- RANDOLPH, M. F. and WROTH, C. P. (1979): An analysis of the vertical deformation of pile groups. *Géot.*, No. 4.
- RANDOLPH, M. F., STEINFELT, J. and WROTH, C. P. (1979a): The effect of pile type on design parameters for driven piles. *Proc. 7th Eur. Conf. SMFE*. Vol. 2, Brighton.
- RANDOLPH, M. F., CARTER, J. P. and WROTH, C. P. (1979b): Driven piles in clay - the effects of installation and subsequent consolidation. *Géot.*, No. 4.
- RANDOLPH, M. F. and WROTH, C. P. (1982): Recent developments in understanding the axial capacity of piles in clay. *Ground Engg.*, No. 7.
- RAUSCHE, F. and GOBLE, G. G. (1979): Determination of pile damage by top measurements. *ASTM STP* 670.
- REESE, L. C. and WELCH, R. C. (1975): Lateral loading of deep foundations in stiff clay. *Proc. ASCE*. GT 7.
- ROLLBERG, D. (1977): Determination of the bearing capacity and pile driving resistance of piles using soundings. *Publ. Inst. Found. Engg., Soil Mech., Rock Mech. and Waterways Constr.* RWTH, Aachen, (3).
- SABINI, G. and SAPIO, G. (1981): Behaviour of small diameter bored piles under axial load. *Proc. 10th ICSMFE*. Vol. 2, Stockholm.
- SANTOYO, E. and GOBLE, G. G. (1981): An experience with dynamically tested piles. *Proc. 10th ICSMFE*. Vol. 2, Stockholm.
- SCHLITT, H. G. (1951): Group pile loads in plastic soils. *Proc. Highway Research Board*. Vol. 31, Washington.
- SCHMIDT, H. G. (1981): Group action of laterally loaded bored piles. *Proc. 10th ICSMFE*. Vol. 2, Stockholm.
- SEED, H. D. and REESE, L. C. (1957): The action of soft clay along friction piles. *Trans. ASCE*. Vol. 122.
- SKEMPTON, A. W. (1951): The bearing capacity of clays. *Proc. of the Building Research Congress*. Vol. 1.
- SKEMPTON, A. W. (1953): Discussion - piles and pile foundations, settlement of pile foundations. *Proc. 3rd ICSMFE*. Vol. 3, Zurich.
- SÖDEBERG, L. O. (1962): Consolidation theory applied to foundation pile time effects. *Géot.*, No. 3.
- STEINFELT, J. S., RANDOLPH, M. F. and WROTH, C. P. (1981): Instrumented model piles jacked into clay. *Proc. 10th ICSMFE*. Vol. 2, Stockholm.
- TAJIMI, H. (1977): Piles subjected to dynamical lateral loading. *Proc. 9th ICSMFE*. Vol. 3, Tokyo.
- TOMLINSON, M. J. (1957): The adhesion of piles driven in clay soils. *Proc. 4th ICSMFE*. Vol. 2, London.
- TOMLINSON, M. J. (1971): Some effects of pile driving on skin frictions. *Proc. Conf. on Behaviour of Piles*. London.
- TONG, Y. X., CHEN, O. H. and CHEN, X. L. (1981): Pile foundations in soft soils. *Proc. 10th ICSMFE*. Vol. 2, Stockholm.
- VELLOSO, P-P. C., ROCHA, E. A., FUJII, J. and RÉMY, J. P. (1981): Tension tests on 30 m steel piles to determine negative friction. *Proc. 10th ICSMFE*. Vol. 2, Stockholm.
- VESIĆ, A. S. (1967): A study of bearing capacity of deep foundations. *Report B-189*, Georgia Inst. of Techn., Atlanta.
- VESIĆ, A. S. (1968): Load transfer, lateral loads and group action of deep foundations. *Symp. on Perf. on Deep Found., Spec. Techn. Publ., 44 ASTM*.
- VESIĆ, A. S. (1975): Principles of pile foundation design. *Duke Univ., Soil Mech. Series*, No. 38.
- VESIĆ, A. S. (1981): Behaviour of pile groups. *Proc. 10th ICSMFE*. Vol. 4, Stockholm.
- VIJAVERGIYA, V. N. and FOCHT, J. A. (1972): A new way to predict capacity of piles in clay. *Offshore Techn. Conf.*, Houston.
- WITAKER, T. (1957): Experiments with model piles in group. *Géot.*, Vol. 7.
- WITAKER, T. and COOKE, R. W. (1966): An investigation of the shaft and base resistance of large bored piles in London clay. *Proc. Symp. on Large Bored Piles*, London.
- WOODWARD, R. J. and BOITANO, J. (1961): Pile loading tests in stiff clays. *Proc. 5th ICSMFE*. Vol. 2, Paris.
- ZEEVAERT, L. (1973): *Foundation Engineering for Difficult Subsoil Conditions*. Van Nostrand Rheinhold Co., New York.

Chapter 4.

Soil mechanics in road construction

4.1 Introduction

The tremendous growth in road transportation and especially the advent and widespread use of motor vehicles in the present century has led to requirements regarding the lay-out and especially the surfacing of roads; requirements which the earth and stone pavements which had slowly developed over the centuries could no longer satisfy. Smooth, durable pavements of high load-bearing capacity and insensitive to atmospheric influences became necessary to make full use of the vast possibilities offered by the motor vehicle and to permit the safe movement of heavy vehicles at speeds which were previously unimaginable. At the same time, allowance also had to be made for new requirements in road planning. The ancient traces closely following the slopes and gradients of the terrain and frequently adhering to historical traditions had to be abandoned; principles of planning developed by scientific research became necessary and roads had to be designed and constructed according to the same engineering principles as were earlier applied only to the railways. The results of this work have, in turn, given added impetus to the development of vehicles, and the successive stages of this mutual interrelationship are reflected in the rapid evolution of road transport, as well as in increasing standards of living.

In early road building, which was an art rather than a science, little care was devoted to the soil forming the foundation of the roads.

In constructing the new types of pavement to meet the aforementioned requirements, the importance of the subsoil was soon realized, in that the durability and soundness of the road depended fundamentally on the quality of the subsoil of the foundation, as well as on the extent to which the soil properties had been allowed for in the course of design. The early attempts to solve these problems followed a purely empirical approach, but this was soon replaced by research giving birth to the science of the soil mechanics of road construction.

In more recent times, further evolution has been prompted by the requirements of air transportation. High-capacity transport places have increased the need for long runways with pavements

capable of resisting severe static and dynamic effects equally. A special branch of soil mechanics devoted to airport runways has evolved; extensive theoretical, research and observational work was started and this has already resulted in considerable achievements.

The need for distinguishing a special branch of soil mechanics for road construction may be questioned, since the physical properties, load-bearing capacity, etc., of the soil are here just as important as in other domains; this question can, however, be answered most pertinently by reference to Fig. 328 (cf. Vol. 1, Fig. 3). The foundations of buildings and other civil engineering structures are almost invariably extended to depths unaffected by frost, desiccation in summer and penetration by the roots of plants. The foundations are supported by a soil the properties of which change but very slightly with temperature. On the other hand, there is no other structure which is exposed as strongly, and at the same time alternately, to such a wide variety of mechanical and climatic influences as the narrow, thin and expensive band of road pavements and

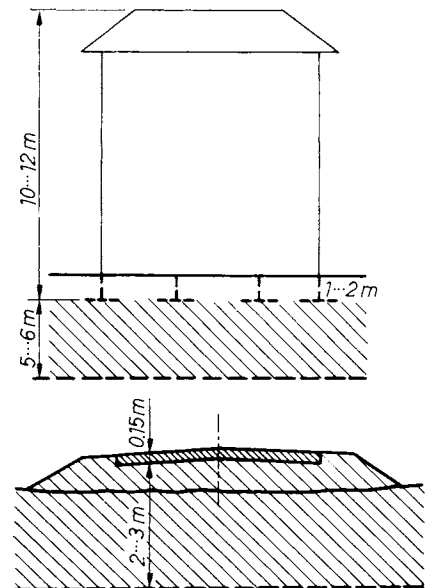


Fig. 328. Relationship between foundation and superstructure in buildings and roads

in combination therewith, the foundation, the earthworks and the subsoil which are exposed to the same effects.

Among the mechanical effects, the vertical static loads, horizontal forces and the impacts and vibrations caused by vehicles must be taken into consideration. The climatic effects are often closely associated with changes in stress conditions; they cause the water content and thus the structure of the soil to change. Most important in this respect is drying accompanied by shrinkage and cracking saturation resulting in a loss of strength, swelling and reduction in load bearing, frost giving rise to heaving by ice and loosening of the soil structure, and finally melting by which the soil is softened and rendered plastic.

In examining the relationship between the subsoil and the road pavement, three principal groups of problems can be distinguished:

1. The combined load-bearing capacity of the pavement and the subsoil, the determination of the ultimate load causing failure, and further dimensioning of the pavement and foundation with regard to the properties of the subsoil.

2. Volume changes of the subsoil and methods to control the detrimental effects thereof.

3. The effect of frost and other atmospheric conditions on the pavement and the subsoil.

The subsequent discussions will be centered around these three groups of problems.

4.2 Soil investigations for line structures

4.2.1 Objectives

The method and extent of soil investigations are governed by the objectives thereof. In our case, the objective is to detect the potentially detrimental and destructive effects of the subsoil and to furnish the designer with all the data on soil and groundwater conditions which he may find necessary for arriving at a rational and economic design. In soil exploration, this objective is realized if the data obtained are sufficient for resolving the requirements listed below correctly.

1. Assessing the correctness of the track envisaged in the horizontal and vertical sense alike.

2. The choice of soils suited to embankment construction.

3. Designing the cross-sections — slopes — of embankments and cuts.

4. Providing data for calculation and distribution of mass, the determination of loosening or densification, estimation of rockwork volumes.

5. The solution of surface and underground drainage problems.

6. Determination of the pavement thickness.

7. Decision on the advisability of soil stabilization method.

8. Testing the local materials for their suitability for stabilization and pavement construction.

The domain of soil exploration for road and railway construction purposes includes the excavation of pits, the sinking of boreholes and the collection of samples. Parallel therewith, the samples must be classified, qualified, and identified visually and by hand. For these reasons, such investigations must always be performed under the supervision of an engineer trained in soil mechanics who is perfectly aware of the objectives, who can appreciate the importance of slight indications which may appear insignificant to the untrained eye, and who can form a picture of the subsoil conditions. Development in this domain tend toward the establishment of small field laboratories for performing the basic soil-physical tests on major construction jobs, only the samples on which special tests are considered necessary being forwarded to a permanent laboratory.

4.2.2 The location and depth of soil exploration

Soil explorations related to road and railway building in Hungary are subject to standard specifications. The main provisions thereof are as follows.

“In locating the exploration sites, attempts should be made to obtain a clear picture of the stratification of soils and of the position of occasional rock layers along the track and in the borrow areas to be investigated. At the sites of major embankments or cuts, where settlement or heave, base failure or sliding are liable to occur in the subsoil, explorations must be extended laterally to obtain information on the position of any soil layer at at least three points. In the case of roads to be constructed over rolling terrain, soil explorations are essential in major fills and cuts at the intersections of the grade and the terrain.

Where earthwork of major extent and significance is contemplated and the individual layers are difficult to trace, the number of explorations must be increased along the profile and in the cross-sections alike.

For roads and railways involving fills and cuts of moderate height, the exploration sites should be spaced at 200 to 250 m on the average. Along sections where the stratification of the subsoil is found to change, or the groundwater table to fluctuate over a wide range, additional explorations should be envisaged at 50 to 100 m distances within the spacings specified above. This applies in particular to cases where the difference between two adjacent explorations is great enough to warrant changes in pavement thickness, filter drains, subgrade, etc. In the case of major differences, an even closer spacing of 30 to 35 m may also be justified.”

„ . . . the depth of exploration is controlled by the soil stratification observed and by the dimensions and type of the structure. The exploration

should be extended to a depth yielding reliable information on the soil layers below the grade which may effect the stability of the structure. Under embankments representing a load less than 60 kN/m^2 and in cuts not deeper than 3.0 m, explorations should be extended to 3 m depth below the terrain or the grade line, but in any case at least to the groundwater table. Under embankments transmitting loads greater than 60 kN/m^2 — where consolidation of the subsoil must be anticipated — the exploration should be deep enough to permit a reliable estimate of the ensuing stress pattern and the magnitude of settlements resulting therefrom. Alternatively, the exploration depth should equal the base width of the cut. Deeper soil layers need not be explored, unless the load-bearing capacity of those perforated is poor. In such cases, the strata should be explored down to the load-bearing layer.

Special care should be exercised in exploring soil layers including peat, marsh and other soils of high organic content. In such cases, exploration must be extended beyond the peat, marsh and organic layers to determine the quality, position

and depth of the load-bearing layers underlying them.

The sites of major cuts should be explored to a depth considered necessary for obtaining information on the hazard of heave, soil failure or sliding, and on the depth and direction of groundwater seepage, as well as on the stratification of the subsoil, for determining reliably the boundaries and inclination of the individual soil layers.”

As a practical rule, it should be noted that for examining the problem of volume changes, explorations extending to about 1.5–2.0 m below the crest of the earthwork are adequate, while as regards frost heave the exploration should be extended at least down to the groundwater table. However, instead of adhering to strict rules, the sites and depths of exploration should be determined individually in each particular case, keeping in mind the objectives mentioned before, the soil conditions encountered and the type of soil.

Prior to field work, all information on local geology and soil conditions should be obtained, geological, pedological and topographic maps of

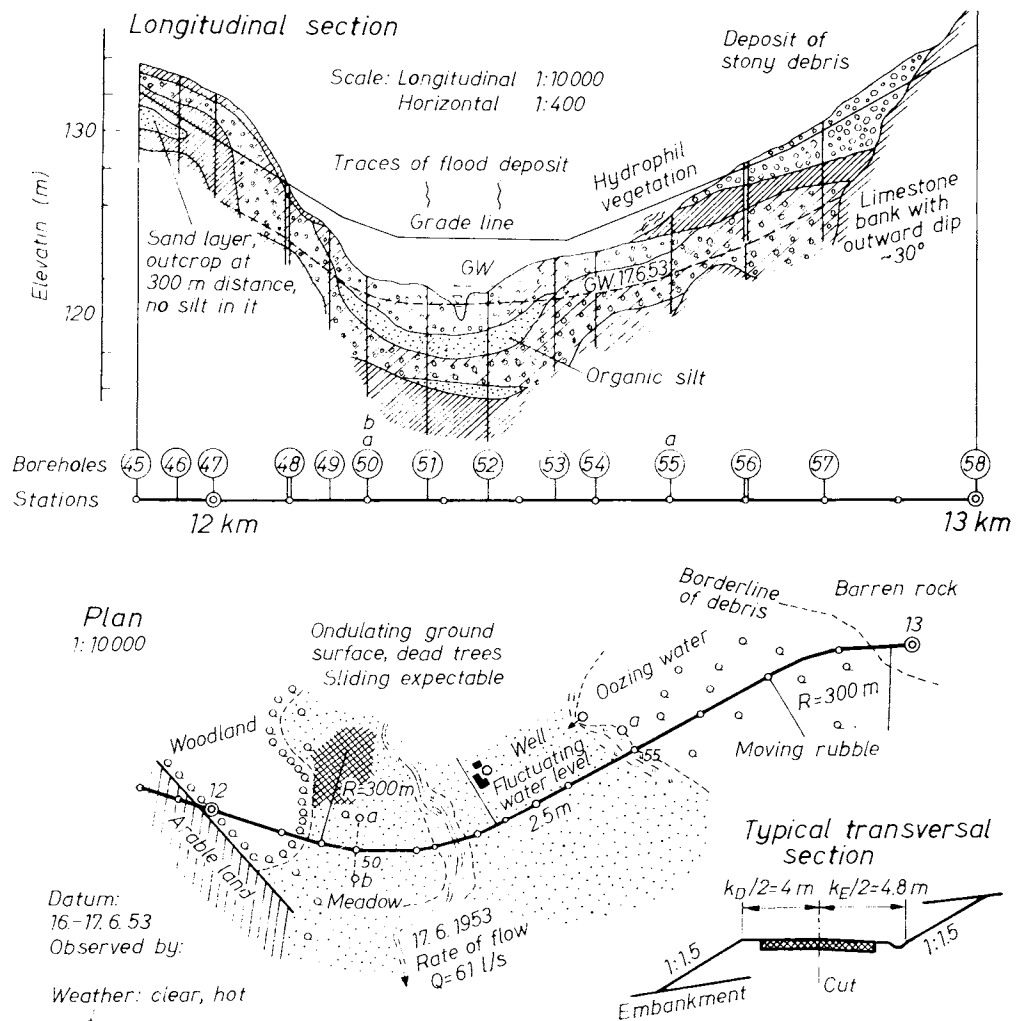


Fig. 329. Demonstrative example for the arrangement of site investigation plans

the area should be studied, together with the results of earlier soil explorations along the first tentative trace indicated on a 1 : 25 000 scale map. The approximate pattern of boreholes should emerge from these studies. In the field, a general inspection trip should first be made. The general topography of the terrain will already convey indications as to whether the soil conditions are highly variable or not. In the light of observations made during the inspection trip, the exploration pattern should be revised and the boreholes definitely located. The exploration itself is performed by the excavation of pits or by sinking boreholes, as a rule using an auger.

Detailed records of the exploration work must be kept, indicating also the land uses in the area (crops, forest, meadow, etc.).

The exploration records should be compiled into a soil profile in the field. Following the practice evolved in the Soviet Union, this should preferably indicate, besides the road profile, the general layout of the trace as well, and it should be accompanied by a compilation of all the data observed in the course of exploration. The quality of surface soils, the outcropping layers, the type of vegetation, the land uses, occasional springs, gorges, the results of geological observations, etc., may also be entered into the layout sketch, along with the technical particulars, such as slopes, standard cross-sections, etc., of the track contemplated. Following such a procedure, this sheet may become virtually a reconnaissance report and may be found highly valuable in determining the laboratory tests needed, in composing the soil mechanical report and in planning. An example of such a reconnaissance report sheet is shown in Fig. 329.

4.3 Structural analysis of pavements

4.3.1 Principles. Structural classification of pavements

Analyses into the load-bearing capacity of pavements differ appreciably from those related to the foundation of buildings. In the latter case, rather large foundations carrying mainly static loads are placed directly on the subsoil, the load is transmitted below the terrain surface along a plane at greater depth and even large foundations display only a slight flexibility. Road pavements, on the other hand, are thin crusts on the surface of the soil, loaded by the vertical and horizontal forces transmitted by the vehicles and interacting with the subsoil in the course of deformations. Their behaviour depends on the relative abilities of the subsoil and the pavement to withstand deformation. This last-mentioned property is used as the criterion for classifying the different types of pavement.

Consider for the time being a pavement of infinite extension (Fig. 330) subject to the concentrated wheel load P . Greater loads are accompanied

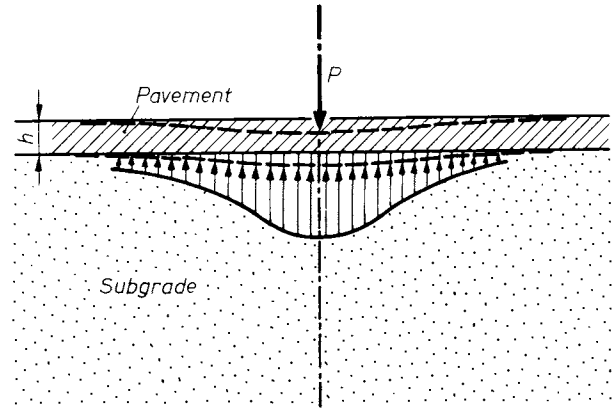


Fig. 330. Deformation of a flexible elastically supported slab of infinite dimensions

by greater deflection of the pavement, as a consequence of which the foundation soil is compressed, evoking a soil reaction which prevents the deflection from increasing further. The ultimate load, i.e. failure, is conceivable in two different ways.

(a) The deflection of the pavement attains a critical value, and the resulting stress in the material of the lower tensioned zone exceeds the tensile strength thereof.

(b) The great deflections cause the foundation to fail, although the pavement itself could still withstand the deflections.

The two factors governing the load-bearing capacity are thus the tensile strength of the pavement material and the ability of the subsoil to deform under vertical loads. The type of pavement depends hereafter on which of the two factors is of critical influence on strength. In case (a), the pavement is termed rigid, and in case (b) flexible. The first group includes the pavements of concrete and similar materials while the second includes macadam, the diverse black pavements, etc. In addition to these two groups consideration must also be given to the case where the surface consists of earth or gravel and where the wheels may cut into the pavement, giving rise to wheel tracks.

The pavements, however, usually consist of several courses each having a specific function. The problem in structural analysis is to determine the thickness and occasionally the strength required for the individual courses. A number of dimensioning methods has been developed for this purpose. The principles underlying these are manifold and involve a wide variety of factors. In the course of evolution the number of factors included has increased gradually and the constants representing the material properties of the subsoil and the pavement have been perfected as observational data and experience became available. The reliability of a particular method depends on the measurement

and empirical data on which it is based and on whether the basic assumption is verified by experimental evidence. No method must be applied without sound judgement and the method suited to a particular case should be selected only after careful consideration.

The behaviour and service life of road pavement structure depend on the following factors.

1. The type and density of traffic and the changes thereof during the service life of the road.
2. The design and the properties of the materials used in the pavement.
3. The physical properties of the subsoil, the scatter of numerical values in space and their variations in time, groundwater conditions.
4. Atmospheric influence, the climate and the environment of the road.

In the pavement structure stresses and deformations are generated by

- (a) static and dynamic loads;
- (b) the movements inherent to the pavement;
- (c) the movements and deformations of the subsoil.

The stresses and deformations must not exceed a certain limit. It will thus be perceived that here again two main problems need to be solved, namely the pavement must be designed to resist failure and harmful deformation with an ample margin of safety.

The problems of dimensioning will be treated subsequently, adopting an approach differing from that followed in the earlier Hungarian editions of the present book. Rather than classifying the methods into groups, the aforementioned four factors will first be analysed, followed by an examination of the stresses and deformations.

In reviewing the historical development of pavement design methods, some interesting features can be detected. We are virtually witnesses of the evolution of a branch of science which, starting from purely empirical foundations, has become increasingly rational. The conventional pavement 60 to 70 years ago was the waterbound macadam, for which a rock base was placed first by hand, using crushed stone for the surface course. At that time no dimensioning was attempted, the thickness of the pavement was controlled by traditions and the level of technology (Fig. 331). Higher traffic loads have subsequently demonstrated that deformations of the subsoil affect both the load-bearing capacity and the durability of the pavement greatly. In order to allow for the deformations, empirical methods have been developed, of which the CBR method is unquestionably most advanced (cf. Section 4.5.2). Investigations have simultaneously been started with the objective of determining the stresses generated in rigid pavements made of concrete numerically. The basic principles of var-

ious dimensioning methods were already available in the nineteen-thirties and as far as the essential features are concerned, the methods developed then are still in general use, although revolutionary changes have occurred meanwhile in road-building materials. In response to the more exacting requirements, pavement systems consisting of several courses have been devised in which the deformation of the subsoil is not the exclusive factor, the subsoil being only an element of the pavement structure.

Once the importance of deformations was recognized, research was started to develop analytical methods for determining the stresses induced in the pavement and in the subsoil. Formulae have been developed for two-layer and multi-layer systems, while the advent of computers has made the development of detailed tables possible. The results of these efforts are, however, of limited practical interest only, since the basic criteria underlying the computations, the Young's moduli of elasticity, the Poisson numbers, the fatigue behaviour, etc., of the diverse materials are not known with the accuracy needed. As a consequence thereof, the role of experience is still very important in the design of pavements.

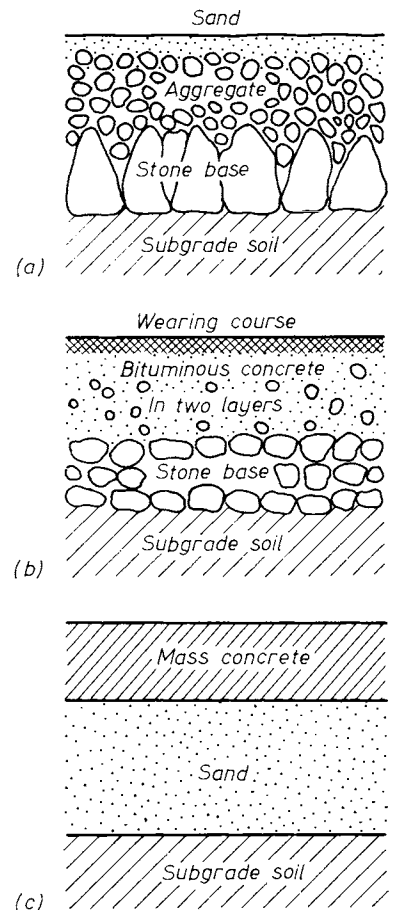


Fig. 331. Pavement types: a — macadam; b — surface treatment; c — concrete slab on granular subbase

4.3.2 Traffic data

Before any structural analysis of a pavement is attempted, information must be acquired on the following traffic data:

- (a) wheel load;
- (b) the arrangement of axles and wheels;
- (c) tyre pressure;
- (d) the frequency of load repetition;
- (e) vehicle speed;
- (f) the pattern of traffic over the width of the road.

The highest permissible wheel loads are specified in the regulations of the various countries. In Hungary the data given in Table 22 apply.

Mention should be made here of the recommendations of the U. N. Economic Commission concerning the heaviest vehicles participating in road traffic (Table 23). Other specifications apply to airport runways; an example from the U.S. is given in Table 24.

Owing to the multitude of wheel and axle arrangements, it is difficult to select the critical one.

Table 22. Permissible load for various vehicles — Hungarian Standard

Two axles	Load per axle Max. total load	80 kN 160 kN
Three axles	Load per double axle Max. total load	145 kN 200 kN

Table 23. Maximum allowable load on vehicles as proposed by the U. N. Economic Commission

	For the first stage construction (kN)	For future performance (kN)
Maximally loaded axle	100	130
Vehicles on two axles	150	190
Vehicles on three axles	200	260
Vehicles on four or more axles	220	260
Semi-trailer	200	350
Truck-train	320	400

Table 24. Design parameters for airports (Civil Aeronautics Administration, Technical Standard order, N6b, 1958)

Classification	Runway		Runway for sight landing	Equivalent wheel load (kN)
	Length (m)	Width (m)	Length (m)	
Local connections	1300	30	120	136
Regional connections	1800	45	150	272
Continental connections	2300	45	150	340
Intercontinental connections	3200	45	150	454

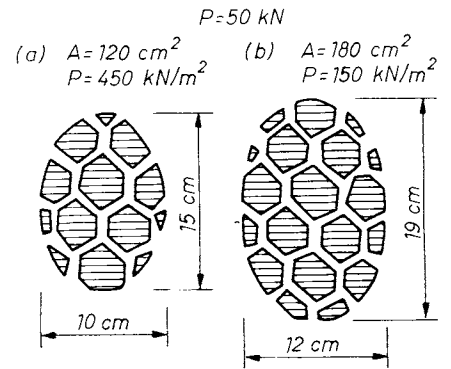


Fig. 332. Contact area below a tyre on the road surface

For this reason the concept of the Equivalent Single Wheel Load (ESWL) has been introduced in the U.S. This is understood as the load acting on a single wheel which gives rise to the same deflection as the entire wheel system considered.

Vehicle loads are transmitted to the pavement through the contact area of the wheel. The contact surface of pneumatic tyres in new condition, at the correct operating pressure and highest allowable load specified by the manufacturer, is an ellipse with 1 : 1.5 axis ratio. In this case the contact surface equals the ratio of the load to the tyre pressure. According to the measurements by TELLER (1954), the actual surface may range from 0.99 to 1.15 times this value. Worn or overloaded tyres produce greater contact areas than new or normally loaded ones. Some experimental results on rigid pavements are given in Table 25.

The results of tests performed with normal automobile tyres of 6.0'' (15 cm) width and 22'' (56 cm) diameter on a smooth soil-cement pavement are shown in Fig. 332. The wheel mass was 500 kg. At higher tyre pressures the print was a regular ellipse with 1 : 1.5 axis ratio. At lower tyre pressures the

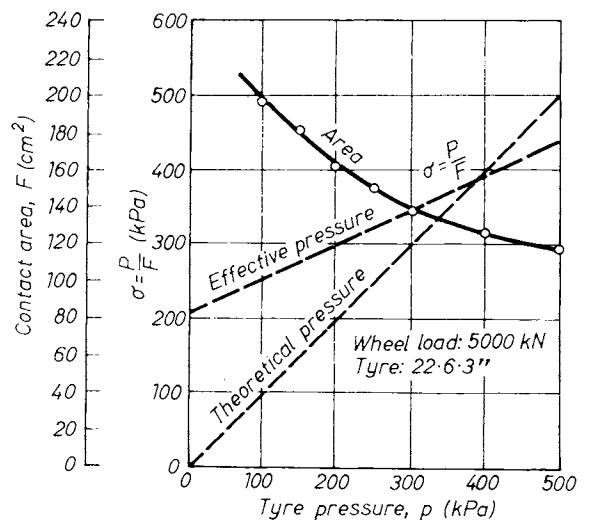


Fig. 333. Relationship between tyre pressure and contact area

Table 25. Characteristics for pneumatic tyres

Identification	Wheel road (kN)	Tyre pressure (kN/m ²)	Case 1: worn tyre				
			P_m (kN/m ²)	max p (kN/m ²)	Contact area (cm ²)	Half-diameters of the ellipse	
						a (cm)	b (cm)
7-24 AS	30	84	140	140	214	11.6	5.9
9-24 AS	50	84	140	140	357	14.9	7.6
11-28 AS	75	84	140	140	536	18.3	9.3
13-30 AS	100	84	140	140	714	21.1	10.8
170-20 AW	75	300	330	330	227	11.9	6.1
10-20 AW	150	400	440	440	341	14.6	7.4

Identification	Wheel road (kN)	Tyre pressure (kN/m ²)	Case 2: overloaded tyre				
			P_m (kN/m ²)	max p (kN/m ²)	Contact area (cm ²)	Half-diameters of the ellipse	
						a (cm)	b (cm)
7-24 AS	30	84	75	113	400	15.8	8.1
9-24 AS	50	84	75	113	667	20.4	10.4
11-28 AS	75	84	75	113	1000	25.0	12.7
13-30 AS	100	84	75	113	1333	28.8	14.7
170-20 AW	75	300	160	240	469	17.1	8.7
10-20 AW	150	400	230	345	653	20.2	10.3

Identification	Wheel road (kN)	Tyre pressure (kN/m ²)	Case 3: new tyre				
			P_m (kN/m ²)	max p (kN/m ²)	F' (cm ²)	a (cm)	b (cm)
9-24 AS	50	84	65	130	769	21.9	11.2
11-28 AS	75	84	65	130	1155	26.3	13.7
13-30 AS	100	84	65	130	1539	31.0	15.8
170-20 AW	75	300	135	270	556	18.6	9.5
10-20 AW	150	400	190	380	789	22.2	11.3

ellipse was elongated, with a section bounded by straight lines at the middle. The area was determined under different axle loads and plotted against the pressure (Fig. 333). From the diagram it will readily be seen that the pressure transmitted to the pavement is not identical with the tyre pressure. Computing and plotting the average contact pressure, an almost linear relationship has been obtained.

MONISMITH (1965) has suggested that this relationship probably follows the diagram in Fig. 334. The distribution of wheel load over the contact surface was studied by TELLER and BUCHANAN (1937). Under balloon tires the distribution was virtually uniform (Fig. 335) and can thus be adopted as the basis of computation. Under metal cart-wheels and solid-rubber tyres (b, c) the differences are greater.

The first loads were usually observed to cause no damage to the pavements, the damage being the result of repeated loadings only. Under repeated loads, the pavement may fail either by fatigue, or by the gradually increasing settlement of the sub-

soil. This observation has led to the more recent conclusion that in dimensioning pavements, allowance must be made not only for the heaviest

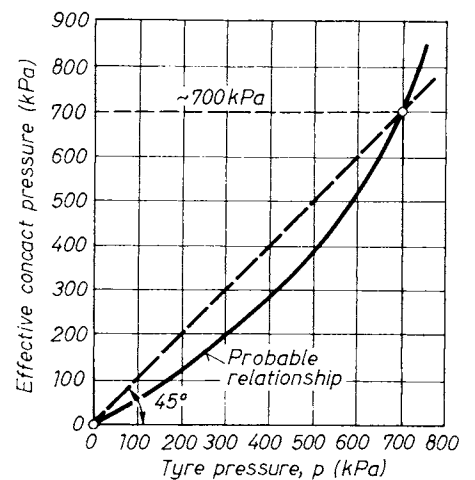


Fig. 334. Relationship between tyre pressure and contact pressure, after MONISMITH (1965)

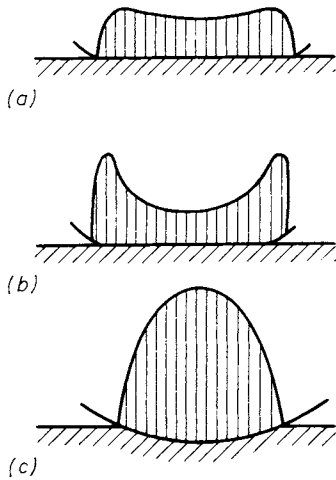


Fig. 335. Contact pressure distribution on the pavement surface:
 a — pneumatic tyre; b — full rubber wheel; c — steel rim

wheel load, but also for the density and volume of traffic, by increasing the design wheel load for roads carrying large traffic volumes. The increment wheel load will be controlled by the number of load repetitions, their distribution on the road surface, as well as wheels carrying different loads.

Efforts to take repeated loads into account have resulted in the introduction of the equivalent wheel load. For example, in California the expression

$$P_{eq} = \frac{P^5 n}{3125} \quad (448)$$

is commonly used. The traffic index is also applied widely according to the formula

$$T_i = 1.3 \left(\frac{P}{227} \right)^{0.5} n^{0.12} \quad (449)$$

Here P is the wheel load in Mp (= 10 kN) units, while n is the number of repetitions anticipated. In some empirical dimensioning methods the necessary pavement thickness is determined on the basis of the T_i value. According to SHERMAN, the equivalent wheel load is related to the magnitude of T_i by the expression

$$T_i = 1.35 (P_{eq})^{0.11} \quad (450)$$

The influence of vehicle speed is reflected primarily in the magnitude of the deflections produced. At higher speeds the deflections will be smaller, but this must not be understood to mean that the stresses will also become lower. This effect is, in general, taken into account by introducing a higher modulus of elasticity into the computation. Thus, e.g. for an asphaltic concrete pavement the values obtained for E were 8.0 and 60.0 kN/cm² under static and rapid, transient loads, respectively. These limits are especially wide in bituminous pavements.

Attention has recently been concentrated on the distribution of traffic on the pavement surface. This is illustrated visually by the runways at airports, where each landing leaves black marks on the concrete slab. These have been used for constructing distribution curves. It was concluded, however, that for arriving at a safe design, the possibility of the full load acting on each 0.1 m² area of the surface cannot be excluded.

4.3.3 Stresses produced by traffic loads in the pavement and in the subsoil

4.3.3.1 Introductory remarks

Stress computations can be based on a variety of assumptions, e.g. by considering the pavement to be elastically bedded on the subgrade (Fig. 336) the compressibility of which is characterized by a single numerical value, namely the bedding coefficient. In other methods the subsoil and the diverse courses of the pavement, as well as the base, are treated as a multi-layer system, the individual layers of which have different moduli of elasticity, but suffer the same deformation. These methods will be dealt with separately.

4.3.3.2 Stresses in pavements on an elastic subgrade

The investigation is based on the plate theory of classical mechanics, in which plates are understood to be load-bearing structures, where the surface in undeformed state, halving the thickness at all points, is plane; the thickness is negligible relative to the other dimensions and no component of the load acts parallel to the middle surface mentioned before. An element of a plate thus defined is shown — in cartesian coordinates — in Fig. 337. The stresses σ_x , τ_{xy} , σ_y and τ_{yx} acting on the side surfaces of the area hdx and hdy may be combined with the bending moments related to unit length

$$M_x = - \int_{-h/2}^{+h/2} \sigma_x z dz; \quad M_y = \int_{-h/2}^{+h/2} \sigma_y z dz. \quad (451)$$

$$M_{xy} = M_{yx} = - \int_{-h/2}^{+h/2} \tau_{xy} z dz.$$

The vertical shear stresses may similarly be combined into shear forces:

$$Q_x = - \int_{-h/2}^{+h/2} \tau_{xz} dz; \quad Q_y = - \int_{-h/2}^{+h/2} \tau_{yz} dz. \quad (452)$$

The forces and bending moments written above are required to meet the conditions of equilibrium. Thus for the projection of the vertical forces

$$\frac{\partial Q_x}{\partial x} + \frac{\partial Q_y}{\partial y} + p = 0.$$

Here p = the uniformly distributed load acting on the elementary surface, $dx \cdot dy$ of the plate. For the moments in the x - z plane

$$\frac{\partial M_x}{\partial x} + \frac{\partial M_{xy}}{\partial y} - Q_x = 0.$$

while for the moments in the y - z plane

$$\frac{\partial M_y}{\partial y} + \frac{\partial M_{xy}}{\partial x} - Q_y = 0.$$

Expressing Q_x and Q_y from the two moment equations and introducing the resulting expressions into the first, we have

$$\frac{\partial^2 M_x}{\partial x^2} + 2 \frac{\partial^2 M_{xy}}{\partial x \partial y} + \frac{\partial^2 M_y}{\partial y^2} = -p. \quad (453)$$

For determining the three bending moments and the two shear forces, the equilibrium conditions (3 equations) are inadequate and the deformations must also be introduced. Just as in the bending theory of beams, simplifying assumptions are inevitable. Thus the following assumptions are made:

1. The compression of the plate in the direction of the z axis is small enough to be neglected.

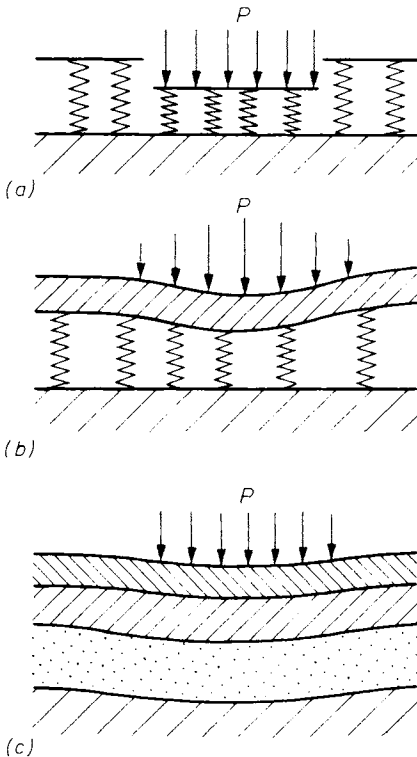


Fig. 336. Models for the mathematical treatment of the system composed of the pavement structure and the subsoil:

a — elastically supported plate within own-strength; b — as before, but having own-strength; c — multi-layered elastic system with substantial friction at the interfaces

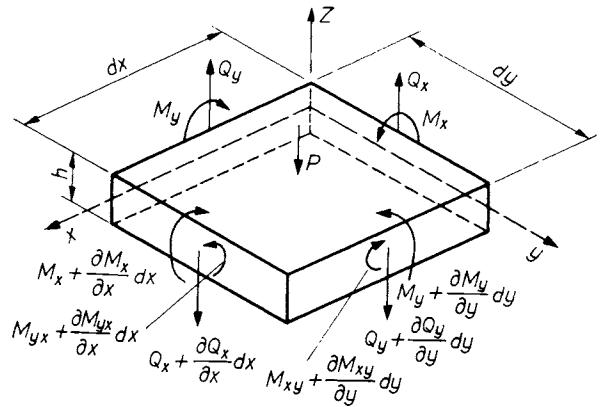


Fig. 337. Forces acting on the elements of a plate

2. The perpendiculars to the middle surface of the plate remain straight after deformation and normal to the deformed middle surface.

3. The normal stress in the direction of the plate thickness is negligible.

With these assumptions, the deformations according to Fig. 338 become

$$u = -z \frac{\partial w}{\partial x}; \quad v = -z \frac{\partial w}{\partial y}$$

and the unit strains are

$$\epsilon_x = \frac{\partial u}{\partial x} = -z \frac{\partial^2 w}{\partial x^2}; \quad \epsilon_y = \frac{\partial v}{\partial y} = -z \frac{\partial^2 w}{\partial y^2},$$

$$\gamma_{xy} = \frac{\partial u}{\partial y} + \frac{\partial v}{\partial x} = -2z \frac{\partial^2 w}{\partial x \partial y}.$$

Introducing Hooke's law

$$\left. \begin{aligned} \sigma_x &= -\frac{Ez}{1-\mu^2} \left(\frac{\partial^2 w}{\partial x^2} + \mu \frac{\partial^2 w}{\partial y^2} \right), \\ \sigma_y &= -\frac{Ez}{1-\mu^2} \left(\frac{\partial^2 w}{\partial y^2} + \mu \frac{\partial^2 w}{\partial x^2} \right), \\ \tau_{xy} &= -\frac{Ez}{1+\mu} \frac{\partial^2 w}{\partial x \partial y}. \end{aligned} \right\} \quad (454)$$

If the stresses expressed by Eqs (454) are introduced into Eqs (451), integration with respect to

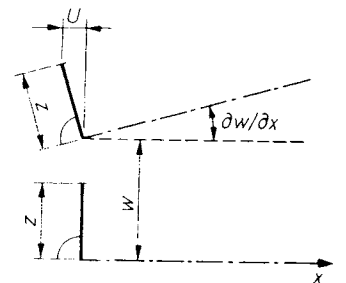


Fig. 338. Calculation of deformations

z becomes possible:

$$\left. \begin{aligned} M_x &= -K \left(\frac{\partial^2 w}{\partial x^2} + \mu \frac{\partial^2 w}{\partial y^2} \right), \\ M_y &= -K \left(\frac{\partial^2 w}{\partial y^2} + \mu \frac{\partial^2 w}{\partial x^2} \right), \\ M_{xy} &= -K (1 - \mu) \frac{\partial^2 w}{\partial x \partial y} \end{aligned} \right\} \quad (455)$$

The expression $K = E h^3 / 12 (1 - \mu^2)$ is called the stiffness number of the plate and is the two-dimensional counterpart of the quantity EI involved in the bending theory of beams.

Combining the moments in Eqs (455) with Eq (453), the fundamental differential equation of plate theory is obtained:

$$\nabla \nabla w = \frac{\partial^4 w}{\partial x^4} + 2 \frac{\partial^4 w}{\partial x^2 \partial y^2} + \frac{\partial^4 w}{\partial y^4} = \frac{P}{K} \quad (456)$$

In the case of circular plates, or such plates of infinite extension, the use of polar coordinates is found more expedient. For an axial symmetrical load, the differential equation takes the form

$$\nabla \nabla w = \frac{P}{K}, \quad (457)$$

where

$$\nabla \nabla = \left(\frac{d^2}{dr^2} + \frac{1}{r} \frac{d}{dr} \right)^2.$$

Changing from the general theory of plates to that applying to plates on an elastic, continuous support, an additional assumption must be introduced. As in the theory of continuously supported beams, WINKLER'S assumption is again resorted to, considering the soil reaction on the base of the plate to be proportionate at any point to the deflection at the same point. Thus

$$p = Cw, \quad (458)$$

where C is called the modulus of subgrade reaction. This assumption is rigorously valid in the case of

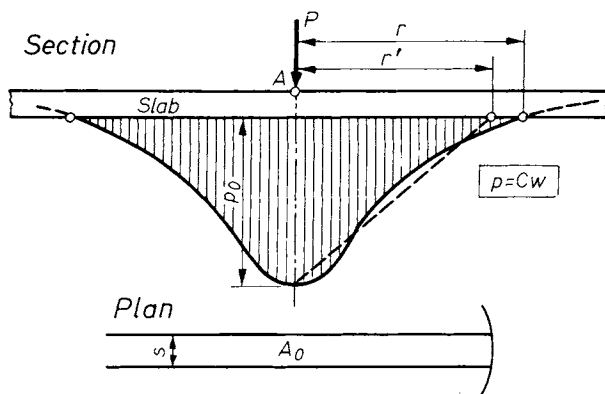


Fig. 339. Stress distribution in the underground below a plate loaded with a singular force

plates supported by a fluid, e.g. ice floes floating on water. In the case of plates resting on soil, the approximation is rather a crude one and some critical remarks will be devoted thereto below.

By introducing the hypothesis expressed by Eq. (458) into Eq. (457), the obstacle to integration is removed. The solution is obtained in terms of the Bessel function involving, for the case of an infinite plate loaded by a concentrated force, the following boundary conditions: the stress is zero at infinity and assumes a finite value under the load, the force P is balanced by the sum of vertical stresses. The corresponding solution given by SCHLEICHER (1926) is

$$w = \frac{P}{4Cl^2} Z_3 \left(\frac{r}{l} \right), \quad (459)$$

where C is the modulus of subgrade reaction,

$$l = \sqrt[4]{\frac{K}{C}} = \sqrt[4]{\frac{Eh^3}{12 C(1 - \mu^2)}} \quad (460)$$

is the representative length (radius of relative plate stiffness) and the term $Z_3 \left(\frac{r}{l} \right)$ is the real part

of the value pertaining to the argument $\left(\frac{r}{l} \sqrt{i} \right)$ of the zero-order, cylindrical Hankel function. Under load $Z_3 = l/2$ and the greatest deflection is

$$w_{\max} = \frac{P}{8 C l^2}.$$

with the peak subgrade stress

$$P_{\max} = Cw_{\max} = \frac{P}{8 l^2}. \quad (461)$$

The stress distribution is depicted in Fig. 339. The reaction p becomes zero at the distance $R = 3.92 l$ from the load.

Replacing the part of the stress distribution diagram extending to this distance by a triangle of identical area, the stress in the plate can be estimated approximately. Considering a strip of width s the resulting moment becomes

$$M = \frac{1}{2} p_0 R' s \frac{1}{3} R' = 0.213 P s,$$

whence the stress induced in the plate having a section modulus $\frac{1}{6} s h^2$ is

$$\sigma = 1.28 \frac{P}{h^2}. \quad (462)$$

The introduction of multiple approximations and simplifying assumptions has led to the elimination of both plate and subgrade stiffnesses from the formula of stresses acting in the plate. For this reason both Eq. (462) and the formally similar

expressions modified on practical, empirical bases yield only crudely approximative results. For more detailed computations the formulae of WESTERGAARD (1947) are considered applicable, because of the smaller number of factors neglected in them, although the difficulties related to the subgrade modulus exist here as well.

The critical situation in a plate of finite extension arises if one of the corners is loaded (Fig. 340). In the simplest method of analysis, the plate is assumed to be perfectly rigid and unsupported in the region around the corner. If the length of the cantilevered part is x , a bending moment $M = Px$ is produced and since the section modulus of the cross-section subjected to bending is $K = \frac{1}{6} 2xh^2$, the resulting flexural stress is

$$\sigma = \frac{M}{K} = 3 \frac{P}{h^2}. \quad (463)$$

The expression is formally identical to the foregoing, the difference between the factors of the term P/h^2 involved in the aforementioned semi-empirical stress formulae ranging, in fact, from 1.28 to 3.0.

Starting from the theoretical considerations expounded before, WESTERGAARD (1947) has developed a method of slab dimensioning, in which the pavement thickness required is determined on the basis of the stresses occurring in rigid plates.

The assumption underlying the theory are as follows:

1. The pavement is elastic, the material having a constant Young's modulus of elasticity E and Poisson's number μ .
2. The pavement is of uniform thickness.

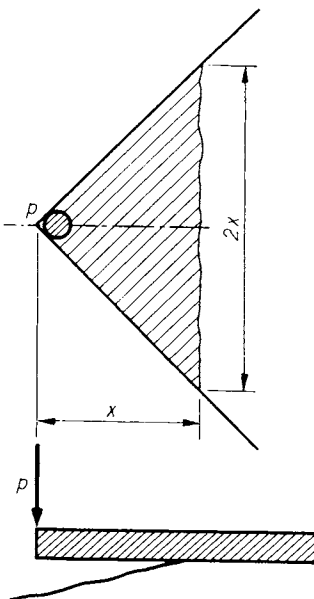


Fig. 340. Load at the corner of a slab.

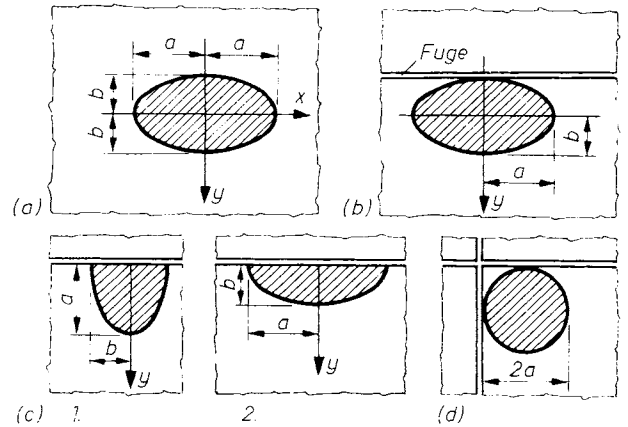


Fig. 341. Load patterns

3. Winkler's assumption, commonly used in the theory of beams supported on an elastic subgrade, applies, i.e. the reactions are directly proportionate to the deflections as expressed by Eq. (458), $p = Cz$.

The loading surface is further assumed to be wider and longer than the thickness of the pavement, implying the validity of the plate-bending theory.

Corresponding to the case of large aircraft, the tyre contact area is assumed to be elliptical in shape, and the load is distributed uniformly over it. The formulae of stresses in the pavement and of the deflections corresponding thereto apply to the loading conditions shown in Fig. 341. Allowance is further made for the ability of certain types of joint to transfer loads. In accordance with the theory of plates on an elastic subgrade (cf. Eq. (460)) the radius of relative plate stiffness is introduced as

$$l^4 = \frac{Eh^3}{12 C(1 - \mu^2)}.$$

A compilation of the formulae for the most important load patterns is presented below.

(A) Load acting remote from any corner or edge

The load acting on the slab is distributed uniformly over the elliptic area described by the equation

$$\frac{x^2}{a^2} + \frac{y^2}{b^2} = 1. \quad (464)$$

The principal tensile stresses σ_x and σ_y in the bottom fibre of the slab under the center of the tyre contact area are:

$$\left. \begin{aligned} \sigma_x \\ \sigma_y \end{aligned} \right\} = \frac{3p}{8\pi h^2} \left[(1 + \mu) \ln \frac{Eh^3}{C \left(\frac{a+b}{2} \right)^4} \mp \mp 2(1 - \mu) \frac{a - b}{a + b} \right]. \quad (465)$$

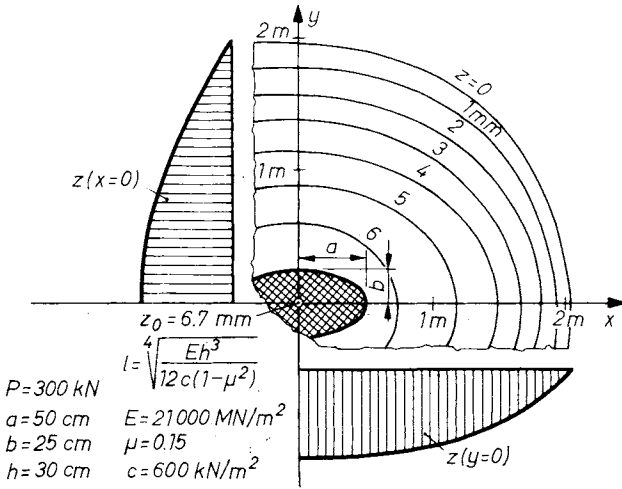


Fig. 342. Contour lines on the deformed surface of a loaded slab

The deflection at any point within, or outside of, the contact area is:

$$z = \frac{P}{8cl^2} \left[1 - \frac{a^2 + b^2 + 4x^2 + 4y^2}{16\pi l^2} \ln \frac{Eh^3}{C \left(\frac{a+b}{2} \right)^4} - \frac{a^2 + 4ab + b^2}{16\pi l^2} + \frac{(a-b)(x^2 - y^2)}{2\pi l^2(a+b)} \right] \quad (466)$$

In order to visualize the deformation of an infinitely large slab, the contour lines of the deformed surface for an actual case are shown in Fig. 342.

(B) Load at the edge of the pavement, or in the vicinity of a joint

The load is next to an edge, or to a joint. The full load is distributed uniformly over an elliptical area, the equation of which is

$$\frac{x^2}{a^2} + \frac{(y-b)^2}{b^2} = 1 \quad (467)$$

The tensile stress in the bottom fibre of the pavement along the edge, at the tangential point of the ellipse, is

$$\sigma_r = \frac{3(1+\mu)P}{\pi(3+\mu)h^2} \left[\ln \frac{Eh^3}{100C \left(\frac{a+b}{2} \right)^4} + 1.84 - \frac{4}{3}\mu + (1+\mu) \frac{a-b}{a+b} + 2(1-\mu) \frac{ab}{(a+b)^2} + 1.18(1+2\mu) \frac{b}{l} \right] \quad (468)$$

The deflection at any point on the axis of symmetry perpendicular to the edge, at a small distance y from, or on the edge itself, is found from the approximate formula

$$z = \frac{P\sqrt{2+1.2\mu}}{\sqrt{Eh^3C}} \left[1 - (0.76 + 0.4\mu) \frac{b}{l} \right] \cdot \left[1 - (0.76 + 0.4\mu) \frac{y}{l} \right] \quad (469)$$

(C) The axis of the contact ellipse is over the edge

P is one-half of the wheel load.

The stress in the bottom fibre under the center of the ellipse is

$$\sigma_e = \frac{3(1+\mu)P}{\pi(3+\mu)h^2} \ln \frac{Eh^3}{100C \left(\frac{a+b}{2} \right)^4} + \frac{3(1+\mu)P}{\pi(3+\mu)h^2} \left[3.84 - \frac{4}{3}\mu - (1-\mu) \frac{a-b}{a+b} + 0.5(1+\mu) \frac{b}{l} \right] \quad (470)$$

The deflection under the center of the ellipse is approximately

$$z = \frac{P\sqrt{2+1.2\mu}}{\sqrt{Eh^3C}} \left[1 - (0.323 + 0.17\mu) \frac{b}{l} \right] \cdot \left[1 - (0.76 + 0.4\mu) \frac{y}{l} \right] \quad (471)$$

For circular tyre contact areas — a case approximated rather by road vehicles — over which the load is uniformly distributed, the stresses due to loads in the interior, on the edge and on the corner of a concrete slab are found from the following formulae.

(a) Load in the interior of the slab, the greatest tensile stress on the bottom face of the slab:

$$\sigma_b = \frac{0.275P}{h^2} (1+\mu) \log \frac{Eh^3}{Cb^4} \quad (472)$$

(b) Load on the edge of the slab, the stress on the bottom face of the slab:

$$\sigma_1 = \frac{0.529P}{h^2} (1+0.54\mu) \left(\log \frac{Eh^3}{Cb^4} - 0.71 \right) \quad (473)$$

(c) Load on the corner of the slab (case D, Fig. 341), the greatest tensile stress in the top plane:

$$\sigma_s = \frac{3P}{h^2} \left\{ 1 - \left[\frac{12(1-\mu)^2C}{Eh^3} \right]^{0.15} (a\sqrt{2})^{0.6} \right\} \quad (474)$$

In the above expressions

$$\begin{aligned} a &= \text{radius of the contact area (circle),} \\ b &= \sqrt{1.6a^2 + h^2} - 0.675 h, \text{ for } a < 1.724 h, \\ b &= a, \text{ for } a > 1.724 h. \end{aligned}$$

TELLER and SUTHERLAND (1943) have arrived at the conclusion that under edge and corner loads, the actual stress in the pavement is greater than that computed from Eqs (473) and (474). For this reason, they have suggested the following formulae, which incorporate empirical modifications:

$$\sigma_r = \frac{0.529 P}{h^2} (1 + 0.54 \mu) \left[\log \frac{Eh^3}{Cb^4} + \log \frac{b}{1 - \mu^2} - 1.079 \right] \quad (475)$$

$$\sigma_e = \frac{3P}{h^2} \left\{ 1 - \left[\frac{12(1 - \mu^2)C}{Eh^3} \right]^{0.3} (a\sqrt{2})^{1.2} \right\}. \quad (476)$$

The stresses due to loads in the interior of the slab surface are, in contrast to the foregoing, smaller than those computed with Westergaard's theory. Starting from the consideration that the subgrade reaction is more concentrated under the load than the deflections (implying that the magnitude of the subgrade reaction decreases with distance from the load center), it was WESTERGAARD himself who suggested modifications. The modified formula is

$$\sigma = \frac{0.275 P}{h^2} (1 + \mu) \left[\log \left(\frac{Eh^3}{Cb^4} \right) - \left(\frac{l}{L} \right)^2 Z \right]. \quad (477)$$

Here L is the radius of the range in which the reactions are rearranged, related to the centerline of the tyre contact area ($L \sim 5l$) and Z is the reduction coefficient ($Z \sim 0.2$).

Starting from the same theoretical foundations, a number of other semi-empirical stress formulae have been suggested. For instance, for a wheel load next to a joint, the stress in the bottom fibre of a concrete slab is, according to the formula of the Portland Cement Association,

$$\sigma = \frac{CP}{h^2} \left[1 - \frac{\sqrt{a/l}}{0.925 + 0.22a/l} \right]. \quad (478)$$

In the absence of load transfer, the coefficient C is 4.2, whereas in cases where the joint is capable of transferring load $C = 3.36$.

A method will be demonstrated subsequently for estimating stresses if load is transferred by the joints between adjacent slabs. Joints of this type are applied mainly in airport runways, examples for such joint designs being shown in Fig. 343. The efficiency of load transfer will be taken into consideration by the coefficient j , with $0 \leq j \leq 1$. For $j = 1$, the deflections of two adjacent slabs are

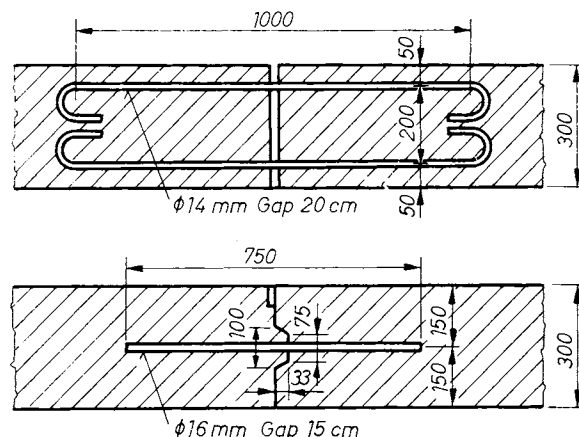


Fig. 343. Devices to promote load transfer at joints

identical along the joint, while for $j = 0$ there is no load transfer and Eqs (465) to (476) apply. The deflections of adjacent slabs should be denoted by z_j and z'_j for the case of load transfer and by z and z' in the absence thereof. The approximate formula

$$z_j - z'_j = (1 - j)z - z' \quad (479)$$

will yield a fair estimate.

The tensile stress in the bottom fibre along the joint is

$$\sigma_j = \left(1 - \frac{1}{2}j \right) \sigma + \frac{1}{2}j\sigma' \quad (480)$$

$$\sigma'_j = \frac{1}{2}j\sigma + \left(1 - \frac{1}{2}j \right) \sigma'. \quad (481)$$

The deflections of the two slabs along the joint are given as

$$z_j = \left(1 - \frac{1}{2}j \right) z + \frac{1}{2}jz', \quad (482)$$

$$z'_j = \frac{1}{2}jz + \left(1 - \frac{1}{2}j \right) z'. \quad (483)$$

Equations (482) and (483) satisfy Eq. (479).

Concerning the dimensioning of rigid pavements the following conclusions may be arrived at from Westergaard's theory.

1. The highest tensile stress in the pavement is directly proportionate to the full load acting.
2. The stresses decrease substantially as the tyre contact area is increased.
3. Edge loads are critical in the majority of practical cases.
4. The stresses depend greatly on pavement thickness.
5. The magnitude of stresses is only moderately influenced by changes in the modulus of subgrade reaction.

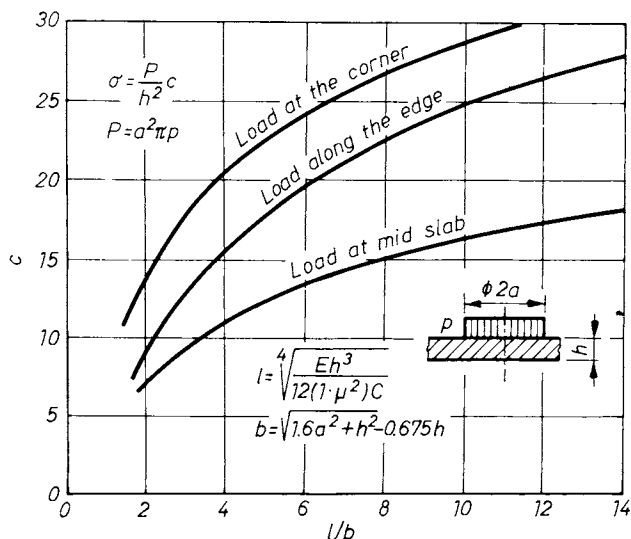


Fig. 344. Diagram to establish the stresses in a slab exposed to circular load

In connection with the theory it should be noted further that the warping stresses due to temperature differentials are neglected, although these may substantially exceed those induced by wheel loads, especially in thick pavements. Neither is any allowance made for the stresses resulting in the subgrade.

A simple diagram is presented in Fig. 344 for estimating the stresses in the pavement under a circular wheel contact area. The influence coefficient c of stresses is obtained therefrom for the three load arrangements indicated, in terms of the ratio l/b . For computing the influence coefficients applying

to the general load pattern, a method was developed by PICKETT and RAY (1951) (cf. YODER, 1959).

Once the stress formulae are available, the problem of pavement dimensioning is greatly simplified. If information is available on the magnitude of the allowable stress in the pavement material, on the elastic constants thereof, as well as on the modulus of subgrade reaction, the thickness of the pavement is readily computed. In the majority of cases, the problem consists of checking the pavement thickness assumed empirically for the resulting stresses.

For direct pavement dimensioning, charts are available indicating the pavement thickness in terms of the wheel load, the tyre inflation pressure, the modulus of subgrade reaction and of the allowable stresses. The charts of major significance have been compiled in Fig. 345 (JELINEK, 1959). These are simple to use, as is demonstrated by the two examples illustrated in Fig. 346.

The modulus of subgrade reaction C is involved in all formulae. This has been defined as the bearing pressure causing unit deflection and it is expressed in kp/cm^3 units. This concept is widely used in the theory of load-bearing structures on an elastic support, although research has provided ample evidence (e.g. TERZAGHI, 1955) indicating that its magnitude must not be regarded as constant, however small the acting load, and besides the load it also depends on the dimensions. According to the theory of elasticity, the deflection under the center of a circular disc loaded by a uniformly distributed force is:

$$y_0 = (1 - \mu^2) \frac{2rq}{E}$$

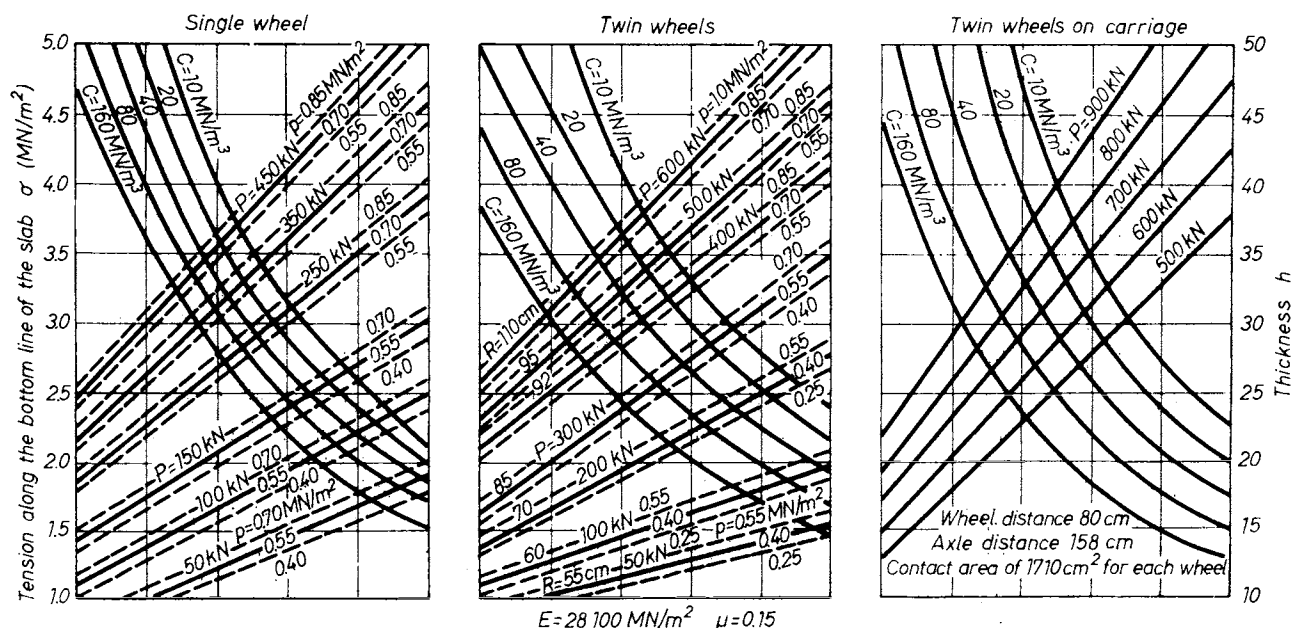


Fig. 345. Design diagrams for concrete slabs (JELINEK, 1959):

$E = 28\,000 \text{ MN/m}^2$; $\mu = 0.15$; C — modulus of subgrade reaction; p — tyre pressure; P — load transmitted by the carriage (half side); R — distance between twin tyres (1 $\text{kp/cm}^2 = 100 \text{ kN/m}^2$; 1 $\text{Mp} = 10 \text{ kN}$; 1 $\text{kp/cm}^3 = 10 \text{ MN/m}^3$)

while the settlement of the rigid plate is

$$y = (1 - \mu^2) \frac{\pi r q}{2 E},$$

whence, remembering that $q = Cy$, and assuming a value $\mu = 1/2$

$$C = \frac{E}{1.5 r}, \text{ or } C = \frac{E}{1.18 r}. \quad (484)$$

The discs used in plate bearing tests may be regarded as rigid rather than flexible.

In the elastic range, the magnitude of the modulus of subgrade reaction will thus be seen to be inversely proportionate to the diameter of the plate. This conclusion is supported by ample experimental evidence. In many cases, however, the elastic range may already be surpassed at deflection as low as 1 mm, which may be offered as an explanation for the fact that beyond a plate diameter of 60 to 80 cm, the modulus of subgrade reaction varies only little with the size of the plate. This is the reason why steel plates of 75 cm diameter are used in field tests. The settlement curve of the loaded plate is observed and plotted against the stress, whereafter the modulus of subgrade reaction C is found from the angle of the secant pertaining to $y = 1.3 \text{ mm} (= 0.05'')$, as shown in Fig. 347.

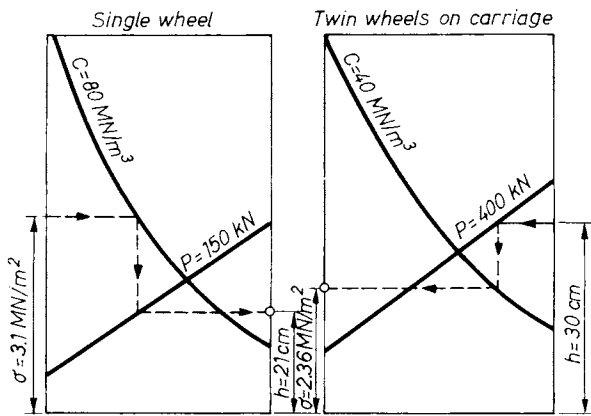


Fig. 346. Scheme to illustrate the use of the diagrams

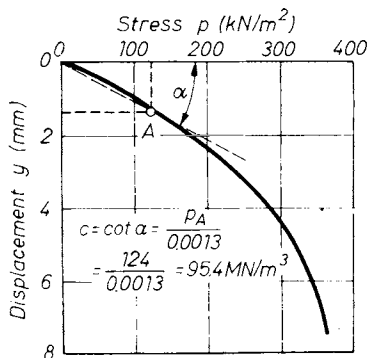


Fig. 347. Determination of the modulus of subgrade reaction

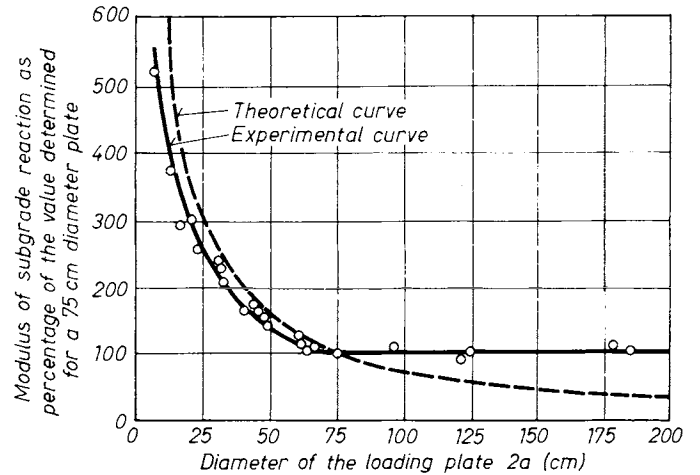


Fig. 348. Modulus of subgrade reaction as a function of the diameter of the plate

The use of plates having a diameter of 75 cm is justified also by Fig. 348, in which the experimental data of several institutions have been compiled. The values of C have been expressed as percentages of the value obtained with 75 cm diameter plates and the theoretical curve has also been entered. For diameters smaller than 75 cm, the departure from the theoretical curve is slight, whereas for larger plates an approximately horizontal straight line is obtained instead of the gradually decreasing theoretical curve. This is because of the development of plastic deformations, which prevent the value of C from decreasing further. The C values determined from field tests with plates smaller than 75 cm diameter should be corrected according to Fig. 348.

4.3.3.3 Stresses and strains in two-layer systems

The three-dimensional problem of stress distribution in a two-layered system (Fig. 349) is accessible to a solution on the basis of the theory of elasticity, if the surface layer — the pavement — and the lower layer of infinite depth — the subgrade — are assumed to be elastic and to have constant moduli of elasticity and Poisson's numbers. Up to certain wheel loads this assumption is likely to hold true, all the more so, since under the rapid transient and frequently repeated loads due to vehicles, the subgrade and the pavement ac-

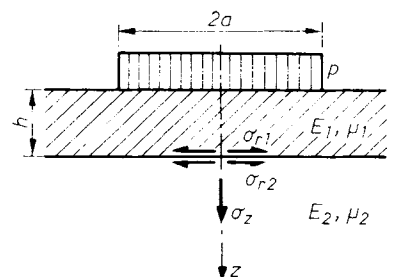


Fig. 349. The two-layer system

Table 26. Influence factors for stresses in the two-layer system—rough interface

h/a	E ₂ /E ₁ = 0.05			E ₂ /E ₁ = 0.1			E ₂ /E ₁ = 0.3		
	σ _z	σ _{r2}	σ _{r1}	σ _z	σ _{r2}	σ _{r1}	σ _z	σ _{r2}	σ _{r1}
1.0	+0.2045	+0.0857	-2.173	+0.2916	+0.105	-1.597	+0.4629	+0.1227	-0.6710
1.111	0.1744	0.0695	-1.924	0.2523	0.0847	-1.424	0.4108	0.0985	-0.6300
1.25	0.1451	0.0544	-1.664	0.2129	0.0667	-1.249	0.3554	0.0764	-0.5743
1.429	0.1170	0.0414	-1.394	0.1741	0.0506	-1.061	0.2976	0.0567	-0.5053
1.667	0.0904	0.0303	-1.117	0.1364	0.0366	-0.862	0.2384	0.0398	-0.4240
2.0	0.0659	0.0206	-0.8424	0.1006	0.0148	-0.657	0.1796	0.0258	-0.3327
2.5	0.0441	0.0128	-0.5809	0.0681	0.0155	-0.458	0.1236	0.0154	-0.2370
3.333	0.0258	0.0071	-0.3481	0.0401	0.0085	-0.276	0.0739	0.0081	-0.1453
5.0	0.0188	0.0031	-0.1623	0.0185	0.0037	-0.130	0.0344	0.0033	-0.0693
10.0	0.0031	0.0008	-0.0418	0.0047	0.0009	-0.030	0.0088	0.0008	-0.0180

h/a	E ₂ /E ₁ = 0.5			E ₂ /E ₁ = 1			E ₂ /E ₁ = 0.0005		
	σ _z	σ _{r2}	σ _{r1}	σ _z	σ _{r2}	σ _{r1}	σ _z	σ _{r2}	σ _{r1}
0.5							+0.0437	+0.0355	-16.40
1.0	+0.5469	+0.1230	-0.3010	-0.646		+0.116	0.0121	0.0092	-5.718
1.111	0.4905	0.1979	-0.2949	0.589		0.097	0.0099	0.0075	-4.834
1.25	0.4298	0.0747	-0.2802	0.524		0.067	0.0079	0.0059	-3.991
1.429	0.3638	0.0642	-0.2554	0.450		0.046	0.0610	0.0045	-3.195
1.667	0.2948	0.0368	-0.2212	0.369		0.028	0.0046	0.0034	-2.456
2.0	0.2240	0.0230	-0.1780	0.284		0.016	0.0032	0.0023	-1.782
2.5	0.1557	0.0129	-0.1298	0.200		0.008	0.0021	0.0015	-1.188
3.333	0.0936	0.0062	-0.0812	0.121		0.003	0.0012	0.0009	-0.6928
5.0	0.0439	0.0024	-0.0392	0.057		0.001	0.0005	0.0003	-0.3164
10.0	0.0112	0.0006	-0.0100	0.015		0.000	0.0001	0.0001	-0.0805

h/a	E ₂ /E ₁ = 0.0025			E ₂ /E ₁ = 0.005			E ₂ /E ₁ = 0.01		
	σ _z	σ _{r2}	σ _{r1}	σ _z	σ _{r2}	σ _{r1}	σ _z	σ _{r2}	σ _{r1}
0.5	+0.1147	+0.0833	-12.45	+0.1696	+0.1184	-10.08	+0.0809	+0.0449	-3.52
1.0	0.0341	0.0222	-4.706	0.0529	0.0323	-4.069	0.0676	0.0365	-3.04
1.111	0.0282	0.0181	-4.010	0.0438	0.0261	-3.493	0.0552	0.0289	-2.57
1.25	0.0227	0.0143	-3.337	0.0355	0.0208	-2.929	0.0436	0.0222	-2.10
1.429	0.0178	0.0110	-2.694	0.0278	0.0158	-2.380	0.0330	0.0163	-1.64
1.667	0.0133	0.0080	-2.087	0.0213	0.0116	-1.850	0.0237	0.0113	-1.22
2.0	0.0094	0.0056	-1.526	0.0150	0.0080	-1.358	0.0156	0.0072	-0.82
2.5	0.0062	0.0036	-1.023	0.0098	0.0054	-0.9133	0.0090	0.0040	-0.49
3.333	0.0035	0.0020	-0.6000	0.0056	0.0028	-0.5343	0.0041	0.0018	-0.23
5.0	0.0016	0.0009	-0.2754	0.0023	0.0011	-0.2459	0.0010	0.0004	-0.06
10.0	0.0004	0.0002	-0.0703	0.0006	0.00002	-0.0627	-	-	-

Table 27. Influence factors for stresses in the two-layer system—frictionless interface

h/a	E ₂ /E ₁ = 0.1		E ₂ /E ₁ = 0.3		E ₂ /E ₁ = 0.5	
	σ _z = σ _{r2}	σ _{r1}	σ _z = σ _{r2}	σ _{r1}	σ _z = σ _{r2}	σ _{r1}
1.0	0.3050	-1.8625	0.5030	-1.1068	0.5979	-0.8122
1.111	0.2633	-1.6689	0.4444	-1.0222	0.5345	-0.7630
1.25	0.2221	-1.4598	0.3833	-0.9202	0.4662	-0.6980
1.429	0.1813	-1.2352	0.3198	-0.7993	0.3933	-0.6159
1.667	0.1420	-1.0006	0.2554	-0.6640	0.3172	-0.5181
2.0	0.1046	-0.7610	0.1916	-0.5156	0.2403	-0.4074
2.5	0.0710	-0.5290	0.1314	-0.3650	0.1663	-0.2913
3.333	0.0416	-0.3184	0.0782	-0.2228	0.0998	-0.1793
5.0	0.0149	-0.0563	0.0363	-0.1056	0.0467	-0.0873
10.0	0.0049	-0.0381	0.0092	-0.0271	0.0119	-0.0220

tually display an elastic behaviour. The theory of elasticity will thus yield the stresses induced in the component layers for which the pavement is then designed.

The two-layer system is shown schematically in Fig. 349. A surface layer of thickness h , Young's modulus of elasticity E_1 and Poisson's number μ_1 , is supported on a subgrade of infinite depth, Young's modulus of elasticity E_2 and Poisson's number μ_2 . A uniformly distributed load p is transmitted to the system by a circular disc of diameter $2a$. The problem consists of determining the stresses in the surface layer and in the subgrade. No more is usually required than to find the stresses in the center line of the load, since these will yield the design value.

Two cases are distinguished:

1. The stresses are perfectly continuous at the interface of the two layers.
2. There is no friction developed at the interface.

The starting basis of the theoretical solution is here again the equation of compatibility. Four stress components other than zero are involved which can be found with the help of the stress function. BURMISTER (1943, 1945, 1956), who was the first to apply the theory of elasticity to the treatment of the two-layer problem, has adopted the following stress function:

$$\Phi = Jmr [Ae^{mz} + Be^{-mz} + Cze^{mz} + Dze^{-mz}]. \tag{485}$$

With due regard to the boundary conditions, the following stress formulae are obtained therefrom.

For the case of perfect continuity:

$$\left. \begin{aligned} \sigma_{r2} &= -\frac{pR(1-N)}{2} \int_0^\infty J_1(mR) \left[\frac{(2-m)e^m - N(2-5m)e^{-m}}{e^{2m} - 2N(1+2m^2) + N^2e^{-2m}} \right] dm, \\ \sigma_z &= -pR(1-N) \int_0^\infty (J_1(mR) \left[\frac{(1+m)e^m - N(1-m)e^{-m}}{e^{2m} - 2N(1+2m^2) + N^2e^{-2m}} \right] dm, \\ \sigma_{r1} &= \frac{E_1}{E_2} \left[\sigma_{r2} - \left(1 - \frac{E_2}{E_1} \sigma_z \right) \right]. \end{aligned} \right\} \tag{486}$$

For the case of a friction-free interface:

$$\sigma_r = pR \int_0^\infty \frac{J_1(mR) \{ [(1+F)m + (1-2F)]e^m - [(2-F)m + (1-2F)]e^{-m} \}}{Fe^{2m} + [2(2F-1)m - (1+2m^2)] + (1-F)e^{-2m}} dm; \tag{487}$$

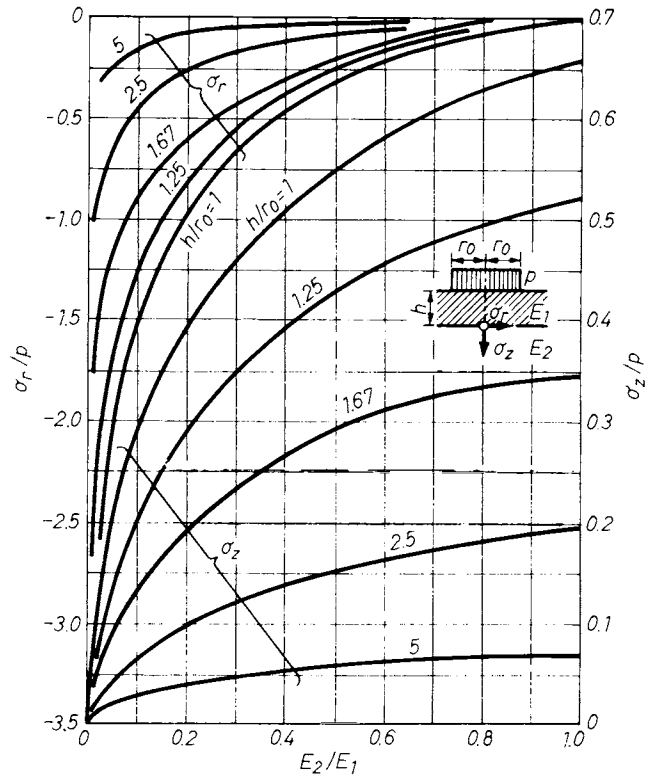


Fig. 350. Vertical and radial stresses at the interface of two layers in the central axis of a uniformly loaded circular plate

$$\sigma_{r2} = \sigma_z = -pR(2F-1) \int_0^\infty \frac{J_1(mR) [(1+m)e^m - (1-m)e^{-m}]}{Fe^{2m} + [2(2F-1)m - (1+2m^2)] + (1-F)e^{-2m}} dm. \tag{488}$$

These stresses are induced in the vertical center line of the symmetrically loaded circular plate and are thus simultaneously principal stresses.

The symbols and terms involved in the foregoing expressions are as follows:

- E_1 = Young's modulus of elasticity of the surface layer,
- E_2 = Young's modulus of elasticity of the subgrade,
- $N = \frac{E_1 - E_2}{E_1 + E_2}$,
- $F = \frac{1}{2} \left(1 + \frac{E_2}{E_1} \right)$,
- $R = a/h$,
- m = a parameter,
- $J_1 mr$ = first-order Bessel-function.

Integration is possible numerically, by successive approximation.

The stresses induced in two-layer systems are found from Tables 26 and 27, or approximately

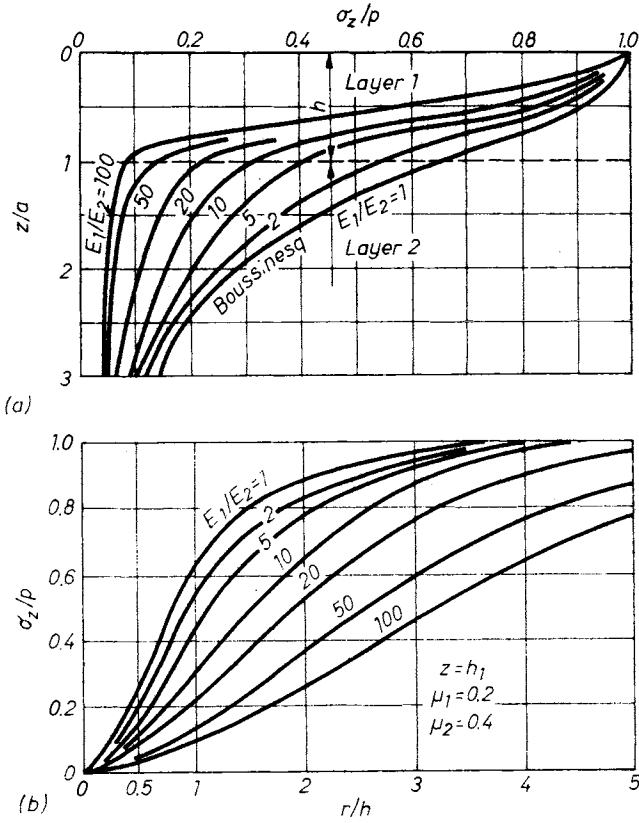


Fig. 351. Stresses in the two-layer system: a — vertical stresses in the line of the load; b — vertical stresses at the interface of the two layers

from the chart in Fig. 350. The considerable influence of the firmer, surface layer is clearly visible from the charts in Fig. 351. The differences relative to the uniform half-space are considerable, especially in the vicinity of the pavement.

It should be noted that in his original paper Burmister dealt with deflections, rather than stresses. He computed the deflection of the surface

in the center line of the load for the case of a rough interface. The results of these computations are reproduced graphically in Fig 352, indicating the values of the settlement coefficient \mathfrak{F} involved in the expression

$$y_0 = \frac{1.5 pa}{E_2} \mathfrak{F} \quad (489)$$

for different values of the ratios h/a and E_1/E_2 .

4.3.3.4 Stresses in three-layer systems

The widespread use of electronic computers has opened new vistas to the solution of engineering problems. Numerical computations have become feasible which were formerly too cumbersome to be practicable. Computers have also been used for the computation of stresses and deflections in layered systems, permitting the compilation of tables and charts. Starting from the foundations laid by ACUM and FOX (1951), WHIFFIN and LISTER (1963) have succeeded in arriving at pertinent conclusions and thus in substantially simplifying the computation of stresses. The results thereof will be described in brief below.

The three-layer system is illustrated in Fig 353. The conclusions are as follows.

1. The ratio of subgrade stresses under two different pavement structures placed on a subgrade with a given Young's modulus of elasticity remains unchanged if the same pavements are constructed on another subgrade with a different modulus of elasticity. The validity of this statement holds true even if the courses of which the two pavements are composed differ in thickness and E -modulus.

2. If a pavement of given thickness, design and modulus of elasticity is placed on different subgrades, the following relationship will be found to

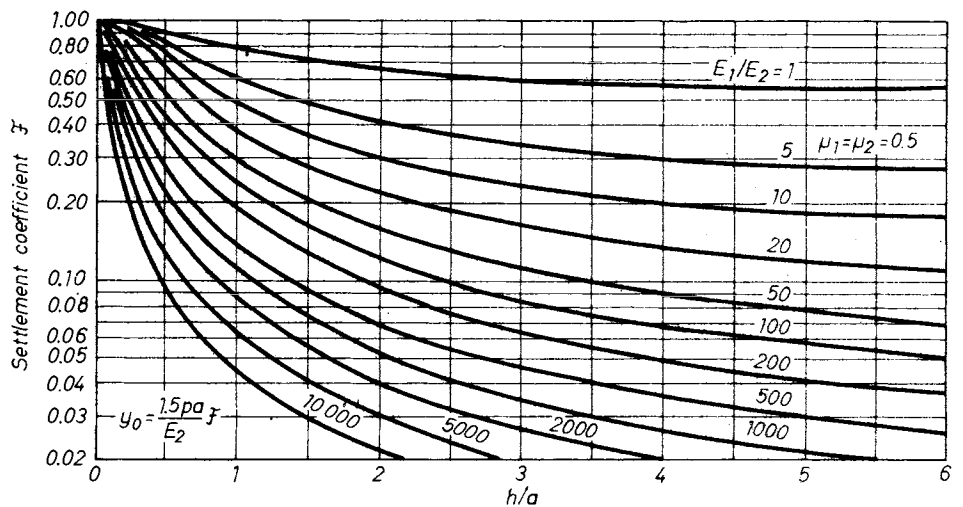


Fig. 352. Influence factors for determining the deflections in the two-layer system

Table 28. Stresses in the three-layer system

$$\alpha_1 = a/h_2 \quad \beta = h_1/h_2$$

$$k_1 = E_1/E_2 \quad k_2 = E_2/E_3$$

Key for use of the Table:

	k_1	
k_2	σ_{z1}	σ_{z2}
	$\sigma_{z1} - \sigma_{r1}$	$\sigma_{z2} - \sigma_{r2}$
	$\sigma_{z1} - \sigma_{r2}$	$\sigma_{z1} - \sigma_{r3}$

$\beta = 2, \alpha_1 = 1$

$k_2 \backslash k_1$	5		10		20		50		100		500	
5	9.51	3.64	6.00	2.59	3.66	1.79	1.87	1.05	1.11	0.690	0.349	0.261
	72.70	15.30	93.90	10.20	113.00	6.44	136.00	3.30	151.00	1.90	187.00	0.513
	14.50	3.06	9.38	2.04	5.66	1.29	2.73	0.66	1.51	0.380	0.374	0.101
10	8.24	2.38	5.06	1.69	3.01	1.16	1.47	0.684	0.852	0.451	0.252	0.169
	79.30	18.70	103.00	12.30	124.00	7.68	148.00	3.85	164.00	2.21	203.00	0.586
	15.80	1.86	10.30	1.23	6.21	0.77	2.96	0.385	1.64	0.221	0.405	0.059
50	6.74	0.860	3.97	0.612	2.23	0.424	1.01	0.252	0.554	0.166		
	95.20	26.00	124.00	16.90	149.00	10.40	178.00	5.12	198.00	2.94		
	19.00	0.519	12.40	0.339	7.44	0.208	3.55	0.103	1.98	0.059		
100	6.43	0.552	3.75	0.397	2.08	0.277	0.921	0.163				
	102.00	29.00	133.00	18.90	161.00	11.60	193.00	5.75				
	20.40	0.290	13.30	0.189	8.04	0.118	3.85	0.058				

$\beta = 1, \alpha_1 = 1$

$k_2 \backslash k_1$	5		10		20		50		100		500	
5	30.30	9.22	20.80	7.14	13.50	5.33	7.26	3.44	4.43	2.36	1.38	0.921
	162.00	37.80	229.00	28.10	300.00	19.70	390.00	11.40	457.00	7.10	594.00	2.11
	32.30	7.56	22.90	5.63	15.00	3.96	7.84	2.29	4.57	1.42	1.19	0.420
10	27.90	6.11	18.70	4.73	11.80	3.53	6.13	2.26	3.60	1.55	1.04	0.599
	173.00	47.10	250.00	35.00	330.00	24.40	431.00	13.90	502.00	8.55	645.00	2.46
	34.70	4.70	25.00	3.50	16.50	2.44	8.66	1.39	5.02	0.86	1.29	0.245
50	25.00	2.23	16.10	1.74	9.76	1.30	4.68	0.833	2.60	0.572		
	201.00	68.20	298.00	50.90	399.00	35.30	523.00	19.50	606.00	11.80		
	40.40	1.37	29.80	1.02	20.00	0.70	10.50	0.392	6.05	0.236		
100	24.30	1.42	15.60	1.11	9.35	0.839	4.40	0.540				
	213.00	75.10	319.00	57.80	428.00	39.80	563.00	22.00				
	42.60	0.76	31.80	0.57	21.40	0.400	11.30	0.22				

$\beta = 1/2, \alpha_1 = 1$

$k_2 \backslash k_1$	5		10		20		50		100		500	
5	66.40	18.10	53.40	15.60	39.90	12.90	24.70	9.42	16.20	7.06	5.48	3.13
	215.00	72.80	366.00	62.00	561.00	49.80	868.00	34.00	116.00	23.80	1687.00	8.60
	43.00	14.60	36.70	12.40	28.10	10.00	17.40	6.81	11.20	4.77	3.37	1.72
10	63.40	12.10	50.40	10.40	37.00	8.59	22.20	6.29	14.20	4.72	4.43	2.09
	223.00	91.70	396.00	78.00	615.00	62.80	963.00	42.90	1244.00	29.80	1866.00	10.50
	44.60	9.20	39.40	7.81	30.70	6.28	19.30	4.29	12.40	2.98	3.73	1.05
50	59.80	4.36	46.70	3.74	33.50	3.14	10.10	2.34	11.60	17.70		
	239.00	134.00	449.00	115.00	730.00	93.30	1180.00	63.90	1541.00	44.20		
	47.80	2.69	44.90	2.30	36.50	1.87	23.60	1.28	15.40	0.88		
100	59.10	2.77	46.00	2.37	32.80	2.00	18.50	1.51				
	244.00	152.00	469.00	130.00	776.00	106.00	1270.00	73.10				
	48.80	1.52	46.90	1.30	38.70	1.06	25.40	0.73				

Table 28 (cont.)

$$\beta = 1/4, \alpha_1 = 1$$

$k_2 \backslash k_1$	5		10		20		50		100		500	
5	94.70	26.50	90.70	24.90	82.10	22.80	64.20	19.40	49.00	16.30	20.80	9.19
	127.00	104.00	301.00	99.00	614.00	90.70	1273.00	75.20	1966.00	61.20	3991.00	30.10
	25.40	20.90	30.20	19.80	30.70	18.20	25.50	15.00	19.70	12.20	8.00	6.03
10	92.80	18.00	88.30	16.60	79.60	15.20	61.20	12.90	45.90	10.90	18.30	6.19
	112.00	134.00	308.00	125.00	657.00	115.00	1404.00	95.60	2195.00	77.90	4500.00	38.00
	22.60	13.40	30.60	12.50	33.00	11.50	28.10	9.56	21.90	7.77	9.00	3.82
50	90.20	6.52	85.50	5.91	76.40	5.38	57.60	4.63	42.20	3.97		
	70.80	197.00	303.00	185.00	725.00	169.00	1657.00	142.00	2668.00	117.00		
	14.20	3.94	30.20	3.69	36.40	3.40	33.10	2.85	26.60	2.33		
100	89.70	4.13	84.90	3.71	75.80	3.37	57.00	2.92				
	50.80	223.00	295.00	208.00	745.00	191.00	1745.00	161.00				
	10.20	2.23	29.40	2.08	37.40	1.91	34.90	1.61				

$$\beta = 2, \alpha_1 = 1/2$$

$k_2 \backslash k_1$	5		10		20		50		100		500	
5	2.85	0.950	1.76	0.670	1.06	0.459	0.522	0.268	0.307	0.175	0.093	0.066
	21.50	4.09	27.20	2.70	32.40	1.69	38.20	0.853	42.10	0.482	50.80	0.131
	4.30	0.817	2.72	0.540	1.62	0.338	0.765	0.170	0.421	0.088	0.101	0.026
10	2.51	0.621	1.52	0.435	0.884	0.297	0.422	0.174	0.241	0.114	0.068	0.042
	23.10	4.96	29.40	3.24	35.00	2.01	41.20	0.999	45.20	0.570	54.90	0.149
	4.62	0.495	2.94	0.323	1.75	0.201	0.825	0.100	0.454	0.057	0.110	0.015
50	2.12	0.220	1.23	0.155	0.692	0.108	0.305	0.064	0.165	0.042		
	27.10	6.80	34.60	4.40	41.20	2.69	48.50	1.32	53.70	0.753		
	5.42	0.136	3.47	0.088	2.06	0.054	0.971	0.026	0.537	0.015		
100	2.02	0.140	1.17	0.101	0.644	0.070	0.281	0.041				
	28.70	7.56	37.00	4.90	44.10	2.99	52.30	1.47				
	5.64	0.076	3.70	0.049	2.21	0.030	1.05	0.015				

$$\beta = 1, \alpha_1 = 1/2$$

$k_2 \backslash k_1$	5		10		20		50		100		500	
5	12.00	2.55	7.72	1.93	4.74	1.42	2.39	0.899	1.40	0.610	0.404	0.235
	66.10	10.90	87.10	7.89	107.00	5.43	132.00	3.07	149.00	1.89	184.00	0.550
	13.20	2.18	8.69	1.58	5.36	1.09	2.64	0.616	1.49	0.376	0.368	0.111
10	11.30	1.66	7.13	1.26	4.29	0.929	2.08	0.586	1.18	0.400	0.318	1.52
	69.10	13.30	92.30	9.68	115.00	6.64	142.00	3.71	160.00	2.26	197.00	0.637
	13.80	1.33	9.22	0.969	5.74	0.664	2.84	0.371	1.60	0.227	0.394	0.064
50	10.50	0.586	6.46	0.453	3.74	0.336	1.71	0.213	0.927	0.145		
	76.10	18.70	104.00	13.70	132.00	9.39	165.00	5.14	186.00	3.08		
	15.20	0.374	10.40	0.275	6.61	0.189	3.30	0.103	1.86	0.062		
100	10.30	0.370	6.32	0.287	3.64	0.215	1.64	0.137				
	79.00	21.10	109.00	15.40	140.00	10.60	175.00	5.75				
	15.80	0.210	10.90	0.154	6.99	0.106	3.50	0.057				

$$\beta = 1/2, \alpha_1 = 1/2$$

$k_2 \backslash k_1$	5		10		20		50		100		500	
5	36.20	5.41	25.60	4.52	17.10	3.64	9.41	2.58	5.76	1.89	1.73	0.815
	144.00	23.20	204.00	19.00	270.00	14.70	363.00	9.69	433.00	6.63	583.00	2.31
	28.80	4.64	20.40	3.81	13.50	2.94	7.26	1.94	4.32	1.32	1.16	0.462
10	35.40	3.52	24.70	2.94	16.30	2.39	8.71	1.69	5.20	1.25	1.46	0.538
	147.00	28.40	211.00	23.30	284.00	18.20	388.00	12.00	465.00	8.18	627.00	2.79
	29.40	2.84	21.10	2.34	14.20	1.83	7.76	1.20	4.65	0.818	1.26	0.279

Table 28 (cont.)

$$\beta = 1/2, \alpha_1 = 1/2$$

$k_2 \backslash k_1$	5		10		20		50		100		500	
50	34.20	1.20	23.60	1.01	15.30	0.835	7.88	0.612	4.51	0.457		
	151.00	39.60	226.00	33.00	314.00	26.10	443.00	17.40	540.00	11.80		
	30.10	0.794	22.50	0.659	15.70	0.522	8.87	0.348	5.40	0.237		
100	33.90	0.748	23.40	0.633	15.10	0.526	7.72	0.390				
	152.00	44.10	230.00	36.80	325.00	29.40	466.00	19.70				
	30.30	0.441	23.00	0.369	16.30	0.294	9.32	0.197				

$$\beta = 1/4, \alpha_1 = 1/2$$

$k_2 \backslash k_1$	5		10		20		50		100		500	
5	74.10	8.79	61.40	8.03	47.50	7.15	30.80	5.80	20.90	4.72	7.30	2.50
	189.00	38.00	312.00	34.70	476.00	30.50	747.00	23.80	984.00	18.60	1582.00	8.52
	37.90	7.61	31.30	6.95	23.80	6.10	15.00	4.77	9.87	3.72	3.17	1.71
10	73.40	5.70	60.60	5.17	46.60	4.60	29.80	3.76	10.90	3.08	6.61	1.65
	186.00	46.50	315.00	42.50	489.00	37.40	783.00	29.50	1045.00	23.10	1713.00	10.60
	37.10	4.65	31.50	4.25	24.50	3.74	15.60	2.95	10.50	2.31	3.43	1.06
50	72.40	1.90	59.60	1.71	45.60	1.52	28.70	1.28	18.80	1.07		
	175.00	63.90	314.00	58.40	508.00	51.90	850.00	41.70	1167.00	33.30		
	34.80	1.28	31.30	1.17	25.40	1.04	17.00	0.836	11.67	0.665		
100	72.40	1.17	59.40	1.04	45.40	0.934	28.50	0.791				
	170.00	70.70	311.00	64.50	513.00	57.50	872.00	46.60				
	34.00	0.707	31.20	0.645	25.70	0.575	17.40	0.466				

exist between the vertical stress σ_{z2} in the pavement-subgrade interface and the modulus E_3 :

$$\sigma_{z2} = \text{const. } E_3^{0.64}. \quad (490)$$

3. The absolute value of the stresses induced in the subgrade decreases if

- (a) the thickness of the surface course;
- (b) the dynamic modulus of elasticity of the surface course;
- (c) the thickness of the second course;
- (d) the dynamic modulus of elasticity of the second course are increased.

4. The ratio of stresses induced in the subgrade under two different pavements by a particular wheel load distributed over a given contact area remains unchanged under a different wheel load and another contact area acting on the pavements.

5. The absolute magnitude of subgrade stresses is a simple function of the radius of the wheel contact area. It is proportionate to $a^{1.9}$ if the unit load p is identical.

6. Under the same wheel contact area, the stress induced in the subgrade will be proportionate to p .

7. The absolute magnitude of the stresses induced in the subgrade is approximately proportionate to the wheel load.

8. For fixed values of h_1, E_1 and E_3 (cf. Fig. 353) the thickness h_2 at which a given constant stress is induced in the subgrade-base course interface is related to the modulus of elasticity of the base as

follows:

$$h_2 = \text{const } E_2^{-0.42}. \quad (491)$$

From conclusions 5 to 7 it follows that

$$\frac{\sigma_{z2}^{(1)}}{\sigma_{z2}^{(2)}} = \frac{CP_1/\pi a_1^2 a_1^{1.9}}{CP_2/\pi a_2^2 a_1^{1.9}} = \frac{P_1}{P_2} \left(\frac{a_2}{a_1}\right)^{0.1}. \quad (492)$$

For normal vehicles the value $(a_2/a_1)^{0.1}$ hardly differs from unity, so that

$$\frac{\sigma_{z2}^{(1)}}{\sigma_{z2}^{(2)}} \approx \frac{P_1}{P_2}.$$

The influence factors of stress (the values of 100 σ/p) have been compiled for a number of cases of practical interest in Table 28. A visual represen-

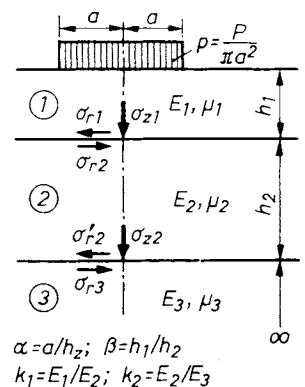


Fig. 353. The three-layer system

tation is given in Figs 354 to 356, the charts providing assistance in estimating the influence of different alternative designs. The charts apply to a particular load and contact surface, but observing the foregoing remarks, they can be extended to other cases as well.

Numerical example. The stresses under the pavement shown in Fig. 357, are to be determined. On the chart in Fig. 356 values are given for the pavement thickness $h_1 = 10$ cm.

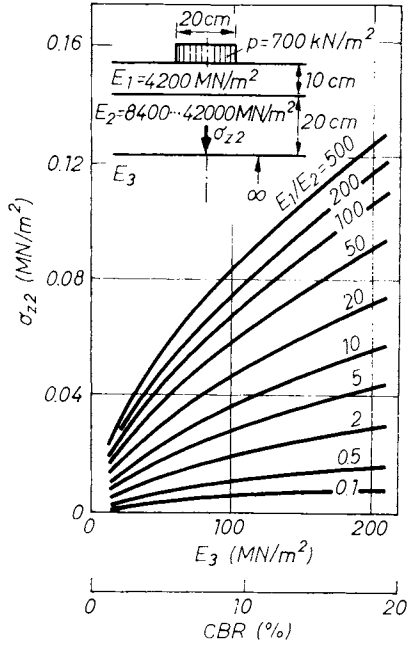


Fig. 354. Influence factors for vertical stresses in the subsoil as functions of soil deformation moduli and subbase quality

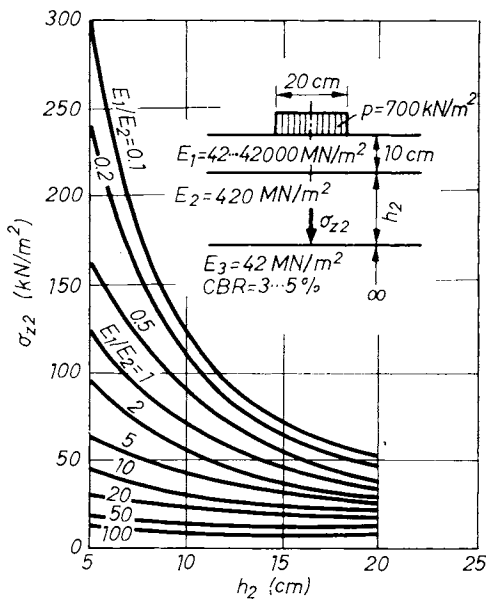


Fig. 355. Influence factors for vertical stresses in the subsoil as functions of the deformation modulus of the slab and the thickness of the subbase

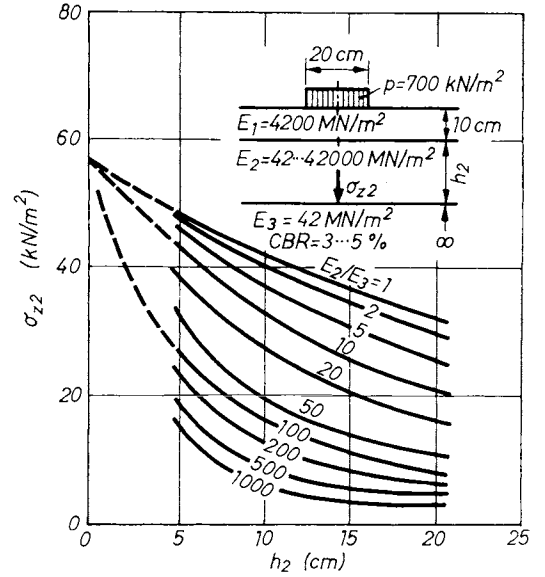


Fig. 356. Influence factors for vertical stresses in the subsoil as functions of deformation modulus and thickness of the subbase

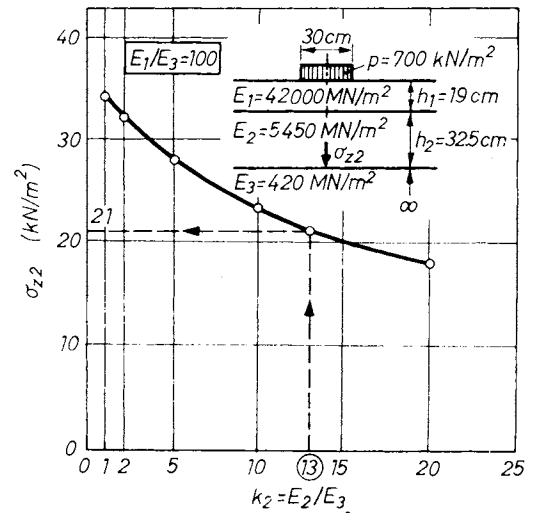


Fig. 357. Data for the numerical example

In this particular case the ratio $\beta = h_1/h_2 = 19/32.5 = 0.58$. The value corresponding to $h_1 = 10$ cm is $h_2 = 10/0.58 = 17.2$ cm. For this value of h_2 a series of σ_z values are determined by varying the value of K_2 . The σ_z values obtained are plotted in a diagram (Fig. 357) and the correct σ_z is found at $K = 13$. The actual stress is computed from Eq. (492), thus

$$\sigma_z = 2.1 \left(\frac{0.48}{0.59} \right)^{1.9} = 1.5 \text{ N/cm}^2.$$

From Figs 354 to 356 σ_{z2} will be seen to increase rapidly with E_2 , particularly for small values of E_2 . On the other hand, it decreases strongly at increasing h_2 values (Fig. 355). As mentioned before, the values here obtained can be converted to other E_3 values by multiplication with $(E_3/420)^{0.64}$. In Fig. 356 the value of σ_{z2} has been plotted against

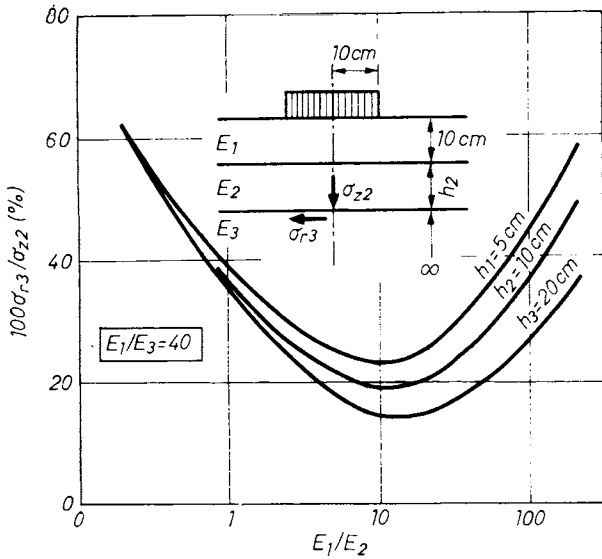


Fig. 358. Varying stress conditions at the top of the subgrade as functions of subbase thickness and the ratio E_1/E_2

the thickness of the base course in terms of the parameter E_2 . The influence of a stronger base (a greater value of h_2) on the stress σ_{z2} is the more pronounced, the lower the value of E_2 .

The horizontal stresses are also of interest to the pavement designer for obtaining a picture of the complete state of stress and thus for performing triaxial compression test with the aim of reproducing the conditions of the pavement. In Fig. 358 the σ_{r3}/σ_{z2} ratio has been plotted against the ratio E_1/E_2 , while the horizontal stresses induced at the bottom plane of the base are shown for two different E_1 values of the surface course in Fig. 359 (the determination of the E value will be discussed later). As is clearly to be seen from the diagrams, the load distributing effect of the base course in-

creases together with the E_2 modulus thereof, but this is accompanied by the development of higher horizontal stresses. These tensile stresses may become especially detrimental in base courses made of a weak concrete (macadam bonded with cement grout, lean concrete). The results of tests performed on beams of lean concrete are shown in Fig. 360, indicating the flexural stress as a function of the modulus of elasticity. In this case, the E value was determined by a dynamic method, by the measurement of resonant frequencies. The horizontal stresses induced in the base course and the flexural strength are compared in Fig. 360. Up to the value $E_2 = 14\,000\text{ MN/m}^2$, the strength will be seen to be lower than the stress computed, so that cracks are liable to develop in the lower side of the base.

The stresses at the interface of the surface and base courses are shown in Fig. 361. In diagram (a) the stress has been plotted against the ratio E_1/E_2 with E_1/E_3 held constant. The diagram indicates thus the increase of the stress σ_{z1} if the E_2 of the base is increased. The curves in Fig. 361b have also been plotted against the ratio E_1/E_2 , but here the ratio E_2/E_3 is constant. Consequently, these charts offer guidance on how to vary the E values in order to control the vertical stresses at the first interface.

Finally, the horizontal stresses at the interface of the first and second layers are plotted in Fig. 362 against the modulus of elasticity of the second layer, for the pavement thickness $h = 10\text{ cm}$. In this particular case, compressive stresses will be induced if the modulus of elasticity of the second layer is of the order of around 1000 kN/cm^2 . The stresses decrease hereafter together with E_2 and become zero at $E_1 \sim E_2$. At low E_2 values very high tensile stresses are induced. The effect of the base thickness h_2 is much inferior to that of the surface course h_1 .

Deformations present hazards for the stability and durability, especially of flexible pavements.

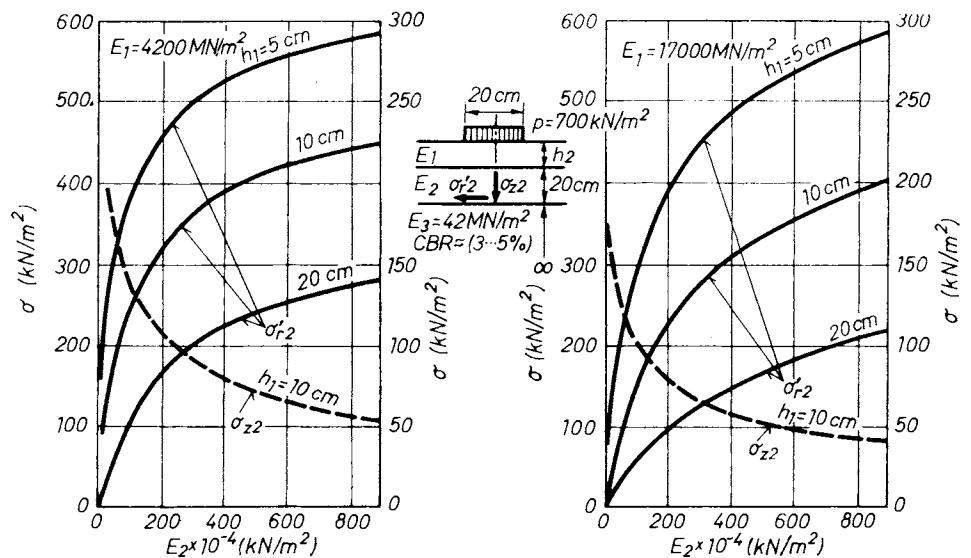


Fig. 359. Relationship between tension stress and modulus of elasticity at the bottom of the subbase

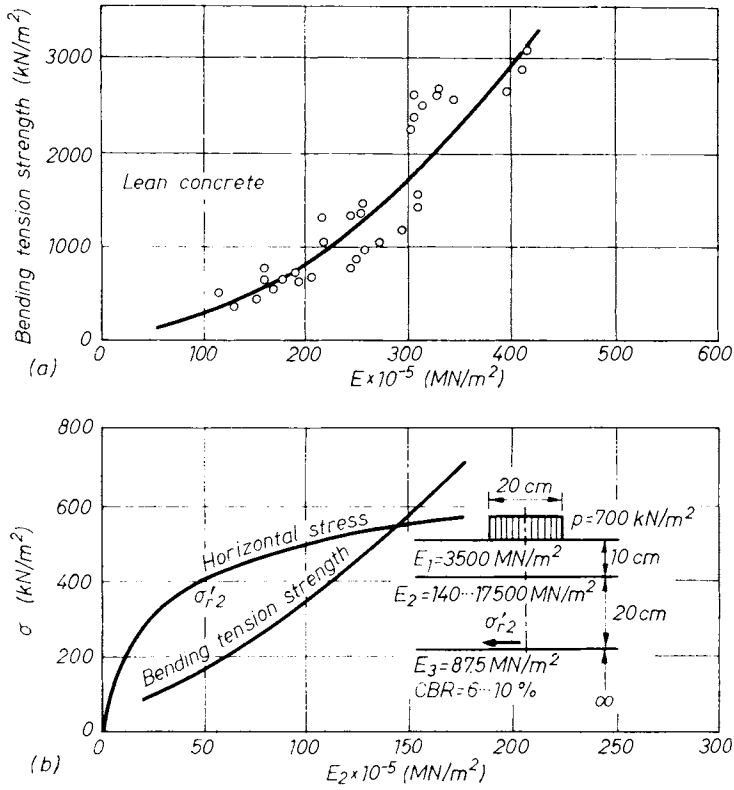


Fig. 360. Comparison of strength and stress in the subbase

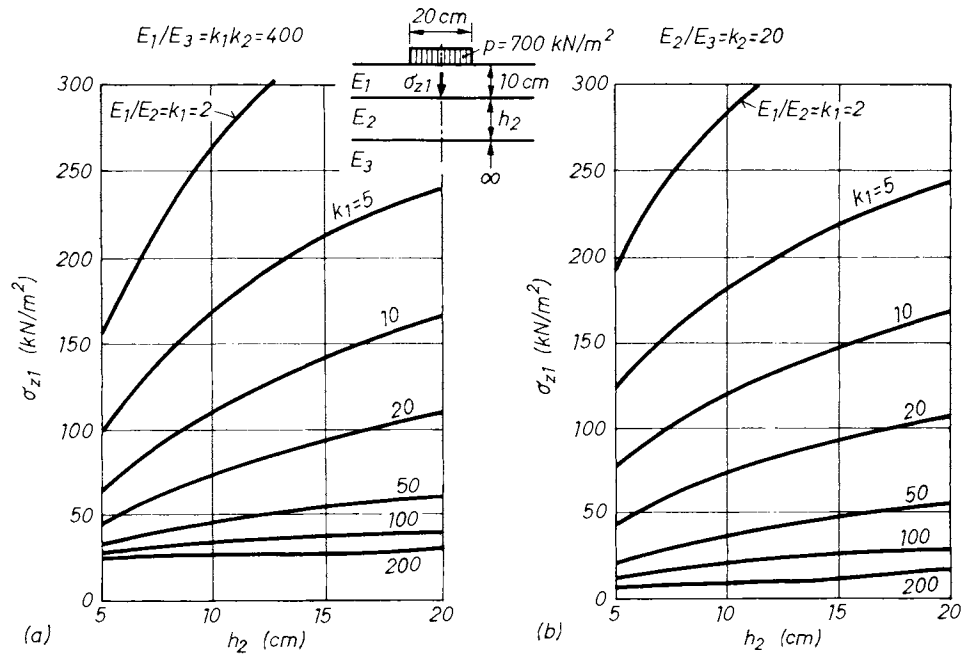


Fig. 361. Values of stresses at the interface of pavement and base as a function of subbase thickness

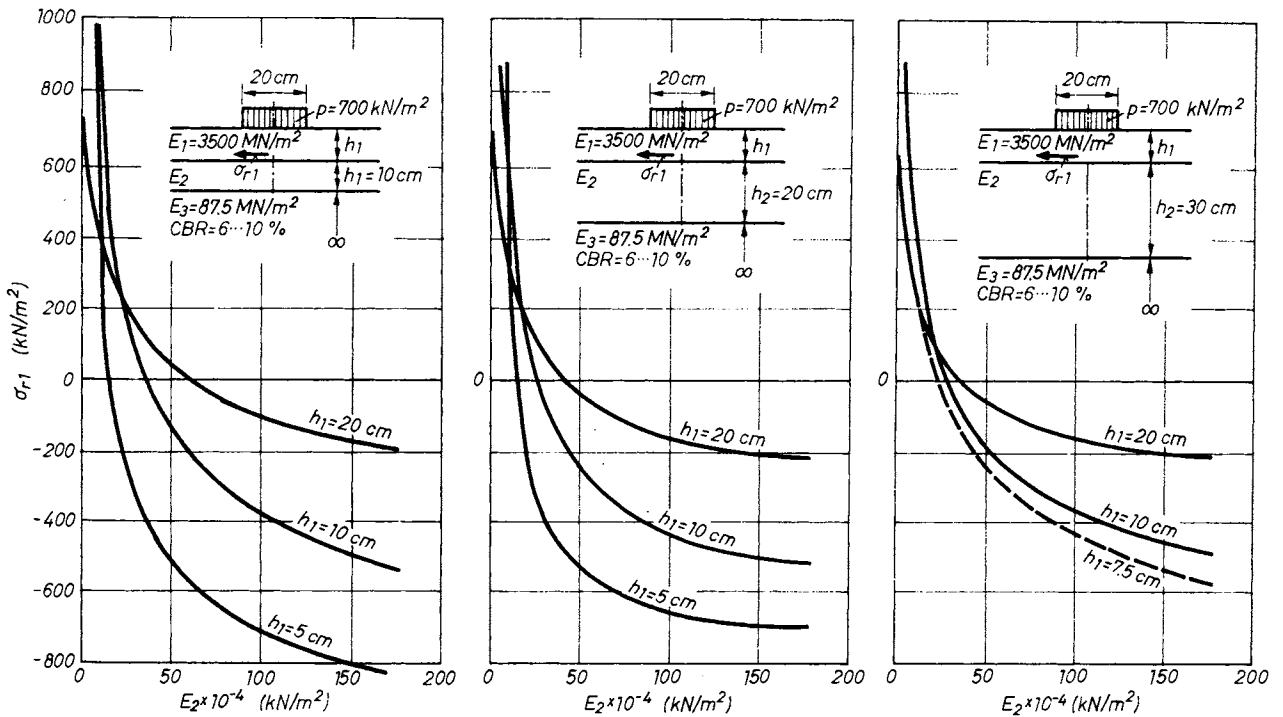


Fig. 362. Horizontal stresses at the interface of pavement and base course

The deformations of two-layer systems are given by the charts of BURMISTER (Fig. 352), whereas neither tables nor diagrams are available for multi-layer systems. According to the example shown in Fig. 363, substantially smaller deflection results from increasing the thickness of the surface layer, whereas increasing h_2 has relatively little effect. If, for example, h_1 is increased from point A to point B, the deflection of the subgrade is reduced by 25%. A reduction of the same magnitude can be achieved by a much greater increase of h_2 only (A-C).

Further data of great interest to the examination of three-layer systems have been contributed by JEUFFROY and BACHELEZ (1963), who have developed detailed charts for the stresses and deflections. An example is shown in Fig. 364. A table for the

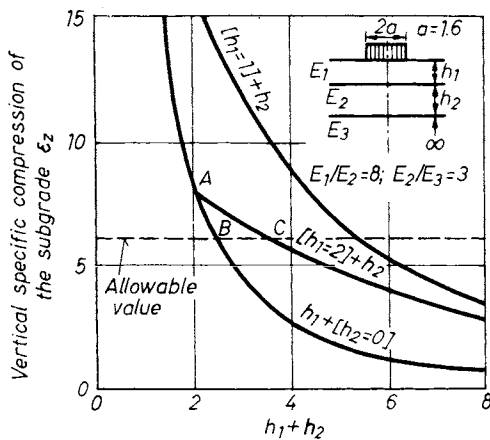


Fig. 363. Influence of layer thickness on deformation

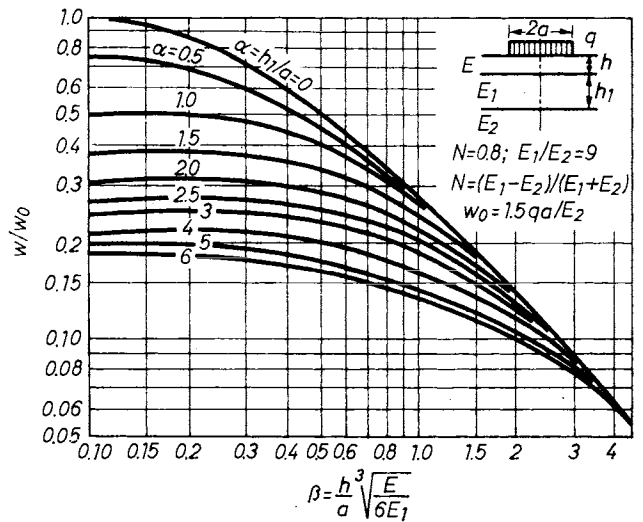


Fig. 364. Deflection (w) at the surface of a pavement structure as a function of material properties and surface load

computation of deflections has been compiled by KIRK (1961). This is reproduced in Table 29.

Concluding the discussion of stresses and deflections in three-layer systems, it may be of interest to quote a few sentences from the book mentioned above. According to JEUFFROY (1967) "... These investigations are still in an initial stage. Any reliance on a purely theoretical method of pavement design would be a grave mistake. The attention of the reader should be directed much rather to the "wide gap" still existing between the theory and the actual facts. This gap will take a long time to close. Nevertheless, the theoretical results have

Table 29. Deflections in the three-layer system after KIRK (1961); values of \mathfrak{F}_3 for the equation $y = 1.5 \frac{Pr}{E_3} \mathfrak{F}_3$

H	a_1	k_2	k_1			
			5	10	20	50
2	1	1	0.4160	0.3050	0.2298	0.1613
		5	1097	1515	1204	0885
		10	1431	1160	0934	0694
		20	1092	0898	0730	0546
		50	0778	0648	0531	0399
1	1	1	5940	4832	3909	2937
		5	2597	2531	2129	1651
		10	2256	1957	1664	1301
		20	1738	1523	1306	1028
		50	1245	1102	0952	0755
0.5	1	1	8301	7405	6429	5139
		5	4176	3823	3423	2860
		10	3166	2925	2651	2241
		20	2430	2253	2058	1759
		50	1727	1607	1479	1280
0.25	1	1	9478	9518	9009	8008
		5	5105	4943	4716	4277
		10	3909	3759	3577	3267
		20	2975	2845	2710	2506
		50	2099	1995	1906	1782
2	0.5	1	3109	2049	1413	9014
		5	1163	0864	0656	0465
		10	0821	0634	0494	0358
		20	0600	0477	0379	0279
		50	0410	0335	0271	0203
1	0.5	1	4160	3057	2298	1613
		5	1730	1403	1140	0858
		10	1258	1050	0871	0668
		20	0936	0799	0673	0524
		50	0650	0567	0485	0381
0.5	0.5	1	5940	4832	3909	2927
		5	2492	2179	1884	1519
		10	1802	1606	1417	1169
		20	1330	1203	1078	0906
		50	0912	0836	0761	0652
0.25	0.5	1	8301	7405	6429	5139
		5	3296	3052	2778	2420
		10	2339	2191	2030	1800
		20	1683	1581	1480	1336
		50	1162	1091	1025	0937

$$H = \frac{h_1}{h_2}; \quad a_1 = \frac{a}{b_2}; \quad k_1 = \frac{E_1}{E_2}; \quad k_2 = \frac{E_2}{E_3}$$

contributed to the better understanding of some of the processes and phenomena involved. Any approach to the complex phenomena taking place in the individual courses of a pavement based on the theory of elasticity would be as futile as an explanation thereof on the basis of experience alone."

The foregoing statements are supported also by the investigations of VESIČ (1964), who arrived at the conclusion that a limited tensile strength is only available in the individual courses of a composite system. Consequently, the behaviour of the system will resemble that of a plate much less than would follow from theoretical considerations. Another fact to be born in mind is that the modulus of elasticity in tension is usually lower.

4.4 Bearing capacity and deformation of pavements and subsoil

4.4.1 Properties of the subsoil

The bearing value is understood as the load causing a 30.5 mm diameter disc to deflect 5 mm. On the basis of the results of diverse statistical analyses, the measurement data will yield information on the load-bearing capacity to be expected in autumn and spring. This, in turn, will indicate the road sections where the capacity specified is not attained and where, e.g. traffic restrictions must be introduced.

The compression modulus is found, in accordance with Swiss standard specifications (SVN 40.315), from the formula

$$M_E = \frac{P_2 - P_1}{s_2 - s_1} d, \quad (493)$$

where p_1 and p_2 are two pressure values, s_1 and s_2 the deflections corresponding thereto, while d is the diameter of the loading plate. From tests performed on the surface of the subgrade, the base and the pavement, the diameters and pressures to be used are given in Table 30, which also shows the lowest required values of M_E .

The equivalent deformation modulus of the pavement structure is

$$E_e = \frac{\pi P}{2 \lambda} \quad (494)$$

with $\lambda = y/d$ denoting the relative deformation coefficient.

The modulus of elasticity is found from the expressions

$$E = \frac{P}{2 ay} (1 - \mu^2) \text{ or } E = \frac{2P}{\pi ay} (1 - \mu^2). \quad (495)$$

The value of 0.5 is usually adopted for μ .

To obtain information on the relative bearing capacity of the subgrade and the individual courses of pavement, the California Bearing Ratio CBR was developed by PORTER (1949) and was used as the basis of a general design method for flexible pavements. The CBR method has since been replaced by more sophisticated procedures, but the CBR value is still found convenient for characterizing the relative strength of the subgrade and the

Table 30. Data for the determination of the modulus of compressibility

	$2a$ (cm)	P_1 (kN/m ²)	P_2 (kN/m ²)	M_E (kN/m ²)
Subgrade	16	50	150	15 000
Subbase	16	150	250	40 000
Pavement	30	250	350	100 000

diverse pavement courses by a single figure, obtained from a simple test.

A compaction test is first performed on the soil sample to furnish the optimum moisture on compaction, as well as the density attainable on the site by the method and equipment used for compaction work. A sample of this density is then prepared in a mould and loaded — through a perforated disc — with a surcharge roughly corresponding to the weight of the actual pavement. The sample is subsequently soaked under water in the mould for 4 days, the expansion during this period being measured continuously. A penetration test is then made, in which a circular piston is forced into the sample at a rate of about 1.3 mm/min and the loads required for 0.6, 1.27, 1.90, 2.54, 5.08, 7.62, 10.16 and 12.7 mm of penetration are recorded. To obtain a clear picture of the penetration process and of the forces required to produce the penetration depths specified, the load-penetration curve is plotted. The resulting penetration resistance is compared with a standard value for crushed stone and expressed as a percentage of the latter. This percentage is termed the CBR value. Thus

$$CBR = 100 \frac{\text{test load}}{\text{standard load}} \quad (496)$$

The CBR test can be performed on undisturbed samples taken in the field, on samples compacted in the laboratory, and on samples soaked as described above.

For computing the CBR values, the following standard loads (CBR = 100%) are needed:

Penetration (mm)	Load (kN/cm ²)
2.54	0.70
5.08	1.06
7.62	1.34
10.16	1.62
12.70	1.83

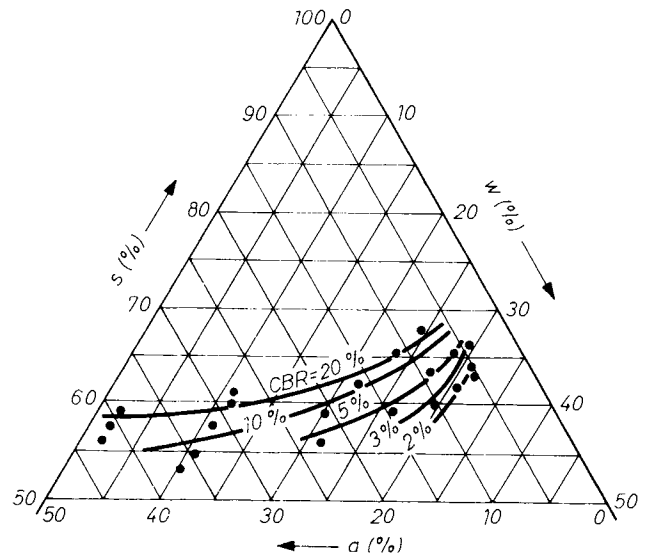


Fig. 366. CBR values depending on phase-conditions: s — solids; a — air; w — water

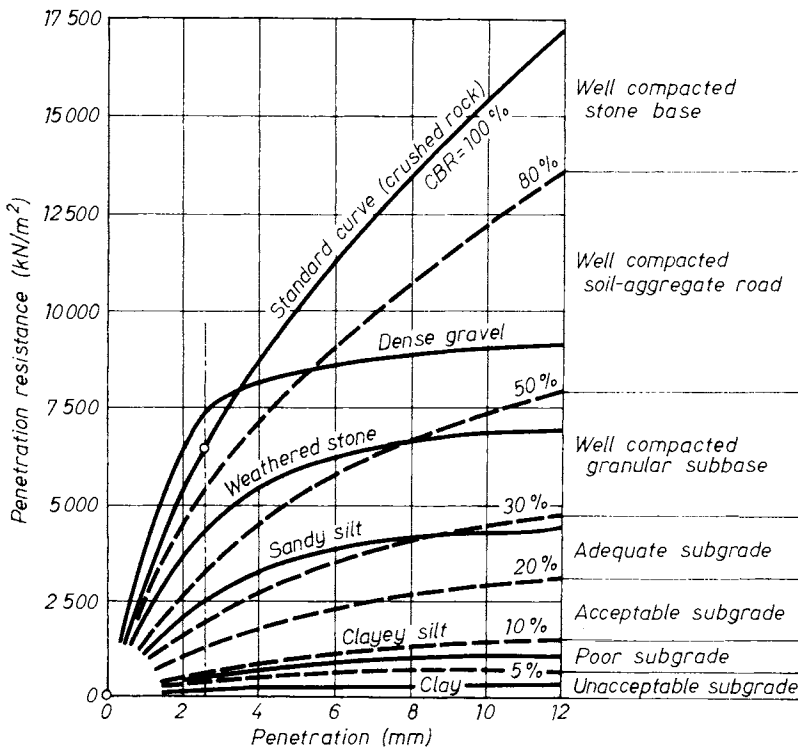


Fig. 365. Curves showing relationship between load and penetration for different soils

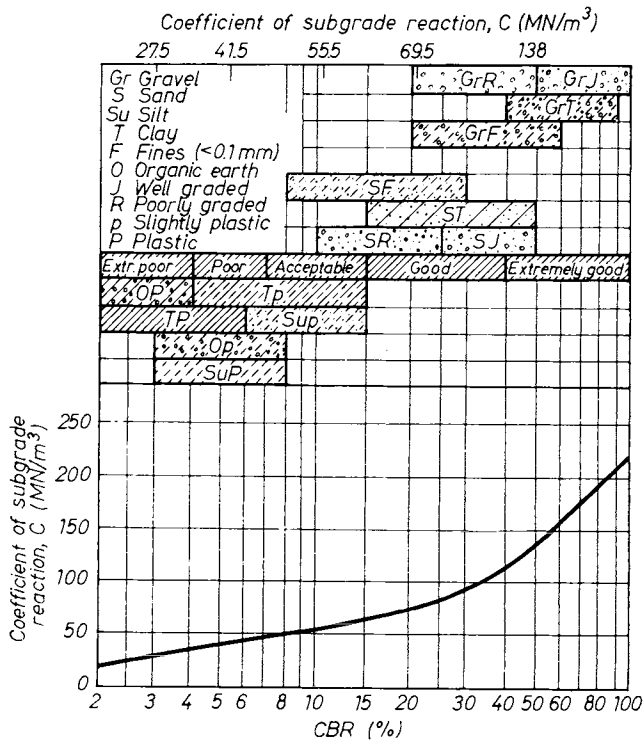


Fig. 367. Relationship between modulus of subgrade reaction and CBR value

Typical test results are shown in Fig. 365, in which the CBR values for 2.54 mm of penetration have also been plotted.

Evidently, the CBR value obtained depends on the condition of the sample tested. In the triangular chart (Fig. 366), the influence of phase composition is illustrated for a silt soil having a plasticity index $I_p = 8\%$ (LAZÁNYI, 1958). The CBR value was found to display a peak in a certain critical condition and to decrease again as the density was further increased. The peak is obtained at saturations $S_r = 0.75$ to 0.80 , owing to the fact that at low moisture contents the pores in the soil communicate with each other, so that no neutral stresses are induced by the penetrating piston. However, once the critical condition is attained only closed air voids remain in the soil, from which the air cannot escape immediately as the load is applied; neutral stresses are developed, as a consequence of which the shear strength and, in turn, the resistance to penetration are reduced.

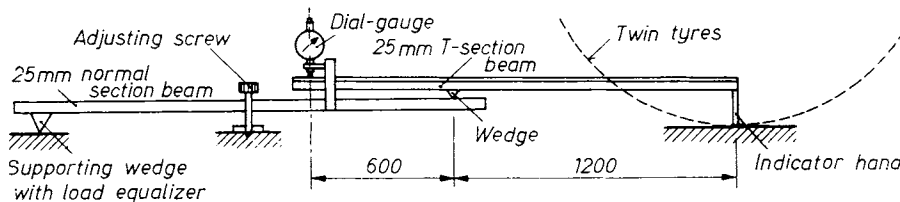


Fig. 368. Modified Benkelmann-rod (BOROMISSZA and GÁSPÁR, 1956; 1968)

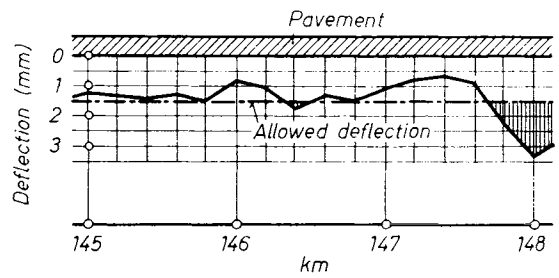


Fig. 369. Results of monitored deformations

With the aim of minimizing the scatter of experimental results, it is preferable not to soak the samples before testing. Instead, they should be tested at different moistures and densities, permitting the phase composition vs. CBR value relationship to be studied.

Road subgrades are required to conform to certain specifications concerned mostly with the density to be attained on a particular job. The density required can be attained, however, only within a certain range of moisture contents, so that the phase composition of a subgrade in the condition meeting the specifications can be allowed to vary within a rather narrow range. It will be realized therefrom that the strength of such soils depends substantially on the type of the soil. Thus, considering, exclusively the soil condition meeting the specifications related to placement, an empiric relationship can be established between the soil type and the strength properties, such as the CBR value, modulus of subgrade reaction, etc. One of these relationships is illustrated in Fig. 367 which can be used to advantage in preliminary estimations.

The tests described in the foregoing, namely the plate bearing and the CBR test, are rather time consuming and cumbersome and thus expensive. This is the reason for the great demand for methods permitting the bearing capacity of a road, or of individual pavement courses to be checked and occasional weak sections rapidly detected. For such purposes, a modified version of the Benkelman rod test was introduced in Hungary (BOROMISSZA and GÁSPÁR, 1956; 1968). From the results of detailed investigations, they arrived at the conclusion that under normal traffic loads, the permanent deformations suffered by a pavement remain small enough to be neglected; the behaviour of the pavement is perfectly elastic and the deflections are proportionate to the load in the greater part of the year. Once these assumptions are accepted as valid, no more than the elastic rebound of the pavement upon relieving the load becomes necessary.

The measurement procedure involves the stationing of a loaded truck, with dual wheels, on the pavement to be tested

and positioning the cantilever arm of the device between the dual wheels (Fig. 368). A reading is taken on the dial gage, whereafter the truck is driven forward. A second reading is taken and the elastic deflection of the pavement is computed from the difference between the two readings. The results of measurements performed at successive points along the pavement are plotted in a profile (Fig. 369) which provides a clear picture about its load-bearing capacity.

4.4.2 Properties of road-building materials

Unfortunately, the information available at present on the strength and deformation properties of the materials used for the diverse courses of pavements is rather incomplete. The determination

Table 31. Modulus of elasticity for different road constructing materials (MN/m²)

Material	E
Asphaltic concrete	280-300
Concrete slab, paving stone	250-280
Sand asphalt	220-240
Macadam	200-220
Coated macadam	150-200
Crushed stone course	140-180
Stone sett, monolithic paving	150-170
Surface treated macadam	120-140
Water bounded aggregate	80-120
Stony bedding course	80-115
Gravelly subbase	80-100
Cement stabilized well graded earth material	60- 90
Bitumen stabilized well graded soil	55- 80
Well graded soil-aggregate	40- 65
Gravelly sand	40- 60
Cement stabilization	40- 60
Bitumen stabilization	35- 50
Silty coarse sand	35- 40
Coarse sand	30- 40

of the conventional strength properties, namely compressive, or tensile strength, is insufficient, since in these tests the state of stress of the sample differs from that in an actual pavement. Moreover, the actual loads are dynamic in character, so that the behaviour under transient load will be decisive. For general information, the normal ranges of deformation characteristics are compiled in Table 31, while for strength properties reference is made to appropriate manuals. The behaviour of road pavements under dynamic loads will be dealt with in Chapter 6.

4.5 Pavement design

4.5.1 Pavement design on the basis of deflection

The most important characteristic of a flexible pavement is its deflection which determines its performance. A simple pavement design procedure, based on deflections, has been proposed by BURMISTER (1943). In it, the surface course, base course, and subbase (AASHO Highway Definitions)

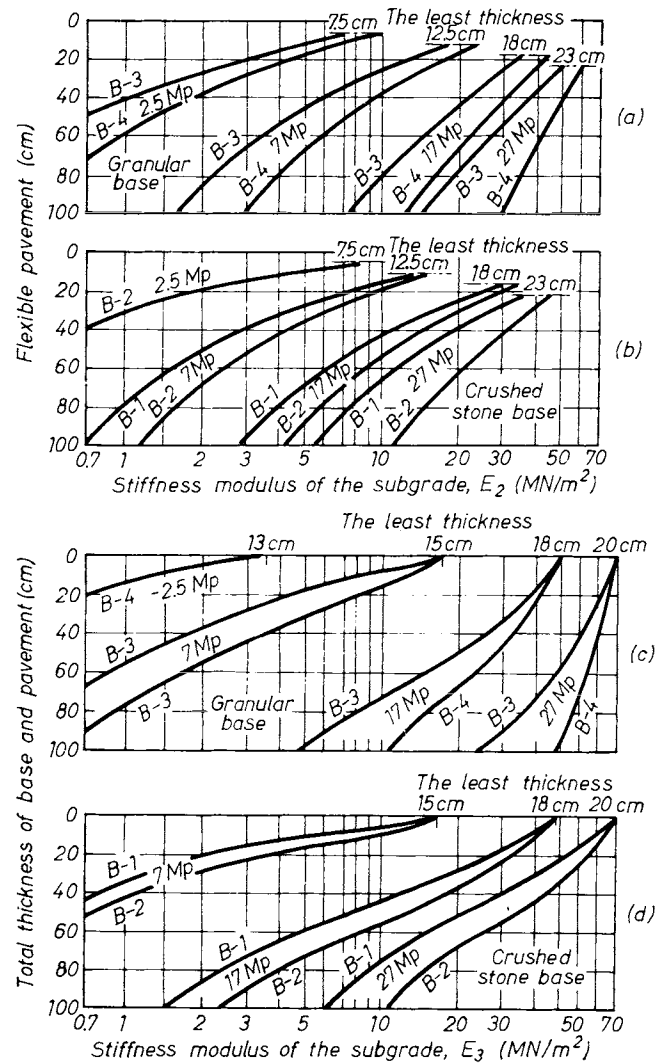


Fig. 370. Design diagrams from BURMISTER (1943)

are compiled into and treated as one layer, and the subgrade is the other layer. Design thickness will be determined on the basis of an allowed maximum 5 mm of deflection. Design charts have been produced using influence factors referring to expected deformations. These graphs are reproduced in Fig. 370a and b.

For the design of rigid pavements, the procedure above has been improved to take the performance of three layers into account — pavement, subbase and subgrade. The necessary thickness of the concrete slab is determined by using partly empirical methods based on allowable stresses caused by the wheel load and additional influences. The thickness of the subbase is determined in order to restrict the deflection of the slab to a maximum of 1 mm. Design curves can be seen in Figs 370 a-d. The set of curves a and c refer to subbases made of gravels, and b and d to crushed aggregates. Indications B-1, B-2, etc. refer to quality, B-1 being

the best, extremely well-compacted aggregate of $E_2 = 700 \text{ kN/m}^2$; B-2 a well-compacted good material of $E_2 = 350 \text{ kN/m}^2$; B-3 a well-graded gravel after careful compaction of $E_2 = 200 \text{ kN/m}^2$; and curves B-4 represent a well-compacted intermediate material of $E_2 = 100 \text{ kN/m}^2$. The modulus of elasticity has been calculated with $E_1 = 21 \text{ MN/m}^2$.

The above described procedure is oversimplified, however, because:

- (a) neither the pavement nor the subbase is fully elastic;
- (b) arbitrary deflection limits were assigned and the actual stresses ensuing remain unknown;
- (c) no representation is given for the repetition and dynamic character of the load.

Another design procedure — which is in use in the U.S.A. and is called the “Navy” procedure — applies also the stress and deflection principles established by BURMISTER.

We have seen earlier that the settlement of a circular rigid plate on homogeneous, isotropic ground surfaces is given as: $y = 1.18 pr/E_2$, and that of a flexible plate as: $y = 1.5 pr/E_2$. To render these formulas applicable in a two-layer system, a coefficient has to be introduced (called the settlement ratio):

$$y = \frac{1.18 pr}{E_2} \bar{\delta}$$

This coefficient, as we have seen, is a function of E_1/E_2 and r/h . E_2 will always be determined on the field by using the plate bearing test (plate diameter $d = 75 \text{ cm}$). The plate should be made absolutely rigid by using insert plates. A similar plate loading test has to be performed on the surface of a previously made pavement of known thickness that has been constructed from the same (or identical) materials as the designed one. E_1 can be calculated from the above formula. When both E_1 and E_2 are known, the way is open to calculating stresses and deformations.

An example will be inserted here to make the procedure more familiar. A pavement is to be designed for accommodating a wheel load $p = 23 \text{ Mp}$ ($= 230 \text{ kN}$). Assumed tire pressure is 10 kp/cm^2 ($= 1 \text{ MN/m}^2$), and so the imprint area is $F = 2300 \text{ cm}^2$ with the radius of the substitutive circle of $r = 27 \text{ cm}$.

Having carried out the plate test on the formation level, we obtain say, $y = 0.5 \text{ cm}$ depression at $p = 1.6 \text{ kp/cm}^2$ pres-

sure. The modulus of elasticity of the soil will then be:

$$E_2 = \frac{3}{8} \frac{pr\pi}{y} = \frac{3}{8} \frac{1.6 \cdot 37.5 \cdot \pi}{0.5} = 142 \text{ kp/cm}^2, \\ = 14.2 \text{ MN/m}^2.$$

A similar experiment should be made on the surface of a pavement of known thickness and of similar material to the designed one and resting on a subgrade with similar attributes (see Fig. 371). From these results we can find the coefficient $\bar{\delta}$:

$$\bar{\delta} = \frac{E_2 y}{1.18 pr} = \frac{142 \cdot 0.5}{1.18 \cdot 3.2 \cdot 37.5}$$

To proceed further we now have to plot the Burmister diagram in the function of r/h as it is in Fig. 372. In our case $r/h = 37.5/15 = 2.5$, and at $\bar{\delta} = 0.5$ we can find the corresponding value $E_2/E_1 \sim 100$, i.e.:

$$E_1 = 100 E_2 = 14200 \text{ kp/cm}^2 = 1420 \text{ MN/m}^2.$$

Now we know E_1 and E_2 , and go on to calculate the settlement ratio for the given loading area:

$$y = 1.5 \frac{pr}{E_2} \bar{\delta}; \bar{\delta} = \frac{E_2 y}{1.5 pr} = \frac{142.0 \cdot 0.5}{1.5 \cdot 10 \cdot 27} = 0.175.$$

With $\bar{\delta} = 0.175$ and $E_2/E_1 = 1/100$, from Fig. 372 we can read $r/h_1 = 0.7$. The desired pavement thickness is therefore: $h_1 = r/0.7 = 27/0.7 = 38.5 \text{ cm}$.

In extremely important cases nine trial sections should be constructed, each 5 m long, with pavement thicknesses of $0.66 h_1$, h_1 , and $1.5 h_1$. Three sections should be situated in cuts, three on embankments and three on sections where the longitudinal alignment is close to the ground surface and where only grubbing and scraping are envisaged. The plate for the loading test should have a diameter as close to that of the imprint area of the loaded wheel as possible. A load is then applied on the plate corresponding to the effective tire pressure, which was $p = 1 \text{ MN/m}^2$ in our example above, and deflections measured. Such results are summarized in the table below:

		Thickness h_1 (cm)	Deflection y (cm)	Reduction factor	Reduced deflection y_m (cm)
Fill	1	25.6	0.59	1.43	0.84
	2	38.5	0.42		0.60
	3	57.6	0.30		0.43
Cut	1	25.6	0.685	1.16	0.80
	2	38.5	0.482		0.56
	3	57.6	0.325		0.38
Ground surface	1	25.6	0.507	1.48	0.75
	2	38.5	0.338		0.50
	3	57.6	0.210		0.31

The last column in the table shows reduced deflections. This modification is to allow for the possibility of moisture uptake in the subsoil and it will be established in the following manner. Compaction tests are carried out and optimum water content and maximum dry bulk density determined for the soils to be tested. Samples 5 cm in diameter and 10 cm high then be prepared from the compacted soil at w_{opt} and at w_{opt} plus 2% water contents,

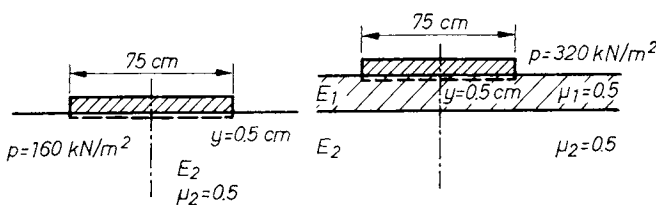


Fig. 371. Plate loading tests for pavement design

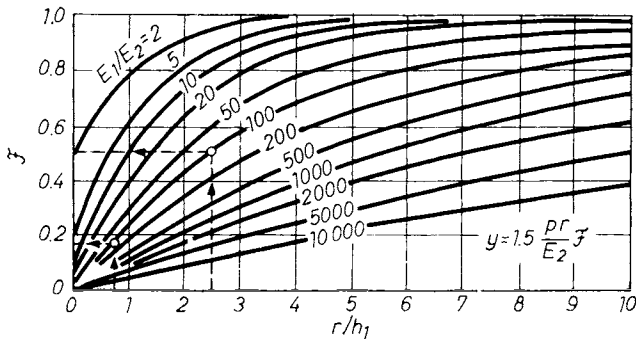


Fig. 372. Influence factors for deformations (after BURMISTER, 1943) as functions of r/h

all compacted to densities of $T_{ry} = 0.95$. The ratio of relevant compressive strengths will represent the reduction factor. The reduced deflection values are then plotted according to Fig. 373; pertinent pavement thicknesses can be read as functions of allowed deformations. In our case $h_1 = 36$ cm, and $h_1^{red} = 45$ cm.

A comprehensive description of McLeod's method must be given to illustrate the progress made in ideas concerning pavement design. This procedure is also based on the plate-loading test, and makes use of the following experience. If a pavement is repeatedly loaded by various weights then a separate deflection curve can be drawn through each load repetition (Fig. 374a). Experience has shown that for any arbitrarily chosen deflection, with various load repetition numbers the ratio of pertinent loads will be a constant value. The ratios given in the figure relate to a certain range of loads only.

The graph in Fig. 374b represents another experience, namely that the ratio of the loads causing $y = 0.88$ cm and $y = 1.25$ cm deflection with $N = 10$ repetitions, is constant.

Harmonizing these two experiences, the diagram in Fig. 374c has been derived. Using this diagram,

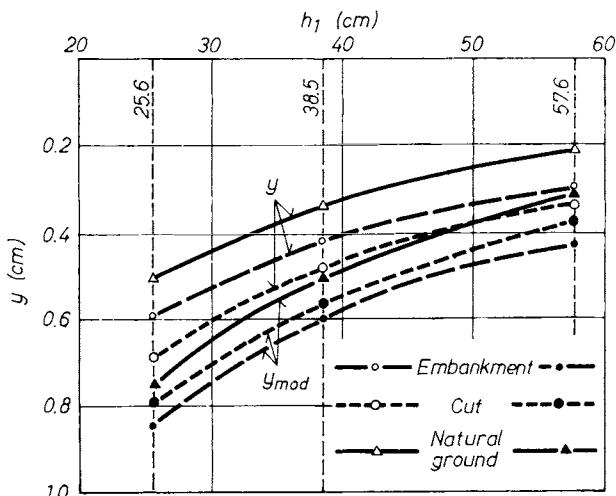


Fig. 373. Definition of final pavement thickness with the help of experimental sections

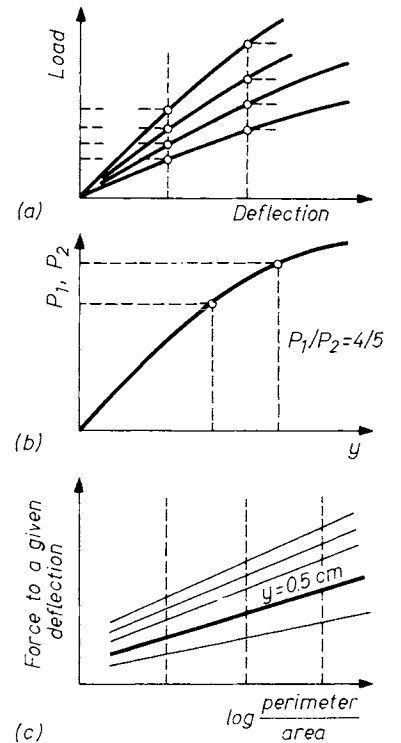


Fig. 374. a — Deflection as a function of load repetition; b — experimental loading diagram; c — design diagram

a quantity can be determined which will characterize the bearing capacity of the ground. Total structure thickness is then found from the expression:

$$h = K \log \frac{P}{S}. \quad (497)$$

K depends on the diameter of the plate used for the test (if $d = 75$ cm, $K = 65$; if $d = 30$ cm, $K = 35$). P is the equivalent wheel load (in $kp = 10$ N), and S is the load which causes a specified deflection with a number of repetitions of $N = 10$ (its value can be read from Fig. 374).

4.5.2 Pavement design on the basis of the CBR-value

In the past there were different sets of curves in use to design pavements on the basis of the CBR-value. The experimental formula to describe the curves was written as:

$$h = 1.33 \sqrt{\frac{P}{\text{CBR}\%} - \frac{P}{5.52 P}} \quad (498)$$

where h is in the necessary thickness of the load bearing layer (cm); P is the wheel load (in $Mp = 10$ kN); and p is the tire pressure (in $kp/cm^2 = 100$ kN/m²). The formula is valid up to $\text{CBR} = \text{maximum } 12\%$.

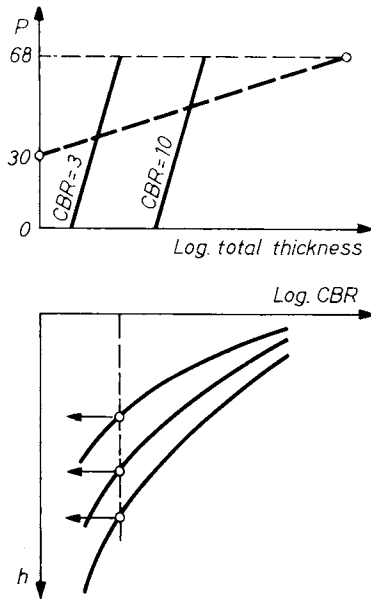


Fig. 375. Elaboration of design curves

The following relations are now available: for identical tire pressures

$$h_2 = h_1 \sqrt{\frac{P_2}{P_1}}$$

and when the wheel load and the CBR are identical

$$\frac{1}{p_1} \frac{1}{p_2} = h_2^2 - h_1^2.$$

Table 32. Constants for the calculation of the CBR-curves (1 psi = 6.89 kPa, 1 lb = 0.45 kg)

1. $\log h = k_{00} + k_{01} \log P + k_1 \log \text{CBR}$

	$p = 100 \text{ (psi); } P \text{ (lb)}$				$p = 200 \text{ (psi); } P \text{ (lb)}$	
	Taxiway		Runway		Runway	
	$h \text{ (cm)}$	$h \text{ (in)}$	$h \text{ (cm)}$	$h \text{ (in)}$	$h \text{ (cm)}$	$h \text{ (in)}$
k_{00}	+0.085	-0.320	+0.039	-0.366	-0.046	-0.451
k_{01}	+0.477	+0.477	+0.477	+0.477	+0.500	+0.500
k_1	-0.566	-0.566	-0.566	-0.566	-0.538	-0.538

2. $\log h = (k_{00} + k_{01} \log p) + (k_{10} + k_{11} \log p) \log (\text{CBR} + 1) + 0.5 \log P$

	$P \text{ (lb)}$			$p \text{ (psi)}$	
	$h \text{ (cm)}$	$h \text{ (in)}$		$h \text{ (cm)}$	$h \text{ (in)}$
k_{00}	+0.403	-0.002	k_{01}	-0.138	-0.138
k_{10}	-1.202	-1.202	k_{11}	+0.244	+0.244

A newer expression has been proposed by NOVAIS FERREIRA and CAMPINOS (1961):

$$\left. \begin{aligned} \log h &= k_{00} + k_{01} \log P + k_1 \log \text{CBR} \\ \text{and} \\ \log h &= (k_{00} + k_{01} \log p) + (k_{10} + k_{11} \log p) \cdot \log (\text{CBR} + 1) + 0.5 \log P. \end{aligned} \right\} (499)$$

The values of the constants k are given in Table 32. Figure 375 offers an insight into the way in which the design curves mentioned have been elaborated. The relation between the wheel load

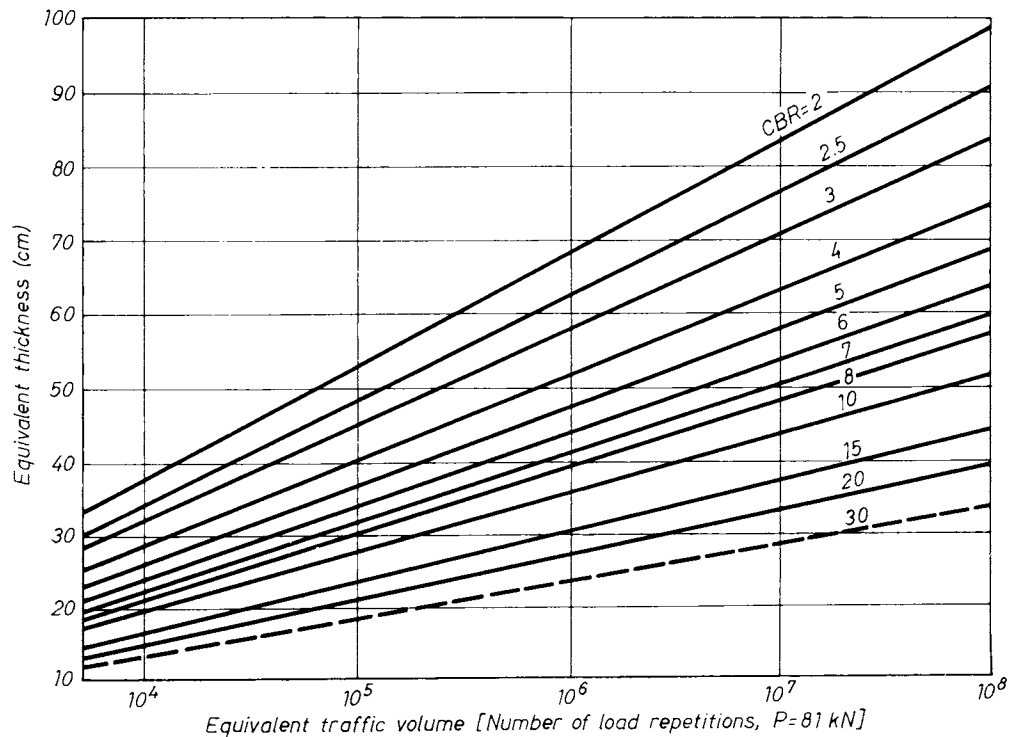


Fig. 376. Design diagram for determination of equivalent thickness

and the thickness of the base plus the subbase are plotted to different CBR-values; the plot shows straight lines when double-logarithmic paper is used. Methods have also been elaborated which enabled drawing the design curves for arbitrarily arranged wheel systems.

Later progressive design methods also took account of traffic distribution patterns along the road with, and the volume of traffic. PELTIER (1955), for example, proposed the following expression:

$$h = \frac{100 + 150 \sqrt{P} \sqrt[10]{\frac{T}{T_0}}}{\text{CBR} + 5} \quad (500)$$

In this expression, T_0 is a base value 100 000 Mp/year (= 1000 MN/year) for a 1 m-wide strip on the pavement surface, and T is the actual value.

SHOCK and FINN (1963) elaborated another expression for asphaltic pavements. First an equivalent thickness is defined as:

$$h_e = 2 h_1 + h_2 + 0.75 h_3,$$

where h_1 represents the thickness of the asphaltic concrete, h_2 that of the load-bearing layer, and h_3 that of the subbase. This value can be obtained for $\text{CBR} = 2.5\%$ from the following equation:

$$h_e = -20.5 + 5.35 \log n + 0.669 P + 0.0932 Pp, \quad (501)$$

where n is the number of load repetitions, P is the load (in 1000 pounds = 4.5 kN), $p = 1$ for single wheels and $p = 0$ for twin wheels.

For the same pavement structure under two different single loads (one of $P = 18$ kip = 81 kN, and the other of wheel load P) an equation can be written, using Eq. (501):

$$5.53 \log n_{18} + 0.669 \cdot 18 = 5.53 \log n_p + 0.669 P$$

and so

$$5.53 \log \frac{n_{18}}{n_p} = 0.669 (P - 18)$$

and

$$f = \frac{n_{18}}{n_p} = 10^{0.121 (P - 18)}. \quad (502)$$

This expression can then be used for design purposes. Figure 376 illustrates the relevant diagram. The second upper line refers to $\text{CBR} = 2.5$; for other CBR-values the pertinent pavement thickness can be found from:

$$h = [-20.5 + 5.53 \log n + 0.691 P + 0.0932 Pp] \left(\frac{2.5}{\text{CBR}} \right)^{0.4} \quad (503)$$

As can be seen, the influence of load repetitions plays a considerable role in these — fairly complicated — experimental expressions.

The following section aims to shed some information (after YODER, 1959) on the performance of some constituent parts of the pavement structure.

Concrete definitely has the property of showing fatigue. Generally, it is supposed that only half of the failure strength might be considered as a long lasting strength of the concrete. Up to this value the concrete can, however, be exposed to load repetitions to an unlimited number. The failure strength of the concrete is normally proportional to the logarithm of the number of repetitions.

Of fatigue in concrete finds, however, its real importance when it is correlated with the fatigue of the subsoil. If the subsoil is a plastic one, its gradually increasing deformation may bring the repeatedly loaded concrete pavement to failure even before the normally assumed fatigue limit ensues. The fatigue of concrete may gain importance in the case of an elastic subsoil where residual deformations are negligible.

The subbase is also exposed to harmful effects under the influence of repeated loading. Some particles of lesser strength may crumble and depreciate this way the grain distribution curve, and consequently also the bearing capacity of the layer. The increasingly greater compression may also evoke the pumping effect.

Repeatedly loaded soils undergo an increased compression, the magnitude of which is proportional to the logarithm of the repetition number (Fig. 377). Flexible pavements mostly fail in spring (tawing!), and hardly in summer, when they are exposed to repeated loads. One interesting

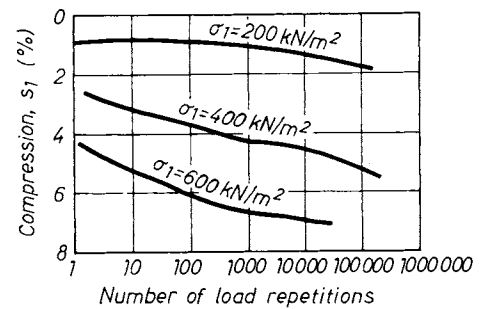


Fig. 377. Compression of clay under repeated loading

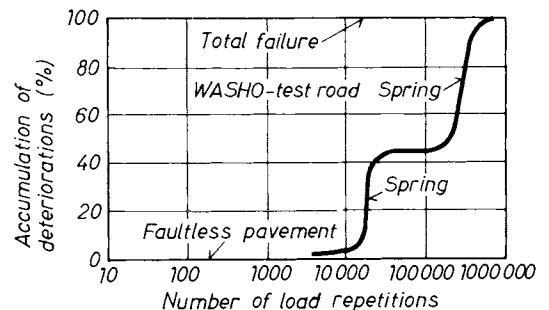


Fig. 378. Deterioration of flexible pavements under the influence of repeated loadings

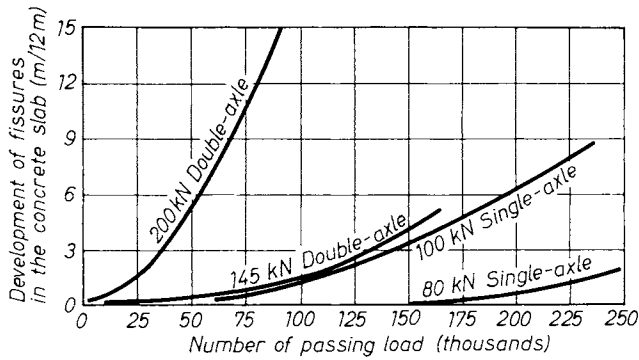


Fig. 379. Development of fissures in rigid pavements as the result of repeated loading

result of the Washo-experimental test is shown in Fig. 378.

Rigid pavements supported immediately by plastic subsoils show almost always the pumping effect when they are submitted to heavy traffic. Granular subsoil or subbase shows a similar effect when the compaction was not made satisfactorily. Fissures and cracks start to develop and advance in number (Fig. 379). Obviously, drainage, temperature, and the condition of the pavement surface have also an important role in this respect.

4.6 Drainage, swelling and shrinkage of the subsoil

The soil layer supporting the pavement is often directly exposed to atmospheric influences. Owing to a variety of effects, the water content may vary between rather wide limits, giving rise to swelling and shrinkage in soils susceptible to volume changes. Moreover, since this change in volume is non-uniform, owing to the heterogeneity of the soil and to other reasons, the bedding of the pavement will also become non-uniform and the external forces acting, e.g. on unsupported parts of the pavement will cause failure and damage. The situation is aggravated by the fact that even slight changes in moisture may cause substantial changes in the bearing capacity of some soils and thus local changes in soil moisture conditions under road pavements may be of considerable influence on road traffic.

The stabilization and control of the condition of road foundations should be considered taking account of all factors affecting moisture movement in the soil. For this reason, the ways must be considered through which water can find access to the soil layer under the pavement. Water may enter from the sides and from below. The possibilities are illustrated in Fig. 380.

Although the penetration of water from above may well be regarded as the most important of these possibilities, it can the most readily be controlled and prevented.

Although the importance of drainage is clearly appreciated by road building engineers — it is proverbial that the three secrets of sound road construction are 1. drainage, 2. drainage, and 3. drainage — it may be well to recall the experience of McADAM: "... The roads can never be rendered thus perfectly secure, until the following principles be fully understood, admitted upon: namely, that it is the native soil which really supports the weight of the traffic; that whilst it is preserved in dry state it will carry any weight without sinking... that if water pass through a road and fill the native soil, the road, whatever may be its thickness, loses support and goes to pieces." (McADAM, I: "Remarks on the present system of road making" London, 1820, 3rd edition, p. 51.)

The penetration of water from the sides presents a more difficult problem. The side ditches that are called upon to collect and remove the surface runoff without damage, may themselves become damaging when blocked or silted up whereby stagnant water can infiltrate into the subsoil, and cause the pavement to deteriorate. It should be realized, however, that a significant portion of the runoff water will anyway find access to the subsoil, before reaching the culvert, even if the ditches are maintained in perfect condition.

From the foregoing the conclusion may be arrived at that preventative measures against the detrimental effects of volume changes are needed even when the water table is located at greater depth.

In the case of roads during rainy weather the top layer of the subsoil becomes saturated and unless controlled, a soft clayey layer of a few cm thick may cause serious damage to the pavement. Rain water seeping across pervious pavements may, logically, have similar consequences.

Careless or poor maintenance may often be responsible for the complete saturation of the subsoil.

A special phenomenon particular to concrete pavements has only recently come to the attention of road-building engineers. The passing vehicles cause the concrete slabs to suffer elastic deformations resulting in a deflection under the load and a slight upwarping at some distance therefrom. The suction exerted by this vertical reciprocating movement tends to lift water from the deeper soil layers as if pumped, towards the pavement. This water then accumulates in the top layer of the subsoil, the soil is remoulded with water by the pumping and the liquid soil is forced to the surface through joints and cracks. The load-bearing capacity is thereby rapidly reduced. In some instances this phenomenon has been observed a few years

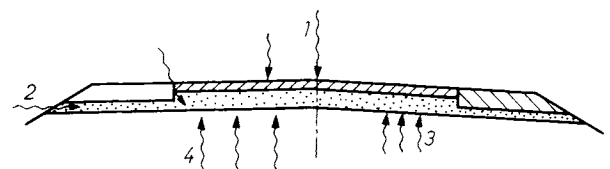


Fig. 380. Water infiltrating in the subgrade: 1 — at joints; 2 — from the inner slope; 3 — via capillarity; 4 — rising flow due to increased head pressure

after a road was completed, especially if, during a certain period, it was called upon to carry traffic of greater weight and volume than normal. Pavements constructed on readily saturating soils are especially susceptible to this effect. The plasticity index (I_p) of such soils ranges from 5 to 10%, they contain low percentages of silt and clay fractions and the influence of their mineral composition is also conceivable as a contributory factor. Another important cause of pumping is insufficient pavement thickness, resulting in great deflections. The provision of a perfect, well-compacted subbase and careful dimensioning are suggested as preventive measures.

Once entered into the soil, the water will continue to move owing to a variety of factors, until a state of equilibrium is reached. Reference is made here not only to the seepage of water proper, but also to the movement of vapour, due to evaporation within the soil which condenses and precipitates under some parts of the pavement. Regular moisture observations in the subsoil of cohesive soils have invariably revealed much higher moisture contents at the centerline under the crown than towards the sides where drying is much more effective. Under pavements constructed on sand where the effect of capillarity is insignificant, this phenomenon was much less pronounced (Fig. 381). This may be offered as an explanation for cracks parallel to the centerline in concrete pavements constructed without soil treatment.

Concerning the movement of water under pavements, mention must be made of the investigations by CRONEY (1952), who has succeeded in clarifying some fundamental problems associated with the migration of "bonded" water. The experimental results were processed in terms of the capillary force pF introduced by SCHOFIELD which is the logarithm of the suction force — that is to say, negative hydraulic pressure — expressed in cm of water column. This value is thus a measure of the force at which water is absorbed by a particular soil. At the saturation limit this value is zero, while in the perfectly dry state it is very high.

In the case of moisture differences in a uniform soil, a suction gradient is created, which tends to re-establish equilibrium conditions. Even at equilibrium moisture contents the actual water content of different soils may differ appreciably. Differences in vapour pressure give rise to similar effects, but these are functions of temperature differences. The pF value is also dependent on temperature and as a resultant effect of these factors, the migration of moisture in the soil will eventually lead to the

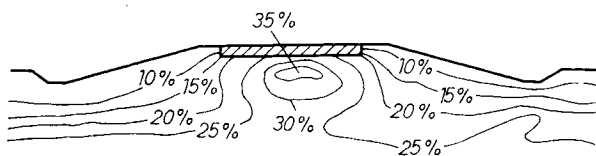


Fig. 381. Moisture distribution below the pavement

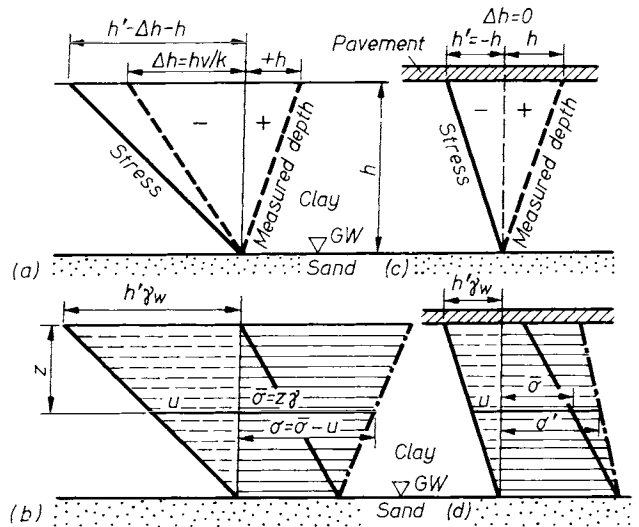


Fig. 382. Stresses in a clay layer:

a — and b — free evaporation at the surface; c — and d — evaporation extruded through the covering courses

distribution shown in Fig. 381. Daily and annual changes in temperature induce a vapour pressure gradient causing the upward movement of water, usually in the form of vapour. Cases have been observed where the pavement has failed as a consequence of the high moisture content in the subgrade, although the climate was very dry with very little annual rainfall. This phenomenon can be attributed to the sole fact that the water was raised in the form of vapour and by condensing under the pavement it has saturated the soil.

Another factor is the heat of hydration generated in the soil upon wetting. Water migration in the soil may be influenced finally by consolidation due to the stresses induced by the traffic.

In cohesive soils the suction effect may be large enough to make the removal of water from the subgrade by gravity alone impossible, since the gravitational drawdown which can be created by means of drain pipes located at small depths [barely attains 10 to 20 kN/m². Therefore, the primary objective should be to prevent water from entering into the soil, since the removal of water which has already entered may often be found impossible.

In cohesive soils any change in moisture is necessarily accompanied by a change in volume. Let us consider the mechanism involved in this process. The starting assumption is that any volume change must be produced by a change in the effective stresses.

A vertical section through the pavement and the subgrade is shown in Fig. 382. Assume the ground-water table to coincide with the bottom of the clay layer. In the original condition prior to the construction of the pavement — Fig. 382a — water is evaporated at the surface at the rate of v (cm³/day/cm² = cm/s). Water is supplied to the clay layer from below and in the case of $v = \text{const.}$ — steady evaporation — upward seepage will be induced

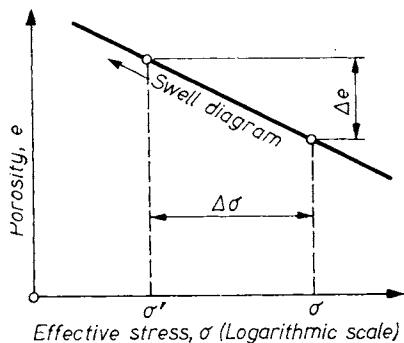


Fig. 383. Determination of swell with the help of the test curve

thereby at the rate v . Any water movement is accompanied by seepage pressures (cf. Vol. 1, Section 5.2). From Darcy's law, the velocity of flow is

$$v = ki; i = \Delta h/h;$$

$$\Delta h = h \frac{v}{k}.$$

The effective stress due to seepage is $+\Delta h\gamma_w$. With the datum plane at the groundwater table, the potential energy is given as $h\gamma_w$. The pressure conditions are indicated in Fig. 382a.

The upward seepage is interrupted by the placement of the pavement. The differential head in the entire layer then necessarily becomes zero (Fig. 382b). If the neutral stresses are known, the effective stresses can be computed, in that the neutral stresses are subtracted from the total stress with due allowance for their sign. The total stress is due to the dead weight. The state of stress has thus been clarified, and it will be realized therefrom that the

effective stress has decreased by $\Delta\sigma$, so that swelling is bound to occur. The extent thereof can be determined from the expansion curve (Fig. 383). The effective stress is reduced by preventing evaporation, i.e. by the construction of the pavement, and this will lead to swelling without any further external effect. The time history of the process resembles that of consolidation.

Actual conditions are much more complicated. Nevertheless, we have succeeded in demonstrating that swelling may be induced by covering a clayey layer. The actual conditions are represented in Fig. 384, where the stress diagrams have been constructed for dry weather, for conditions following a storm, during the process of swelling, in saturated conditions, and finally in the state prevailing with swelling has terminated.

Owing to the number of factors involved, the liability of volume changes is usually assessed by empirical methods. The criterion for the need of control measures is the linear shrinkage of the soil; once this exceeds 5%, the soil is considered expansive and control measures must be envisaged. This empirical rule of thumb has been found applicable to the majority of cases.

The main principle in controlling the undesirable effects of volume changes is to avoid the presence of expansive soils directly under the pavement and further to design the road cross-section in such a way as to confine moisture changes in the subgrade to a narrow range.

As regards fills, care should be taken to avoid the placement of expansive soils around the top of the embankment. Where no appropriate soils are available from cuts or borrow pits, the expansive soil must be mixed with a suitable, granular material. The mixing ratio should be determined by laboratory tests. Where no mixing is practicable,

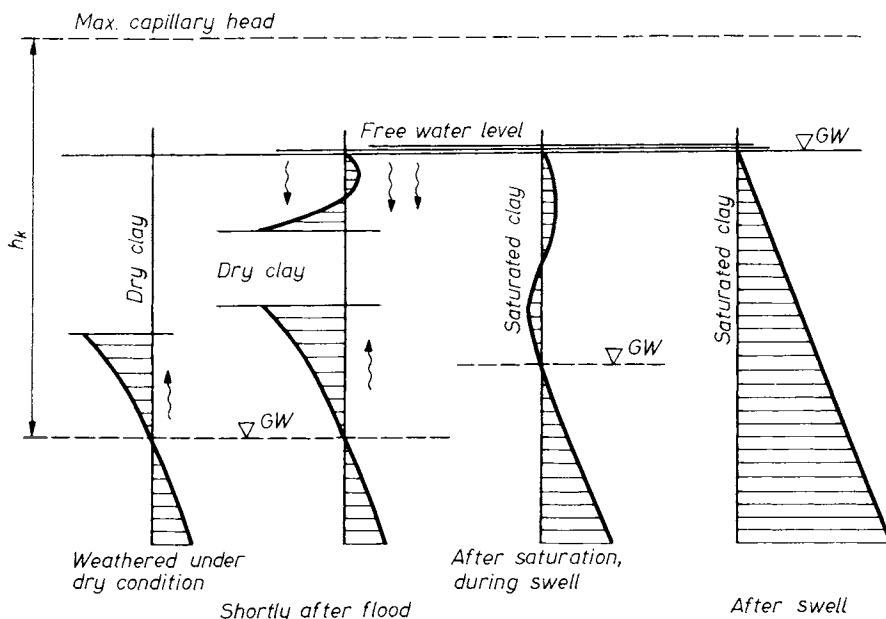


Fig. 384. Stresses in a clay layer under actual conditions

which contingency is liable to occur mainly in cuts, a subbase will become necessary under the pavement. The function thereof is to maintain the moisture content of the underlying expansive soil at a constant value. For this reason, the subbase must consist of pervious soil, expediently of sand, with a silt content not exceeding 3%. The subbase is called upon to provide rapid drainage of the water infiltrating from above, thereby preventing non-uniform saturation of the subgrade; likewise, in the case of moisture migration from below, it should provide uniform support to the pavement by eliminating or distributing minor volume changes. The surface of an expansive subgrade should be finished with slopes of 2 to 4% in both directions, compacted carefully by means of a smooth roller, to facilitate the rapid drainage of infiltrating water. The correct design of shoulders is also of importance. These should be made of impervious, but non-expansive, lean silt. The bottom depth of the side ditches is also an essential factor. Great care should be devoted to preventing the entrance of water under the pavement from a side ditch even if some silt is deposited in the ditch.

The arrangement of the filter layer applied to control volume changes in the cross-section is exemplified in Fig. 385a. Concerning the design of the cross-section, it should be noted further that the edges of the filter layer should be supported by a gravel strip to prevent it from scouring. Another arrangement, suggested by JÁRAY, is shown in Fig. 385b.

For the filter layers to be effective, the permeability of the filter medium must be higher than the rate of infiltration, otherwise the filter layer will become saturated, drastically reducing the bearing capacity of the pavement structure under high impact loads. In a saturated condition the filter layer, which at the same time serves as the subbase, will fail to distribute the load, neutral stresses will be induced and wheel loads will be transmitted directly to the subgrade (Fig. 386).

The water which has entered the filter layer is drained laterally and a drawdown curve is developed. The drainage volume is computed as follows:

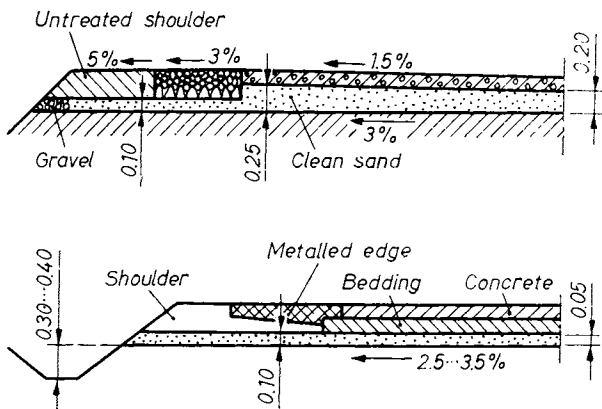


Fig. 385. Construction of filter layers

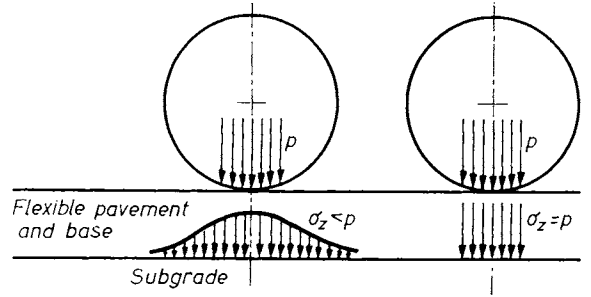


Fig. 386. Saturation of a granular subbase causes alteration in stress distribution

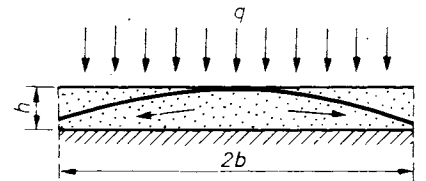


Fig. 387. Sideward movement of water in a filter layer

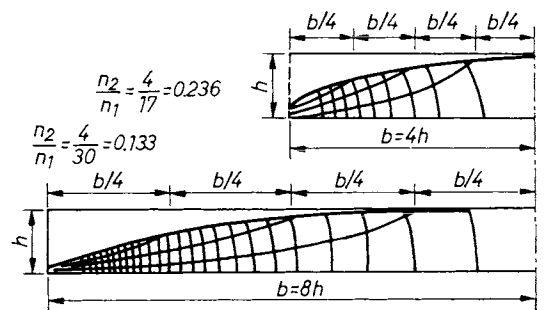


Fig. 388. Flow net diagram in the filter layer; finding the shape factor

The section through the filter layer is shown in Fig. 387. Water enters from above at the rate q , the subgrade is impervious. Under steady conditions, the volume $Q = qb$ must be drained in unit time. According to DARCY, $Q = kiF$. Here i is assumed to be proportionate to the ratio h/b , while the actual cross-sectional area is $1 \cdot h$. Consequently

$$Q \sim k \frac{h}{b} h = k \frac{h^2}{b}$$

The rate of infiltration being $q = Q/b$,

$$q \sim k \left(\frac{h}{b}\right)^2; \tag{504}$$

$$\frac{q}{k} \sim \left(\frac{h}{b}\right)^2$$

The above qualitative statement can be specified in quantitative terms as well, by constructing flow patterns for different h/b values and plotting the shape factors obtained against h/b . Two such flow patterns are illustrated in Fig. 388. The upper curve

is not a streamline, but the limit of saturation, where $u = 0$.

Using the familiar formula, the discharge conveyed is obtained as

$$Q = kh \frac{n_2}{n_1}; q = \frac{Q}{b} = k \frac{h}{b} \frac{n_2}{n_1},$$

or

$$\frac{q}{k} = \frac{n_2}{n_1} \frac{h}{b}.$$

In the case of thin filter layers $n_2/n_1 \sim h/b$ (Fig. 388), so that

$$\frac{q}{k} = \left(\frac{h}{b}\right)^2,$$

which means to say that Eq. (504) is suited to quantitative estimates as well. For particular values of h/b and k it is thus possible to determine the critical intensity q , or, if q is known, the filter layer can be dimensioned to provide the necessary drainage.

Consider for example the problem of draining a 1200 m long airport runway. Down to a depth of 2 m the subsoil consists of clean sand, underlain by impervious soil. The permeability of the sand is $k = 2 \cdot 10^{-2}$ cm/s. No drainage will be provided, unless $q < k(h/b)^2 = 2 \cdot 10^{-2} (2/600)^2 = 1.3 \cdot 10^{-6}$ cm/s.

For the practical details and design alternatives of drainage, reference is made to the book by KÉZDI and MARKÓ (1969).

4.7 Frost susceptibility of the subsoil

4.7.1 Introduction

Owing to the critical role of frost damage in road construction, it is deemed necessary to deal with the general problem of frost susceptibility in the subsoil in the context of highway soil mechanics, including also a brief description of the frost phenomena encountered with other structures as well.

In the case of roads, frost action is controlled by four factors, namely

1. meteorological conditions, climate;
2. soil and groundwater conditions;
3. traffic conditions;
4. quality of the pavement.

In general, significance is attributed to the first two factors only, although essentially frost damage becomes observable almost without exception as a consequence of traffic, its magnitude and extent depending on the type and quality of the pavement. This is the reason why the inclusion of such factors is also justified.

In the literature on soil mechanics two approaches have thus far been adopted for treating the

problem of frost damage. One avenue of approach is a purely empirical one, involving investigations into the frost damage observed. From the statistical processing and regular observations of frost damage, certain rules are evolved which serve as criteria for frost susceptibility. In the other approach, theoretical research and advanced mathematical methods are applied to explore the laws governing frost penetration in soils and the control measures are adjusted to the theoretical results obtained. In view of the semi-empirical approach particular to soil mechanics, each of the above methods is bound to remain ineffective if applied separately.

4.7.2 Meteorology

The meteorological characteristics of frost are duration of the freezing season and frost intensity. The former is understood to be the period of time between the first and last days with freezing temperatures within a season, during which periods of thaw may also occur. On freezing days the lowest daily temperature is below the freezing point, whereas on frost days the soil is frozen for the whole day, i.e. the highest daily temperature remains below freezing point. A freezing season may consist of several freezing periods, the latter being understood as an uninterrupted sequence of freezing days. Day with an average temperature below freezing point are termed cold and an uninterrupted sequence of cold days is referred to as a cold period. Frost intensity means the lowest temperature attained, while the average temperature in a cold period is the average intensity thereof.

These characteristics are influenced by the geographical situation and elevation above sea level of the location considered, further by the topography and the vegetation of the terrain.

For comparing freezing periods and freezing seasons, the total heat deficiency has been introduced as the product of the number of days within a freezing period and of the mean temperature and expressed in hours, or °C-days.

The variations in air and soil temperatures during the winter of 1939–40 in Budapest are shown in Fig. 389. The daily average temperature has been plotted in the upper part of the diagram, while the isotherms plotted against depth and time are shown in the lower part. The soil temperature is seen to follow the variations in air temperature with a certain time lag. At the end of the lower diagram thawing from above and from below is observable.

The average and extreme values of soil temperature have been plotted, on the basis of data for 20 years in Fig. 390.

Concerning frost susceptibility the total heat deficiency is of paramount significance. This is determined for a freezing period by plotting the days on the horizontal axis of a coordinate system,

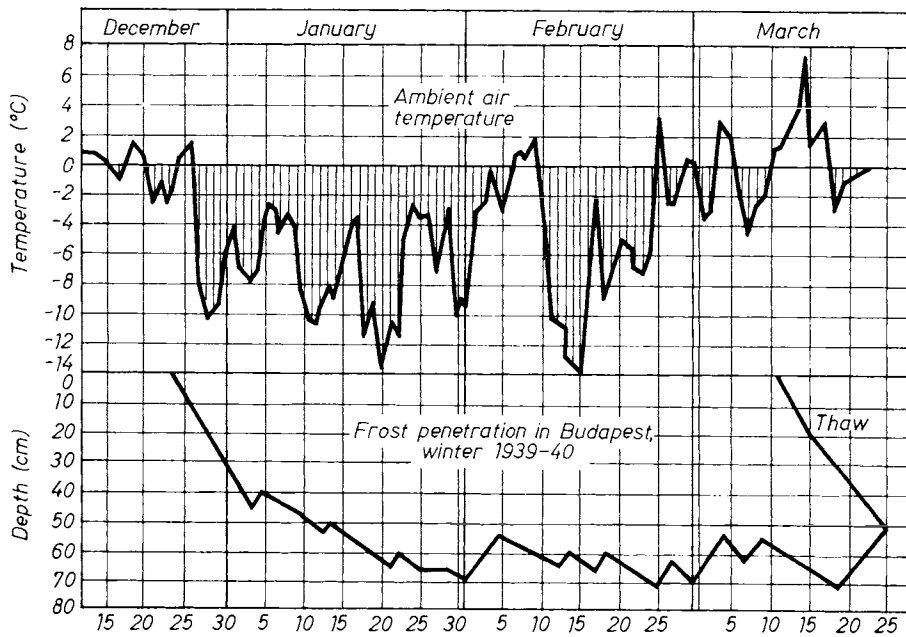


Fig. 389. Ambient air and soil temperature in Budapest during the winter 1939-40

while the daily average temperatures are plotted on the vertical axis.

The average value thereof at Budapest is 150°C-days, but the fluctuation about this average may attain considerable amplitudes in both directions.

Other important factors involved in soil frost studied are the volumetric heat c of the soil, defined as the amount of heat needed for raising the temperature of a 1 kg soil mass by 1°C. The magnitude thereof depends, in general, on temperature. The thermal conductivity λ is understood to be the amount of heat transferred across a soil layer 1 cm thick at a differential temperature of 1°C during one hour. The product $c\lambda$ is called the volumetric heat capacity of the soil and is the amount of heat by which the temperature of one volume unit is raised by 1°C.

It is also usually found expedient to trace the integral curve of temperatures. From this diagram the freezing and thawing indices can be determined according to Fig. 391. Their magnitude is calculated either on the basis of the air-temperature (measured at a height of 1.35 m above the surface) or on that of the soil surface.

A problem of paramount importance in road-building is associated with the rate of frost penetration. Theoretical studies (e.g. JUMIKIS, 1955; SCHAIBLE, 1957; KLENGEL, 1968) have shown the soil temperature to vary according to the curves in Fig. 392 if the variation of the surface temperature follows a sine curve.

The results of practical interest derived from the theoretical studies is that the total heat deficiency and the depth of frost penetration are related by a power function, which plots as a straight line in a log-log system of coordinates. This conclusion has been verified by the statistical processing of mea-

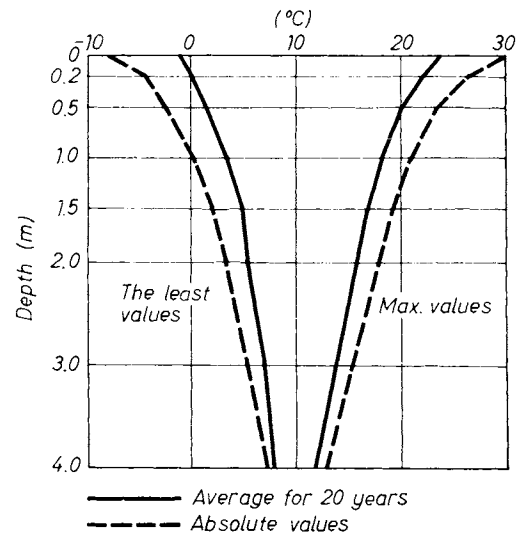


Fig. 390. Fluctuation of soil temperature with depth

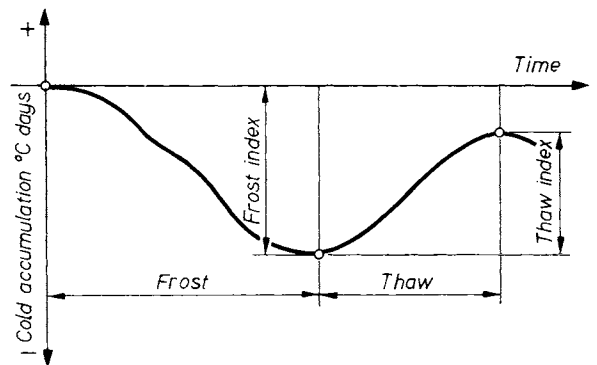


Fig. 391. Definition of frost and thaw indices

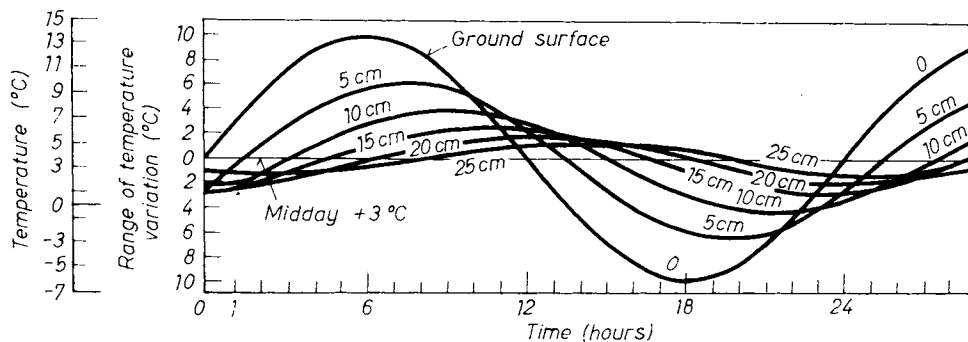


Fig. 392. Theoretical isotherms of soil temperature variation

surement data. The depth of frost penetration has further been found to depend on the freezing index, on the moisture content and the dry unit weight of the soil. From the observation data detailed charts have been constructed (cf. Fig. 393, U.S. Army, Eng. Div.).

Measurement data from Hungary and other countries were collected and processed by GÁSPÁR (1959) and plotted in the diagram shown in Fig. 394, without taking the properties of the subgrade into consideration. The diagram represents the relationship between the depth of the 0 and -2 °C isotherms and the total heat deficiency.

4.7.3 Forms of ice segregation in the soil

Depending on the hydrological and meteorological conditions prevailing, as well as on the type of soil, the water on the surface or within the soil may freeze in a variety of forms.

The case of mass freezing is the most simple of these. In this case the entire mass of the saturated soil freezes, the individual particles being surrounded by ice crystals. This form of freezing is observable in sands and gravels whereas in cohesive soil it occurs only under circumstances when the cooling rate is high enough to provide no opportunity for water migration in the soil. Virtually the entire water volume present in the pores of such soils is freely draining, the freezing thereof controlled by the laws applying to normal, Newtonian water. Freezing is thus not accompanied by changes in the soil structure and the original bearing capacity is retained, even in the case of thawing, consequently no hazards are caused to the pavement or to other structures.

In so far as the volume changes associated with mass freezing are concerned, a distinction must be made, according to BESKOW, between saturated and three-phase soils. No volume change occurs in

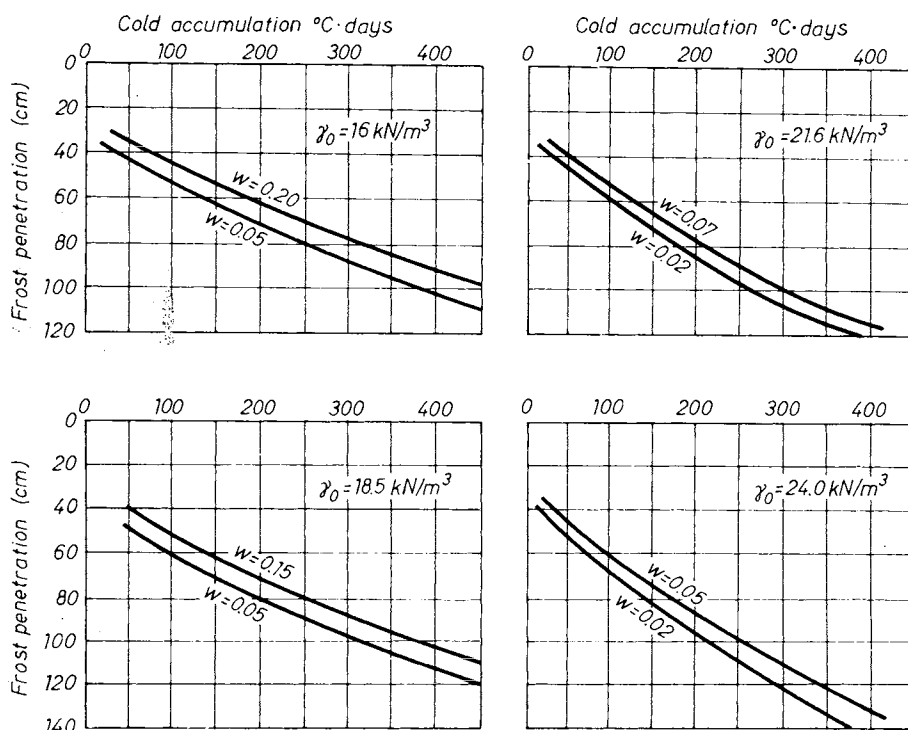


Fig. 393. Frost penetration as a function of accumulated cold hours (heat deficiency) for various soil conditions

the first case if the soil affected by frost penetration communicates with the unconfined groundwater, since the water volume which has become excessive in the soil on account of expansion due to freezing is displaced towards the groundwater. In three-phase soils the interstitial water is situated around the contact points of the soil particles. As long as the pressure acting on the soil is low, this water will freeze in the form of ice crystals, accompanied by a slight expansion.

In the course of mass freezing the water content in the soil remains unchanged.

The frost action most critical to road building is the formation of ice lenses. Exploring and investigating the soil at the site of actual frost damage, the soil will be found to be penetrated by more or less horizontal ice sheets with thicknesses ranging from 1–2 mm to several cm and spaced closely to each other. In fine sandy and silt soils the sheets are, as a rule, thin but closely spaced, whereas in clayey soils ice lenses of greater thickness will be observable at greater distances. The soil between the ice lenses is loose, appearing almost dry. A regularity of considerable interest and of critical importance to the frost problem will be recognized if the moisture content of such soils is determined before freezing and after the formation of ice lenses. The result will resemble that shown in Fig. 395. The moisture content in the vicinity of the ice lenses will be observed to have increased substantially over the original condition. Consequently, some soils have the ability of absorbing water from the surrounding, still unfrozen zone, which is then accumulated in the form of ice lenses.

The water accumulated in the ice lenses may be attributed to two sources. In moist soils which are, however, prevented from communicating with the unconfined groundwater, and thus from receiving additional supplies, no more water than that already present in the soil is concentrated in lenticular form. The volume of this water being insignificant only a few thin lenses will be formed and the process is terminated within a short time. Systems of this type are called closed and no more water than the moisture content of the soil is dis-

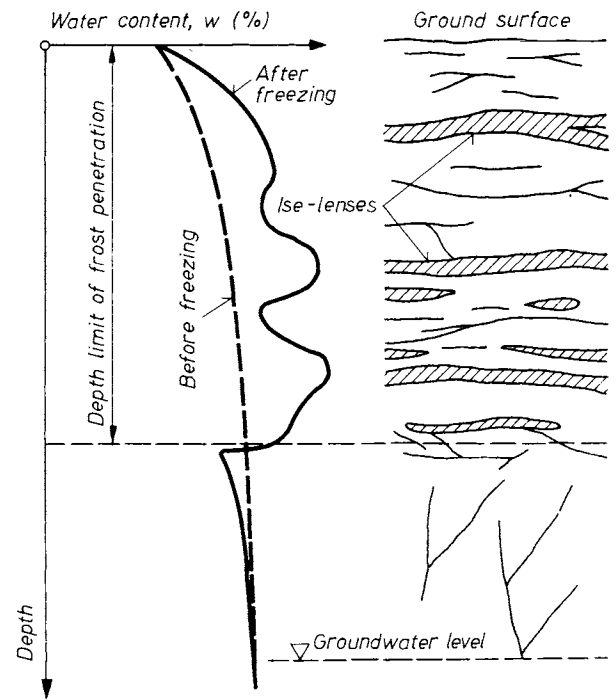


Fig. 395. Moisture dispersion before and after frost

tributed in a different pattern by freezing. No heave of the surface is experienced, probably on account of the fact that the expansion corresponding to the thickness of the lenses is compensated by the shrinkage of the parts of the soil from which water is withdrawn.

The situation will be different where the zone of frost penetration is continually supplied from the groundwater by capillary rise. In the groundwater below the freezing depth the water is free to move. In such cases the water volume used for the formation of ice lenses is continually supplied by capillarity. Systems of this type are referred to as open. In particular cases supply may be secured by surface waters which have infiltrated into the soil and accumulated at certain locations.

The ice lenses are in general situated parallel to the soil surface, in a direction perpendicular to the temperature gradient. Since the lenses invariably grow in the direction of the least resistance, the terrain surface is raised in the process, the total heave being equal to the aggregate thickness of the ice lenses.

Open and closed systems are illustrated diagrammatically in Fig. 396, with Fig. 397 showing the progress of frost penetration and the development of frost heave. The data in Fig. 398 are also of interest. Here the extent of frost heave is shown according to the investigations by DÜCKER (1956, 1964) for media composed of uniform grains, and plotted against the characteristic particle diameter.

This value will be seen to increase rapidly in the finer fractions. The rate of frost penetration is

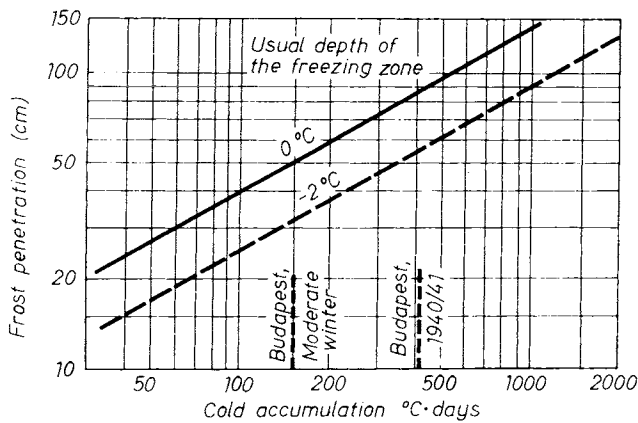


Fig. 394. Depth of frost penetration after GÁSPÁR (1959)

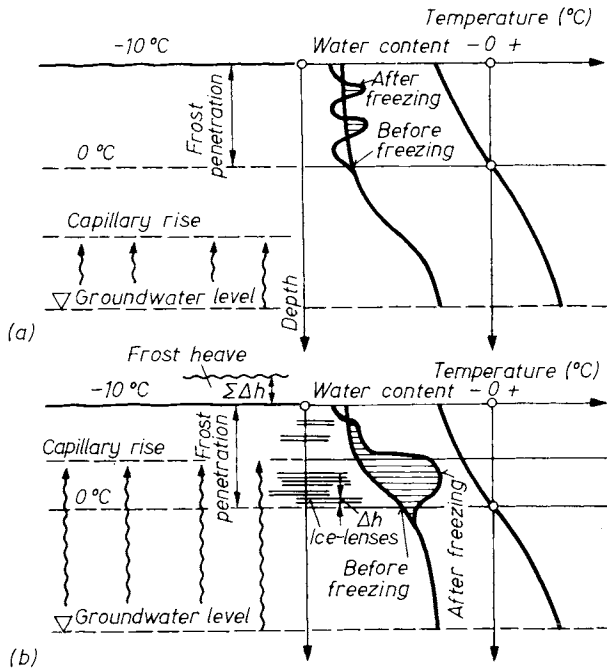


Fig. 396. Idea of open or closed systems for ice-lens formation: a — closed system when water supply is excluded; b — open system with water supply allowed

plotted in the same diagram. The two data, namely the extent of frost heave and the rate of frost penetration are used by DÜCKER as the criterion of frost susceptibility of a particular soil. The degree of frost depth is accordingly

$$f\% = \frac{\text{frost heave } (E, \text{ mm})}{\text{thickness of frozen layer } (H, \text{ mm})} \cdot 100.$$

The magnitude of this factor is also plotted for the individual particle fractions in Fig. 398. According to DÜCKER, assuming an average porosity of $n = 20\%$, a degree of frost susceptibility

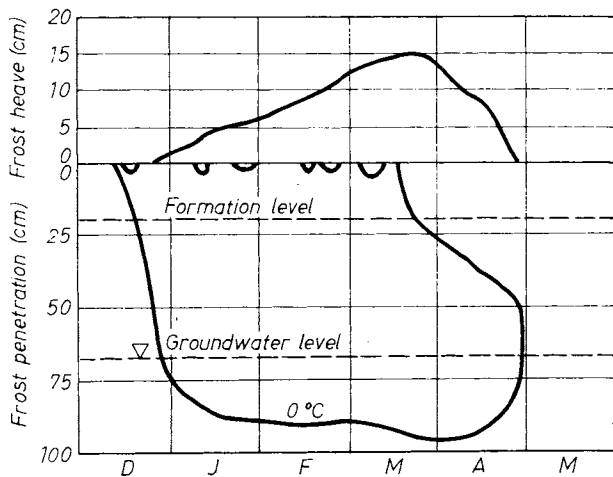


Fig. 397. Frost penetration and frost heave with the passage of time

greater than $f = 3\%$ is indicative of ice lens formation, of lenticular ice segregation.

Hazards to buildings and structures supported by the soil are presented only by lenticular freezing and, as will be perceived from the foregoing, this liability prevails in fine-grained soils only. Frost action in coarse-grained media takes the form of mass freezing. The rate of cooling is another factor in frost action. As indicated by both laboratory freezing tests and observations in the field slow cooling rates are more conducive to ice lens formation than rapid rates. At very high cooling rates, mass freezing will occur even in fine-grained soils.

Finally, the development of frost heave is influenced also by the load acting on the soil. From the theory of consolidation it will be recalled that an increase of stress at a point within the soil will displace some of the water from the soil. The thickness of the water films is reduced thereby, affording less opportunity of water supply towards the frozen areas. In other words this implies that the extent of frost heave is reduced by the pressure due to an external load acting on the surface of a freezing soil mass.

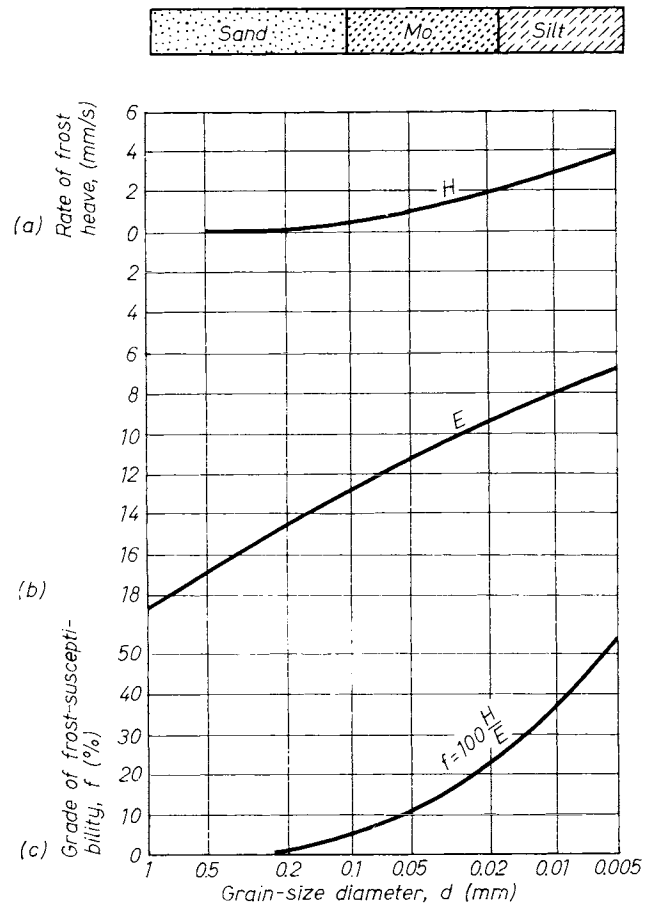


Fig. 398. Dückers' experimental results (1956); dependence on grain size:

a — rate of heave; b — rate of frost penetration; c — degree of risk

The following physical explanation may be offered for the formation of ice lenses. The freezing point of the adsorbed water in the vicinity of the particle surface is below 0 °C. Adsorption forces, chemical effects and free ions are responsible for this effect. This reduction is the more pronounced, the smaller the pores within the soil. Consequently, in a cohesive soil, in the undisturbed state, the freezing point of water tends to vary from point to point. In the vicinity of particle surfaces, the water molecules are subjected to high electric forces and the freezing point is thus well below 0 °C. On the other hand, in the pore water filling the particle interstices, normal properties prevail, and the freezing point is at 0 °C. Once the temperature decreases to below 0 °C individual ice crystal nuclei are formed in these larger pores. Freezing is accompanied by the expansion of the water volume, the ice exerting a wedging pressure on the surrounding soil.

The crystallisation force of the growing ice crystal attracts the water molecules from the surrounding soil and water is thereby removed from the adsorption films as well. The balance of the water film is thus upset, the free potential tends to com-

plete the film and as a consequence water is raised from the deeper layers. The process of freezing is thus accompanied by two types of water migration, namely (a) suction of water from the lower layers in a manner resembling capillary movement, and (b) displacement of local interstitial water towards the freezing soil masses. The water suction under (a) must not be mistaken for capillary action, since in this case no meniscus-effect is present. Capillary tension will be recalled as developing exclusively at interfaces between solid, liquid and gaseous media, as a consequence of surface tension. Experiments have shown, however, the aforementioned suction force and the capillary rise to represent forces of identical orders of magnitude. The water volume which is potentially transported by capillarity in a particular soil, under particular conditions upward, is termed for brevity the "capillary capacity". This capillary capacity may be assumed to represent the upper limit of the water volume which can be raised by the suction exerted by the growing ice crystals. The atmosphere in the soil interstices is saturated with water vapour and if the pressure prevailing in the vicinity of the growing ice crystal is lower than in the deeper

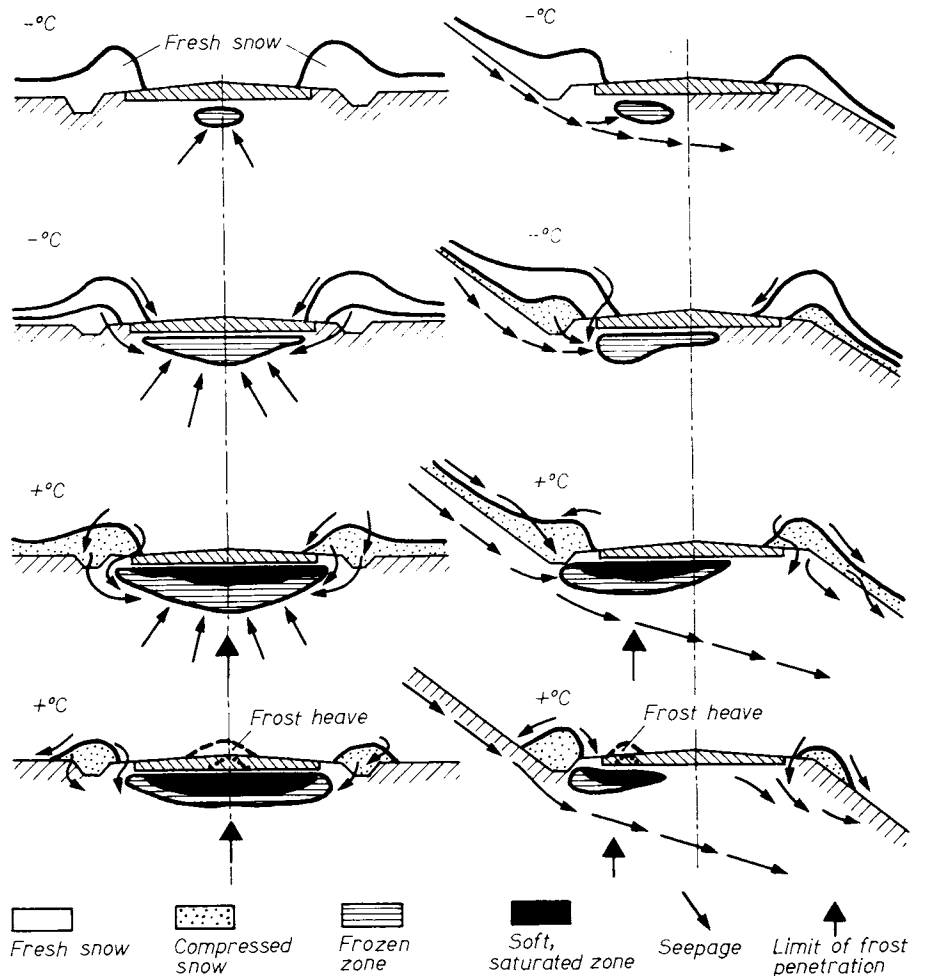


Fig. 399. Frost and thaw processes in the underground

layers, the vapour will migrate upward, to precipitate and freeze subsequently as a consequence of the temperature difference.

From the foregoing it can be concluded that ice lenses will not form unless the following three conditions are satisfied simultaneously:

- the temperature decreases to below 0 °C;
- the subsoil is susceptible to frost;
- the supply of water is secured.

4.7.4 Frost and thaw damage

Frost damage takes, on the one hand, the form of unequal pavement heave, and on the other, and this is the greater liability, of increasing the moisture content in the subgrade under the pavement, thereby saturating the surrounding soil and reducing its bearing capacity upon thawing. Repeated cycles of freezing and thawing will completely change the structure of the soil, virtually eliminating its bearing capacity, so that the pavement is deteriorated by the traffic it is bound to carry in such periods. The typical damages observable in the diverse pavement structures will be described as follows.

Water-bound macadam pavements already suffer deterioration during the freezing period. Ice lenses tend to raise the stones and longitudinal cracks develop with frost heave in an irregular pattern. If the snow is removed, the opportunity for frost penetration is increased, resulting in more extensive heave. A sudden rise in temperature will cause the pavement and a relatively thin layer of the subgrade to thaw, leaving some of the subgrade in a frozen condition. The frozen layer is impervious, leading to the development of a saturated, loosened layer with no bearing capacity. Traffic loads acting on a pavement in this condition result in the rapid deterioration thereof. The process described is illustrated in Fig. 399.

A hand-placed rock base on frost-susceptible soil will suffer frost deterioration by the mechanism shown in Fig. 400 (SCHAIBLE, 1957). The rocks of the base penetrate increasingly deeper into the softening subgrade.

Flexible, asphaltic pavements assume an undulating surface under frost action, subsequently developing a network of cracks. The cracks provide

access for infiltrating water into the subgrade, the soil is remoulded by the pumping action of traffic, the bearing capacity is minimized and deterioration proceeds at a high rate.

The slabs of concrete pavements are raised by frost heave, the joint sealing is damaged, opening a path for water infiltration from above. The support of the concrete slab becomes non-uniform, so that the edges, or corners thereof will break under load. Properly dimensioned rigid pavements behave better than flexible structures in withstanding frost heave, non-uniform deflection and settlement upon thawing, since the wheel load is distributed over a larger surface.

4.7.5 Frost criteria

In assessing the potential damages by frost action and thawing the following questions must be answered:

1. What is the depth of frost penetration during the freezing season?
2. What form of ice segregation is liable to occur, and is the formation of ice lenses to be anticipated?
3. Is the supply of water ensured?

1. The depth of frost penetration is always associated with the depth of the 0 °C isotherm. This depth can be found from Figs 393 and 394. The total heat deficiency is determined most expediently by consulting a meteorologist. The variations in temperature for the past thirty years should be studied, the total heat deficiency computed and, omitting a few extreme values, the design value adopted. As far as applicable, allowance should be made for the microclimate of the track envisaged, comparing the environments and soil conditions at the observing station and at the proposed construction site. According to current Hungarian practice, in locations where the total heat deficiency remains below 500 °C-days, a depth of 80 cm is commonly adopted as the design value for frost penetration and when this value is higher, a depth of 100 cm may be used. These figures are to a certain extent on the conservative side. A margin of safety must be included, since frost damage is extremely expensive to repair (in Hungary attaining an order of magnitude of a hundred million forints annually), whereas appreciably smaller expenditures are needed for preventive measures. The experience gained in the recent past during several long and severe winters with subsequent sudden thawing, have further revealed that the “ageing” of a road is accompanied by a higher frost susceptibility which can probably be attributed to changes in the water regime of the subgrade and the environment brought about by the construction of the road. Owing to the foregoing considerations, the depth of frost penetration to be used as design criterion should be adopted carefully, preferably using a pessimistic approach.

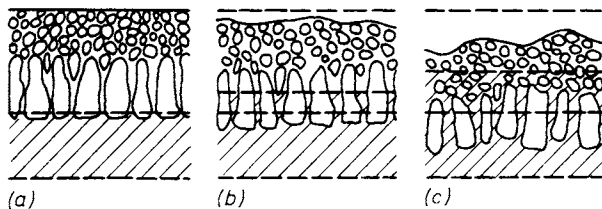


Fig. 400. Harmful effect of frost in a porous pavement structure:
 a — original structure; b — softened earth rises high; c — crushed stone base merges into the soil

2. Attempts to find an answer to this question have resulted in the development of several frost-susceptibility criteria, of which the one originated by CASAGRANDE (1934) has been commonly used. According to this criterion, in a uniformly graded soil ($U = 5$) ice lenses will develop if the total silt fraction ($d = 0.02$ mm) is greater than 10%. Soils having a mixed granulometry ($U = 15$) and containing 3% or more of silt should already be regarded as frost susceptible. The corresponding granulometric ranges are shown in Fig. 401 and the application of the criterion is facilitated by the diagram in Fig. 402. CASAGRANDE's criterion is rather conservative and not supported in all respects by more recent research. A further objection is that the granulometric curve is taken as the only criterion of frost susceptibility. This has since been

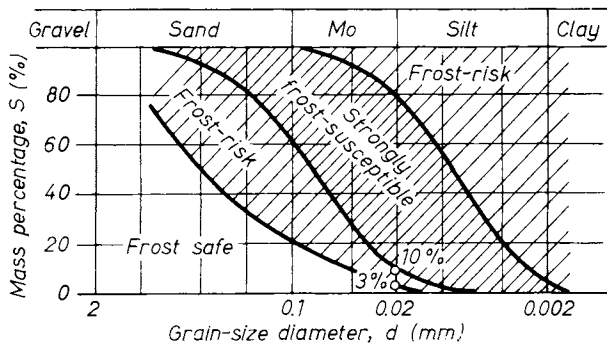


Fig. 401. Frost criterion after CASAGRANDE (1934): grain-size distribution curves

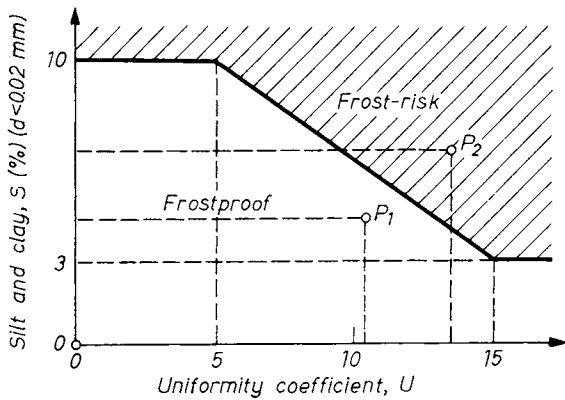


Fig. 402. Diagram for speedy decision as to frost risk

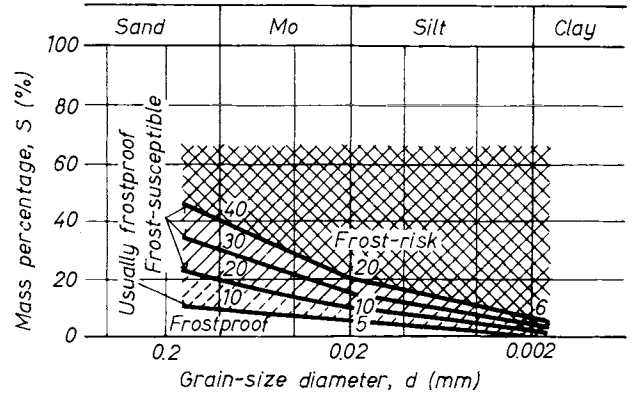


Fig. 403. Frost criterion after SCHAIBLE (1957)

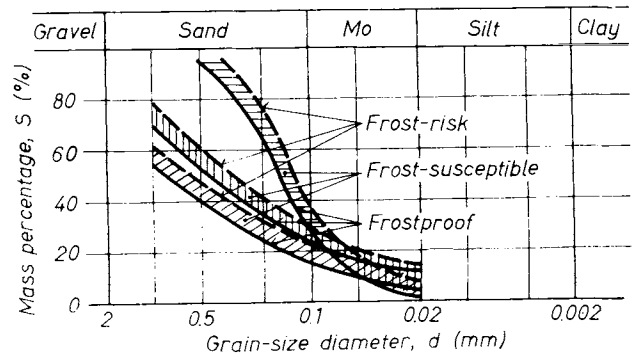


Fig. 404. Frost criterion after GÁSPÁR (1958)

recognized as one of the most important factors, but one which alone is not decisive.

On the basis of detailed investigations, three degrees of frost susceptibility have been suggested by SCHAIBLE (1957). Adopting several particle diameters, he has distinguished non-susceptible, frost sensitive and frost susceptible soils. The criteria have been compiled in Table 33 and represented graphically in Fig. 403.

Special care should be exercised with soils containing weathered rock debris. Physical and chemical weathering due to traffic loads and atmospheric influences tend to increase the amount of fine grains, as a consequence of which the frost susceptibility of the soil is increased.

In Hungary a criterion was suggested by GÁSPÁR (1958) and this is indicated in Table 34, with the corresponding granulometric curves in Fig 404.

Table 33. Determination of frost-susceptibility after SCHAIBLE (1957)

Grade	Proportion of fines (%)			Judgement of risk about frost or thaw damage	
	Clay ($d < 0.002$)	Clay and silt ($s < 0.02$)	Clay and silt + Mo ($d < 0.1$)	Theoretically	In practice
I	0	0... 5	5... 10	No harm	Frost safe
II	1	5... 10	10... 20	Slight damage	
III	2	10... 15	20... 30	Moderate singular damage	Frost-susceptible
IV	4	15... 20	30... 40	Serious damage	
V	6	20	40		Exposed to damage

Table 34. Determination of frost-susceptibility after GÁSPÁR (1958)

Grade	Soil type	Particle size distribution (%)		Judgement of risk about frost-susceptibility
		S(d = 0.02 mm)	S(d = 0.1 mm)	
a	Gravel	6	< 15	Frost-safe
	Coarse sand	5	< 20	
	Fine sand	4	< 25	
b	Gravel	6 ... 15	15 ... 20	Frost-susceptible
	Coarse sand	5 ... 10	20 ... 30	
	Fine sand	4 ... 8	25 ... 35	
c	Gravel	15	> 25	Susceptible in greater degree
	Coarse sand	10	> 30	
	Fine sand	8	> 35	
	Cohesive soils			
d	Mo	$I_p > 0.12$		Highly frost-susceptible
	Silt	$I_p < 0.12$		

The aforementioned frost-susceptibility criteria are compared in Fig. 405. In the criteria of CASAGRANDE, GÁSPÁR and SCHAIBLE, one, two and three particle diameters are involved, respectively, and the corresponding percentages by weight are specified for the individual ranges. The above sequence at the same time implies the severity of the criteria. For practical purposes the observation of GÁSPÁR's criterion is generally recommended in Central Europe. For assessing the subgrades of highways of primary importance, as well as of airport runways, the criterion of CASAGRANDE should be applied, whereas for roads of lesser significance that of SCHAIBLE should suffice.

The information compiled in Table 35 will provide assistance in rapidly assessing the degree of frost susceptibility in the field.

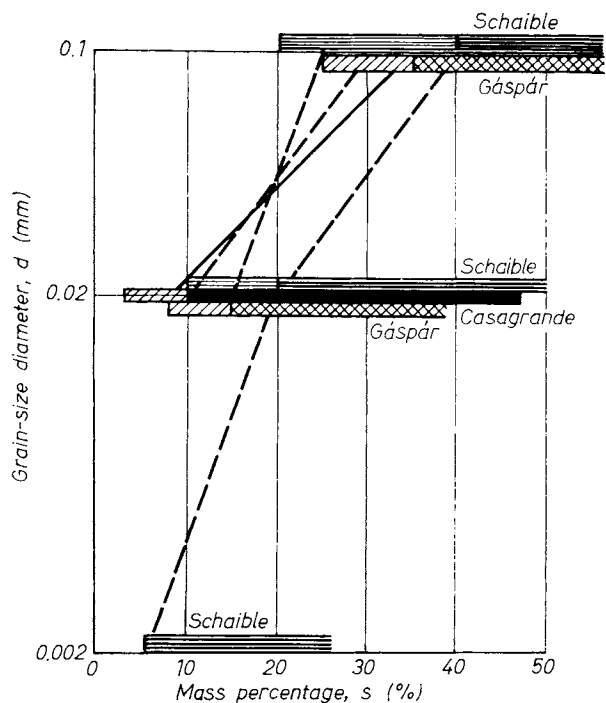


Fig. 405. Comparison of different frost criteria

Some authors find it appropriate to classify the frost action on the basis of frost heave. The following relation exists between the suction force (P_p) attached to a given suction pressure (P), the permeability of the soil (k_D), and frost heave:

$$k_D - \frac{P_p}{l} = v = \frac{h}{1.09 \Delta T}, \quad (505)$$

where l = distance between the lowest ice lens and the water table,
 v = velocity of water seepage,
 ΔT = passing time,
 1.09 = the coefficient of expansion by freezing.

Several researches attached great importance to crystallization forces in the process of ice lens building, but, according to their investigations, these were in the range and magnitude of the capillary forces. A similar opinion has been expressed by KÖGLER *et al.* (1936) who found it appropriate to put the capillary force in Eq. (505), which they calculate from the capillary uplift (H) reduced by the resistance suffered in the course of rising:

$$q = k \frac{H - l}{l}, \quad (506)$$

where k is the coefficient of permeability at 10 °C. The authors classify frost susceptibility on the basis of Eq. (506), but regard frost heaves of up to 2 cm as generally acceptable. The principles of this so-called Freiberg-criterion can be seen in Fig. 406. The three zones in the figure are characterized as:

- a = harmless,
- b = frost susceptible for long duration of frost, or non-homogeneous soils,
- c = very dangerous.

It is claimed that the validity of these criteria has been confirmed by field tests.

Table 35. *In situ* determination of frost-susceptibility

Identification	Description of soil	Grade of frost-susceptibility
A	Organic soils	I
B	Soils abundant in stone and gravel 1. No bounding agent present, crumbles easily 2. Bounding agents present, forms clods	I II
C	The water saturated soil becomes gleaming when shaken in the hand: water recedes into the pores when pressed between the fingers	III
D	The soil consists of a fine-grained mass 1. forms sandy clumps; fine grains are not visible by the naked eye; 2. forms hard clods (a) can be rolled (b) can not be rolled; pulverized	I II III

Equation (506) and some conclusions drawn therefrom need some correction however (RÉTHÁTI, 1960) because

- (a) the equation is valid only in the lower capillary zone where the soil is saturated (here: $H = h_c$);
- (b) above this zone not only the path-time curve but also the degree of saturation changes (diminishes as it becomes farther away from the water table).

Departing from Jáky's experiments which describe the capillary rise (h) in time (t) — with the exception of the initial rising phase — by the expression

$$h = at^b, \tag{507}$$

the quantity of water delivered by capillarity can be written as

$$q = \frac{S_r n b h}{t}, \tag{508}$$

where S_r is the degree of saturation at the desired elevation, and n is the porosity of the soil. The function $S_r(h)$ can be determined in the laboratory (RÉTHÁTI, 1960).

3. A detailed hydrogeological study must be performed before an answer to this question can be given. The height to which groundwater table rises in the winter season should be found in order to determine whether the suction force acting is sufficient or not to provide the supply of water under the particular geometrical conditions.

4.7.6 Frost control methods

As mentioned in the introduction to the present chapter, pavement damage due to frost action is liable to occur where three conditions are satisfied simultaneously, namely a frost-susceptible soil, a source of water supply and freezing temperature of sufficient duration. The third of these factors is particular to a given site and thus beyond control. For this reason, any control measure must be directed towards the elimination of one of the first two factors.

The first factor can be eliminated by modifying the properties of the soil. This may be accomplished by mixing an imported soil with the original so that the resulting soil mix should no longer satisfy the criterion of frost susceptibility. On occasion certain chemicals may be used for this purpose.

These methods are cumbersome and expensive to realize in practice and therefore, also because of the heterogeneity of the soils encountered in Hungary, they have never been generally adopted in that country.

For preventing water from being supplied, one of the following methods may be adopted.

A granular layer of sufficient depth to intercept the capillary rise may be placed under the pavement. Gravel, crushed stone or even slag may be used as the material for this subbase. It is essential to envisage a sand layer of moderate thickness between the coarse-grained subbase and the frost-susceptible subgrade, otherwise the pores between the coarse particles would be plugged.

The most widely used method consists of removing the frost-susceptible soil and of constructing a base course of sufficient thickness. An example for the design thereof is illustrated in Fig. 407.

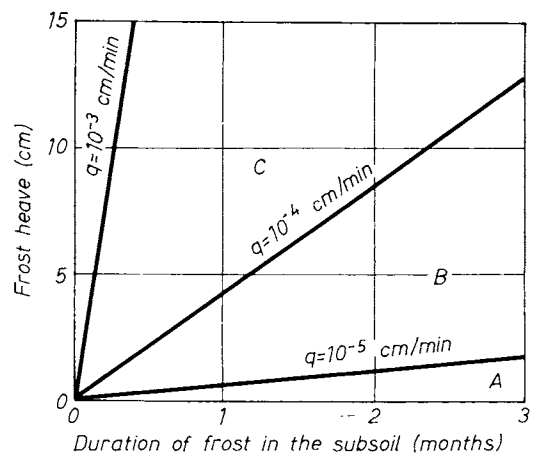


Fig. 406. The Freiberg-criterion

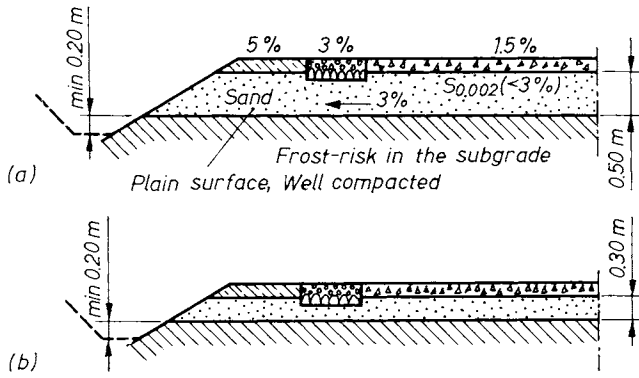


Fig. 407. Sites of the preventive layer in the cross-section

The base course serves at the same time to increase the load-bearing capacity, sometimes permitting reduced pavement thicknesses. In Hungarian practice, the thickness of this layer is commonly determined according to the criteria compiled in Table 36. Similar criteria, suggested

Table 36. Required thickness of frost-preventive layers (Hungarian Standard)

Subsoil according to Table 34	Depth of the water table below formation level in December	Depth between the bottom of the preventive layer and that of the load-bearing course
a	down to F (-2)	According to bearing capacity
b	2 F (-2)	According to bearing capacity
	F (-2) ... 2 F (-2)	0.8 F (-2)
c	2 F (-2) ... 3 F (-2)	0.8 F (-2)
	F (-2) ... 2 F (-2)	0.9 F (-2)
d	3 F (-2) ... 4 F (-2)	0.9 F (-2)
	F (-2) ... 3 F (-2)	F (-2)

F (-2) = frost penetration depth of the isotherm -2 °C

by the highway research institute in the Federal Republic of Germany (SIEDEK and VOSS, 1956), are given in Table 37.

Other potential methods include drainage of the subgrade under the pavement, or lowering the groundwater table by longitudinal drains. These

methods only prove successful, however, in exceptional cases, since it is precisely the frost-susceptible soils which can only be slightly drained by gravity.

Filter drains of this type are entirely ineffective where the capillary rise is greater ($h > 1.50$ m). No improvement can be expected from the provision of deep side ditches and on occasion this may even result in increased frost action.

Another alternative consists of raising the grade, thus increasing the distance between the groundwater table and the depth of frost penetration. According to another solution an isolating layer of dried peat, straw, brushwood, etc., is applied. In recent times plastic foils have been used experimentally but these attempts appear to have remained unsuccessful, mainly due to the fact that the foil prevents evaporation and the moisture content is likely to increase beneath it.

The detailed description of the design parameters of the foregoing methods belongs to the domain of highway engineering and will therefore be omitted here.

References

ACUM, W. E. A. and FOX, L. (1951): Computation of load stresses in a three-layer elastic system. *Proc. Inst. Civ. Engg.*, London.

BURMISTER, D. M. (1943): The theory of stresses and displacements in layered systems and applications to the design of airport runways. *Proc. Highway Research Board*, Vol. 23.

BURMISTER, D. M. (1945): The general theory of stresses and displacements in layered systems. *Proc. HRB*, Vol. 23.

BURMISTER, D. M. (1956): Stress and displacement characteristics of a two-layer rigid base soil system. *Proc. HRB*, Vol. 35.

CASAGRANDE, A. (1934): Bodenuntersuchungen im Dienste des neuzeitlichen Strassenbaues. *Strassenbau*, 25.

CASAGRANDE, A. (1935): Ice - pressure - deformations in clay soils. *Engg. News Rec.*, Vol. 25.

DÜCKER, A. (1956): Gibt es eine Grenze zwischen frostsicheren und frostempfindlichen Lockergesteinen? *Strasse und Autobahn*, No. 3.

DÜCKER, A. (1964): Vorschlag einer Einteilung und Kennzeichnung der Lockergesteine (Erdstoffe) für erdbautechnische Zwecke. *Strasse und Autobahn*, 15.

GÁSPÁR, L. (1959): Calculation of frost penetration depth from air temperature data. (In Hungarian.) *Mélyépítéstudományi Szemle*, No. 10.

GÁSPÁR, L. (1964): Some practical aspects of the economical compaction of earthworks. (In Hungarian.) *Mélyépítéstudományi Szemle*, 10.

Table 37. Required thickness of the frost-preventive layer after SIEDEK and VOSS (1956)

total sample	Percent by weight (%)		Required thickness (cm)			Minimum depth of the formation level (cm) below pavement surface		
	for particles $d < 2$ mm		dry		wet	dry		wet
	$d < 0.02$ mm	$d < 0.10$ mm	earth-work	subsoil		earth work	sub-soil	
0 ... 3	—	—	—	—	—	—	—	—
3 ... 6	down to 10	down to 20	—	—	30	—	—	60
6 ... 10	down to 15	down to 30	20	30	30	50	60	60
> 10	> 15	> 30	30	40	40	60	70	70

- JEUFFROY, G. and BACHELEZ, J. (1963): Note on a method analysis for pavements. *Int. Conf. on the Structural Design of Asphalt Pavements*, Michigan.
- JUMIKIS, A. R. (1955): *The frost penetration problem in highway engineering*. The Brunswick, Rutgers Univ. Press.
- KÉZDI, A. and MARKÓ, I. (1969): *Erdbauten, Schutz und Entwässerung*. Werner, Düsseldorf.
- KIRK, J. M. (1966): Tables of radial stresses in top layer of three-layer elastic system at distance from load axis. *Highway Res. Rec.*, No. 145.
- KLENGEL, K. J. (1968): *Frost und Baugrund.*, VEB Verlag für Bauwesen, Berlin.
- KÖGLER, F., SCHEIDIG, A. and LEUSSINK, H. (1936): Beiträge zur Frostfrage im Strassenbau. *Bodenmechanik und neuzeitlicher Strassenbau*.
- LAZÁNYI, I. (1958): Experiments with the CBR-method. (In Hungarian.) *ÉKKME Közöny*, Vol. IV.
- NOVAIS-FERREIRA, H. and CAMPINOS, J. (1961): A mathematical method of determining the thickness of flexible pavements based on CBR. *Proc. 5th ICSMFE*. Vol. 2. Paris.
- PELTIER, R. (1955): *Manuel de laboratoire routier*. Dunod, Paris.
- PORTER, O. J. (1949): Development of the original method for highway design. *Pros. ASCE*. Vol. 75, pp. 11–17.
- REICHERT, J. (1958, 1959): Essais de chargements répétés sur un massif de limon. I–II, *Centre de Recherches Routières*, Bruxelles.
- RÉTHÁTI, L. (1960): Capillary properties of soils. *Acta Techn. Acad. Sci. Hung.* Tom. XXIX. fasc. 1–2.
- SCHAIBLE, L. (1957): *Frost- und Tauschaden an Verkehrsweegen und deren Bekämpfung*, Ernst, Berlin.
- SCHLEICHER, F. (1926): Zur Theorie des Baugrundes. *Der Bauingenieur*, pp. 931–949.
- SHOOK, J. F. and FINN, F. N. (1963): Thickness design relationships for asphalt pavements. *Proc. Int. Conf. on the Struct. Design of asphalt pavements*. Univ. of Michigan.
- SIEDEK, P. and VOSS, R. (1956): *Beurteilung der Tragfähigkeit schwerbelasteter Strassen durch den Plattendruckversuch*. Ernst, Berlin.
- TELLER, L. W. and SUTHERLAND, H. B. (1943): The structural design of concrete pavements. *Public Roads*, 23.
- TERZAGHI, K. (1955): Evaluation of coefficients of subgrade reaction. *Géotechnique*, No. 5.
- WESTERGAARD, H. M. (1947): New formulas for stresses in concrete pavements of airfields. *Proc. ASCE*. 73.
- YODER, E. J. (1959): *Principles of Pavement Design*. Wiley, New York.

Chapter 5.

Improvement of the physical properties of soils

5.1 Introduction

The physical properties of natural soils and of man-made earth structures are often poorer than may be required for a particular project, in that their shear strength may be too low, their compressibility, water content or permeability too high, etc. The solution to a particular engineering problem may basically be approached from three different directions:

(a) The soil layers of inferior quality are relieved from bearing loads, or from withstanding water pressure, etc. This method is adopted for instance when the load of a building is transferred to a sound layer situated at greater depths by means of piles or caissons, or when a highly pervious soil is confined by a sheet pile cutoff extended into a lower impermeable layer.

(b) The poor soil layer is removed from under the structure and replaced by a soil having the required properties. This method is applicable in the case of tall buildings, but even more so in earthwork foundations, where e.g. a highly compressible peat mass is removed by excavation or blasting. Removal may be complete or partial, in the latter case the poor soil being excavated to a certain depth only, or in the form of vertical columns, i.e. a distributing layer, or alternatively sand or gravel columns are adopted.

(c) The third method consists essentially of changing and improving the properties of a particular natural soil by some kind of treatment to make it better suited for the purpose envisaged.

5.2 Compaction of soils

The most ancient soil improving method is compaction. With the advance of technology two main branches have developed in this field: compaction at the surface and deep compaction. When compacting effort is exercised at the surface, its impact embraces the upper top 20 to 50 cm layer below the surface. ("Heavy tamping" does not belong to this category despite the fact that the energy is transmitted at the ground surface.) Due to significant differences between

them, the two branches have to be dealt with separately, though some regularities are relevant to each procedure.

5.2.1 Compaction at the surface

5.2.1.1 *The significance of compacting*

Depending on their purpose, earth structures are required to conform to desired characteristics. These are most often associated with stability, durability, low permeability and resistance to deformation.

In planning compaction operations, the engineer is usually faced with three problems.

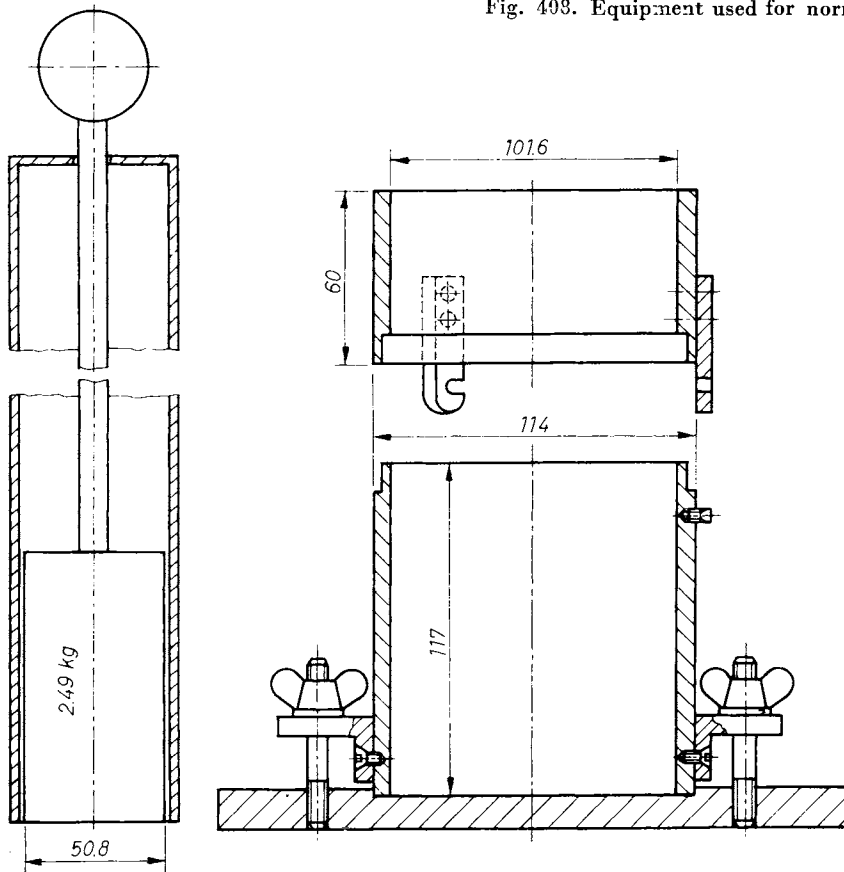
1. Determination of the required soil density. Any decision in this respect should take into consideration the purpose for which the earth structure is to be constructed. In some earth structures adequate strength, in others a specified degree of permeability, may be the dominant requirement. Once the desired values of the coefficient of permeability, shear strength, or modulus of compressibility are established, the density to be attained during construction can be found from laboratory and/or field tests.

2. The second problem is related to the selection of compaction equipment and methods by which the required density can most economically be attained.

3. Compaction operations at the site must be supervised and the results thereof checked continuously by a method yielding data in the shortest possible time, to see whether the values specified have actually been attained or not.

The importance of proper compaction has only been recognized in the last few decades. In the past, e.g. in carrying out the large railway projects of the 19th century, it was generally believed that adequate compaction of the loosely spread soil could be attained solely under the influence of the traffic of the earth-hauling vehicles. The importance of consolidation that is believed to occur during a winter period during which construction work is suspended, has generally been overestimated.

Fig. 403. Equipment used for normal and modified Proctor compaction tests



5.2.1.2 Factors affecting the compaction effort

In the first volume of the present book, a test is described by which the optimum water content and the maximum dry density attainable with a given compaction effort can be determined. In this test a soil sample is placed into a cylinder in loose layers and each layer is compacted by a prescribed number of blows with a standard weight. The device is shown in Fig. 408. The major data of tests used for determining the “normal” and the “modified” Proctor densities are compiled in Table 38. The test is repeated at several different water contents and the water content and dry bulk density are determined for each. The relationship thereof is then plotted in a diagram.

The curves obtained (cf. Vol. 1, Section 2.3.6, Figs 63–64) — called Proctor curves after their originator — display a typical shape, from which the optimal water content of compaction and

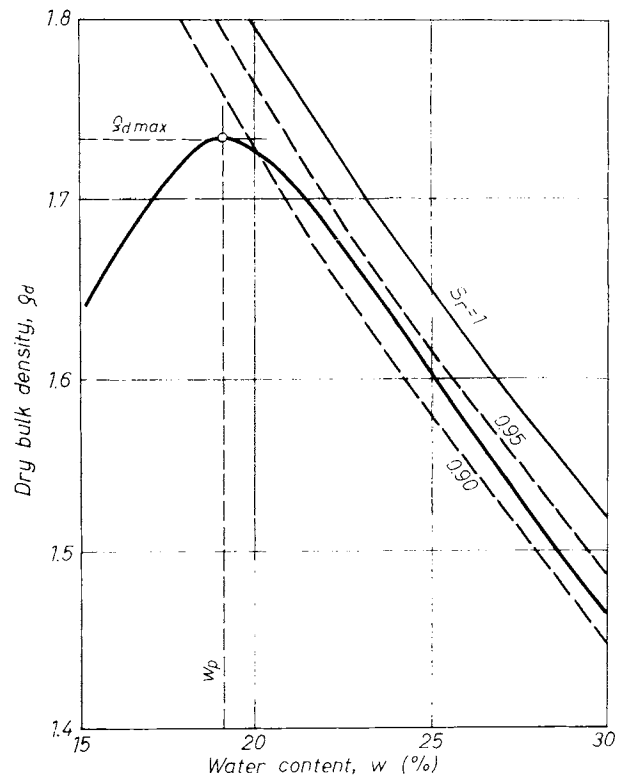


Fig. 409. Characteristic shape of a compaction curve

Table 38. Testing methods to find Proctor densities

Description	Volume of the sample (cm ³)	Number of layers	Mass of the tamper (kg)	Drop (mm)	Number of drops
Standard	2080	3	2.5	305	25
Modified	2080	5	4.5	460	55

further the "normal" or "modified" Proctor densities are obtained (Fig. 409). The $w - \gamma_0$ relationship for saturated conditions or for a given saturation S_r may also be plotted in the diagram, according to the expression

$$\gamma_0 = \frac{\gamma_s}{1 + \frac{w\gamma_s}{S_r\gamma_w}}$$

The Proctor curve will always remain below the saturation line $S_r = 1$, since the air can never be completely removed by tamping. The shape of the Proctor curve is in agreement with practical experience, according to which neither completely saturated nor desiccated soils can be effectively compacted. In the first case, the soil will yield laterally under the weight, or transient neutral stresses will be generated, whereas in the second case most of the compaction effort will be consumed in breaking up hard lumps.

There are cases where the Proctor curve assumes a shape differing from those shown before. For some clays, in addition to the peak, it may also display a minimum, in the range of smaller water contents, implying that dry soil is again more readily compacted. A Proctor curve of this type is illustrated in Fig. 410.

This shape may also be encountered in sandy gravels. The probable reason thereof is that owing to the menisci a certain cohesion is introduced by surface tension, increasing the resistance to the compaction effort.

The peak of the Proctor curve is usually associated with a certain degree of saturation. This value remains unchanged if the test is repeated

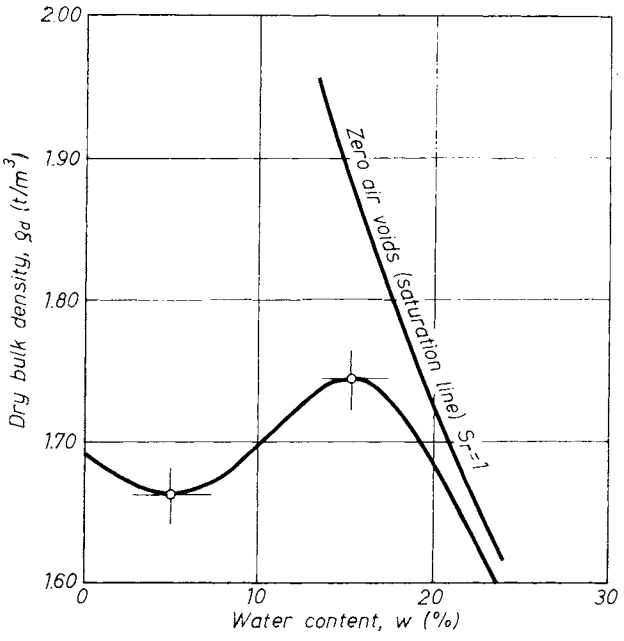


Fig. 410. Compaction curve with two prominent peaks

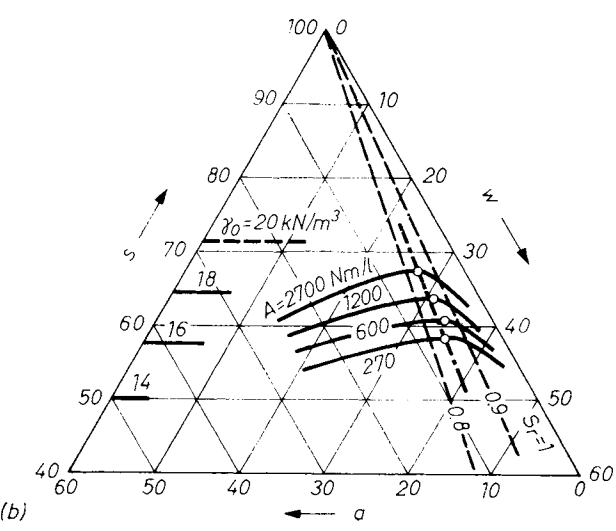
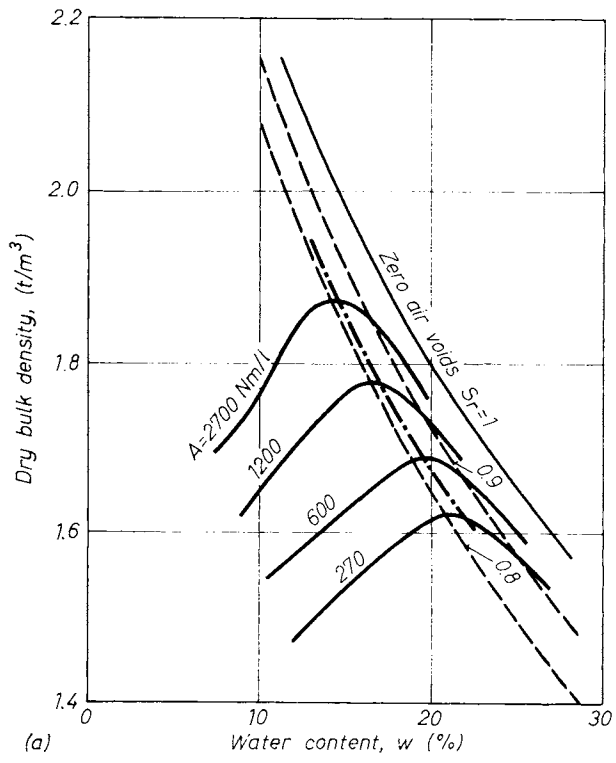


Fig. 411. a — Relationship between water content and dry density for different compacting efforts and degrees of saturation; b — compaction curves as plotted in a triangular diagram

with a different, e.g. higher, compacting effort. This implies, on the other hand, that the peak, the optimum moisture, will necessarily be shifted to the left. Proctor curves for successively increasing compaction efforts are shown in Fig. 411.

In a lecture delivered in 1964, the senior author attempted a physical explanation for the shape of the Proctor curve. For this purpose the curve has been plotted as illustrated in Fig. 412, indicating the change in the whole volume as a function of saturation. The relationship thus obtained

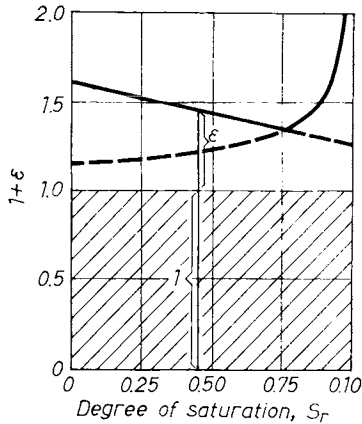


Fig. 412. Representation of the compaction curve as a function of saturation

consisted of two different sections. The section $S_r = 0$ to 0.85 was found to be linear in the great majority of the cases examined so far; moreover, having repeated the test on the same soil sample with different compaction efforts, the results plotted to parallel straight lines in the first section. The second section assumed the shape of a rapidly rising curve more or less asymptotically approaching the $S_r = 1$ axis.

A reasonable physical explanation can be offered for this shape of the curve. At the saturation values corresponding to the left-hand branch, water is present in the soil — mostly in the form of a film adsorbed on the particle surfaces. The “mobility” of the particles and, in turn, the effectiveness of compaction will increase together with the thickness of the water film, since the viscosity thereof decreases rapidly with the distance from the solid surface (Fig. 413). Below certain values of S_r relative movement of the particles is made possible by the air present in the soil. If the specific surface of the soil is f

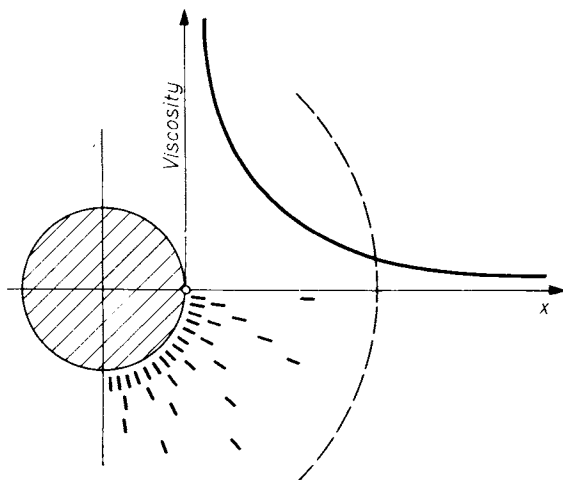


Fig. 413. Effect of molecular forces in the grain–water system: loosening toughness with increased distance

(cm^2/g) and the particles are assumed to be spherical in shape, then the average particle diameter is

$$d = \frac{6}{f\gamma_s}$$

and at the water content w the thickness of the water film around the particle becomes

$$\delta = \frac{w\gamma_0 d}{\sigma\gamma_w} = \frac{w}{f\gamma_w}$$

Assuming e.g. a particle diameter of $d = 0.001$ cm the specific surface is

$$f = \frac{6}{0.001 \cdot 2.6} = 2310 \text{ cm}^2/\text{g}$$

and the water content corresponding to a water film of $\delta = 0.5 \mu\text{m}$ is $w = 100 \delta f \gamma_w = 15\%$.

Thus it will be readily understandable that at similar and smaller moisture contents, the viscosity of the water film will present an obstacle to compaction. Considering the law of viscosity, it can be demonstrated that $e = bS_r$, so that the reduction in the void ratio is directly proportional to saturation. This linear relationship can hold true up to certain degrees of saturation only, since it is impossible to squeeze water from the soil even by static compaction. Assuming, however, that air can be removed during the short time available — compaction being the consequence thereof — the density attainable should, in principle, be inversely proportional to saturation.

In other words, at $S_r = 0$ it should be possible to compact the soil up to the density $e = 0$ (or to the $e - e_{\text{min}}$ value). At $S_r = 1$, on the other hand, no compaction occurs at the given water content. Consequently

$$e = \frac{e_{\text{min}}}{1 - S_r}$$

It should be evident that of the two equations, namely $e = e_0 - bS_r$ and $e = e_{\text{min}}/(1 - S_r)$, the one yielding the higher e value, i.e. the lower density, will be applicable. The point of intersection of the two curves (Fig. 412) will represent the optimal water of compaction.

5.2.1.3 Pores in soil mixtures

In soil mechanics, but mainly in connection with concrete technology, considerable efforts have been devoted to the determination of the granulometry conducive to the smallest pore volume. In the domain of concrete technology these investigations have failed to produce explicit results. It was found that the strength of a concrete made with the “best” aggregate may even be smaller than that of a concrete mixed with another aggregate, since other factors, e.g. consistency, were often predominant. Concerning soil

mechanics it may be concluded in general that soils graded uniformly, i.e. having a higher uniformity coefficient U , are compacted more readily, with a smaller compaction effort, since then the voids between the coarse particles are filled by the finer fractions. The theoretical arrangement shown in Fig. 414a will, however, never occur in practice, the corresponding grain-size distribution curve (Fig. 414b) representing a purely theoretical, unrealistic case.

The greatest density of a soil consisting of two or three components, i.e. size fractions, will be obtained at a specific mixing ratio. An explanation for this phenomenon has already been presented in Vol. 1, Section 3.2, where several examples have also been quoted. The size distribution of pores in granular media has also been discussed there, together with the changes in this distribution as a consequence of compaction. Studies of this type will play an important role in compaction problems.

In the interpretation of experimental results the analogy to be demonstrated subsequently will present a highly visual picture.

If a substance is dissolved in the molten product of another, the interaction between the molecular

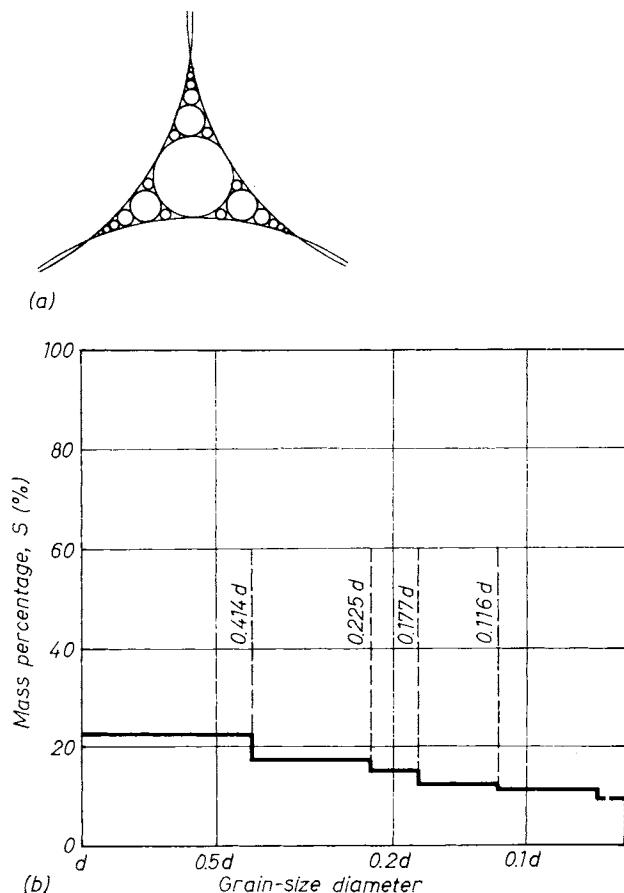


Fig. 414. a — The densest arrangement of spheres of different diameters; b — the grain-size distribution for the above arrangement

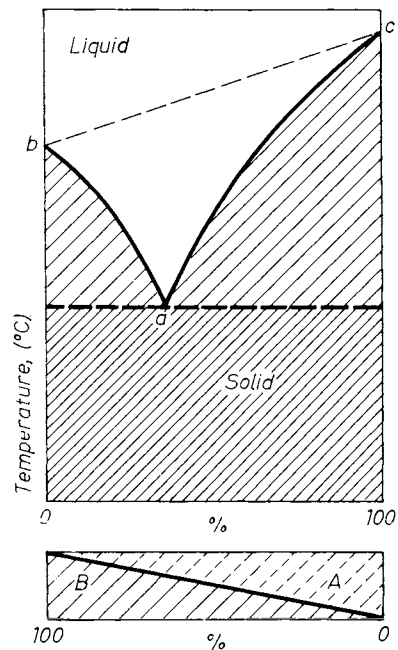


Fig. 415. Melting point of mixtures in the function of their percentages

components will produce a uniform solution. In the course of this process the mutual attractive forces between molecules of the same kind, as well as the dispersive forces — which depend on temperature — tend to decrease, so that the melting point, which is a function of temperature, is lowered (Fig. 415). The lowest value is named the eutectic point (point a in Fig. 415). Considering that soils consist of discrete components, which occur in variable proportions by weight in the granular medium, and further that temperature is a measure of the free energy of a system comprising several components and a quantity positively related to the volume of the system at constant pressure, the analogy between molecular and macromeritic fluids will become apparent. The free energy of the system is the greater, the higher its porosity; the latter also controls the volume of the system. Porosity in macromeritic systems thus assumes the role of temperature and conversely, the temperature of fluids may be regarded a measure of their "porosity".

Numerous investigations aimed at the determination of the density of two-component systems have been reported on in the literature (e.g. RODE, 1952). A mixture of spheres having two different diameters, d_1 and d_2 , was found to display, in the loosest arrangement, a porosity invariably lower than that of a mass containing uniform spheres only. The phenomenon observed here is the same as in the phase diagram of Fig. 415. Experimental results supporting this conclusion are compiled in Fig. 416 (FURNAS, 1931). The normal porosity was $n = 50\%$, the diverse curves apply to two-component granular

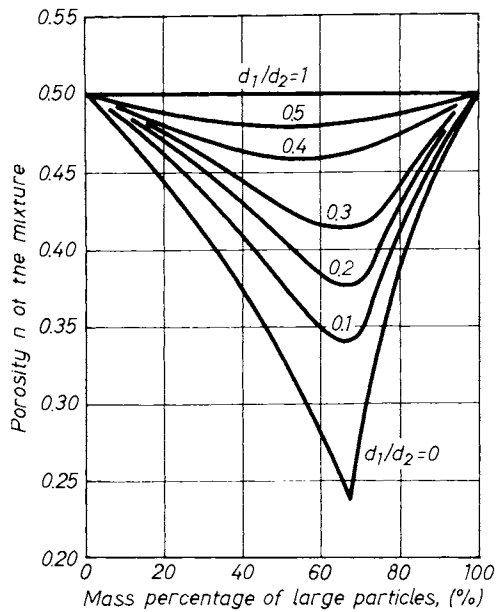


Fig. 416. Densities of two-component mixtures (FURNAS, 1931)

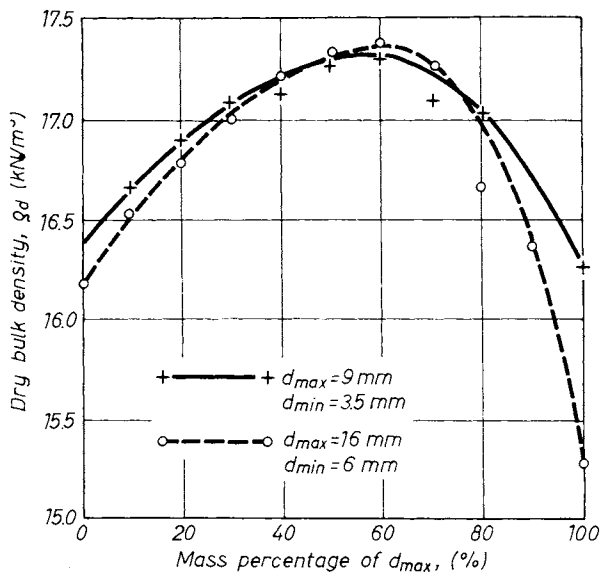


Fig. 417. Dry densities of two-component mixtures (LEUSSINK and KUTZNER, 1962)

media with different d_1/d_2 values. The greatest density was invariably obtained at a particular mixing ratio. The ratio d/d_2 applies to the case where the voids of a coarse component (sand, gravel) are filled with fine clay. Similar results have been attained by LEUSSINK and KUTZNER (1962) and further, at the laboratory of the Technical University of Budapest (Kézdi). Some of the results are reproduced in Fig. 417.

A system of three components has two degrees of freedom (FINDLAY, 1951). The condition of the system depends on the relative concentration of

the three components and on porosity. Mixtures of three-size fractions compacted with the same effort will display porosities similar to those shown in Fig. 418, in a diagram of the three components. The character of the diagram is again identical with the phase diagram of different fluid mixtures. Point K (the eutectic point) is situated on one side of the triangle, since the three components can be mixed in any proportion.

A result of considerable interest is shown in Fig. 419. The loosest and densest porosities of different sand mixtures are plotted in a triangular diagram. Figure 419 shows the difference between the two values.

An experimental approach is suggested for determining the composition of a soil mixture which is readily and economically compacted for a specific purpose.

The behaviour of granular media is governed, besides their porosity, also by the size of the pores. These pores have been studied by the senior author (KÉZDI, 1979). The pores of a particular sample were filled with gelatine, after the solidification of which the pore units could be measured and their volume computed. The volumetric distribution curves have been determined from a sufficiently large number of measurement data and plotted for both the solid particles and the pores. Two examples are shown in Fig. 420 where the distribution of pore sizes was determined for dense and loose conditions. By plotting the difference between the two curves, it will be observed that the reduction is most pronounced at a certain pore size.

Tendencies experienced in the capillary rise of water let us conclude that the moisture distribution in the upper capillary zone is in conformity with the distribution of the pores (RÉTHÁTI, 1960). Thus in most cases we will be close to reality when we describe the pore-distribution curve by the lognormal distribution function.

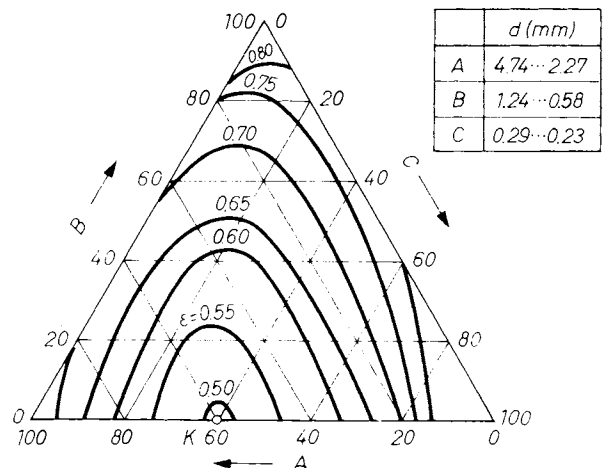


Fig. 418. Porosity in a three-component mixture as the function of the loosest arrangement

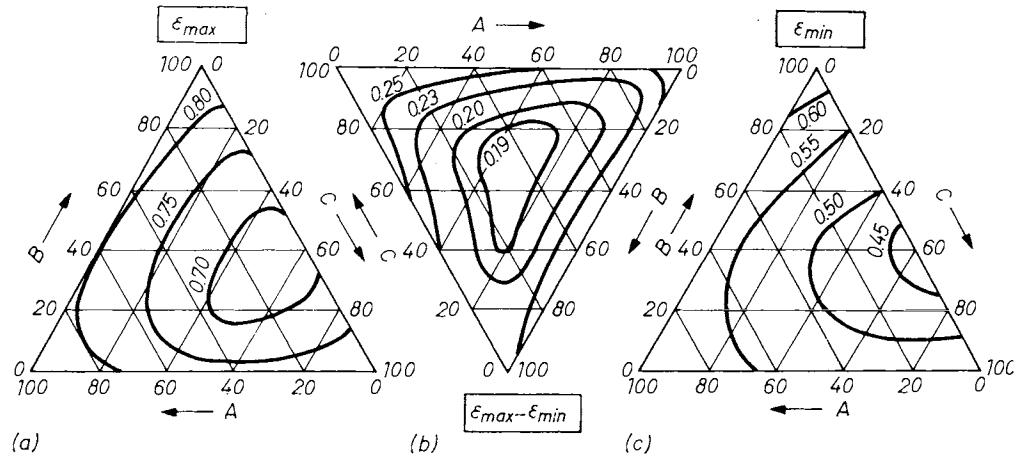


Fig. 419. Porosity values of three-component mixtures in their loosest and densest arrangements showing the ranges of the three components: $A = 0.58 \dots 0.29$ mm; $B = 0.29 \dots 0.22$ mm; $C = 1.24 \dots 0.58$ mm; a — porosity in the loosest stage; b — porosity in the densest stage; c — porosity ranges as functions of composition

5.2.1.4 The effect of compaction on the physical properties of soils

The main factors affecting the behaviour of a compacted soil mass are the density (T_{ry} , or e), degree of saturation (S_r), and the microstructure. Each of these factors is in turn determined by the compaction water content, compaction energy and compaction method.

Microstructure can be defined in the first approximation as the degree of preferred orien-

tation of clay particles (RESENDIZ, 1977). Two main factors determine the microstructure: 1. the magnitude of interparticle repulsive forces, and 2. the angular deformations induced by compaction (kneading effect).

A general representation of the structure of compacted soils is shown in Fig. 421 (McRAE, 1959): the drawings on the left-hand side illustrate the structure of soils compacted on the “dry side”, i.e. at moisture contents lower than the optimum determined by the Proctor test. The right-hand side shows the results of compaction on the wet side. The structure of sand and gravel is unaffected, only the void ratio is reduced by compaction. With cohesive soils the situation is different, since compaction on the wet side tends, in general, to produce a much more oriented structure. At higher moisture contents the individual particles are surrounded by a water film of greater thickness and this lends increased mobility to the flat flaky particles, thus enabling them to assume positions perpendicular to the compacting force. In dry condition, on the other hand, an irregular, un-oriented structure results. These differences have important consequences for the behaviour of the compacted soil.

The effects of changes in the clay structure are illustrated in Fig. 422 for a greater and a smaller compaction effort (LAMBE, 1960).

In the condition corresponding to point A, the water content is so low that the repulsive forces between the particles are smaller than the attractive forces, the resultant force being attraction. The particles are consequently coagulated without any regular pattern. The repulsive forces increase together with the moisture content and the particles are dispersed. In this condition they tend more readily to assume a regular pattern. The higher degree of orientation is accompanied by higher densities, so that the dry density increases up to point B. Although the degree of orientation continues to increase at even higher

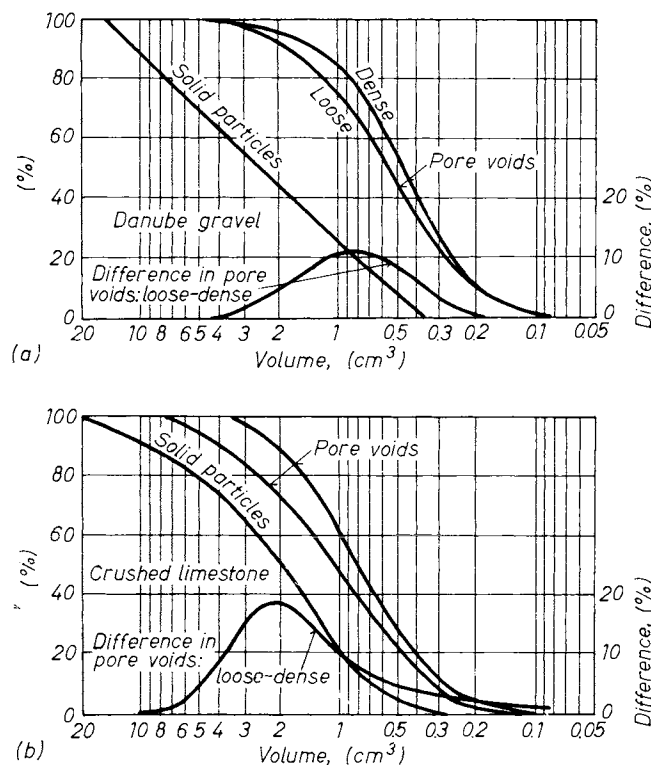


Fig. 420. Volumetric distribution of solid grains and pores: a — sandy gravel from the Danube; b — crushed limestone

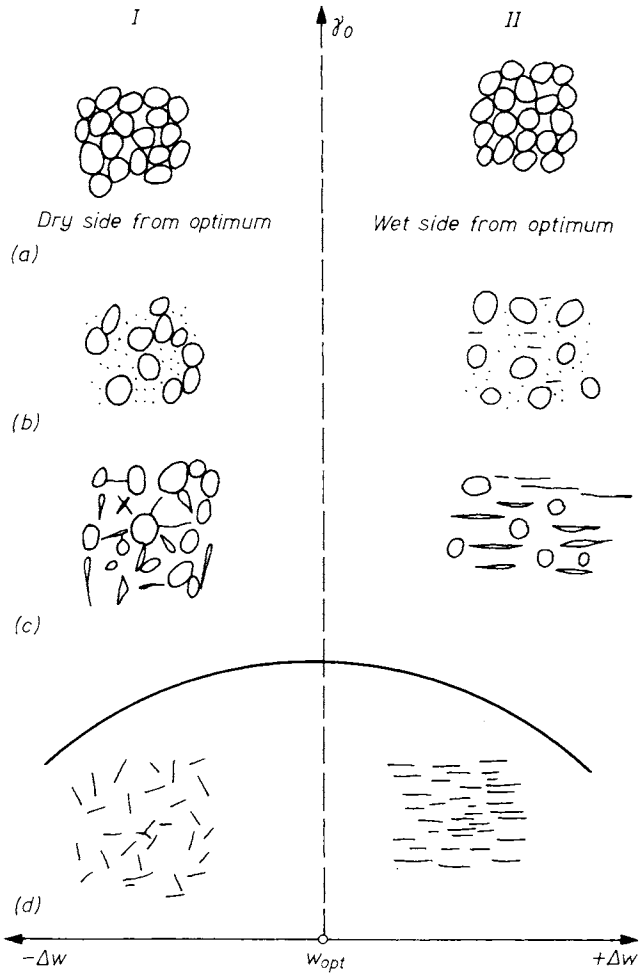


Fig. 421. Structure of different soils after compaction: I — initial stage on the dry side from optimum; II — initial stage on the wet side from optimum; a — sand and gravel; b — silty and clayey sand and gravel; c — silt and clay of low plasticity; d — silt and clay of high plasticity

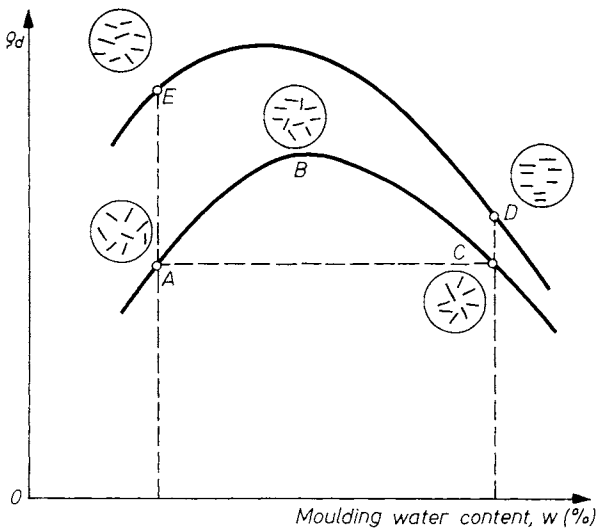


Fig. 422. Variation of the soil structure during compaction

moisture contents, the unit weight will decrease owing to water occupying a growing volume. Greater compaction efforts will always result in a higher degree of orientation and thus in a higher density (Fig. 422).

The degree of particle orientation can be measured quantitatively by the optical methods developed by MITCHELL (1956). The results shown in Fig. 423 have been published, among others, by PACEY (1956). These correspond to the drawings shown in Fig. 422 and provide the corresponding numerical values. The influence of structure on some of the important soil properties has been studied by SEED and CHAN (1959).

The influence on shrinkage is illustrated in Fig. 424. The shrinkage of samples compacted on the dry side is seen to be considerably smaller. The influence of structure is demonstrated even more clearly if soil samples are prepared with the same moisture content and compacted to the same density, but with different structures. This is realized by allowing the samples compacted on the dry side to absorb water. Comparing the linear shrinkage of the samples compacted on the wet side, i.e. of dispersed structure with that of samples compacted on the dry side but subsequently moistened, the results shown in Fig. 425 will be obtained, indicating a much smaller shrinkage for the samples compacted on the dry side. On the other hand, when absorbing water, these samples will display a much greater shrinkage, since the soil is much farther from the equilibrium moisture and the particles are much less oriented.

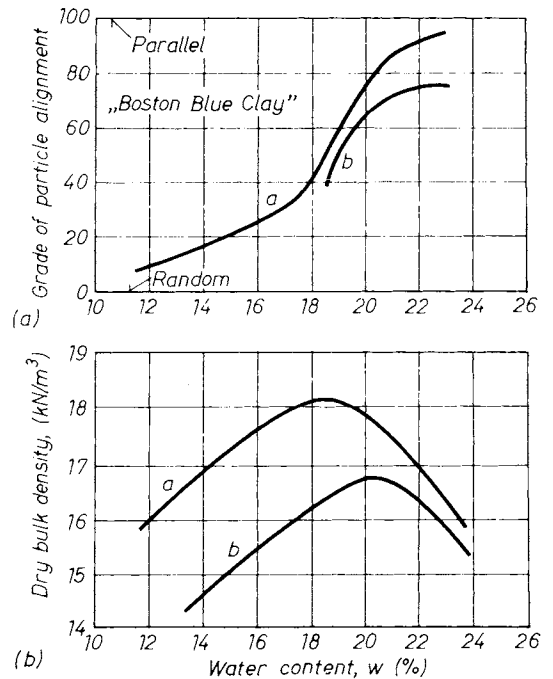


Fig. 423. Influence of moulding water content on the structure of compacted soils for different compacting efforts

When two samples of the same water content are compacted under different compaction energies, the expansivity will be higher in the sample compacted with the higher compaction energy (Fig. 426) (MARSAL and RESENDIZ, 1975).

As will be demonstrated subsequently, the strength and deformation characteristics of soils are also influenced by the structure. However, before embarking upon this important problem, the influence of structure will be examined in the case of granular soils. Evidently, these have no structure proper, only the solid and fluid phases are arranged in different patterns (cf. Vol. 1, p. 119, Fig. 88). At the optimum moisture level, the structure *b* changes to *c*. Here the air-filled

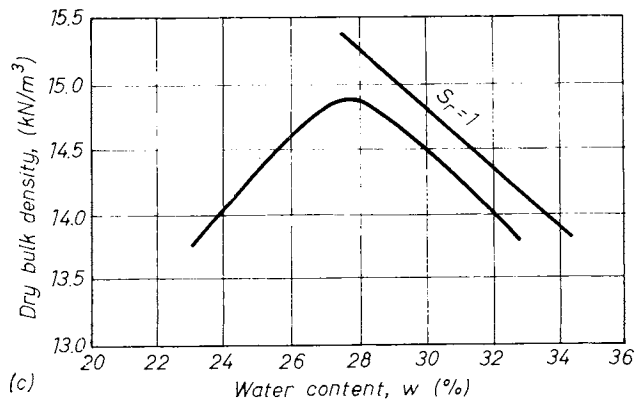
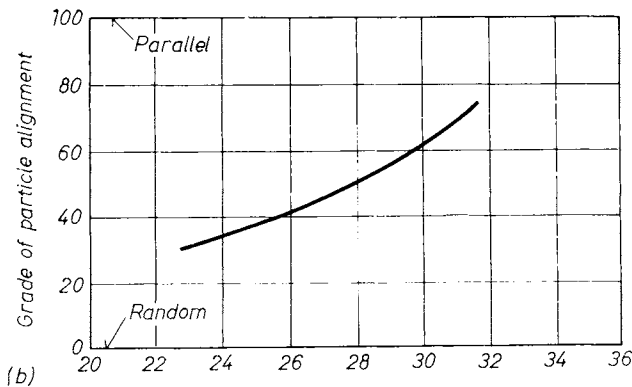
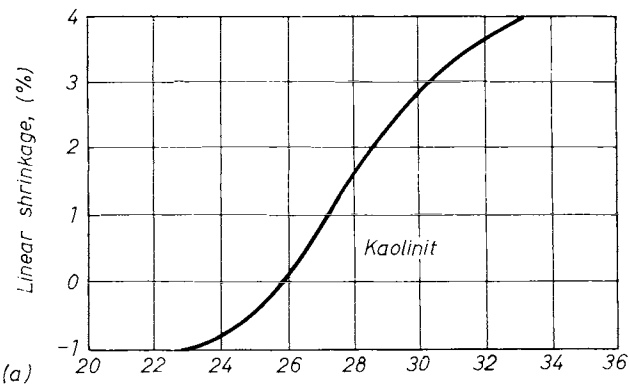


Fig. 424. Influence of the soil structure on shrinkage: a — shrinkage as a function of moulding water content; b — order of disposition; c — compaction curve

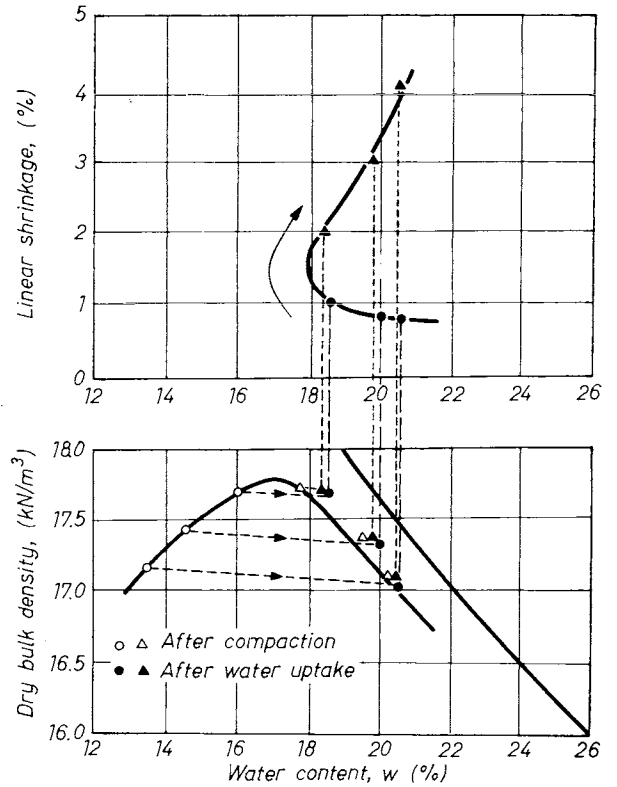


Fig. 425. Shrinkage of compacted samples after water uptake

pores are still communicating, so that it is mainly air that is expelled by compaction. On the other hand, the majority of the solid particles is enveloped by a water layer, enabling them to become rearranged more readily into a denser packing.

Extending the concept of structure also to the arrangement of coarse and fine particles raises the question, in which way is the density attainable influenced by the uniformity of grain-size distribution. This question has been examined in detail in experiments at the laboratory of the Geotechnical Department of the Technical University of Budapest (KABAI, 1968). The granulometric curves of soils produced artificially by mixing are shown

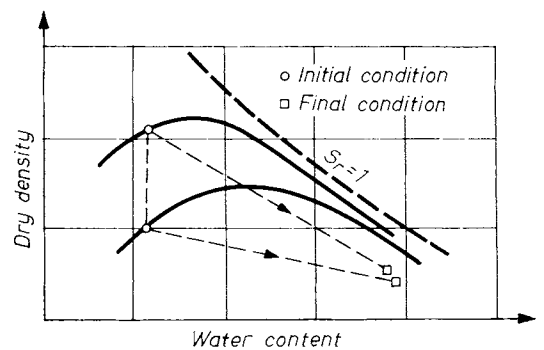


Fig. 426. Expansivity of two clay samples at the same water content under two different compacting efforts (MARSAL and RESENDIZ, 1975)

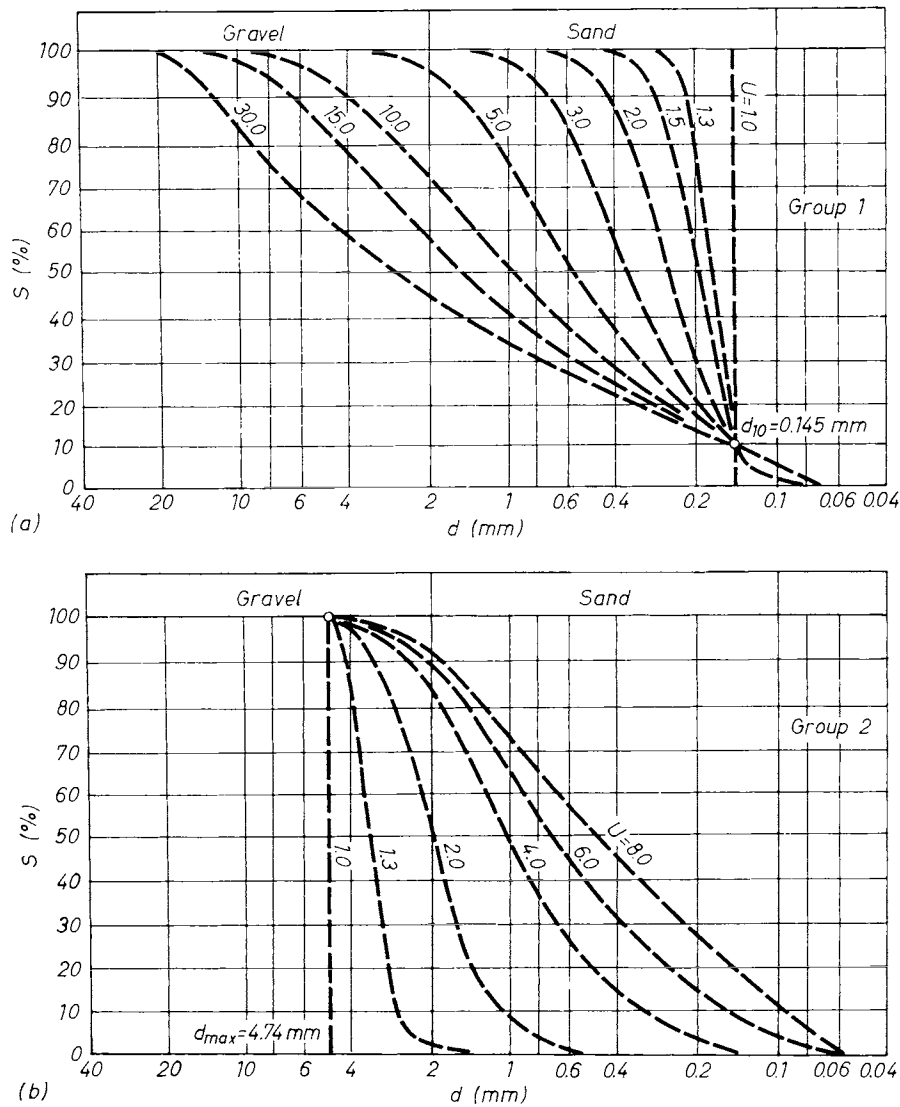


Fig. 427. Grading of the investigated soils

in Fig. 427. The curve of each soil belonging to Group 1 passes through the point $d_{10} = 0.145$ mm, $S = 10\%$, the uniformity coefficient ranges from $U = 1$ to 30. In Group 2 the greatest size is identical ($d_{max} = 4.74$ mm), but the grading is different with $U = 1$ to 8. The optimum water content was found to depend on the uniformity coefficient, in that w_{opt} decreased as U was increased. The relationship is indicated in Fig. 428 for two different compactive efforts, namely $A_1 = 20$ and $A_2 = 3500$ kNm/m³, the first representing manual, the second mechanical compaction. As is to be seen, the decrease of w_{opt} at higher U values is considerable. This is probably due to the fact that soils having higher U values produce higher densities, so that less water is needed for developing the water films ensuring the optimum moisture.

The effect of compaction on the dry density of soils belonging to Group 1 is displayed in Fig. 429,

where the variation in dry density is plotted against the compactive effort per unit volume. The curves originate at the $A = 0$ value from γ_0 values the magnitude of which increases with the uniformity coefficient. In other words, the void ratio in the loosest condition is the lower, the higher the value of U . It is interesting to note that the shape of the curves is virtually identical, thus the increment dry density γ_0 produced by a particular compactive effort A shows but slight differences at different U values, as will be perceived from Fig. 430, where the γ_0 values are plotted against A . The higher density attained by compaction is thus primarily the consequence of the lower void ratio already pertaining in the less uniformly graded soil under uncompacted conditions, the compactive effort producing a largely identical reduction of the pore volume.

The influence of uniformity in response to compaction, viz. on the γ_0 value attainable for

a given compactive effort, is illustrated in Fig. 431. The diagram definitely reflects the fact that uniform grain-size distribution is an important factor in compactibility; the effect of grain size itself being slight in the case of sands.

The results of the foregoing study may be summarized as follows:

- the density of a loosely dumped granular material is the greater, the higher the uniformity coefficient;
- the optimum moisture of compaction is the smaller, the wider the range of grain sizes in the soil;
- a given compactive effort applied to the sands used in the experiments has largely produced the same increase in density, the influence of the void ratio in the loosest state being negligible;
- the density γ_0 attained depends primarily on the granulometry of the soil and increases together with the uniformity coefficient.

The last of these statements has long been known, the results presented have provided additional numerical evidence.

From the results of these experiments the following conclusion of major interest has been arrived at. The numerical value of the degree of compaction $T_{r\gamma}$ is hardly affected by the uniformity of the granular medium, i.e. sand. This fact is positively demonstrated by the curves in Fig. 432, in which the compaction curve, viz. the increase in density γ_0 , is plotted against the compaction energy for two mixtures having dif-

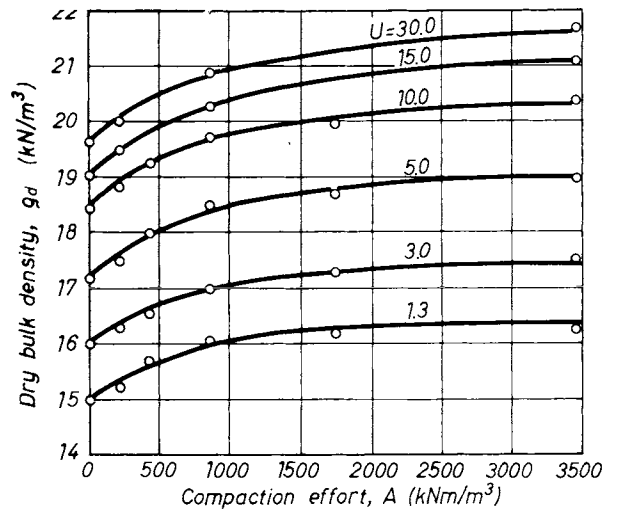


Fig. 429. Effect of compaction on dry density

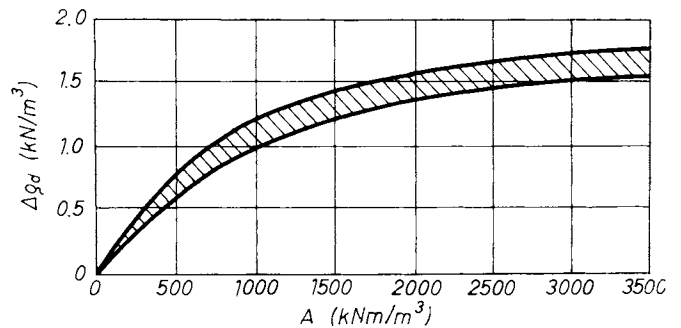


Fig. 430. Dry density increases as the compacting energy increases

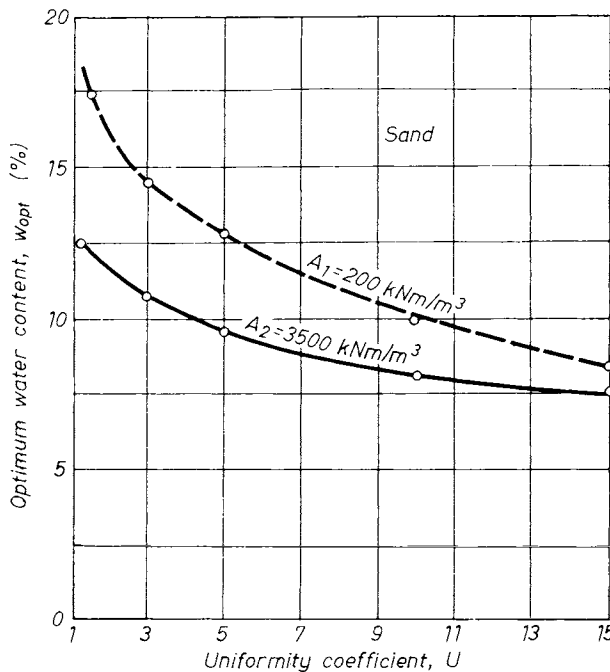


Fig. 428. Optimum water content as a function of uniformity coefficient

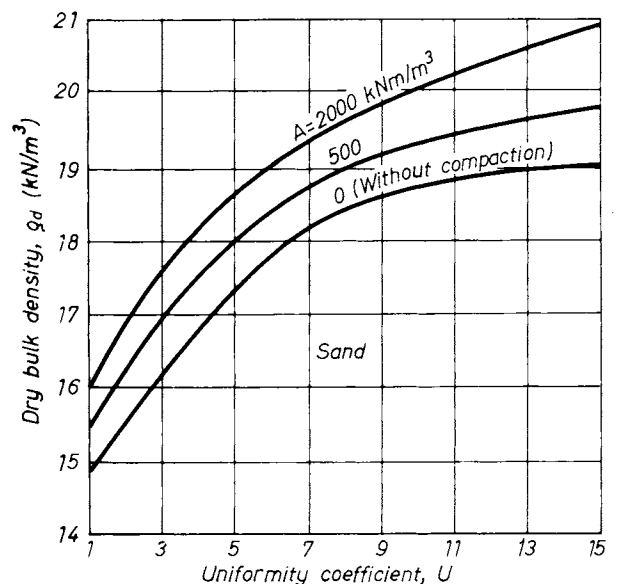


Fig. 431. Contribution of the uniformity coefficient to attainable max. dry density

ferent U values. From these curves the value of T_{ry} can be computed (Fig. 432b). Once the desired value of T_{ry} has been specified for a particular earth structure (e.g. $T_{ry} = 90\%$ in the figure) the specific compactive effort needed for attaining that value can be found from the curves computed. Although the effort needed for compacting the soil with the higher U value is undeniably smaller, the difference is practically insignificant (16%).

This, however, should not be misunderstood to imply that the uniformity of gradation is unimportant in granular soils. In the final count, what we are interested in is the strength, durability and low compressibility of the soil and these are guaranteed by a high angle of internal friction and a high compression modulus, rather than by a high T_{ry} value. These factors, in turn, depend on the absolute magnitude of the density attained, and not on T_{ry} . A particular value is attained in the more uniformly graded soil with a smaller effort, thus at lower cost.

It should be pointed out also that besides the position, the shape of the Proctor curve is also determined by the type and texture of the soil. The coarser the grains, the closer to each other the two limbs of the curve are situated. The same trend will be observed for the U value as well.

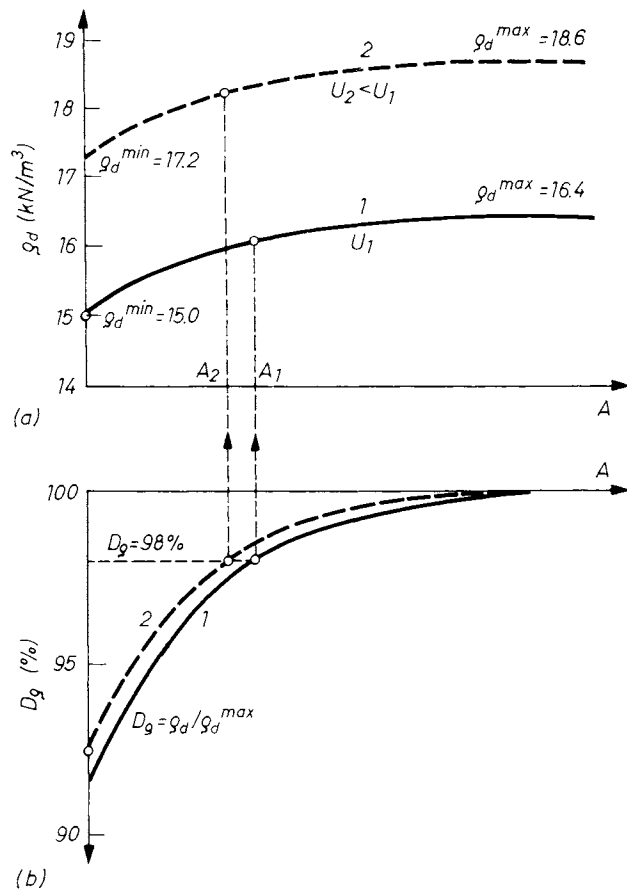


Fig. 432. a — Compaction curves ($g_d = f(A)$) for two soils of different U ; b — variation of relative density as a function of compaction energy

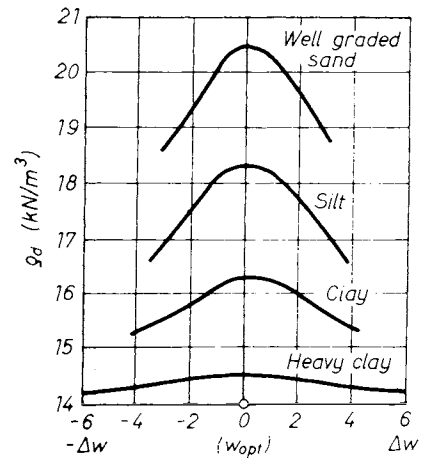


Fig. 433. Compaction curves plotted symmetrically to $w = w_{opt}$.

Consequently, the soils which are coarser, or have a higher U value, are thus more susceptible to changes in moisture. A change as small as 2 to 3% may already cause an appreciable reduction in dry density. This susceptibility will become even more conspicuous, if the compaction curves are plotted in the manner shown in Fig. 433, i.e. by plotting the w_{opt} values on the vertical axis. The coarser the soil, the higher the dry density attainable and the more readily it responds to changes in moisture.

The compactive effort required also depends on temperature. In warm weather higher densities are attainable at lower w_{opt} values. The logical explanation of this phenomenon is that the viscosity of the pore water decreases as the temperature increases, lending greater mobility to the particles.

5.2.1.5 Density, moisture and strength

In cohesionless granular soils the problem is a fairly simple one, in that a virtually positive relation exists between the void ratio and the shear strength.

In cohesive soils the situation is much more complicated, since the shear strength depends on the condition of the soil and on the method of compaction. Compacted soils are almost invariably unsaturated and structured, the anisotropy being caused by compaction itself.

For this reason the familiar fundamental equation becomes

$$\tau_s = (\sigma - u) \tan \Phi' + c'$$

and the concept of effective stress is inapplicable to compacted cohesive soils.

In unsaturated soils the pores are filled with water and air, the pressures in the two are not necessarily equal. The air is dissolved in the pore water to an extent depending on pressure, it may

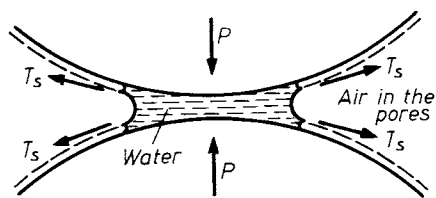


Fig. 434. Active surface stresses between two soil particles

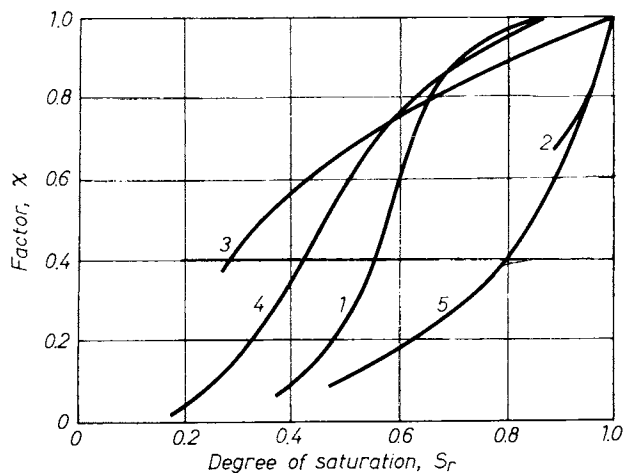


Fig. 435. Variation of the parameter χ with the degree of saturation for different cohesive soils 1 to 5

form closed bubbles in the water, or it may communicate with the atmosphere. The compressibility of such soils will consequently differ from that of saturated ones. The state of stress is further influenced by additional stresses prevailing between the particles due to the surface tension of water (Fig. 434).

With the foregoing considerations in mind, the effective stresses in unsaturated soils are described according to BISHOP (1955) by the expression

$$\bar{\sigma} = \sigma - p_l + \chi(p_l - u), \quad (509)$$

where $\bar{\sigma}$ is the effective stress directly related to strength and volume changes, σ is the total stress, p_l is the pressure in the pore water and u is the neutral stress prevailing in the water, while χ is an empirical factor whose magnitude varies between 0 and 1, depending on the degree of saturation. The $\chi = f(S_r)$ relationship has been reproduced (after BISHOP and DONALD) in Fig. 435.

The term $(p_l - u)$ is thus a positive additive to the effective stress enabling the soil to absorb water. At the same time it is indicative of the actual condition relative to the equilibrium moisture content.

The condition immediately after compaction is illustrated by an example after SEED and CHAN (1959). Three compaction curves are shown in

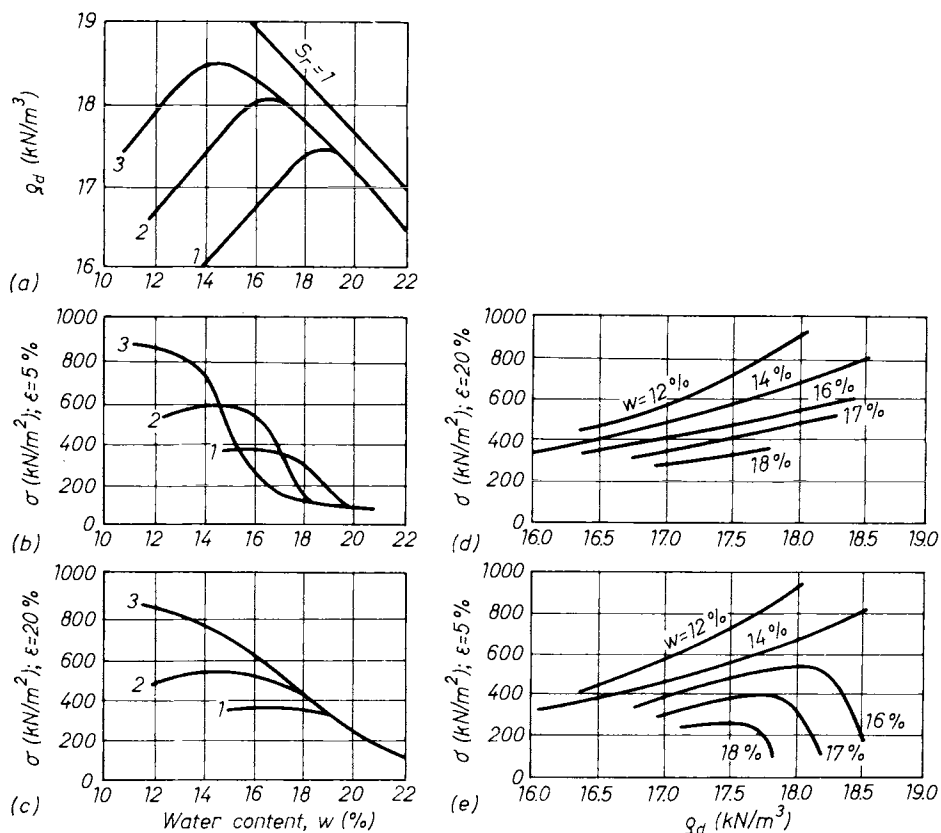


Fig. 436. Illustration of effects introduced by soil structure:

a — compaction curves for three different stress conditions; b — and c — stress values causing 5 and 20% deformations, respectively; d — and e — stress values causing these deformations as functions of dry densities

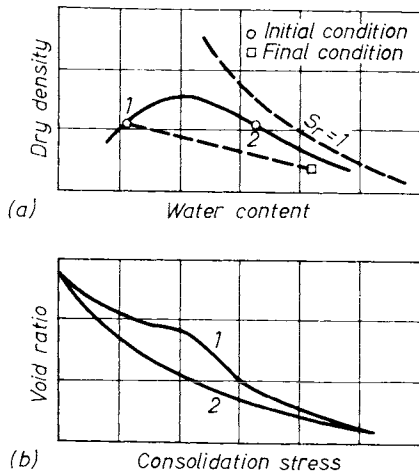


Fig. 437. Expansivity (a — swelling under access of water) and compressibility (b — void ratio vs. pressure) of two clay samples compacted to the same dry density below and above w_{opt} . (MARSAL and RESENDIZ, 1975)

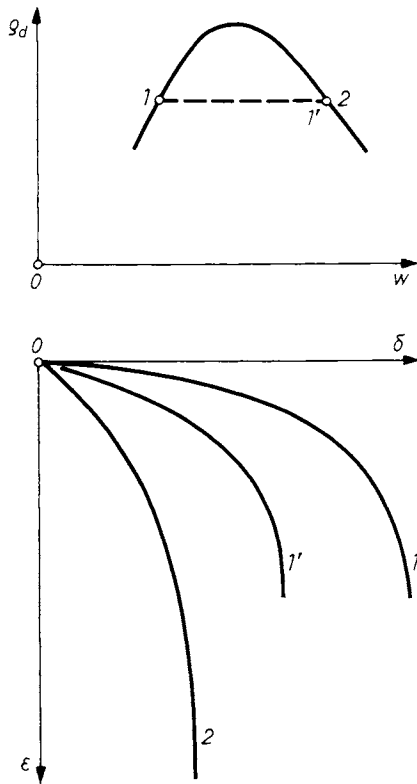


Fig. 438. Strength of compacted samples of the same density but of different structures

Fig. 436. The clay has been compacted by kneading at three different stresses.

Compression tests have been performed on the compacted specimens, the deformation curves yielding the stresses causing 5 and 20% deformation. These have been plotted for each Proctor curve in Fig. 436 and c as a function of water content. The stress pertaining to small compression values (5%) is seen to decrease beyond a certain γ_0 value. Greater densities are thus, paradoxically, accompanied by lower strength. Considering the compact curves, this phenomenon will be observed to appear at a high degree of saturation, i.e., in the case of compaction on the wet side, where the texture is composed of dispersed particles and compaction gives rise to the development of pore-water pressure. It seems thus safe to conclude that strength increases with density as long as the texture remains unchanged.

If two samples are compacted to the same dry density at water contents below and above the optimum, their relative compressibility will be like that shown in Fig. 437. As is seen, under increasing load, the void ratio versus load curve for the sample compacted on the wet side of optimum shows a steadily decreasing slope (curve 2). That of the sample compacted on the dry side of optimum has two portions, each similar to a curve, linked by a transition with a rapidly increasing slope (curve 1).

Compacted clays may exhibit appreciable thixotropic effects, i.e. the ability to gain strength with time at rest after compaction at constant water content and density (SEED and CHAN, 1959; MITCHELL, 1961). MITCHELL has suggested that compacting a thixotropic clay creates a somewhat dispersed structure that is compatible with the compacting energy. The natural tendency may be for the clay to flocculate, however, so that on completion of compaction, the clay structure may

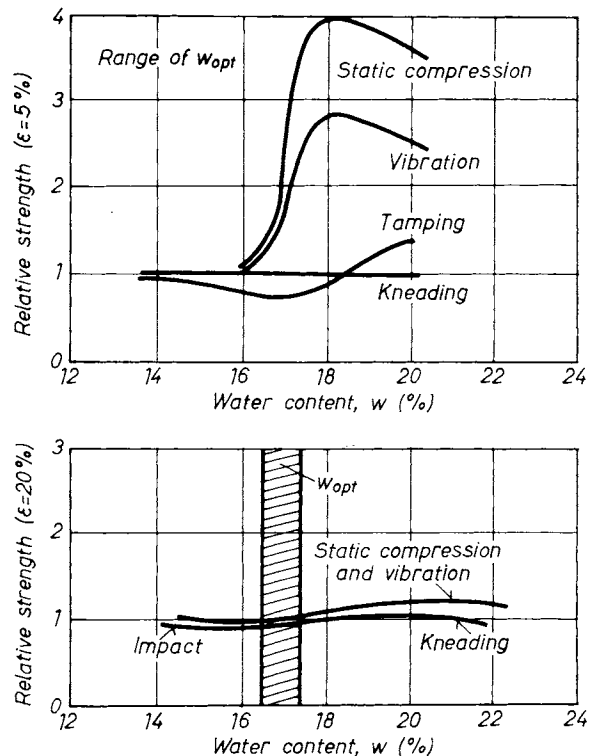


Fig. 439. Relative strength of samples compacted by different methods

undergo a small but significant, time-dependent transition to a more flocculated state. At the same time, changes in adsorbed water structure probably take place, because the measurement has shown water pressure to decrease with time after compaction (BISHOP *et al.*, 1960). Both of these effects tend to create a stronger material.

The soil placed in an embankment, a dam, or in the subgrade of a pavement may absorb water during the service life of the structure. This will cause loss of strength, with adverse consequence on stability or load-bearing capacity. This is the reason prompting a study into the effect of moisture uptake on compacted soils. Two samples of the same soil are compacted to the same dry density, one on the dry side (1), the second on the wet (2) and the first is then saturated without allowing it to swell (Fig. 438). The first sample will, in general, display greater strength. This difference is also due to structure. Compaction has imparted a coagulated structure to sample 1, which it has retained even after saturation. This is the reason for the greater strength.

The effect of some compaction methods on strength is demonstrated in Fig. 439. The relative strength, *versus* the ratio of the strength observed to that displayed by a sample compacted to about the same density by kneading, is plotted on the vertical axis. Two diagrams have been plotted, the first showing the strength pertaining to 5, the second that to 25% deformation. The method of compaction will be clearly observed to have hardly any effect on strength, as long as compaction is performed on the dry side, whereas on the wet side the differences are wide. Strength

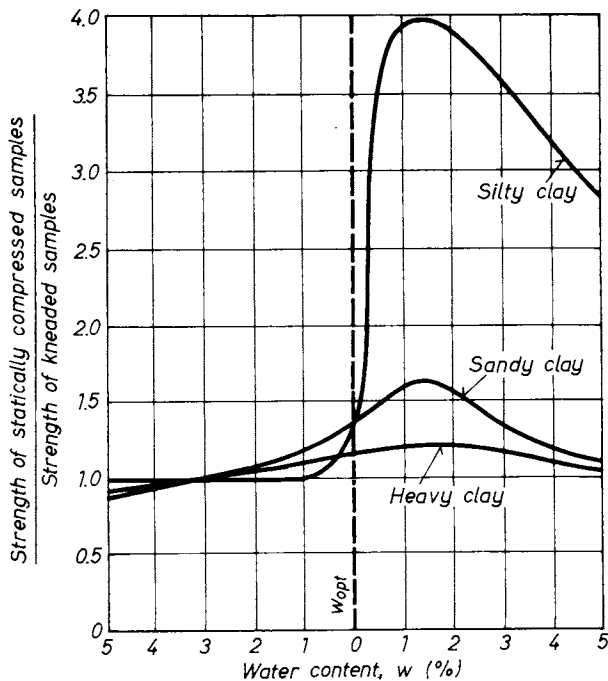


Fig. 440. Strength of different soils when compacted by different methods

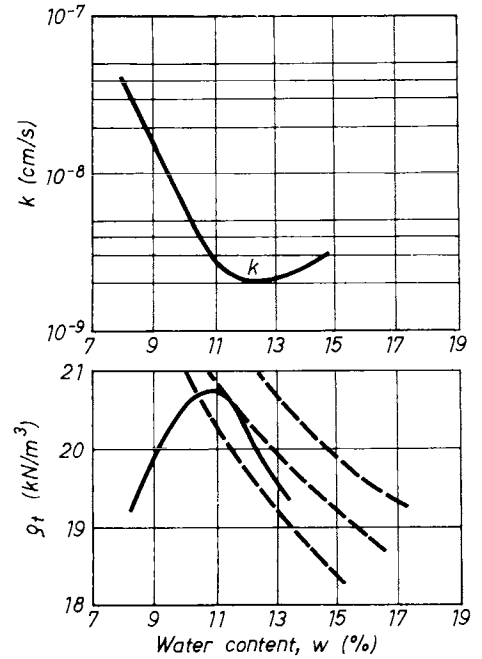


Fig. 441. Variation of permeability in compacted samples at the equilibrium stage

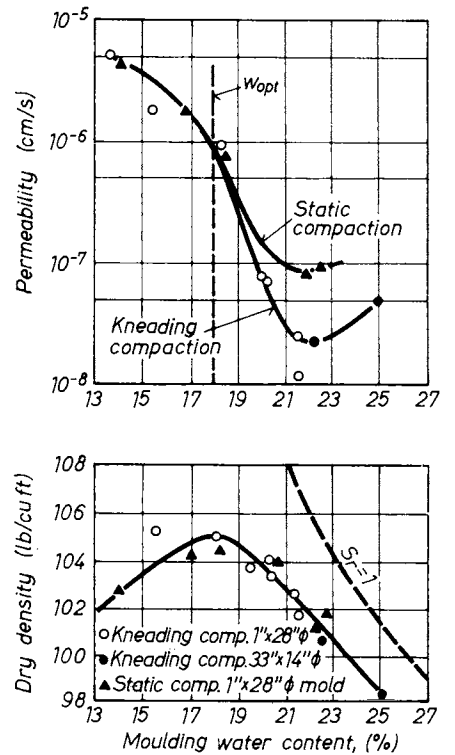


Fig. 442. Influence of micro-structure on permeability of a silty clay (MITCHELL *et al.*, 1965)

is seen to increase in the sequence kneading, tamping, vibration, static pressure. The uniformity of orientation and pore-water pressure appear to decrease in this order and the most coagulated

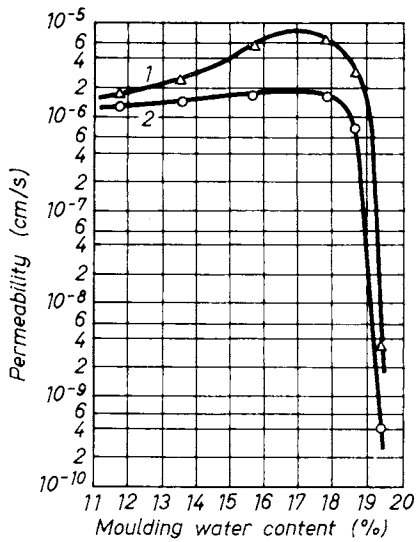


Fig. 443. Effect of aging on the permeability of a compacted silty clay:
 1 — samples tested 21 days after compaction; 2 — samples tested immediately after compaction (MITCHELL *et al.*, 1965)

structure to yield the greatest strength. The plot of strengths pertaining to 25% compression will, however, reveal no differences those between structuring, and thus strength, being obliterated by the great deformations.

The aforementioned differences are shown for several soil types in Fig. 440, where the effects of static pressure and kneading are compared.

5.2.1.6 The effect of compaction on permeability

In cohesive soils, permeability also depends on structure, as exemplified by Fig. 441. The compacted samples have been tested at constant volume and permeability determined at equilibrium. On the dry side, *k* was found to decrease rapidly with increasing moisture and to reach a lowest value at $w = w_{opt}$, increasing again slightly beyond this point.

In Fig. 442 the effects of both compaction method and compaction water content are included (MITCHELL *et al.*, 1965).

If a transition to a more flocculent structure takes place to cause thixotropic hardening, it would be expected that the permeability should increase as well, because the more flocculent structure should have a larger effective pore size. In order to investigate the effect of aging, two sets of specimens were compacted by MITCHELL *et al.* (1965). One set was tested immediately after compaction, and the other was aged at constant water content and density for 21 days and then tested. The results are shown in Fig. 443. This is one of the risks involved in extrapolation of laboratory measurements to field conditions.

The response of compacted soils to water is of particular interest in the case of dams and flood levees. The effect of repeated cycles of wetting and drying has been studied by PORTER (1955), who found that compacted clays will not disintegrate, only swell and shrink, if the uptake and loss of water occurs at a slow rate. Density has suffered no change even after several cycles of wetting and drying. Fast rates of changes in moisture will, on the other hand, cause the soil to crack and disintegrate.

5.2.1.7 Relationship between the index properties and compaction characteristics of soils

Table 39 has been compiled by GÁSPÁR (1964) and it indicates the modified Proctor density for different types of soil. Experience in Hungary has demonstrated the validity of these data. Empirical formulae have also been given by GÁSPÁR for finding the optimum water content. The diagrams plotted from these are shown in Fig. 444. The value of γ_0^{max} is from tables. The relationship between the Atterberg limits and w_{opt} has also been plotted in Fig. 444.

Results from the U. S. A. are shown as illustrative examples of the great number of tables and diagrams. The chart of Fig. 445 (AASHTO T 99-49), compiled on the basis of 972 experiments, is most

Table 39. Characteristic compaction parameters for typical Hungarian soils, after GÁSPÁR (1964)

Soil type	W_{opt}	γ_{0max} (kN/m ³)
Silty gravel, silty broken stone	5. . 10	20.0. . 22.5
Sandy gravel, gravelly coarse sand	4. . 7	19.5. . 21.0
Silty sand	$U > 5$	19.0. . 20.5
	$U = 2.5. . 5.0$	18.2. . 19.5
Fine sand	$U = 1.3. . 2.5$	17.0. . 18.2
Sand from the shore of Lake Balaton	$U = 1.3. . 1.7$	15.8. . 16.6
Silty Mo	$I_p = 5. . 10\%$	19.0. . 19.8
Silt	$I_p = 10. . 15\%$	18.5. . 19.5
Clay	$I_p = 15. . 25\%$	17.5. . 19.2
Heavy clay	$I_p = 25. . 45\%$	16.5. . 18.0

simple to use. Further studies were conducted in 1961 from the results of which the following formulae were derived (RING and SALLBERG, 1962):

$$\ln w_{opt} = 0.784 \ln w_L + 1.378(f_a + 100) - 6.586 \quad (510)$$

and

$$\ln \gamma_{0max} = 3.127 - 0.567 \ln (w_P + 20) - 0.110 \ln f_a \quad (511)$$

The formulae are represented graphically in Fig. 446, indicating at the same time the range used for compiling the formula. In these expressions f_a is the mean of the ordinates pertaining to the values $d = 2.0, 0.42, 0.047, 0.02, 0.005$ and 0.001 mm on the grain-size distribution curve.

5.2.2 Deep compaction

5.2.2.1 Blasting

Deep compaction by detonation of buried explosives can provide a rapid, low cost means for soil improvement. The general procedure consists of (MITCHELL, 1981):

1. installation of a pipe by jetting, vibration, or other means to the desired depth of charge placement;
2. placement of the charge in the pipe;
3. backfilling the hole;
4. detonation of charges according to a pre-established pattern.

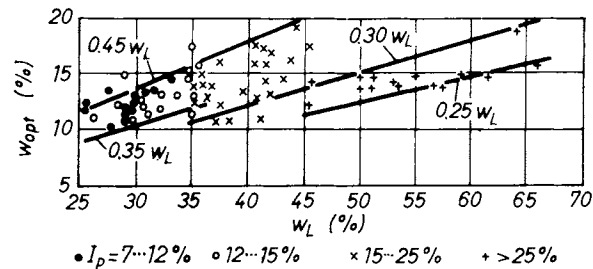


Fig. 444. Observed optimum water content values

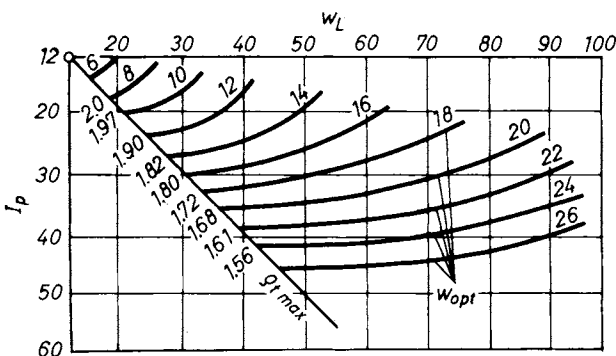


Fig. 445. Diagram to find compaction parameters

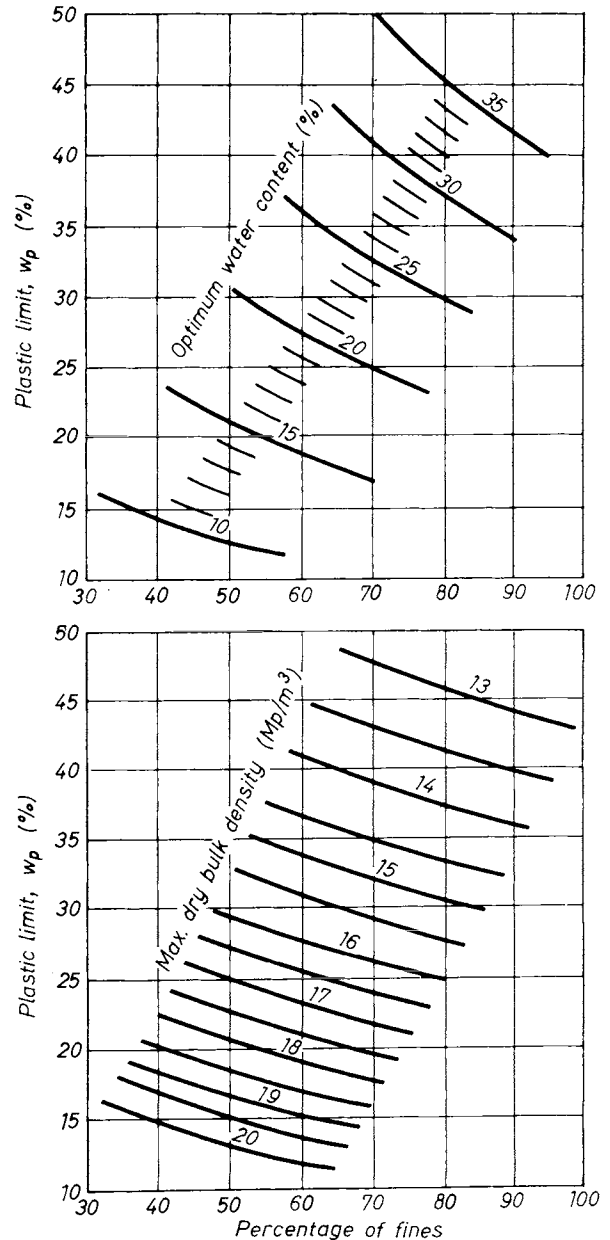


Fig. 446. Experimental relationships to find w_{opt} value

The explosives used include dynamit, TNT, and ammonite. Detailed descriptions of blasting are given by IVANOV (1967); MITCHELL (1970); LITVINOV (1973, 1976); DONCHEV (1980) and others.

Saturated clean sands are well suited for densification by blasting. Success in any case depends on the ability of the shock wave generated by the blast to break down the initial structure, and create a liquefaction (see Chapter 6) for a sufficient period to enable particles to rearrange themselves in a denser packing.

There are no generally accepted theoretical design procedures for densification by blasting, field trials are therefore usually used prior to execution.

Table 40. Parameters for estimating blast pressures and impulse values (IVANOV, 1967)

Soil type	Gas content (%)	k_1	μ_1	k_2	μ_2
Sand below water table	0	600	1.05	0.080	1.05
	0.05	450	1.5	0.075	1.10
	1	250	2.0	0.045	1.25
	4	45	2.5	0.040	1.40
Moist sand (8–10% water) (2–4% water)	—	7.5	3.0	0.035	1.50
	—	3.5	3.3	0.032	1.50

The required disruptive stress will increase with depth, and the effective radius of influence will decrease. The magnitudes of the shock wave pressure, P_{\max} (in $\text{kp}/\text{cm}^2 = 100 \text{ kN}/\text{m}^2$), and the impulse per unit area, I (in $\text{kp} - \text{s}/\text{cm}^2 = 100 \text{ kN} - \text{s}/\text{m}^2$), are given by IVANOV (1967) as follows:

$$P_{\max} = k_1 \left(\sqrt[3]{\frac{C}{R}} \right)^{\mu_1} \quad (512)$$

and

$$I = k_2 \sqrt[3]{C} \left[\sqrt[3]{\frac{C}{R}} \right]^{\mu_2}, \quad (513)$$

in which C is the size of charge (kg of TNT), R is the distance from centre of charge (m), μ_1 and μ_2 are empirical coefficients to be taken from Table 40.

A hydro-blasting technique has been used very successfully and economically for compaction of collapsible loess deposits (LITVINOV 1973, 1976; DONCHEV, 1980). Although collapse of the loess can often be accomplished by flooding alone, it has been found that more uniform results can be achieved more quickly and economically by this method.

5.2.2.2 Vibrocompaction

The process of vibrocompaction is thoroughly reviewed in the presentation by MITCHELL (1981). The procedures are characterized by the insertion of a cylindrical or torpedo-shaped probe into the ground, followed by vibration during withdrawal. In a number of these methods a granular backfill is added, so that a compacted sand or gravel column is left behind within the mass of sand compacted. Sinking of the probe to the desired treatment depth is usually accomplished using vibratory methods, often supplemented by water jets at the tip. Injection of air at the same time has been found to facilitate penetration to large depths. Upward directed water jets along the sides have also been found helpful in some cases. Soil gradations suitable for densification by vibrocompaction are indicated in Fig. 447. Such methods used at present include:

(a) Terraprobe method. This method (ANDERSON, 1974) uses a Foster Vibrodriver pile hammer on top of a 0.76 m diameter open tubular probe (pipe pile) that is 3 to 5 m longer than the desired penetration depth. The unit operates at a frequency of 15 Hz and a vertical amplitude of 10–25 mm. It exercises marginal effectiveness in the upper 3 to 4 m of the zone to be densified.

(b) Vibroflotation. The equipment consists of three main parts: the vibrator, extension tubes, and a supporting crane. The vibrator is a hollow steel tube containing an eccentric mass mounted on a vertical axis in the lower part, so as to transmit horizontal vibration. Vibroflot sinking rates of 1 to 2 m/min and withdrawal/compaction rates of about 0.3 m/min are typical. Water pressures of up to 0.8 MPa and flow rates up to 3000 l/min may be used to facilitate penetration. Sand backfill is consumed at a rate of up to 1.5 m^3/m during the compaction process.

(c) Vibrocomposer method (MURAYAMA, 1958). The apparatus and procedure used in this system are shown in Fig. 448. A casing pipe is driven to the desired depth by a vibrator at the top. A sand charge is then introduced into the pipe, the pipe is withdrawn part way while compressed air is blown down inside the casing to hold the sand in place. The pipe is vibrated down to compact the sand pile and enlarge its diameter. The process is repeated until the pipe reaches the ground surface.

(d) Soil vibratory stabilizing method (SVS or Toyomenka method). This type of compaction combines the vertical vibration of a vibratory driving hammer and the horizontal vibration of a Vilot depth compactor. The Vilot is a special probe of about the same size as the Vibroflot units. Sand backfill is used, but water is not jetted for either the sinking or the compacting process.

BROWN (1977) has defined a suitability number for vibroflotation backfills that is given by:

$$\text{SN} = 1.7 \sqrt[3]{\frac{3}{(d_{50})^2} + \frac{1}{(d_{20})^2} + \frac{1}{(d_{10})^2}} \quad (514)$$

in which d_i are the 50, 20 and 10% grain-size diameters in mm. Corresponding suitability numbers and backfill ratings are

0–10	excellent,
10–20	good,
20–30	fair,
30–50	poor,
> 50	unsuitable.

The lower the suitability number, the faster the vibroflot can be withdrawn while still achieving acceptable compaction.

(e) The Vibro-Wing method (BROMS and HANSON, 1984). It consists in principle of a 15 m-long steel rod with a number of wings welded to it. The unit is driven down into the fill using a high

capacity vibratory hammer and then slowly pulled out during continued vibration. The time needed for driving and withdrawal of the unit is about one and five minutes, respectively, the sand being compacted both during the driving and when the unit is being retrieved. When the pore-water pressure corresponds to the total overburden pressure the effective stress is reduced to zero and the soil becomes liquified. Liquefaction occurs first locally around the vibrating wings and it spreads gradually as the pore-water pressure increases around the vibrating unit. If the soil contains layers with low permeability, which is often the case in hydraulic fills, the effectiveness of the method is increased if the sand is relatively coarse, since a longer time will be required for the dissipation of the excess pore-water pressure. The efficiency of the Vibro-Wing method is affected by the size and location of the wings (e.g. in coarse sand the wings should be relatively short and be placed relatively far apart).

5.2.2.3 Heavy tamping

Soil compaction by heavy tamping involves repeated dropping of heavy masses onto the ground surface. The method is also termed dynamic compaction (consolidation), or pounding. When applied to partly saturated soils, the densification process is essentially the same as that for impact compaction (Proctor) in the laboratory (MITCHELL, 1981). In the case of saturated cohesionless soils liquefaction can be induced, and the densification process is similar to that accompanying blasting and vibro-compaction. The effectiveness of the method in saturated, fine-grained soils is uncertain; both success and failure have been reported.

The pounders used for heavy tamping may be concrete blocks, steel plates, or thick steel shells filled with concrete or sand, and may range from one or two up to 200 tons in mass. Drop heights of up to 40 m have been used.

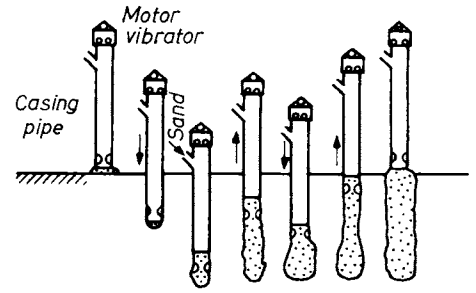


Fig. 448. Construction of compaction piles by the Composer system (MURAYAMA, 1958)

Two or three coverages of an area may be required, separated by time intervals dependent on the rate of dissipation of excess pore water pressure and regain of strength. The general response of the ground as a function of time after coverage is shown in Fig. 449.

The degree of soil improvement depends on soil type, water conditions, and input energy per unit area. Finer grained soils cannot be strengthened to the same level as can coarser materials. Soft layers of clay and peat inhibit high degrees of compaction of adjacent cohesionless material because of their flexibility (MITCHELL, 1981).

Of particular interest is the depth of influence. MÉNARD and BROISE (1975) proposed using

$$D = \sqrt{W \cdot H}, \tag{515}$$

where D is the maximum depth to be influenced (m), W is the falling weight (in metric tons) and H is the height of drop (m).

LEONARDS *et al.* (1980) analysed seven cases and concluded that

$$D = 0.5 \sqrt{W \cdot H} \tag{516}$$

was more appropriate, and LUKAS (1980) suggested that

$$D = (0.65 \text{ to } 0.80) \sqrt{W \cdot H} \tag{517}$$

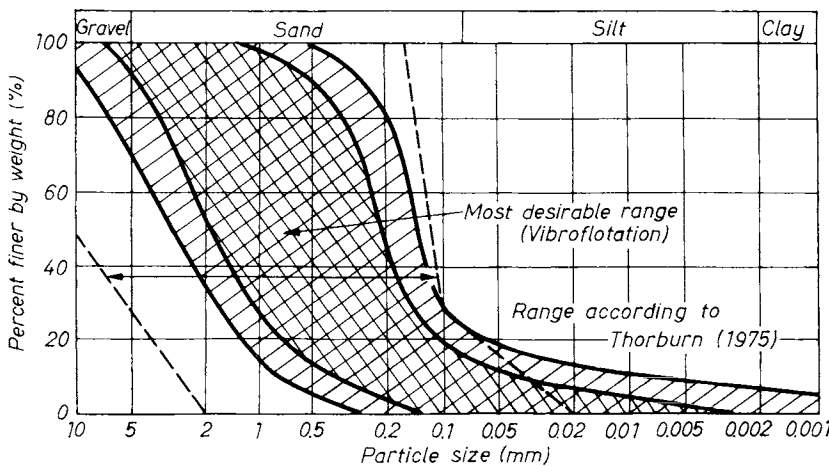


Fig. 447. Range of particle-size distributions suitable for densification by vibrocompaction (MITCHELL, 1981)

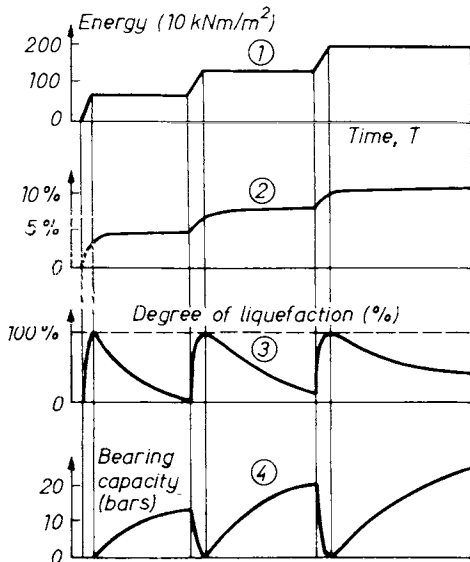


Fig. 449. Ground response with time after successive coverages of dynamic consolidation (MÉNARD and BROISE, 1975):
 1 — applied energy (tm/m²); 2 — volume change with time; 3 — ratio of pore pressure to initial effective stress; 4 — variation of bearing capacity

was the best suited formula for the eight cases that he studied.

The depth of influence depends on other factors as well in addition to the impact energy. Soil type may be expected to be the most important. A crane drop is less efficient than a free drop. The presence of soft layers induces a damping effect on dynamic forces (MITCHELL, 1981).

JESSBERGER and BEINE (1981) explain the principle of the compaction by heavy tamping within the framework of fundamental laws of soil mechanics. For this purpose laboratory tests were carried out — with DYNO-class equipment, and with a fine sand and a silt — to measure the basic parameters and to find a correlation between stress conditions and compaction effects. The experiments carried out on dry sand proved that

$$\Phi_{\text{dyn}} = \Phi_{\text{stat}}$$

When water-saturated silt was tested, the total vertical stress remained constant, whereas the total horizontal stress increased to a limiting

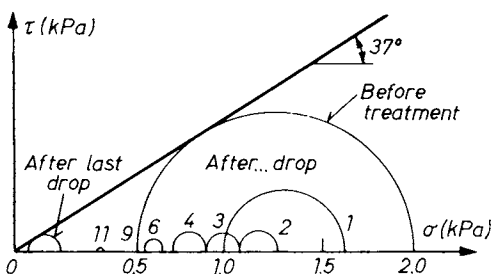


Fig. 450. Effective stresses in water saturated silt under impact loading (JESSBERGER and BEINE, 1981)

value. The effective vertical and horizontal stresses can be calculated from the measurements. The results of a typical trial run are shown in Fig. 450. The state of stress before treatment and after various number of drops are drawn in the form of Mohr's circle using effective stresses. Before treatment the effective vertical stress has a value of $\bar{\sigma}_z = 2.0$ kPa, the effective horizontal stress $\bar{\sigma}_h = 0.48$ kPa. (The state before treatment is characterized as a state of failure.)

During treatment the stress $\bar{\sigma}_z$ decreases immediately after the first single drop because of increase in pore-water pressure. After the first two drops $\bar{\sigma}_h$ increases with increase of $\bar{\sigma}_z$, but with further drops it decreases too. After the eight drops $\bar{\sigma}_h$ has a larger value than $\bar{\sigma}_z$. After the last drop the Mohr circle again touches the failure envelope. At this state the pore-water pressure has reached its maximum, given by the specific weight of the soil. Further drops would damage the soil structure, so that the number of drops until this state is reached is a limiting value for treatment. During the following consolidation the effective stresses increase, $\bar{\sigma}_h$ reaching a larger value than before treatment. The increase of effective stresses is accompanied by settlements at the soil surface.

Amount and type of the dynamic loading can be estimated by measuring the retardation a of the falling weight. By use of Newton's law the stress at the soil surface ($\sigma_{0, \text{dyn}}$ in kN/m²) is calculated from the equation:

$$\sigma_{0, \text{dyn}} = a \frac{m}{A}, \quad (518)$$

in which m is the mass of the poulder (kg), A is the base area of the poulder (m²).

According to the trials of JESSBERGER and BEINE (1981):

$$a = \alpha \sqrt{2gH}, \quad (519)$$

where α (1/s) is a constant of proportionality.

The fact that the maximum retardation is independent of m/A means that heavy tamping in the field can be simulated by laboratory tests. The stress at the soil surface, necessary for compaction down to the required depth z_0 , is dependent on this depth. For estimating the stress distribution under dynamic loading the methods of FRÖHLICH (1934) and KÖGLER and SCHEIDIG (1948) are used. The equations are:

$$\frac{\sigma_{z, \text{dyn}}}{\sigma_{0, \text{dyn}}} = 1 - \left(\frac{z}{\sqrt{z^2 + r^2}} \right)^v \quad (520)$$

and

$$\frac{\sigma_{z, \text{dyn}}}{\sigma_{0, \text{dyn}}} = \left(1 + \frac{z}{r} \tan \theta_0 \right)^{-2}, \quad (521)$$

respectively. In the equations z is the depth, r is the radius of the loaded area, θ_0 is the angle of

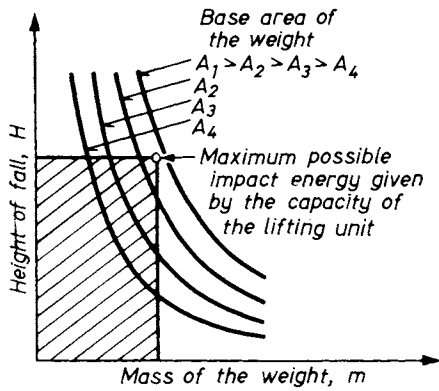


Fig. 451. Design chart for heavy tamping for $z = \text{const.}$ (JESSBERGER and BEINE, 1981)

load distribution, ν is the factor of concentration, and $\sigma_{0, \text{dyn}}$ can be calculated from Eqs (518) and (519).

The required stress $\sigma_{z, \text{dyn}}$ and the parameters α and θ_0 (or ν) have to be determined before the design charts are drawn. As the equations contain four variables (m, H, A, z_0), it is necessary to set one parameter constant to get the dependencies of the three others. The depth z_0 is given by ground conditions, and the working parameters have to be chosen in the design procedure. The laboratory test results are used to prepare a design chart similar to that in Fig. 451. For a constant A various combinations of mass and height can be

used. The possible values are given by the capacity of the lifting unit used, indicated by the hatched zone in Fig. 451.

5.3 Mechanical stabilization

The purely mechanical process of attaining and conserving higher strength of any earth structure by mixing certain soils and compacting the mix carefully, is referred to as mechanical stabilization. This implies that no other additives are used.

Practical experience has shown that for effective mechanical stabilization, the grain-size distribution of a soil should remain between certain limits. These limits are shown in Fig. 452 for a variety of purposes. Attempts have been made to develop formulae for ideal gradation. One of these formulae, suggested by TALBOT, is

$$S = \left(\frac{d}{d_{\text{max}}} \right)^m \tag{522}$$

Another, according to ROTHFUCHS (1935) is

$$S = \frac{d^m - d_0^m}{d_{\text{max}}^m - d_0^m} \tag{523}$$

In this formula, m is an empirical coefficient usually entered with values of 0.4 to 0.5. The specifications of the AASHO (1958) are reproduced in Table 41, while those on the Atterberg limits are given in Table 42.

Table 41. Grading for mechanically stabilized soil-aggregate roads (AASHO*, 1958)

Sieve designation		Percentage by mass passing sieves			
		A	B	C	D
Classification I (coarsely grained)					
	76.2 mm	100			
	50.8 mm	—	100		
	37.6 mm	—	—	100	
	25.4 mm	35 ... 65	50 ... 80	—	100
4	4.76 mm	10 ... 30	15 ... 35	20 ... 40	25 ... 45
200	0.076 mm	—	—	10	10
Classification II (mediately grained)					
	76.2 mm	100			
	50.8 mm	—	100		
	37.6 mm	—	—	100	
	25.4 mm	45 ... 75	50 ... 80	—	100
4	4.26 mm	15 ... 45	20 ... 50	25 ... 55	30 ... 60
10	2.00 mm	—	—	—	20 ... 50
200	0.076 mm	10	12	12	12
Classification III (stabilized)					
	76.2 mm	100			
	50.8 mm	65 ... 100	100		
	37.6 mm	—	70 ... 100	100	
	25.4 mm	45 ... 75	55 ... 85	70 ... 100	100
	18.8 mm	—	50 ... 80	60 ... 90	70 ... 100
	9.4 mm	30 ... 60	40 ... 70	45 ... 75	50 ... 80
4	4.76 mm	25 ... 50	40 ... 60	30 ... 60	35 ... 65
10	2.00 mm	20 ... 40	20 ... 50	20 ... 50	25 ... 50
40	0.42 mm	10 ... 25	10 ... 30	10 ... 30	15 ... 30
200	0.076 mm	3 ... 10	5 ... 10	5 ... 15	5 ... 15

* AASHO — American Association of State Highway Officials

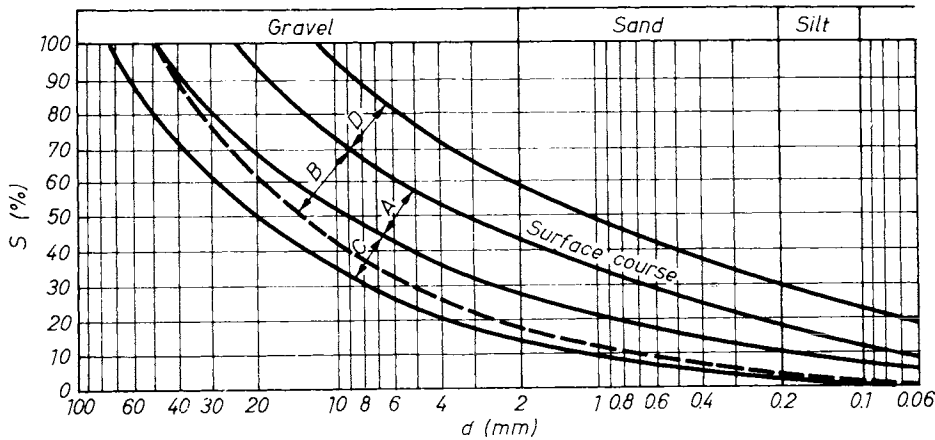


Fig. 452. Grading bands of mixtures suitable for stabilization: A — optimal for base and surfacing courses; B — still useful mixtures; C — band range for wearing courses

Table 42. Requirements in respect of consistency limits

Classification	Layer	I_p	w_L
II	Load-bearing course	< 6	< 25
	Wearing course	< 6	< 25
III	Load-bearing course	< 6	< 25
	Wearing course	4 . . . 9	< 35

Soils meeting the above requirements are but rarely encountered in the field. The material having the desired properties must usually be produced by blending; the corresponding methods have been described in Vol. 1, Section 2.1.7. It should be further noted that blending ratios giving the highest possible uniformity coefficient will prove the most satisfactory.

The strength of the stabilized soil depends on the strength of adhesion and — disregarding the properties of the binding agent — on the density and moisture of the blend. An increasing degree of moisture will cause a pronounced loss in strength. The effect of saturation by capillary rise was found to be the greater, the lower the density of the soil in the original condition.

5.3.1 Cement stabilization

In cement stabilization, a mix consisting of pulverized soil, portland cement and water is produced, resulting in a new material known as soil cement. Owing to its superior strength and durability, low compressibility, and its resistance to water, hot weather and frost, this material is suited for pavements, base courses, canal linings, foundations, etc.

The mechanism by which the stabilizing action of cement is realized differs in fine- and coarse-grained soils (the latter term applying to fine- and medium-grained sands). In fine-grained silts and

clays the hydrating cement develops strong bonds between the mineral particles, resulting in a cemented matrix which encases the unbonded soil grains. The honeycomb structure of the matrix is responsible for the strength of the final product, the strength of the clay particles within the matrix being rather low. The bonds prevent the particles from moving relative to each other, thereby minimizing plasticity and increasing shear resistance. The clay particles are coagulated by the lime liberated in the course of hydration, reducing their affinity to water and thus the swelling and shrinking properties of the soil.

The cementing action in the more granular soils is due to a mechanism resembling that in concrete, with the difference, however, that the voids in the aggregate are not completely filled by the cement paste. Firm bonds are developed only at the points of contact of the aggregate grains ("point weld"). No continuous matrix is created. The strength of the cementing action will increase directly with the density of grading and with the number of contact areas and inversely with the size of the pores.

For a detailed treatment of the chemical processes in soil cement, reference is made to the book "Soil Stabilization" by the senior author (1967).

A wealth of data has been published in the literature concerning the strength of soil cement. The diagram in Fig. 453 has been plotted on the basis of experimental results. The compressive strength of compacted cylindrical samples containing 8% by weight of Class 500 cement and cured for 7 days has been plotted into the triangular diagram. The sides of the triangle indicate the sand content ($d > 0.1$ mm), the silt + clay content ($d < 0.1$ mm), as well as the air- and water content in % by volume. This manner of presentation is convenient, on the one hand, for demarcating the range in which a cement treatment of a soil is at all feasible and in which

strength can be tested. Also, a clear picture is obtained of the influence of density and moisture content. Further information of interest may be found in Fig. 454, showing, again for a particular cement content of the mix, the strength thereof as a function of the percentages by volume of the solids, water and air. This diagram also indicates the range of optimal mix composition. The influence of density will be seen to be especially pronounced, in that an increase in the unit weight of 10% results in a gain in strength of 30 up to 40%.

A result of particular interest is indicated in Fig. 455, where the compressive strength of a silt-sand mixture has been plotted against the mix ratio while the cement content being maintained constant. The dry unit weights and uniformity coefficients have also been entered. All three curves attain a peak value at the same mix ratio. The greatest strength and density are found where U assumes its highest value. A positive relationship was found to exist between U and the compressive strength (Fig. 455b). For different mix ratios of the same U value, identical strengths were obtained.

Most soils to be stabilized by cement treatment must be pulverized before adding the cement and mixing with water. The mix must be subsequently compacted. Strength is also influenced by these processes.

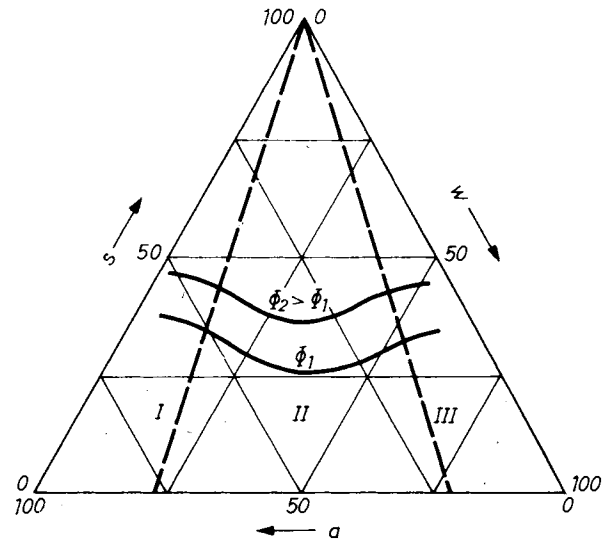


Fig. 454. Strength of field road construction materials represented in the phase-diagram

In a number of applications, the tensile, or flexural strength of the cement-treated soil is also of interest. The corresponding investigations have revealed that the improvement of these properties, attainable primarily by increasing the cement content, is in general slight. Increased cement contents of the mix have, on the other

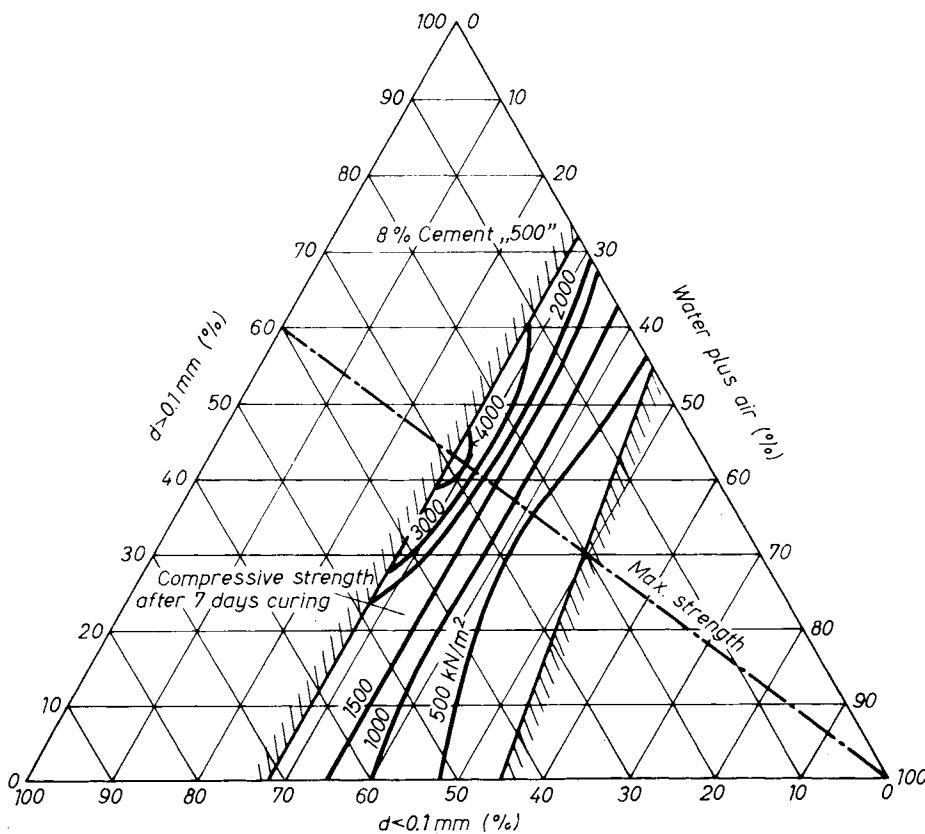


Fig. 453. Strength of soil-aggregate road construction materials with 8% (by volume) cement added

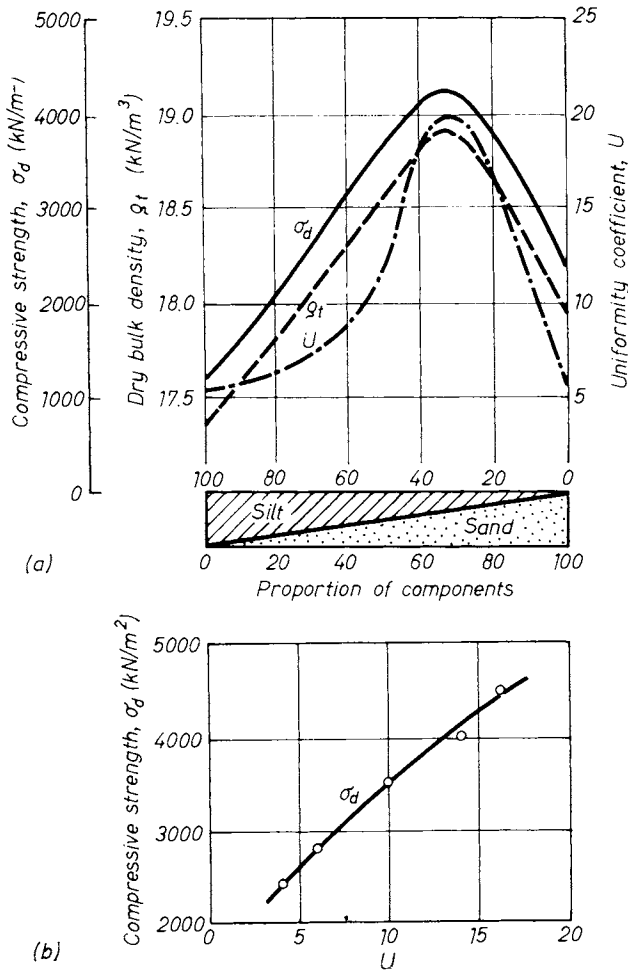


Fig. 455. a — Compressive strength, dry density and uniformity coefficient as functions of proportioned materials; b — compressive strength as a function of uniformity coefficient

hand, a marked influence on the Atterberg limits and on volume changes, as shown by the example in Fig. 456. The granulometric curves of soils suited for cement treatment are shown in Fig. 457.

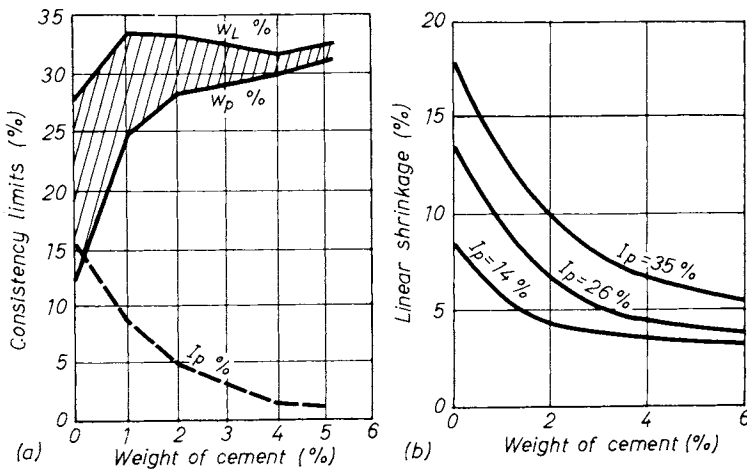


Fig. 456. Variation of the Atterberg-limits and linear shrinkage with cement addition

5.3.2 Lime stabilization

Cohesive soils mixed with lime, in the form of pulverized quicklime, slaked (hydrated) lime, or lime slurry, and subsequently compacted will produce a stabilized soil. The reaction between the lime and the clay minerals present in the soil invariably results in changing the plastic properties and structure of the soil and thereby in a higher bearing capacity. The physical and chemical processes involved have largely been clarified (cf. eg. JESSBERGER, 1967; KÉZDI, 1967). The most impor-

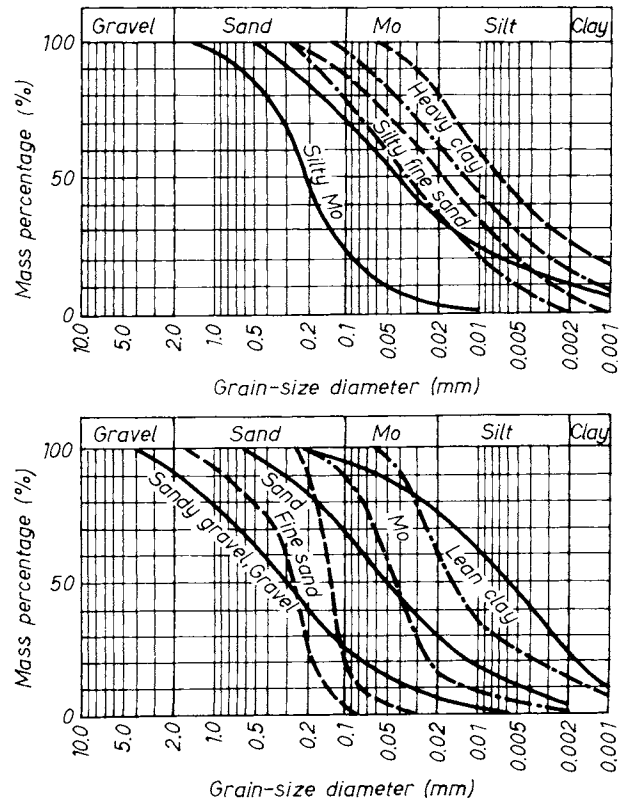


Fig. 457. Grain-size distribution curves of materials suitable for cement stabilization

tant changes in soil properties include (JESSBERGER, 1967):

- coagulation, aggregation;
- reduced affinity to water;
- improved compactibility;
- higher strength.

These changes are related primarily to the change taking place in the soil structure. The change in the Proctor curve is illustrated in Fig. 458, showing the increase in w_{opt} and the decrease in maximum dry density. A major advantage of lime treatment is that the compaction properties of a wet soil can be materially improved thereby. Changes in structure are offered as an explanation for the lowering of the dry density obtainable with a given compactive effort, in that water is needed for hydration restricting the mobility of the coagulated particles.

Another important effect is that cohesive soils treated with lime display virtually no swelling and shrinkage is also greatly diminished.

The most important effect of lime treatment is the gain in strength, the extent of which depends on several factors. According to Fig. 459 the influence of aging time is insignificant, as long as the lime content is small, but it increases together with the lime percentage. The cementation process takes place at a rather slow rate and even tests performed after 28 days do not yield the eventual strength values.

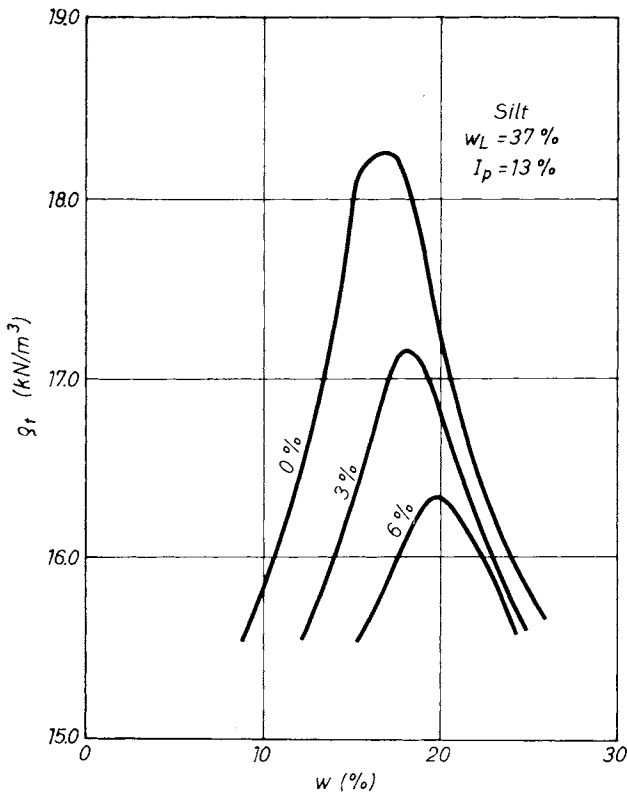


Fig. 458. Effect of lime addition on compaction curves

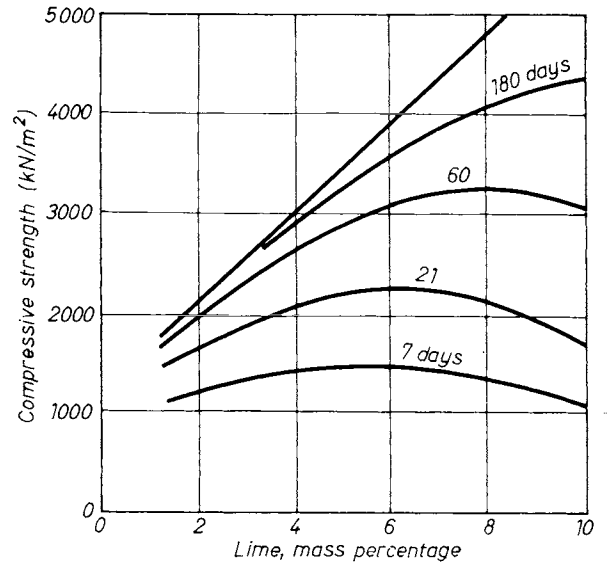


Fig. 459. Effect of aging on the strength of lime stabilized soil

As regards response to lime treatment, soils are classified according to the grain-size distribution curves into the groups shown in Fig. 460. Soils belonging to Group A are too coarse to be processed and are thus unsuited to lime stabilization. In Group B — sands — lime treatment remains similarly ineffective, the soils still being too coarse. The addition of lime results in no gain in strength, since the carbon dioxide of the air finds no access to the stabilized layer. The group in which lime treatment can be applied effectively has been denoted by C. Rather than the grain-size distribution, it is the mineralogical-chemical effect of the fine components which is decisive in such soils. The soils belonging to Group D are again unsuited to lime treatment, since these are too heavy and thus uneconomical to process.

The improvements in the engineering character of lime-soil mixtures are attributed to four basic reactions. These, based on currently available literature, and on THOMPSON'S (1966) reference, include the followings.

1. Cation exchange. The general order of replaceability of the common cations associated with soils is given by the lyotropic series, $Na^+ < K^+ < Ca^{++} < Mg^{++}$. Any cation will tend to replace the cations to the left of it, and monovalent cations are usually replaceable by multivalent cations. In some cases, the exchange complex is practically Ca^{++} saturated before the lime addition and cation exchange does not occur, or is minimized.

2. Flocculation and agglomeration. These reactions result in apparent change of the texture and — together with the cation exchange — are primarily responsible for the changes in plasticity, shrinkage, and workability characteristics, but not

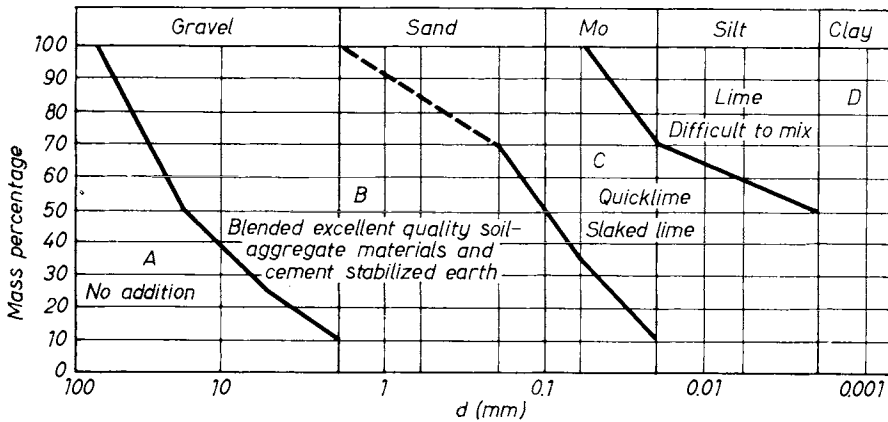


Fig. 460. Grain-size distribution curves of materials suitable for lime stabilization

for strength increase of lime-soil mixtures (THOMPSON, 1966).

3. Lime carbonation. Lime reacts with carbon dioxide to form the relatively weak cementing agents Ca and Mg carbonate.

4. Puzzolanic reaction. This is a reaction between soil silica and/or alumina and lime to form various types of cementing agents. These latter are generally regarded as the major source of strength increases.

According to THOMPSON'S experiments (1966), optimal lime addition is in the range of 3 to 7% by weight. The strength increase can be characterized by the so-called "lime reactivity" which is the result of a subtraction:

$$LR = q_{uk} - q_n, \quad (524)$$

where q_n means the unconfined compression strength of the natural soil, and q_{uk} the maximal unconfined compression strength of the lime-treated soil (independently of the quantity of lime added). The values for Eq. (524) were established by the author on samples compacted at their optimum water content and cured for 28 days. It was found that the "lime reactivity" increased with the pH of the mixture, but decreased considerably when the mass contained organic carbon; with over 1% organic content, lime addition was practically ineffective. The author expressed his opinion that lime treatment would have the best efficiency with soils of substantial Si or Al content.

QUEIROZ (1981) demonstrated, on the basis of his experiments, that the correlation between LR and the SiO_2 or Al_2O_3 content of the soil was not too close ($r = 0.46$ and $r = 0.43$ for the soils tested). When, on the other hand, the regression analysis was based on the amorphous constituents of these compounds, the correlation coefficient improved substantially ($r = 0.79$ and $r = 0.69$). The less crystalline the clay mineral, the more easily the Si/Al will be available for reaction; if

there are amorphous constituents present, the lime will immediately react with them. These experiments have further confirmed that all other geotechnical properties of the clay (w_L , w_P , D_r , etc.) were almost irrelevant in respect to the LR-value.

5.3.3 Bitumenous soil stabilization

The combination of soils with water and bitumen is accompanied by complicated physical and chemical processes. The objective of such treatment is to coat the individual particles with a bituminous film, which is, on the one hand, thin enough not to reduce radically the frictional resistance to the relative movement of the particles and, on the other hand, thick enough to cement the discrete solids. To produce this condition, the steady load must be high enough to squeeze the bitumen from the area surrounding the point of contact. The bitumen film will then coat several particles (Fig. 461), which are more or less in direct contact with each other. Shear stresses in a similar system will cause the coating film to rupture at several points

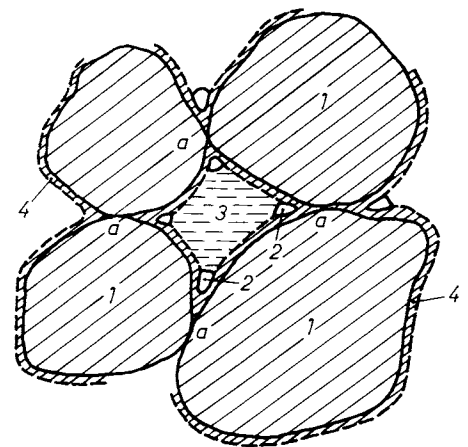


Fig. 461. Bitumen-bounded sand:
1 — solid soil particle; 2 — air bubble; 3 — pore water; 4 — bitumen film; a — contact points between soil particles

and induce frictional resistances of considerable magnitude. The coat is reformed as soon as there is no movement. The surroundings of the contact points are protected from water by the bitumen, preventing the water from entering re-establishing the bonding effect.

Practical experience has shown air-dry and very wet soils not to mix readily with bitumen, while soils with moistures from $w = 4$ to 12% present no difficulty. Surface tension between the individual components and the magnitude of the energy of wetting have been suggested as explanations for this phenomenon. No material can be coated with another, unless the adhesion between the two materials is superior to the bond strength of one of them. Adhesion conditions at 20 °C are shown in Fig. 462, from which it will be perceived that the grains in a dry mass are surrounded primarily by air, the little water present being confined to the corners between the particles. The bitumen added will thus displace the bonded air

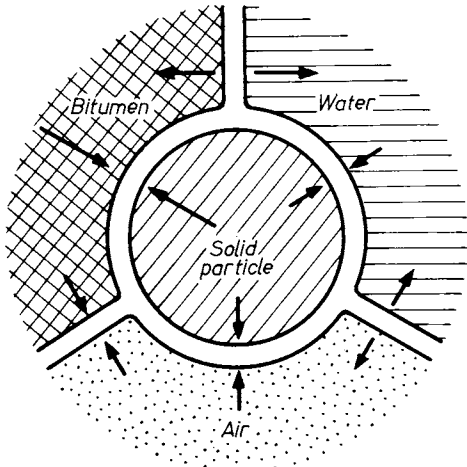


Fig. 462. Specific adhesion between components of bitumen-bounded materials

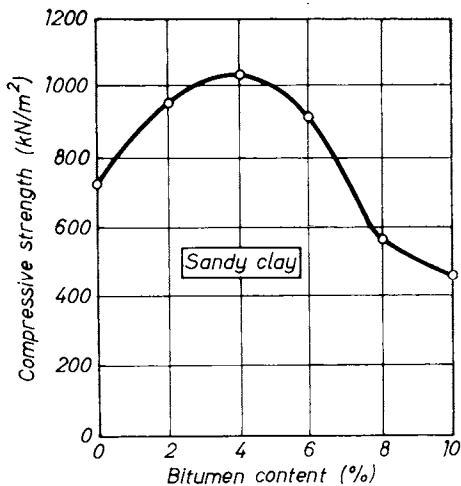


Fig. 463. Strength in a bitumen-bounded soil mass

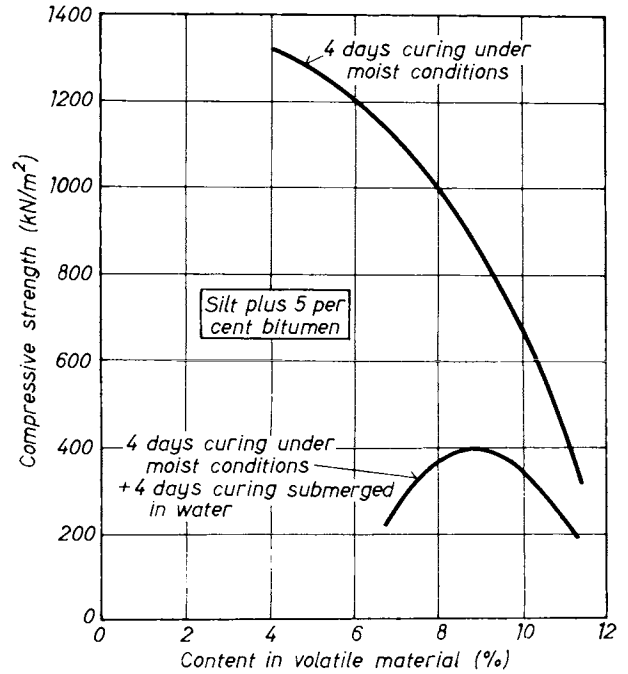


Fig. 464. Influence on strength of aging below water

layer and no coating film will be formed. Conversely, too much water will be present not only in the corners but also in the large pores, forming a thin envelop around the particles. A bitumen-to-solid bond could only be realized by displacing the pore water and by removing the water film. This, however, is impossible because of differences in adhesive forces. There is consequently an optimal water content at which the bonding force and thus strength are greatest.

As is seen in Fig. 463, the strength of the compacted mix depends on the amount of bitumen added, the optimal value being obtained at around 4%. This is due to the structure of soils stabilized by bitumen, as well as to the fact that the dry density attainable with a particular compactive effort decreases as the bitumen content is increased. Low bitumen contents may lead to swelling, loosening and deterioration of the structure, especially in cohesive soils which the small amount of bitumen fails to render impervious. The samples are, therefore, cured for four days in a humid atmosphere and are then submerged in water for another four days. The strength loss caused by such curing provides the clues needed for determining the optimum bitumen content. The results of similar tests are shown in Fig. 464.

According to practical experiments, the soil types suited to successful bituminous stabilization should have the following properties.

1. The diameter of the coarsest particle should not exceed one-third of the thickness of the treated soil layer.

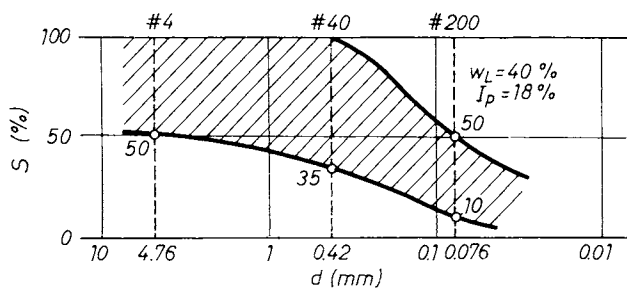


Fig. 465. Grain-size distribution curve of materials suitable for bitumen stabilization

2. The grain-size distribution curve should lie in the shaded area in Fig. 465.
3. The liquid and plastic limits should be lower than 40 and 18%, respectively.

The compaction characteristics (w_{opt} , $\gamma_{0,max}$) of the soil vary with the bitumen content mostly as indicated by Fig. 466, viz. the optimum moisture increases as the maximum dry density is reduced.

The amount of bitumen needed is found simply, in terms of the granulometry, from the formula (JOHNSON, 1957):

$$p = 0.015a + 0.02b + 0.03c + 0.09d. \quad (525)$$

Here p is the percentage of bitumen without solvent, based on dry weight of the soil, while the quantities a , b , c and d are found from Fig. 467.

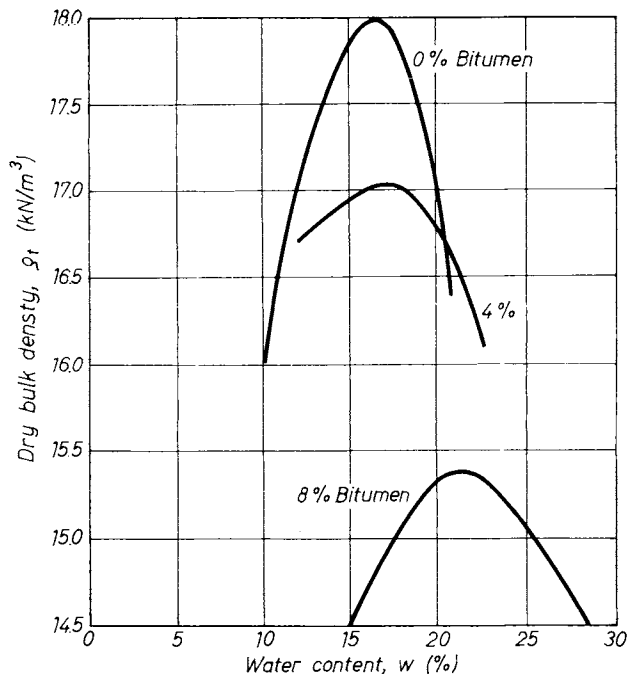


Fig. 466. Influence of bitumen addition on compaction parameters

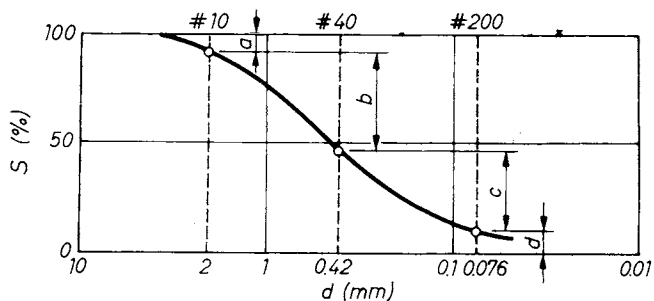


Fig. 467. Determination of design parameters for Eq. (525)

The magnitude of the fine fraction (< 0.076 mm) is considered decisive. The results obtained by Eq. (525) plotted as $p = f(d)$, fit a straight line which is described by the expression

$$p[\%] = 2.75 + 0.064d.$$

5.3.4 Miscellaneous soil improvement methods

Promising stabilizing results have been achieved in Japan by using multivalent cations. MATSUO and KAMON (1981) used poly-aluminium chlorite (PAC) and pulverized iron (Fe^{+++}) for this purpose. The former disperses the clay particles by its cation exchange capacity, while the latter enhances a cementation effect through oxidation and provides a stronger bound through adsorption in the inter-clay particles and intra-aggregates.

WAGENER *et al.* (1981) applied chemical stabilization for a reconstruction job at a reservoir and its surrounding dam. The soil was a dispersive clay of high Na content and of high ESP-value (ESP — exchangeable sodium percentage). Gypsum was used as the stabilizing agent. 3.8 kg/m^3 gypsum was needed to lower the original $ESP = 25\%$ to 5% , which was sufficient to restore stable conditions to the site.

5.3.5 Deep mixing methods

The *in situ* mixing of admixtures with soft, fine grained soils to form columns, piers, and walls has been studied and applied extensively in practice during the last several years (BROMS and BOWMAN, 1976, 1979; PILOT, 1977; TERASHI *et al.*, 1979). Columns are produced by feeding a metered quantity of stabilizing agent into a soft clay mass through a rotary drill equipped with a special auger bit both to advance to the desired depth and to mix the soil and the admixture during withdrawal. Figure 468 is a schematic diagram of the process as used for the construction of a lime column in Sweden. When quicklime (CaO) is used the heat of hydration can be substantial, and the drying of the surrounding soil due to this and to the consumption of water by hydration can be significant. BROMS and BOWMAN (1979)

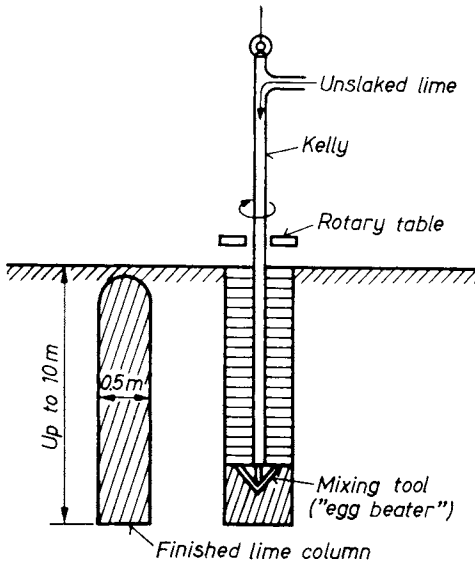


Fig. 468. Manufacture of a lime column using the Swedish system (MITCHELL, 1981)

note that typically the clay in lime columns is 100 to 1000 times more permeable than in the untreated state. As a consequence the columns can act as vertical drains, thus accelerating settlements.

5.4 Soil improvement by precompression

Any substantial load placed on the ground before construction begins decreases the porosity and the water content of the subsoil, and so contributes to improving the shear strength and to lessening the compressibility. Thus, precompression is particularly well suited to use with soils that undergo large volume decrease and strength increase under sustained static loads and when there is sufficient time available for the required compression to develop. The soil types best suited to this method are saturated soft clays, compressible silts, organic clays and peats.

If the available time is short the consolidation can be enhanced by the installation of drains (Section 5.4.2). Also electro-osmotic procedures may be advantageous in such cases (Section 5.4.3).

The following types of surcharge loads may be considered (MITCHELL, 1981):

- (a) earth fill as the most commonly used type;
- (b) water in tanks used for small areas, and water in lined ponds for larger areas;
- (c) vacuum preloading by pumping from beneath an impervious membrane placed over the ground surface; this can produce surcharge loads of up to 60 to 80 kPa (HOLTZ and WAGER, 1975);
- (d) anchor and jack systems can be devised for special cases;
- (e) groundwater lowering provides an increase in consolidation pressure equal to the unit weight of water times the drawdown distance.

Preloading by vacuum, water table lowering, and electro-osmosis offer the advantage that no stability problems will arise.

Precompression has been used successfully to improve the soils for buildings, embankments, highways, runways, tanks and bridges.

5.4.1 Precompression without drains

Precompression is normally accomplished by providing a preloading procedure which involves the placement (and later removal) of an earth fill (or some other equivalent dead load), to compress the soil below the proposed foundation prior to construction. If the intensity of the load from the dead weight is greater than the pressure under the final load, this is called overloading or surcharging. The excess load intensity above the final load (p_f) will be called the surcharge (p_s), and p_s/p_f will be defined as the surcharge ratio (ALDRICH, 1965).

Design may have two main goals:

- to determine that surcharge (p_s) that will produce the desired settlement (compression) in the time available, or
- to determine the consolidation time belonging to p_s .

As extended areas are usually involved, the relevant calculations may follow the one-dimensional consolidation theory proposed by TERZAGHI. Reality is not so simple, however, because the following problems may arise in the course of the design:

- the rate of consolidation may vary among the strata;
- there may be some considerable secondary consolidation in some soils;
- modifications might be required when the soil reveals non-homogeneous properties, or
- the subsoil contain various layers.

If there is no expected secondary consolidation, the time-dependent-settlement will develop accord-

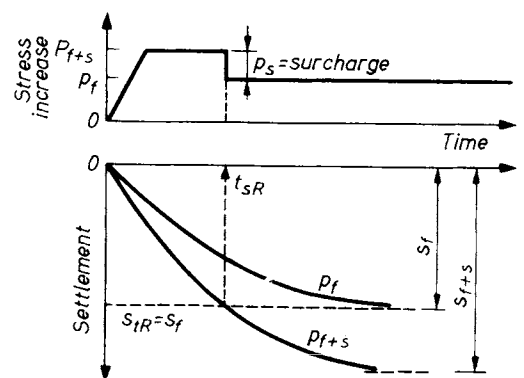


Fig. 469. Compensation for primary compression using surcharge loading (MITCHELL, 1981)

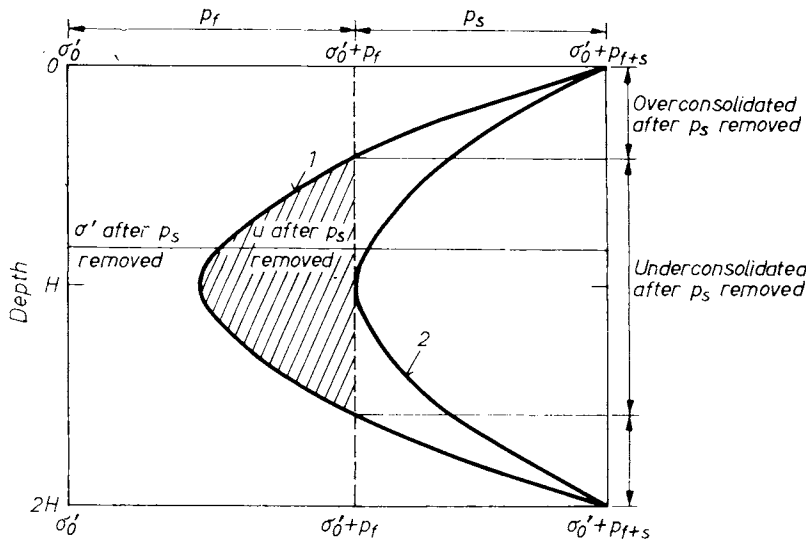


Fig. 470. Pore-pressure distribution after removal of the surcharge load at time t_{sR} (MITCHELL, 1981):
 1 — pore-pressure distribution at t corresponding to \bar{U}_{sR} ; 2 — pore-pressure distribution required to prevent further settlement if p_s is removed

ing to the scheme given in Fig. 469 (ALDRICH, 1965, in MITCHELL, 1981). If the surcharge were left in place until time t_{sR} , then the layer would have settled as much as under the permanent load alone, i.e. $s_{fR} = s_f$. At this time the layer would have reached an average degree of consolidation \bar{U}_{sR} given by

$$\bar{U}_{sR} = \frac{s_f}{s_{f+s}} \tag{526}$$

By the time the average percentage consolidation has reached the required value, the centre of the compressible layer might yet be far from having been consolidated to the required stress corresponding to the final load (Fig. 470). To eliminate any primary consolidation after the construction, all segments of the stratum must be consolidated to an intergranular pressure equal to or greater than the stress experienced under the final load (ALDRICH, 1965). Although the process of unloading the overconsolidated zones near the drainage boundaries will generally not lead to significant heave (JOHNSON, 1970), the additional consolidation in the central portion may be important. Thus, the surcharge should be left in place until the pore pressure at the most critical point (i.e. where the consolidation will occur at the latest, generally at the midplane) attains the consolidation ratio U_z given by

$$(U_z)_{f+s} = \frac{P_f}{P_f + P_s} \tag{527}$$

Time periods t required to reach U_{sR} and U_z can be found by using the Terzaghi theory and the consolidation coefficient c_v according to

$$t = \frac{TH^2}{c_v} \tag{528}$$

A solution for the secondary consolidation has been presented by MITCHELL (1970). This problem emerges mostly where organic clays or peats are present. The idea is to estimate the total settlement under p_f as the sum of that due to primary and secondary (s_s) compressions anticipated to occur in the life span of the structure. The secondary compression, s_s , can be determined from

$$s_s = C_\alpha H_p \log \frac{t}{t_p} \text{ where } t > t_p, \tag{529}$$

in which C_α is the vertical strain per log cycle increase in time subsequent to the end of the primary consolidation at t_p , and H_p is the layer thickness at time t_p . The analogous equation to (527) for the critical point is:

$$(U_z)_{f+s} = \frac{s_f + C_\alpha H_p \log \left(\frac{t}{t_p} \right)}{s_{f+s}} \tag{530}$$

The nature of secondary compression is such that some time after the removal of the surcharge p_s , the secondary compression will reappear under p_f . This effect is, however, small and can be neglected (JOHNSON, 1970a).

If preloading is carried out in a manner such that all, or part of the surcharge material is presumably displaced before the construction begins (e.g. in the case of reservoir tanks) a recompression process in the underground has to be reckoned with (ALDRICH, 1965; JOHNSON, 1970a).

Column footings may cause hardly any stress increase at the centre of the compressible stratum but the increase near the top of the stratum may be considerable. It is desirable therefore to use low contact pressures, thereby minimizing the amount of the surcharge load required (JOHNSON, 1970a).

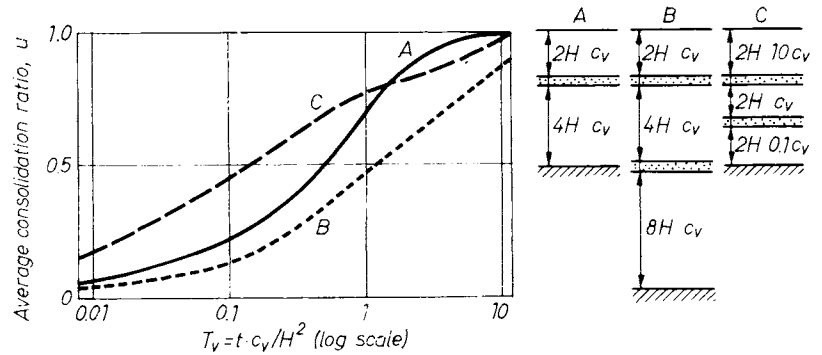


Fig. 471. The U vs. T_v curve can take various shapes, depending on geometry and c_v (STAMATOPOULOS and KOTZIAS, 1983)

STAMATOPOULOS and KOTZIAS (1983) observed that the shape of s vs T_v curves may differ widely. Mostly the three types illustrated in Fig. 471 are prevalent. The shapes in cases A to C can be reproduced theoretically by assuming the stratification shown in the figure. The overall clay layer, surrounded by a free draining material, is divided into horizontal sublayers separated by seams of free draining sand or silt. It is further assumed that these sublayers have equal compressibility and may have equal or different c_v values. The authors provided calculation methods to cope with all these problems.

The time rate and the magnitude of settlement of large scale preloading can be reliably predicted from a test fill (STAMATOPOULOS and KOTZIAS, 1983). The settlement vs. time curves in Fig. 472 afford a comparison between the behaviour of the large scale preloading and that of the test fill. The two curves in the figure are similar in shape and the one corresponding to the full scale loading gives about 3.5 times the settlement due to the test fill, i.e. the settlements are nearly proportional to the heights of fill, 11 m : 3.4 m.

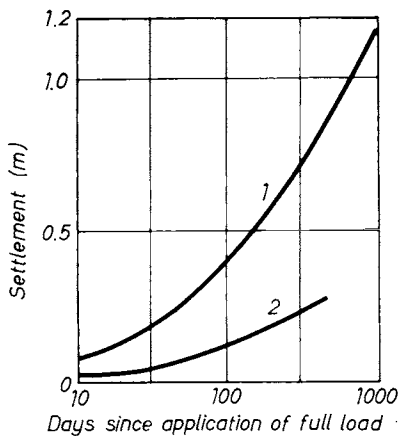


Fig. 472. The Ratio of settlement during preloading to settlement of test fill is about the same as the ratio of heights of fill (STAMATOPOULOS and KOTZIAS, 1983)

1 — fill crest 100 m · 43 m, height 11 m; 2 — fill crest 60 m · 40 m, height 3.4 m

5.4.2 Precompression with vertical drains

Initially, engineering practice applied only sand drains generally using 200 to 500 mm diameter holes with 1.5 to 6.0 m spacing distances. Prefabricated drains were introduced in 1937, soon after the application of sand drains. First on the market was the KJELMANN cardboard drain which is a 3.5 mm by 100 mm band made up of two cardboard strips with ten longitudinal grooves. Features (width, thickness, grooves) of the newly produced prefabricated drains imitate very closely that of the prototype, the cardboard wick (such as: Geodrain, Castle Board, Bidim, Alidrain, etc.). The drains usually have a core of plastic material with a filter sleeve of paper or some other fibrous material, usually of plastic.

KJELMANN (1948) stated that “the draining effect of a drain depends to a great extent upon the circumference of its cross-section, but very little upon its cross-sectional area” and that “certain considerations show that the cardboard which is as effective as a circular drain with a 1 in radius”. This statement has since been proved by several observations, for example, by the test run represented in Fig. 473 (HANSBO and TORSTENSSON, 1977).

Since the first use of vertical sand drains, the drains have been installed by the following methods (JOHNSON, 1970b): 1 — closed mandrel — driven, 2 — closed mandrel — jetted, 3 — open mandrel — driven, 4 — open mandrel — jetted, 5 — rotary drill, 6 — rotary jet, 7 — continuous auger — solid stem, 8 — continuous auger — hollow stem, 9 — bucket auger, and 10 — vibratory driving.

Another aspect is to classify displacement and non-displacement drains. The influence of the technology used is principally weighted according to the degree of soil disturbance caused; this may have the consequence of decreasing the c_v value or arranging a narrowed spacing. Displacement drains additionally — at least transitionally — lessen the shear strength of the soil, which may cause stability problems. This fact, as well as the short installation period would in many cases give preference to the use of prefabricated drains (HANSBO and TORSTENSSON, 1977).

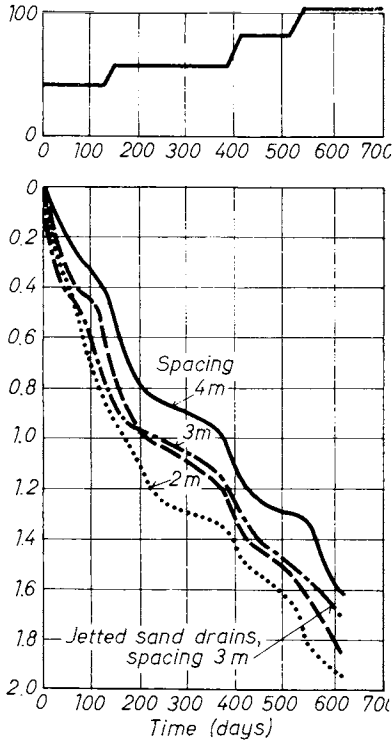
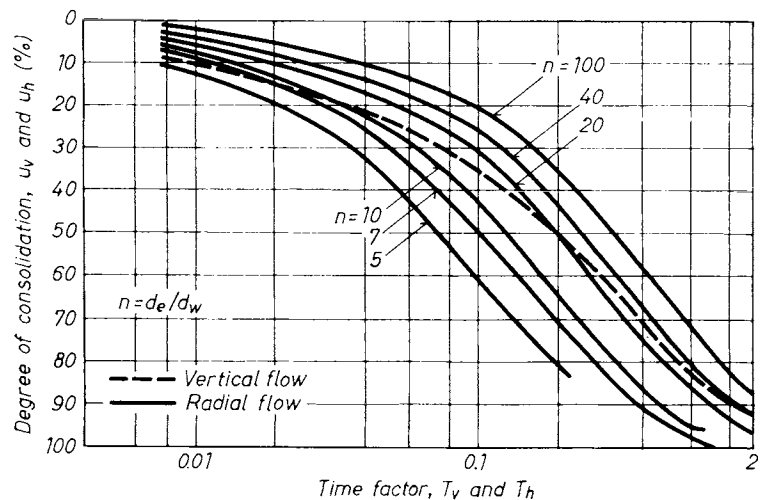


Fig. 473. Measured settlements in test areas with Geodrains and jetted sand drains of 0.28 m diameter (HANSBO and TORSTENSSON, 1977)

The theory of consolidation for the design of vertical sand drains considers combined radial and vertical pore-water flow to the drains; it has been elaborated by CARILLO (1942), and in detail by BARRON (1948), as an extension of TERZAGHI's work. Combined vertical and radial flow can be treated analitically as separate vertical and radial flow problems. The excess pore-water pressure ratios at any time for these separate types can be multiplied together to determine their combined effect, i.e.:

$$\bar{U} = 1 - \left(\frac{\bar{u}}{u_0} \right)_{v-h} = 1 - \left(\frac{\bar{u}}{u_0} \right)_v \left(\frac{\bar{u}}{u_0} \right)_h \quad (531)$$

Fig. 474. Consolidation solution for radial flow and equal vertical strain at the ground surface (BARRON, 1948)



The time of consolidation is

$$t = \frac{T_v H^2}{c_{v-h}} = T_v H^2 \frac{a_{v-v} \gamma_w}{k_v (1 - e_0)} \quad (532)$$

for vertical consolidation, and

$$t = \frac{T_h H^2}{c_{v-h}} = T_h H^2 \frac{a_{v-v} \gamma_w}{k_h (1 - e_0)} \quad (533)$$

for radial (horizontal) consolidation.

Relations, T_v , U_v and T_h , U_h are illustrated in Fig. 474. These include also the distance between the drains (s) because d_e means the diameter of the influence zone around the drain. In case of a rectangular drain arrangement $d_e = 1.13 s$, for triangular locations $d_e = 1.05 s$ are appropriate. Thus Eqs (531) to (533) and Fig. 474 supply all necessary design data. As can be seen, the process is far more influenced by the spacing of the drains than by the diameter of the drain.

Assuming that

- the permeability of the drain is infinite in comparison with that of the clay;
- Darcy's law is valid;
- consolidation due to vertical flow is negligible compared to that due to radial flow, the time of consolidation t can be determined according to:

$$t = \frac{d_e^2 \mu}{8c_h} \ln \frac{1}{1 - \bar{U}_h} \quad (534)$$

where

$$\begin{aligned} \mu &= \frac{n^2}{n^2 - 1} \left[\ln n - 0.75 + \frac{1}{n^2} \left(1 - \frac{1}{4n^2} \right) \right] \cong \\ &\cong \frac{n^2}{n^2 - 1} [\ln n - 0.75 - n^{-2}] \quad (535) \end{aligned}$$

and

$$n = d_e/d_w$$

(where d_w is the diameter of the drain).

The equivalent diameter of a band-shaped drain of width b and thickness t can be expressed as

$$d_w = \frac{2(b + t)}{\pi} \quad (536)$$

In practice, drain spacing is seldom below 0.8 m. For prefab drains we thus find $n > 12$ (or $n > 8$ for the Colbond drain). This justifies a further simplification of μ in Eq. (535), which might be taken as:

$$\mu = \ln n - 0.75 \quad (\text{HANSBO, 1979}) \quad (537)$$

Some modifications have been proposed recently in respect of these design formulas. A drain with infinite permeability in the longitudinal direction does not exist (among other things the drain has a certain well resistance). If it is assumed that the discharge capacity of the drain is q_w , and that the permeability of the soil is k_c (Darcy's law is assumed to be valid), then μ in Eq. (535) should be replaced after HANSBO (1979) by

$$\mu \cong \ln n - 0.75 + \pi z(2l - z) \frac{k_c}{q_w} \quad (538)$$

where l is the length of the drain when it is open at one end only (half length of the drain when open at both ends), z is the distance from the open end of the drain ($0 < z < 2l$).

Darcy's law is not valid, however, for slow flow velocities. It is generally accepted in such cases to use the expression:

$$v = Ki^n \quad (539)$$

A new solution to the "equal strain" consolidation theory based on this exponential law was presented by HANSBO (1960). For example, when $n = 1.5$, the new theory gives:

$$t = \frac{\alpha}{\lambda} d_e^2 \sqrt{d_e \cdot \gamma_w / \Delta \bar{u}_0} \left(\frac{1}{\sqrt{1 - \bar{U}_h}} - 1 \right) \quad (540)$$

where $\Delta \bar{u}_0$ is the average excess pore pressure at $t = 0$, α is a function of $d_e/d_w (= n)$ (Fig. 475), λ is the coefficient of consolidation in horizontal

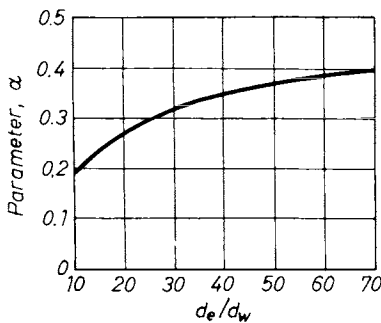


Fig. 475. Parameter α vs. d_e/d_w (HANSBO, 1979)

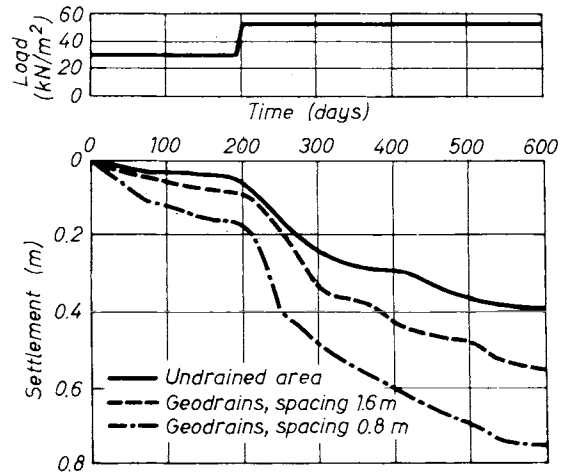


Fig. 476. Measured settlements in undrained and drained areas (HANSBO and TORSTENSSON, 1977)

non-Darcian pore-water flow:

$$\lambda = \frac{KE_s}{\gamma_w} \quad (541)$$

Experience and observation confirm that a preloading procedure combined with subsoil drainage is almost inefficient if the pressure on the layer is less than the preconsolidation pressure (Fig. 476).

5.4.3 Precompression by electro-osmosis

Electro-osmotic treatment might be efficient and economical with certain soils and in a restricted volume. Its mechanism has been explored recently by GRAY and MITCHELL (1967), and the relevant consolidation theory has been elaborated by ESRIG (1968), WAN and MITCHELL (1976) and by MITCHELL and WAN (1977).

The water flow rate, q_h , in the one-dimensional direct current field is initially

$$q_h = k_e i_e A = k_i I \quad (\text{m}^3/\text{s}) \quad (542)$$

where k_e is the electro-osmotic coefficient of permeability ($1 \cdot 10^{-9}$ to $7 \cdot 10^{-9}$ m/s per V/m), i_e is the electrical potential gradient (V/m), A is the cross-sectional area (m^2), k_i is the water flow per unit time per ampere ($\text{m}^3/\text{s}/\text{A}$), and I is the current (A).

The time t for a given degree of consolidation is:

$$t = \frac{TL^2}{c_v} \quad (543)$$

where T is a time factor, L is the electrode spacing, and c_v is the coefficient of consolidation. Values of T for different degrees of consolidation for the case of parallel plate electrodes with a linear variation in voltage between them are given in Table 43 (MITCHELL, 1981). Measurements of

Table 43. Time factor for various degrees of consolidation (MITCHELL, 1981)

Degree of consolidation \bar{u} (%)	Time factor, T	
	Linear V variation	Infinite initial gradient
0	0	0
10	0.05	0.001
20	0.10	0.007
30	0.16	0.017
40	0.22	0.02
50	0.29	0.05
60	0.38	0.07
70	0.50	0.10
80	0.66	0.14
90	0.95	0.20

JOHNSTON and BUTTERFIELD (1977) indicate that rather than a linear variation in voltage between electrodes, an instantaneously infinite electrical gradient develops initially at the anode, which decreases in a consistent manner to a uniform gradient at the completion of consolidation. Values of T for these conditions are also listed in Table 43. (It can be seen that consolidation occurs more rapidly for the latter case.)

Electro-osmosis may be effective and economical under the following conditions (MITCHELL, 1981):

1. saturated silts or silty clay soils;
2. normally consolidated conditions;
3. low pore-water electrolyte concentration.

BALLY (1984) introduced a parameter c , which when used, the product $\rho \cdot k_e \cdot c$, gives a dimensionless quantity, where ρ (Ω/cm) is the electrical resistivity, k_e ($\text{cm}^2/\text{s V}$) the electro-osmotic coefficient of permeability, c ($\text{mA} - \text{h}/\text{cm}^3$) the "specific consumption of electricity".

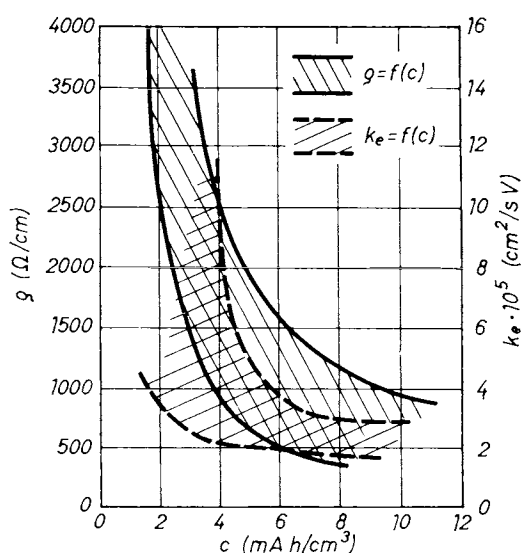


Fig. 477. Ranges suitable for electro-osmotic and electrokinetic soil treatment (BALLY, 1984)

Putting these three parameters in a single diagram (as in Fig. 477), two characteristic regions can be distinguished:

- the area on the left which is favourable for electro-osmotic treatment due to the great permeability and low specific consumption of electricity;
- the area on the right with high c and low k_e values, thus reflecting a small suitability of the soil to electro-osmotic filtration, but a favourable behaviour concerning electrochemical processes.

5.5 Grouting of soils

Though the technology of the grouting was well developed by a number of researchers (JOOSTEN, JØRGENSEN and others) more than half a century ago, its elevated cost has prevented a frequent application thereof. Generally, it might be economical in cases where the mass or volume to be stabilized is small, or when this method is simpler than any other method would be (for example, in the case of a damaged duct).

Four alternatives to this soil improvement method are distinguished:

- (a) Permeation grouting in which the grout fills up the voids and pores in the soil without provoking changes in the volume or structure of the original ground. This has two alternatives: (1) the particulate grouts or injections, and (2) the chemical grouts.
- (b) Electro-chemical grouting as a special case of electro-osmotic treatment (3).
- (c) Displacement (compaction) grouting in which a stiff mixture fills the voids and compresses the surrounding soil.

A short summary of the four mentioned methods is given in the following sections, but a detailed discussion of the problem will be omitted here.

5.5.1 Particulate grouts (injections)

Particulate grouts are generally made of cement, soil, or clay and mixtures of these. Chemical additives are sometimes used to facilitate penetration, to prevent cement flocculation and to control setting times. A part of the cement might be substituted by appropriate industrial waste materials e.g. furnace slag.

Clay or bentonite suspensions are non-hardening materials, so, in themselves — without the addition of cement — these are only good for sealing or waterproofing.

Acceleration of setting (when it is necessary, for instance due to speedy groundwater movement) can be enhanced by adding CaCl_2 , water-glass, or NaCl .

Particulate grouts cannot be injected as permeation grouts into soils finer than medium to coarse sands. Two groutability ratios that have proved useful, are:

$$(a) N = \frac{(d_{15})_{soil}}{(d_{85})_{grout}}$$

$N > 24$: grouting consistently possible,
 $N < 11$: grouting not possible;

$$(b) N_c = \frac{(d_{10})_{soil}}{(d_{95})_{grout}}$$

$N_c > 11$: grouting consistently possible,
 $N_c < 6$: grouting not possible.

5.5.2 Chemical grouts

Two methods are distinguished in this category: one-shot and two-shot procedures. The latter might be subdivided as to whether the second shot is also a fluid or a gas.

Commonly used agents and attained strengths are listed in Fig. 478. The figure reveals that chemical grouting would be successful for fine grained soils as well (contrary to particulate grouts) due to the low viscosity of the fluid.

Water-glass ($Na_2O \cdot nSiO_2 \cdot mH_2O$) was the first agent to be used in practice, and it is frequently used. Coming in contact with reagents the amount of Na_2O decreases and flint-molecules form aggregates. The higher the concentration of the water-glass and the shorter the setting time the higher the gel-strength will be. The gel undergoes further alterations as time passes (syneresis = aging) which adds to its strength, but in the meantime the permeability of the product will also increase. The grade of the syneresis depends on grain size (see Fig. 479) and on the bounding force between the grains and the gel.

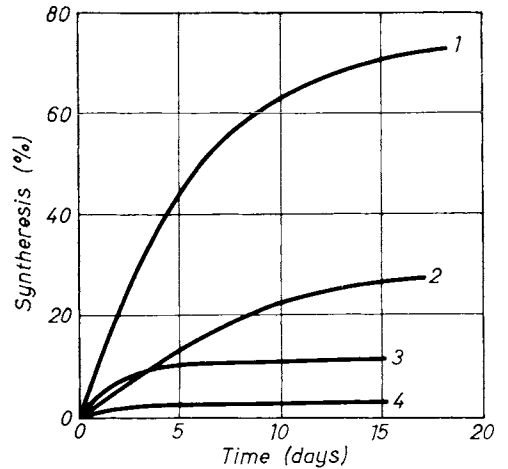
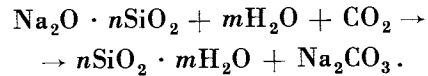


Fig. 479. Variation of syneresis with grain size: 1 — pure gel; 2 — gravel ($d = 1.6$ to 8 mm); 3 — pebbles ($d = 1.0$ to 3.2 mm); 4 — sand ($d = 0.06$ to 1.25 mm)

The reagent of the water-glass is usually $CaCl_2$ or $MgCl_2$, but gases were also applied in recent years (CO_2 , fluoride-gas, ammonium-gas). For the reagent CO_2 (JOOSTEN, 1931; JORGENSEN, 1935), the reaction is



More recently organic reagents are also being used (Nobel-Bozel, Pecler, Solétanche-procedure).

5.5.3 Electro-chemical grouting

Electro-osmosis is most efficient in soils that contain predominantly bound water, compared to free water. This feature is, however, characteristic just for those soils that are not prone to receive fluid using classic grouting methods. Because the

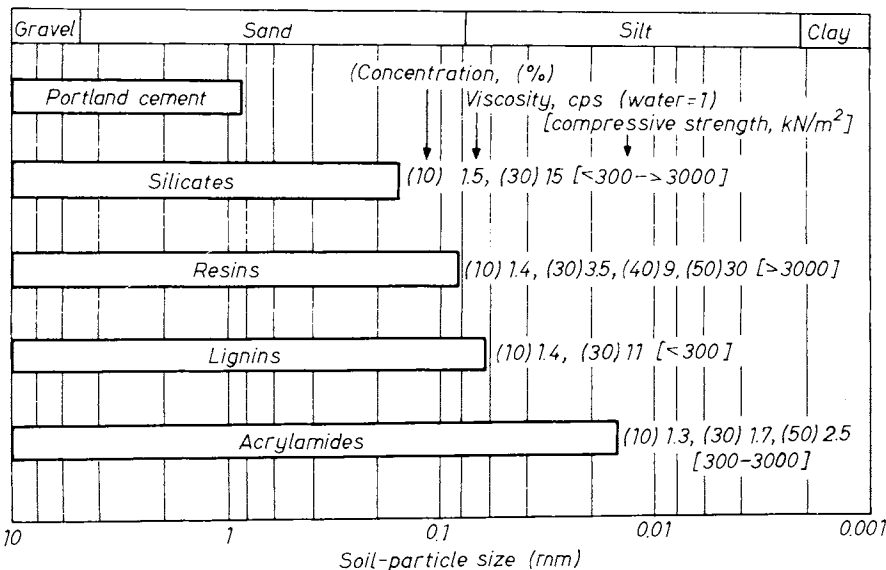


Fig. 478. Soil-particle sizes for different grout types and grouted soil properties (MITCHELL, 1981)

coefficient of electro-osmotic permeability, k_e , is insensitive to particle size and generally falls within a narrow range of about 1 to 7 times 10^{-9} cm/s per V/cm, a unit electrical gradient (one V/cm) can be more effective than a unit hydraulic gradient for moving fluids through finer grained soils.

Chemical stabilizers are introduced at the anode and carried toward the cathode by means of electrical gradients of the order of 50 to 100 V/m.

Two alternatives are known for this method. One is to convey appropriate compounds (CaCl_2 , AlCl_3) to the soil which alter the composition of the adsorptive complex, decrease the affinity toward moisture and thus the capability for volume change as well, and improve compressibility properties. The other procedure aims to achieve a considerable strength increase in the soil normally by using two fluids, mostly water-glass and one kind of reagent.

The stabilization of a potentially liquefiable sand has been investigated by YAMANOUCHI and MATSUDA (1975). The concept was to fill the voids with a gel or colloidal material. Silicate solutions, bentonite, and aluminium hydroxide were investigated as injection materials. The results demonstrated a marked increase in resistance to liquefaction after treatment.

KATTI *et al.* (1981) produced very convincing results in salty soft marine clays. Laboratory experiments indicated that

- (a) unconfined compression strength changed considerably, both according to depth and the distance from the anode;
- (b) efficiency could be enhanced by changing the polarity.

5.5.4 Displacement grouting

A highly viscous soil, cement, and water displacement grout acts as a radical hydraulic jack that compresses the surrounding soil. This type of soil

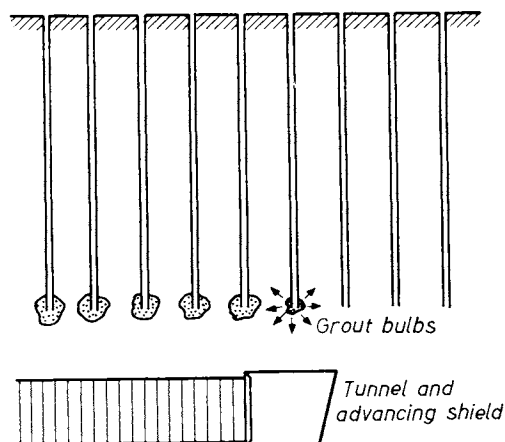


Fig. 480. Compaction grouting during tunnelling to prevent settlement

improvement can be used in partly saturated soils and loose materials containing void spaces (GRAF, 1969; WARNER, 1978). An interesting actual application is illustrated in Fig. 480: settlement of the ground surface was eliminated by producing "grout bulbs" at the construction site of the underground railway in Baltimore (Hayward Baker Co., 1980). Pumping pressures averaged about 2 MPa, injection depths were about 12 m, and work was carried out at a distance of about 2 m behind the shield.

5.6 Thermal stabilization

5.6.1 Stabilization by heating

The basic conception of this procedure can be retraced to very ancient times (brick baking), but its application as a soil improving method goes only back to the nineteen-thirties.

The effect of heat appears in two forms: moisture is evaporated and minerals or compounds are submitted to an irreversible chemical transformation. In the range of 130 to 250 °C, free and adsorptive water is dispelled from the soil; between 500 and 600 °C the intercrystalline water also is dissipated from the clay minerals. Between 700 and 800 °C the carbonates start to decompose, and above 1200 °C the heat melts the silicates, but colloidal particles begin to bake together sooner.

Under the influence of heat:

- (a) compressive and shear strengths increase;
- (b) compressibility diminishes;
- (c) tendency toward subsidence;
- (d) volume change ceases.

To produce the effects under *c* and *d*, 500 °C and 700 to 800 °C are needed, respectively.

Most successful applications have been experienced in partly saturated fine grained soils such as collapsible loess. A significant gas permeability is desirable to permit both the removal of water vapor and the exhaustion of stabilizing compounds which are sometimes used. Solutions are also known where special chimneys have been provided 70 to 90 cm distant from the burning hole to carry off the exhaustion gases (BELES and STANCU-LESCU, 1958).

Results from several sites, summarized by LITVINOV (1960), indicated an approximate doubling of the friction angle, an order of magnitude increase in cohesion intercept, and a five-fold decrease in compressibility.

5.6.2 Stabilization by freezing

Artificial freezing increases the soil strength intermittently and provides protection against groundwater flow. It can be extremely well

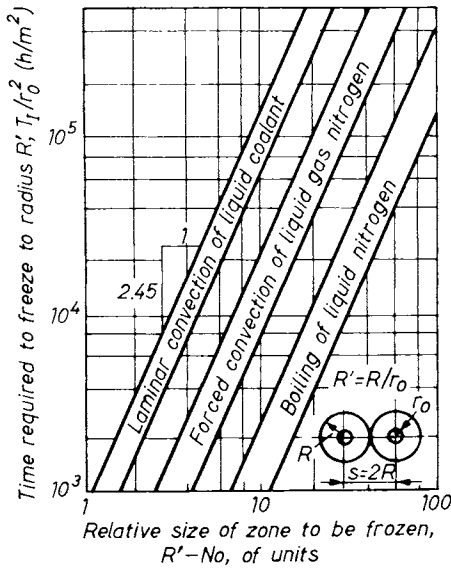


Fig. 481. Determination of required freezing time (SCHUSTER, 1972)

applied in loose soils when cuttings 6 to 8 m deep or foundation pits are excavated, or tunnels are constructed. Due to the high cost and consumption of time its use was for a long time neglected; a recent revival of this method is probably explained by the development technologies using liquid nitrogen for this purpose. This gain in prestige can be appreciated from the fact that even symposia have been organized recently on the topic of "Ground Freezing", held at the Ruhr Univ., Bochum.

The thermal energy and time required to complete freezing may be approximately calculated using two-dimensional heat conduction theory for heterogeneous profiles finite element or finite difference procedures. The most important factors governing cost are the size and spacing of the freezing pipes (SCHUSTER, 1972). Figure 481 can be used for estimation of the time required to freeze to a radius R using freeze pipes of radius r_0 .

The volumetric expansion of frozen water attains 9%, and the building of ice lenses is a common phenomenon; this may be harmful in the presence of silts and clays (TAKAGI, 1978; JONES and BROWN, 1978).

5.7 Soil reinforcement

The term "soil reinforcement" is not yet used uniformly in the literature. All authors agree that reinforced earth (terre armée) and soil nailing belong to this group; but there are authors (e.g. BARTOS, 1979; MITCHELL, 1981) who also include micro-piles (root piles) in this category. It is therefore probably convenient to count any procedure as reinforcement which

- favourably influences the compressive-, tensile-, and shear strength and compressibility in the soil;
- is not listed in Sections 5.2 to 5.6.

5.7.1 Reinforced earth

This is a construction developed and patented by French engineer, VIDAL (1966). It consists of a facing wall and compacted soil backfill reinforced with thin metallic strips. The strips, usually galvanized steel, absorb tensile stresses within the backfill by strip/soil skin friction. This holds the soil together as an integral mass, known as the "reinforced earth volume". The reinforcing strip lengths are usually about 0.7 to 0.8 times the height of the wall.

The facing elements, normally interlocking concrete panels, are not structural members; these serve only to retain the soil between strips near the outer edge of the backfill and to make the structure more appealing to the eye. The panels are bolted to the reinforcing strips to keep the facing in place, and the entire structure (facing, backfill, reinforcement) behaves as a single unit. Reinforced earth structures possess flexibility too and can tolerate some deformation without distress.

The steel strips convey some apparent cohesion to the soil. Linear tensile reinforcements exert their greatest strengthening effort when they are oriented in the direction of the principal strain extension (BASSETT and LAST, 1978; JEWELL, 1980).

The measurement of the apparent friction coefficient, f^* , between soil and reinforcements has been made using several test types as shown in

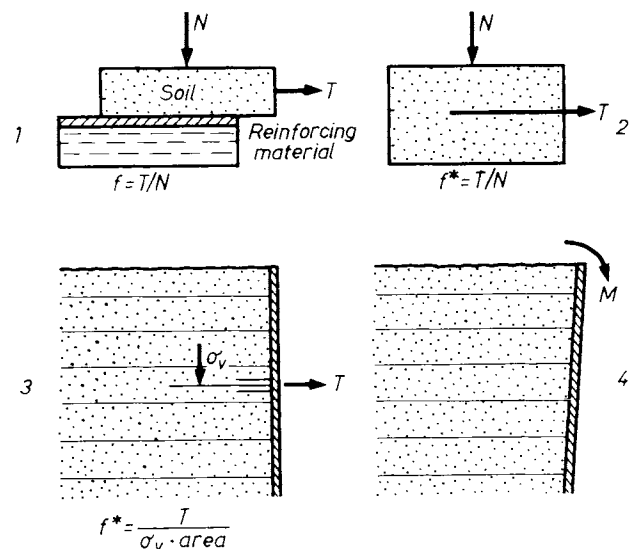


Fig. 482. Types of test for measurement of soil-reinforcement friction (MITCHELL, 1981):
1 — direct shear test; 2 — pull out test in shear box; 3 — pull out test on wall; 4 — pull out test by rotation

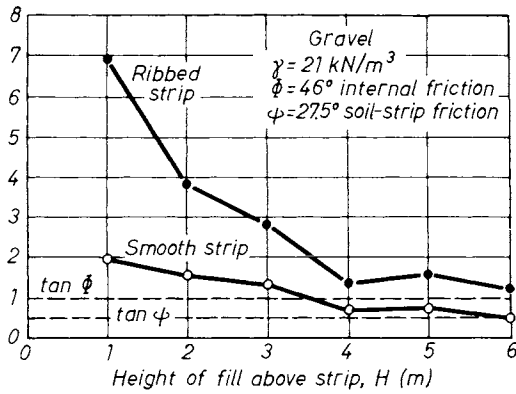


Fig. 483. Effect of overburden pressure on the apparent friction coefficient f^* (ALIMI *et al.*, 1977)

Fig. 482 (MITCHELL, 1981). The values of f^* have been shown (e.g. MCKITTRICK, 1979) to vary with type of reinforcement, type and density of backfill (compaction), and confining pressure. The influence of overburden pressure of f^* for smooth and ribbed strip reinforcement is shown in Fig. 483 (ALIMI *et al.*, 1977). It has also been observed that the heavier the overburden, the more displacement is needed to fully mobilize the maximum friction. These tests have shown that f^* increases with length and decreases with width of the reinforcement.

One current specification requires that the I_p of backfill be less than 6%, Φ be greater than 34°, and that there be less than 15% by weight of particles finer than 15 μm (MITCHELL, 1981).

A safety factor of at least 1.5 against strip pull-out is usually required, and the maximum tensile stress in the reinforcement must be less than that allowable for the material. The requirement for strip pull-out conditions is:

$$\frac{2bf^*le\sigma'_v}{\sigma_hSV} \geq 1.5, \quad (544)$$

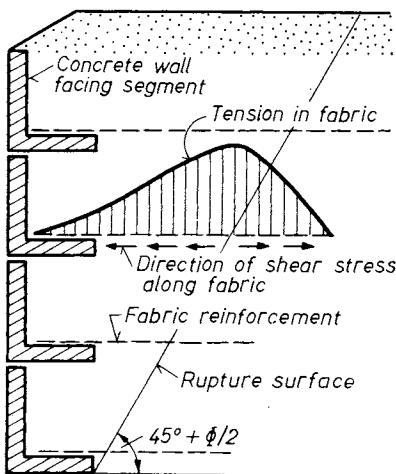


Fig. 484. Decreasing the earth pressure by means of synthetic fabrics (after Broms: BARTOS, 1979)

in which b is the strip width, $\sigma'_v = \gamma h$, S is the horizontal spacing of reinforcements, and V is their vertical spacing. The maximum tensile stress, f_t , in the reinforcement can be found from:

$$f_t = \frac{\sigma_h \cdot S \cdot V}{A_s}, \quad (545)$$

where A_s is the cross-sectional area of the reinforcement.

Geotextiles are going to be used more frequently for the reinforcement of soil masses. With the advent of second and even third generation textiles for use in ground engineering the term “fabrics” has largely been replaced by “geotextiles” (after GIROUD) and “geogrids” (after INGOLD, 1984).

Geotextiles can serve several functions, including repair, reinforcement, drainage, erosion control, forms and impermeable membranes, and can be used for retaining walls to lessen the earth pressure (Fig. 484). An important field for using geotextiles has been found in the construction of temporary roads over marshes, peat soils, and compressible clays. The textile sheet between the surface of the soft soil and the gravel base serves both to separate the materials and prevent their mixing, and to spread vertical vehicle loads over the foundation base, thus reducing the induced shear stresses (KOERNER and WELSH, 1980).

5.7.2 Soil nailing

The nails used for this purpose are usually steel rods, 20 to 30 mm in diameter, that are grouted into predrilled holes or driven using a percussion drilling device. The aim of soil nailing is mostly to stabilize hill sides and outer cut slopes. (Their effect is similar to that of root piles.) Their length may be of the order 50% of the height of the excavation to be supported.

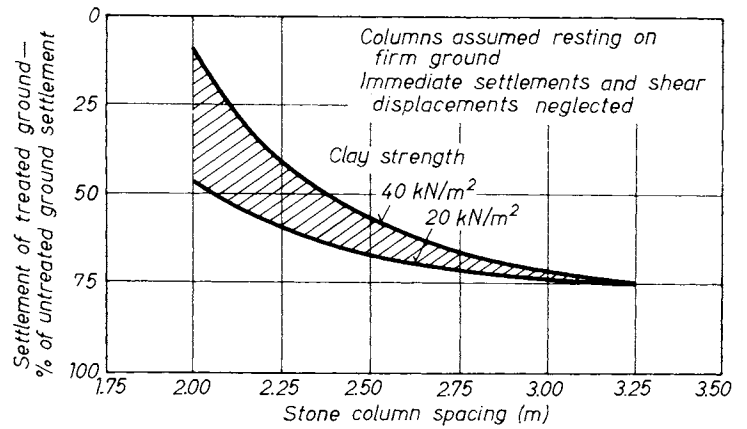
Design principles are the same as in reinforced earths, inasmuch the nails are provided to absorb tension stresses and also here the bar yield strength and the pull-out resistance are the two determinant design parameters.

There are also solutions that combine the characteristic features of nailing and reinforced earth (BANG *et al.*, 1980).

5.7.3 Soil and stone columns

Compacted stone (gravel, sand) columns provide vertical support for overlying structures or embankments and function as drains for soft soil. They can be used also to resist shear in horizontal and inclined directions. They can also be used to prevent liquefaction (SEED and BOOKER, 1977). Column diameter are generally 0.6 to 1.0 m, and length may attain up to 20 m.

Fig. 485. Effect of stone columns on anticipated foundation settlement (GREENWOOD, 1970)



“Vibrocompaction” produces similar soil columns, therefore some of the methods described in Section 5.2.2.2 could have been categorized under this group.

Square or triangular grid patterns are used with centre to centre column spacings of 1.5 to 3.5 m. The entire foundation area may be covered with an additional coverage around the perimeter to include stresses spread with depth (MITCHELL, 1981).

The load capacity of the column is controlled by the passive resistance of the soft soil that can be mobilized to withstand radial bulging and by the friction angle of the compacted material of the column. Design values of 20 to 30 tons (= 200 – 300 kN) per column are typical for columns in soft to medium stiff clays. Both limit analyses (HUGHES and WITHERS, 1974) and experience (THORNBURN, 1975) indicate that the allowable vertical stress, σ_v , on a single column can be expressed by

$$\sigma_v = \frac{25\tau_f}{FS}, \quad (546)$$

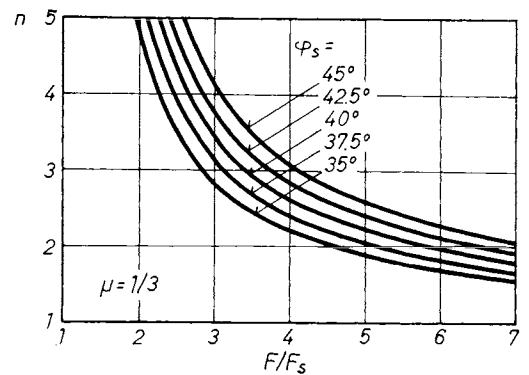


Fig. 486. Estimation of how stone columns reduce settlement (PRIEBE, 1976)

where τ_f is the undrained shear strength of the soft ground, and FS is the factor of safety (abt. $\cong 3$).

The settlement of a stone column foundation depends on the column spacing. The settlement of a single column is in the range of 5 to 10 mm under

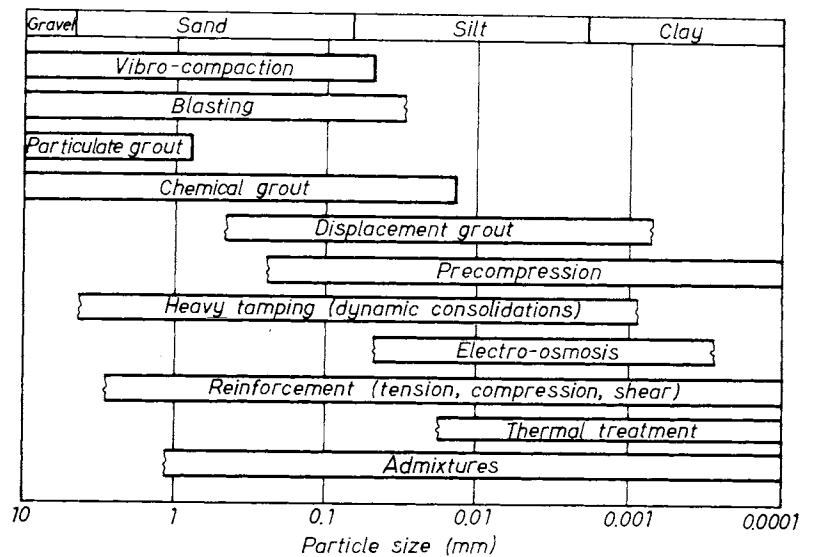


Fig. 487. Applicable grain-size ranges for different stabilization methods (MITCHELL, 1981)

the design load, but the settlement of a large loaded area supported by stone columns, will be about 5 to 10 times greater than this. Estimated settlement of treated ground as a function of soil strength, and column spacing is shown in Fig. 485. The ratio n of original settlement to that lessened by the soil column is considered by PRIEBE (1976). He suggests calculating it according to Fig. 486.

5.8 Choosing the appropriate method for soil improvement

The decision to select the most appropriate method among those described in Sections 5.2 to 5.7 must depend on weighing up several aspects, such as: the properties of the soil to be treated; available time; improvement costs in relation to overall investment costs; available equipment and materials; environmental issues; local experience, and so on.

Figure 487 illustrates improvement methods relating each one to the range of soil grain sizes for which it is most applicable (MITCHELL, 1981).

References

- ALDRICH, H. P. (1965): Precompression for support of shallow foundations. *Proc. ASCE*. Vol. SM 2.
- ALIMI, I., BACOT, J., LAREAL, P., LONG, N. T. and SCHLOSSER, F. (1977): Etude de l'adhérence "Sol-Armature". *Proc. 9th ICSMFE*. Vol. 1, Tokyo.
- ANDERSON, R. D. (1974): New method for deep sand vibratory compaction. *Proc. ASCE*. No. Co. 1.
- BALLY, R. J. (1984): The electro-chemical characteristics of the soil. *Proc. 6th Conf. SMFE*. Budapest.
- BANG, S., SHEN, C. K. and ROMSTAD, K. M. (1980): Analysis of an earth-reinforcing system for deep excavation. *Transport. Research Record*, 749.
- BARRON, R. A. (1948): Consolidation of finegrained soils by drain wells. *Trans. ASCE* (113).
- BARTOS, M. J. Jr. (1979): 101 uses for earth reinforcement. *Civil Engg. ASCE*. Jan.
- BASSETT, R. H. and LAST, N. C. (1978): Reinforcing earth below footings and embankments. *Proc. ASCE Symposium on Earth Reinforcement*. Pittsburgh.
- BELES, A. A. and STANCULESCU, I. I. (1958): Thermal treatment as a means of improving the stability of earth masses. *Géotechnique*, No. 4.
- BROMS, B. B. and BOMAN, P. (1976): Stabilization of deep cuts with lime columns. *Proc. 6th Eur. Conf. SMFE*. Vienna, 1/3-2.
- BROMS, B. B. and BOMAN, P. (1979): Lime columns — a new foundation method. *Proc. ASCE*. GT 4.
- BROMS, B. B. and HANSON, O.: (1984): Deep compaction with the Vibro-Wing method. *Ground Engg.*, No. 5.
- BROWN, R. E. (1977): Vibrofloatation compaction of cohesionless soils. *Proc. ASCE*. SM 4.
- CARILLO, N. J. (1942): Simple two- and three-dimensional cases in the theory of consolidation of soils. *Journal Mathematics and Physics* (21).
- DONCHEV, P. (1980): Compaction of loess by saturation and explosion. *Proc. Int. Conf. Compaction*, Paris.
- ESRIC, M. I. (1968): Pore pressures, consolidation, and electrokinetics. *Proc. ASCE*. SM 4.
- FINDLAY, A. (1951): *The phase rule*. Campbell and Smith, Dover Publ. Inc., New York.
- FRÖHLICH, O. (1934): *Druckverteilung im Baugrunde*. Springer, Vienna.
- GRAF, E. D. (1969): Compaction grouting technique and operations. *Proc. ASCE*. SM 5.
- GRAY, D. H. and MITCHELL, J. K. (1967): Fundamental aspects of electro-osmosis in soils. *Proc. ASCE*. SM 4.
- GREENWOOD, B. A. (1970): Mechanical improvement of soils below ground surface. *Proc. Conf. Ground Engg.*, Inst. of Civil Engineers, London, 11-22.
- HANSBO, S. (1960): Consolidation of clay, with special reference to influence of vertical sand drains. *Swedish Geot. Inst. Publ.*, No. 18.
- HANSBO, S. (1979): Consolidation of clay by band-shaped prefabricated drains. *Ground Engg.* (12).
- HANSBO, S. and TORSTENSSON, B. A. (1977): Geodrain and other vertical drain behaviour. *Proc. 9th ICSMFE*. Vol. 1, Tokyo.
- HOLTZ, R. D. and WAGER, O. (1975): Preloading by vacuum-current prospects. *Transp. Res. Record*. 548.
- HUGHES, J. M. O. and WITHERS, N. J. (1974): Reinforcing soft cohesive soil with stone columns. *Ground Engg.*, May.
- INGOLD, T. S. (1984): Geotextiles as earth reinforcement in the United Kingdom. *Ground Engg.*, No. 3.
- IVANOV, P. L. (1967): *Compaction of non-cohesive soils by explosions*. Izd. Literaturi po Stroitelstvo, Leningrad.
- JESSBERGER, H. L. and BEINE, R. A. (1981): Heavy tamping: theoretical and practical aspects. *Proc. 10th ICSMFE*. Vol. 3, Stockholm.
- JEWELL, R. A. (1980): Some factors which influence the shear strength of reinforced sand. *CUED D-Soils TR 85*, Cambridge Univ.
- JOHNSON, S. J. (1970a): Precompression for improving foundation soils. *Proc. ASCE*. SM 1.
- JOHNSON, S. J. (1970b): Foundation precompression with vertical sand drains. *Proc. ASCE*. SM 1.
- JOHNSTON, I. W. and BUTTERFIELD, R. (1977): A laboratory investigation of soil consolidation by electro-osmosis. *Austral Geomech. J.*, No. G7.
- JONES, J. S. and BROWN, R. E. (1978): Design of tunnel support systems using ground freezing. *Proc. 1st Int. Symp. on Ground Freezing*. Bochum.
- KABAI, I. (1968): The compactibility of sands and sandy gravels. *Proc 3rd ICSMFE*. Budapest.
- KATTI, R. K., DONGARWAR, D. W. and PATWARDHAN, S. H. (1981): Studies of electrochemical hardening of marine clay. *Proc. 10th ICSMFE*. Vol. 3, Stockholm.
- KÉZDI, Á. (1967): *Stabilized Earth Roads*. (In Hungarian). Akadémiai Kiadó, Budapest.
- KÉZDI, Á. (1979): *Soil Physics — Selected Topics*. Elsevier Sc. Publ. Co., Amsterdam — Akadémiai Kiadó, Budapest.
- KJELMANN, W. (1948): Consolidation of fine-grained soils by drain wells. *Trans. ASCE*. Vol. 113.
- KOERNER, R. M. and WELCH, J. P. (1980): *Construction and Geotechnical Engineering Using Synthetic Fabrics*. Wiley, New York.
- KÖGLER, F. and SCHEIDIG, A. (1948): *Baugrund und Bauwerk*. Ernst, Berlin.
- LAMBE, T. W. (1960): Compacted clays structure, engineering behaviour. *Trans., ASCE*, Vol. 125, p. 1.
- LEONARDS, G. A., CUTTER, W. A. and HOLTZ, R. D. (1980): Dynamic compaction of granular soils. *Proc. ASCE*, GT. 1.
- LITVINOV, I. M. (1960): Stabilization of settlement and weak clayey soils by thermal treatment. *Highway Res. Board Spec. Rep.*, No. 60.
- LITVINOV, I. M. (1973): Deep compaction of soils with the aim of considerably increasing their carrying capacity. *Proc. 8th ICSMFE*. Vol. 4.1, Moscow.
- LITVINOV, I. M. (1976): Blast compaction of collapsible soils at the construction site of a large industrial plant. *Osnov. Fund. Meh. Gruntov*, No. 4.
- LUKAS, R. G. (1980): Densification of loess deposits by pounding. *Proc. ASCE*. GT 4.
- MATSUO, S. and KAMON, M. (1981): Soil stabilization by multivalent cations. *Proc. 10th ICSMFE*. Vol. 3, Stockholm.
- MARSAL, R. J. and RESENDIZ, D. (1975): *Presas de Tierra y Envocamiento*, Limusa, Mexico, D. F., oh. 9.
- McKITTRICK, D. P. (1979): Reinforced earth, application of theory and research to practice. *Ground Engg.*, No. 1.
- MÉNARD, L. and BROISE, Y. (1975): Theoretical and practical aspects of dynamic consolidation. *Géotechnique*, No. 1.

- MITCHELL, J. K. (1961): Fundamental aspects of thixotropy in soils. *Trans. ASCE*. Vol. 126.
- MITCHELL, J. K. (1970): In-place treatment of foundation soils. *Proc. ASCE*. SM 1.
- MITCHELL, J. K. (1981): Soil improvement—state of the art report. *Proc. 10th ICSMFE*. Vol. 4, Stockholm.
- MITCHELL, J. K. et al. (1965): Permeability of compacted clay. *Proc. ASCE*. SM 4.
- MITCHELL, J. K. and WAN, T. Y. (1977): Electro-osmotic consolidation—its effect on soft soils. *Proc. 9th ICSMFE*. Vol. 1, Tokyo.
- MURAYAMA, S. (1958): Method to install sand piles by vibrating casing pipes. *Japanese Patent* No. 266080.
- PILOT, G. (1977): Methods of improving the engineering properties of soft clay—state of the art report. *Proc. Int. Symp. on Soft Clay*, Bangkok.
- PRIEBE, H. (1976): Abschätzung des Setzungsverhaltens eines durch Stopfverdichtung verbesserten Baugrundes. *Die Bautechnik*, No. 5.
- QUEIROZ, DE CARVALHO, J. B. (1981): Amorphous materials and lime stabilized soils. *Proc. 10th ICSMFE*, Vol. 3, Stockholm.
- RESENDIZ, D. (1977): Slopes in compacted soils—state of the art report. *Proc. 9th ICSMFE*. Vol. 2, pp. 591–599. Tokyo.
- RÉTHÁTI, L. (1960): Capillary properties of soils. *Acta Techn. Acad. Sci. Hung.*, Tom. XXIX, fasc. 1–2.
- RODE, A. A. (1952): *Pochvennaya vlaga*. Izd. Ak. Nauk SSSR, Moscow.
- SEED, H. B. and CHAN, C. K. (1959): Compacted clays. *Proc. ASCE*. SMF Div., Oct.
- SEED, H. B. and BOOKER, J. R. (1977): Stabilization of potentially liquefiable sand deposits using gravel drains. *Proc. ASCE*. GT 7.
- SCHUSTER, J. A. (1972): Controlled freezing for temporary ground support. *Proc. 1st North Amer. Rapid Excavation and Tunnelling Conf.*, Vol. 2.
- STAMATOPOULOS, A. C. and KOTZIAS, P. C. (1983): Settlement-time predictions in preloading. *Proc. ASCE, J. of Geot. Engg.*, No. 6.
- TAKAGI, S. (1978): Segregation freezing as the cause of suction force for ice lens formation. *Proc. 1st Int. Symp. on Ground Freezing*, Bochum.
- TERASHI, M., TANAKA, H. and OKUMURA, T. (1979): Engineering properties of lime-treated marine soils and D. M. method. *Proc. 6th Asian Reg. Conf. on SMFE*, 11/19.
- THOMPSON, M. R. (1966): Lime reactivity of Illinois soils. *Proc. ASCE*. Vol. SM 5.
- THORNBURN, S. (1975): Building structures supported by stabilized ground. *Géotechnique*, 25.
- VIDAL, H. (1966): La terre armée. *Ann. de l'Inst. Techn. de Bâtiment et des Trav. Publ.*, Nos 223–229.
- WAGENER, F. von M., HARMSE, H. J. von M., STONE, P. and ELLIS, W. (1981): Chemical treatment of a dispersive clay reservoir. *Proc. 10th ICSMFE*. Vol. 3, Stockholm.
- WAN, T. Y. and MITCHELL, J. K. (1976): Electro-osmotic consolidation of soils. *Proc. ASCE*. GT 5.
- WARNER, J. (1978): Compaction grouting— a significant case history. *Proc. ASCE*. GT 7.
- YAMANOUCHI, T. and MATSUDA, S. (1975): Stabilization of sand feasible to liquefaction by means of a kind of grouting applying electro-osmosis. *Proc. Symp. Recent Dev. in the Analysis of Soil Behaviour*. Kensington.

Chapter 6.

Soil dynamics

6.1 Introduction

If an elastic, or elastically supported structure is disturbed by the sudden application or release of a force, the static equilibrium of the reactions at the supports and of the forces acting within the individual elements is also disturbed and the system will start vibrating. The response of a structure to a transient disturbance, *viz.* the magnitude, mode and variation with time of the resulting vibrations, will depend on the material, dimensions, support, etc., of the structure itself, as well as on the actual disturbance. The free response of a structure to an initial displacement or velocity will take the form of free vibrations. The complexity of a dynamic system is indicated by the number of degree of freedom the system possesses. This equals the number of independent coordinates in terms of which the displacement of the system can be completely described. A three-dimensional rigid body subject to no restriction requires six coordinates to specify its position completely, namely three linear displacements and three angular rotations, thus it has six degrees of freedom.

A body subject to a rapidly varying, repeated disturbing force will also start vibrating. The mode of vibration will depend on the magnitude, direction and point of application of the disturbing forces, but also on the properties of the body and on the support conditions. The disturbing force is harmonic in the majority of cases and the response of the structure takes the form of forced vibrations.

In structures supported on soil, both types of vibration are liable to occur. A blast, a single-acting pile driver, etc., will generate free vibrations in the structure and thus in the subsoil as well. The soil particles are displaced from their original position and will start vibrating owing to their inertia. The amplitude and propagation velocity of the waves induced in the soil will vary with the kind and magnitude of the disturbing force, and will depend also on the type and condition of the soil. Conversely, any periodically acting machine, such as continuously operating pile

drivers, rail or road traffic, will induce forced vibrations. The foundation and, in turn, the subsoil will suffer continuous impacts generating vibrations.

If the source of the periodic disturbance is located outside the structure considered, the pulses will be transmitted to it by the soil. The vibrations in the latter propagate in a manner similar to sound. The velocity of propagation is controlled by the soil characteristics, this offers the possibility of non-destructive soil exploration.

The conventional static methods and soil physical characteristics discussed in the foregoing sections are insufficient to describe the dynamic behaviour of soils. Special methods of investigation are therefore needed; the response of soil masses to vibrations and the propagation of waves have had to be studied, along with the effect of dynamic forces on the soil physical properties. Advances in industrialisation have raised problems related to machine foundations, and the growing dynamic loads on road and runway pavements present problems of growing importance and complexity; thus the soil engineer is compelled to devote greater attention to the problems of soil dynamics.

Even more formidable problems have recently been encountered. For example, space research calls for very special foundations for launching pads and the size of hydroelectric generators and other machines continues to grow. The devastating earthquakes that have occurred during the past few decades (e.g. Valdivia, Skopje, Tashkent, Anchorage, Niigata, etc.) have also contributed to directing attention to the dynamic behaviour of soils. The influence of vibrations in changing soil physical properties has indeed been utilised in the construction industry in solving a number of technological problems encountered in practice, e.g. vibratory compaction or the vibratory driving of piles and sheet piles, to mention only a few. Blasting is also likely to find even more widespread application in the future.

In view of the foregoing considerations, the present chapter will be devoted to some problems in soil dynamics.

6.2 Theory of vibrations

Consider a rigid footing supported on a uniform soil. The footing should be assumed to be acted upon by concentric, vertical forces alone and to perform vertical movement only (Fig. 488). The forces acting on the footing are the external periodic disturbing force $P = P(t)$ and the force due to the dead weight (mass) of the footing, the latter being excited to move. This force is consequently an inertial force and its magnitude is obtained as the product of mass and acceleration, namely $m d^2z/dt^2$. The third force is the similarly vertical, periodic restoring force, namely reaction and one of the major aims of dynamic analysis is its determination. The forces are in dynamic equilibrium at any instant

$$m \frac{d^2z}{dt^2} + P(t) = Q(t). \quad (547)$$

The disturbing force $P(t)$ is, in the majority of cases, a periodic function of time, viz. harmonic. According to the generating effect, the peak magnitude thereof may or may not depend on frequency. In practice, two kinds of disturbance are encountered, namely constant, where $P = P_0$ and quadratic, where $P = m_0 r \omega^2$.

The magnitude of the force Q depends on the displacement z , viz. on the depth and rate of penetration of the footing into the soil. In general

$$Q(t) = Q \left(z, \frac{dz}{dt} \right). \quad (548)$$

Solutions of the differential equation (547) are available for a few simple $Q(t)$ functions only. This function of two variables is commonly assumed to be composed of two terms

$$Q = Q_1(z) + Q_2(dz/dt). \quad (549)$$

The first term represents the dynamic load – settlement diagram of the soil, viz. the load – settlement relationship. This diagram is usually called the response curve of vibration and may be sub-linear, linear or supralinear, i.e. it may deviate from the straight line upward or downward (Fig. 489). In the case *a* (sublinear), the system becomes softer with increasing displacement, whereas in case *c* (supralinear) it becomes stiffer.

The second term in Eq. (549) represents damping, which is termed linear if the force causing the vibration to diminish is proportionate to the

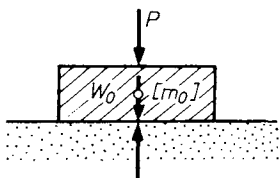


Fig. 488. Forces acting on the footing

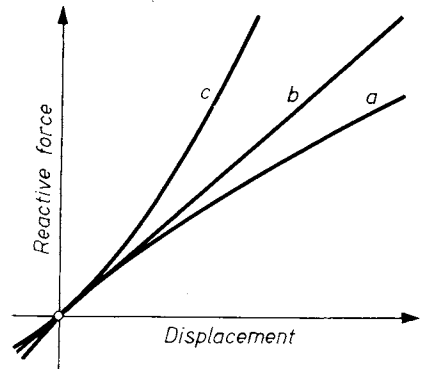


Fig. 489. Guide lines of vibration

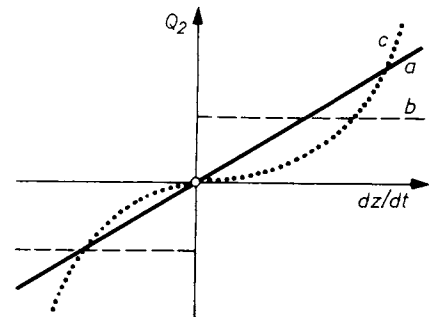


Fig. 490. Practically experienced attenuations: *a* – viscous damping; *b* – friction in dry stage; *c* – air-, or water resistance

velocity of movement. The expression “viscous damping” is also common.

Other kinds of damping, due to dry friction (Coulomb), or air or hydraulic resistance are also frequently encountered in practice. The former is unrelated to velocity and always acts in a direction opposite thereto, whereas the latter are proportionate to the square of velocity (Fig. 490).

Equation (547) should be written for the simplest conceivable case, where the function $Q(t)$ is of the form in Eq. (549) with Q_1 and Q_2 being linear functions of the corresponding variables. Thus $Q_1 = Kz$ and $Q_2 = cdz/dt$. In this way the simplest basic equation in vibration theory is obtained

$$m \frac{d^2z}{dt^2} + c \frac{dz}{dt} + Kz = P(t). \quad (550)$$

The constants involved in the equation are

- m = the mass of the vibrating body,
- c = the damping factor,
- K = the spring constant.

6.3 Solutions of the basic equation

6.3.1 General case

Assume a harmonic, sinusoidal disturbing force acting on the footing. Then

$$P(t) = P_0 \sin \omega t \quad (551)$$

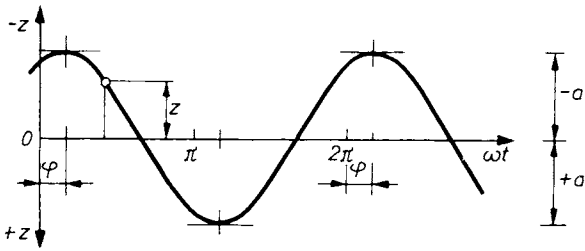


Fig. 491. Time-path curve of swinging

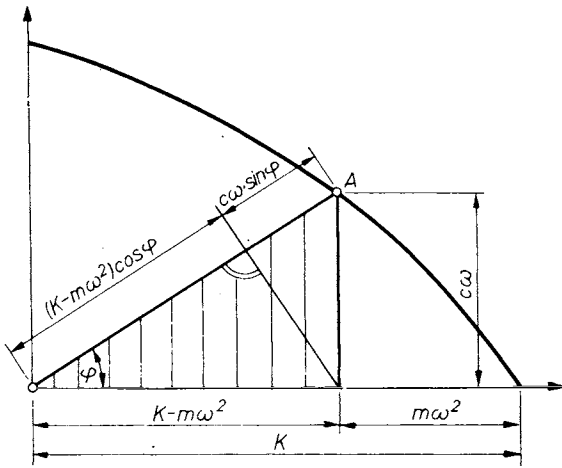


Fig. 492. Illustration of the equation describing enforced attenuated swinging

and a particular solution $z = f(t)$ of Eq. (550) is written simply as*

$$z = a \cos(\omega t - \varphi). \quad (552)$$

The time-displacement curve is thus a cosine function with maximum amplitude a and phase angle φ (cf. Fig. 491).

Upon substitution into Eq. (550),

$$(K - m\omega^2) \cos \varphi + c\omega \sin \varphi = \frac{P_0}{a}. \quad (553)$$

The relationship is represented according to Fig. 492, by a right-angled triangle (Runge). A change in frequency will cause point A on the hypotenuse to describe a parabola, the angle at the origin O denoting the phase angle. From this diagram the expressions for amplitude a and phase angle φ are written directly as

$$a = \frac{P_0}{\sqrt{(K - m\omega^2)^2 + c^2\omega^2}}, \quad (554a)$$

$$\tan \varphi = \frac{c\omega}{K - m\omega^2}. \quad (554b)$$

* For the detailed mathematical treatment of the problem, reference is made to the literature at the end of this chapter.

The physical interpretation of the notation $2\sqrt{mK} = c_k$ introduced here will be explained subsequently. The solution $z = f(t)$, namely the time-displacement curve of vibration, is given therewith as

$$z = \frac{P_0}{K} \cdot \frac{1}{\sqrt{\left(1 - \frac{\omega^2}{\omega_0^2}\right)^2 + \left(2 \frac{c}{c_k} \frac{\omega}{\omega_0}\right)^2}} \cdot \sin \left[\omega t - \arctan \frac{2 \frac{c\omega}{c_k \omega_0}}{1 - \frac{\omega^2}{\omega_0^2}} \right]. \quad (555)$$

The widest amplitude is

$$a_{\max} = N_1 a_1 = \frac{a_1}{\sqrt{\left[1 - \frac{\omega^2}{\omega_0^2}\right]^2 + \left(2 \frac{c}{c_k} \frac{\omega}{\omega_0}\right)^2}}, \quad (556)$$

where $a_1 = P_0/k$, viz. the compression of the system under the static load P_0 , and $\omega_0 = \sqrt{K/m}$.

6.3.2 Special cases

Before embarking upon analysis of the general solution, the special cases will first be considered. Setting both $P(t)$ and c in Eq. (550) equal to zero, viz. in the absence of an external disturbing force and of damping, the expression reduces to

$$m \frac{d^2z}{dt^2} + Kz = 0 \quad (557)$$

the familiar solution of which is

$$z = C_1 \sin t \sqrt{\frac{K}{m}} + C_2 \cos t \sqrt{\frac{K}{m}}. \quad (558)$$

C_1 and C_2 are constants of integration. Assume the mass to be displaced from its original position by the distance z_0 and subsequently to be released. Counting time from this instant, the initial conditions become

$$\text{for } t = 0, z = z_0 \text{ and } dz/dt = 0.$$

Upon substitution we have

$$z = z_0 \cos t \sqrt{\frac{K}{m}}. \quad (559)$$

Equation (559) is the expression of undamped vibration, the period T of which is the time required for one complete cycle, during which the quantity $t\sqrt{K/m}$ varies from 0 to 2π (Fig. 493). Thus

$$T \sqrt{\frac{K}{m}} = 2\pi \text{ or } T = 2\pi \sqrt{\frac{m}{K}}. \quad (560)$$

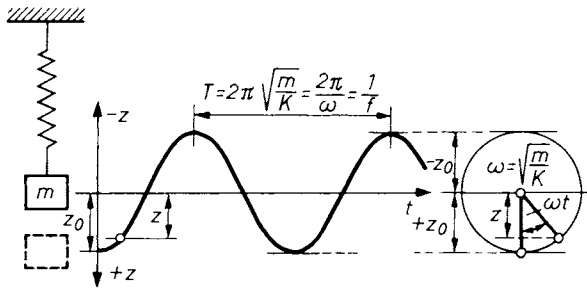


Fig. 493. Graphical illustration of undamped free swing

The quantity $\sqrt{K/m}$ is the circular natural frequency of vibration with the dimension s^{-1} (measured in radians per second) and is substantially the angular velocity

$$\omega_0 = \sqrt{\frac{K}{m}} \quad (561)$$

of the rotating vector characterizing vibration.

The inverse of the period T is called the natural frequency in cycles (the number of revolutions by the vector) per second

$$f_0 = \frac{1}{T} = \frac{1}{2\pi} \sqrt{\frac{K}{m}} = \frac{1}{2\pi} \sqrt{\frac{Kg}{G}} = \frac{\omega_0}{2\pi} \quad (562)$$

denoted as cps or Hz (Hertz).

This spring is compressed under the static load G by the distance

$$\delta_0 = G/K$$

or

$$\frac{K}{m} = \frac{g}{\delta_0} \text{ and } \omega_0 = \sqrt{\frac{g}{\delta_0}} \quad (563)$$

With δ_0 specified in cm units, the frequency becomes

$$f_0 = \frac{\omega_0}{2\pi} = \frac{1}{2\pi} \sqrt{\frac{g}{\delta_0}} = \frac{5}{\sqrt{\delta_0}} \text{ s}^{-1} = \frac{300}{\sqrt{\delta_0}} \text{ min}^{-1} \quad (564)$$

Substitution of ω_0 from Eq. (562) into Eq. (559) yields

$$z = z_0 \cos(\omega_0 t).$$

The position of the revolving vector of length z_0 (Fig. 494) is described by the function

$$\beta = \beta(t) = \omega_0 t,$$

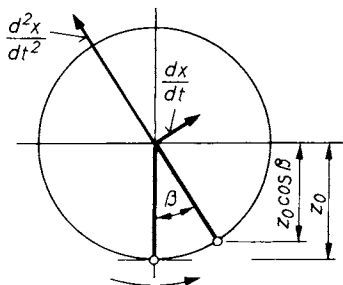


Fig. 494. Position of vector z_0

where

$$\omega_0 = \frac{d\beta}{dt}$$

is the angular velocity. The velocity and acceleration of motion are

$$\frac{dx}{dt} = -z_0 \omega_0 \sin(\omega_0 t); \quad \frac{d^2x}{dt^2} = -z_0 \omega_0^2 \cos(\omega_0 t). \quad (565)$$

The only physical parameter involved in these expressions is the spring constant (stiffness) K , with the physical interpretation given in Eq. (563) and defined in the foregoing for a single spring, or for a single set of springs. The behaviour of the composite system will depend on whether the

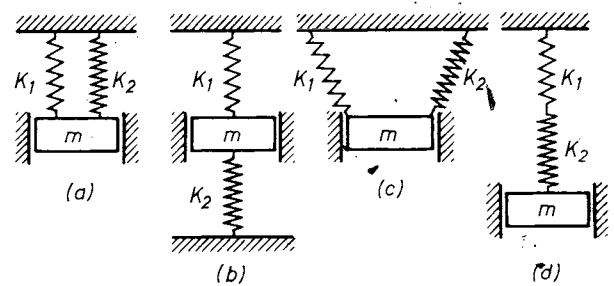


Fig. 495. Spring assemblies coupled in parallel (a, b, c) and in series (d)

springs are connected in parallel or in series. For instance, in cases (a) and (b) in Fig. 495, unit vertical displacement of the mass will induce the spring force (strain energy) $K_1 + K_2$. The natural frequency of the system is thus

$$\omega_0 = \sqrt{\frac{K_1 + K_2}{m}}.$$

In the case c the total elongation due to unit force is the sum of the elongations of the two springs loaded by the same force: $1/K_1 + 1/K_2$. Thus the spring constant of the system is

$$K = \frac{1}{\frac{1}{K_1} + \frac{1}{K_2}}.$$

For several parallel-connected springs

$$K = \sum_{i=1}^n K_i > K_i^{\max} \quad (566a)$$

for springs connected in series

$$\frac{1}{K} = \sum_{i=1}^n \frac{1}{K_i}; \quad K < K_i^{\min}. \quad (566b)$$

Actually, all free vibrations are attenuated because of the frictional (etc.), forces induced; the amplitude diminishes gradually and all vibra-

tions are eventually damped out. With regard to this fact, the equation applying to the second special case is derived from Eq. (550)

$$m \frac{d^2z}{dt^2} + c \frac{dz}{dt} + Kz = 0. \quad (567)$$

The differential equation is solved by substituting $z = e^{st}$

$$e^{st} \left(s^2 + \frac{c}{m} s + \frac{K}{m} \right) = 0 \quad (568)$$

and if $z = e^{st}$ is actually a solution, the term in brackets must become zero, i.e.

$$s = s_{12} = -\frac{c}{2m} \pm \sqrt{\left(\frac{c}{2m}\right)^2 - \frac{K}{m}} \quad (569)$$

and the general solution is

$$z = C_1 e^{s_1 t} + C_2 e^{s_2 t}. \quad (570)$$

Where the square root in Eq. (569) is a real number, two negative roots are obtained and the solution is the algebraic sum of two exponential curves. The dashed line in Fig. 496 shows the solution for the case $C_1 = 1$ and $C_2 = -2$. It will be observed therefrom that no "vibration" occurs in this case, the mass displaced returning to the equilibrium position with gradually diminishing velocity (creeping motion). In this case, viz. for $[(c/2m)^2 > K/m]$, damping is too heavy and no vibration will occur as long as

$$c_k = 2 \sqrt{mK} = 2m\omega_0 \quad (571)$$

reaches the value of critical damping. Conversely, for $c < c_k$, Eq. (569) yields complex roots. With the substitutions

$$\sqrt{\frac{c^2}{4m^2} - \frac{K}{m}} = i\omega \quad \text{and} \quad \frac{c}{2m} = \rho,$$

the general solution becomes

$$z = e^{-\rho t} (Ae^{i\omega t} + Be^{-i\omega t}).$$

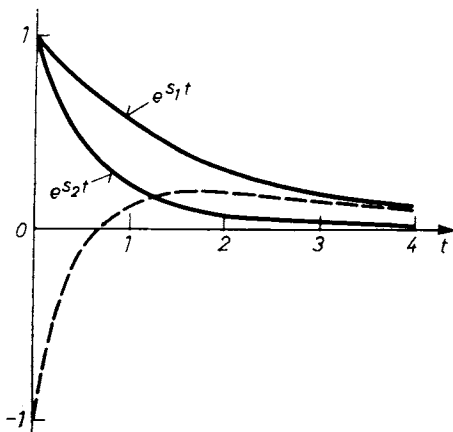


Fig. 496. Motion of a system characterized by one degree of freedom when damping exceeds the critical value

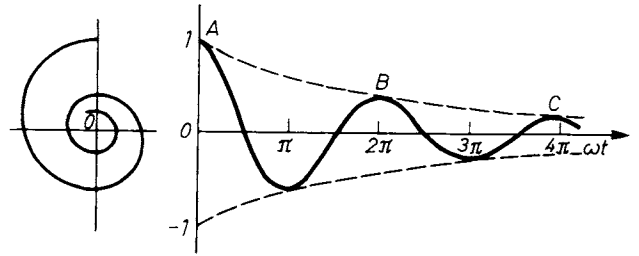


Fig. 497. Damped swinging when damping effect is below the critical value

Introducing Euler's relation

$$e^{\pm iy} = \cos y + i \sin y;$$

so that

$$z = e^{-\rho t} \{ (A + B) \cos \omega t + i(A - B) \sin \omega t \}.$$

The arbitrary constants are written as

$$i(A - B) = C_1$$

and

$$A + B = C_2,$$

thus

$$z = e^{-\rho t} (c_1 \cos \omega t + c_2 \sin \omega t)$$

with the solution

$$z = e^{-\frac{c}{2m} t} [C_1 \cos \omega t + C_2 \sin \omega t], \quad (572)$$

where

$$\omega = \sqrt{\frac{K}{m} - \frac{c^2}{4m^2}}. \quad (573)$$

Equation (572) will plot as a sine curve with successively diminishing amplitudes between the exponential curve and the reflected image thereof (Fig. 497).

For $c^2/4m^2 = K/m$, viz. $c = c_k$, the characteristic equation (568) has two identical real roots and the two constants give no solution. Substituting into Eq. (550) will show the solution to be obtained by the function

$$z = Bte^{-\frac{c}{2m} t}.$$

At greater t value, z tends to zero, i.e. the motion is again aperiodic.

The extent of damping is found by considering two successive maxima of the curve. During the time $2\pi/q$ the amplitude decreases from

$$C_1 e^{-\frac{c}{2m} t} \quad \text{to} \quad C_1 e^{-\frac{c}{2m} (t + \frac{2\pi}{q})}.$$

The ratio of the two is the logarithmic decrement

$$\ln \delta = \frac{\pi c}{mq} = \text{const.}$$

i.e. the amplitude decreases according to a geometric series.

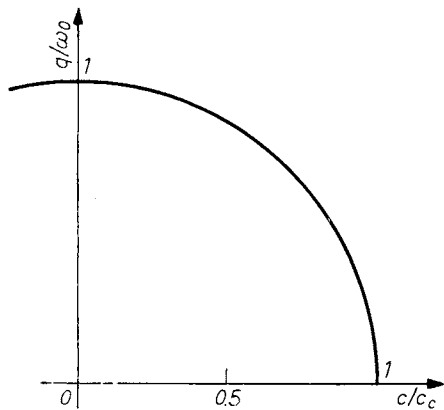


Fig. 498. Natural frequency of a system with one degree of freedom as a function of damping

The ratio of the frequency of free damped vibration to that of free undamped vibration is from Eq. (572) with regard to Eq. (571),

$$\frac{q}{\omega_0} = \sqrt{1 - \left(\frac{c}{c_k}\right)^2}$$

This relationship is plotted in Fig. 498. The resulting curve is a circle; for $c = c_k$ we have $q = 0$. Since the tangent to the curve at the point $c = 0$ is horizontal, under the damping conditions commonly encountered in practice ($c/c_k < 0.2$) the natural frequencies hardly differ from the natural frequencies of the undamped system ($\sqrt{K/m}$) and may for all practical purposes be considered constant.

The last special case, namely that of forced, undamped vibrations will be considered in connection with the general solution.

6.3.3 Determination of the relevant dynamic quantities

Returning to the solution of Eq. (550), given by Eqs (554) and (555), the results are clearly illustrated by the graphical representation. From the treatment of the special cases it will be seen directly that ω_0 in Eq. (561) is the natural frequency of the free vibrations of the system, c is the damping coefficient and c_k the critical value thereof. N_1 is the ratio of the widest amplitude to the displacement under a static force and is therefore called the (dynamic) magnification factor, or gain.

The solution is written in the form

$$z = a_1 N_1 \sin(\omega t - \varphi), \tag{574}$$

where

$$\tan \varphi = \frac{2 \frac{c}{c_k} \frac{\omega}{\omega_0}}{1 - \frac{\omega^2}{\omega_0^2}} = \frac{c\omega}{K - m\omega^2}. \tag{575}$$

φ is the phase angle. The vibration is a harmonic one, and has a frequency equal to that of the disturbing force, but lags behind the latter by the phase angle φ .

The magnification factor N_1 and the phase angle φ are plotted against the frequency of the disturbing force and the natural frequency in Figs 499 and 500. The parameter of the curves is c/c_k . The curve pertaining to the parameter value $c/c_k = 0$ in Fig. 499 applies to undamped vibrations. Damping will be seen to reduce the amplitude of

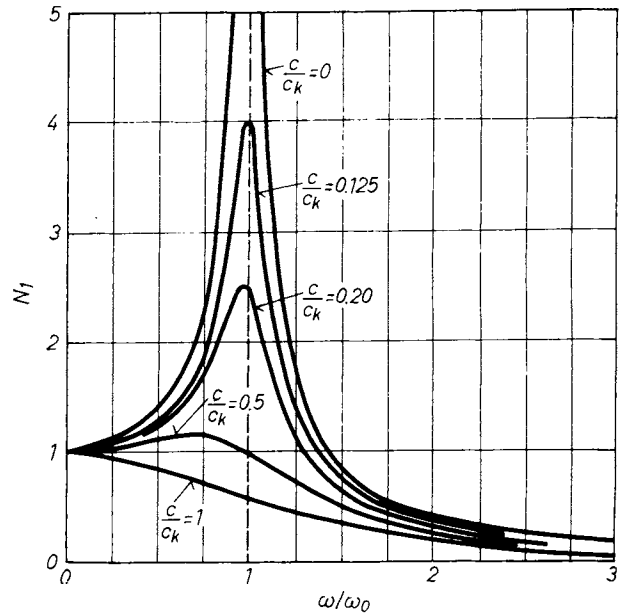


Fig. 499. Magnification factors for enforced damped swinging motions

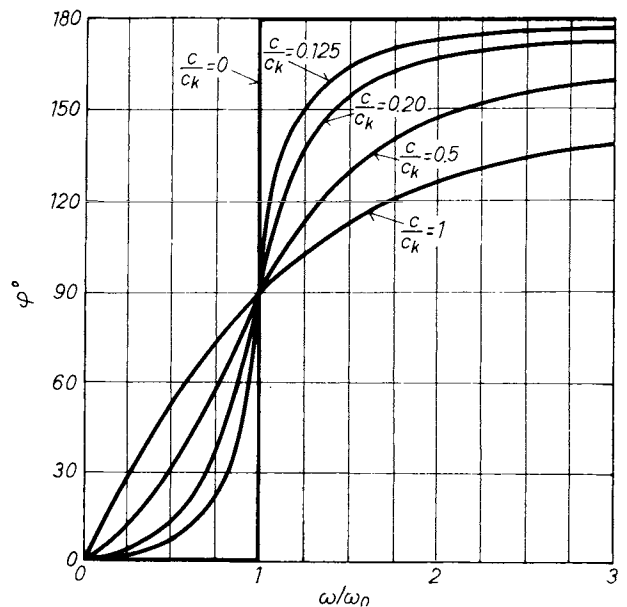


Fig. 500. Phase-angles between force and displacement as functions of frequency and damping

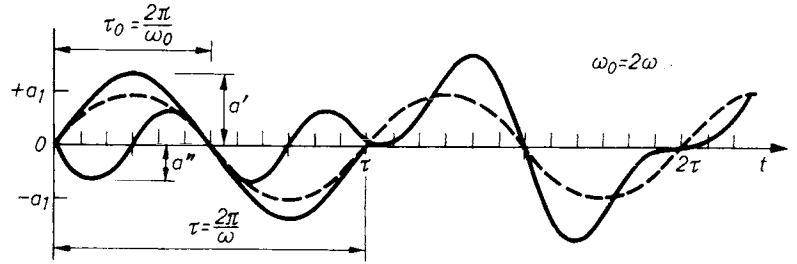


Fig. 501. Time-path curve of an enforced undamped swinging system for $\omega/\omega_0 = 0.5$

forced vibrations. The solution for the case $c/c_k = 0$ is

$$z = \frac{a_1}{1 - \frac{\omega^2}{\omega_0^2}} \sin \omega t. \quad (576)$$

This is the particular solution of the inhomogeneous differential equation. The general solution is found by adding the general solution Eq. (558) of the homogeneous equation. Thus

$$z = C_1 \sin \omega_0 t + C_2 \cos \omega_0 t + \frac{a_1}{1 - \frac{\omega^2}{\omega_0^2}} \sin \omega t. \quad (577)$$

For $C_2 = 0$, transformation yields

$$z = \frac{a_1}{1 - \frac{\omega^2}{\omega_0^2}} \left(\sin \omega t - \frac{\omega}{\omega_0} \sin \omega t \right). \quad (578)$$

Vibration accordingly consists of two parts, namely the first part where

$$z' = \frac{a_1}{1 - \frac{\omega^2}{\omega_0^2}} \sin \omega t \quad (578a)$$

is the forced vibration with the circular frequency ω and the amplitude

$$a' = \frac{a_1}{1 - \frac{\omega^2}{\omega_0^2}} = N_1 a_1.$$

$N_1 = \omega_0^2/(\omega_0^2 - \omega^2)$ is the magnification factor in the case $c = 0$ (cf. Fig. 499).

The second part of the solution

$$\begin{aligned} z'' &= \frac{a_1}{1 - \omega^2/\omega_0^2} \frac{\omega}{\omega_0} \sin \omega t = \\ &= a_1 N_1 \frac{\omega}{\omega_0} \sin \omega t \end{aligned} \quad (578b)$$

is a free vibration with the circular frequency ω_0 and the amplitude

$$a'' = a_1 N_1 \frac{\omega}{\omega_0}.$$

The resultant vibration is thus the sum of two vibrations and is no longer harmonic. For the case $\omega/\omega_0 = 0.5$, the time-displacement curve of vibration is shown in Fig. 501. The variation of the disturbing force with time is indicated by the dashed line. The force is seen to have increased due to the dynamic effect. The magnification factor $N_1 = 1/(1 - 1/4) = 1.33$, so that the amplitude of the forced vibration is $a' = 1.33a_1$, and that of the free vibration is $a'' = 1.33 \cdot 1/2a_1 = 0.67a_1$.

The resultant time-displacement curve of free and forced vibrations assumes an interesting shape if the vibrations differ from each other but little. The widest amplitude will vary periodically, the phenomenon being known as beating. The frequency thereof is $\omega_0 - \omega$ and the circular frequency $2\pi/(\omega_0 - \omega)$. The time-displacement curve of beating is shown in Fig. 502.

For $\omega = \omega_0$ and $c = 0$ the magnification factor N tends to infinity. This is the case of resonance

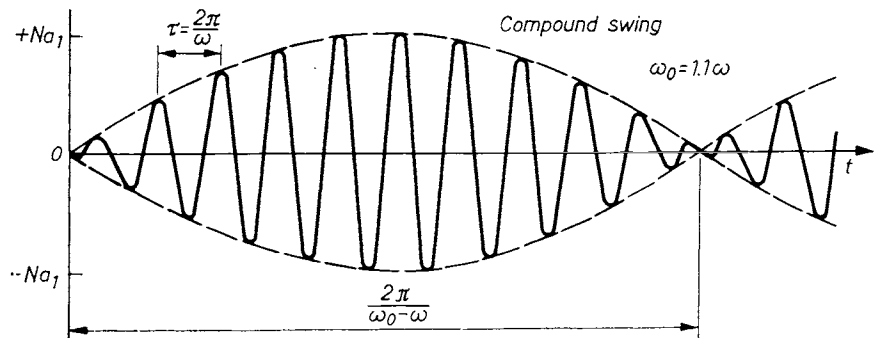


Fig. 502. Time-path curve for compound swinging

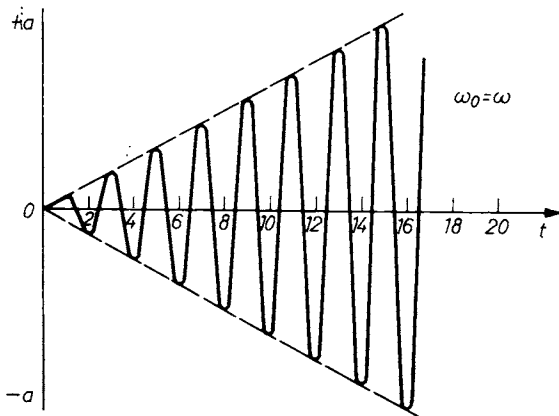


Fig. 503. Time-path curve for resonance

at undamped vibration. The disturbing force always acts on the vibrating body at a time and in a direction such as to increase the amplitude thereof, so that the maxima of the force increase to infinity as a linear function of time (Fig. 503).

Damped vibrations invariably have smaller amplitudes than undamped ones. Moreover, the greatest value of N_1 is a finite one and resonance occurs at a frequency slightly lower than that corresponding to $\omega/\omega_0 = 1$, at

$$\omega_1 = \omega_0 \sqrt{1 - \frac{1}{2} \left(\frac{2c}{\omega_0} \right)^2} \quad (579)$$

In practical systems, however, the ratio ω_1/ω_0 differs but slightly from unity and thus the approximation $\omega_1 \sim \omega_0$ is acceptable. At resonance the amplitude is

$$z_0 = \frac{P_0}{2k \frac{c}{c_k}} \quad (580)$$

6.4 Rocking vibrations

The vibrations considered in the foregoing were caused by a vertical disturbing force, the line of action and point of attack of which remained unchanged during vibration, the magnitude being the only variable. The vibration of a body acted upon by a moment varying periodically with time will be examined subsequently after BARKAN (1962). Assume the moment to vary according to the function $M = M_0 \sin \omega t$ and to act in one of the principal planes of inertia of the body (Fig. 504).

In cases where the resistance to sliding on the base is large enough, the moment will cause the body to rotate through the angle α . The equation of motion is then

$$-J_0 \frac{d^2\alpha}{dt^2} + \Sigma M_i = 0, \quad (581)$$

where J_0 is the moment of inertia of the mass about the axis of rotation and ΣM_i is the moment of all external forces about the same axis. Moments are due to the dead weight of the body and to soil reaction. The magnitude of the former is haQ , while for computing the latter the soil reaction must first be found. The soil resistance acting on the elementary area dF situated at the distance ξ from the axis of rotation is

$$dR = C_\alpha \xi \alpha dF,$$

whence the elementary moment

$$dM_r = -\xi dR = -C_\alpha \xi^2 \alpha dF,$$

and the total reacting moment becomes

$$M_r = -C_\alpha \alpha \int \xi^2 dF = -C_\alpha J,$$

with J denoting the moment of inertia of the base about the axis of rotation.

Together with the disturbing moment, the equation of motion is

$$J_0 \frac{d^2\alpha}{dt^2} + (C_\alpha J - Qh) \alpha = M_0 \sin \omega t. \quad (582)$$

The case $M_0 = 0$ yields the equation of free rocking vibrations

$$J_0 \frac{d^2\alpha}{dt^2} + (C_\alpha J - Qh) \alpha = 0 \quad (583)$$

the solution of which is

$$\alpha = C \sin(\omega_x t + \alpha_0), \quad (584)$$

wherein

$$\omega_x^2 = \frac{C_\alpha J - Qh}{J_0} \quad (585)$$

is the natural frequency of rocking vibrations, while C and α_0 are constants, whose magnitude depends on the initial conditions. The solution of Eq. (582) is formally identical with the expression of vertical forced vibrations, with P , m and ω_0

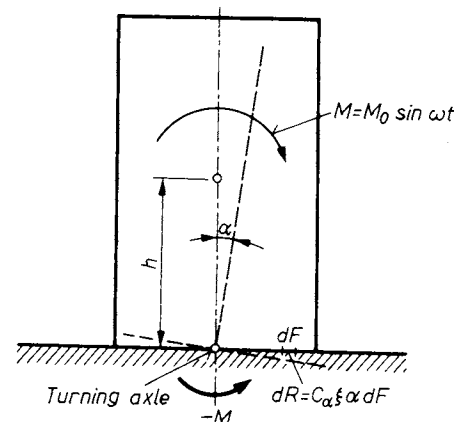


Fig. 504. Elastically supported mass under the influence of periodic movement

being replaced by M, J_0 and ω_z . The amplitude of forced vibrations is thus

$$a_z = \frac{M}{J_0(\omega_z^2 - \omega^2)}. \quad (586)$$

The problem of rocking vibrations arises mainly in the case of tall machine foundations, which are acted upon by a disturbing moment or a disturbing horizontal force. In such cases the natural frequency is found from Eq. (585).

Before any practical application of the theoretical results in Sections 6.3 and 6.4 can be attempted, numerical values must be assigned to the constants involved in Eq. (550). The question arises, how far are we justified in regarding these quantities as constant within the system consisting of the structure and the subsoil? The quantities in question are:

- the spring constant (stiffness) K ;
- the mass of the system m ;
- the damping coefficient c ;
- the disturbing force $P(t)$.

Before embarking upon this subject, the effect of vibrations on the soils and on the physical properties thereof must be examined.

6.5 Non-linear vibrations

In deriving the basic equation in Section 6.2, it was pointed out that the terms involved therein are in general non-linear, in contrast with the assumption made there. The response curve has also been defined as representing the relationship between displacement and the restoring force. A non-linear response curve implies that the natural frequency of the system is not constant. Thus a sublinear response curve means that the natural frequency decreases with increasing amplitude, since the restoring force diminishes (Fig. 505).

Consider now the case of non-linear vibrations starting with the conditions of free vibrations. The differential equation of motion is

$$m = \frac{d^2z}{dt^2} + f(z), \quad (587)$$

where $Q = Q_1(z)$ is the non-linear restoring force [cf. Eqs (547) and (549)]. Equation (587) can also be written in the form

$$m \frac{d^2z}{dt^2} = m \frac{dv}{dt} = m \frac{dv}{dz} \frac{dz}{dt} = m v \frac{dv}{dz} = -f(z),$$

whence, upon integration with respect to z ,

$$m \frac{v^2}{2} = \int_{z_{\max}}^z -f(z) dz. \quad (588)$$

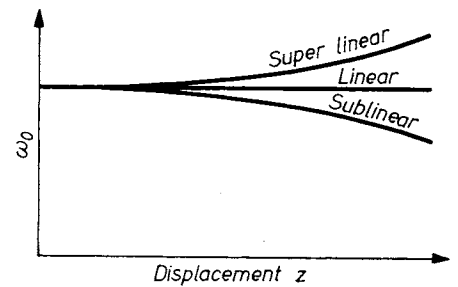


Fig. 505. Natural frequency as a function of displacement

The limits of integration are the maximum amplitude z_{\max} , where $v = 0$, and an arbitrary intermediate value z . From Eq. (588)

$$v = \sqrt{\frac{2}{m}} \sqrt{\int_{z_{\max}}^z -f(z) dz} = \frac{dz}{dt}$$

and the time during which the mass point moves from z_{\max} to z is

$$t = \sqrt{\frac{m}{2}} \int_{z_{\max}}^z \frac{dz}{\sqrt{\int_{z_{\max}}^z -f(z) dz}}.$$

The second integration between $z = z_{\max}$ and $z = z_0 = 0$ yields the natural frequency as

$$\frac{1}{f_0} = \frac{2\pi}{\omega_0} = T = \sqrt{8m} \int_{z_{\max}}^0 \frac{dz}{\sqrt{\int_{z_{\max}}^z -f(z) dz}}. \quad (589)$$

Theoretically, Eq. (589) can be used to find the natural frequency for any response curve. Exact integration is, however, possible only in a few cases of practical interest, but a solution can always be found by adopting a numerical, or graphical approach.

In the case of non-linear damping, the natural frequency retains the value $\sim K/m$. The attenuation of amplitudes can be determined by iterative, numerical or graphical integration, but the step-by-step procedure is somewhat lengthy. A fair approximation is obtained by equating the energy consumed by friction to the decrement kinetic energy of the system. The loss in energy is computed knowing the character of movement. Assume the movement to be harmonic, $z = z_0 \sin \omega t$. The damping force is $Q_2 = f(dz/dt)$ and the work performed during one cycle is

$$A = \int_0^T f \left(\frac{dz}{dt} \right) dz = \int_0^T f \left(\frac{dz}{dt} \right) \frac{dz}{dt} dt = z_0 \int_0^{2\pi} f \left(\frac{dz}{dt} \right) \cos \omega t d(\omega t).$$

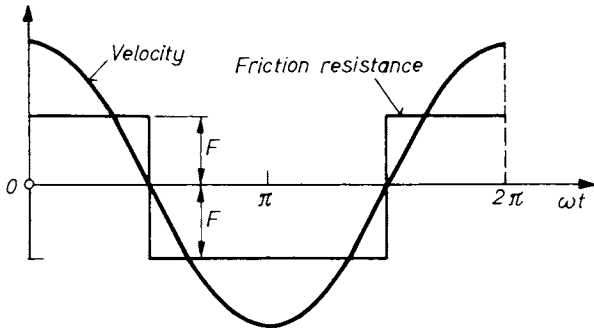


Fig. 506. Friction as a damping force

The decrement kinetic energy is

$$\begin{aligned} \frac{1}{2} m\omega^2 z_0^2 - \frac{1}{2} m\omega^2 (z_0 - \Delta z)^2 &= \\ = m\omega^2 z_0 \Delta z - \frac{1}{2} m\omega^2 (\Delta z)^2 &\approx m\omega^2 z_0 \Delta z. \end{aligned}$$

Equating the two expressions, the change in amplitude during one cycle is

$$\Delta z = \frac{1}{m\omega^2} \int_0^{2\pi} f \left(\frac{dz}{dt} \right) \cos \omega t d(\omega t). \quad (590)$$

As an example, the case of friction is first examined where $f(dz/dt) = \pm F$. The velocity is shown as a function of the damping force in Fig. 506. The integral in Eq. (590) consists of four identical parts:

$$4 \int_0^{\pi/2} F \cos \omega t d(\omega t) = 4T$$

and the amplitude decreases in a single cycle by

$$\Delta z = \frac{4F}{m\omega^2} = 4 \frac{F}{K} \frac{K}{m} \frac{1}{\omega^2} = 4 \frac{F}{K} \quad (591)$$

and thus four times as much as the compression of the spring under the static force F . The amplitudes thus decrease arithmetically, whereas in the case of viscous friction they decrease according to a geometric sequence.

The next case considered is that of forced vibration in combination with a non-linear restoring force. The relevant differential equation of motion is

$$m \frac{d^2 z}{dt^2} + f(z) = P_0 \cos \omega t. \quad (592)$$

Assume the solution to consist of an expression of the form $z = z_0 \cos \omega t$. The mass force is $m d^2 z / dt^2 = m z_0 \omega^2 \cos t$, the maximum of which is $-m\omega^2 z_0$ and this occurs simultaneously with the maxima of the disturbing force P_0 and the restoring force $f(z_0)$. Equation (592) applies to any

instant of motion, thus also to the position $z = z_0$. Here

$$-m\omega^2 z_0 + f(z_0) = P_0,$$

so that

$$f(z_0) = P_0 + m\omega^2 z_0. \quad (593)$$

At $z = 0$ the three forces simultaneously become zero and are thus in equilibrium. In the case of $f(z) = Kz$ each of the three terms in Eq. (592) is proportionate to $\sin \omega t$ and division thereby yields Eq. (593); $f(z_0) = Kz_0$ and the condition of equilibrium is satisfied for all intermediate values between $z = 0$ and $z = z_0$, but not for $f(z) \neq Kz$. An approximate solution is therefore sought, in which equilibrium is established at least in the points $z = \theta$ and $z = z_0$. The amplitude of forced vibrations is thus obtained from Eq. (593).

Preferably, a graphical approach is adopted, in which the forces are plotted on the vertical and the displacement z_0 on the horizontal axis. The left-hand side of Eq. (593) is the equation of the non-linear spring characteristic curve, while the quantity on the right-hand side — the sum of the disturbing force and the maximum value of the inertia force — can be represented by a straight line intersecting the vertical axis at the point P_0 , and inclined at $\arctan(m\omega^2)$ (cf. Fig. 507).

The z_0 value pertaining to an assumed ω value can thus be determined in this manner. In other words, one point on the resonance curve of non-linear vibration is obtained.

In the case of low frequencies, only a single point of intersection (e.g. A_1) is obtained whereas

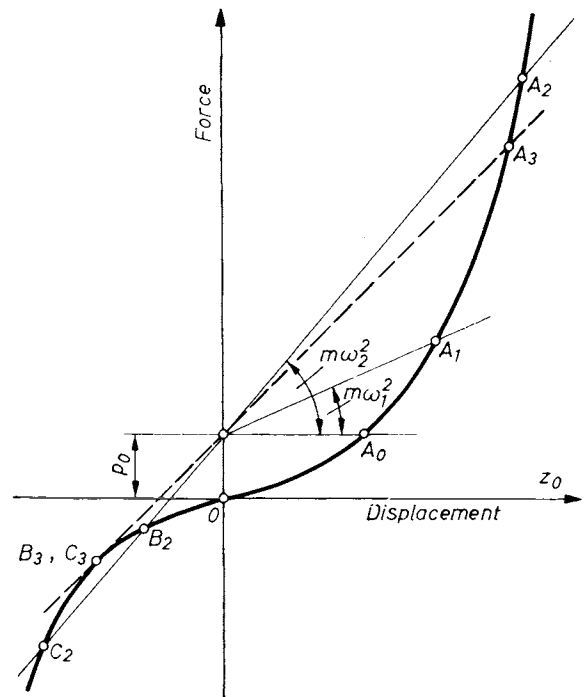


Fig. 507. Approximative determination of the resonance curve for non-linear swinging

at higher frequencies three points (A_2, B_2 and C_2) will result and thus three solutions exist. The plot of the z_0 values against ω thus constructed defines a non-linear resonance curve as illustrated in Fig. 508, which corresponds to the curve in Fig. 499.

Resonance curves for the three types can be seen in Fig. 509 and for these, the always present attenuation should be reckoned with. Own-frequencies are not stable values. Increasing the frequency in the supra-linearity stage causes the amplitude — after reaching point B — to fall suddenly to point C , from where it decreases gradually as ω is further increased. When the investigation begins at a high ω -value, the section

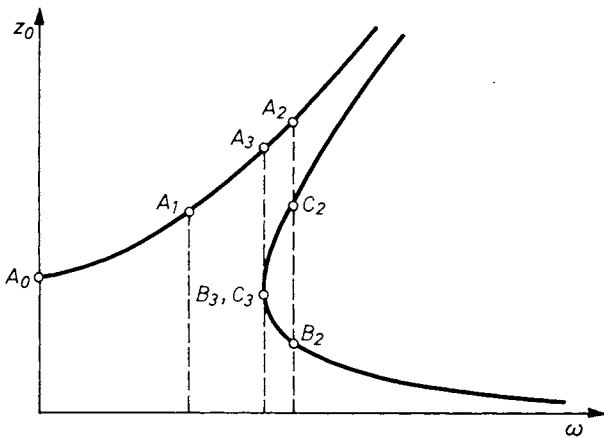


Fig. 508. Resonance curve determined graphically

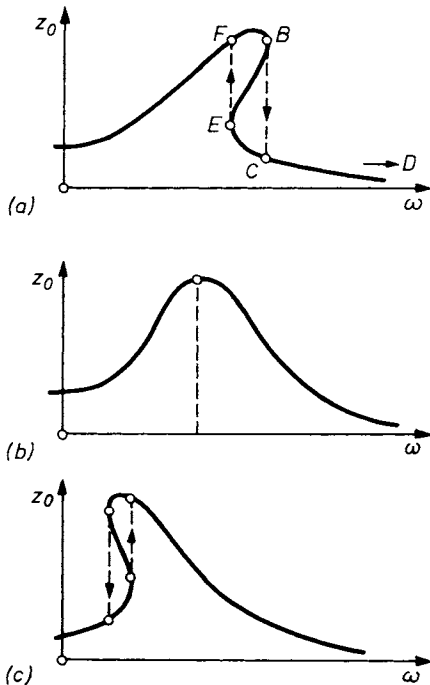


Fig. 509. Resonance curves for:
a — super linear; b — linear; and c — sub-linear vibrations

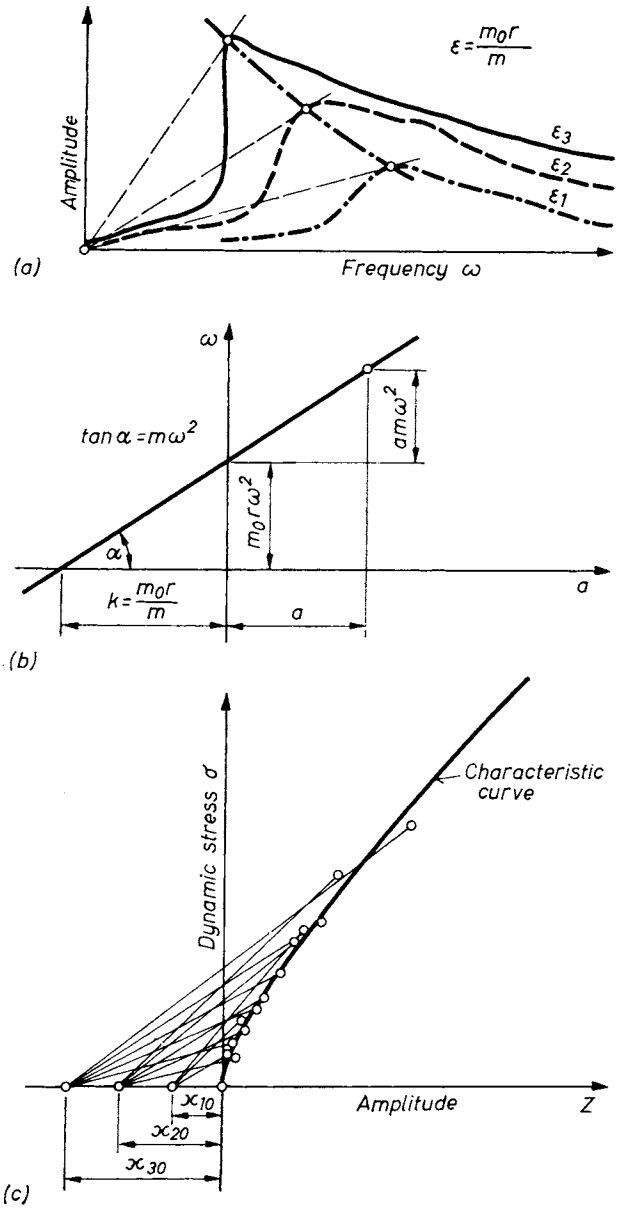


Fig. 510. Drawing the dynamic characteristic curve from known resonance curves

DCE develops, and at point E the amplitude will suddenly reach the value marked as point F .

LORENZ (1950) concluded that the characteristic can be determined by means of experimentally established resonance curves by using the method proposed by DEN HARTOG (1947). Assume that they are known for three eccentricity levels of the rotor. These curves can be seen in Fig. 510; their pattern is typically sublinear. In order to draw the characteristic curve a pair of points ω and z have to be chosen on the amplitude curve. Then a coordinate system should be selected and the amplitudes plotted on the abscissa and the dynamic stresses induced in the soil as the ordinates. The coefficient of eccentricity $\epsilon = m_0 r / m$ (in which m_0 is the mass of the rotor, r is the

diameter, m is the vibrating mass and product m_0r is the generating momentum) should be plotted on the negative side of the amplitude curve (Fig. 510b). A straight line should be drawn from this point with the inclination $m\omega^2/F$; the intersection of this line with the amplitude z will supply one point of the characteristic curve. Repeating this procedure, the whole curve can be produced.

The following expression has been suggested by LORENZ (1950) to describe the characteristic curve:

$$\sigma = az + \frac{bz}{d + z}, \quad (594)$$

where the soil stress σ is composed of a dynamic and a static component

$$\sigma = \sigma_{st}(1 + 0.04\epsilon n^2), \quad (595)$$

where

$$\sigma_{st} = \frac{G}{F} \text{ is the static soil stress;}$$

$$\epsilon = \frac{m_0rg}{G} \text{ the eccentricity factor;}$$

$$n = \text{the frequency.}$$

The three constants involved in Eq. (594) are found from the resonance values obtained by dynamic soil tests performed at three different eccentricities. These being known, the amplitudes are computed from Eq. (594) as

$$z = \frac{a - b}{2a} - \frac{d}{2} + \sqrt{\left(\frac{a - b}{2a} - \frac{d}{2}\right)^2 + \frac{\sigma d}{a}} \quad (596)$$

and the bedding coefficient is the slope of the tangent

$$c = c(\sigma) = \frac{d\sigma}{dz} = a + \frac{bd}{(z + d)^2}. \quad (597)$$

The bedding coefficient determined in this manner is then used in dimensioning machine foundations.

For further detailed treatment of the problem reference is made to the books by LORENZ and KLEIN (1966), KAUDERER (1958), NOVAK (1957) and DEN HARTOG (1947).

The stress deformation relationship in soils has been found to be non-linear in practice, regardless of whether the load is static or dynamic. The deformation curves obtained by applying and

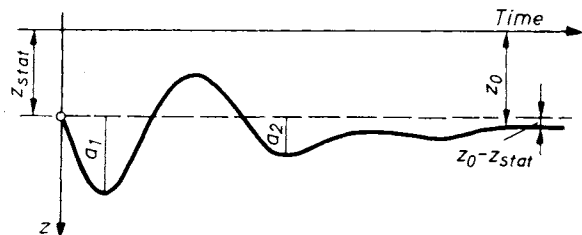


Fig. 511. Time-path curve of a damped swing

removing different loads producing the same stress will display a hysteresis loop. The greater the absorbing capacity of a particular material, the greater the area of the hysteresis loop will be; in other words, the less elastic its behaviour, the greater its capacity for absorbing mechanical work which is irreversibly converted into heat. This part ΔA of the work performed equals the area of the hysteresis loop. Denoting the total work performed by loading up to the greatest deformation by A , the ratio

$$\psi = \frac{\Delta A}{A} \quad (598)$$

may be termed the absorption coefficient, which represents the energy related to the total work A absorbed by the material during a single loading cycle.

A block supported on a soil and acted upon by a single transient force will perform free vibrations, the time-displacement curve of which is shown in Fig. 511. In a linear system the restoring force (the soil reaction) at the maximum amplitude is $Q = Ka_1$, the energy of vibration being

$$A_1 = Ka_1 \frac{a_1}{2} = \frac{K}{2} a_1^2.$$

At the second peak

$$A_2 = \frac{K}{2} a_2^2$$

and the energy absorbed

$$\Delta A = \frac{Ka_1^2}{2} \left(1 - \frac{a_2}{a_1}\right),$$

so that the absorption coefficient becomes

$$\psi = 1 - \left(\frac{a_2}{a_1}\right)^2.$$

It can be demonstrated that in vibrating systems having a single degree of freedom, the maxima of two successive amplitudes are

$$a_1 = a \exp(-cT/4); \text{ and } a_2 = a \exp(5cT/4).$$

Here c is the damping coefficient, T is the period of vibration and a the amplitude of undamped vibration.

Upon substitution

$$\psi = 1 - \exp(-2cT). \quad (599)$$

Experience has shown ψ to depend on the rate of load application, on frequency and on the soil stress to a limited extent only; the influence of soil conditions and granulometry being more pronounced. For instance at $d = 0.1$ to 0.25 mm we have $\psi = 0.04$, while at $d = 1$ to 2 mm it is 0.79 .

The magnitude of ψ and of the damping coefficient can be computed from time-displacement curves determined by measurement.

6.6 Dynamic soil characteristics

6.6.1 Shear strength

It should be made clear at the outset that the changes caused by dynamic effects in the physical parameters of soils are up to now but imperfectly understood. There is ample empirical evidence available to indicate that shear strength (the values of Φ and c), permeability, pore-water pressure and the Young's modulus of elasticity are among the properties substantially affected by vibrations.

The effect on the angle of internal friction in sand was studied by BARKAN (1962) by means of a special direct shear apparatus which enabled him to subject soil samples to the effect of different frequencies. Coulomb's friction law was found also to apply to sands acted upon by dynamic forces: $\tau_s = \sigma \tan \Phi$ (Fig. 512); but it was also found that the angle of friction depends also on frequency and amplitude. In the initial period of vibration, first slight consolidation and then loosening were observed.

The variation of the friction coefficient with the amplitude and frequency of vibration is shown in Fig. 513. The influence of amplitude is unmistakable in that Φ decrease as a is increased. The influence of frequency is more complex, in that a sudden drop in the value of $\tan \Phi$ occurs as the frequency is increased beyond a certain critical value. An interesting and rather unambiguous relationship is obtained by plotting the coefficient of friction against the ratio $\eta = b/g$ (Fig. 514), where b and g are the accelerations of vibration and of gravity, respectively. To describe this relationship BARKAN has suggested the empirical formula

$$\frac{\tan \Phi_{\text{dyn}} - \tan \Phi_v}{\tan \Phi_{\text{stat}} - \tan \Phi_v} = \exp(-\beta\eta), \quad (600)$$

where $\tan \Phi_{\text{stat}}$ is the coefficient of friction determined by a static test, $\tan \Phi_v$ is the asymptote of the curve in Fig. 514, while β is a constant whose value for dry, medium sand is $\beta = 0.23$.

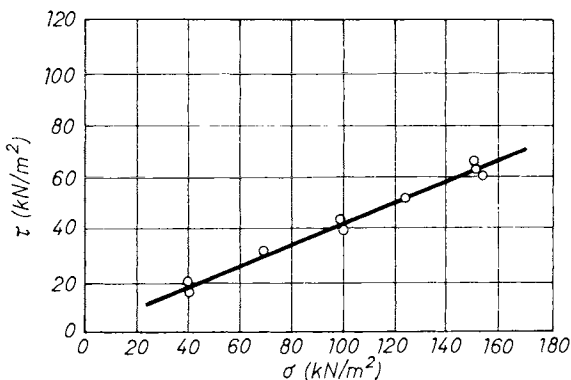


Fig. 512. Coulomb's friction law for dynamically operated probes

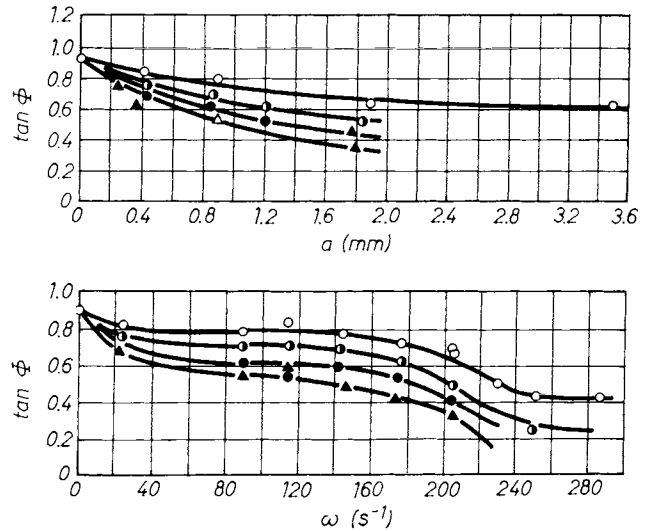


Fig. 513. Angle of internal friction in sand depending on the frequency and the amplitude of vibration

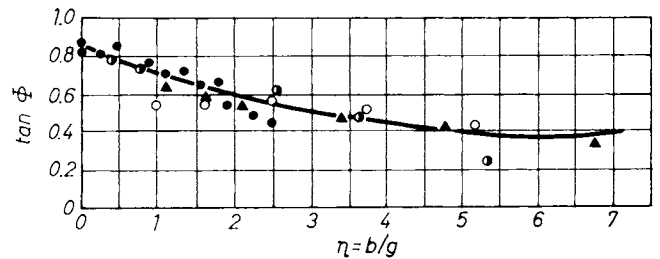


Fig. 514. Angle of internal friction in sand depending on relative acceleration

Vibration affects the coefficient of friction by temporarily reducing the number of contact points between vibrating particles. The result of the shear test is expressed as

$$\tan \Phi = \frac{\tau}{\sigma}$$

To determine the quantities τ and σ , the T and N forces are divided by the total cross-sectional area resisting shear. In contrast to this simplified situation, actual contact between particles is confined to minute, discrete areas and it is in these latter where the frictional resistances are developed. The formula should thus be rewritten into the form

$$\tan \varphi = \frac{T}{N} = \frac{T/\alpha A}{T/\beta A},$$

where α and β are the ratios of the sums of the elementary areas perpendicular to the direction of shearing and the normal force, respectively, to the total area. The effect of vertical vibrations probably consists in reducing α to a smaller extent than β , as a consequence of which $\tan \Phi$ is reduced. The effect of vibration is thus to decrease, at a

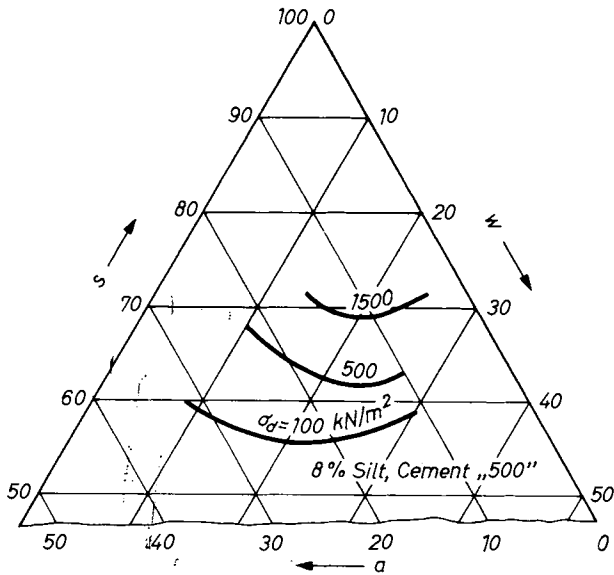


Fig. 515. Coefficient of friction as a function of phase composition

given instant, the size of the contact areas in the cross-section, the probability of reduction increasing with amplitude and frequency.

Understanding the influence of density and moisture on the dynamic behaviour of soils would be of considerable interest. Owing to experimental difficulties, the problem has not been satisfactorily clarified thus far, but this influence is not expected to be a simple one.

Consider first the role of moisture. The investigations by BARKAN (1962) have revealed a water content at which the reduction of the angle of internal friction is minimal. This effect is related to the structure of granular soils. In such soils two critical water contents have been shown to exist (cf. Vol. 1, Fig. 170) concerning resistance to forces and further air- and water permeability (cf. Vol. 1, Section 6.2.5). At saturation values below the lower limit, water is only present in the corners between the particles, the communicating passages being filled with air. The air permeability of the soil is thus great, while the relative water permeability is zero. Above the upper critical value, on the other hand, air is present in the soil, in the form of bubbles, which are displaced together with the water. Consequently, the air permeability is zero at this moisture. Below the critical lower and above the critical upper moisture contents, the effect of vibration is necessarily greater than in the range enclosed, since the continuous air and water matrix, respectively, guarantees a greater mobility to the particles. Owing to this increased mobility, the extent of reduction is more pronounced in the lower and upper ranges.

BARKAN's experimental results plotted in a triangular diagram, are shown in Fig. 515, indicating the values of $\tan \Phi$ at two different frequencies in terms of the phase composition. In the

ranges I and III, friction between the particles may even disappear completely, the material behaving like a dense, viscous fluid. Objects placed on the surface of such sands will sink if their specific gravity is greater than the unit weight of the water-solid particle mixture and will float on the surface in the opposite case.

IMAI (1977) proposed determining the dynamic shear modulus from standard penetration test results. Having evaluated 950 tests he has found with good approximation the formula

$$G_d = 120N^{0.737} \quad (601)$$

(with the correlation coefficient $r = 0.888$).

Investigating the relationship between dynamic and static shear moduli, IMAI (1977) established (from 218 pairs of values) the formula

$$G_d = 510 G_s^{0.781} \quad (602)$$

SEED and SILVER (1972) produced the formula

$$G_d = 1000 K \cdot \sigma_v^m \quad (603)$$

in which σ_v is the applied vertical confining pressure, m is the exponent, K_m is a coefficient whose value varies with the shear strain. Figure 516 presents the relationship between shear modulus and shear strain, and damping factor and shear strain at low confining pressures. These relations have been obtained from simple shear tests; the simple shear apparatus was suitably modified for cyclic strain applications. The material tested was the Crystal Silica No. 20 sand ($d_{10} = 0.5$ mm; $U = 1.5$).

6.6.2 Compressibility

The density of granular soils subject to dynamic effects is controlled mainly by the acceleration ratio $\eta = b/g$. In addition thereto, the hydrostatic

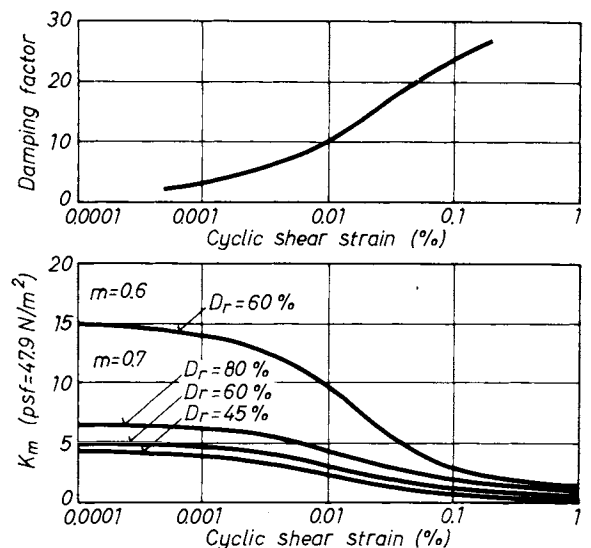


Fig. 516. Shear moduli and damping characteristics of silica sand at very low confining pressures (SEED and SILVER, 1972)

compression stresses acting simultaneously are also of interest, in that consolidation increases as this stress is reduced. Experiments performed at several amplitudes and frequencies have yielded the average dynamic compression curve shown in Fig. 517. The curves for other types of soil are identical in shape and yield to the equation

$$\frac{de}{d\eta} = -\alpha(e - e_{\min}), \quad (604)$$

whence

$$e = e_{\min} + C \exp(-\alpha\eta).$$

For $\eta = 0, e = e_0$ and thus $C = e_0 - e_{\min}$, so that

$$e = e_{\min} + e_0 - e_{\min} \exp(-\alpha\eta). \quad (605)$$

The magnitude of the coefficient α depends on the water content, as indicated in Fig. 518. The role of sand structure, reflected by a lower and an upper critical condition will again be observed. Dynamic compaction of sands is thus effective either in the dry or in the saturated condition.

Since the void ratio is reduced by vibration, it would be logical to conclude that the permeability coefficient is also reduced. This, however, is not the case, in that k increases together with $\eta = b/g$. This effect is more pronounced in fine sands (Fig. 519). This phenomenon can again be explained by the fact that the number of contact points at any instant is reduced by vibration, enabling a greater number of passages to develop.

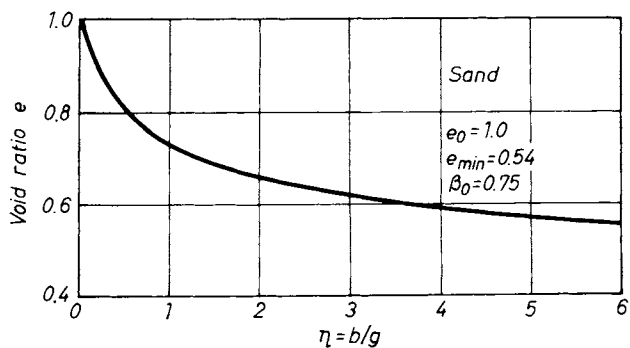


Fig. 517. Dynamically compressed sand — compressive curve

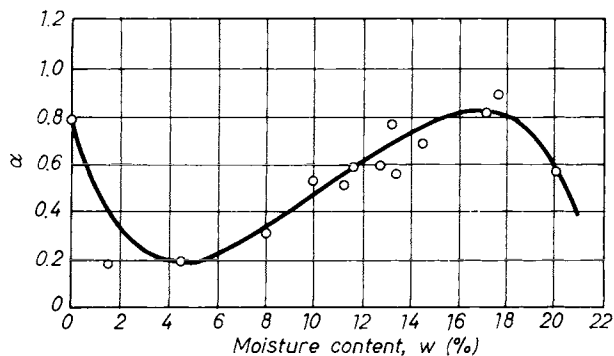


Fig. 518. Limiting values of α by dynamic compression

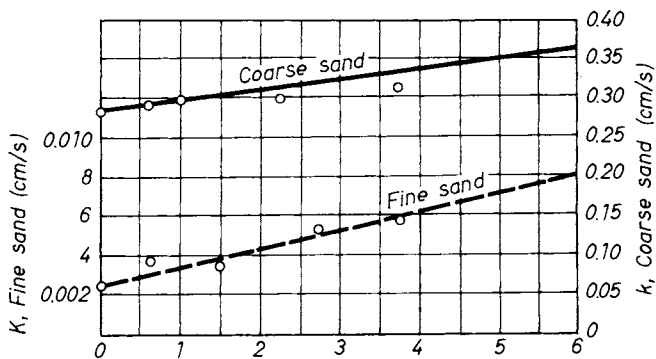


Fig. 519. Variation of permeability caused by vibration

Though the fully saturated state might be the most perilous one for cohesionless soils (see Section 6.6.5) even dry and partly wet sands are exposed to substantial deformations. During the San Fernando earthquake of 1971, for example, compaction of a 12 m deep sand fill resulted in settlements of 10 to 15 cm at a building constructed on spread footings near the surface. In the Skopje earthquake of 1963, severe damage to major structures was attributed to differential settle-

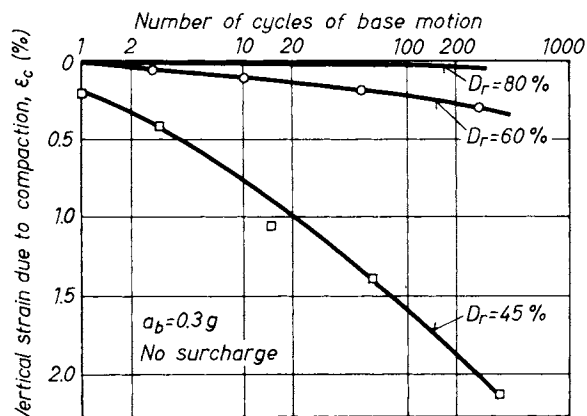


Fig. 520. Effect of relative density on settlement of a sand layer in the shaking table test (SEED and SILVER, 1972)

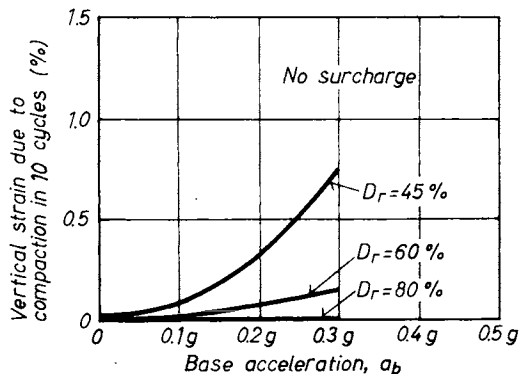


Fig. 521. Effect of relative density on settlement of a sand layer in shaking table test (SEED and SILVER, 1972) ($1 \text{ kp} = 10 \text{ N}$)

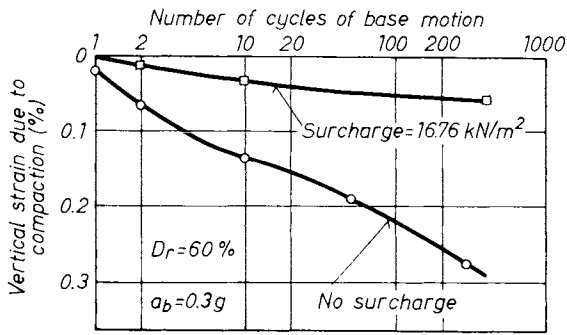


Fig. 522. Effect of surcharge pressure on settlement of sand layer in shaking table test (SEED and SILVER, 1972)

ments resulting from the compaction of pockets of loose sand underlying the foundations.

Recently it has been discovered and observed that a fundamental differentiation is needed between vertical displacements induced by the vertical and the horizontal components of ground shaking.

D'APPOLONIA (1968) describes tests in which samples of fine sand were placed in containers at very low density and then subjected to vertical

vibrations. It was found that even under no surcharge very little densification occurred until the acceleration reached about 1 g. WHITMAN and ORTIGOSA (1969) concluded that: (a) when the dynamic stresses are small, no noticeable densification occurs for $a < 1 g$; (b) when the dynamic stresses are small compared to the initial overburden stresses, there is no noticeable densification, (c) vertical acceleration during earthquakes can cause very little densification.

It may be concluded from these studies that the settlement of sand during earthquakes is produced mainly by the horizontal components of ground shaking. Impressive experiments have been conducted in this respect (SEED and SILVER, 1972) with the help of a shaking table. Accordingly, the vertical displacement is influenced by:

- relative density of the soil (D_r);
- base acceleration (a_b);
- number of cycles;
- surcharge.

The experimental results described in Section 6.6.1 are reproduced in Figs 520 to 522. By their use, diagrams can be constructed which give the

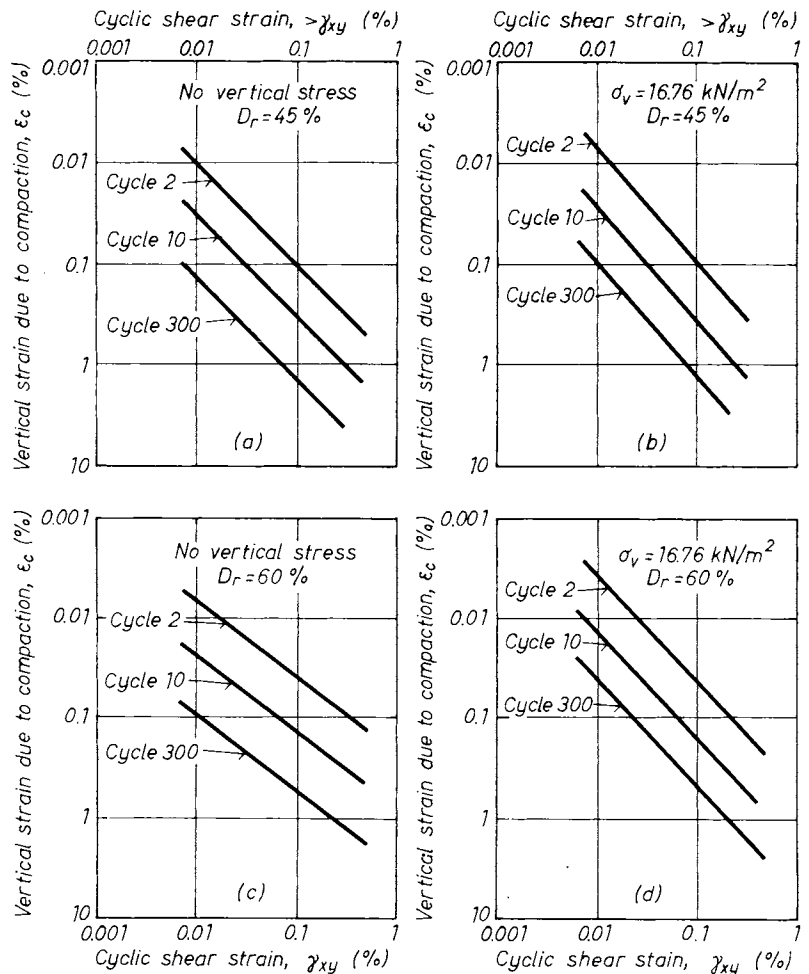


Fig. 523. Vertical settlement-shear strain relationship for silica sand: a, b — $D_r = 45\%$; c, d — $D_r = 60\%$ (SEED and SILVER, 1972)

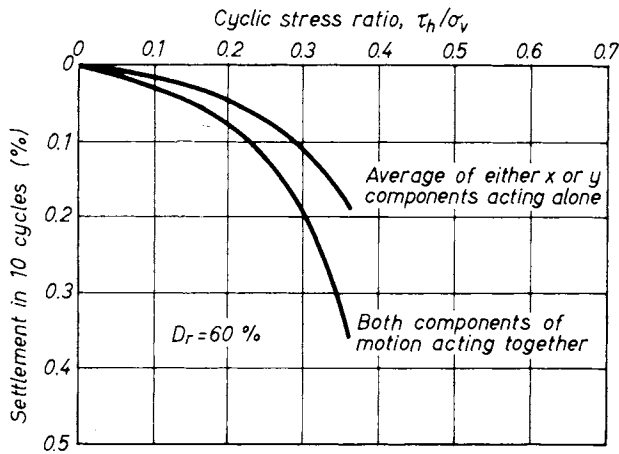


Fig. 524. Settlement of dry sand under unidirectional and multidirectional shaking (SEED *et al.*, 1978)

vertical strain, ϵ_c , as a function of D_r , σ_v , γ_{xy} , and n (Fig. 523).

Though the vertical component would normally not induce, in itself, a considerable displacement, experiments have confirmed that it can be a contributive factor in enhancing the effect of the horizontal component. PYKE *et al.* (1975) have shown that the settlement of dry sands is relatively greater under multidirectional shaking than under unidirectional shaking of similar magnitude. This is illustrated in Fig. 524, where the settlement in 10 cycles of loading is shown as a function of the cyclic stress ratio, τ_h/σ_v , in which τ_h is the horizontal shear stress, and σ_v is the applied vertical stress (SEED *et al.*, 1978). For a given value of the stress ratio it may be seen that the settlement caused by the combined motion is approximately equal to the sum of the settlement caused by the X and Y components separately. However, because the stress-settlement relationship is non-linear, the stress-ratio causing a given settlement for the combined motions is typically only about 20% less than the stress ratio that causes the same settlement under a single component.

6.6.3 Natural frequency and spring constant

As mentioned above, the behaviour of a vibrating system comprising a mass point and the soil is governed by the constants involved in the basic equation.

In the present paragraph these constants will be examined in greater detail.

From the very beginning, research has been concerned with the determination of the natural frequency, rather than with the spring constant K . From Eq. (564)

$$K = 4\pi^2 f_0^2 \frac{G}{g}, \tag{606}$$

so that the spring constant is found from measured values of the natural frequency. The ratio

$$k = \frac{K}{F} = \frac{4\pi^2}{g} f_0^2 p_{stat}$$

is called the dynamic bedding coefficient and is defined as the dynamic load causing a settlement of 1 cm, while p_{stat} is the static bearing pressure G/F .

The natural frequency is found from a model test performed on site, using a vibrator (Fig. 525) as the source of the disturbing force of controlled frequency and amplitude (SCHULTZE and MUHS, 1967). A vibration transducer is mounted on the vibrator, the rate of which is then accelerated to a preset value. The phase and amplitude of the vibrations performed by the vibrator are measured at constant frequency. The test is repeated at several frequencies and by plotting the amplitudes measured against the disturbing force, a resonance curve (Fig. 526) is obtained. The resonant frequency is found by drawing a tangent to this curve through the origin of the coordinate system, the point of tangency indicating the natural frequency.

The method is applicable to cases where the disturbing force increases as the square of frequency, this being the situation with the vibrator.

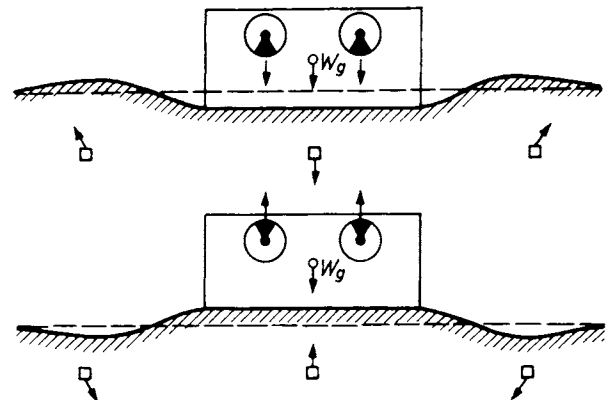


Fig. 525. Scheme of a swinging machine

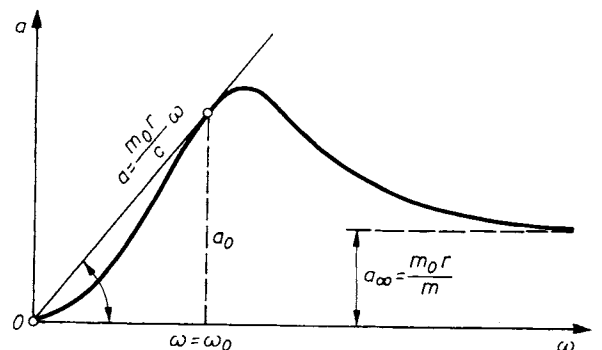


Fig. 526. Design of the resonance curve in the case of a force which acts at the square of the frequency

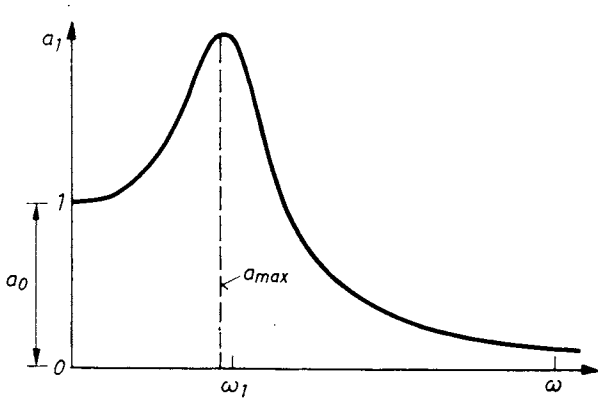


Fig. 527. Resonance curve originated by a constantly acting force

The disturbing force is the centrifugal force of the rotating masses, so that

$$P_0 = m_0 r \omega^2,$$

where m_0 is the rotating mass and r is the excentricity thereof. From Eq. (554)

$$a = \frac{m_0 r \omega^2}{\sqrt{(K - m\omega^2)^2 + c^2 \omega^2}}.$$

Reducing the fraction by ω^2 , the transition $\omega \rightarrow \infty$ will reveal the asymptote of the curve

$$a_\infty = \frac{m_0 r}{m}. \tag{607}$$

Since m_0 and r are known, the magnitude of the vibrating mass can be computed. Resonance occurs, if $\omega = \omega_0 (f = f_0)$. The equation of the tangent to this point is

$$a = \frac{m_0 r}{c} \omega,$$

showing that the tangent actually passes through the origin. The spring constant is found from ω_0 as

$$K = m\omega_0^2;$$

the slope of the foregoing tangent yields the damping coefficient

$$c = \frac{m_0 r}{a_0} \omega_0, \tag{608}$$

where a_0 is the amplitude measured at resonance.

The constants involved in the basic equation can thus be determined with the help of the resonance curve obtained by direct measurement.

Tests performed with a constant disturbing force, the magnitude of which is unaffected by frequency, commonly yield a curve resembling that shown in Fig. 527. The analytical expression of the curve is given by Eq. (574), revealing the case of forced, damped vibrations.

At $\omega = 0$ the amplitude is

$$a_0 = a_1 \frac{P}{K}$$

and thus, a_0 being known, the spring constant becomes

$$K = \frac{P_0}{a_0}.$$

The damping coefficient cannot be determined unless the values of a_{\max} and ω_1 are known. The term under the square root sign in Eq. (554) is differentiated with respect to ω :

$$[-2m(K - m\omega^2) + c^2] \omega = 0. \tag{609}$$

The two solutions are

- (a) $\omega = 0$;
- (b) $\omega^2 = (2Km - c^2)/2m^2$.

For $c^2 > 2Km$ the maximum occurs at $\omega = 0$ (c is greater than c_k), for $c^2 < 2Km$, at the frequency

$$\omega_1^2 = \frac{2Km - c^2}{2m^2}$$

and has the magnitude

$$a_{\max} = \frac{P_0}{K} \frac{2Km/c^2}{\sqrt{4Km/c^2 - 1}}. \tag{610}$$

The pair of values ω_1 and a_{\max} yields the damping coefficient

$$c = m \sqrt{2 \frac{K}{m} - 2\omega_1^2} = m \sqrt{2} \sqrt{(\omega_0^2 - \omega_1^2)}. \tag{611}$$

Where the mass is unknown, the following approximate formulae can be used

$$c \approx \frac{P_0}{a_{\max} \omega_1} \text{ and } m \approx \frac{K}{\omega_1^2}. \tag{612}$$

The accuracy of approximation will be the better, the smaller the ratio c/c_k .

In analysing the model experiments described above, a difficulty has been encountered on account of the fact that the subsoil is involved in the dynamic process not only as an elastic support, and as a damping medium, but also as a mass affected. The magnitude of the resonant mass depends on the data concerning the vibrator. Equation (562) must therefore be written in the following form:

$$f_0 = \frac{1}{2\pi} \sqrt{\frac{K}{M}} = \frac{1}{2\pi} \sqrt{\frac{kFg}{a}} = \frac{1}{2\pi} \sqrt{\frac{kFg}{G_g + G_t}}, \tag{613a}$$

where the spring constant is written in the form $K = kF$, F is the area in plan, G_g is the weight of the vibrator and G_t that of the resonant soil

mass. For determining the natural frequency, the "reduced natural frequency" was suggested by TCHEBOTARIOFF and WARD (1948). This is found by rearranging Eq. (562) as follows:

$$f_0 = \frac{1}{2\pi} \sqrt{\frac{F}{G_g}} \sqrt{\frac{k \cdot g}{1 + \frac{G_g}{G_t}}} = \frac{1}{\sqrt{P}} f_{or}. \quad (613b)$$

The experimental data published have been compiled by these authors and the natural frequency entered in a log-log plot against the contact area. Depending on whether the subsoil was cohesive clay or granular sand, the points fitted two parallel straight lines as illustrated in Fig. 528. This can be used for finding the reduced natural frequency and, in turn, the natural frequency itself. According to NOVAK (1957) the weight of the resonant soil mass is found from the expression

$$G_t = fF^{4/3},$$

where f is an empirical coefficient.

For estimating the magnitude of the spring constant, BARKAN (1962) has put forward the formula

$$k_2 = k_1 \sqrt{\frac{F_1}{F_2}}, \quad (614)$$

where k_1 and k_2 are the bedding coefficients pertaining to the areas F_1 and F_2 respectively.

The corresponding pair of values being known, the bedding coefficient can thus be found for any area.

It should be noted that the foregoing two empirical relationships are in complete agreement, since the reduced natural frequency can also be written in the form

$$f_{cr} = \sqrt{k} \sqrt{\frac{g}{1 + \frac{G_g}{G_t}}} = C \sqrt{k}$$

thus

$$\frac{f_{or1}^2}{f_{or2}^2} = \frac{k_1}{k_2}.$$

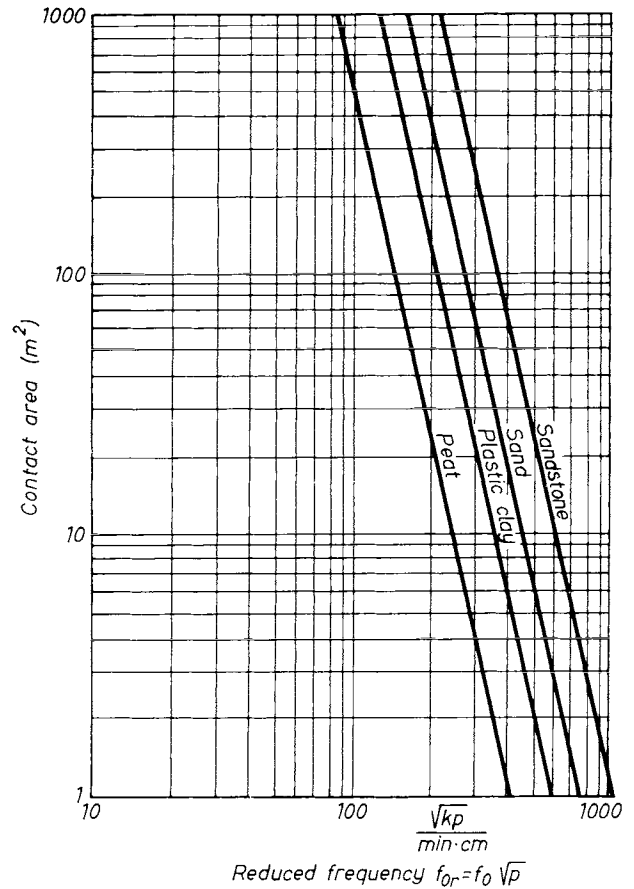


Fig. 528. Relationship between contact area and reduced natural frequency

On the other hand, according to BARKAN

$$\frac{k_1}{k_2} = \sqrt{\frac{F_2}{F_1}}$$

hence

$$\frac{f_{or1}^A}{f_{or2}^A} = \frac{F_2}{F_1}$$

and

$$F_1 f_{or1}^A = F_2 f_{or2}^A = \text{const.}$$

Table 44. Dynamic bedding coefficient of subgrade reaction for a 10 m² contact area, after BARKAN (1962)

Class	Soil type	Allowable bearing capacity under static load σ_{zu} (kN/m²)	Coefficient of subgrade reaction k (MN/m³)
I	Moderate bearing capacity (plastic cohesive soils) mediately loose silty fine sand; soils from class II and III with interlaced mud or peat	15	30
II	Mediately hard cohesive soils (plasticity limit) mediately dense sand	15...35	30...50
III	Hard cohesive soils: dense sand or gravel	35...50	50...100
IV	Rock	> 50	> 100

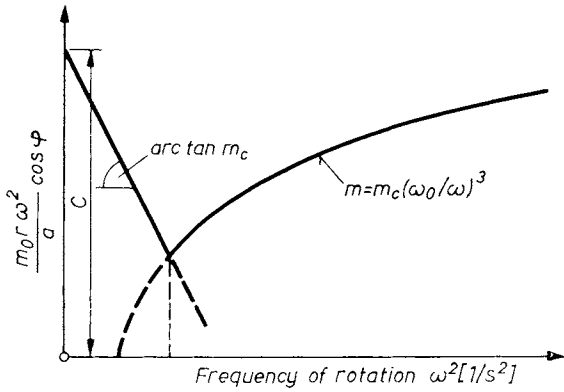


Fig. 529. Dependence of the function $m_0 r \omega^2 \cos \varphi / a$ on ω^2 (after HEUKELOM, 1957)

so that

$$F = \frac{\text{const.}}{f_{or}^4}$$

thus

$$\log F = \log (\text{const}) - 4 \log f_{or},$$

the equation describing the parallel straight lines of TCHEBOTARIOFF.

Numerical values of the dynamic bedding coefficient[†] are compiled for information in Table 44, in which the values of k are given after BARKAN for a block of 10 m² plan area. For other areas these values can be transformed using Eq. (614).

Another method for finding the dynamic constants, suggested by HEUKELOM (1957), consists of plotting the quantities

$$\left. \begin{aligned} \frac{m_0 r \omega^2}{a} \cos \varphi &= K - m \omega^2 \\ \frac{m_0 r \omega}{a} \sin \varphi &= c \end{aligned} \right\} \quad (615)$$

against ω^2 . These result directly from Eqs (554). At low frequencies a straight line is obtained, the spring constant K is read at $\omega^2 = 0$ and the slope is found as m_c , the resonant soil mass (Fig. 529). According to HEUKELOM, if $\omega \leq \omega_0$, then $m_b = \text{const.} = m_c$ and if $\omega > \omega_0$, then $m_b = m_c (\omega_0 / \omega)^3$, so that a radically different line is obtained for higher frequencies. The two lines intersect at the frequency ω_0 .

The vibrator is designed to transmit periodic pulses also as horizontal force to the soil. With this arrangement the dynamic shear modulus can be determined. The natural frequency is found from Eq. (585), neglecting the term Qh

$$f_x = \frac{\omega_x}{2\pi} \sqrt{\frac{C_x J}{J_0}}$$

whence

$$C_x = 4\pi^2 \frac{J_0}{J} f_0^2. \quad (616)$$

6.6.4 Propagation of waves in the soil

The intensity of any pulse transmitted to the soil will diminish in the course of spreading with the distance from the point of disturbance. For practical considerations information is needed as to whether the vibrations at a particular point are detrimental or not to the human organism, to the source of vibration itself or to any other structure.

The type of vibration induced by a transient force, and further the velocity of propagation, depend on the elastic properties of the soil and on the configuration of the surface. A particle will start vibrating during the passage of the wave front. During a cycle of period T_0 , the wave front travels the distance $l = T_0 v$, where l is the wave length.

The waves may be classified into several types. In seismology distinction is made between mass waves propagated within the interior of the mass and surface waves. The mass waves may be compression or longitudinal waves also referred to as P -waves or undae primae, and transverse or shear waves, also known as S -waves or undae secundae. The concepts of wavelength, frequency and period are assumed to be familiar to the reader. The two different wave types are illustrated in Fig. 530. Assuming the medium to be uniform and isotropic, the propagation velocity of the compression wave is

$$v_1 = \sqrt{\frac{Eg(1 - \mu)}{(1 - \mu - 2\mu^2)}}, \quad (617)$$

where E = the Young's modulus of elasticity,
 μ = Poisson's number,
 γ = the bulk density,
 g = gravitational acceleration.

Shear waves are substantially transverse waves, where the particles are displaced in a direction

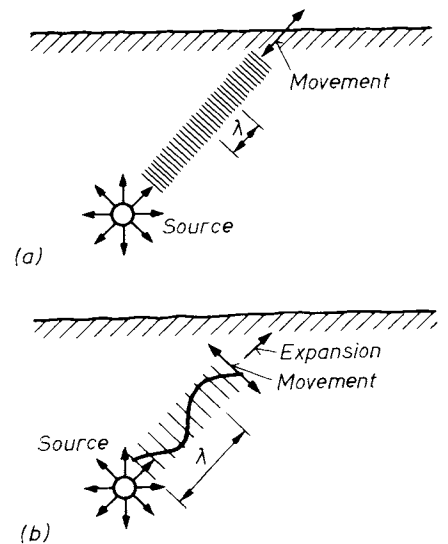


Fig. 530. Wave types in the underground: a — P -waves (longitudinal waves); b — S -waves (transversal waves)

perpendicular to that of wave propagation, the velocity of the latter being

$$v_z = \sqrt{\frac{Eg}{2\gamma(1 + \mu)}} \tag{618}$$

The value of v_2 is always lower than v_1 , the variation thereof with the Poisson's number of the medium being illustrated in Fig. 531. At a Poisson's number $\mu = 0.5$, the velocity $v_1 \rightarrow \infty$, while v_2 has the finite value $\sqrt{Eg/3\gamma}$.

Velocities actually measured in different types of soil are compiled in Table 45.

Table 45. Propagation of transversal wave velocities during dynamic soil investigation

Soil type	v (m/s)
Sand, according to conditions	100 ... 250
Sand and gravel	180 ... 550
Silt	150 ... 200
Clay, according to water content	120 ... 700
Weathered limestone	250
Sound sandstone	1100

Surface waves having their origin in the semi-infinite uniform or stratified medium and propagating along the surface, or along the interface

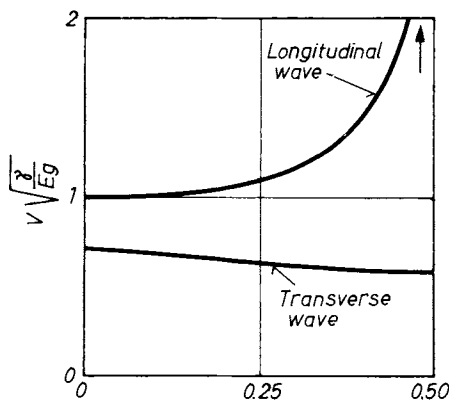


Fig. 531. Relationship between Poisson's number and wave velocity

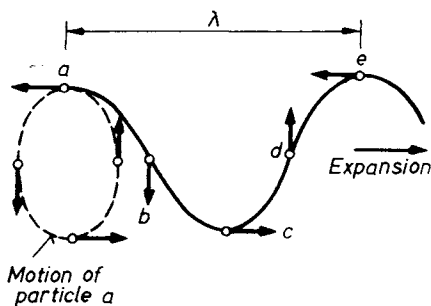


Fig. 532. Development of the Rayleigh-type wave

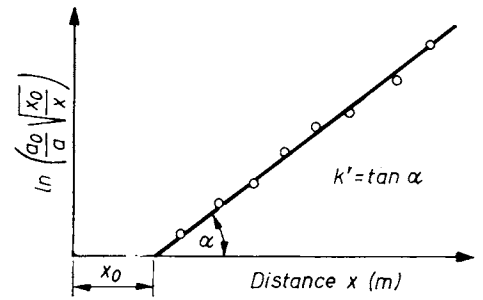


Fig. 533. Determination of the absorption coefficient

between two layers, are termed Rayleigh waves and have the propagation velocity

$$v_r = \beta v_2, \tag{619}$$

where

$$0.919 \leq \beta \leq 0.955 \text{ for } 0.25 \leq \mu < 0.5.$$

Rayleigh waves resemble water waves but the direction of movement is different. The individual particles describe elliptical paths as shown in Fig. 532. Love waves are also surface waves resembling the S-waves, with the surface particles moving perpendicular to the direction of wave propagation. The influence of these waves is limited to a rather thin layer below the surface.

The amplitude of these waves diminishes exponentially with the distance x from the point of disturbance according to the formula

$$a = a_0 \sqrt{\frac{x_0}{x}} \exp[-k'(x - x_0)/\lambda], \tag{620}$$

where a and a_0 are the amplitude at the distances x and x_0 , respectively, k' is the wave absorption coefficient and $\lambda = \frac{v}{n}$ is the wave length.

For disturbances other than sinusoidal, the following expression has been suggested

$$a = a_0 \frac{x_0}{x} \exp[-k'(x - x_0) \lambda]. \tag{621}$$

According to FÖRTSCH (1954, 1956) the energy is absorbed owing to Coulomb friction within the soil structure, whereas in saturated soils this is due to the viscosity of pore water.

In order to determine the magnitude of the absorption coefficient, the amplitudes are measured at different distances from the disturbance and the quantities $\ln(a/a_0 \sqrt{x_0/x})$ are then plotted against x (Fig. 533). In uniform soils, since

$$\ln(a_0/a \sqrt{x_0/x}) = k'(x - x_0),$$

a straight line is obtained, the slope thereof yielding the magnitude of k' . This value is unrelated to frequency and may, therefore, be regarded a physical property of the soil and a measure of the difference between the behaviour

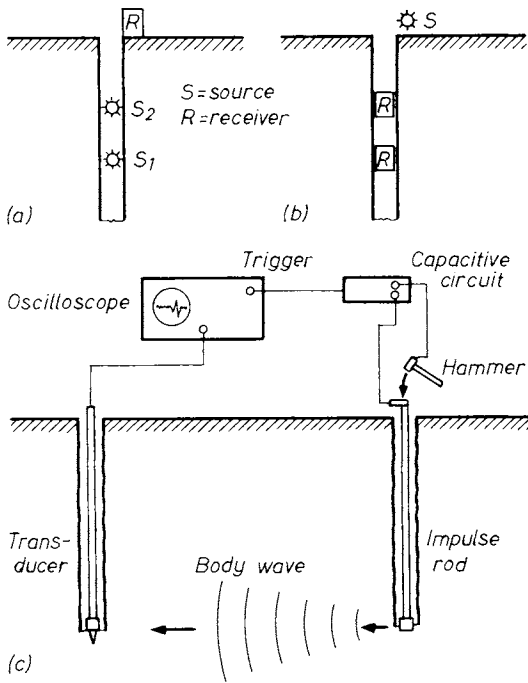


Fig. 534. Field test procedures to evaluate v_s : a — up-hole; b — down-hole; c — cross-hole method (YOSHIMI, 1977)

of the soil and of an elastic medium. The expression $a = a_0 \sqrt{x_0/x}$ applies to the elastic half-space rather than Eq. (620).

Numerical values of k' are given in Table 46 after FÖRTSCH (1940). Once k' is known, the amplitude at any distance from the disturbance can be computed, provided that the amplitude and the frequency of the disturbance are known. From the amplitude and frequency, the acceleration is found as

$$b = 4 \pi^2 f^2 a. \quad (622)$$

Seismic measurements can establish values of the shear wave velocity, v_s , within a rock or soil

Table 46. Coefficient of absorption for different soils, after FÖRTSCH (1940)

Soil type	k'
Loess, silty loess	0.215
Diluvian clay	0.146
Lias clay	0.350
Silty sand	0.425
Silty gravel	0.105
Medium sand	0.620
Fine sand	0.5 . . . 0.6

mass. Then the low amplitude shear modulus can be calculated from

$$G_0 = \rho v_s^2, \quad (623)$$

in which ρ is the mass density.

For detailed information on the wave velocity and on the variation of v_s with depth, surface refraction, steady-state vibration and borehole techniques can be used. Up-hole and down-hole tests can be performed with one borehole, while cross-hole tests require two or more boreholes.

In the up-hole method, the excitation is provided at various depths within the borehole and the sensor is placed at the surface (Fig. 534a), while for the down-hole method the excitation is applied at the surface and one or more sensors are placed at different depths within the hole (Fig. 534b).

In the cross-hole method (STOKOE and WOODS, 1972; WOODS, 1978; HOAR and STOKOE, 1981, etc.) at least two boreholes are needed, one for the impulse and the other for the sensors. As shown in Fig. 534c the impulse rod is struck at the top end and an impulse travels down the rod and is transmitted to the soil at the bottom. This shear impulse creates shear waves which travel horizontally through the soil to the vertical motion sensor located in the second hole, and the time required for the shear wave to traverse this known distance is recorded.

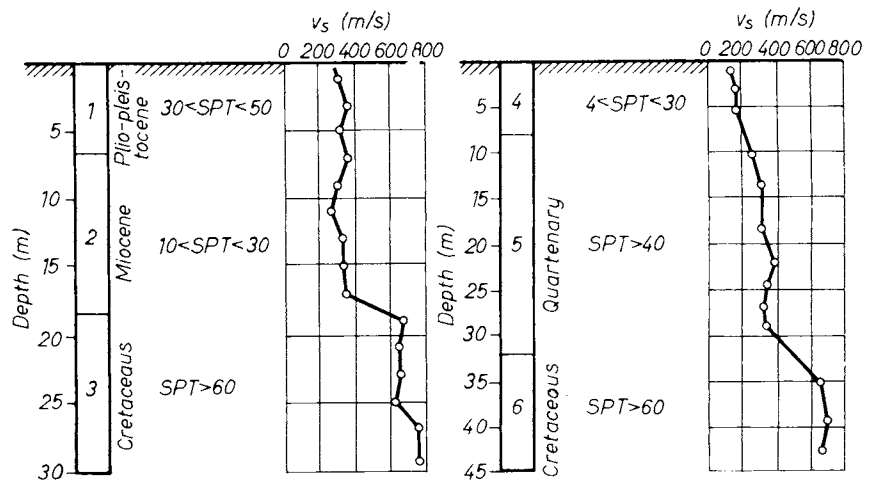


Fig. 535. Typical shear wave velocities from cross-hole test (RODRIGUES, 1981)

Travel velocity can be measured in the following manner. (HOAR and STOKOE, 1981). Typical seismic-wave travel time records are analyzed by identifying initial wave arrivals. Then either the direct travel time from the source to the receiver, or the interval travel time between two receivers for the same impulse are determined. Interval travel times may also be determined by using points on the waveform other than the initial wave arrival, such as the first through, first cross-over point, or first peak after the initial arrival. Using points on the wave-form other than the initial arrival tends to produce longer interval travel times and therefore slower velocities, due to wave spreading. Interval travel times generally produce more consistent and reliable velocity profiles.

Figure 535 is inserted here to provide two examples on the variation of v_s according to depth (stratification). These profiles have been determined by RODRIGUES (1981) by using the cross-hole method.

In the case of the P -wave velocity (v_p) a clear contrast is often found between above and below groundwater level. On the other hand, in the case of S -wave velocity (v_s) there is a good correlation with the mechanical properties of the soil layers. These facts support the general explanation that — though v_p depends on the bulk modulus of the soil skeleton and the pore water — v_s depends on the structural elasticity of the soil skeleton (IMAI, 1977). This is a good interpretation of Japanese statistics which proves that the distribution of v_s is more regular than that of v_p , if the investigated soils are grouped according to their geological age and origin. This is also the reason for v_s having a closer correlation with SPT results and q_u -s, than v_p has.

IMAI (1977) proposed two formulas as being valid for the entirety of Japanese soils investigated:

$$v_s = 91N^{0.337} \quad (r = 0.889) \quad (624)$$

and

$$v_s = 134q_u^{0.443}, \quad (625)$$

where v_s is in m/s, and q_u has to be substituted in kp/cm^2 ($= 100 \text{ kN/m}^2$). Closer correlations can be found, however, if the classification of data follows the geological subdivision.

Knowing v_s and v_p also Poisson's ratio can be established from the formula:

$$\nu = \frac{1 - 2 \left(\frac{v_s}{v_p} \right)^2}{2 - 2 \left(\frac{v_s}{v_p} \right)^2}. \quad (626)$$

6.6.5 Liquefaction of soils

A qualitative understanding of liquefaction and its effects was first presented by CASAGRANDE in 1936. Since then it has been recognized that when alternating loads are applied to saturated cohesionless soils from which drainage is restricted, the pore-water pressure may even rise to a value

equal to the total confining pressure. In the latter case, the effective confining pressure on the soil becomes zero, and the soil loses its ability to resist shear deformation. The soil is then said to have liquefied.

6.6.5.1 Mechanism and definition of liquefaction

In a narrow sense of the word, liquefaction means a complete loss of shear strength which can occur when a loose cohesionless soil is subjected to shear stress, either monotonic or cyclic. In a broader sense, this term has also been used to denote a partial loss of shear strength due to build-up of pore-water pressure, e.g. "partial liquefaction", by TAYLOR (1948), "initial liquefaction with limited shear strain potential", by SEED *et al.* (1975), or "cyclic liquefaction" by CASAGRANDE (1976). The "incipient failure state" or "limit equilibrium" of a saturated sand under cyclic loading defined by WANG (1981) is the state at which the shear stress is just balanced by the shear resistance.

The sudden collapse of a soil structure is preceded by a gradual buildup of pore-water pressure with negligible shear strain (Fig. 536). The tendency of the soil to contract due to cyclic shear is counteracted by a rebound due to the reduction in the effective stress to satisfy the conditions of constant volume and constant total stress (YAGI, 1972; MARTIN *et al.*, 1975).

The results shown in Fig. 536 can be summarized as in Fig. 537. The solid curve in insert (a) shows the shear stress amplitude τ_d plotted against the number of cycles to initial liquefaction N_i , which denotes "a condition where . . . the residual pore-water pressure on completion of any full stress cycle becomes equal to the applied confining pressure" (SEED *et al.*, 1975). The dashed line in Fig. 537a can be obtained by plotting the number of cycles to failure, N_f , corresponding to a failure

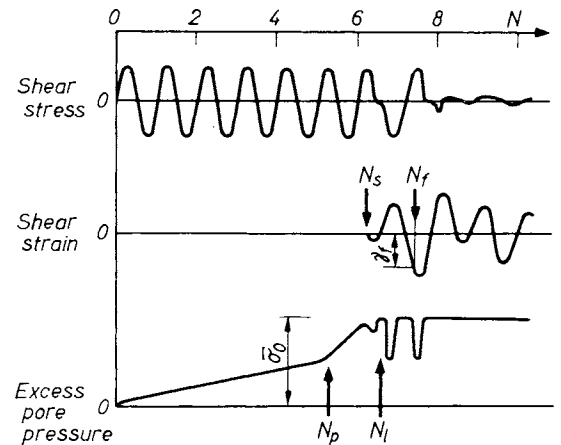


Fig. 536. An example of undrained cyclic simple shear test on loose saturated sand (YOSHIMI, 1977)

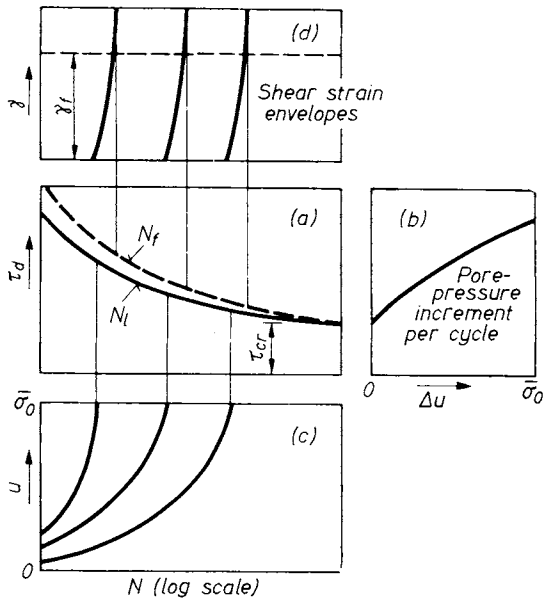


Fig. 537. Typical result of undrained cyclic shear test on loose saturated sand (YOSHIMI, 1977)

strain, γ_f . The difference between N_i and N_f is small because the strain increases rapidly after the pore pressure becomes equal to the applied confining pressure, $\bar{\sigma}_0$. It is evident from Fig. 537 that there is a threshold shear stress amplitude, τ_{cr} , below which the pore pressure does not build up at all (YOSHIMI, 1977).

Pore-water pressure increases in dense sand as well, because this is contractive during shear at small strains, but the condition of zero effective stress occurs only momentarily when the shear stress is zero, and the soil retains considerable shear modulus even after the initial liquefaction. In fact, a dense soil cannot be strained beyond a certain limit regardless of the level of shear stress amplitude, provided it stays below the static shear strength. This phenomenon has been called "cyclic mobility" by CASTRO (1975), "initial liquefaction with limited shear strain potential" by DE ALBA *et al.* (1976), or "cyclic liquefaction" by CASAGRANDE (1976).

The coarser granular soils exhibit great stability because their high permeability would either preclude a full development of pore-water pressure, or reduce the duration of the fully liquefied condition (WONG *et al.*, 1975; SEED and BOOKER, 1976).

Laboratory tests by numerous investigators (e.g., FLORIN and IVANOV, 1961; LEE and SEED, 1967; PEACOCK and SEED, 1968) have shown that for a given initial density, the stress required to initiate liquefaction increases with the initial confining pressure. The effect was also shown in the field during the Niigata earthquake where the soil under a 2.7 m deep fill remained stable, but similar soils surrounding the fill liquefied extensively (SEED and IDRIS, 1967). This phenomenon can be interpreted in the following way (SEED and IDRIS, 1971).

If the soil column above a soil element at depth h behaved as a rigid body and the maximum ground surface acceleration were a_{max} (Fig. 538), the maximum shear stress on the soil element would be:

$$(\tau_{max})_r = \frac{\gamma \cdot h}{g} a_{max} \quad (627)$$

Because the soil column behaves as a deformable body, the actual shear stress at depth h , $(\tau_{max})_d$ will be less than $(\tau_{max})_r$, and might be expressed by

$$(\tau_{max})_d = r_d (\tau_{max})_r \quad (628)$$

Computations of the value r_d for a wide variety of earthquake motions and soil conditions having sand in the upper 15 m have shown that r_d falls within the range of values shown in Fig. 539. Referring to these facts and other observations FERRITTO and FORREST (1977) concluded that liquefaction is practically excluded from depths below 15 m.

The vulnerability to liquefaction during an earthquake depends on the magnitude of the stresses or strains induced in it. SEED and IDRIS (1971) mention as an example the earthquakes experienced at Niigata in Japan during the last 370 years. Based on contemporary records the authors discovered that severe damages (owing to

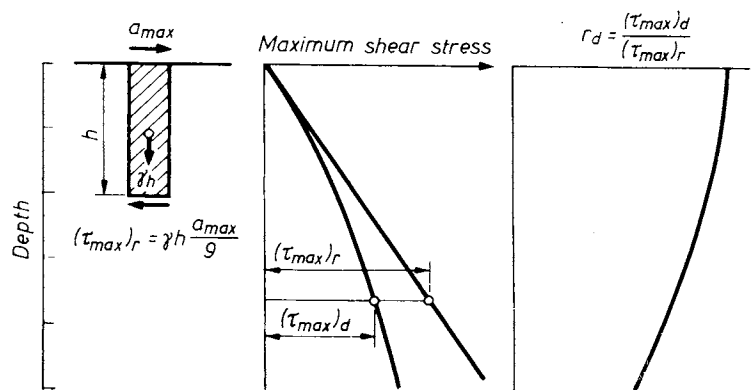


Fig. 538. Determination of maximum shear stress (SEED and IDRIS, 1971)

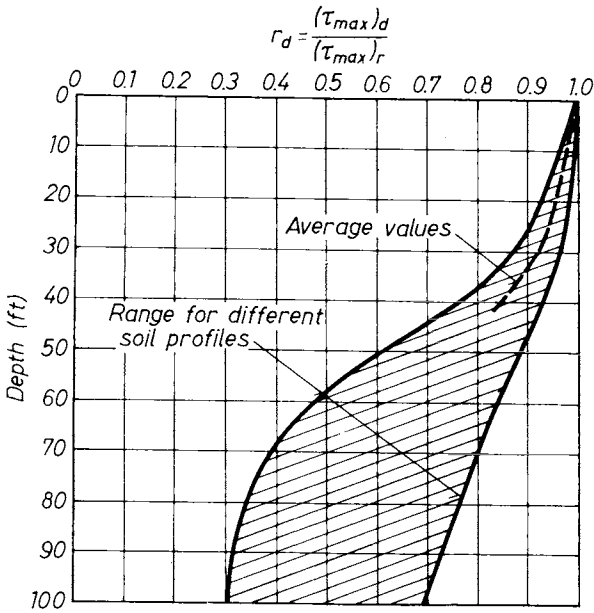


Fig. 539. Range of values of r_d for different soil profiles (SEED and IDRIS, 1971) (1 ft = 0.3048 m)

liquefaction) were only caused in three instances when the ground acceleration exceeded 0.13g. A contributive factor is naturally, also the duration of shaking (see Section 6.6.5.2).

For a given magnitude of earthquake, M , there appears to be a limiting epicentral distance, R , beyond which liquefaction is unlikely to occur. The limiting distance, R in km, for $M \geq 6$ may be expressed as (KURIBAYASHI and TATSUOKA, 1975):

$$\log R = 0.77M - 3.6. \quad (629)$$

6.6.5.2 Laboratory testing of liquefaction

Appropriate laboratory testing methods include:

- the shaking table test;
- triaxial compression;
- the simple shear test.

Because for undrained testing conditions the sample must be enclosed in a constant volume system, the simple shear device developed by

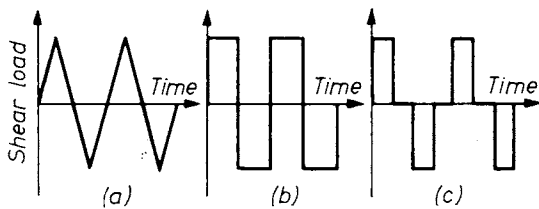


Fig. 540. Alternative wave forms of shear loading (FINN et al., 1971)

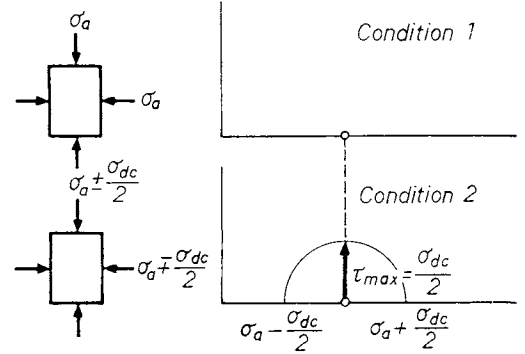


Fig. 541. Cyclic loading triaxial test (SEED and PEACOCK, 1971)

ROSCOE (1953) or a torsional shear device with lateral confinement appear to be the only equipment available to produce these test conditions (SEED and PEACOCK, 1971). The device developed by Roscoe and fellow investigators is a purpose-oriented suitable instrument ("UBC machine") which has the additional capacity of applying alternating shear loads ($\Delta\tau_{xy}$) so soil samples. Tests are normally carried out under frequencies of 1-2 Hz. The wave forms of shear loading (deviator stresses) are shown in Fig. 540. Variant (c) is justified by the fact that a more meaningful insight into the liquefaction process might be obtained if the loading cycle contains a short period of zero load which might allow full equalization of the pore pressure and allow the shear load being measured in the absence of inertia effects (SEED and PEACOCK, 1971).

Most researchers prefer, however, the triaxial testing method, due to its simplicity. In this type of test, a sample is initially consolidated under an ambient pressure σ_a , producing a stress condition as shown by Condition 1 in Fig. 541. The sample is then subjected to an increase in axial stress of an $\sigma_{dc}/2$ and a simultaneous reduction in lateral stress of equal amount. The normal stress on a 45° plane remains unchanged, but a shear stress of $\sigma_{dc}/2$ develops on the plane. The stress changes are then reversed so that the direction of application of shear stress on the 45° plane is reversed; thus, on this plane the normal stress remains constant. The conditions on the 45° plane are thus similar to those on the horizontal plane for the field loading condition (SEED and LEE, 1966). In dealing with saturated samples, the same effective stress conditions can be produced more conveniently by keeping the lateral stress constant and cycling the axial stress by $\pm\sigma_{dc}$, but the general principles are more correctly illustrated by the changes shown in Fig. 541 (SEED and PEACOCK, 1971).

PEACOCK and SEED (1968) summarized the disadvantageous aspects of the triaxial testing method in four points.

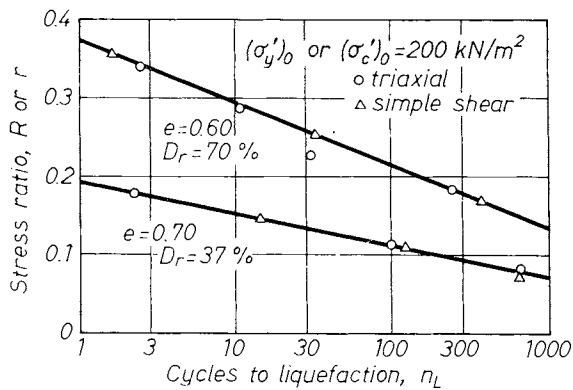


Fig. 542. Comparison of liquefaction resistance of a sand in simple shear and triaxial compression (FINN *et al.*, 1971)

1. In the field there is a reorientation of the principal stress directions: the major one is initially vertical and rotates through some angle $\theta = 0 - 40^\circ$, to the right and left of its initial position. (In the triaxial test this angle is 90° .)

2. In the field the soil element is initially consolidated under K_0 conditions ($\sigma_x = K_0\sigma_z$); the triaxial test requires the adaptation of a value of K_0 equal to unity.

3. In the field, deformations are presumed to occur under plane-strain conditions, whereas they occur in all three principal stress directions in the triaxial compression test.

4. Under the idealized field loading condition (or in the simple shear test) the intermediate principal stress has a value corresponding to plane-strain conditions; in the triaxial compression test, however, the intermediate principal stress has a value equal to the major principal stress during one half of the loading cycle and equal to the minor principal stress during the other half of the cycle.

As the shear test with a saturated sand is far more complicated than a triaxial test, some researcher attempted to compare the results of the two testing methods, or to produce a formula by which it would be possible to recalculate one from the other. FINN *et al.* (1971) proposed taking the "initial effective stress ratio" for the triaxial test as

$$R = \frac{\Delta\sigma_d}{2(\sigma'_c)_0}, \quad (630)$$

and for the simple shear test as

$$r = \frac{2\Delta\tau_{xy}}{(\sigma'_y + K_0\sigma'_y)_0}. \quad (631)$$

In these: $(\sigma'_y)_0$ is the initial vertical effective stress, $(\sigma'_c)_0$ is the initial hydrostatic effective stress. If these ratios are used as parameters, the results of the two testing methods are well comparable as Fig. 542 demonstrates.

SEED and PEACOCK (1971) suggested that the stress ratio τ_h/σ'_{vc} causing initial liquefaction under cyclic simple shear condition might be related to the stress ratio $\sigma_d/2\sigma'_a$ causing initial liquefaction in a cyclic triaxial test by a correction factor, c_r , in which

$$\frac{\tau_h}{\sigma'_{vc}} = c_r \frac{\sigma_d}{2\sigma'_a}. \quad (632)$$

It has been mentioned previously that there is a difference in respect of liquefaction between isotropic and anisotropic consolidation. The influence of K_0 can well be observed in Fig. 543 in which is plotted the relationship between the cyclic shear stress and the number of stress cycles required to cause liquefaction for samples having the same void ratio and the same vertical stress, but different initial value of K_0 (SEED and PEACOCK, 1971). The values of K_0 were obtained by over-consolidating the samples, and the values of K_0 shown were determined from the test data relating K_0 to OCR obtained by HENDRON (1963). It is apparent that the stress required to cause failure increases with increasing values of K_0 .

This phenomenon has been described by ISHIIHARA *et al.* (1977) in the following manner. Initially a soil element is subjected to a vertical effective stress σ'_v and a horizontal stress $K_0\sigma'_v$. If the deposit becomes liquified, the soil element will be subjected to a hydrostatic pressure equal to σ'_v , both vertically and horizontally. Thus, there is an increase or decrease in total stress by an amount of $(1 - K_0)\sigma'_v$ in the horizontal direction. Since the change in total stress occurs under an undrained condition, an accompanying change in pore pressure by an amount of

$$\Delta u_s = \frac{2}{3} (1 - K_0) B\sigma'_b \quad (633)$$

must occur where B is the pore-pressure coefficient. It is possible to define the stress ratio causing liquefaction in isotropically consolidated

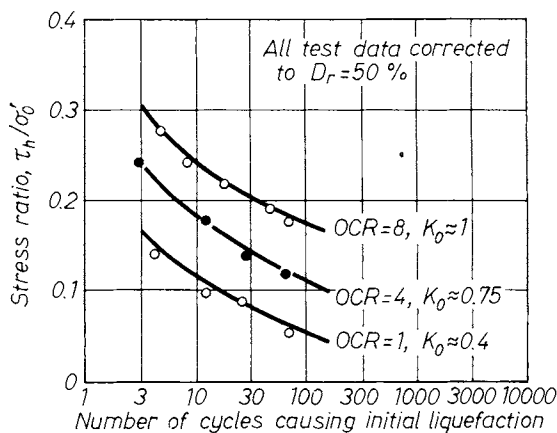


Fig. 543. Influence of initial principal stress ratio on stresses causing liquefaction in simple shear tests (SEED and PEACOCK, 1971)

specimens with a certain number of cycles by the term $(\tau_h/\sigma'_v)_I$. In this case the total pressure σ'_v will be transformed into pore pressure. However, when $K_0 \neq 1$, and the sample is subjected to the same number of cycles the portion of the initial stress that is transformed into pore pressure should be equal to

$$\sigma'_v - \Delta u_s.$$

This concept is based on the assumption that the pore pressure, Δu_s , is not induced by the cyclic stress but is produced through a gradual shift in the geostatic stress system from an initial K_0 -state to a liquified state under isotropic compression. Therefore, if the stress ratio inducing liquefaction in an anisotropically consolidated sample is denoted as $(\tau_h/\sigma'_v)_A$, the following relationship results:

$$\left(\frac{\tau_h}{\sigma'_v - 2(1 - K_0) B\sigma'_v/3} \right)_A = \left(\frac{\tau_h}{\sigma'_v} \right)_I. \quad (634)$$

Rearranging Eq. (634) gives:

$$\left(\frac{\tau_h}{\sigma'_v} \right)_A = \frac{1 + 2K_0}{3} \left(\frac{\tau_h}{\sigma'_v} \right)_I, \quad (635)$$

which compares cyclic strength under isotropic and anisotropic states.

If we really want to simulate reality, it should be based on the assumption of selecting $\Delta\tau$ and N_c (the number of cycles). SEED and IDRIS (1971) proposed taking $\Delta\tau$ as the 65% of the value calculated from Eq. (627). As for N_c , their suggestion was to take it in function of the magnitude:

$$\begin{aligned} \text{for } M = 7 \quad N_c &= 10, \\ M = 7.5 \quad N_c &= 20, \\ M = 8 \quad N_c &= 30. \end{aligned}$$

As several studies have shown that for any test condition the cyclic shear stress causing liquefaction is approximately directly proportional to the initial effective normal stress (σ'_0 or σ'_v), the test results can usually be expressed in terms of the ratio τ_h/σ'_0 , which will lead to liquefaction or any given soil and test condition (SEED and PEACOCK, 1971) (See Fig. 524).

There is a still wider difference between unidirectional and multidirectional shaking in the case of a saturated sand than in the case of a dry sand; this is illustrated in Fig. 544 (SEED *et al.*, 1978).

6.6.5.3 Local measurements and observations

For the determination of the possibility of perilous liquefaction probes are at present preferred in practice. The aim of these investigations is to produce reliable relationships between probing parameters and the probability of liquefaction.

The most part of the observations recorded are related to actual earthquakes. By comparing the standard penetration blow counts (N) before and

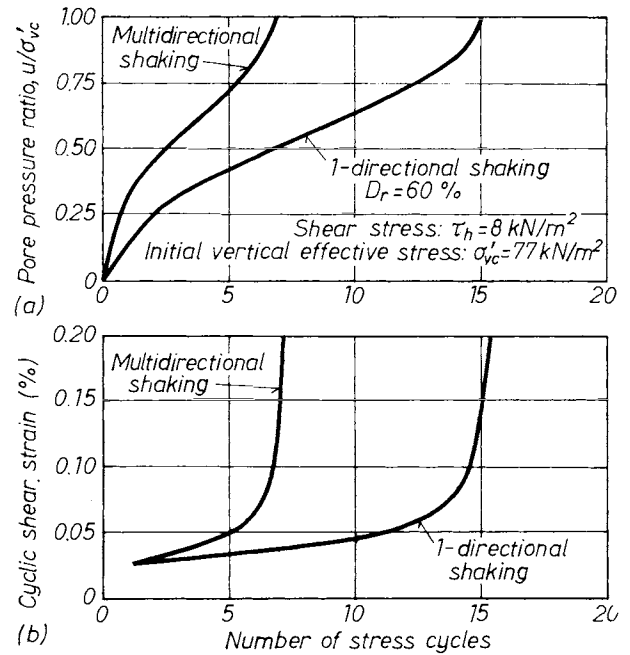


Fig. 544. a — Typical rates of pore pressure; b — cyclic strain development for sand (SEED *et al.*, 1978)

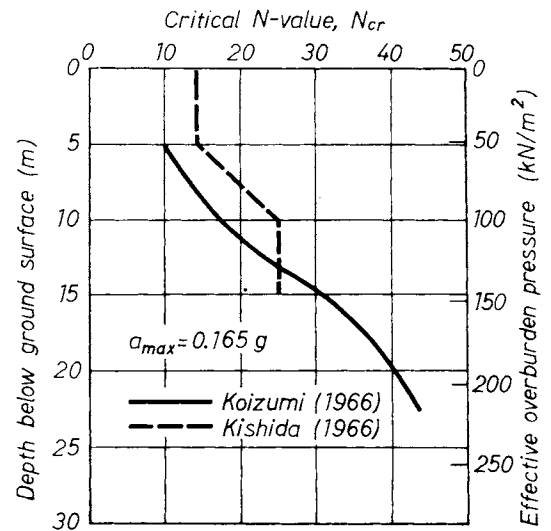


Fig. 545. Empirical criteria of liquefaction for the Niigata earthquake of 1964 (KOIZUMI, 1966; KISHIDA, 1966)

after the Niigata earthquake of 1964 ($M = 7.5$), KORZUMI (1966) proposed a “critical blow count, N_{cr} ”, as shown in the solid line in Fig. 545, on the basis of the hypothesis that the soil that had liquified should have experienced an increase in its blow count. Thus, the blow count before the earthquake, that had fallen on the left side on the N_{cr} -curve, increased as a result of the earthquake, and those on the right side decreased. KISHIDA (1966) plotted the blow count and showed that the data points could be separated into two groups by the dashed lines as shown in Fig. 545, i.e. those on

the left side suffered heavy damage, and those on the right, lighter damage.

SEED and IDRIS (1971) conceived the following categories for cases where the groundwater table was at 1.5 m depth below the surface, by using data from the literature:

Maximum ground surface acceleration	Liquefaction very likely	Liquefaction potential depends on soil type and earthquake magnitude	Liquefaction very unlikely
0.10 g	$D_r < 33$	$33 < D_r < 54$	$D_r > 54$
0.15 g	$D_r < 48$	$48 < D_r < 73$	$D_r > 73$
0.20 g	$D_r < 60$	$60 < D_r < 85$	$D_r > 85$
0.30 g	$D_r < 70$	$70 < D_r < 92$	$D_r > 92$

These values can also be correlated with the SPT-values if the relationships developed by

GIBBS and HOLTZ (1957) between N , D_r and the effective overburden pressure are used. The results of such recalculations are shown in Fig. 546 (SEED and IDRIS, 1971).

Another data processing method is to relate the number of blows to the ratio of τ/σ'_0 . Figure 547 is a reproduction of such calculations made by SEED *et al.* (1983). The corrected value N_1 of N is:

$$N_1 = C_N N,$$

where C_N can be extracted from the N_c -curves in the insert (b). Note that SEED *et al.* (1983) have used a previous relationship, but MARCUSON and BIEGANOUSKY (1976) made another proposition and in recent times the curves shown in the figure are applied.

SEED *et al.* (1983) further presented an approximate relationship for the case of Static Cone Penetration Test explorations. For any sand, the

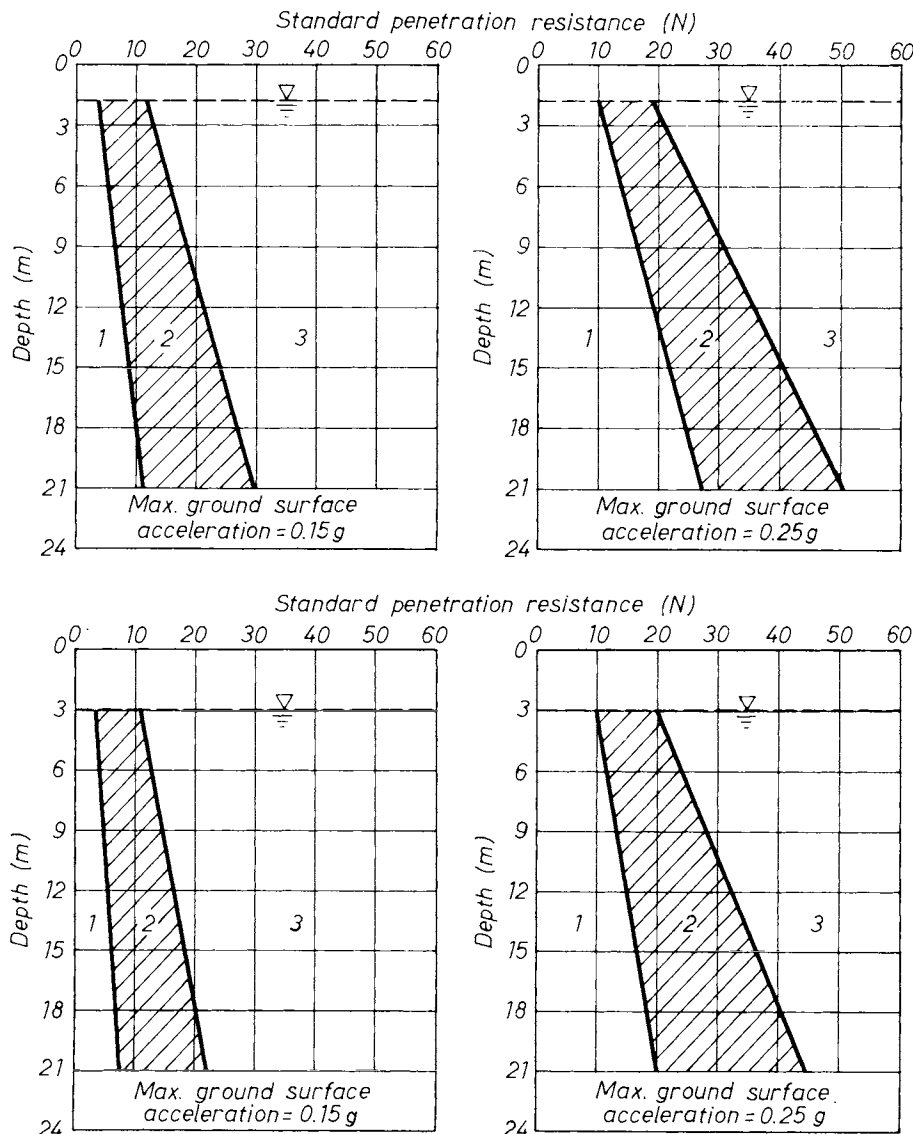


Fig. 546. Liquefaction potential evaluation charts for sands with water table at depth of about 1.5 m (a) and 3.0 m (b)

1 — liquefaction very likely; 2 — liquefaction potential depends on soil type and earthquake magnitude; 3 — liquefaction very unlikely (SEED and IDRIS, 1971)

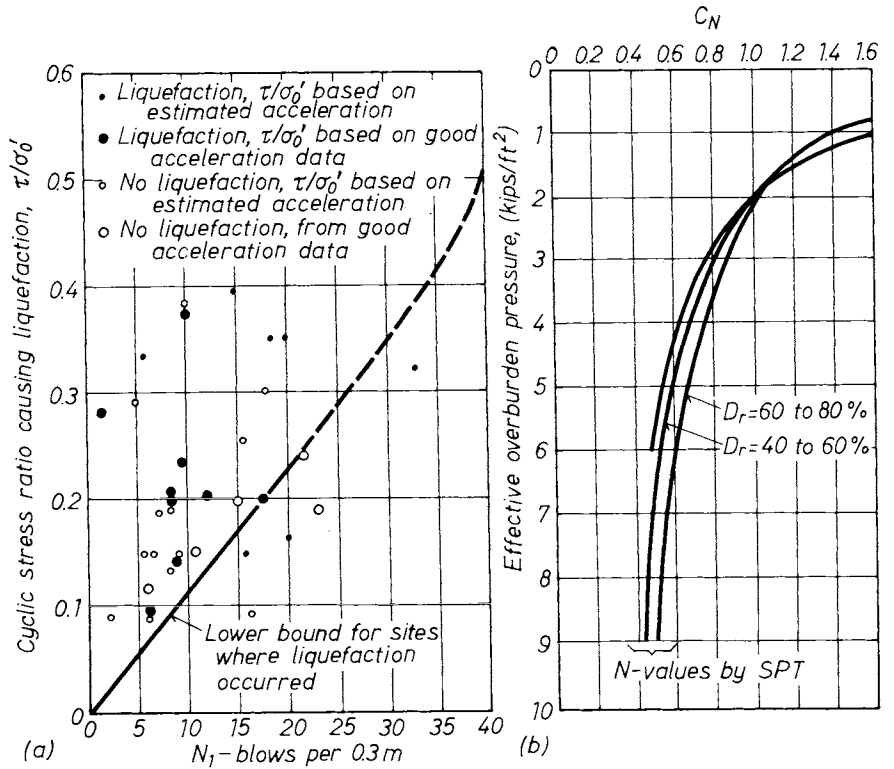


Fig. 547. a — Correlation between stress ratio causing liquefaction in field and N_1 ; b — relationship between C_N and effective overburden pressure

value of q_{cl} can be determined from the value of q_c measured at any depth:

$$q_{cl} = q_c C_N,$$

for which C_N -values are read-off from the curve shown in Fig. 547. The probability of liquefaction can then be determined from Fig. 548.

After the Chinese Building Code (valid from 1974), the critical value of the standard penetration resistance, N_{cr} , separating liquefiable from non-liquefiable conditions to a depth of approximately 15 m, can be determined by

$$N_{cr} = \bar{N} [1 + 0.125(d_s - 3) - 0.05(d_w - 2)], \tag{636}$$

in which d_s is the depth to the sand layer under consideration (in m), d_w is the depth of water below ground surface (in m), and \bar{N} is a function of the shaking intensity as follows:

Modified Mercalli intensity	\bar{N} in blows per 0.3 m
VII	6
VIII	10
IX	16

Equation (636) reflects among other things, also the fact that the risk of liquefaction decreases when the water table is deeper.

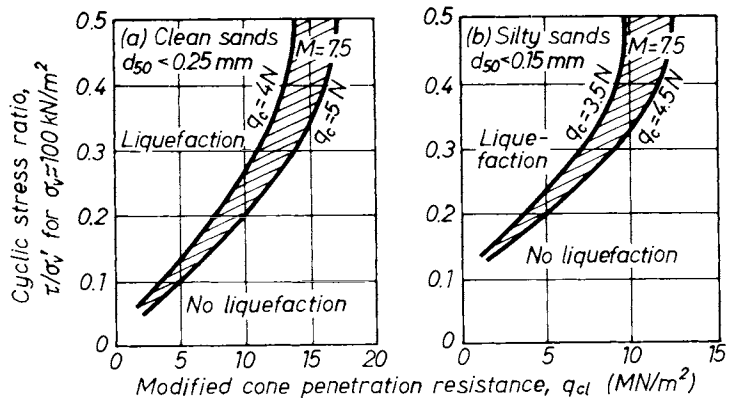


Fig. 548. Proposed correlation between liquefaction resistance of sands for level ground conditions and cone penetration resistance (SEED *et al.*, 1983)

6.6.5.4 Damage caused by liquefaction and appropriate preventive measures

Since the phenomenon of liquefaction has become recognized, damages caused by several ancient and recent earthquakes could have been attributed to the presence of saturated sand layers.

Extensive liquefaction occurred, for example, in the level sandy ground in Niigata, Japan, during the earthquake of 1964 ($M = 7.5$; epicentral distance 55 km). In the most heavily damaged area, 40 out of 63 buildings on shallow foundations and 49 out of 75 buildings on short piles settled more than 50 cm and/or tilted more than 1.0 degree (YOSHIMI, 1977). Similar damages were recorded during the earthquake in Alaska in 1964.

Major landslides, lateral movements of bridge supports and failure of waterfront retaining structures have all been observed in recent years as a result of liquefaction.

SEED (1968) presented a comprehensive review of landslides due to soil liquefaction during 37 earthquakes. The slope failures observed during these and more recent earthquakes have been classified into the following types (YOSHIMI, 1977):

- flow slides due to liquefaction of cohesionless soils comprising the slopes;
- slope failures due to liquefaction of thin layers of sand;
- slope failures of predominantly cohesive soils due to liquefaction of sand lenses;
- slumping of embankments on firm foundation due to cyclic deformation.

In addition, many failures of earth retaining structures have been reported as due to liquefaction of the backfill.

Recent research (e.g. NATARAJA and GILL, 1983) reveals that high ocean waves are also prone to produce considerable liquefaction on the shores.

When a proposed site is judged susceptible to liquefaction, it is wise to reconsider the relocation of the site, to apply some kind of stabilization, or to use pile foundations. Densification of soils by vibroflotation and a variety of deep compaction techniques (see Chapter 5) have been employed in places to prevent damage. The beneficial effects of coarse backfill in preventing pore pressure build-up or in reducing the duration of liquefaction were pointed out by YOSHIMI and KUWABARA (1973), and confirmed by YAMANOUCHI *et al.* (1976). Lowering the groundwater table tends to reduce the potential damage due to liquefaction for the following two reasons (YOSHIMI, 1977):

- it increases the liquefaction resistance of the saturated part of the soil by increasing the effective stress;
- it increases the thickness of the unsaturated part of the soil.

When piles are recommended, the loss of lateral resistance and frictional resistance should be taken in account in assessing their bearing capacity and deformation.

6.7 Dynamic problems of structures

6.7.1 Machine foundations

6.7.1.1 Theoretical aspects

Foundation engineering for machines causing vibration has gradually developed into a special discipline. There is an ample literature available on the problem in which all aspects are treated in detail (e.g. RAUSCH, 1959; BARKAN, 1962; KLOTTER, 1951). For this reason, the present consideration will be confined to the essential features of the problem in order to illustrate the practical application of the theoretical considerations dealt with in the foregoing sections. The extent to which such applications to problems in soil dynamics are justified will be examined first in the light of the results of recent large-scale experiments. In the United States, detailed experiments were carried out between 1960 and 1963 by the U.S. Army Waterways Experimental Station on foundations subject to dynamic loads. The foundations supported on loess and sandy soils had diameters from 1.5 to 5.0 m. The results of major interest are reproduced in Fig. 549, in which the ratio of amplitudes computed on the basis of the elastic half space to those actually observed are plotted against the ratio of the greatest acceleration by gravity. The first conclusion of general interest was that the results obtained by assuming the elastic half-space are satisfactory for practical purposes, a difference of

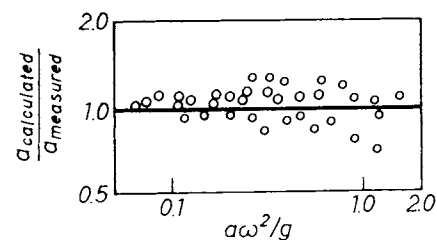


Fig. 549. Results of large-scale tests: comparison of measured and calculated values

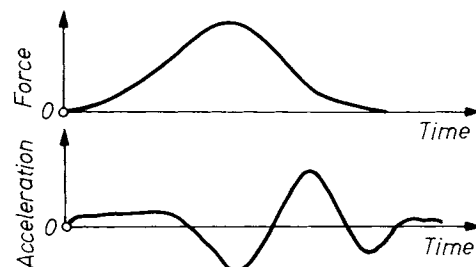


Fig. 550. Measured forces and time-path curves

100% being considered acceptable at the present state of knowledge. Moreover, the influence of soil type was found to be insignificant.

The agreement between theoretical and experimental results was likewise found satisfactory in experiments made at the University of Michigan with Ottawa sand. One of the results is shown in Fig. 550. The variation of acceleration with time was derived from the latter, while the variations of the force were used to compute the same curve in a computer by the theoretical relationships applying to the elastic half space. The agreement between the two curves was satisfactory.

In designing machine foundations, the following dynamic problems are encountered:

- check for resonance;
- determination of the dynamic reactions;
- estimation of the soil stresses.

The first problem is solved by computing the natural frequency. The formulae involved have been given in the earlier sections under Eqs (562a) and (562b). The extent to which the system is out of tune with respect to resonance, is clearly indicated by the expression

$$N = \frac{\omega_0^2}{\omega_0^2 - \omega^2}.$$

The allowable values of the ratio ω/ω_0 , or of N are mentioned in the standard specifications of the various countries.

The disturbing force is determined as a function of machine type. For example, in the case of piston engines the overturning moment M depends on the torque on the cross head: $M = Pr$. The forces are induced by the gas pressure acting on the piston, further by the inertia of the reciprocating parts of the crank mechanism. The variations in pressure are obtained from the indicator diagram of the engine and the magnitude thereof is unrelated to the machine speed. (Disturbance unrelated to frequency.) The inertia forces are proportionate to the square of the angular velocity. (Quadratic disturbance.) The forces proper are found from the indicator diagram (cf. KLOTTER, 1951). The centrifugal forces in rotating machines cause quadratic disturbance, the disturbing force being

$$P_0 = m_0 r \omega^2,$$

where m_0 is the revolving mass, r the excentricity which occasionally results from deflection of the shaft.

Let us now estimate the force transmitted by the vibrating system to the foundation and to the soil. The magnification factor has been defined as the ratio of the widest amplitude of forced vibration to the static compression. The magnitude thereof is plotted against the ratio ω/ω_0 . This factor has been shown to apply also to the case of

damped vibrations. The static compression is $z_{st} = P_0/K$, so that the magnification factor is

$$\begin{aligned} N &= \frac{z_0}{z_{st}} = \frac{z_0}{P_0/K} = \frac{Kz_0}{P_0} = \\ &= \frac{\text{max. restoring force}}{\text{max. disturbing force}} = \frac{\text{transmitted force}}{\text{disturbing force}} = \\ &= \text{transmittance.} \end{aligned}$$

The greatest reaction is obtained as

$$P_{dyn} = NP_{max}. \tag{637}$$

Foundations of vibrating systems are designed to minimize the force transmitted to the soil, when the foundation is perfectly rigid. In this case the natural frequency is infinitely large and $\omega/\omega_0 \rightarrow 0$, corresponding to point A in Fig. 499. The force transmitted in this case equals the disturbing force. The magnification factor increases with the ratio ω/ω_0 and becomes infinitely large as this ratio attains unity (resonance). Beyond this value, it decreases again and to attain a natural frequency much lower than the disturbing frequency, the support should be soft enough to have $\omega/\omega_0 > \sqrt{2}$, otherwise $N > 1$.

Vibrating systems on foundations supported by means of steel springs should be regarded as undamped. On the other hand, the damping effect of foundations resting directly on the soil, or on a layer of cork or rubber is no longer negligible. Resonance will occur according to one of the curves in Fig. 499. The force transmitted to the foundation consists of two parts, namely the restoring force Kz_0 and the damping force, the phase angle between the two being 90° . The resultant, or the total transmitted force is

$$P_{dyn} = z_0 \sqrt{K^2 + (c\omega)^2}. \tag{638}$$

The magnitude of the ordinate z_0 is given by Eq. (555), so that the force transmitted becomes

$$P_{dyn} = P_0 \frac{\sqrt{1 + \left(\frac{c\omega}{R}\right)^2}}{\sqrt{\left(1 - \frac{\omega^2}{\omega_0^2}\right)^2 + \left(2 \frac{c}{c_k} \frac{\omega}{\omega_0}\right)^2}}. \tag{639}$$

P_0 being the greatest disturbing force, the magnification is

$$\sqrt{\frac{1 + \left(\frac{2c}{c_k} \frac{\omega}{\omega_0}\right)^2}{\left(1 - \frac{\omega^2}{\omega_0^2}\right)^2 + \left(2 \frac{c}{c_k} \frac{\omega}{\omega_0}\right)^2}}. \tag{640}$$

This relationship is plotted in Fig. 551 for some values of c/c_k . Damping will be seen to be effective only for $\omega/\omega_0 < \sqrt{2}$.

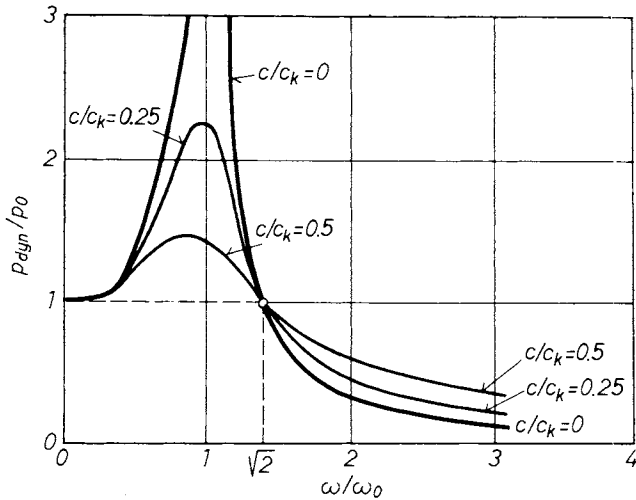


Fig. 551. Values of transferred dynamic forces

Concerning the foundation of vibrating systems, an examination of this diagram will lead to the following important conclusions.

- The application of a stiff support is advisable in cases where the ratio ω/ω_0 is close to zero. In such cases the load is virtually static.
- In the case of a soft support (high values of ω/ω_0), only a fraction of the disturbing force is transmitted to the foundation. Thus for effective elimination of vibration, such foundations should be adopted.
- In cases where $\omega/\omega_0 < \sqrt{2}$, the force transmitted is effectively reduced by damping. Consequently, absorbing devices are applied to advantage in this range only.
- In cases where $\omega/\omega_0 > \sqrt{2}$, no damping is advisable, as this would impair transmission. In this range the provision of damping is justified where the machine is liable to pass the resonance band during acceleration or slowing down, since damping is highly effective in this band.

6.7.1.2 Numerical examples

1. The weight of a machine is $G = 25.00$ kN, that of the rotor 1.50 kN and the excentricity of the latter is $r = 2$ cm. The machine is supported on springs the stiffness of which is $K = 18.00$ kN/cm. The frequency of the disturbing force is $f = 600$ cycles/min = 10 cycles/s. Find the force transmitted by the machine to the foundation.

The disturbance force is due to the centrifugal force of the revolving mass and has the magnitude

$$P = mr \omega^2,$$

$$m = \frac{G}{g} = \frac{1500 \text{ N}}{981 \text{ cm s}^{-2}} = 1.55 \text{ N s}^2 \text{ cm}^{-1},$$

$$\omega = 2 \pi f = 6.28 \cdot 10 = 62.8 \text{ s}^{-1},$$

$$P_0 = 1.55 \cdot 2 \cdot 62.8^2 = 12090 \text{ N} = 12.09 \text{ kN}.$$

The natural frequency is

$$\omega_0 = \sqrt{\frac{Kg}{G}} = \sqrt{\frac{18.00 \text{ kNcm}^{-1} \cdot 981 \text{ cm s}^{-2}}{25.00 \text{ kN}}} = 26.6 \text{ s}^{-1}$$

or

$$f_0 = \frac{\omega_0}{2\pi} = 4.24 \text{ s}^{-1} = 254 \text{ c/min}.$$

The support is thus soft, since $\omega/\omega_0 = f/f_0 = 600/254 = 2.36$.

Since forced vibrations without damping are considered, the magnification factor equals the transmission factor

$$N = \left| \frac{1}{1 - 2.36^2} \right| = 0.223.$$

The force transmitted is thus $P = 12.09 \cdot 0.223 = 2.69$ kN.

2. Examine for the same foundation the change in the transmission factor in the presence of damping. The damping coefficient is $c = 73.5$ N s/cm. The critical damping is

$$c_k = 2\sqrt{mk} = 2\sqrt{1.55 \text{ N/cm s}^2 \cdot 18000 \text{ N/cm}} = 334 \text{ N s/cm}$$

and

$$c/c_k = 73.5/334 = 0.22.$$

The transmission factor is thus

$$\sqrt{\frac{1 + (2 \cdot 0.22 \cdot 2.36)^2}{(1 - 2.36^2)^2 + (2 \cdot 0.22 \cdot 2.36)^2}} = 0.307$$

and the force transmitted $P = 3.71$ kN and is thus greater than in the first example.

The force transmitted depends on frequency and since the machine operated beyond the resonance range $\omega/\omega_0 \simeq 1$, during acceleration it is bound to pass the resonant frequency. For this reason, the variation of the force transmitted during acceleration should be examined. The result obtained is shown in Fig. 552, indicating (a) the variation of the transmission factor and (b) the variation of the magnitude of the force transmitted on the base of the bedding. Evidently, allowance had to be made in the computation for the variation of the disturbing force with frequency, the particular case being that of quadratic excitation. The curves representing the case without damping have also been plotted and are valuable for estimating the forces induced. If the rate of acceleration is known, the variation of the forces with time can also be plotted.

3. A machine supported on a concrete block of dimensions 2 by 4 by 1.60 m transmits only a vertical periodic disturbing force to the soil, which is wet, silty fine sand.

The weight of the machine is 180.00 kN, that of the revolving part 1.10 kN. The eccentricity is $r = 12$ cm. The frequency of the disturbing force is $n = 700$ cpm = 11.67 cps. The total weight is

$$G = (2 \cdot 4 \cdot 1.6) 2.2 + 180 = 462 \text{ kN.}$$

The static bearing pressure is thus

$$\sigma = \frac{462000}{200 \cdot 400} = 5.8 \text{ N/cm}^2.$$

First find the natural frequency. Using the "clay" line of the diagram of TSHEBOTARIOFF, the reduced natural frequency is obtained in terms of the base area $F = 8 \text{ m}^2$ as

$$n_{or} = 445 \text{ cpm kp cm}^{-1}.$$

The natural frequency is thus

$$n_0 = \frac{n_{or}}{\sqrt{p}} = \frac{445}{\sqrt{0.58}} = 584 \text{ cpm} = 9.73 \text{ cps.}$$

Then compute the dynamic bedding coefficient using the natural frequency.

From the expression $\omega_0 = \sqrt{K/m}$ the stiffness is

$$K = m\omega_0^2 = 4\pi^2 \frac{G}{g} n_0^2$$

and the dynamic bedding coefficient

$$k = \frac{K}{F} = \frac{4\pi^2 G n_0^2}{Fg} = \frac{4 \cdot 9.89 \cdot 462000 \text{ N} \cdot 9.73^2 \text{ s}^{-2}}{400 \cdot 200 \text{ cm}^2 \cdot 981 \text{ cm s}^{-2}} = 22 \text{ N/cm}^2.$$

Assume damping to be slight, the damping coefficient $c = 0.18 \cdot 10^2 \text{ kN cm}^{-1} \text{ s}$ and the critical damping coefficient, from the formula, is:

$$c_k = \sqrt{2mK} = 1.8 \cdot 10^2 \text{ kN cm}^{-1} \text{ s,}$$

so that $c/c_k = 0.01$.

The magnification factor is then

$$N = \frac{1}{\sqrt{\left(1 - \frac{\omega^2}{\omega_0^2}\right)^2 + \left(2 \frac{c}{c_k} \frac{\omega}{\omega_0}\right)^2}} = \frac{1}{\sqrt{\left(1 - \frac{700^2}{584^2}\right)^2 + \left(2 \cdot 0.1 \frac{700}{584}\right)^2}} = 2.13.$$

The peak value of the disturbing force ($\omega = 2\pi n$)

$$P_0 = m_0 r \omega^2 = \frac{1.1 \text{ kN} \cdot 12 \text{ cm}}{981 \text{ cm s}^{-2}} \cdot (6.28 \cdot 11.67)^2 \text{ s}^{-2} = 72.4 \text{ kN.}$$

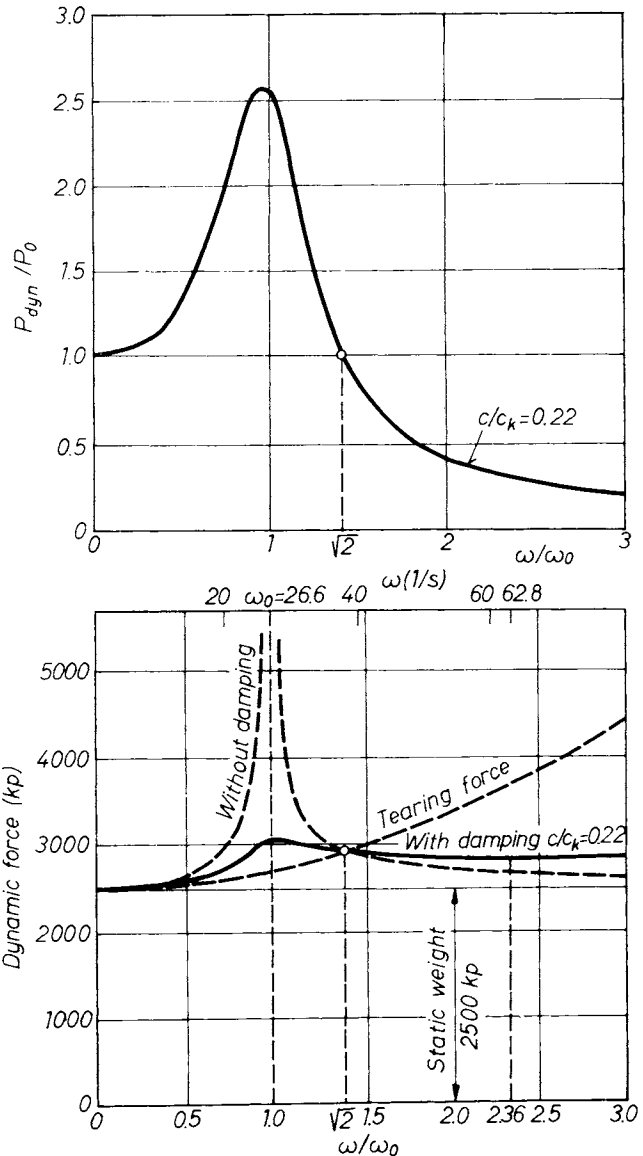


Fig. 552. Numerical example

The maximum amplitude ($K = kF$) is

$$a_0 = \frac{P_0}{K} N_1 = \frac{72400 \text{ N}}{22 \text{ N/cm}^2 \cdot 200 \cdot 400 \text{ cm}^2} \cdot 2.13 = 0.0875 \text{ cm.}$$

This is thus the amplitude with which the whole foundation vibrates, its magnitude being in general beyond the allowable value.

4. Find the vibrations at 10 m distance from the center of the foundation block if the propagation velocity of the waves is $v = 1200$ m/s and the absorption coefficient $k' = 0.215$.

The wave length is thus

$$\lambda = \frac{v}{f} = \frac{1200 \text{ ms}^{-1}}{11.67 \text{ s}^{-1}} = 94.5 \text{ m.}$$

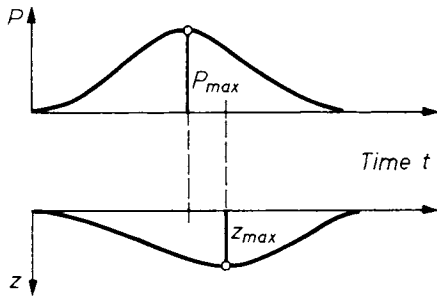


Fig. 553. Force pattern and deflection in the case of a pavement

At distance $x_0 = 2$ m the amplitude from the foregoing example is $a_0 = 0.0875$ cm so that at 10 m distance the amplitude from Eq. (621) is

$$a = 0.0875 \text{ cm} \sqrt{\frac{2.0 \text{ m}}{10.0 \text{ m}}} e^{\frac{-0.215 \cdot (10-2) \text{ m}}{94.5 \text{ m}}} = 0.0875 \cdot 0.447 \cdot 0.98 = 0.0384 \text{ cm}.$$

These amplitudes are too wide, the foundation is unacceptable and the design must be modified.

6.7.2 The dynamic behaviour of road pavements

The dimensioning of road pavements has been dealt with in detail in Chapter 4. The pavement was assumed to be acted upon by a single wheel load, or by some equivalent traffic, emphasizing, however, that the load is actually a dynamic one and that vibrations are induced in the pavement and in the subgrade which result in dynamic effects. In the majority of dimensioning procedures this circumstance has been allowed for by introducing a safety factor. In recent years the dynamic behaviour of road pavements has been studied intensively (NIJBOER, 1956, 1957, VAN DER POEL, 1953, HEUKELOM and FOSTER). Research into these problems has been prompted by the continuous increase in the weight and velocity of vehicles whence an increasing magnitude of the dynamic effects. Much important knowledge has been gained from these studies, but it would still be premature to consider the introduction of new "dynamic" methods of dimensioning. On the other hand, the dynamic studies made in the field have contributed to our understanding of actual pavement behaviour. The tests are non-destructive and no sampling is involved. They can be applied to the checking of longer road sections as well.

HEUKELOM has demonstrated (1961) that, at constant frequency, the road pavement can be treated as a linear system. For these tests in Great Britain, light vibrators were initially used (JONES, 1962), but heavier equipment was subsequently found to produce more relevant results. The method adopted for testing depended on whether a

relative comparison of different pavement structures, or the behaviour of a particular pavement under traffic was the objective of the study. In the first case, steady vibrations are induced by a vibrator and the conventional dynamic quantities are measured, whereas in the second the impacts imparted to the pavement by the traffic must be simulated.

The concept of "dynamic stiffness" has been introduced by VAN DER POEL (1951). If $P = P_0 \cdot \sin \omega t$ is the disturbing force and $z = z_0 \sin (\omega t - \varphi)$ is the amplitude, then the dynamic stiffness is

$$S = \frac{P_0}{z_0}, \tag{641}$$

or in combination with Eq. (554)

$$S = \sqrt{(k - m\omega^2)^2 + c^2\omega^2}. \tag{642}$$

Experiments have shown S to depend on frequency.

A wheel rolling along the pavement will induce a different kind of disturbance. Plotting the force transmitted and the deflection in a particular cross-section against time, the curves shown in Fig. 553 will be obtained. The maximum deflection will be seen therefrom to occur somewhat later than P_{max} . The stiffness under traffic is thus

$$T = \frac{P_{max}}{Z_{max}}. \tag{643}$$

S and T are usually of unequal magnitude and the time-lag between the maxima is the phase difference according to Eq. (579).

A simplified model of a system consisting of subgrade and pavement is illustrated in Fig. 554.

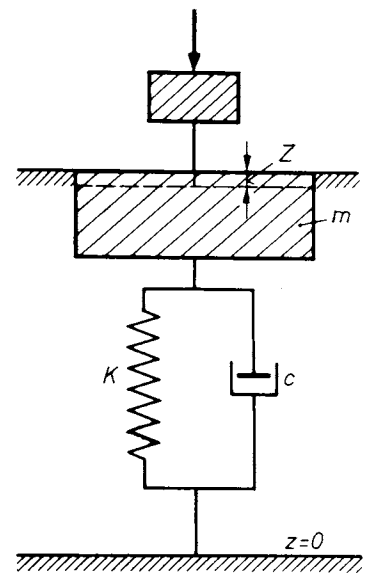


Fig. 554. Model for investigating the dynamic performance of pavement structures

The dynamic constants

$$S \cos \varphi = K - m \omega^2, \tag{644}$$

$$S \sin \varphi = c\omega,$$

measured at different frequencies, are plotted against ω^2 or ω . From the second plot the value of c is obtained directly at $\omega = 0$. $S \cos \varphi$ is plotted against ω^2 and the value of K is obtained at $\omega = 0$. At low frequencies the points plot on straight lines, the slope of the first yielding the value of m (Fig. 555). The value of K may be regarded a measure of the dynamic behaviour of the pavement structure.

As mentioned before, K is a function of frequency. At low frequencies the linear extension according to Fig. 555 is acceptable, but at high frequencies the following empirical expression applies

$$S \cos \varphi = K - \frac{\text{const.}}{\omega}. \tag{645}$$

In this range, K is found from the relationship $S \cos \varphi = F(1/\omega)$ (Fig. 555). The two diagrams are preferably combined in a single figure as shown in Fig. 555.

The dynamic characteristics suited to assessing pavement behaviour and to comparing different designs are obtained in the manner described above. However, the displacements under traffic differ from these (see Fig. 553), so that the dynamic stiffness of the pavement under traffic must also be examined. For small phase angles one solution of the basic equation is

$$z = \frac{P_0}{S} \left(\sin \omega t - \omega \sqrt{\frac{m}{K}} e^{-\omega t/2m} \sin \sqrt{\frac{K}{m}} t \right). \tag{646}$$

Values computed by the above equation for some loads are shown in Fig. 556, where the full

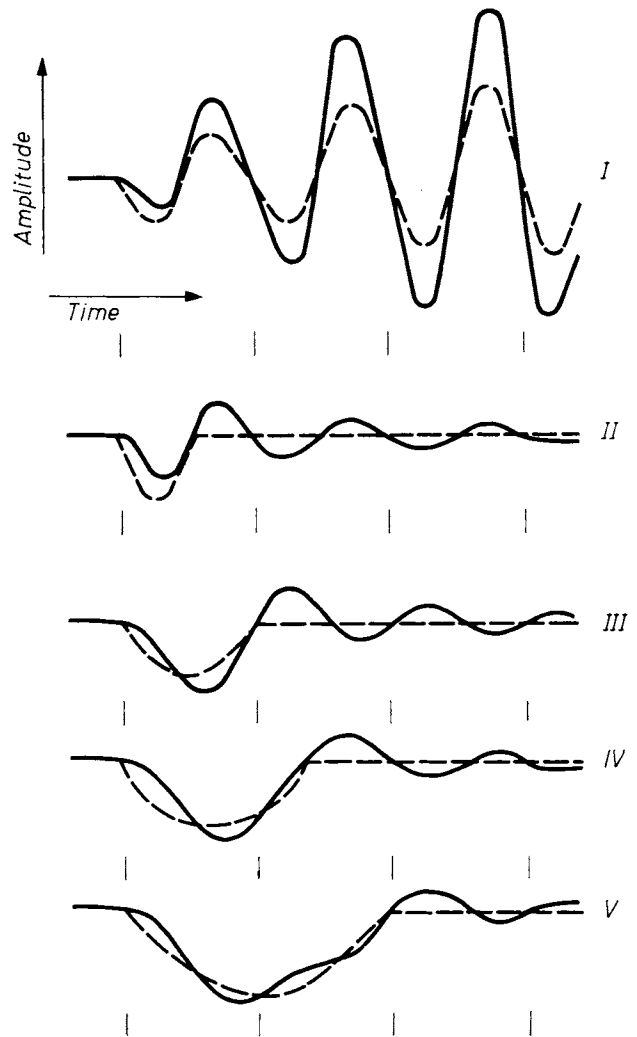


Fig. 556. Swinging of pavement structures

line applies to the whole vibrating mass, while the dashed lines indicate the “elastic” stiffness for the elastic medium at the same K values. The time-displacement curve I applies to steady vibrations. The amplitudes increase successively, the system attaining the peak value after several cycles. The curves II-IV indicate the deflections under passing vehicles for impacts represented by the half-period of a sinusoidal curve at different frequencies. The frequency is assumed to correspond to normal traffic condition. The theoretical curves were found to be in fair agreement with the experimental results.

It will be seen from the curve that the greatest deflection of the structure agrees closely with the theoretical deformation of the elastic medium. Consequently, the value of T virtually equals that of K . Further studies have shown the traffic stiffness to be

$$T = K (\pm 20\%).$$

The frequency of vibrations is of the same order of magnitude as the vehicle speed in km/h units.

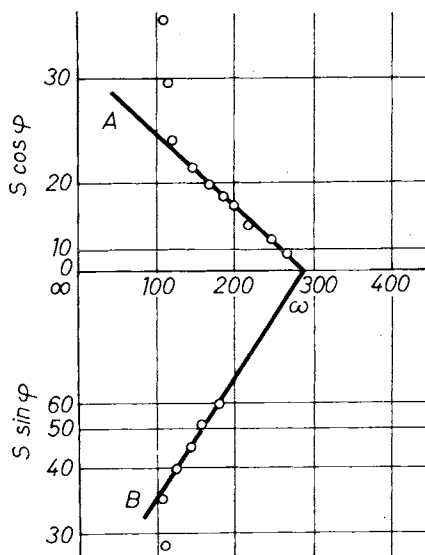


Fig. 555. Determination of dynamically determinant values

6.7.3 The effect of vibrations on slope stability

The stability and structural integrity of structures is endangered in a variety of ways by the vibrations, either artificially induced or due to earthquakes. Of this wide spectrum of problems, only a small detail, the stability of slopes, will be treated here. The examination of other structures is associated with problems which would exceed the scope of the present book by far and extend to the domain of seismology and they will, therefore, not be considered here.

The stability of a slope bounding a vibrating earth mass will now be examined (SEED and GOODMAN, 1963; SEED, 1966). It is desired to find the critical acceleration at which the slope becomes unstable. Consider for this purpose the equilibrium of a block — an elementary soil mass — situated in the slope surface (Fig. 557). A given acceleration will produce a force of magnitude $bG/g = \eta_k G$, sliding being caused by the components parallel to the slope of this force and of that due to gravity. Sliding is resisted by the shear $\tau = \sigma \tan \Phi$ mobilised on the base area of the block. Sliding will occur if the resultant of G and $\eta_k G$ and the force Q includes the angle Φ with the perpendicular to the sliding surface, as indicated in the vector diagram. The acceleration producing this condition will be the critical, the “failure” acceleration. The magnitude thereof is b_k , the dynamic force being $\eta_k G$, where $\eta_k = b_k/g$.

From the vector triangle

$$\frac{\eta_k G}{\sin(\Phi - \beta)} = \frac{G}{\sin[90^\circ - (\Phi - \beta - \vartheta)]}$$

and

$$\eta_k = \frac{\sin(\Phi - \beta)}{\cos(\Phi - \beta - \vartheta)} \quad (647)$$

For $\vartheta = \theta$ (horizontal acceleration)

$$\eta_{kh} = \tan(\Phi - \beta) \quad (648)$$

The variation of η_k for different values of $\Phi - \beta$ is shown in Fig. 558. Denoting the static safety factor of the slope by v , the acceleration ratio at failure will become

$$\eta_k = \frac{\sin \Phi (v - 1)}{v \sqrt{1 + \frac{\tan^2 \Phi}{v^2}}} \quad (649)$$

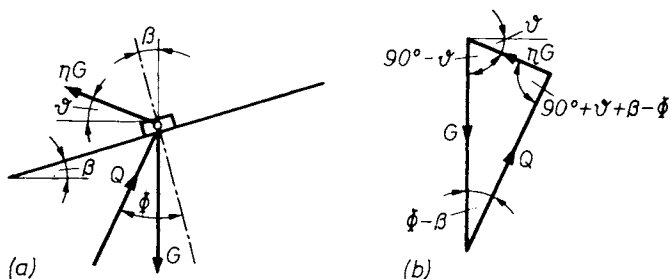


Fig. 557. Effect of earthquake acceleration: a — forces acting on the soil element; b — vector triangle in the limiting stage

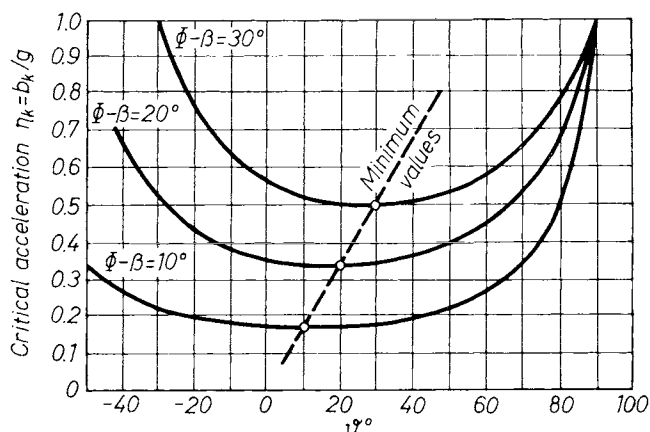


Fig. 558. Diagram for calculating the critical acceleration

A slope inclined at $\beta = 25^\circ$ with $\Phi = 36^\circ$ resists sliding with a safety factor $v = \tan 35^\circ / \tan 25^\circ \cong 1.5$. The condition of limit equilibrium occurs at the acceleration ratio $\eta_k = b_k/g = 0.1$.

Pseudostatic methods are often employed for the investigation of dams and embankments. In this approach, the stability of a potential sliding mass is determined as for static loading conditions and the effects of an earthquake are taken into account by including an equivalent horizontal force, acting on the potential sliding mass, in the computations (SEED *et al.*, 1975). The horizontal force representing earthquake effects is expressed as the product of the weight of the sliding mass under consideration and a seismic coefficient, k . The value of this coefficient is normally selected on the basis of the seismicity of the region (e.g. values in California range from a lower limit of 0.05 to an upper limit of about 0.15).

6.7.4 Behaviour of retaining walls

The design of retaining walls for dynamic (seismic) effects has first been dealt by MONONOBÉ (1929), MONONOBÉ and MATSUO (1929) and OKABE (1926); Coulomb's sliding wedge theory has been extrapolated for this case. According to the authors

$$E_{AE} = 0.5\gamma H^2(1 - k_v)K_{AE} \quad (650)$$

where

$$K_{AE} = \frac{\cos^2(\Phi - \theta - \beta)}{\cos \theta \cos^2 \beta \cos(\delta + \beta + \theta)}$$

$$\left[1 + \sqrt{\frac{\sin(\Phi + \delta) \sin(\Phi + \theta - i)}{\cos(\delta + \beta + \theta) \cos(i - \beta)}} \right]^2 \quad (651)$$

In the equations $\theta = \tan^{-1} k_h/(1 - k_v)$, $\delta =$ angle of friction between the wall and soil, $\beta =$ slope of the wall to the vertical, $i =$ slope of the ground surface, $k_h =$ horizontal acceleration per g .

RICHARDS and ELMS (1979) proved after the evaluation of this equation that this theory may

in many cases lead to absurd conclusions. The authors pointed out that it was completely inaccurate to neglect the inertia of the wall and that this assumption was unconservative, since it was actually the weight of the wall which provided most if not all of the resistance against movement. They deduced the following relation from the equilibrium of acting forces:

$$W_w = \frac{0.5\gamma H^2 [\cos(\delta + \beta) - \sin(\delta + \beta) \tan \Phi_b]}{\tan \Phi_b - \tan \theta} K_{AE} \quad (652)$$

where W_w is the weight of the wall, Φ_b is the angle of the reactive force at the base with the vertical. The same expression can be transformed into

$$W_w = \frac{[\cos(\delta + \beta) - \sin(\delta + \beta) \tan \Phi_b]}{(1 - k_v)(\tan \Phi_b - \tan \theta)} E_{AE} \quad (653)$$

Equations (652) and (653) can be evaluated in a straightforward manner to provide the weight of the wall required. Essentially, this weight is the dynamic thrust, as computed by the MONONOBE-OKABE analysis, multiplied by a wall inertia factor C_{IE} , that is

$$W_w = C_{IE} E_{AE} = C_{IE} 0.5 \gamma H^2 (1 - k_v) K_{AE} \quad (654)$$

in which

$$C_{IE} = \frac{\cos(\delta + \beta) - \sin(\delta + \beta) \tan \Phi_b}{(1 - k_v)(\tan \Phi_b - \tan \theta)} \quad (655)$$

The relative importance of the two dynamic effects (i.e. the increased thrust on the wall due to inertia forces on the sliding wedge and the increase in driving force due to the inertia of the wall itself) can be seen by normalizing them with regard to

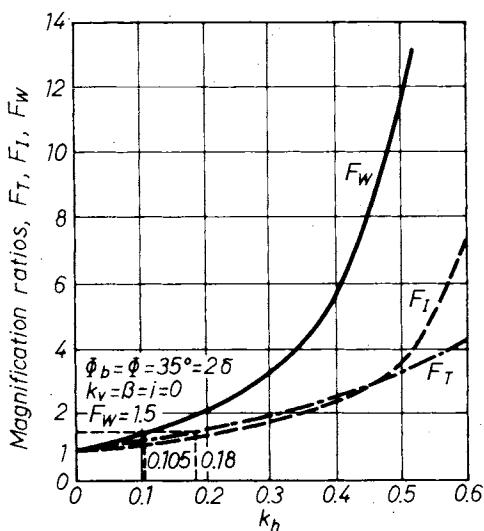


Fig. 559. Variation of soil thrust factor F_T , wall inertia factor F_I and combined dynamic factor F_w with horizontal acceleration (RICHARDS and ELMS, 1979)

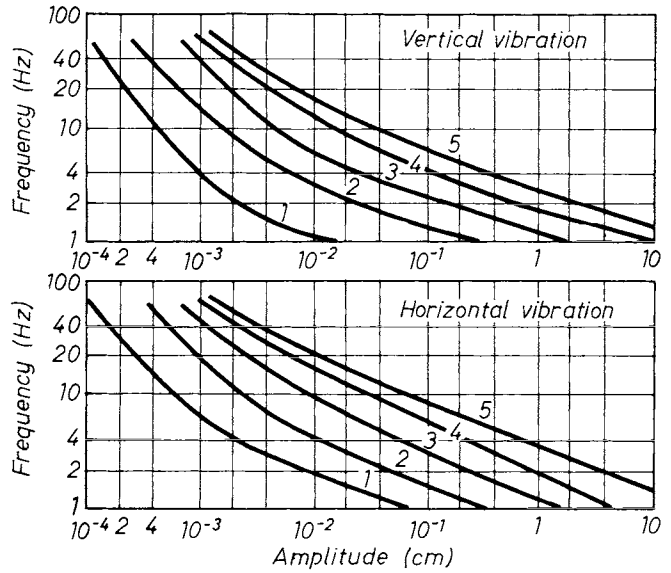


Fig. 560. Human sensitivity to vibrations: 1 — just sensitive 2 — well sensitive 3 — strongly sensitive 4 — harmful when experienced for longer periods; 5 — absolutely disturbing and harmful

the static values. Thus we may define a soil thrust factor

$$F_T = \frac{K_{AE}(1 - k_v)}{K_A} \quad (656)$$

and a wall inertia factor

$$F_I = \frac{C_{IE}}{C_I}$$

in which

$$K_A = \frac{\cos^2(\Phi - \beta)}{\cos^2 \beta \cos(\delta + \beta) \left[1 + \sqrt{\frac{\sin(\delta + \Phi) \sin(\Phi - i)}{\cos(\delta + \beta) \cos(\beta - i)}} \right]^2} \quad (657)$$

and

$$C_I = \frac{\cos(\delta + \beta) - \sin(\delta + \beta) \tan \Phi}{\tan \Phi_b} \quad (658)$$

The product F_w of the thrust and inertia factors is a safety factor applied to the weight of the wall to allow for the effects of soil pressure and wall inertia:

$$F_w = F_T F_I = \frac{W_w}{W}, \quad (659)$$

in which W is the weight of the wall required for equilibrium in the static case.

For a static design safety factor of some value F_w on the weight of the wall, the critical horizontal acceleration can be read directly from Fig. 559. If, for example, a wall were designed for $F_w = 1.5$, then for the parametric values specified in Fig. 559, motion would occur at $k_h = 0.105$. Neglecting wall inertia, this value would be $k_h = 0.18$.

6.7.5 Effect of vibrations on buildings

ZELLER suggested using the following formula to discern the harmfulness of vibrations

$$\chi = \frac{b^2}{n} = 16 \cdot \pi^4 \cdot n^3 \cdot a^2 \text{ (in cm}^2/\text{s}^3\text{)}, \quad (660)$$

where n is the frequency, and a is the amplitude.

Human sensitivity to vibrations — on the basis of observations — is represented in Fig. 560. Buildings may suffer damage from vibrations when the value of χ attains 25 to 100 cm²/s³.

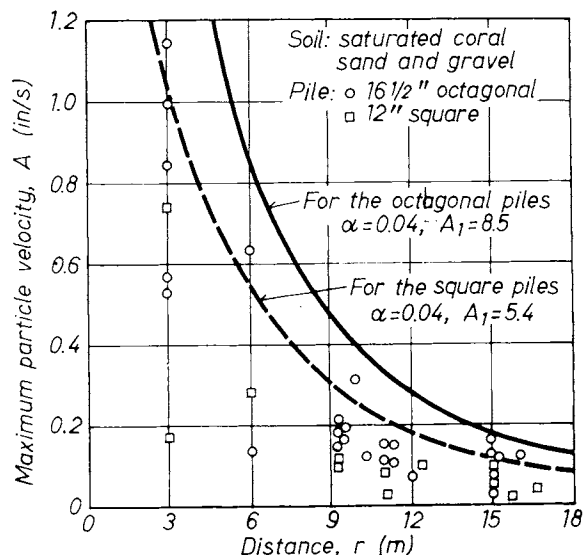


Fig. 561. $A-r$ relationship from a case study (Lo, 1977) (1 in = 25.4 · 10⁻³ m)

WISS (1968) recommended the “peak particle velocity” as the best parameter to assess the damage potential of ground vibration. The author concluded that 5 cm/s was a good criterion for residential structures and 10 cm/s for commercial and engineered structures to avoid damage due to vibrations.

The effect of pile driving can be computed on the basis of the formula suggested by Lo (1977). The results of a survey made on site are represented in Fig. 561.

In Switzerland a Code has been constructed on the basis of over 200 vibration measurements to detect those limiting values which may cause light damage in buildings (appearance of fissures, peeling, etc.) (STUDER and SUESSTRUNK 1981). The knowledge of four characteristics is needed to assess the degree of peril

- the parameters of the vibrating source;
- the properties of the structure;
- the condition of the building;
- geological situation.

The decisive design term will be the peak particle velocity.

References

BARKAN, D. D. (1962): *Dynamics of Bases and Foundations*. McGraw-Hill, New York.

CASAGRANDE, A. (1936): Characteristics of cohesionless soils affecting the stability of slopes and earth fills. *J. of Boston Soc. of Civ. Engs.*, January.

CASAGRANDE, A. (1976): Liquefaction and cyclic deformation of sands: a critical review. *Harvard Soil. Mech. Series*. No. 81.

CASTRO, G. (1975): Liquefaction and cyclic mobility of saturated sands. *Proc. ASCE*. GT 6.

D'APPOLONIA, E. (1968): Dynamic loadings. *ASCE Speciality Conf.*, Cambridge.

DE ALBA, P. SEED, H. B. and CHAN, C. K. (1976): Sand liquefaction in large-scale simple shear test. *Proc. ASCE*. GT 9.

DEN HARTOG, J. P. (1947): *Mechanical Vibrations*. McGraw-Hill, New York.

FERRITTO, J. M. and FORREST, J. B. (1977): Sitting structures in seismic liquefaction areas. *Proc. 9th ICSMFE*. Vol. 2, Tokyo.

FINN, W. D. L., PICKERING, D. J. and BRANSBY, P. L. (1971): Sand liquefaction in triaxial and simple shear tests. *Proc. ASCE*. SM 4.

FLORIN, V. A. and IVANOV, P. L. (1961): Liquefaction of saturated sandy soils. *Proc. 5th ICSMFE*. Vol. 1, Paris.

GIBBS, H. J. and HOLTZ, W. G. (1957): Research on determining the density of sand by spoon penetration test. *Proc. 4th ICSMFE*. Vol. 1, London.

HENDRON, A. J. Jr. (1963): The behaviour of sand in one-dimensional compression. *Thesis. presented to Univ. of Illinois*.

HEUKELOM, W. (1957): Über die mechanischen Elemente, die Steifigkeit von Strassenkonstruktionen beherrschen. *Report M 23020, Kozinklijke Shell Lab.* Amsterdam.

HOAR, R. J. and STOKOE, K. H. (1981): Crosshole measurement and analysis of shear waves. *Proc. 10th ICSMFE*. Vol. 3, Stockholm.

IMAI, T. (1977): P- and S-wave velocities of the ground in Japan. *Proc. 9th ICSMFE*. Vol. 2, Tokyo.

ISHIHARA, K., IWAMOTO, S., YASUDA, S. and TAKATSU, H. (1977): Liquefaction of anisotropically consolidated sand. *Proc. 9th ICSMFE*. Vol. 2, Tokyo.

KAUDERER, H. (1958): *Nichtlineare Mechanik*. Springer, Berlin.

KISHIDA, H. (1966): Damage to reinforced concrete buildings in Niigata city, with special reference to foundation engineering. *Soil and Foundation*, Vol. 6, No. 1.

KLOTTER, K. (1951): *Technische Schwingungslehre*. Springer, Berlin.

KOIZUMI, Y. (1966): Changes in density of sand subsoil caused by the Niigata earthquake. *Soil and Foundation*, Vol. 6, No. 2.

KURIBAYASHI, E. and TATSUOKA, F. (1975): Brief review of liquefaction during earthquakes in Japan. *Soil and Found.*, Vol. 15, No. 4.

LEE, K. L. and SEED, H. B. (1967): Cyclic stress conditions causing liquefaction of sand. *Proc. ASCE*. SM 6.

LO, M. B. (1977): Attenuation of ground vibration induced by pile driving. *Proc. 9th ICSMFE*. Vol. 2, Tokyo.

LORENZ, H. (1950): Der Bauground als Federung und Dämpfung schwingender Körper. *Bauing*, No. 10.

LORENZ, H. and KLEIN, G. (1966): *Grundbaudynamik*. Gruntaschenbuch. Vol. I, 2nd ed., Berlin/München.

MARCUSON, W. F., and BIEGANOUSKY, W. A. (1976): Laboratory Standard Penetration Test on fine sands. *Proc. ASCE*. GT 6.

MARTIN, G. R., FINN, W. D. L. and SEED, H. B. (1975): Fundamentals of liquefaction under cyclic loading. *Proc. ASCE*. GT 5.

MONONOBE, N. (1929): Earthquake proof construction of masonry dams. *Proc. World. Eng. Congress*, Vol. 9, p. 275.

MONONOBE, N. and MATSUO, H. (1929): On the determination of earth pressures during earthquakes. *Proc. of World Engg. Conf.*, Vol. 9.

NATARAJA, M. S. and GILL, H. S. (1983): Ocean wave-induced liquefaction analysis. *Proc. ASCE, J. of Geot. Engg.*, No. 4.

- NOVAK, M. (1957): Über die Nichtlinearität der Vertikal-schwingungen von starren Körpern auf dem Baugrunde. *Acta Technica* 5, 6, Praha.
- OKABE, S. (1926): General theory of earth pressure. *J. of Japanese Soc. of Civ. Engrs.* Vol. 12, No. 1.
- PEACOCK, W. H. and SEED, H. B. (1968): Sand in liquefaction under cyclic loading simple shear conditions. *Proc. ASCE*, SM 3.
- PYKE, R. H., SEED, H. B. and CHAN, C. K. (1975): Settlement of sands under multidirectional shaking. *Proc. ASCE*, GT 4.
- RAUSCH, E. (1959): *Maschinenfundamente und andere dynamische Bauaufgaben*. 3rd ed., VDI Düsseldorf.
- RICHARDS, R. and ELMS, D. G. (1979): Seismic behaviour of gravity retaining walls. *Proc. ASCE*, GT 4.
- RODRIGUES, L. F. (1981): Shear wave studies by cross-hole method. *Proc. 10th ICSMFE*, Vol. 3, Stockholm.
- ROSCOE, K. H. (1953): An apparatus for the application of simple shear to soil samples. *Proc. 3rd ICSMFE*, Vol. 1, Zürich.
- SCHULTZE, E. and MUHS, H. (1967): *Bodenuntersuchungen für Ingenieurbauten*. 2nd ed., Springer, Berlin.
- SEED, H. B. (1966): A method for earthquake resistant design of earth dams. *Proc. ASCE*. SM 1.
- SEE, H. B. (1968): Landslides during earthquakes due to soil liquefaction. *Proc. ASCE*. SM 5.
- SEED, H. B. and BOOKER, J. R. (1976): Stabilization of potentially liquefiable sand deposits using gravel drain systems. *Report No EERC 76-10*. Univ. of California.
- SEED, H. B. and IDRIS, I. M. (1967): Analysis of soil liquefaction at Niigata earthquake. *Proc. ASCE*. SM 3.
- SEED, H. B. and IDRIS, I. M. (1971): Simplified procedure for evaluating soil liquefaction potential. *Proc. ASCE*. SM 9.
- SEED, H. B. and LEE, K. M. (1966): Liquefaction of saturated sands during cyclic loading. *Proc. ASCE*. SM 6.
- SEED, H. B. and PEACOCK, W. H. (1971): Test procedure for measuring soil liquefaction characteristics. *Proc. ASCE*. SM 8.
- SEED, H. B. and SILVER, M. L. (1972): Settlement of dry sands during earthquakes. *Proc. ASCE*. SM 4.
- SEED, H. B., IDRIS, I. M., MAKDISI, F. and BENERJEE, N. (1975): Evaluation of soil liquefaction potential during earthquakes. *Report No. EERC 75-28*, Univ. of California.
- SEED, H. B., PYKE, R. M. and MARTIN, G. R. (1978): Effect of multidirectional shaking on pore pressure development in sands. *Proc. ASCE*. GT 1.
- SEED, H. B., IDRIS, I. M. and ARANGO, I. (1983): Evaluation of liquefaction potential using field performance data. *Proc. ASCE. J. of Geot. Engg.*, No. 3.
- STOKOE, K. H. and WOODS, R. D. (1972): In situ shear wave velocity by cross-hole method. *Proc. ASCE*. SM 5.
- STUDER, J. and SUESSTRUNK, A. (1981): Swiss standard for vibrational damage to buildings. *Proc. 10th ICSMFE*. Vol. 3, Stockholm.
- TAYLOR, D. W. (1948): *Fundamentals of Soil Mechanics*. Wiley, New York.
- TCHEBOTARIOFF, G. P. and WARD, E. R. (1948): The resonance of machine foundations and the soil coefficients which affect it. *Proc. 2nd ICSMFE*. Vol. 1, Rotterdam.
- WANG, W. S. (1981): Saturated sands under cyclic loading. *Proc. 10th ICSMFE*. Vol. 3, Stockholm.
- WHITMAN, R. V. and ORTIGOSA, P. O. (1969): Densification of sand by vertical vibrations. *Proc. 4th World Conf. on Earthquake Engg.*, Santiago.
- WISS, J. F. (1968): Effects of blasting vibrations on buildings and people. *Civ. Engg. ASCE*, July.
- WONG, R. T., SEED, H. B. and CHAN, C. K. (1975): Cyclic loading liquefaction on gravelly soils. *Proc. ASCE*. GT 6.
- WOODS, R. D. (1978): Measurement of dynamic soil properties. *Proc. Earthquake Engg. and Soil Dynamics, ASCE*. Vol. 1, Pasadena.
- YAGI, N. (1972): Volume change and excess pore pressure of sand due to cyclic shear. (In Japanese.) *Proc. 7th Conf. Jap. Soc. SMFE*.
- YAMANOUCHI, T., KOREEDA, K. and SAKAGUCHI, O. (1976): Shirasu soils in Kogoshima. *Tsuchito-Kiso, Jap. Soc. SMFE*. Vol. 24, No. 7.
- YOSHIMI, Y. (1977): Liquefaction and cyclic deformation of soils under undrained conditions. *Proc. 9th ICSMFE*. Vol. 2, Tokyo.
- YOSHIMI, Y. and KUWABARA, F. (1973): Effect of subsurface liquefaction on the strength of surface soil. *Soils and Found.*, Vol. 13, No. 2.

Author index

- Aas 49
Acum 244
Airy 112
Aköz 221
Aldrich 305, 306
Alimi 314
Altes 133
Amann 143
Anagnostopoulos 30
Anderson 294
Au 143
Auviner 215, 216
- Babkov 127, 137
Bachelez 251
Bakht 224
Balasubramaniam 186, 193
Baligh 50
Balla 96–98
Bally 310
Banerjee 185, 196, 208, 211
Bang 314
Barata 151
Barkan 326, 331, 332, 337, 338, 348
Barron 73, 308
Bartolomey 193, 197
Bartos 313
Bassett 313
Bazaraa 152
Beine 296
Beles 312
Bell 171
Berezantsev 124, 188, 200, 206
Bernatzik 41
Bertram 78
Beskow 266
Biarez 98
Bieganousky 346
Bishop 24, 25, 26, 28, 30–33, 289, 291
Bjerrum 145, 148, 151, 168, 187
Boitand 186
Booker 314, 342
Boromissza 254
Borowiczka 138
Borozuk 168
Boussinesq 109, 124, 126, 138, 139, 141, 194, 196
Bowman 304
Brandl 136–137
Brenner 193
Breth 143
Brinch Hansen 98, 100, 116, 131, 175
Brisette 151
Broise 295
Broms 184, 185, 197, 208, 219, 294, 304
Brown 294, 313
Buchanan 233
Budin 146
Buisman 90
Bukowski 127, 137
- Burland 167, 169, 170, 186, 193, 197, 200
Burmister 135, 136, 151, 243, 244, 251, 255
Butterfield 310
- Campinos 258
Caquot 89, 90, 98, 176, 189, 191
Carillo 308
Casagrande 13, 60, 62, 63, 271, 341, 342
Castro 342
Cauchy 110
Cedergren 82, 83
Chan 284, 289, 290
Chapman 72, 73, 74
Chin 219
Christensen 54
Clark 217, 218
Clemente 216
Cole 217
Cooke 196, 197, 203, 207
Cox 159
Coyle 195, 197, 220, 225
Cronney 261
Culmann 15, 16
- DA'ppolonia 141, 151, 195, 334
Davies 185, 208, 211
Davis 143, 145, 146, 195, 201, 205
De Alba 342
De Beer 99, 191, 192
Den Hartog 329, 330
Deninger 166
Donald 289
Donchev 294
Dücker 267
Dubrova 101
- Eggestad 151
Elms 354
Engesser 53
Erlenbach 158
Ewert 132
- Feda 133, 134
Feld 70, 159
Fellenius 17, 18, 30, 34
Ferritto 342
Findlay 282
Finn 259, 344
Fischer 139
Flaate 193
Fleming 87
Flores-Berrounes 185
Florin 342
Focht 186
Forrest 342
Förtsch 339
Fox 244
Francescon 184
- Franke 224
Fraser 164
Fredlund 28, 32
Fröhlich 22, 43, 107, 118, 120, 138, 177, 296
Frontard 48
Furnas 281
- Gáspár 254, 266, 271, 292
Geddes 195
Gibbs 346
Gilboy 63
Gill 348
Giroud 105, 314
Goble 221, 223
Goodman 354
Gorbunov-Posadov 166
Graf 312
Grasshof 166
Gray 309
Greenwood 30
Grivas 69
- Hanell 215, 216
Hansbo 307, 309
Hansson 294
Hendron 344
Herrera 178
Hetényi 166
Heukelom 338, 352
Hoar 340, 341
Holtz 305, 346
Homes 106
Horvat 214, 216
Housel 151
Hruban 119
Hu 98
Huder 32
Hughes 315
- Idriss 342, 345, 346
Imai 332, 341
Ingold 314
Inoue 159, 214
Ishihara 344
Ivanov 294, 342
Iwakiri 171
- Jaeger 224
Janbu 26, 27, 28, 32, 186
Jaropolskii 108
Jáky 16, 23, 24, 55, 94, 96, 108, 133, 158, 273
Járay 263
Jegorov 134, 146
Jelinek 123, 134, 138, 187, 192, 193, 240
Jessberger 296, 300, 301
Jeuffroy 251
Jewell 313
Johnson 304, 306, 307

- Johnston 310
 Jones 313, 352
 Joosten 310, 311
 Jorgensen 310, 311
 Jumikis 265

K
 Kabai 285
 Kamon 304
 Kany 132, 166
 Katti 312
 Kauderer 330
 Kay 220, 225
 Kérisel 98, 145, 159, 176, 186, 191, 192, 216
 Kézdi 49, 70, 71, 106, 135, 199, 200, 264, 282, 298, 300
 Kirk 251
 Kishida 160, 345
 Kjellmann 307
 Klein 330
 Klengel 265
 Klotter 348, 349
 Koerner 194, 314
 Kögler 166, 272, 296
 König 166
 Kötter 97
 Koizumi 345
 Kotzias 307
 Koutsoftas 217
 Krahn 28, 32
 Krizek 93
 Krsmanović 166
 Kuribayashi 343
 Kusurelis 107
 Kutzner 282
 Kuwabara 348

L
 Lacy 159, 223
 Ladányi 192
 Lambe 147, 150, 283
 Langejan 70
 La Rochelle 31
 Lazányi 254
 Lazard 66
 Lebuis 45
 Lee 342, 343
 Leonards 50, 295
 Leroueil 143
 Leske 107
 Leussink 168, 177, 178, 282
 Lindquist 188
 Lister 244
 Littlejohn 171
 Litvinov 294, 312
 Lo 356
 Logeais 160
 Lorenz 127, 329, 330
 Lu 209, 221
 Lukas 295
 Lumb 176
 Lundgren 94, 175

Mac
 MacDonald 145, 167, 168, 170
 MacLeod 171, 257
 Mangel 90
 Malik 172
 Manfredini 45
 Marguerre 134
 Marguson 346
 Mariupolskii 104
 Markó 49, 70, 71, 264
 Marr 171, 172
 Marsal 285
 Martin 341
 Maslov 108
 Matsuda 312
 Matsuo 304, 354
 Mattes 195

Mc
 McAdam 260
 McKinley 160
 McKitterick 314
 McRae 283
 Melan 122
 Ménard 142, 152, 295
 Meyerhof 70, 94–96, 98, 101, 105, 152, 164, 167, 168, 184, 186, 187, 188, 191, 192, 199, 201, 218
 Middlebrook 70
 Mindlin 195, 201, 210
 Mitchell 284, 290, 305, 306, 309, 310, 313–316
 Mizuno 94
 Monismith 233
 Mononobe 354
 Morgenstern 28, 29, 32, 33
 Mors 103
 Mortensen 94
 Morton 143
 Muhs 99, 101, 102, 335
 Müller 152

N
 Natarja 348
 Newmark 127, 131
 Nijboer 352
 Norlund 188
 Novais Ferrera 258
 Novak 330

O
 Odemark 136
 Ohde 118, 125, 166
 Okaba 214, 216
 Okabe 354
 Olko 217, 218
 Ortigosa 334
 Oreo 210, 212

P
 Pacey 284
 Papadopoulos 30
 Partos 194
 Peacock 342, 343, 344, 345
 Peck 145, 151, 152, 168, 200
 Peltier 259
 Penman 173
 Petaja 188
 Pickett 240
 Pilot 304
 Porkovskii 135–136, 137
 Polshin 168, 169, 170
 Popova 134
 Porter 252, 292
 Poulos 143, 145, 146, 185, 195, 197, 201, 203, 205, 208, 210, 213, 224
 Parakash 101
 Prandtl 89, 90, 93, 98, 189, 191
 Price 28, 29, 33
 Priebe 316
 Promboon 193
 Puzirjevskii 107, 108
 Pusch 142
 Pyke 335

Q
 Quartre 145
 Queiroz 302

R
 Raes 90
 Randolph 184, 185, 195, 196, 197, 203, 224
 Rausch 348
 Rausche 223
 Ray 240
 Reese 195, 197, 198, 209, 213, 220, 221, 225
 Reissner 93
 Rendulič 53, 54
 Repnikov 166
 Resendiz 178, 283, 285

Ré
 Rétháti 108, 144, 153, 154, 155, 156, 157, 158, 161, 162, 169, 179, 282
 Richards 354
 Ring 293
 Rissman 45
 Rode 281
 Rodrigues 341
 Rollberg 219
 Romualdi 195
 Roscoe 343
 Rotfuchs 297
 Rudnickii 151

S
 Sabini 188, 219
 Sallberg 293
 Santoyo 221
 Sapio 188, 219
 Saran 101
 Scarlett 87
 Schaible 265, 270, 271
 Scheidig 166, 296
 Schields 105
 Schleicher 120, 236
 Schlitt 199
 Schmidt 212
 Schofield 261
 Schultze 99, 100, 152, 166, 168, 176, 177, 335
 Schuster 313
 Schwarz 54
 Seed 195, 198, 284, 289, 290, 314, 332, 334, 335, 341–346, 348, 354
 Selnes 193
 Shanon 13
 Sherif 152, 157, 168
 Sherman 234
 Shock 259
 Sichardt 73
 Siedek 274
 Sievering 177
 Silver 332, 334
 Simons 143
 Singh 67, 69, 176
 Skempton 51, 145, 148, 167, 168, 170, 192, 197, 200, 206
 Södeberg 184
 Sokolovskii 94
 Som 143
 Stamatoopoulos 307
 Spencer 28, 29, 30, 33
 Stanculescu 312
 Steenfelt 184, 194
 Steinbrenner 127
 Stokoe 340, 341
 Strohschneider 54
 Studer 356
 Suesstrunk 356
 Sutherland 239

T
 Tajimi 214
 Takagi 313
 Takano 160
 Takeo mogami 126
 Talbot 297
 Tatsuoka 343
 Tavenas 31, 143
 Taylor 20, 21, 24, 40, 44, 50, 80, 341
 Teller 232, 239
 Terashi 304
 Terzaghi 46, 77, 90–95, 143, 151, 162, 168, 200, 240, 205, 308
 Thompson 301, 302
 Thornburn 315
 Timoshenko 115, 169
 Tokar 168, 169, 170
 Tomlinson 186
 Tong 200, 217, 222

Tortensson 307, 309
Tran-Vo-Nhiem 105
Tshebotarioff 168, 337, 338
Tsytovitch 85, 137

Valerio 210, 212
Van der Poel 352
Van der Veen 214, 216
Vanmarke 70
Varga 105-106
Velloso 216
Vesić 86, 88, 186, 190, 192, 199, 200,
208, 225, 252
Viberg 39, 45, 49, 51
Vidal 313
Vijavergija 186
Vogel 146
Voss 274

Wagener 304
Wager 305
Wan 309
Wang 341
Ward 337
Wardle 164
Warner 312
Weber 125
Weiffin 244
Weiss 101
Welch 209, 213, 221
Welsh 314
Westergraad 137-138, 237, 239
Windgate 163
Wiss 356
Withaker 197, 199
Withers 315
Wong 342
Woods 340
Woodward 186
Wright 31, 32
Wroth 167, 169, 170, 184, 195, 196, 197,
203

Zeevaert 146, 187
Zeller 356
Zhukov 173

Yagi 341
Yamanouchi 312, 348
Yoder 240, 259
Yoshimi 342, 348

Subject index

- Absorption coefficient** 330
adhesion factor for piles 186
Airy function 112
angular distortion 168
- strain 167
- velocity 322
artesian water 72, 73
- Bearing-capacity factor** 90
Benkelman road test 254
bituminous coating (for piles) 216
body force 41
- Californian Bearing Ratio (CBR)** 252-255, 257-259
central safety factor 68, 80
chimney drain 81
circular natural frequency 322
C-method 166
coefficient of secondary consolidation 146
- of the shaft pressure 186
- of volume compressibility 144
cold period 264
compaction methods 291
conical fill 12
- hallow 12
conventional safety factor 68
counterweight 56
cross-hole test 340
curvature radius 167
cylindrical cavity expansion 185
- Damping** 320
- factor 320
deflection ratio 167
depth factor 19, 20, 100
direction of the tilt 155
disturbing force 320
down-hole test 340
duration of the freezing season 264
dynamic bedding coefficient 335
- shear modulus 332
- stiffness 352
- Earthquake** 13, 37
eccentrically loaded footing 101, 102, 106, 107
effective base area 101
electro-osmotic coefficient 309
E-method 166
equation of compatibility 111, 112
equivalent ground surface 94
- single wheel load 232
eutectic point 281
- Fissured clay** 48
Frankfurt clay 143
freezing day 264
- period 264
- Freiberg-criterion** 272
frost day 264
- heave 272
- index 265
- intensity 264
- penetration 270
- General shear failure** 86, 90
geotextile 314
Gibson-type soil 208, 211
graded filter 71
- Heat deficiency** 264
hog 167
horizontal displacement 168
- Ice lense** 267
imperfect drain 74
inclination (obliquity) factor 100, 101
inclinometer 45
influence radius 185, 196
- Lime reactivity** 302
limiting tensil strain 169
line of thrust 27
local shear failure 87, 94
loess 49, 137, 158, 294
London clay 51, 143
lyotropic series 301
- Magnification factor** 324, 349
mass freezing 266
method of slices 21
micro-pile 313
microstructure 283
mixed filter 78
Monte Carlo method 69, 176
mosaic structure 48, 49, 51
multidirectional shaking 335
multiple filter 78
- Natural frequency** 322
neutral point 215
- Oedometer test** 147
- Partial coefficient of safety** 175
pF value 261
phase of compression 85
probability of failure 68, 69, 70
Proctor curve 278
punching shear failure 87
P-wave 338
- Quick clay** 49
- loading 143
- Radius of influence** 73
Rayleigh wave 339
- relative deflection (sag, hog)** 167
- pile compressibility ratio 185
- pile flexibility ratio 185
- plate stiffness 237
response curve 320
root pile 313
rotation 167
- Safety margin** 68, 69, 107
sag 167
seepage force 41
self-filtration 78
settlement coefficient 244
shape factor 98-100, 102
silos 143, 178
specific subsidence 158
spring constant 320, 322
stability number (factor) 18, 20, 40, 44
standard penetration test (method) 152, 177, 341, 345, 346
static cone penetrometer 222, 346
stiffness ratio (factor) 164, 165
stress concentration factor 118
- path 32, 145, 147, 148
subsidence 158, 159
substitutive thickness 136
surcharge ratio 305
SUS (Toyomenka) method 294
S-wave 338
Swedish method 17, 33
syneresis 311
- Terraprobe method** 294
terre armée 313
thaw index 265
theoretical slope 16
thermal conductivity 265
tilt 167
time factor (T) 156
Toyomenka (SUS) method 294
traffic index 234
transfer curve 187
trial ramming 220
- UBC machine** 343
unidirectional shaking 335
up-hole test 340
- Vibrocomposer method** 294
vibroflotation 294
Vibro-Wing method 294
volumetric heat 265
- Wheel load** 232

Contents of Volume 1

Soil Physics

Scope aims and methods of soil mechanics

The main problem of soil mechanics

Origin of soils. Soil properties

Origin and formation of soils
Physical properties of soils

Constituent parts of soils

The solid part
Unit weight of solid particles
Particle-size distribution of soils
Water and air in soil
Phase composition of soils
Consistency limits

Soil structure

Structure of gravels and sands
Properties of fine soil particles
Structure of cohesive soils
Organic constituents in soils
Harmful constituents in soils

Classification of soils

General considerations
Main soil types: their identification and nomenclature
Soil classification based on grain size
Soil classification based on consistency limits
Soil classification standards

Stresses in soils

Effective and neutral stresses
Stresses in soil: steady flow of water
Stresses in soils due to volume changes
:

Flow of water in soil

Flow of water through soil due to gravity
Two-dimensional potential flow
Capillary movement of water
Drainage of saturated soils by gravity
Movement of water in saturated soils due to electric current
Flow of water by heat action

Soil strength

General discussion
Calculation of stresses

Failure criteria
Physical causes of friction and cohesion
Measurement of shear strength
Shear strength of cohesionless soils
Shear strength of cohesive soils

Deformation of soils

Deformation during confined compression
Rheological properties of soils
Compression due to repeated loading
Sudden compression (structural collapse)

Earth pressure problems

Earth pressure at rest
Limit states of equilibrium in the half-space
Retaining wall problems
Pressure of cohesive soils
Passive earth pressure

Contents of Volume 2

Soil Testing

Soil exploration

Survey of soil exploration methods
Guidelines for preliminary investigations; geological studies
Soil exploration by direct methods
Sounding
The extent of soil exploration and subsoil testing

Laboratory investigations

Character and order of the examinations
Characteristics for soil classification and identification
Grain-size distribution
Determination of the Atterberg limits
Water movements in soils
Soil strength and deformation
Chemical tests

Investigation of groundwater

Exploration of groundwater conditions
Field determination of the coefficient of permeability

Investigation of the load-bearing capacity

Load test
Test piling
Pile loading test

Earthwork investigations

The importance of and role played by such investigations
Field determination of the phase composition and the water content, respectively
Determination of earthwork permeability
In situ pore-water pressure measurement
Earthwork strength characteristics

Contents of Volume 4

Application of Soil Mechanics in Practice; Examples and Case Histories

Introduction

Stability of earthworks (in general)

Settlement of embankments
Stability of embankments
Compaction of earthworks
Geotechnics of earthworks on railways

Stability of earthworks limited by water bodies

Seepage through a dam
Examination of a sudden drawdown effect
Internal erosion and piping
Examination of old dams made of cohesive soils
Soil investigation of a water reservoir
Investigation of a small-size dam
Stability of flood-protective dams
Protective layer above a plastic foil employed for protection
against seepage

Large dams, pumping sites and cuts produced by mining and industrial operations

Dumps made using dry technologies
Hydraulic fills
Geotechnical aspects of open cast mines

Landslides

Effects that initiate surface movement
Types of landslides
Stratum (translation) slides
Prevention and rehabilitation
Examples and case studies

Retaining walls

Types of retaining structures
Design of retaining walls
Damage to retaining walls
Reconstruction and reinforcement of retaining walls
Case studies

Foundations of buildings

Conclusions derived from failures
Foundations on swelling soils
Foundations on loess
Damage to non-structural elements
The effect of groundwater on deterioration of buildings
Case studies

Appendix

Examination of flocculant treated soils
Deterioration of a sewer under the load of the overburden